# Effect of Corrosion on the Flexural and Shear Responses of Reinforced Concrete Beams Subjected to Quasi-Static and Blast Loads

By

**Wesam Mustafa Jumaa Njeem**

Thesis submitted to the University of Ottawa

in partial fulfilment of the requirements for the degree of

**Doctor of Philosophy**

in Civil Engineering




Department of Civil Engineering

Faculty of Engineering

University of Ottawa

© Wesam Mustafa Jumaa Njeem, Ottawa, Canada, 2021

# Abstract

The aim of this research project is to investigate, experimentally and analytically, the effects of reinforcement corrosion on the flexural, shear and blast behaviours of reinforced concrete beams. As part of the experimental study, twenty-four beams reinforced were tested under quasi-static and simulated blast loads using the University of Ottawa Shock tube. All beams had dimensions of 125 mm x 250 mm x 2400 mm and were tested under four-point bending. Tension reinforcement consisted of either 2 – 10M ($\rho$= 1%) or 2 – 15M bars ($\rho$= 1.6%) for the flexure dominant specimens, and 2 – 25 M bars ($\rho$= 4%) for the shear-dominant specimens. In all cases, transverse reinforcement consisted of 6 mm stirrups spaced at s = 100 mm (d/2) throughout the beam span. Eighteen of the specimens were subjected to an accelerated corrosion process to induce different amount of mass loss in the longitudinal and transverse steel reinforcement. The test variables included: the type of corrosion (i.e. on the longitudinal or transverse reinforcement), the amount of corrosion (i.e. % mass loss in the steel reinforcement) and the extent / location of corrosion on the tension steel reinforcement (i.e. over the full length, middle span or end spans).

The results from the experimental tests showed that corrosion of the tension and transverse steel reinforcement decreased the strength and ductility of the reinforced concrete beams under static loading, ultimately changing the failure mode. Similarly, the results from the blast tests showed that corrosion of the longitudinal and transverse reinforcement affected maximum displacements and support rotations, reduced blast capacity, increased damage and fragmentation, and ultimately changed the failure process from ductile to brittle. Results under both static and blast loads were sensitive to the amount and extent/location of the corrosion.

As part of the analytical study, the static results were predicted using 2D finite nonlinear element (FE) modelling. The effects of corrosion were considered using several modeling features including: reduction in steel bar cross-sectional area, modification of the steel stress-strain response, and introducing corrosion-induced cracking using applied pre-strains. The predicted results from the FE simulations were to provide acceptable predictions in terms of load capacity and failure mode when compared to the experimental static test results.

The blast results were predicted using two approaches, including: 1) single-degree of freedom (SDOF) analysis (with the resistance functions developed using FE modelling); and 2) the blast

analysis capabilities of FE software VecTor2. Overall both approaches led to acceptable predictions of maximum mid-span displacements when compared to the experiments.

## Acknowledgements

First and foremost, I must thank GOD Almighty for giving me the strength and the opportunity to accomplish and complete this thesis.

I would like to express my deepest and sincere appreciation and gratitude to my supervisors Dr. Hassan Aoude, Dr. Beatriz Martin-Perez and Dr. Ahmad Jrade for their continued support and encouragement throughout my PhD study and also for their help, patience, motivation and guidance.

Also, I would like to express my appreciation to Dr. Muslim Majeed and Dr. Gamal Elnabelsya for their continuous help in the structural lab.

In addition, my deepest gratitude goes to my colleagues Roukaya Bastami, Charlemagne Charles, Hyunchul Jung, Jordan Gandia, Yang Li, co-op students for their help during the construction, testing and the analysis of my beams.

I would like also to give big thank to my mother, my father, my siblings, my wife and my daughter for giving me the strength to complete this thesis and for their support and encouragement during my study especially in the tough times, without them I could not achieve this.

# Notations

| Symbol | Definition |
|---|---|
| $\alpha_{pit}$ | Pitting factor |
| $\Delta A_{pit}$ | Area reduction due to pitting |
| $A_{bar}$ | Original cross-section area of bar |
| $\mathcal{E}_{sy}$ | Yield strain |
| $\mathcal{E}_{su}$ | Ultimate strain |
| $\alpha_{pit}^{max}$ | Sever reduction percentage |
| $\lambda$ | Ultimate strain in corroded state |
| $\alpha_1$ | Regression coefficient |
| $A_{corr}$ | Section loss |
| $\lambda_0$ | Ultimate strain in un-corroded state |
| $f^*_c$ | Reduced compressive strength |
| K | Coefficient related to bar roughness and diameter |
| $\varepsilon_1$ | Average tensile strain in the cracked concrete |
| $\varepsilon_{co}$ | Strain at the peak compressive stress ($f_c$) |
| $\varepsilon_{corr}$ | Pre-strain |
| $d'$ | Expanded diameter |
| $d$ | Original diameter |
| $b_f$ | Increased width by corrosion |
| $b_0$ | Original width |
| $n_{bars}$ | Number of the bars in the top layer |
| $d_s(t)$ | Thickness of corrosion product form |
| $v_c$ | Poisson's ration of concrete |
| $f_t$ | Tensile strength of concrete |
| $E_{ef}$ | Effective elastic modulus of concrete ($a = (d_b + 2d_0)/2$) |
| $d_b$ | Diameter of reinforcement bars |
| $d_0$ | Thickness of the annular layer of concrete pores |
| $b$ | The outer radii of the thick wall cylinder ($b = S/2$) |

| | |
|---|---|
| $S$ | Rebar spacing |
| $\tau_{bu}$ | Ultimate bond strength of uncorroded and corroded reinforcing bars |
| $f'_c$ | Concrete compressive strength |
| $c$ | Concrete cover depth |
| $D$ | Diameter of steel bar |
| $E_c$ | Modulus of elasticity |
| $w_{ori}$ | Original weight of the steel bar |
| $w_{corr}$ | Weight of steel bar after corrosion |
| $d_{corr}$ | Diameter of corroded steel bar |
| $a$ | Value of 2 for uniform corrosion |
| $x(t)$ | The corrosion penetration depth |
| $A_{s(red)}$ | Reduction in steel bar area |
| $A_s$ | Original steel bar area |
| $A_{s(corr)}$ | Corroded steel bar area |
| $f_y$ and $f_u$ | Yield and ultimate stresses in the corroded state |
| $f_{y0}$ and $f_{u0}$ | Yield stress and ultimate stress in the un-corroded state |
| $\alpha_y$, $\alpha_u$ and $\alpha_1$ | Regression coefficients |
| $f_s$ | Steel stress |
| $f_y$ and $f_u$ | Yield and ultimate stresses |
| $\varepsilon_s$ | Steel strain |
| $\varepsilon_y$, $\varepsilon_{sh}$ and $\varepsilon_u$ | Yield, hardening and ultimate strains of steel reinforcement |
| $A_{s(exp)}$ | Total expanded area of corroded steel bar |
| $\mu$ | Ratio of steel-to-corrosion product density |
| $x$ | The penetration of corrosion |
| $d_{exp}$ | Expanded diameter of corroded steel bar |
| $\varepsilon$ | Corrosion-induced strain in the reinforcement |
| $\varepsilon_{avg}$ | Average of corrosion-induced strains for both legs of the stirrup |
| $\varepsilon_1$ | Corrosion-induced strain for the first leg of the stirrup |
| $\varepsilon_2$ | Corrosion-induced strain for the second leg of the stirrup |
| $b$ | Beam width |
| DIF | Dynamic increase factor |

| | |
|---|---|
| $\dot{\varepsilon}$ | Strain rate |
| $DIF_y$ | Dynamic increase factor at yield |
| $DIF_u$ | Dynamic increase factor at ultimate |
| $K_{LM}$ | Load-mass transformation factor |
| m | Mass of the system |
| $u(t)$ and ü(t) | Beam mid-span displacement and acceleration |
| R(u(t)) | Beam resistance function |
| APr(t) | Loading function |
| A | The impacted area of the LTD |
| Pr(t) | The idealized triangular pressure-time history |

# Table of Contents

**Abstract** ... **ii**
**Acknowledgements** ... **iv**
**Notations** ... **v**
**Table of Contents** ... **viii**
**List of Figures** ... **xiv**
**List of Tables** ... **xxvi**
**Chapter 1: Introduction** ... **1**
1.1 Introduction ... 1
1.2 Research Significance ... 2
1.3 Thesis Objectives and Scope ... 3
1.3.1 Objectives ... 3
1.3.2 Scope ... 3
1.4 Thesis Organization ... 4
**Chapter 2: Literature Review** ... **6**
2.1 Chapter Overview ... 6
2.2 Mechanism of Corrosion in Reinforced Concrete Beams ... 6
2.3 Previous Studies on the Static Behaviour of Corroded Reinforced Beams Tested Statically ... 8
2.3.1 Flexural Behaviour ... 8
2.3.2 Shear Behaviour ... 21
2.3.3 General Guidelines for Modeling Corrosion in RC Beams ... 31
2.3.4 Previous Studies of Corrosion Modeling in RC Beams ... 34
2.4 Previous Studies on the Behaviour of Corroded Reinforced Concrete Beams Tested under Impact Test and Blast Loading ... 43
2.4.1 Impact Test ... 43
2.4.2 Blast Loading ... 45
2.5 Research Gap ... 47
**Chapter 3: Experimental Program** ... **48**
3.1 Chapter Overview ... 48
3.2 Beams Geometry ... 48
3.2.1 10M Group ... 52

3.2.2 15M Group ..... 52
3.2.3 25M Group ..... 52
3.3 Materials ..... 53
3.3.1 Concrete Mix ..... 53
3.3.2 Steel Reinforcement Bars ..... 54
3.4 Construction Procedure ..... 57
3.4.1 Preparation ..... 57
3.4.2 Mixing and Curing ..... 62
3.4.3 Concrete Properties at Fresh State ..... 62
3.4.4 Concrete Properties at Hardened State ..... 64
3.5 Corrosion Acceleration Process ..... 66
3.6 Experimental Tests Setup ..... 69
3.6.1 Static Loading Test ..... 69
3.6.2 Blast Loading Test (Dynamic) ..... 70
3.6.2.1 Shock Tube ..... 70
3.6.2.2 Lateral Load Transfer Device ..... 73
3.6.2.3 Supports ..... 74
3.6.2.4 Data Acquisition System ..... 75
3.6.2.5 Pressure Sensors ..... 75
3.6.2.6 Strain Gauges ..... 75
3.6.2.7 Linear Variable Displacement Transducer (LVDT) ..... 75
3.6.2.8 High-Speed Video Cameras ..... 75
3.6.2.9 Testing Procedure ..... 76
3.7 Mass Loss Measurement ..... 78
**Chapter 4: Experimental Results: Details Results from the Static Tests ..... 80**
4.1 Introduction ..... 80
4.2 Summary of Results ..... 81
4.3 Detailed Experimental Results ..... 84
4.3.1 10M Group ..... 84
4.3.1.1 10M: Control (0% mass loss) (CB-10M-0%) ..... 84
4.3.1.2 10M: Mid-span corrosion – 13% mass loss (B-MC-10M-13%) ..... 87
4.3.1.3 10M: Mid-span corrosion – 14% mass loss (B-MC-10M-14%) ..... 91

4.3.1.4 10M: End/Side corrosion – 11% mass loss (B-SC-10M-11%) ..... 96
4.3.1.5 10M: Full length Corrosion - 13% mass loss (B-FC-10M-13%) ..... 100
4.3.2 15M group ..... 104
4.3.2.1 15M: Control (0% mass loss) (CB-15M-0%) ..... 104
4.3.2.2 15M: Mid-span corrosion – 10% mass loss (B-MC-15M-10%) ..... 107
4.3.3 25M Group ..... 111
4.3.3.1 25M: Control – 0% mass loss (CB-25M-0%) ..... 111
4.3.3.2 25M: Shear corrosion – 10% mass loss (B-SHC-25M-10%) ..... 114
4.3.3.3 25M: Shear corrosion – 12% mass loss (B-SHC-25M-12%) ..... 118
**Chapter 5: Discussion of Static Results ..... 123**
5.1 Chapter Overview ..... 123
5.2 Effects of mid-span corrosion ..... 124
5.2.1 10M group: CB-10M-0% vs B-MC-10M-14% and B-MC-10M-13% ..... 124
5.2.2 15M group: CB-15M-0% vs B-MC-15M-10% ..... 127
5.3 Effects of corrosion in the end span region ..... 130
5.3.1 10M group: CB-10M-0% vs B-SC-10M-11% ..... 130
5.4 Effects of corrosion over the full span ..... 133
5.4.1 10M group: CB-10M-0% vs B-FC-10M-13% ..... 133
5.5 Effect of corrosion location (mid, end and full span corrosion) ..... 136
5.5.1 10M group: B-MC-10M-14% vs B-SC-10M-11% vs B-FC-10M-13% ..... 136
5.6 Effects of corrosion in the shear reinforcement ..... 139
5.6.1 25M group: CB-25M-0% vs B-SHC-25M-12% and B-SHC-25M-10% ..... 139
**Chapter 6: Dynamic Experimental Results ..... 142**
6.1 Chapter Overview ..... 142
6.2 Summary of the Results ..... 142
6.3 Detailed Experimental Results ..... 146
6.3.1 10M Group ..... 146
6.3.1.1 10M: Control (0% mass loss) (CB-10M-0%) ..... 146
6.3.1.2 10M: Mid-span corrosion-11% mass loss (B-MC-10M-11%) ..... 151
6.3.1.3 10M: Mid-span corrosion-15% mass loss (B-MC-10M-15%) ..... 156
6.3.1.4 10M: Full length corrosion-12% mass loss (B-FC-10M-12%) ..... 161
6.3.1.5 10M: End/side corrosion-7% mass loss (B-SC-10M-7%) ..... 166

6.3.1.6 10M: Mid-span corrosion- 22% extreme mass loss (B-EMC-10M-22%)..... 171
6.3.1.7 10M: cover-removal with mid-span corrosion – 5% mass loss (B-CR-MC-10M-5%)..... 175
6.3.2 15M Group..... 178
6.3.2.1 15M: Control (0% mass loss) (CB-15M-0%)..... 178
6.3.2.2 15M: Mid-span corrosion – 12% mass loss (B-MC-15M-12%) ..... 183
6.3.2.3 15M: Mid-span corrosion – 17% extreme mass loss (B-EMC-15M-17%) ..... 188
6.3.2.4 15M: Cover-removal with mid-span corrosion - 4% mass loss (B-CR-MC-15M-4%)..... 192
6.3.3 25M Group..... 195
6.3.3.1 25M: Control (0% mass loss) (CB-25M-0%)..... 195
6.3.3.2 25M: shear corrosion – 11% mass loss (B-SHC-25M-11%)..... 199
6.3.3.3 25M: shear corrosion – 12% mass loss (B-SHC-25M-12%)..... 203
**Chapter 7: Discussion of Blast Results..... 207**
7.1 Chapter Overview..... 207
7.2 Effect of mid-span corrosion..... 208
7.2.1 10M group: CB-10M-0% vs B-MC-10M-11% vs B-MC-10M-15% vs B-EMC-10M-22%..... 208
7.2.2 15M group: CB-15M-0% vs B-MC-15M-12% vs B-EMC-15M-17%..... 213
7.3 Effect of end-span corrosion..... 217
7.3.1 10M group: CB-10M-0% vs B-SC-10M-7%..... 217
7.4 Effect of full-span corrosion..... 220
7.4.1 10M group: CB-10M-0% vs B-FC-10M-12%..... 220
7.5 Effect of corrosion location (mid, end and full span)..... 223
7.5.1 10M group: B-MC-10M-11% vs B-SC-10M-7% vs B-FC-10M-12%..... 223
7.6 Effect of cover-removal with mid-span corrosion..... 226
7.6.1 10M group: CB-10M-0% vs B-CR-MC-10M-5%..... 226
7.6.2 15M group: CB-15M-0% vs B-CR-MC-15M-4%..... 229
7.7 Effect of shear-span corrosion..... 232
7.7.1 25M group: CB-25M-0% vs B-SHC-25M-11% vs B-SHC-25M-12%..... 232
7.8 Effects of corrosion on residual static capacity..... 235
7.8.1 CB-10M-0% vs B-SC-10M-7%..... 235
7.8.2 CB-10M-0% vs B-FC-10M-12%..... 238

7.9 Static vs Dynamic resistance ..... 240
**Chapter 8: Finite Element Analysis of Corrosion-Damaged Beams Under Static Loading ..... 242**
8.1 Chapter Overview ..... 242
8.2 Numerical Methodology ..... 242
8.2.1 Reduction of steel bar area ..... 246
8.2.2 Modified and unmodified stress-strain of corroded and un-corroded steel bars ..... 247
8.2.3 Corrosion-induced cracking ..... 250
8.3 Mesh Size Sensitivity ..... 253
8.4 Crack width sensitivity ..... 256
8.5 Sensitivity of different corrosion modeling features on the FE model results ..... 257
8.6 Numerical Results ..... 258
8.6.1 Flexure-governed beams ..... 258
8.6.1.1 Control Beams (0% mass loss): CB-10M-0% and CB-15M-0% ..... 258
8.6.1.2 Mid corrosion: B-MC-10M-13%, B-MC-10M-14% and B-MC-15M-10% ..... 263
8.6.1.3 Corrosion at the ends (B-SC-10M-11%) ..... 271
8.6.1.4 Full corrosion (B-FC-10M-13%) ..... 274
8.6.2 Shear-governed beams ..... 277
8.6.2.1 Control shear beam (CB-25M-0%) ..... 277
8.6.2.2 Shear corrosion beams (B-SHC-25M-10%) and (B-SHC-25M-12%) ..... 280
**Chapter 9: SDOF Analysis of Corrosion-Damaged Beams under Blast Loading ..... 285**
9.1 Chapter Overview ..... 285
9.2 Procedure of SDOF Analysis Approach ..... 285
9.3 Corrosion inducing-cracking ..... 287
9.4 SDOF approach results ..... 288
9.4.1 Flexure-governed beams ..... 288
9.4.1.1 Control beams (0% mass loss): CB-10M-0% and CB-15M-0% ..... 288
9.4.1.2 Specimens undergoing corrosion at mid-span ..... 293
9.4.1.3 Specimen undergoing corrosion at end supports ..... 305
9.4.1.4 Specimen undergoing corrosion along the entire span ..... 308
9.4.2 Shear-governed beams ..... 310
9.4.2.1 Control shear beam CB-25M-% ..... 310
9.4.2.2 Shear corrosion beams: B-SHC-25M-11% and B-SHC-25M-12% ..... 312

**Chapter 10: Finite Element Analysis of Corrosion-Damaged Beams Under Blast-Loading ..... 315**
10.1 Chapter Overview ..... 315
10.2 Modelling Methodology ..... 315
10.2.1 Corrosion inducing-cracking ..... 316
10.3 Mesh size sensitivity ..... 317
10.4 Dynamic increase factor (DIF) sensitivity ..... 321
10.5 Damping ratio sensitivity ..... 324
10.6 Numerical results for all beams ..... 328
10.6.1 Flexure-governed beams ..... 328
10.6.1.1 Control beams (0% mass loss): CB-10M-0% and CB-15M-0% ..... 328
10.6.1.2 Specimens subjected to corrosion at mid-span ..... 334
10.6.1.3 Specimen subjected to corrosion at the ends ..... 353
10.6.1.4 Specimen subjected to full corrosion ..... 359
10.6.2 Shear-governed beams ..... 362
10.6.2.1 Control shear beam CB-25M-0% ..... 362
10.6.2.2 Corroded shear-governed beams ..... 366
**Chapter 11: Conclusions and Recommendations ..... 369**
11.1 Conclusions ..... 369
11.2 Limitations ..... 372
11.3 Recommendations for future work ..... 372
**References ..... 374**

# List of Figures

Figure 2-1 Corrosion effects in RC flexural members (Reproduced from Soltani et al., 2019)..... 6
Figure 2-2 Corrosion Mechanism (Reproduced from Hansson et al., 2012)..... 7
Figure 2-3 Beam dimensions and results from Al-Sulaimani et al. (1990) ..... 8
Figure 2-4 Beam dimensions from Rodriguez et al. (1997) ..... 9
Figure 2-5 Beam dimensions and results from Mangat and Elgarf (1999)..... 10
Figure 2-6 Beam dimensions and results from Castel et al. (2000)..... 11
Figure 2-7 Beam dimensions and results from El-Maaddawy et al. (2005) ..... 12
Figure 2-8 Beam dimensions and results from Azad et al. (2007) ..... 13
Figure 2-9 Beam dimensions and results from Torres-Acosta et al. (2007)..... 13
Figure 2-10 Beam dimensions and results from Oyado et al. (2011) ..... 14
Figure 2-11 Beam dimensions and results from Xia et al. (2012)..... 15
Figure 2-12 Beam dimensions and results from Zhu et al. (2013) ..... 16
Figure 2-13 Beam dimensions and results from Liu et al. (2016) ..... 17
Figure 2-14 Beam dimensions and results from Dong et al. (2017)..... 18
Figure 2-15 Beam dimensions from Lu et al. (2018)..... 18
Figure 2-16 Beam dimensions and results from Higgins and Farrow (2006) ..... 21
Figure 2-17 Beam dimensions and results from Juarez et al. (2011)..... 22
Figure 2-18 Beam dimensions and results from Wang et al. (2011) ..... 23
Figure 2-19 Beam dimensions and results from Khan et al. (2014) ..... 24
Figure 2-20 Beam dimensions and results from Lachemi et al. (2014)..... 25
Figure 2-21 Beam dimensions and results from Xue et al. (2014) ..... 26
Figure 2-22 Beam dimensions and results from Wang et al. (2015) ..... 27
Figure 2-23 Beam dimensions and results from El-sayed et al. (2016)..... 28
Figure 2-24 Beam dimensions and results from Imam and Azad. (2016)..... 28
Figure 2-25 Beam dimensions and results from Zhang et al. (2019)..... 29
Figure 2-26 Finite element mesh and results from Coronelli and Gambarova (2004) ..... 33
Figure 2-27 Corrosion modelling and results from Dekoster et al. (2003)..... 35
Figure 2-28 Beam dimensions and results from Francois et al. (2006)..... 36
Figure 2-29 Beam dimensions and results from Kallias and Rafiq (2010)..... 37
Figure 2-30 Beam dimensions and results from Sanchez et al., (2010) ..... 39

Figure 2-31 Beam dimensions and results from Bernard (2013) ..... 41
Figure 2-32 Beam dimensions and results from Dai et al. (2016) ..... 44
Figure 2-33 Beam dimensions and results from Tamai et al. (2020) ..... 45
Figure 3-1 The geometry of the beams with reinforcement details ..... 50
Figure 3-2 GALDABINI SUN 60 Universal Floor Standing Testing Machine, Ottawa University ..... 54
Figure 3-3 Stress-strain curves for each steel bar ..... 56
Figure 3-4 Formwork of the beams ..... 58
Figure 3-5 Forming steel cages ..... 59
Figure 3-6 U-shaped stirrups ..... 59
Figure 3-7 Steel cages of the beams ..... 60
Figure 3-8 Strain gauges application steps ..... 61
Figure 3-9 Placing electrical wires at different locations on the beams ..... 61
Figure 3-10 Concrete mixer ..... 62
Figure 3-11 Sample of slump test ..... 64
Figure 3-12 Cylinder compressive testing machine ..... 64
Figure 3-13 Stress-strain curve for concrete ..... 66
Figure 3-14 Concrete cylinder after testing ..... 66
Figure 3-15 Beams inside the tank ..... 67
Figure 3-16 Corrosion setup components ..... 67
Figure 3-17 Typical beam after corrosion process ..... 67
Figure 3-18 Static load test setup ..... 69
Figure 3-19 Shock-tube ..... 71
Figure 3-20 Typical beam with blast test setup ..... 72
Figure 3-21 Isotropic view of lateral load transfer device (reproduced from Bastami, 2019) ..... 73
Figure 3-22 Support details (reproduced from Bastami, 2019) ..... 74
Figure 3-23 Camera validation ..... 76
Figure 3-24 Typical blast shots for each group of beams ..... 77
Figure 3-25 Breaking the beams ..... 79
Figure 3-26 Corroded steel bar before cleaning ..... 79
Figure 3-27 Tools and materials for steel bar cleaning ..... 79

Figure 3-28 Cleaning process ..... 79
Figure 3-29 Corroded steel bar after cleaning ..... 79
Figure 4-1 Key static test load-deflection parameters ..... 81
Figure 4-2 Experimental results for all beams in the 10M, 15M and 25M groups..... 82
Figure 4-3 Experimental results: Load-displacement response (CB-10M-0%) ..... 85
Figure 4-4 Experimental results: strains and crack widths (CB-10M-0%)..... 85
Figure 4-5 Main events during testing (CB-10M-0%) ..... 86
Figure 4-6 Mass loss distribution along the middle length of the tensile bars (B-MC-10M-13%) ..... 88
Figure 4-7 Cracking in the beam before testing (B-MC-10M-13%) ..... 88
Figure 4-8 Experimental results: load-displacement response (B-FC-10M-13%) ..... 89
Figure 4-9 Experimental results: crack widths (B-MC-10M-13%)..... 89
Figure 4-10 Main events during testing (B-MC-10M-13%)..... 90
Figure 4-11 Mass loss distribution along the middle length of the tensile bars (B-MC-10M-14%) ..... 92
Figure 4-12 Cracking in the beam before testing: B-MC-10M-14%..... 92
Figure 4-13 Experimental results: load-displacement response (B-MC-10M-14%)..... 93
Figure 4-14 Experimental results: crack widths (B-MC-10M-14%)..... 93
Figure 4-15 Main events during testing (B-MC-10M-14%)..... 94
Figure 4-16 Bar rupture and concrete damage at the end of testing (B-MC-10M-14%)..... 95
Figure 4-17 Mass loss distribution along the ends length of the tensile bars (B-SC-10M-11%) . 97
Figure 4-18 Cracking in the beam before testing (B-SC-10M-11%) ..... 97
Figure 4-19 Experimental results: load-displacement response (B-SC-10M-11%) ..... 98
Figure 4-20 Experimental results: crack widths (B-SC-10M-11%) ..... 98
Figure 4-21 Main events during testing (B-SC-10M-11%)..... 99
Figure 4-22 Mass loss distribution along the entire length of the tensile bars (B-FC-10M-13%) ..... 101
Figure 4-23 Cracking in the beam before testing (B-FC-10M-13%) ..... 101
Figure 4-24 Experimental results: load-displacement response (B-FC-10M-13%) ..... 102
Figure 4-25 Experimental results: crack widths (B-FC-10M-13%) ..... 102
Figure 4-26 Main events during testing (B-FC-10M-13%)..... 103

Figure 4-27 Beam collapse with severe spalling and bar rupture (B-FC-10M-13%)..... 103
Figure 4-28 Experimental results: load-displacement response (CB-15M-0%)..... 105
Figure 4-29 Experimental results: strains and crack widths (CB-15M-0%)..... 105
Figure 4-30 Main events during testing (CB-15M-0%) ..... 106
Figure 4-31 Mass loss distribution along the middle length of the tensile bars (B-MC-15M-10%) ..... 108
Figure 4-32 Cracking patterns of the beam before testing (B-MC-15M-10%) ..... 108
Figure 4-33 Experimental results: load-displacement response (B-MC-15M-10%)..... 109
Figure 4-34 Experimental results: strains and crack widths (B-MC-15M-10%)..... 109
Figure 4-35 The main events through loading stages (B-MC-15M-10%)..... 110
Figure 4-36 Severe buckling and spalling (B-MC-15M-10%)..... 110
Figure 4-37 Experimental results: load-displacement response (CB-25M-0%)..... 112
Figure 4-38 Experimental results: crack widths (CB-25M-0%)..... 112
Figure 4-39 The main events during testing (CB-25M-0%)..... 113
Figure 4-40 Buckling of top bars in shear span region (CB-25M-0%) ..... 113
Figure 4-41 Mass loss distribution along the stirrups in shear span (B-SHC-25M-10%)..... 115
Figure 4-42 Cracking in the beam before testing (B-SHC-25M-10%)..... 115
Figure 4-43 Experimental results: load-displacement response (B-SHC-25M-10%) ..... 116
Figure 4-44 Experimental results: strains and crack widths (B-SHC-25M-10%) ..... 116
Figure 4-45 Main events during testing (B-SHC-25M-10%)..... 117
Figure 4-46 Buckling of the longitudinal bars and loss of side cover (B-SHC-25M-10%) ..... 117
Figure 4-47 Mass loss distribution along the stirrups in shear span (B-SHC-25M-12%)..... 119
Figure 4-48 Corrosion-induced cracking in the beam before testing (B-SHC-25M-12%) ..... 119
Figure 4-49 Experimental results: load-displacement response (B-SHC-25M-10%) ..... 120
Figure 4-50 Experimental results: strains and crack widths (B-SHC-25M-12%) ..... 120
Figure 4-51 Main events during testing (B-SHC-25M-12%)..... 121
Figure 4-52 Rupture of stirrups and severe concrete damage (B-SHC-25M-12%)..... 122
Figure 5-1 Load-deflection comparison: effect of mid-span corrosion (10M group) ..... 125
Figure 5-2 Failure mode comparison: effect of mid-span corrosion (10M group)..... 125
Figure 5-3 Comparison of key results: effect of mid-span corrosion (10M group)..... 126
Figure 5-4 Load-deflection comparison: effect of mid-span corrosion (15M group) ..... 127

Figure 5-5 Failure mode comparison: effect of mid-span corrosion (15M group)..... 128
Figure 5-6 Comparison of key results: effect of mid-span corrosion (15M group)..... 129
Figure 5-7 Load-deflection comparison: effect of end-span corrosion (10M group)..... 131
Figure 5-8 Failure mode comparison: effect of end-span corrosion (10M group) ..... 131
Figure 5-9 Test results comparison: effect of end-span corrosion (10M group) ..... 132
Figure 5-10 Load-deflection comparison: effect of full-span corrosion (10M group) ..... 134
Figure 5-11 Failure mode comparison: effect of full-span corrosion (10M group) ..... 134
Figure 5-12 Test results comparison: effect of full-span corrosion (10M group) ..... 135
Figure 5-13 Load-deflection comparison: effect of corrosion location (10M group) ..... 137
Figure 5-14 Failure mode comparison: effect of corrosion location (10M group)..... 137
Figure 5-15 Test results comparison: 10M group (effect of corrosion location)..... 138
Figure 5-16 Load-deflection comparison: effect of corrosion in stirrups (25M group) ..... 140
Figure 5-17 Failure mode comparison: effect of corrosion in stirrups (25M group)..... 140
Figure 5-18 Test results comparison: 25M group (effect of corrosion mass loss in stirrups) .... 141
Figure 6-1 Photos of the beams at the end of blast testing ..... 145
Figure 6-2 Reflected pressure, impulse and mid-span displacement histories (CB-10M-0%)... 147
Figure 6-3 Beam damage after the blast shots (CB-10M-0%) ..... 148
Figure 6-4 Blast load resistance and strain time history curves (CB-10M-0%)..... 149
Figure 6-5 Residual test results (CB-10M-0%) ..... 150
Figure 6-6 Mass loss distribution along the middle length of the tensile bars (B-MC-10M-11%) ..... 152
Figure 6-7 Cracking in the beam before testing (B-MC-10M-11%)..... 152
Figure 6-8 Reflected pressure, impulse and mid-span displacement histories (B-MC-10M-11%) ..... 153
Figure 6-9 Beam damage after testing (B-MC-10M-11%)..... 154
Figure 6-10 Blast load resistance curves (B-MC-10M-11%)..... 155
Figure 6-11 Mass loss distribution along the middle length of the tensile bars (B-MC-10M-15%) ..... 157
Figure 6-12 Beam cracking before testing (B-MC-10M-15%) ..... 157
Figure 6-13 Reflected pressure, impulse and mid-span histories (B-MC-10M-15%)..... 158
Figure 6-14 Beam damage after testing (B-MC-10M-15%)..... 159

Figure 6-15 Blast load resistance and strain time history curves (B-MC-10M-15%) ..... 160
Figure 6-16 Mass loss distribution along the entire length of the tensile bars (B-FC-10M-12%) ..... 162
Figure 6-17 Beam cracks before testing (B-FC-10M-12%) ..... 162
Figure 6-18 Reflected pressure, impulse and mid-span displacement histories (B-FC-10M-12%) ..... 163
Figure 6-19 Beam damage after testing (B-FC-10M-12%) ..... 164
Figure 6-20 Residual test results (B-FC-10M-12%) ..... 165
Figure 6-21 Mass loss distribution along the ends length of the tensile bars (B-SC-10M-7%) . 167
Figure 6-22 Cracking in the beam before testing (B-SC-10M-7%) ..... 167
Figure 6-23 Reflected pressure, impulse and mid-span displacement histories (B-SC-10M-7%) ..... 168
Figure 6-24 Beam damage after testing (B-SC-10M-7%) ..... 169
Figure 6-25 Residual test results (B-SC-10M-7%) ..... 170
Figure 6-26 Mass loss distribution along the middle length of the tensile bars (B-EMC-10M-22%) ..... 172
Figure 6-27 Corrosion-induced cracking in the beam before testing (B-EMC-10M-22%) ..... 172
Figure 6-28 Reflected pressure, impulse and mid-span displacement histories (B-EMC-10M-22%) ..... 172
Figure 6-29 Beam damage after testing (B-EMC-10M-22%) ..... 173
Figure 6-30 Strain time history in the tension 10M bars (B-EMC-10M-22%) ..... 174
Figure 6-31 Mass loss distribution along the middle length of the tensile bars (B-CR-MC-10M-5%) ..... 176
Figure 6-32 The condition of the beam before testing (B-CR-MC-10M-5%) ..... 176
Figure 6-33 Reflected pressure, impulse and mid-span displacement histories (B-CR-MC-10M-5%) ..... 176
Figure 6-34 Beam damage after testing (B-CR-MC-10M-5%) ..... 177
Figure 6-35 Reflected pressure, impulse and mid-span displacement histories (CB-15M-0%). 179
Figure 6-36 The beam damage after testing (CB-15M-0%) ..... 180
Figure 6-37 Blast load resistance and strain time history curves (CB-15M-0%) ..... 181
Figure 6-38 Residual test results (CB-15M-0%) ..... 182

Figure 6-39 Mass loss distribution along the middle length of the tensile bars (B-MC-15M-12%) ..... 184
Figure 6-40 The condition of the beam before testing (B-MC-15M-12%) ..... 184
Figure 6-41 Reflected pressure, impulse and mid-span displacement histories (B-MC-15M-12%) ..... 185
Figure 6-42 Photos of the beam damage after testing (B-MC-15M-12%) ..... 186
Figure 6-43 Blast load resistance curve and strain time history curves (B-MC-15M-12%) ..... 187
Figure 6-44 Mass loss distribution along the middle length of the tensile bars (B-EMC-15M-17%) ..... 189
Figure 6-45 Condition of the beam before testing (B-EMC-15M-17%) ..... 189
Figure 6-46 Reflected pressure, impulse and mid-span displacement (B-EMC-15M-17%) ..... 189
Figure 6-47 The condition of the beam after testing (B-EMC-15M-17%) ..... 190
Figure 6-48 Strain time history curve (B-EMC-15M-17%) ..... 191
Figure 6-49 Mass loss distribution along the middle length of the tensile bars (B-CR-MC-15M-4%) ..... 193
Figure 6-50 The condition of the beam before testing (B-CR-MC-15M-4%) ..... 193
Figure 6-51 Reflected pressure, impulse and mid-span displacement histories (B-CR-MC-15M-4%) ..... 193
Figure 6-52 Beam damage after testing (B-CR-MC-15M-4%) ..... 194
Figure 6-53 Reflected pressure, impulse and mid-span displacement (CB-25M-0%) ..... 196
Figure 6-54 Blast load resistance and strain time history curves (CB-25M-0%) ..... 196
Figure 6-55 The condition of the beam after the blast test (CB-25M-0%) ..... 197
Figure 6-56 The residual test results (CB-25M-0%) ..... 198
Figure 6-57 Mass loss distribution along the stirrups in the shear span (B-SHC-25M-11%) ..... 200
Figure 6-58 The beam before testing (B-SHC-25M-11%) ..... 200
Figure 6-59 Reflected pressure, impulse and mid-span displacement (B-SHC-25M-11%) ..... 200
Figure 6-60 Damage in the beam after testing (B-SHC-25M-11%) ..... 201
Figure 6-61 Blast load resistance and strain time history curves (B-SHC-25M-11%) ..... 202
Figure 6-62 Mass loss distribution along the stirrups in the shear span (B-SHC-25M-12%) ..... 204
Figure 6-63 The condition of the beam before testing (B-SHC-25M-12%) ..... 204
Figure 6-64 Reflected pressure, impulse and mid-span displacement (B-SHC-25M-12%) ..... 204

Figure 6-65 The damage of the beam after the test (B-SHC-25M-12%) ..... 205
Figure 6-66 Blast load resistance and strain time history curves (B-SHC-25M-12%)..... 206
Figure 7-1 Displacements for blast 1-2: effect of mid-span corrosion (10M group)..... 210
Figure 7-2 Failure mode: effect of mid-span corrosion (10M group) ..... 211
Figure 7-3 Damage and fragmentation at failure: effect of mid-span corrosion (10M group)... 212
Figure 7-4 Displacements: effect of mid-span corrosion (15M group) ..... 214
Figure 7-5 Failure mode and damage: effect of mid-span corrosion (15M group) ..... 215
Figure 7-6 Fragmentation at failure: effect of mid-span corrosion (15M group) ..... 216
Figure 7-7 Displacements: effect of end-span corrosion with 7% mass loss (10M group)..... 218
Figure 7-8 Failure mode: effect of end-span corrosion with 7% mass loss (10M group) ..... 219
Figure 7-9 Dynamic reactions: effect of end-span corrosion with 7% mass loss (10M group) . 219
Figure 7-10 Displacements: effect of full span corrosion at 12% mass (10M group)..... 221
Figure 7-11 Failure mode: effect of full span corrosion at 12% mass loss (10M group)..... 222
Figure 7-12 Displacements: effect of corrosion locations in the 10M group ..... 224
Figure 7-13 Failure mode: effect of corrosion locations in the 10M group..... 225
Figure 7-14 Displacements: effect of corrosion and cover-removal in the mid-span (10M group) ..... 227
Figure 7-15 Failure mode: effect of corrosion and cover-removal in the mid-span (10M group) ..... 228
Figure 7-16 Displacements: effect of corrosion and cover-removal in the mid-span (15M group) ..... 230
Figure 7-17 Failure mode: effect of corrosion and cover-removed at mid-span (15M group ).. 231
Figure 7-18 Displacements: effect of shear corrosion in the 25M group ..... 233
Figure 7-19 Failure mode: effect of shear corrosion in the 25M group..... 234
Figure 7-20 Dynamic reactions: effect of shear corrosion in the 25M group..... 234
Figure 7-21 Residual test results: effect of end-span corrosion with 7% mass loss..... 236
Figure 7-22 Photos of the beams (CB-10M-0% and B-SC-10M-7%) before and after the residual test..... 237
Figure 7-23 Residual test results: effect of full-span corrosion at 12% mass loss ..... 238
Figure 7-24 Photos of the beams (CB-10M-0% and B-FC-10M-12%) before and after the residual test ..... 239

Figure 7-25 Comparison of static vs dynamic resistance ..... 241
Figure 8-1 Typical finite element meshes for 10M, 15M and 25M groups..... 244
Figure 8-2 Uniform corrosion..... 246
Figure 8-3 Stress-strain curves for un-corroded and corroded steel bars (10M, 15M and 6.3 mm) ..... 248
Figure 8-4 Defining steel reinforcement properties in VecTor2 ..... 249
Figure 8-5 Applying corrosion-induced strains on stirrups in RC beam (adapted from Bernard, 2013) ..... 251
Figure 8-6 Locations of applied equivalent pre-strains for various beam types..... 252
Figure 8-7 Mesh sizes considered in the analysis of beam CB-10-0% (flexure-dominant) ..... 254
Figure 8-8 Mesh size sensitivity in beam CB-10M-0%..... 255
Figure 8-9 Mesh sizes considered in the analysis of beam CB-25M-0% (shear-dominant) ..... 255
Figure 8-10 Experimental vs simulated load-deflection curves for beam CB-25M-0% ..... 256
Figure 8-11 Crack width sensitivity: results for beams CB-10M-0% and CB-25M-0%..... 257
Figure 8-12 Load-deflection curves: 10M and 15M controls..... 260
Figure 8-13 Failure mode and cracking patters (experimental vs simulation) ..... 260
Figure 8-14 Finite element results of beam (CB-10M-0%)..... 261
Figure 8-15 Finite element results of beam (CB-15M-0%)..... 262
Figure 8-16 Load-deflection responses for three beams with mid-corrosion ..... 266
Figure 8-17 Failure mode and crack patterns (experimental vs simulation) ..... 267
Figure 8-18 Finite elements results of (B-MC-10M-13%) (case 4) ..... 268
Figure 8-19 Finite element results of beam (B-MC-10M-14%) (case 4) ..... 269
Figure 8-20 Finite element results of beam (B-MC-15M-10%) (case 5) ..... 270
Figure 8-21 Load-deflection responses of B-SC-10M-11%..... 272
Figure 8-22 Experimental failure mode vs simulation of B-SC-10M-11% (case 4) ..... 272
Figure 8-23 Finite elements results of beam B-SC-10M-11% (case 4)..... 273
Figure 8-24 Load-deflection responses of beam B-FC-10M-13% ..... 275
Figure 8-25 Experimental failure mode vs simulation for beam B-FC-10M-13% (case 4) ..... 275
Figure 8-26 Finite element results of beam B-FC-10M-13% (case 4) ..... 276
Figure 8-27 Experimental and simulation load-deflection responses for CB-25M-0% ..... 278
Figure 8-28 Experimental failure mode vs simulation for beam CB-25M-0% ..... 278

Figure 8-29 Finite element results of beam CB-25M-0% ..... 279
Figure 8-30 Experimental and simulation responses of beams with corroded stirrups ..... 282
Figure 8-31 Failure mode comparison between experimental and simulation beams (case 4) .. 282
Figure 8-32 Finite element results of beam B-SHC-25M-10% (case 4) ..... 283
Figure 8-33 Finite element results of beam B-SHC-25M-12% (case 4) ..... 284
Figure 9-1 RCBlast software interface after analysis ..... 287
Figure 9-2 FE model ..... 290
Figure 9-3 Predicted (SDOF) vs experimental displacements (CB-10M-0%) ..... 291
Figure 9-4 Predicted (SDOF) vs experimental displacements (CB-15M-0%) ..... 292
Figure 9-5 FE models for beams undergoing corrosion at mid-span..... 297
Figure 9-6 Predicted (SDOF) vs experimental displacements (B-MC-10M-11%) ..... 298
Figure 9-7 Predicted (SDOF) vs experimental displacements (B-MC-10M-15%) ..... 299
Figure 9-8 Predicted (SDOF) vs experimental displacements (B-EMC-10M-22%)..... 300
Figure 9-9 Predicted (SDOF) vs experimental displacements (B-CR-MC-10M-5%)..... 301
Figure 9-10 Predicted (SDOF) vs experimental displacements (B-MC-15M-12%) ..... 302
Figure 9-11 Predicted (SDOF) vs experimental displacements (B-CR-MC-15M-4%)..... 303
Figure 9-12 Predicted (SDOF) vs experimental displacements (B-EMC-15M-17%)..... 304
Figure 9-13 FE model of beam undergoing corrosion at the ends..... 305
Figure 9-14 Predicted (SDOF) vs experimental displacements (B-SC-10M-7%)..... 307
Figure 9-15 FE model of beam undergoing corrosion along its entire length ..... 309
Figure 9-16 Predicted (SDOF) vs experimental displacements (B-FC-10M-12%)..... 309
Figure 9-17 FE model of CB-25M-0%..... 311
Figure 9-18 Predicted (SDOF) vs experimental displacements (CB-25M-0%) ..... 311
Figure 9-19 FE models of beams undergoing stirrup corrosion ..... 313
Figure 9-20 Predicted (DIF) vs experimental (B-SHC-25M-11%) ..... 313
Figure 9-21 Predicted (DIF) vs experimental (B-SHC-25M-12%) ..... 314
Figure 10-1 FE models and idealized blast pressure-time history..... 316
Figure 10-2 Mesh sizes considered in the analysis of the control beams ..... 318
Figure 10-3 Mesh size sensitivity: displacement-time histories..... 319
Figure 10-4 Mesh size sensitivity: average displacement ratios and comparison of displacements
..... 320

Figure 10-5 DIF sensitivity analysis: sample displacement-time histories ..... 322
Figure 10-6 DIF sensitivity: average displacement ratios and comparison of displacements .... 323
Figure 10-7 Damping ratio sensitivity for control beams: CB-10M-0% and CB-15M-0% ..... 326
Figure 10-8 Damping ratio sensitivity for corroded beams: B-MC-10M-11% and B-MC-15M-12% ..... 327
Figure 10-9 FE models of control beams..... 330
Figure 10-10 Idealized blast pressure-time history for beams CB-10M-0% and CB-15M-0% . 330
Figure 10-11 Predicted vs experimental results for beams CB-10M-0% and CB-15M-0% ..... 331
Figure 10-12 Predicted vs experimental reactions for beams CB-10M-0% and CB-15M-0% .. 332
Figure 10-13 Cracking patterns of FE model vs experimental for beam CB-10M-0%..... 333
Figure 10-14 Cracking patterns of FE model vs experimental for beam CB-15M-0%..... 333
Figure 10-15 FE models for specimens with mid-corrosion ..... 338
Figure 10-16 Idealized blast pressure-time history for beam B-MC-10M-11%..... 339
Figure 10-17 Predicted vs experimental results for beam B-MC-10M-11%..... 339
Figure 10-18 Predicted vs experimental dynamic reactions for beam B-MC-10M-11%..... 340
Figure 10-19 Cracking patterns of FE model vs experimental for beam B-MC-10M-11%..... 340
Figure 10-20 Idealized blast pressure-time history for beam B-MC-10M-15%..... 341
Figure 10-21 Predicted vs experimental results for beam B-MC-10M-15%..... 341
Figure 10-22 Predicted vs experimental reactions for beam B-MC-10M-15%..... 342
Figure 10-23 Cracking patterns of FE model vs experimental for beam B-MC-10M-15%..... 342
Figure 10-24 Idealized blast pressure-time history for beam B-EMC-10M-22% ..... 343
Figure 10-25 Predicted vs experimental results for beam B-EMC-10M-22% ..... 343
Figure 10-26 Predicted reactions for beam B-EMC-10M-22%..... 344
Figure 10-27 Cracking patterns of FE model vs experimental for beam B-EMC-10M-22% .... 344
Figure 10-28 Idealized blast pressure-time history for B-CR-MC-10M-5%..... 345
Figure 10-29 Predicted vs experimental results for beam B-CR-MC-10M-5% ..... 345
Figure 10-30 Predicted reactions for beam B-CR-MC-10M-5% ..... 346
Figure 10-31 Cracking patterns of FE model vs experimental for beam B-CR-MC-10M-5% .. 346
Figure 10-32 Idealized blast pressure-time history for beam B-MC-15M-12%..... 347
Figure 10-33 Predicted vs experimental results for beam B-MC-15M-12%..... 347
Figure 10-34 Predicted vs experimental reactions for beam B-MC-15M-12%..... 348

Figure 10-35 Cracking patterns of FE model vs experimental for beam B-MC-15M-12%..... 348
Figure 10-36 Idealized blast pressure-time history for beam B-CR-MC-15M-4%..... 349
Figure 10-37 Predicted vs experimental results for beam B-CR-MC-15M-4%..... 349
Figure 10-38 Predicted reactions for beam B-CR-MC-15M-4% ..... 350
Figure 10-39 Cracking patterns of FE model vs experimental for beam B-CR-MC-15M-4% .. 350
Figure 10-40 Idealized blast pressure-time history for beam B-EMC-15M-17%..... 351
Figure 10-41 Predicted vs experimental results for beam B-EMC-15M-17% ..... 351
Figure 10-42 Predicted reactions for beam B-EMC-15M-17%..... 352
Figure 10-43 Cracking patterns of FE model vs experimental for beam B-EMC-15M-17% .... 352
Figure 10-44 FE model of beam B-SC-10M-7%..... 354
Figure 10-45 Idealized blast pressure-time history for beam B-SC-10M-7%..... 355
Figure 10-46 Predicted vs experimental results for beam B-SC-10M-7%..... 356
Figure 10-47 Predicted vs experimental reactions for beam B-SC-10M-7%..... 357
Figure 10-48 FE model vs experimental cracking patterns for beam B-SC-10M-7% ..... 358
Figure 10-49 FE model of beam B-FC-10M-12%..... 360
Figure 10-50 Idealized blast pressure-time history for beam B-FC-10M-12%..... 360
Figure 10-51 Predicted vs experimental results for beam B-FC-10M-12%..... 360
Figure 10-52 Predicted reactions for beam B-FC-10M-12% ..... 361
Figure 10-53 Cracking patterns of beam B-FC-10M-12%..... 361
Figure 10-54 FE model for control beam CB-25M-0%..... 363
Figure 10-55 Idealized blast pressure time-history vs experimental for beam CB-25M-0%..... 364
Figure 10-56 Predicted vs experimental results for beam CB-25M-0%..... 364
Figure 10-57 Predicted vs experimental reactions for beam CB-25M-0%..... 365
Figure 10-58 Failure mode and cracking patterns for beam CB-25M-0%..... 365
Figure 10-59 FE models of corroded shear-governed beams..... 367
Figure 10-60 Idealized blast pressure time-history for corroded shear-governed beams..... 367
Figure 10-61 Predicted vs experimental results of corroded shear-governed beams ..... 368
Figure 10-62 Failure mode and cracking patterns of corroded shear-governed beams..... 368

# List of Tables

Table 2-1 Summary of the studies on flexural response: part one ..... 19
Table 2-2 Summary of the studies on flexural response: part two ..... 20
Table 2-3 Summary of the studies on shear response ..... 30
Table 2-4 Summary of the studies on corrosion modeling ..... 42
Table 3-1 Main properties of the beams ..... 51
Table 3-2 Concrete mix components ..... 53
Table 3-3 Physical and average mechanical properties of steel bars ..... 55
Table 3-4 Concrete properties at fresh state ..... 63
Table 3-5 Concrete compressive strength (cylinders) for each beam ..... 65
Table 3-6 Applied current and corrosion rates with duration of application ..... 68
Table 3-7 Blast shots properties ..... 78
Table 4-1 Key load-deflection results for all beams ..... 83
Table 4-2 : Key results: CB-10M-0% ..... 84
Table 4-3 : Key results: B-MC-10M-13% ..... 87
Table 4-4 : Key results: B-MC-10M-14% ..... 91
Table 4-5 : Key results: B-SC-10M-11% ..... 96
Table 4-6 : Key results: B-FC-10M-13% ..... 100
Table 4-7 : Key results: CB-15M-0% ..... 104
Table 4-8 : Key results: B-MC-15M-10% ..... 107
Table 4-9 : Key results: CB-25M-0% ..... 111
Table 4-10 : Key results: B-SHC-25M-10% ..... 114
Table 4-11 : Key results: B-SHC-25M-12% ..... 118
Table 6-1 Blast test results for all beams ..... 143
Table 6-2 CSA S850 damage levels (reproduced from the CSA S850 Standard) ..... 143
Table 6-3 Key blast test results: CB-10M-0% ..... 147
Table 6-4 Key results: B-MC-10M-11% ..... 152
Table 6-5 Key results (B-MC-10M-15%) ..... 157
Table 6-6 Key results (B-FC-10M-12%) ..... 162
Table 6-7 Key results (B-SC-10M-7%) ..... 167
Table 6-8 Key results (B-EMC-10M-22%) ..... 171

Table 6-9 Key results (B-CR-MC-10M-5%) ..... 175
Table 6-10 Key results (CB-15M-0%) ..... 179
Table 6-11 Key results (B-MC-15M-12%) ..... 184
Table 6-12 Key results (B-EMC-15M-17%) ..... 188
Table 6-13 Key results (B-CR-MC-15M-5%) ..... 192
Table 6-14 Key results (CB-25M-0%) ..... 196
Table 6-15 Key results (B-SHC-25M-11%) ..... 199
Table 6-16 Key results (B-SHC-25M-12%) ..... 203
Table 7-1 Key results: effect of mid-span corrosion and mass loss ..... 209
Table 7-2 Key results: effect of mid-span corrosion (15M group) ..... 214
Table 7-3 Key results: effect of end-span corrosion (10M group) ..... 218
Table 7-4 Key results: effect of full span corrosion at 12% mass loss (10M group) ..... 220
Table 7-5 Key results: effect of corrosion location in the 10M group ..... 224
Table 7-6 Key results: effect of corrosion and cover-removal in the mid-span ..... 226
Table 7-7 Key results: effect of corrosion and cover-removal in the mid-span (15M group) ..... 229
Table 7-8 Key results: effect of shear corrosion in the 25M group ..... 233
Table 8-1 Constitutive models used in FE analysis for 10M and 15M groups ..... 245
Table 8-2 Constitutive models used in FE analysis for 25M group ..... 245
Table 8-3 Equivalent pre-strains with corresponding mass loss ..... 253
Table 8-4 FE analysis cases considering different corrosion modelling features ..... 257
Table 8-5 Experimental and simulation results for CB-10M-0% and CB-15M-0% ..... 259
Table 8-6 Experimental and simulation results for beams with mid corrosion ..... 265
Table 8-7 Experimental and simulation results of beam B-SC-10M-11% ..... 271
Table 8-8 Experimental and simulation results of beam B-FC-10M-13% ..... 275
Table 8-9 Experimental and simulation results of beam CB-25M-0% ..... 278
Table 8-10 Summary of the experimental and simulation results of beams with corroded stirrups ..... 281
Table 9-1 Dynamic increase factors for reinforced concrete design (UFC-3-340-02, 2008) ..... 286
Table 9-2 Equivalent pre-strains with corresponding mass loss ..... 287
Table 9-3 Idealized blast properties and analysis results ..... 289
Table 9-4 Summary of analysis results for control beams ..... 290

Table 9-5 Idealized blast properties and analysis results ..... 296
Table 9-6 Summary of analysis results for beams with corrosion at mid-span ..... 296
Table 9-7 Idealized blast properties and results for beam B-SC-10M-7% ..... 306
Table 9-8 Idealized blast properties and results for beam B-FC-10M-12% ..... 308
Table 9-9 Idealized blast properties and results for control beam CB-25M-0% ..... 310
Table 9-10 Idealized blast properties and results for beams undergoing stirrup corrosion ..... 312
Table 10-1 Equivalent pre-strains with corresponding mass loss ..... 316
Table 10-2 Mesh sensitivity: data analysis ..... 318
Table 10-3 DIF sensitivity: data analysis ..... 322
Table 10-4 Damping ratio sensitivity: data analysis ..... 325
Table 10-5 Summary of the FE results for 10M/15M control beams ..... 329
Table 10-6 Summary of FE results for specimens subjected to mid-span corrosion ..... 337
Table 10-7 Summary of the FE and experimental results for beam B-SC-10M-7% ..... 354
Table 10-8 Summary of the FE results for beam B-FC-10M-12% ..... 359
Table 10-9 Summary of the FE results for beam CB-25M-0% ..... 363
Table 10-10 Summary of the FE results for corroded 25M beams ..... 366

# Chapter 1: Introduction

## 1.1 Introduction

Corrosion of steel reinforcement is considered one of the main deterioration mechanisms of reinforced concrete (RC) structures. In the presence of sufficient quantities of chloride ions and/or carbonation of the concrete cover, corrosion leads to damage of the protective passive film around the steel reinforcement. This corrosion process reduces the cross-sectional area of the longitudinal and transverse reinforcement, which can degrade the load-carrying capacity of RC members. In addition to the reduction of the steel cross-sectional area, the lower-density by-products of the corrosion process can exert an expansion on the surrounding concrete, eventually leading to cover cracking (Bicer et al., 2018). Likewise, corrosion leads to a deterioration of the bond between the steel bars and concrete, which can also influence the ultimate strength, deformation capacity and ductility of RC flexural members (Hou et al., 2019). The degradation of bond also reduces stiffness and increases deflections (Zhang et al., 2018). Thus, corrosion of steel reinforcement is a major problem which can affect the safety and service life of RC structures (Li et al., 2018).

As noted by Zhang et al. (2019), Soltani et al. (2019) and others, corrosion of steel reinforcement is the most influencing factor affecting the durability and maintenance of RC infrastructure, especially in marine and cold climate environments due to exposure to chlorides from seawater or de-icing salts, respectively. The problem of deterioration due to corrosion is especially problematic in North America. In the United States, the 2017 American Society of Civil Engineering (ASCE) Infrastructure Report Card gave grades of C+ and D+ when rating "overall" and "bridge" infrastructure, respectively (ASCE, 2017; Soltani et al., 2019). Deterioration is also a major problem that affects the safety and service life of Canada's RC infrastructure (Mirza, 2006). Indeed, failures such as the "de la Concorde" overpass collapse in Laval, QC, Canada in 2006 put into evidence the consequences of deterioration on the safety of concrete structures in Canada (Mitchel et al., 2011; Wood, 2008). Thus, it is of great importance to investigate the effects of corrosion on the structural behaviour of RC structures.

Nowadays, it becomes increasingly important to ensure that critical RC structures are blast-resistant due to the increased risks from malicious and accidental explosions. While previous blast research has primarily focussed on civilian and military buildings, critical bridges, transportation

assets and parking garages are also vulnerable to blast loads (Williamson et al., 2011). Since such structures can be affected by corrosion, there is a need for experimental and analytical research on the blast behaviour of corrosion-affected RC structures and components.

### 1.2 Research Significance

Over the years, extensive studies have focussed on the structural evaluation of corrosion-damaged RC structures. Soltani et al. (2019) presented a comprehensive review of 33 previous studies from 1955 to 2017, which examined the shear and flexural behaviour of RC beams. Among these studies the vast majority focussed on the behaviour of beams subjected to quasi-static conditions, with a few studies conducted under cyclic or reverse-cyclic loads. Conversely, research on the impact and blast response of corrosion-affected RC beams is very limited (indeed, a review of literature reveals a single experimental study, conducted on a limited number of beams, tested under impact loads). Thus there is an important need for experimental and numerical research on the blast behaviour of corrosion-damaged RC beams.

Corrosion can also affect the anchorage regions of the longitudinal tensile reinforcement in RC beams. However, a review of the literature indicates only limited studies have examined the flexure response of RC beams when the tensile reinforcement is corroded at different locations (mid length, full length and end lengths). Thus, there is also a need for further experimental and numerical research to better understand the influence of location of longitudinal reinforcement corrosion on the static and dynamic flexure behaviour of corrosion-damaged RC beams.

Finally, in addition to experimental research, there is a need to develop numerical approaches that can be used to predict the blast behaviour of corrosion-damaged RC structures, including the use of simplified tools commonly used in engineering practice (such as single-degree-of-freedom analysis), and more advanced finite-element modelling.

## 1.3 Thesis Objectives and Scope

### 1.3.1 Objectives

The main objective of this thesis is to gain a better understanding of the effects of reinforcement corrosion on the blast behaviour of RC structures, with the focus on flexural members. The thesis also aims at a better understanding of the effect of influential parameters such the extent and location of reinforcement corrosion on the static and blast response of RC beams. Furthermore, the thesis aims at demonstrating the ability of two-dimensional (2D) nonlinear finite element (FE) modelling to reliably predict the static and blast responses of corrosion-damaged RC beams.

### 1.3.2 Scope

The thesis scope includes experimental and analytical/numerical components. The experimental program includes twenty-four beams which are tested under quasi-static bending and simulated blast loads using the University of Ottawa Shock-tube.

The experimental research program includes the following aspects:

- Investigates the effect of longitudinal reinforcement corrosion on the flexural response of RC beams subjected to quasi-static and simulated blast loads;
- Investigates the effect of transverse reinforcement corrosion on the shear and flexural response of RC beams subjected to quasi-static and simulated blast loads;
- Examines the effect of influential parameters such as % of steel mass loss and corrosion location on the static and blast response of RC beams.

The numerical research program includes the following aspects:

- Investigates the ability of 2D nonlinear FE modelling to predict the shear and flexural response of corrosion-affected RC beams under static loading;
- Investigates the ability of Single Degree of Freedom (SDOF) analysis to predict the maximum displacement response of corrosion-affected RC beams under blast loading;
- Investigates the ability of 2D nonlinear FE modelling to predict the shear and flexural response of corrosion-affected RC beams under blast loading;

## 1.4 Thesis Organization

This thesis consists of eleven chapters which are listed as follows:

***Chapter 1: Introduction***

- Provides an introduction to the thesis topic, and clarifies the thesis objectives.

***Chapter 2: Literature Review***

- Presents background information on the mechanism of corrosion and summarizes previous studies, which have focused on the flexural, shear and impact / blast behaviours of corroded RC beams, and presents an overview of corrosion modeling in RC beams.

***Chapter 3: Experimental Program***

- Describes the experimental program of the thesis, which includes overview of the test matrix, details of the specimen design, material parameters, corrosion acceleration process, tests set ups and testing procedures.

***Chapter 4: Static Experimental Results***

- Presents detailed experimental results of ten beams, which were tested under quasi-static loading.

***Chapter 5: Discussion of Static Results***

- Discusses the effects of the test parameters on the static performance of the beams. The effects are examined by comparing the maximum strength, maximum displacement, stiffness, ductility, toughness, and failure mode of the beams.

***Chapter 6: Dynamic Experimental Results***

- Presents the experimental results of fourteen beams tested under blast loading using the shock-tube.

***Chapter 7: Discussion of Blast Results***

- Discusses the effects of the test parameters on the blast performance of the beams. The effects are examined by comparing the maximum and residual displacements, support rotations, blast capacities, failure modes, damage and fragmentation.

***Chapter 8: Finite Element Analysis of Corrosion-Damaged Beams under Static Loading***

- Presents the first phase of the numerical research program, which aims to predict the behaviour of the beams under static loading, and provides a comparison between the FE and the experimental results.

***Chapter 9: SDOF Analysis of Corrosion-Damaged Beams under Blast-Loading***

- Presents the second phase of the numerical research program, which aims to predict the blast response of the beams using single degree of freedom (SDOF) analysis, and provides a comparison between the experimental and analytical maximum displacements.

***Chapter 10: Finite Element Analysis of Corrosion-Damaged Beams under Blast Loading***

- Presents the last phase of the numerical research program, which aims to predict the full dynamic response of the tested beams under blast-loading using 2D FE modelling, and provides a comparison between the FE and the experimental results.

***Chapter 11: Conclusions and Recommendations***

- Summarizes the conclusions from the experimental and numerical research programs, and provides recommendations for future research.

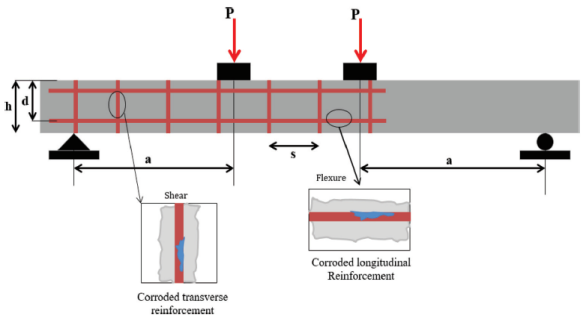
# Chapter 2: Literature Review

## 2.1 Chapter Overview

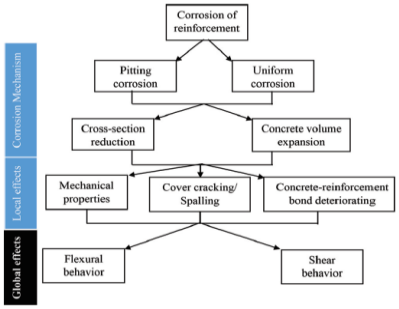
Corrosion of steel reinforcement is one of the most significant deterioration mechanisms in reinforced concrete structures. The focus of this chapter is to provide a comprehensive review of previous studies on the impact of corroded steel reinforcement on the structural behaviour of reinforced concrete beams under static-four-point bending and blast loadings, including both flexural and shear governed responses.

## 2.2 Mechanism of Corrosion in Reinforced Concrete Beams

As shown in **Figure 2-1 (a)**, corrosion in reinforced concrete flexural members leads to a reduction in the cross-sectional area of the longitudinal and transverse steel bars and reduces the bond between the steel reinforcement and surrounding concrete. In addition to the negative influence on flexural and shear capacity, these mechanisms affect ductility, reduce maximum displacements and lead to bond and anchorage failures, as (illustrated in **Figure 2-1 (b)**) Soltani et al., (2019). The corrosion process also leads to the formation of corrosion by-products, which leads to extra expansion on the surrounding concrete, resulting in cracking and spalling of the concrete cover.




a) Corrosion of the longitudinal and transverse reinforcement in RC beams




b) Effects of corrosion on load-carrying capacity and stiffness of concrete beams

Figure 2-1 Corrosion effects in RC flexural members (Reproduced from Soltani et al., 2019)

The corrosion process in reinforced concrete structures is an electrochemical process involving reactions at anodic and cathodic half-cells at the microscopic and/or macroscopic levels. The

anodic iron dissolution reaction at high pH solutions and in the absence of chloride ions is given by:

$$Fe \rightarrow Fe^{2+} + 2e^{-} \quad (2\text{-}1)$$

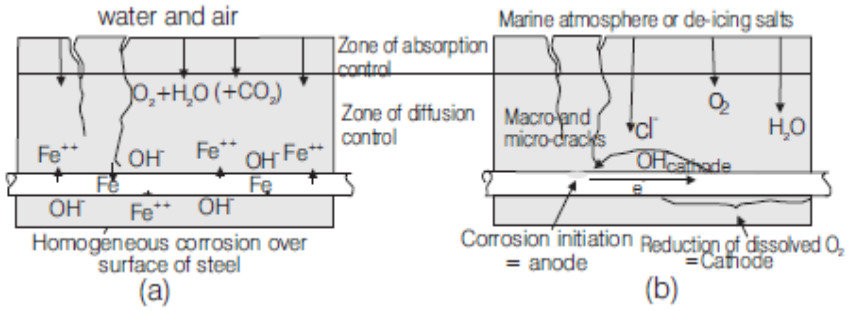
The anodic reaction is balanced by the following cathodic reaction:

$$1/2O_2 + H_2O + 2e^{-} \rightarrow 2OH^{-} \quad (2\text{-}2)$$

The combination of $Fe^{2+}$ and $OH^{-}$ ions produce a stable passive film as shown in **Figure 2-2 (a)**.

**Figure 2-2 (b)** shows that $Cl^{-}$ ions compete with $OH^{-}$ ions to react with $Fe^{2+}$ ions, forming soluble complexes that damage the passive film. The soluble iron-chloride complexes diffuse away from the steel bars, resulting in the formation of expansive corrosion products. The free $Cl^{-}$ ions migrate back to the anode reacting more with the iron of the steel bar (Hansson et al., 2012).

Reinforced concrete structures exposed to a salty environment, where de-icing salts are widely used, have the reinforcement de-passivated when enough chloride ions penetrate the concrete cover, leading to the corrosion process initiation (Rivera-Corral et al., 2017). The high alkali content in the concrete protects the reinforcement against corrosion by forming a passive film on the surface of the steel bars in the concrete. However, this passive film can be damaged by a high content of chloride ions and low pH in the concrete, leading to steel corrosion. Thus, the composition and microstructure of the steel reinforcement have a big influence on the forming and breaking of the passive film (Bertolini et al., 2013). Factors that contribute to steel corrosion in concrete are low pH around the steel bars and the ingress of $CO_2$, $O_2$ and chloride-laden water through the cracks of the concrete cover reaching the surface of the steel bars (Song et al., 2019).




(a) Formation of passive film on the steel bar. (b) Chloride induced active corrosion of steel bar in concrete

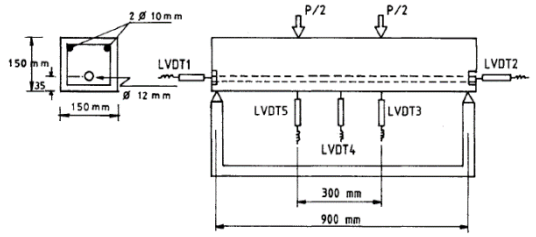
Figure 2-2 Corrosion Mechanism (Reproduced from Hansson et al., 2012)

## 2.3 Previous Studies on the Static Behaviour of Corroded Reinforced Beams Tested Statically

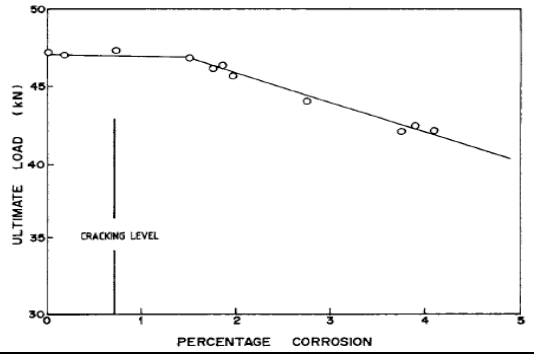
This section reviews some previous studies that investigated the flexural and shear behaviour of corroded reinforced concrete beams tested under static loading. **Tables 2-1** to **2-4** summarize these studies, including material properties, specimen details and test setup used. More details are provided in the following sub-sections.

### 2.3.1 Flexural Behaviour

Al-Sulaimani et al. (1990) studied the impact of reinforcement corrosion and cracking on the capacity and the bond behaviour between steel reinforcement and concrete by testing 24 reinforced concrete beams with dimensions of 150×150×1,000 mm as shown in **Figure 2-3 (a)**. The test program included four stages, and the corrosion process was applied to the entire length of the bottom steel bar in the third and fourth stages. The top steel bars and stirrups were isolated from the bottom steel bar to avoid corrosion. The reinforced concrete beams were tested under four-point bending test. The results from the study showed that the ultimate bond capacity decreased with the increase of corrosion level. In addition, there was no effect on the ultimate flexural load at a corrosion level of 1.5%; however, the ultimate load was reduced by 12% at a corrosion level of 4.5% as illustrated in **Figure 2-3 (b)**.




a) Dimensions of the beams




b) Ultimate load vs corrosion levels

Figure 2-3 Beam dimensions and results from Al-Sulaimani et al. (1990)

Rodriguez et al. (1997) investigated the corrosion process and the impact of different corrosion levels on the load-carrying capacity and serviceability of reinforced concrete beams; 31 reinforced

concrete beams were built with dimensions of 150×200×2,050 mm and 150×200×2,300 mm as presented in **Figure 2-4**. The study program included casting six types of reinforced concrete beams, and the corrosion was applied to the bottom bars, top bars and stirrups based on the type of reinforced concrete beam. Four-point bending test was used to test all the beams. From the obtained results, it was observed that the corrosion process in the reinforced concrete beams increased their deflections and crack widths at service load, and it decreased their strength at ultimate load. Moreover, the failure mode for the tested beams was due to shear in most cases.

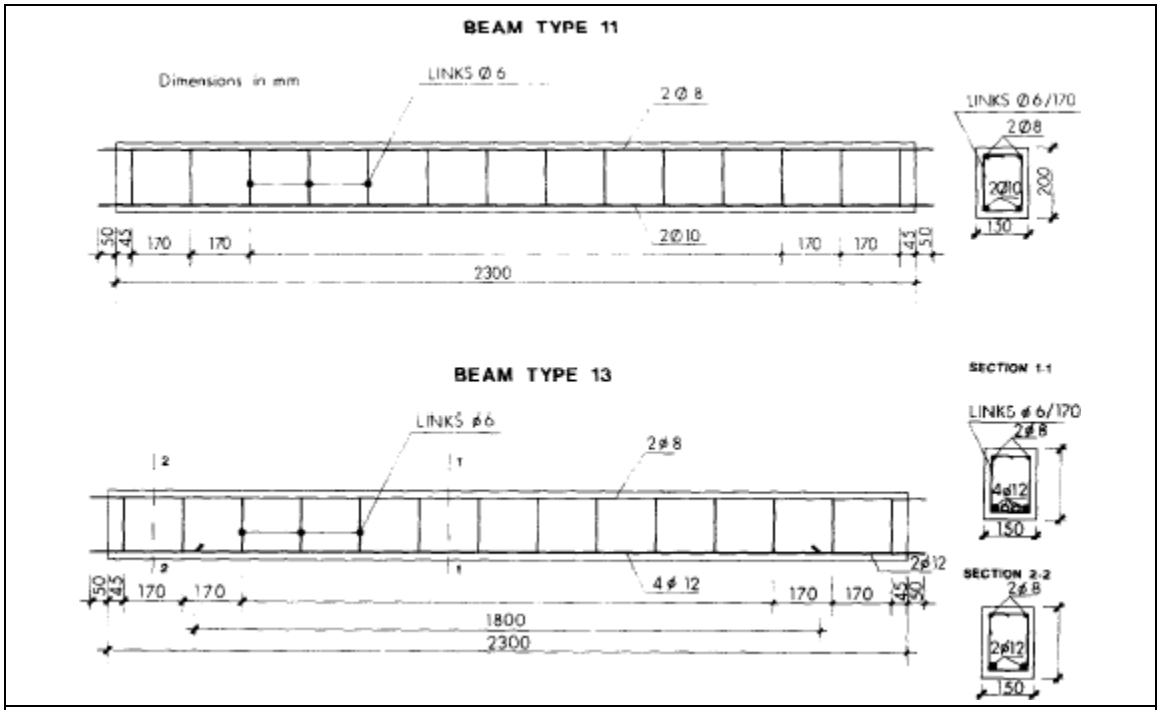
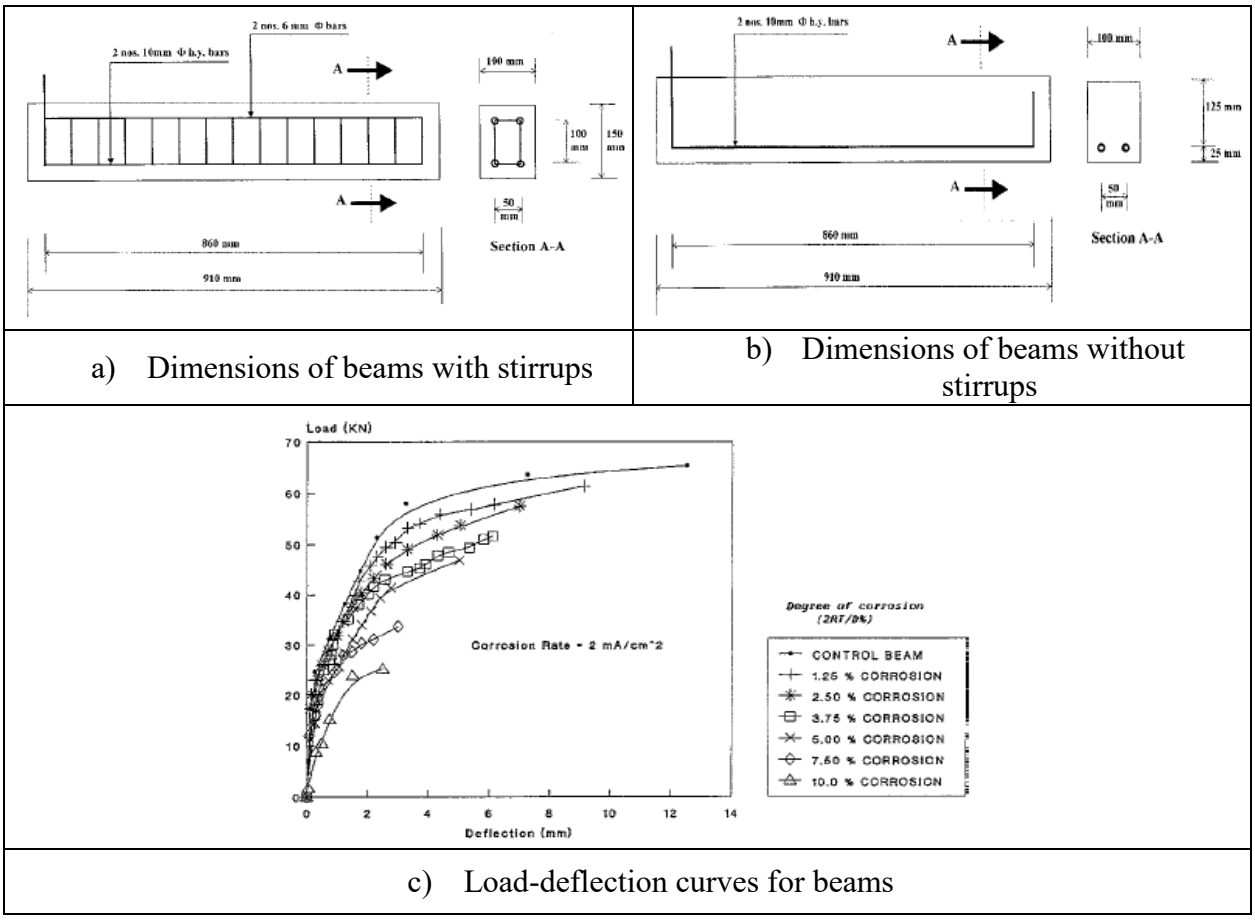



Figure 2-4 Beam dimensions from Rodriguez et al. (1997)

Mangat and Elgarf (1999) studied experimentally the residual flexural capacity of 111 corroded reinforced concrete beams at different levels of corrosion. The reinforced concrete beams were constructed with and without stirrups with dimensions of 100×150×910 mm as shown in **Figure 2-5 (a)** and **Figure 2-5 (b)**. The accelerated corrosion process was applied to the entire length of the tensile reinforcing bars. All the reinforced concrete beams were tested using four-point bending test. The flexural load capacity and deflection of the reinforced concrete beams were affected by the corrosion process as illustrated in **Figure 2-5 (c)**. The residual strength of the beams was reduced due to loss of bond between the steel bar and the concrete.



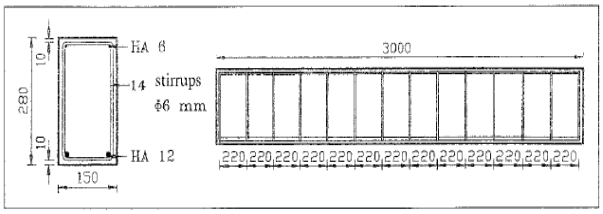

a) Dimensions of beams with stirrups

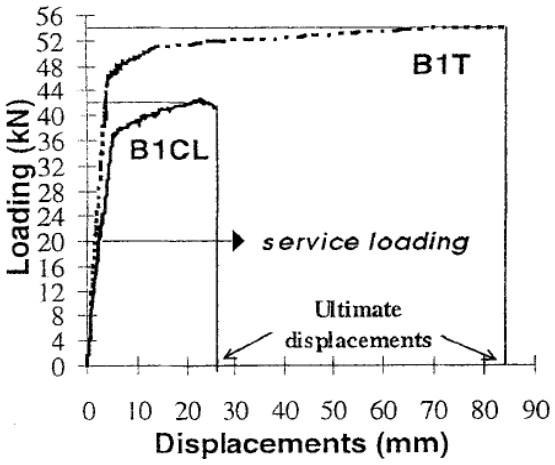
b) Dimensions of beams without stirrups

c) Load-deflection curves for beams

Figure 2-5 Beam dimensions and results from Mangat and Elgarf (1999)

Castel et al. (2000) assessed the mechanical properties of corroded reinforced concrete beams when compared with non-corroded ones. Four reinforced concrete beams were built with dimensions of 150×280×3,000 mm as shown in **Figure 2-6 (a)**. The corrosion process was applied on the entire beams by spraying them with salt fog (NaCl). According to the procedure of this study, all the beams were tested under sustained load using a three-point bending test. The results illustrated that the cracks on the compression zone did not influence the mechanical properties of corroded reinforced concrete beams. The stiffness of the corroded beams was reduced by 35% due to the bond decay between the steel and concrete in the tension zone. The residual bearing capacity of the corroded beams was affected only by reducing the cross-section area of the tensile steel reinforcement. In addition, the ductility was reduced by 70% in the corroded beams as shown in **Figure 2-6 (b)**.



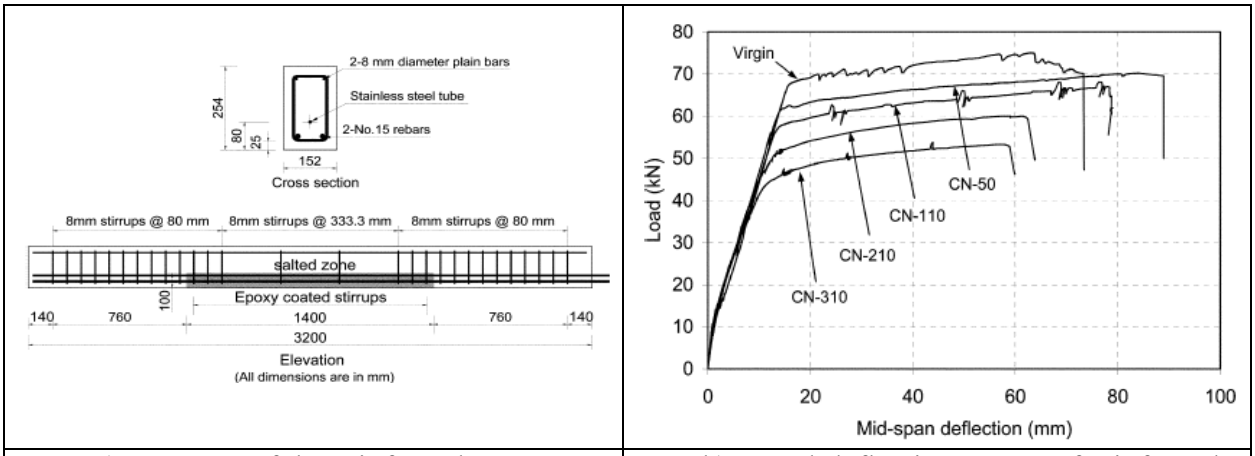




a) The geometry of the beams

b) Load-deflection curves for corroded (B1CL) and uncorroded (B1T) beams

Figure 2-6 Beam dimensions and results from Castel et al. (2000)

El Maaddawy et al. (2005) investigated the performance of reinforced concrete beams under a corrosion process and sustained loads. Nine reinforced concrete beams were constructed with dimensions of 152×254×3,200 mm as presented in **Figure 2-7 (a)**. The middle span of the corroded beams was cast by adding 2.25% salt into the concrete mix at a height of 100 mm and length of 1,400 mm, confining the corrosion region on the tensile bars at the mid region of the reinforced concrete beams. The stirrups in the corrosion region were coated with epoxy, and the contact points between stirrups and longitudinal steel bars were wrapped with plastic tape to avoid corrosion. Four corroded beams were tested under sustained loading (equivalent to approximately to 60% of the yielding moment of the control beam) using four-point bending test during the corrosion process, whereas the other four corroded beams were tested the same as the control beam under four-point bending test only. The results showed that the load-carrying capacity of the beams was reduced due to the corrosion process. In addition, there was a slight effect of flexural cracks resulting from sustained loading on the steel mass loss and the reduction of the beams' capacity. The deflection capacity of the corroded beams was reduced when the mass loss of steel reached 15% and above as illustrated in **Figure 2-7 (b)**.

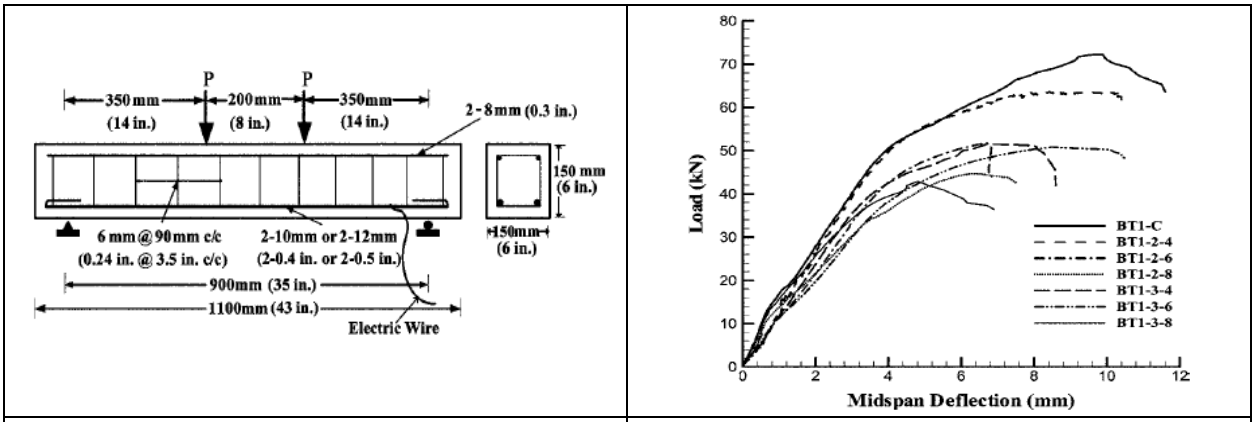



a) Lay-out of the reinforced concrete beams

b) Load-deflection curves of reinforced concrete beams

Figure 2-7 Beam dimensions and results from El-Maaddawy et al. (2005)

Azad et al. (2007) focused on evaluating the flexural behaviour of corroded reinforced concrete beams and predicting the residual flexural strength by developing a model based on the experimental results. The experimental program of this study consisted of 56 reinforced concrete beams with dimensions of 150×150×1,100 mm as presented in **Figure 2-8 (a)**. The corrosion process was accelerated on the entire length of the tensile steel bars and stirrups at different periods of 4, 6 and 8 days; however, the compression steel bars were coated by epoxy to avoid corrosion. Under a four-point bending test, all reinforced concrete beams were tested statically. The obtained results showed that the corroded beams were affected with the increase of mass loss percentage as illustrated in **Figure 2-8 (b)**. The maximum mass loss percentage reached was 34.8%. The residual flexural strength of corroded reinforced concrete beams was predicted using a numerical model with acceptable accuracy at low corrosion rates. Moreover, the load-deflection behaviour of the corroded beams was softer than the uncorroded ones due to loss of flexural stiffness.

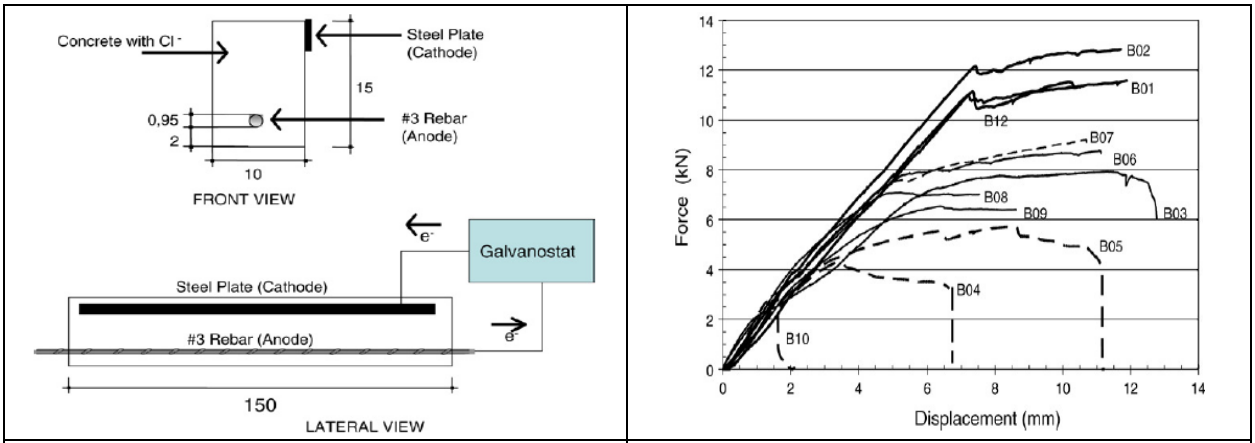



a) Reinforcement layout of the beams

b) Load-deflection curves for the beams

Figure 2-8 Beam dimensions and results from Azad et al. (2007)

Torres-Acosta et al. (2007) discussed the flexural capacity reduction of corroded reinforced concrete beams in a humid environment. Twelve reinforced concrete beams were constructed with one steel bar in the tension zone and with dimensions of 100×150×1,500 mm, as shown in **Figure 2-9 (a)**. The corrosion process was accelerated on the entire length of the tensile bar for a period of 40, 80 and 200 days. This study used three-point bending test to examine all the beams. The results showed that cracks evolved rapidly in a dry environment when compared to a wet environment. During the acceleration process of corrosion, the pitting formation on the surface of the steel bar was increased in the wet environment. In addition, the flexure load capacity was reduced due to pitting corrosion as illustrated in **Figure 2-9 (b)**.

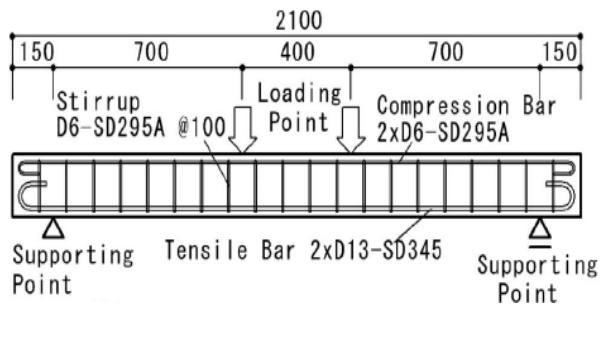



a) The geometry of the specimen

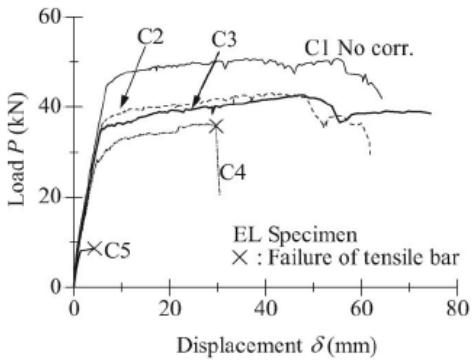
b) Load-deflection curves

Figure 2-9 Beam dimensions and results from Torres-Acosta et al. (2007)

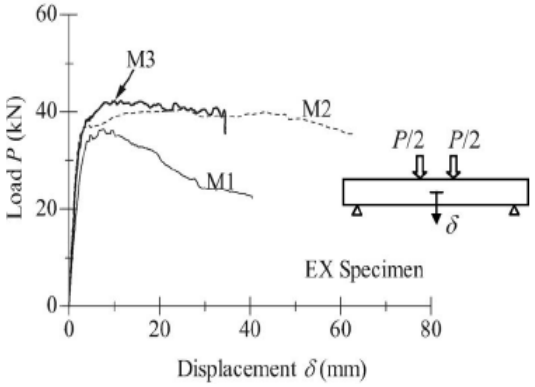
Oyado et al. (2011) also examined the performance of corroded reinforced concrete beams under different corrosion-inducing regimes. This study consisted of thirteen reinforced concrete beams with dimensions of 100×200×2,100 mm as presented in **Figure 2-10 (a)**. The corrosion process was applied on the whole reinforcement cage of the beams using either a salty environment (EX specimens) for a period of time ranging between 20 months and 12 years or an accelerated electric corrosion process (EL specimens) for a time period that did not exceed 54 days. All the reinforced concrete beams were tested under four-point bending test. The beams that were corroded using a salty environment had a higher steel mass loss than those corroded with an accelerated corrosion process. Furthermore, the majority of the corroded reinforced concrete beams failed due to concrete compression failure after the tensile steel bars had yielded. **Figure 2-10 (b)** and **Figure 2-10 (c)** show the results of the accelerated corroded beams (EL) and long-term corroded beams (EX), respectively.




a) The dimension of the beams



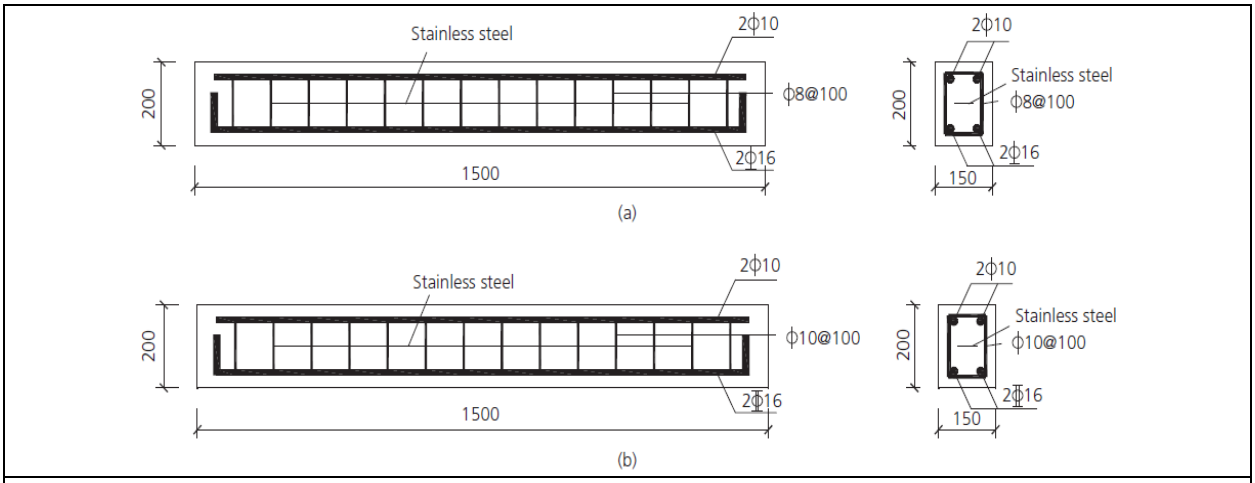

b) Load-deflection curves of accelerated corroded beams (EL)



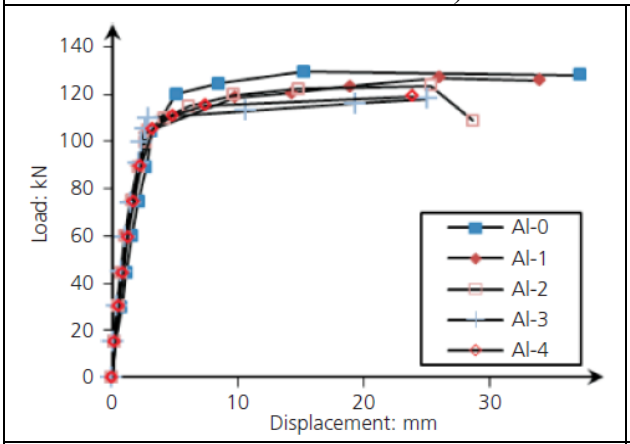

c) Load-deflection curves of long-term corroded beams (EX)

Figure 2-10 Beam dimensions and results from Oyado et al. (2011)

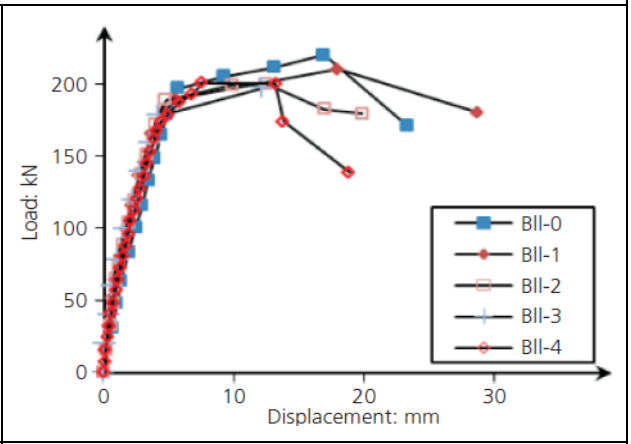
Xia et al. (2012) aimed to investigate the flexural strength of corroded reinforced concrete beams under different levels of corrosion and to predict their residual flexural strength. This investigation included twenty reinforced concrete beams with dimensions of 150×200×1,500 mm, as shown in **Figure 2-11 (a)**. The beams were divided into two types (Al and Bll) based on the concrete mix and the stirrups diameter. The corrosion zone was on the mid-span of the tensile steel bars with a length of 1,000 mm. The beams were tested under four-point bending. At a corrosion level of 12% mass loss, the stiffness and flexural capacity of the reinforced concrete beams were reduced, and the maximum and average corrosion- induced crack widths were increased. In addition, the failure mode of the beams changed from ductile to brittle failure when the corrosion level reached 12%. **Figure 2-11 (b)** and **Figure 2-11 (c)** illustrate the load-deflection curves for beams type Al and Bll, respectively.




a) The dimensions of the beams



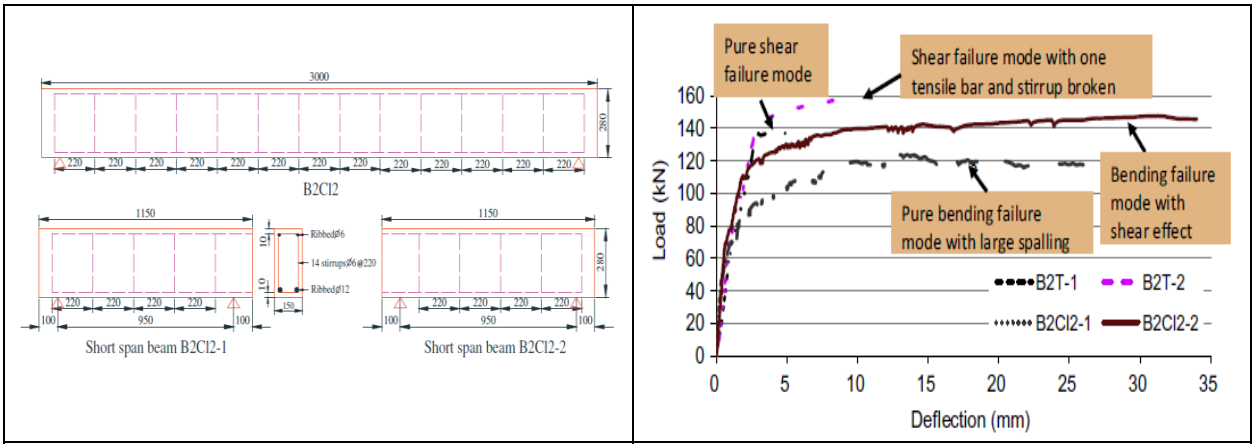

b) Load-deflection curves of beam type Al




c) Load-deflection curves of beam type Bll

Figure 2-11 Beam dimensions and results from Xia et al. (2012)

Zhu et al. (2013) evaluated the behaviour of reinforced concrete beams subjected to a corrosion regime for 26 years. Four reinforced concrete beams were built with dimensions of 150×280×1,150 mm as illustrated in **Figure 2-12 (a)**. The corrosion process was applied on the entire reinforcement of the beams using a saline environment while they were under sustained loading. All the reinforced concrete beams were tested under three-point bending test. The results showed that the control beams failed in shear, while the corroded beams failed in flexure due to the impact of the corrosion process. **Figure 2-12 (b)** shows the load-deflection behaviour of the beams after testing.

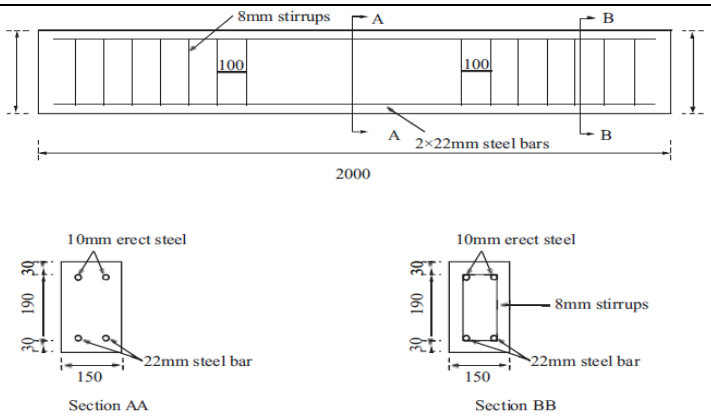



a) Dimensions of the beams

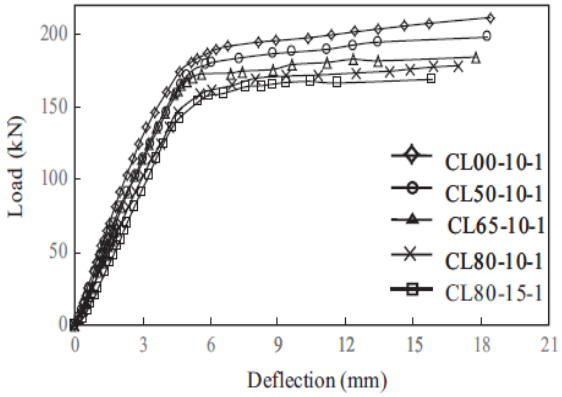
b) Load-deflection curves of the beams

Figure 2-12 Beam dimensions and results from Zhu et al. (2013)

Liu et al. (2016) intended to evaluate the flexural behaviour, residual capacity and ductility of corroded reinforced concrete beams under sustained loading. Twelve reinforced concrete beams were constructed without stirrups in the pure bending-moment region and had dimensions of 150×250×2,000 mm as shown in **Figure 2-13 (a)**. The corrosion process was accelerated on the entire length of the tensile reinforcement only, and the stirrups were coated with epoxy resin to prevent corrosion. A four-point bending test was used to test all the reinforced concrete beams statically under sustained loads. The results show that the flexural rigidity, maximum strength capacity and the ductility ratio of corroded reinforced beams under heavy simultaneous sustained loads (up to 80% of the ultimate load) were reduced as presented in **Figure 2-13 (b)**. However, the ductility ratio was affected mostly by the levels of sustained loads.




a) The geometry of the beams

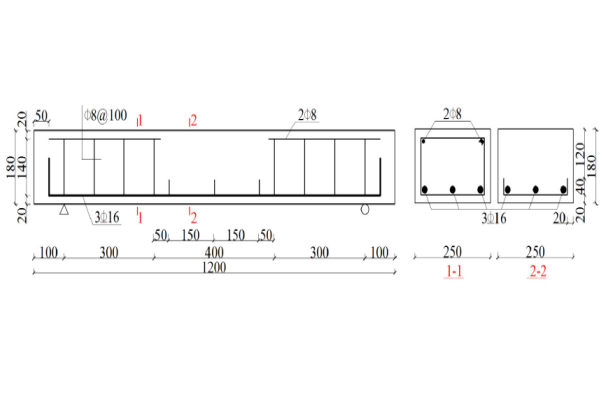



b) Load-deflection curves of beams

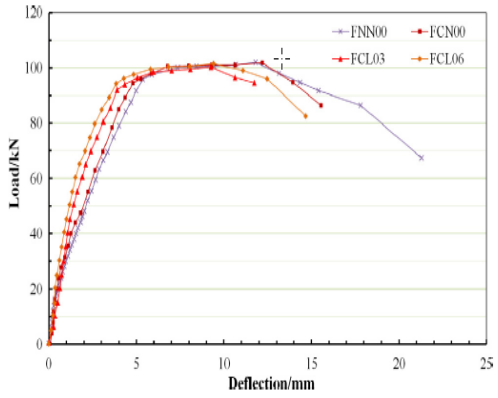
Figure 2-13 Beam dimensions and results from Liu et al. (2016)

Dong et al. (2017) focused on experimentally assessing the crack propagation and flexural response of corroded reinforced concrete beams having rectangular cross-section under simultaneous sustained loading. Seven reinforced concrete beams were constructed with dimensions of 250×180×1,200 mm as shown in **Figure 2-14 (a)**. In the shear span, stirrups were spaced at 100 mm, while mid-span U-shaped stirrups were used at a spacing of 150 mm. The corrosion region was mainly distributed on the tensile bars in the mid-span of the reinforced concrete beams for a length of 400 mm. The behaviour of the reinforced concrete beams was examined using four-point bending test. The results of this study illustrated that corroded reinforced concrete beams under simultaneous sustained loading experienced severe cracks. Furthermore, the sustained loading did not affect the maximum capacity of the corroded beams with low corrosion levels (2% and 3% mass loss); however, at this level of corrosion the ductility

of the beams was decreased. **Figure 2-14 (b)** illustrates the load-deflection behaviour of the beams after testing.




a) Beams dimensions




b) Load-deflection curves of the beams

Figure 2-14 Beam dimensions and results from Dong et al. (2017)

Lu et al. (2018) examined the fatigue life of reinforced concrete beams with corroded reinforcement. This examination included fourteen reinforced concrete beams with dimensions of 120×200×1,700 mm as illustrated in **Figure 2-15**. The corrosion process was accelerated on the tensile reinforcement in the mid region of the reinforced concrete beams for a length of 500 mm, along which there were no stirrups. Two types of tests were conducted: monotonic static loading and simultaneous fatigue loading. The fatigue performance of the corroded reinforced concrete beams was affected significantly in terms of crack patterns, ductility, fatigue life and stiffness. The fatigue life of the corroded beams decreased as the maximum fatigue load and corrosion levels were increased. Finally, under simultaneous fatigue loading and corrosion, both uniform and pitting corrosion occurred simultaneously in the reinforced concrete beams.

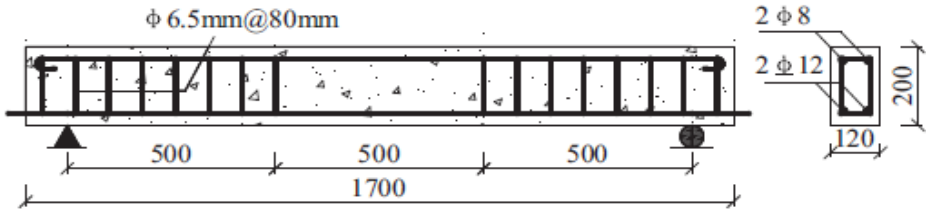



Figure 2-15 Beam dimensions from Lu et al. (2018)

Table 2-1 Summary of the studies on flexural response: part one

| Focus | Authors | No. of beams | Beam dimensions | | | $f'_c$ (MPa) | Longitudinal reinforcement | | Stirrups | | Concrete cover (mm) | Salt (%) | Mass loss (%) | Corrosion location | Corrosion method, | $\mu A/cm^2$ or current (A) | Corrosion duration (days) | Test type |
|---|---|---|---|---|---|---|---|---|---|---|---|---|---|---|---|---|---|---|
| | | | B (mm) | H (mm) | L (mm) | | Top | Bottom | Size (mm) | S* (mm) | | | | | | | | |
| Flexural response | Al-Sulaimani (1990) | 24 | 150 | 150 | 1000 | 40 | 2-10 | 1-12 | 6 | 50 | - | - | - | B*FL*, Stirrups | Acc* | 2000 | - | 4PB* |
| | Rodriguez et al (1997) | 31 | 150 | 200 | 2050 2300 | 34-52 | 2,4-8 | 2-10,12 | 6 | 85, 150, 170 | - | 3 | - | Whole beam | Acc* | 100 | - | 4PB* |
| | Mangat and Elgarf (1999) | 111 | 100 | 150 | 910 | 40 | 2-6 | 2-10 | 6 | 70 | 25 | 1, 3.5 | 1.25-10 | B*FL* | Acc* | 1,2,3,4 *10^3 | 0.5 to 16 | 4PB* |
| | Castel et al (2000) | 4 | 150 | 280 | 3000 | 45 | 2-6 | 2-12 | 6 | 220 | 10 | - | - | Whole beam | Saline Env* | - | 4745 | SL*, 3PB* |
| | El-Maaddawy et al (2005) | 9 | 152 | 254 | 3200 | 40.5 | 2-8 | 2-15 | 8 | 80, 333 | 25 | 2.25 | 8.9 – 31.6 | B*ML* | Acc* | 215mA | 50,110, 210,310 | SL*, 4PB* |
| | Azad et al (2007) | 56 | 150 | 150 | 1100 | 40.7 | 2-8 | 2-10,12 | 6 | 90 | 25, 36,40 | 2, 5 | 5.4 – 34.8 | B*FL*, Stirrups | Acc* | 2000, 3000 | 4, 6, 8 | 4PB* |
| | Torres-Acosta et al (2007) | 12 | 100 | 150 | 1500 | 27 | - | 1-10 | - | - | 20 | 3 | 5, 10, 15 | B*FL* | Acc* | 80 | 40, 80, 200 | 3PB* |
| | Oyado et al (2011) | 13 | 100 | 200 | 2100 | 21.7-42.3 | 2-6 | 2-13 | 6 | 100 | - | 3 | 50 | Whole beam | Env*, Acc* | - | 600 to 4380 | 4PB* |
| | Xia et al (2012) | 20 | 150 | 200 | 1500 | 25.9, 35.6 | 2-10 | 2- 16 | 8, 10 | 100 | 30 | 5 | 4- 12 | B*ML* | EM*, Acc* | 200 | 4 to 98 25 to 78 | 4PB* |
| | Zhu et al (2013) | 4 | 150 | 280 | 1150 | 60 | 2-6 | 2-12 | 6 | 220 | 10, 14 | - | 20.5 – 34.28 | Whole beam | Saline Env* | - | 9490 | SL*, 3PB* |

S*: Spacing. B*: Bottom. FL*: Full length. ML*: Mid length. EM*: Electro-migration. Acc*: Accelerated corrosion process. SL*: sustained loads. 4PB*: Four-point bending test. 3PB*: Three-point bending test. Env*: Saline environment.

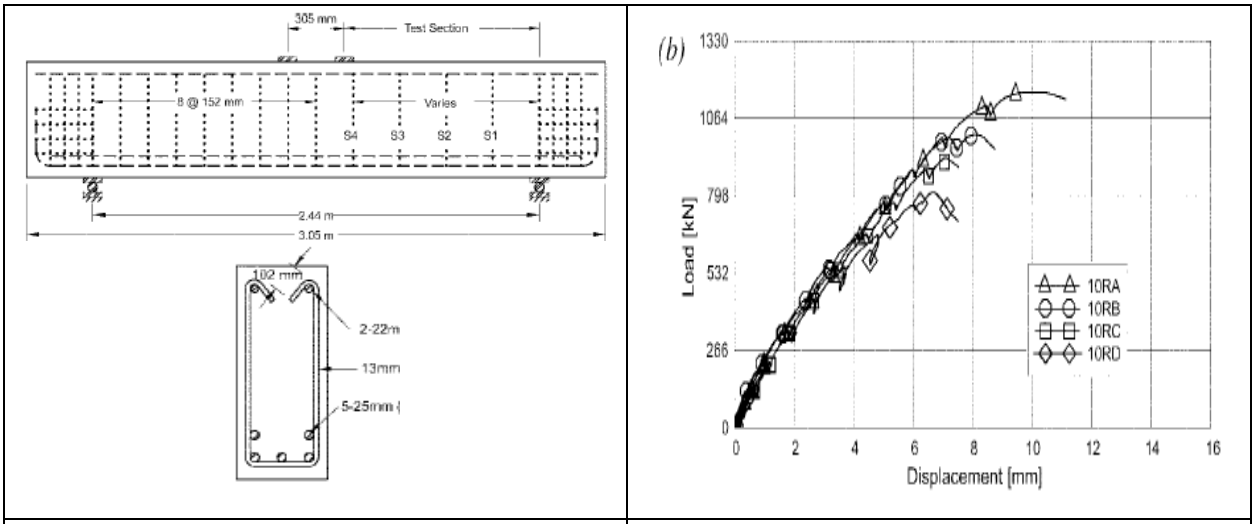
Table 2-2 Summary of the studies on flexural response: part two

| Focus | Authors | No. of beams | Beam dimensions | | | $f'_c$ (MPa) | Longitudinal reinforcement | | Stirrups | | Concrete cover (mm) | Salt (%) | Mass loss (%) | Corrosion location | Corrosion method, | $\mu A/cm^2$ or current (A) | Corrosion duration (days) | Test type |
|---|---|---|---|---|---|---|---|---|---|---|---|---|---|---|---|---|---|---|
| | | | B (mm) | H (mm) | L (mm) | | Top | Bottom | Size (mm) | S* (mm) | | | | | | | | |
| Flexural response | Liu et al (2016) | 12 | 150 | 250 | 2000 | 40 | 2-10 | 2-22 | 10 | 100 | 30 | 5 | - | B*FL* | Acc* | 2.5A | 10, 15 | SL*, 4PB* |
| | Dong et al (2017) | 7 | 250 | 180 | 1200 | 35.4 | 2-8 | 3-16 | 8 | 100 | 20 | 5 | 2, 3 | B*ML* | EM*, Acc* | 100 | 98 | SL*, 4PB* |
| | Lu et al (2018) | 14 | 120 | 200 | 1700 | 32.74 | 2-8 | 2-12 | 6.5 | 80 | - | 5 | 4.03 – 18.55 | B*ML* | Acc* | 1327-6635 | - | SL*, 4PB* |

S*: Spacing. B*: Bottom. FL*: Full length. ML*: Mid length. EM*: Electro-migration. Acc*: Accelerated corrosion process. SL*: sustained loads. 4PB*: Four-point bending test.

### 2.3.2 Shear Behaviour

Higgins and Farrow. (2006) investigated the shear behaviour and shear capacity of corroded reinforced concrete beams. The reinforced concrete beams were constructed with three different cross-sections (rectangular, T and IT); eight of the reinforced concrete beams had rectangular cross-section with dimensions of 254×610×3,050 as shown in **Figure 2-16 (a)**. The corrosion process was accelerated on the stirrups on one side of the beams for a length of 1,068 mm (test section in **Figure 2-16 (a)**), and the stirrups located on the opposite side as well as the flexural reinforcement were epoxy coated to prevent corrosion of the steel. The corroded reinforced concrete beams were tested under four-point bending. The results showed that the cross-section of the corroded stirrups was reduced due to severe local pitting corrosion leading to a decrease in the capacity and ductility of the reinforced concrete beams, as illustrated in **Figure 2-16 (b)**.




a) Beams geometry | b) Load-deflection curves of the beams

Figure 2-16 Beam dimensions and results from Higgins and Farrow (2006)

Juarez et al. (2011) studied the effect of moderate and severe corrosion levels on the ultimate shear strength of reinforced concrete beams. Sixteen reinforced concrete beams were built with dimensions of 200×350×2,000 mm as shown in **Figure 2-17 (a)**. These beams were classified into two groups with different spacing between stirrups: 150 mm and 200 mm. The beams were constructed without compression steel bars and with stirrups along the 600-mm shear span. The tensile steel bars were epoxy coated to avoid corrosion. All beams were tested using four-point bending test. From the results, it was observed that the ultimate shear strength of the reinforced

concrete beams was decreased by 30% at moderate and severe corrosion levels (20% and 50% steel mass loss, respectively) due to loss of the bond between the stirrups and concrete as presented in **Figure 2-17 (b)** and **Figure 2-17 (c)**. The ductility of the beams was also reduced due to the increase in corrosion level.

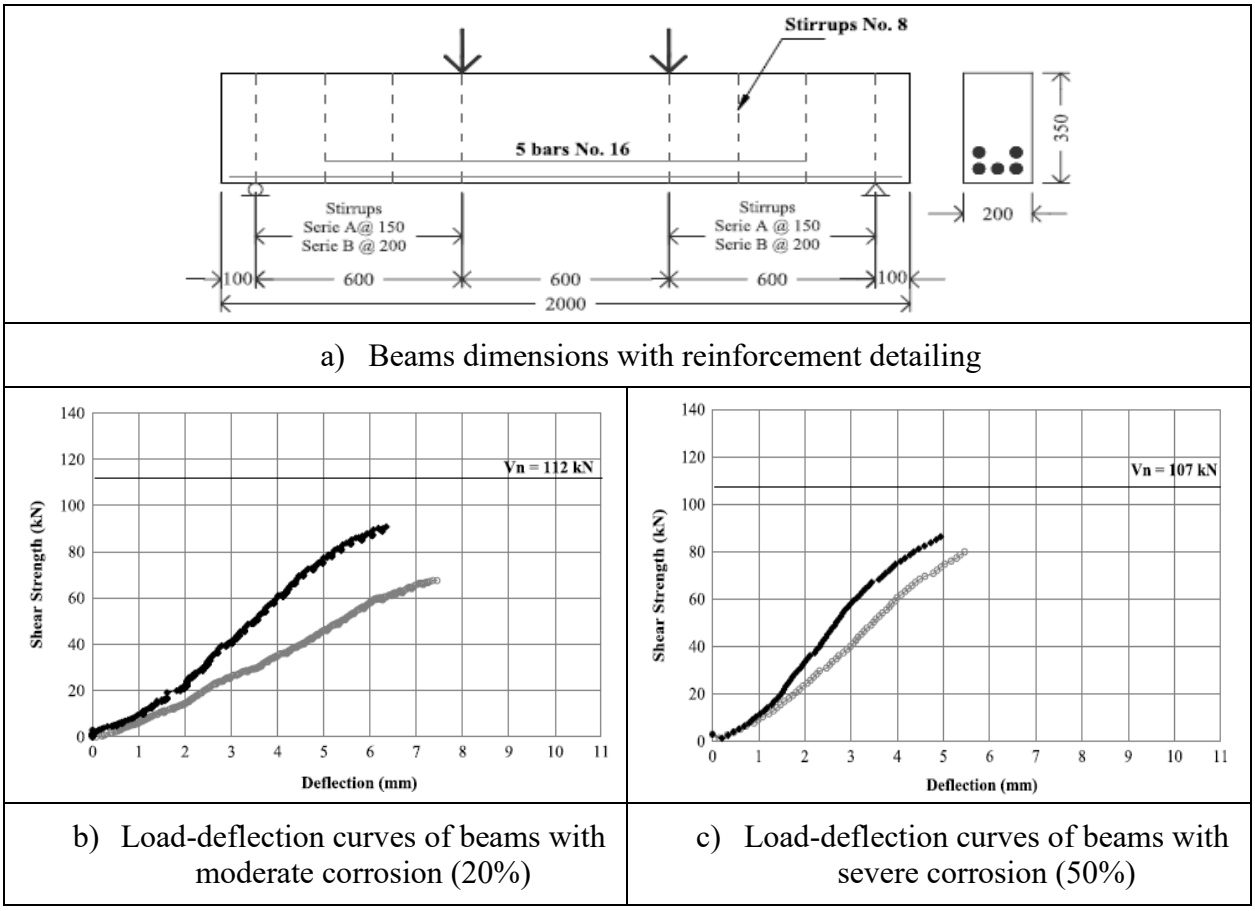
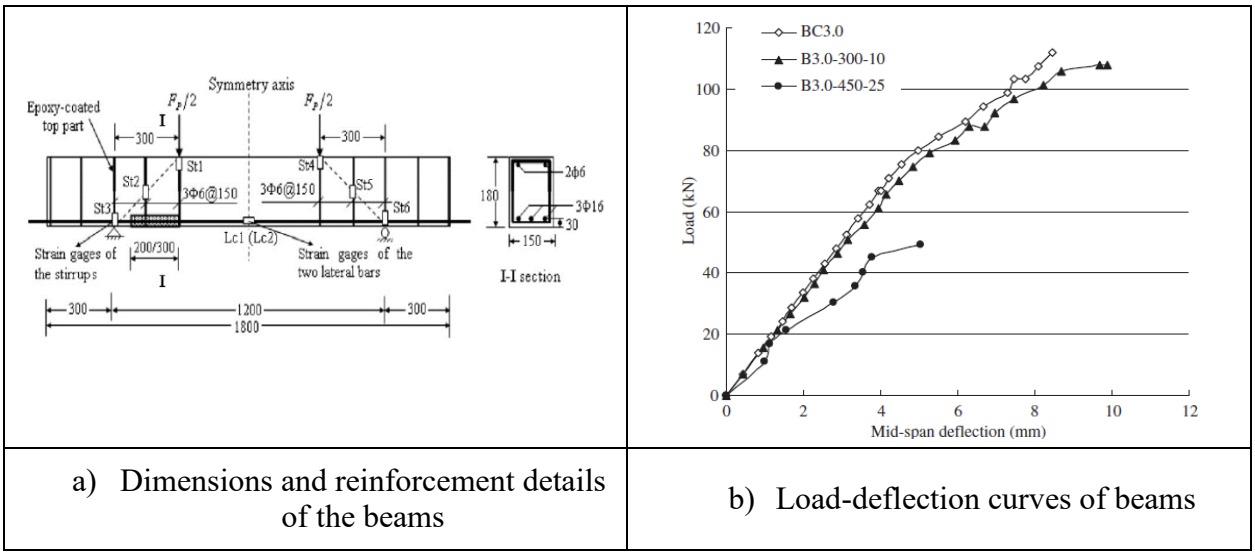



Figure 2-17 Beam dimensions and results from Juarez et al. (2011)

Wang et al. (2011) evaluated the effects of corrosion on one side of the shear span, which was partially damaged, on the load capacity of corroded reinforced concrete beams. This study included fourteen reinforced concrete beams with dimensions of 150×180×1,800 mm as illustrated in **Figure 2-18 (a)**. These beams were designed by considering the followings: two shear span-to-effective depth ratios of 2 and 3, two different partial lengths, and three bond characteristics (complete bond loss, moderate and high reduction in bond strength). The lengths of the partially damaged region were 200 mm and 300 mm for a shear span-to-effective depth ratio of 2 and 300 mm and 450 mm for a shear span-to-effective depth ratio of 3. An accelerated corrosion regime

was applied on the longitudinal bars and stirrups located in this region. All the reinforced concrete beams were tested under four-point monotonic loading. From the testing results, it was observed that the corroded beams with 10% mass loss still behaved in a ductile manner. The beam with the longest partial damage length and high level of corrosion displayed the lowest load capacity, irrespective of the shear span-to-effective ratio. Furthermore, the failure mode of the corroded beams was brittle with reduction of the load capacity due to a 25% steel mass loss on the longitudinal reinforcement and severe pitting and rupture of stirrups, as illustrated in **Figure 2-18 (b)**.

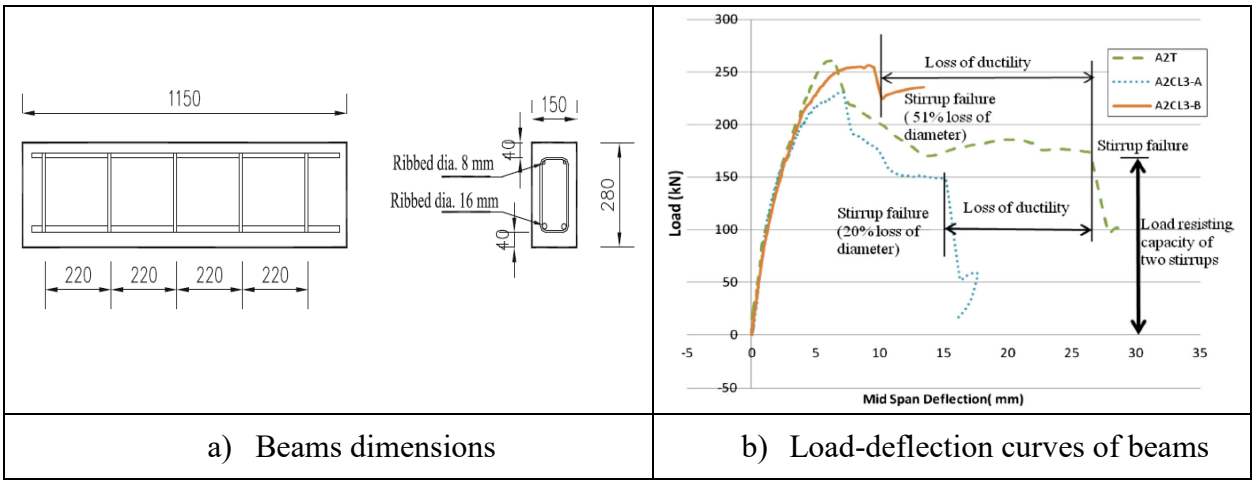



a) Dimensions and reinforcement details of the beams

b) Load-deflection curves of beams

Figure 2-18 Beam dimensions and results from Wang et al. (2011)

Khan et al. (2014) evaluated the effect of long-term corrosion on the shear behaviour of reinforced concrete beams. Three reinforced concrete beams were built with dimensions of 150×280×1,500 mm as shown in **Figure 2-19 (a)**. The corrosion process was induced on the whole reinforced concrete beam using a saline environment. The beams were stored under sustained loading using a three-point bending test. The corrosion process applied to the beams did not change their failure mode. The mass loss induced on the stirrups caused a loss in the ductility of the reinforced concrete beams. On the other hand, the corroded longitudinal steel bars barely decreased the load-bearing capacity of the reinforced concrete beams as shown in **Figure 2-19 (b)**.

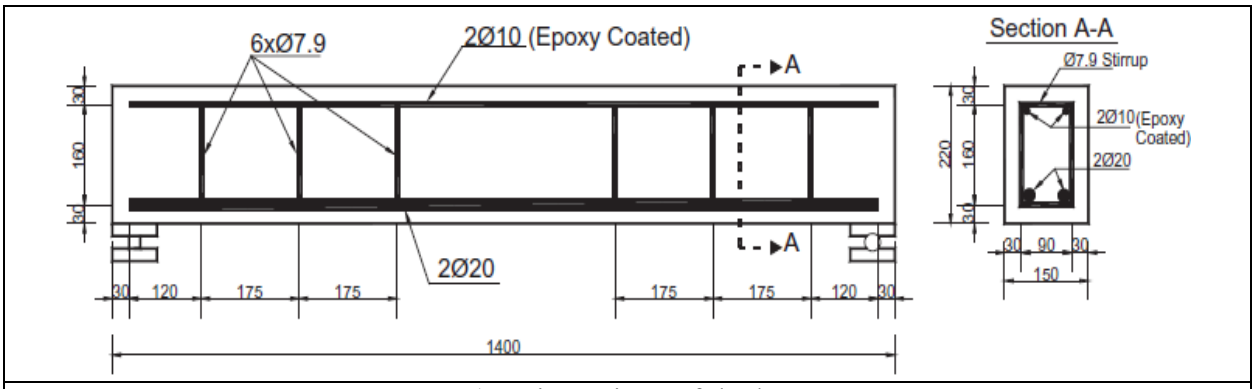



a) Beams dimensions

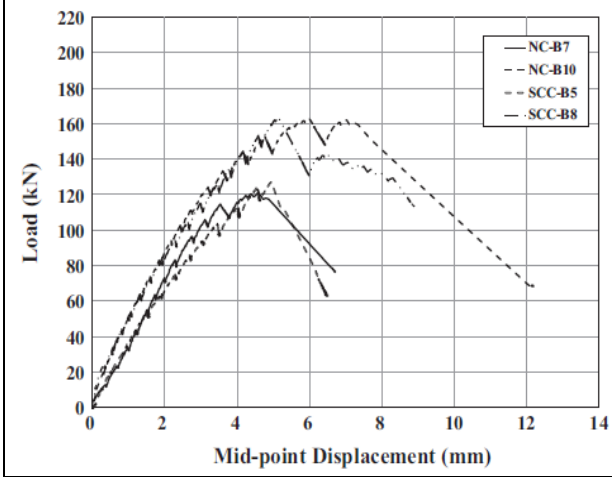
b) Load-deflection curves of beams

Figure 2-19 Beam dimensions and results from Khan et al. (2014)

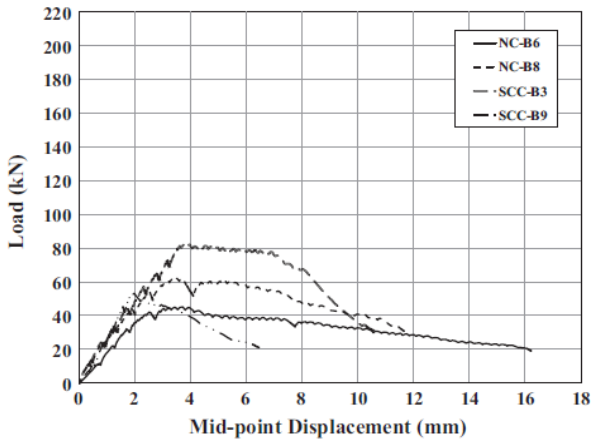
Lachemi et al. (2014) inspected the shear response of self-consolidating concrete (SCC) beams under the influence of corrosion. Twenty reinforced concrete beams with dimensions of 150×220×1,400 mm were constructed, as shown in **Figure 2-20 (a)**, with either normal concrete (NC) or SCC. The corrosion process was accelerated on both the tensile steel bars and stirrups of the reinforced concrete beams. However, the compression steel bars were coated with epoxy to prevent corrosion. The reinforced concrete beams response was tested using a four-point bending test. The study results showed that the load capacity, stiffness and energy dissipation of the corroded reinforced concrete beams were rapidly decreased at corrosion levels of 10%, 15% and 20% steel mass loss as illustrated in **Figure 2-20 (b)** and **Figure 2-20 (c)**. In addition, the bond strength between the concrete and reinforcement was reduced due to large cracks on the beams. The corrosion level had a significant impact on changing the failure mode of the reinforced concrete beams (NC and SCC). Moreover, the failure mode of both the NC and SCC corroded beams was flexure-shear failure, shear failure and bonding failure.




a) Dimensions of the beams



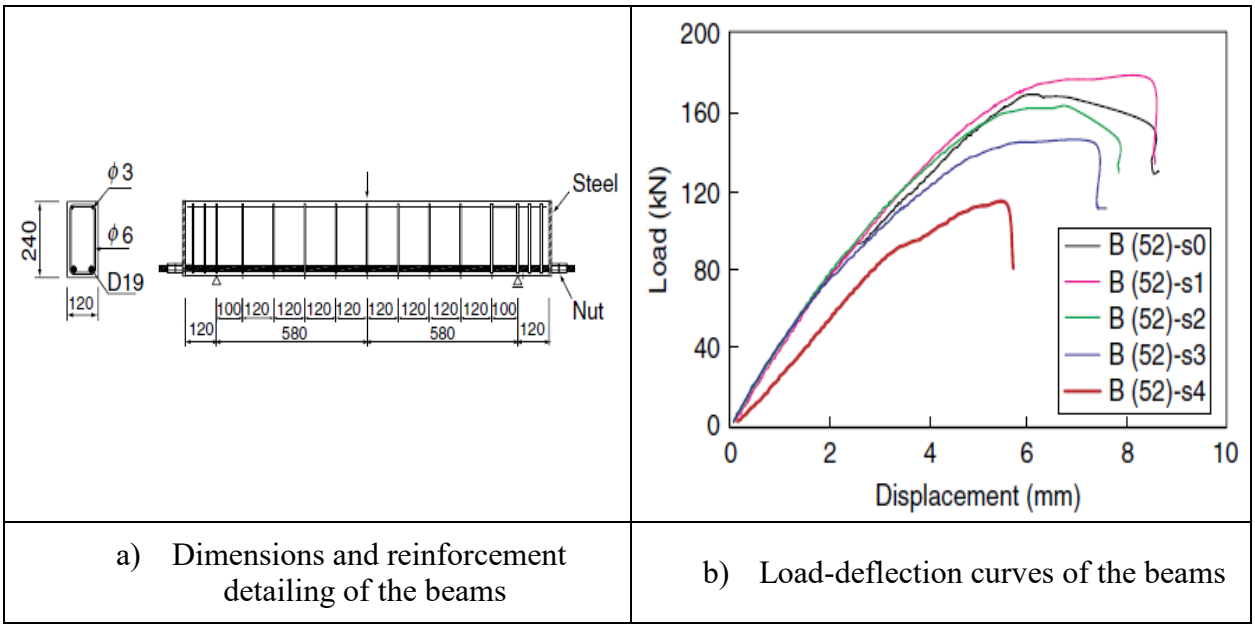

b) Load-deflection curves of the beams with 10% mass loss




c) Load-deflection curves of the beams with 20% mass loss

Figure 2-20 Beam dimensions and results from Lachemi et al. (2014)

Xue et al. (2014) studied the effect of corroded stirrups on the shear behaviour of reinforced concrete beams. The experimental program included thirteen reinforced concrete beams with dimensions of 120×240×1,400 mm as illustrated in **Figure 2-21 (a)**. The tensile steel bars in the reinforced concrete beams were fixed from outside using nuts to prevent anchorage failure. The corrosion process was applied on the stirrups only, and the contact points between the longitudinal steel bars and stirrups were isolated to ensure corrosion occurred only on the stirrups. The shear behaviour of the reinforced concrete beams was investigated using a three-point bending test. The shear strength of the reinforced concrete beams with corroded stirrups was decreased due to 32% steel mass loss, as shown in **Figure 2-21 (b)**. In addition, severe corroded stirrups in the reinforced concrete beams led to diagonal tension failure and a reduction of stiffness and shear strength.

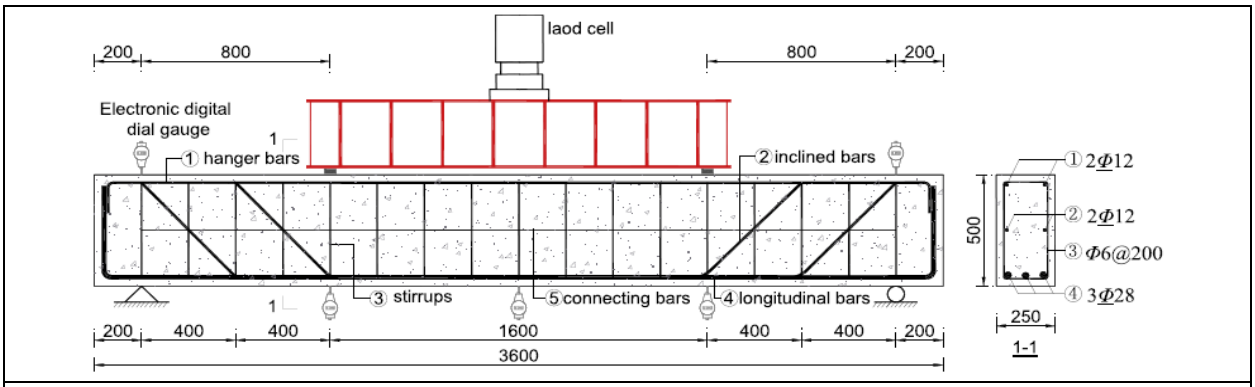



a) Dimensions and reinforcement detailing of the beams

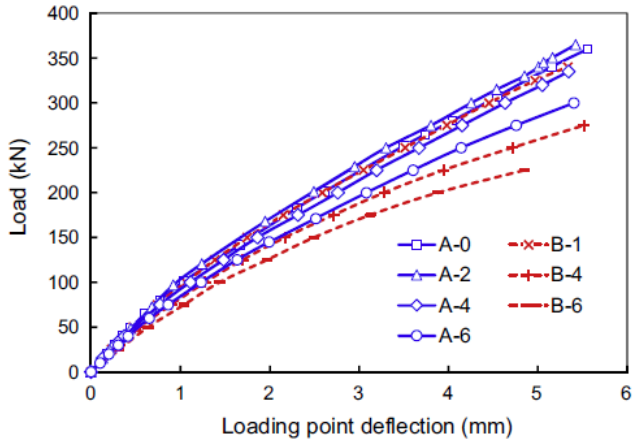
b) Load-deflection curves of the beams

Figure 2-21 Beam dimensions and results from Xue et al. (2014)

Wang et al. (2015) examined the impact of corrosion on two types of shear reinforcement (stirrups and inclined bars) in reinforced concrete beams. This study consisted of fourteen reinforced concrete beams with dimensions of 250×500×3,600 mm as illustrated in **Figure 2-22 (a)**. The corrosion process was applied on the beams in two stages: first on stirrups only by insulating the longitudinal reinforcement and inclined bars using epoxy coating and tape, and second, on both stirrups and inclined bars. All the reinforced concrete beams were tested statically under four-point bending. The results showed that low levels of corrosion (up to 10% steel mass loss) on the stirrups and inclined bars had a slight influence on the shear strength and initial shear stiffness; however, high levels of corrosion (up to 68% steel mass loss) on the stirrups and inclined bars reduced the post-cracking shear stiffness, as shown in **Figure 2-22 (b)**. Furthermore, the failure mode of the reinforced concrete beams with corroded stirrups and inclined bars was not affected, even though the corroded reinforcement ruptured early.



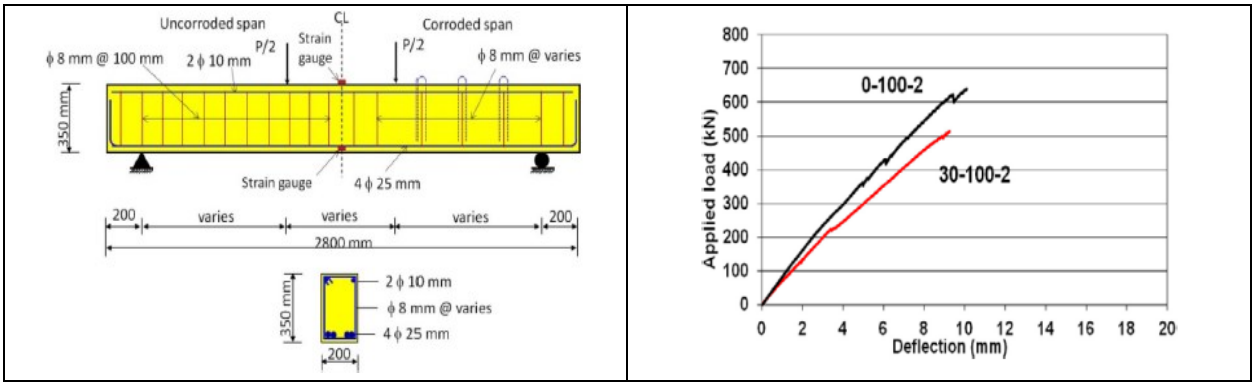

a) Beams details




b) Load-deflection curves of the beams

Figure 2-22 Beam dimensions and results from Wang et al. (2015)

El-Sayed et al. (2016) conducted an experimental program to study the impact of the corroded stirrups on the shear response and strength of reinforced concrete beams. This study included fourteen reinforced concrete beams with dimensions of 200×350×2,800 mm as presented in **Figure 2-23 (a)**. These beams were reinforced with epoxy coated steel bars at the tension and compression zones to ensure corrosion occurred on the stirrups only. Moreover, the longitudinal reinforcement was wrapped with electrical tape at the point of contact with the stirrups to prevent any electrical connection. All the reinforced concrete beams were tested by four-point bending. The results showed that the stiffness and shear strength of the corroded reinforced concrete beams were reduced when compared with the control beams, and this reduction was more significant at high corrosion levels (up to 24% steel mass loss) as shown in **Figure 2-23 (b)**. Failure of beams with corroded stirrups was due to stirrups rupture.

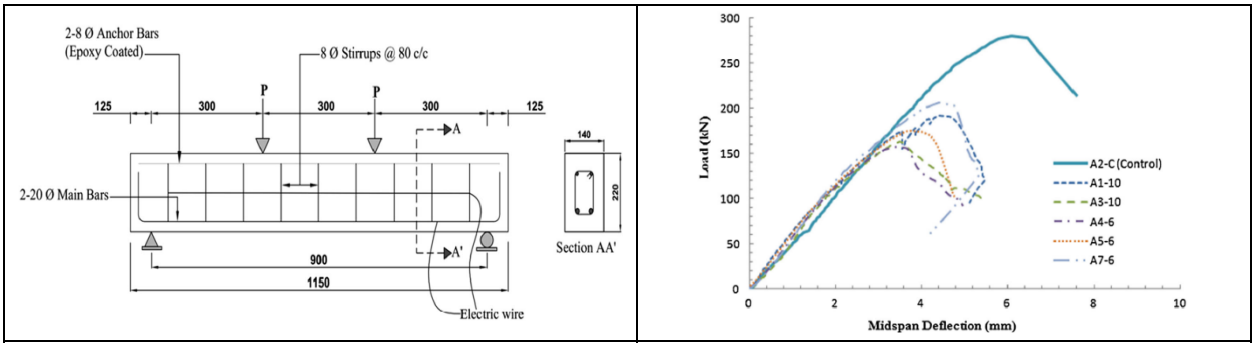



a) Details of the beams

b) Load-deflection curves of beams with stirrup spacing of 100mm and a/d=2

Figure 2-23 Beam dimensions and results from El-sayed et al. (2016)

Imam and Azad (2016) investigated experimentally the effect of corroded stirrups on the strength capacity of reinforced concrete beams and used the experimental results to predict the residual shear capacity. This investigation consisted of seventeen reinforced concrete beams with dimensions of 140×220×1,150 mm and 150×240×1,150 mm, as illustrated in **Figure 2-24 (a)**. The compression bars were coated with epoxy to prevent corrosion; however, the tension bars were left uncoated and exposed to the same corrosion regime as the stirrups. All the reinforced concrete beams were tested statically under four-point bending. From the results, it was found that the most important parameters that initiate damage in the corroded reinforced concrete beams were corrosion rate (2 mA/cm$^2$) and the duration of the corrosion process (up to 10 days). **Figure 2-24 (b)** shows the load-deflection behaviour of the corroded (up to 39% steel mass loss) and uncorroded (control) reinforced concrete beams.

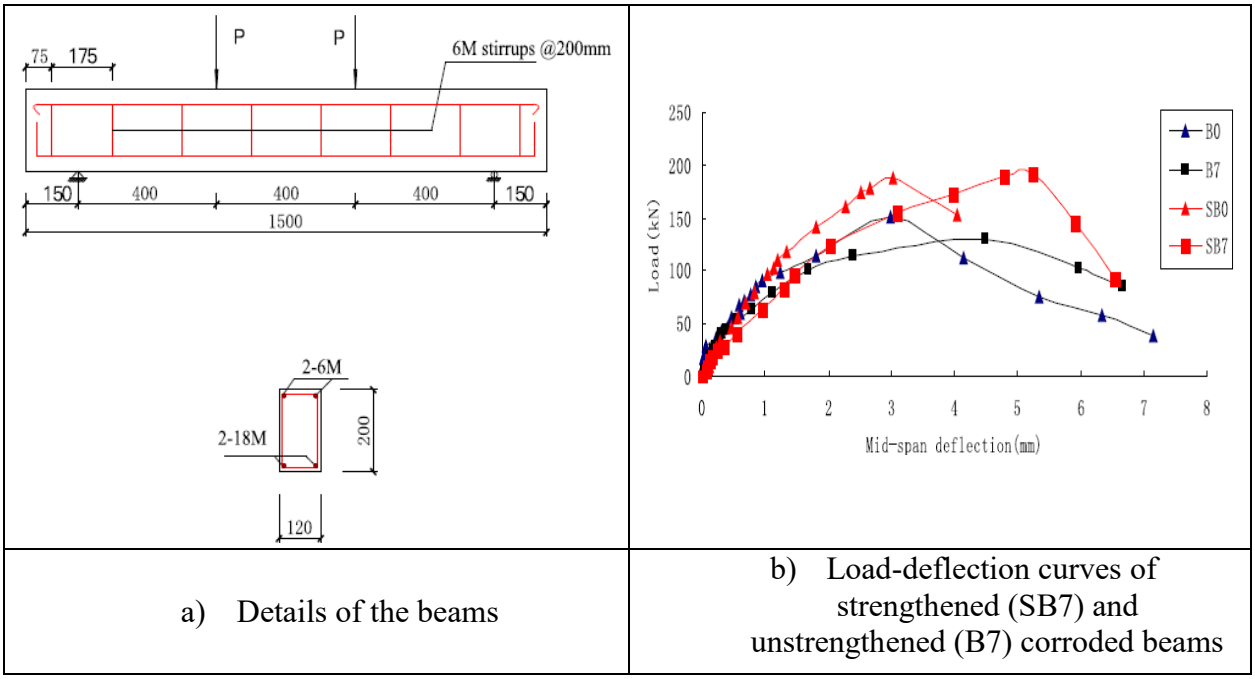



a) Beams details

b) Load-deflection curves of the beams

Figure 2-24 Beam dimensions and results from Imam and Azad. (2016)

Zhang et al. (2019) studied the shear behaviour of reinforced recycled aggregate concrete (RRC) beams with corroded stirrups and strengthened with sheets of carbon fiber reinforced polymer (CFRP). Ten reinforced concrete beams were constructed with dimensions of 120×200×1,500 mm as illustrated in **Figure 2-25 (a)**. The intersections between stirrups and longitudinal reinforcement were insulated to ensure the corrosion occurred only on the stirrups. The CFRP sheets were placed on the shear zones at a spacing of 100 mm. All the reinforced concrete beams were tested using four-point bending. The test results highlighted that using CFRP sheets on corroded RRC beams decreases the extension of diagonal cracking and delays the critical cracks. The failure mode of the strengthened corroded RRC beams and strengthened reinforced concrete beams was shear failure. **Figure 2-25 (b)** shows the behaviour of strengthened and unstrengthened corroded beams.




a) Details of the beams

b) Load-deflection curves of strengthened (SB7) and unstrengthened (B7) corroded beams

Figure 2-25 Beam dimensions and results from Zhang et al. (2019)

Table 2-3 Summary of the studies on shear response

| Focus | Authors | No. of beams | Beam dimensions | | | $f'_c$ (MPa) | Longitudinal reinforcement | | Stirrups | | Concrete cover (mm) | Salt (%) | Mass loss (%) | Corrosion location | Corrosion method, | $\mu A/cm^2$ or current (A) | Corrosion duration (days) | Test type |
|---|---|---|---|---|---|---|---|---|---|---|---|---|---|---|---|---|---|---|
| | | | B (mm) | H (mm) | L (mm) | | Top | Bottom | Size (mm) | S* (mm) | | | | | | | | |
| Shear response | Higgins and Farrow (2006) | 8 | 254 | 610 | 3050 | 29.3 - 33.4 | 2-22 | 5-25 | 13 | 203, 254 ,305 | 25, 38 | - | 12, 20, 40 | Stirrups | Acc* | 600 | 35 to 169 | 4PB* |
| | Juarez et al (2011) | 16 | 200 | 350 | 2000 | 21 | - | 5-16 | 8 | 150, 200 | - | 3.5 | 20, 50 | Stirrups | w/d*, Acc* | 100 | 80, 120 | 4PB* |
| | Wang et al (2011) | 14 | 150 | 180 | 1800 | 30 | 2-6 | 3-16 | 6 | 150, 200 | 16 | 5 | 10 - 25 | LR*, Stirrups | Acc* | - | - | 4PB* |
| | Khan et al (2014) | 3 | 150 | 280 | 1150 | 45 | 2-8 | 2-16 | 8 | 220 | 40 | - | - | Whole beam | Saline Env* | - | 9490 | SL*, 3PB* |
| | Lachemi et al (2014) | 20 | 150 | 220 | 1400 | 45.5, 42.9 | 2-10 | 2-20 | 8 | 120, 175 | 30 | 5 | 5,10,15 ,20 | Stirrups, B*FL* | Acc* | 1A | 15,30,45 ,60 | 4PB* |
| | Xue et al (2014) | 13 | 120 | 240 | 1400 | 33.1 – 35.1 | 2-10 | 2-19 | 6 | 90,100, 120 | - | 3 | 4 – 32 | Stirrups | Acc* | 1000 | 2 - 20 | 3PB* |
| | Wang et al (2015) | 14 | 250 | 500 | 3600 | 25.96-38.32 | 2-12 | 3-28 | 6 | 200 | - | 5 | 4.23-68.35 | Shear bars | Acc* | 1830 | - | 4PB* |
| | El-sayed et al (2016) | 14 | 200 | 350 | 2800 | 38 | 2-10 | 4-25 | 8 | 100-200 | 20 | 2 | 12.3-24 | Stirrups | Acc* | 400 | 30, 120 | 4PB* |
| | Imam and Azad (2016) | 17 | 140, 150 | 220, 240 | 1150 | 31.5, 37.4 | 2-8 | 2-20 | 8 | 80 | 32, 40 | 3 | 16.79-38.72 | Stirrups | Acc* | 5.91A, 6.36A | 6 and 10 | 4PB* |
| | Zhang et al (2019) | 10 | 120 | 200 | 1500 | 36.5 | 2-6 | 2-18 | 6 | 200 | - | 5 | 1.5-13.7 | Stirrups | Acc* | 270 | 0,1,2,3, 4,5,6,7 | 4PB* |

S*: Spacing. Acc*: Accelerated corrosion process. 4PB*: Four-point bending test. LR*: Longitudinal reinforcement. w/d*: wet/dry cycles. Env*: Saline environment. SL*: sustained loads. 3PB*: Three-point bending test. B*: Bottom. FL*: Full length.

### 2.3.3 General Guidelines for Modeling Corrosion in RC Beams

Coronelli and Gambarova (2004) proposed a finite element procedure for modeling corroded reinforced concrete beams to predict their structural behaviour. Concrete was modelled by 4-4-node plane stress elements, while steel reinforcement was modeled using 2-node truss elements. The bond action between concrete and steel bars was modelled through link elements. **Figure 2-26 (a)** shows constitutive models used for concrete, steel and bond. **Figure 2-26 (b)** shows a typical finite element mesh whose geometry or associated mechanical properties are modified to account for corrosion-induced damage. The proposed procedure included the followings:

- Reducing the cross-sectional area of the corroded longitudinal steel bars and stirrups that are attacked by either chloride ingress or carbonation. The reduction percentage of steel bar cross-section due to corrosion pitting is done through a pitting factor $\alpha_{pit}$, defined as:

  $$\alpha_{pit} = \frac{\Delta A_{pit}}{A_{bar}} \quad (2\text{-}3)$$

  where: $\alpha_{pit} = 0$ in virgin material. $\Delta A_{pit}$ = Area reduction due to pitting and $A_{bar}$ = original cross-section area of bar.

- Changing the ductility of the corroded steel bars due to the pitting process of chloride ingress. This change can be done by considering the severe reduction on the cross-section area of steel bar in the ultimate strain of the steel bar as shown in this equation:

  $$\mathcal{E}_{su} = \mathcal{E}_{sy} + (\mathcal{E}_{su} - \mathcal{E}_{sy})\,(1 - \alpha_{pit} / \alpha_{Pit}^{max}) \text{ for } \alpha_{Pit} < \alpha_{Pit}^{max} \quad (2\text{-}4)$$

  where: $\mathcal{E}_{sy}$ = yield strain, $\mathcal{E}_{su}$ = ultimate strain, $\alpha_{Pit}^{max}$ = Severe reduction percentage which ranges from 0.5 to 0.1.

  Another approach adapted from Lay et al. (2003) is used as follows:

  $$\lambda = (1 - \alpha_1 * A_{corr}) * \lambda_0 \quad (2\text{-}5)$$

  where: $\lambda$ = ultimate strain in the corroded state, $\alpha_1$ = regression coefficient, $A_{corr}$ = section loss, $\lambda_0$ = ultimate strain in the uncorroded state.

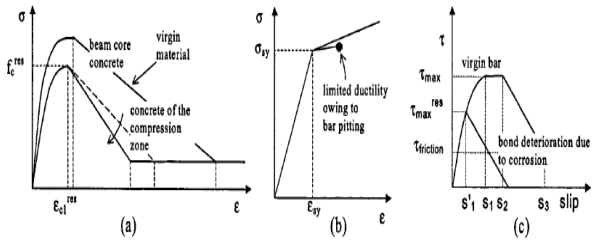
- Reducing the compressive strength due to cracking and spalling of the concrete cover. according to the following model (Vecchio and Collins, 1986):

  $$f^*_c = f_c / 1 + K\,\varepsilon_1 / \varepsilon_{co} \quad (2\text{-}6)$$

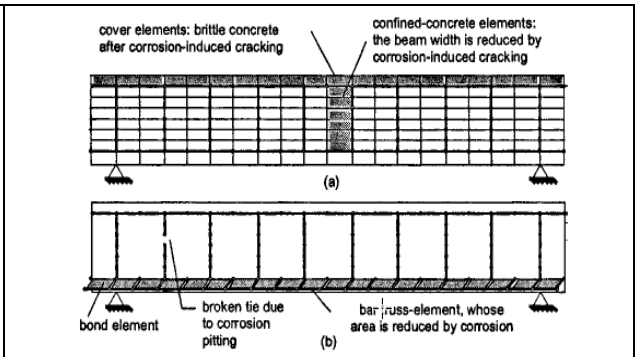
  where: K = coefficient related to bar roughness and diameter, $\varepsilon_1$ = average tensile strain in the cracked concrete, and $\varepsilon_{co}$ = strain at the peak compressive stress ($f_c$).

- Changing the strength and ductility of the reinforced concrete beams in compression due to induced micro-cracking by expansion of steel bars.
- Changing the tension stiffening of corroded tensile steel bars due to losing concrete cover and bond between concrete and steel bars.
- Changing the bond between steel bars and concrete depending on the corrosion level as illustrated in **Figure 2-26 (c)**.

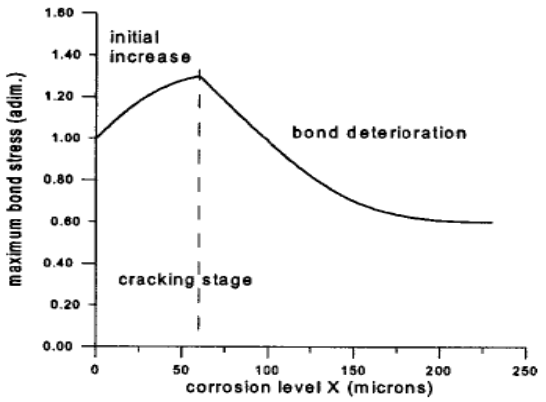
**Figure 2-26 (d)** and **Figure 2-26 (e)** show a comparison between experimental results and finite element results for un-corroded and corroded beams tested under four-point bending, respectively. The results demonstrate that the analytical assessment of corroded reinforced concrete beams can be achieved by simulating concrete cover spalling, reducing the cross-sectional area of corroded steel bars, and decreasing the cross-section of the beam, which leads to deterioration of the stiffness and bond conditions between concrete and steel reinforcement. As result, the strength and ductility of the corroded reinforced concrete beams are affected.



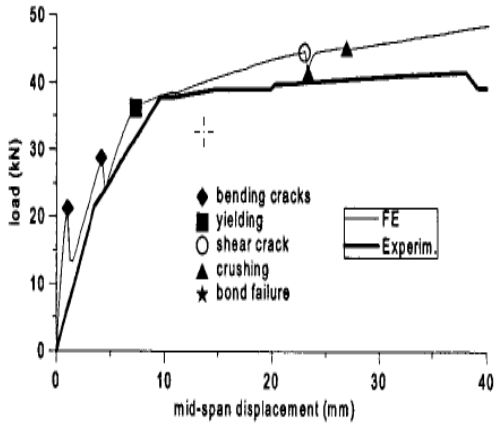

a) Constitutive models a) concrete, b) steel and c) bond



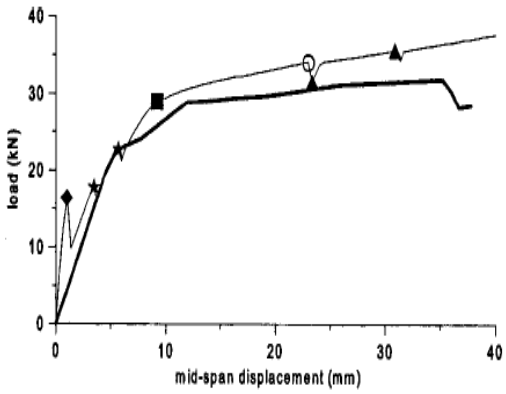

b) Finite element mesh




c) Variation of bond strength with corrosion level




d) Non-corroded beam Type 11, No. 11.1

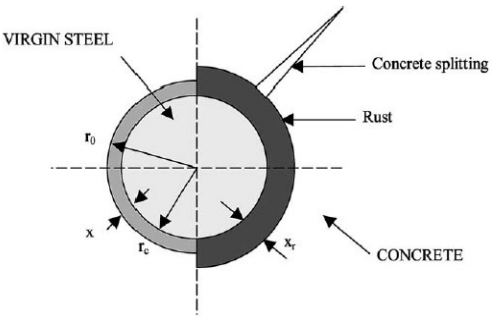



e) Corroded beam Type 11, No. 11.5

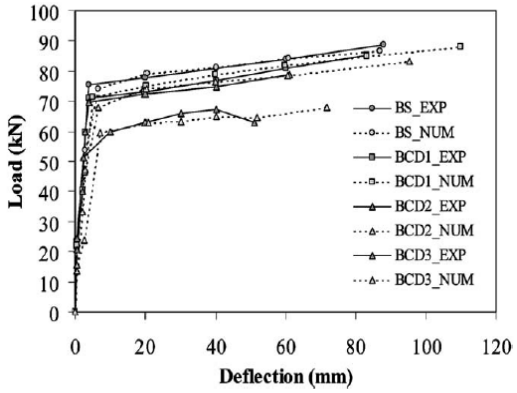
Figure 2-26 Finite element mesh and results from Coronelli and Gambarova (2004)

### 2.3.4 Previous Studies of Corrosion Modeling in RC Beams

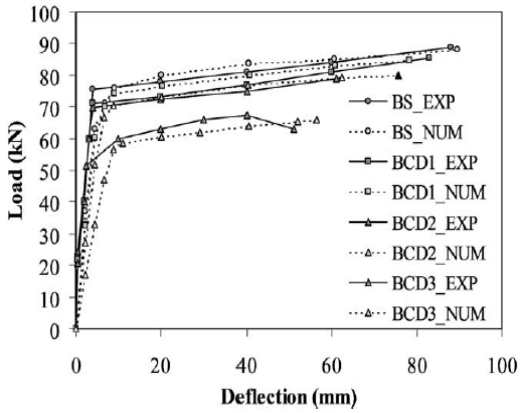
Dekoster et al. (2003) proposed a finite element model to evaluate the flexural response of corroded reinforced concrete beams. The corroded beams were modelled using the CASTEM 2000 software. The concrete model was modelled by either an elasto-plastic model based on smeared cracking or by a damage approach in which the concrete modulus was modified using a damage variable (D), whose value varied between 0 (virgin material) and 1 (failure). The steel reinforcement was modeled using an elasto-plastic model with two-node linear bar elements. Rust was modelled as an elastic interface material between the steel and concrete to simulate the increase in volume of the initial steel section, as illustrated in **Figure 2-27 (a)**. The proposed model was validated using the data of two experimental studies on beams with different dimensions and reinforcement data. **Figure 2-27 (b)** and **Figure 2-27 (c)** show the load-deflection curves for both the experimental and numerical results assuming uniform corrosion along the tensile reinforcement using the elasto-plastic (EPA) and damage (DA) approaches, respectively. The results demonstrated that the most fundamental parameters for modeling the flexural behaviour of corroded reinforced concrete beams were the mass loss of the steel bars and the degradation of the steel-concrete interface based on a layer of rust elements. In addition, the finite element results had acceptable results in terms of stiffness, yield load and maximum load when compared with the experimental ones. However, the ultimate deflection of the modeled beams was different than that of three experimental beams. A parametric analysis of the size of the layer of rust elements concluded that this should be small.




a) Cross-section of corroded steel bars



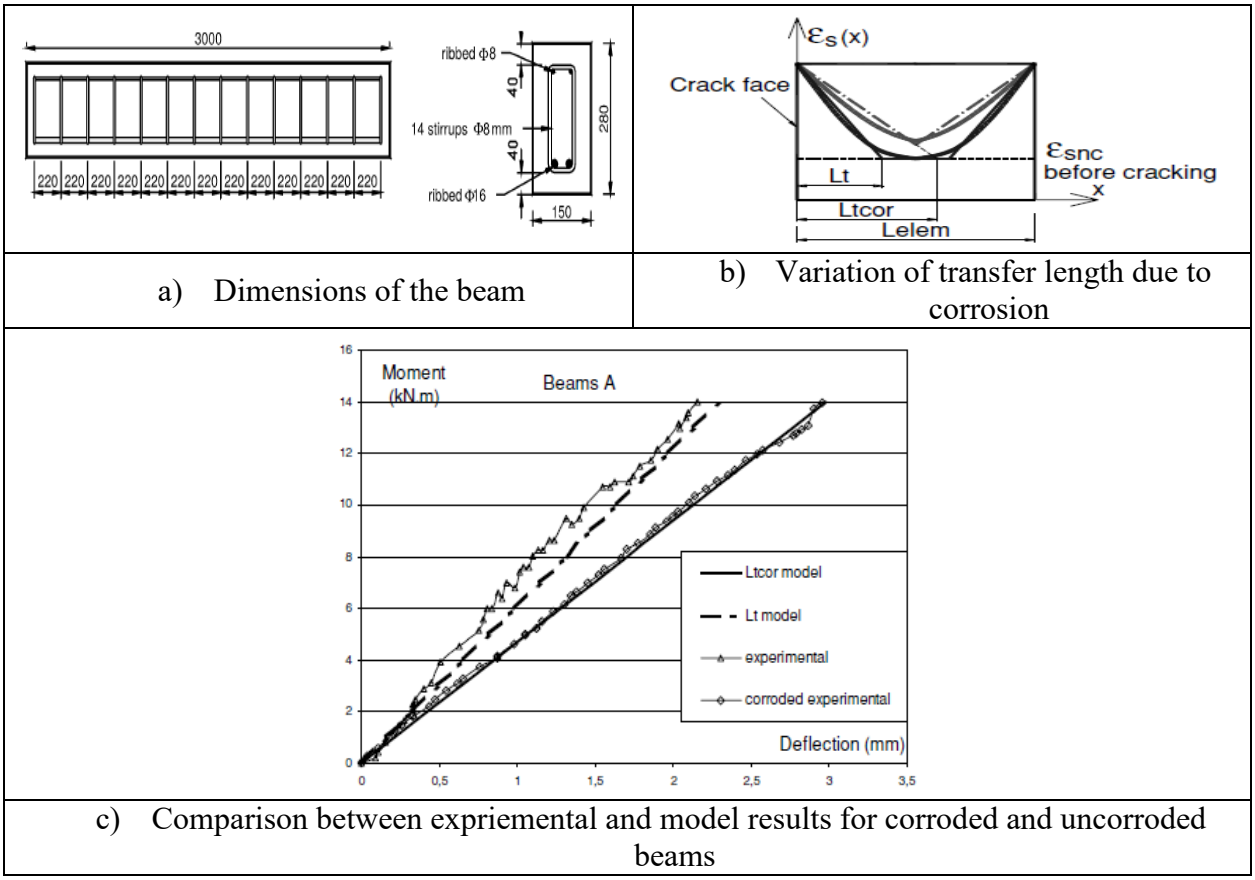

b) Load–deflection curves, EPA, rust element size of 1 mm




c) Load–deflection curves, DA, rust element size of 1 mm

Figure 2-27 Corrosion modelling and results from Dekoster et al. (2003)

François et al. (2006) proposed a model using finite element analysis to evaluate the mechanical behaviour of corroded reinforced concrete beams tested under three-point bending. The mechanism of the model relied on the execution of macro-elements with a length equal to the distance among two flexural cracks and the height equal to the beam height. The feasibility of the proposed model was assessed by using experimental data from corroded reinforced concrete beam tests, as shown in **Figure 2-28 (a)**. **Figure 2-28 (b)** shows that the transfer length between concrete and steel bars was increased to consider the effect of corrosion on the bond between concrete and steel bars in the damaged region of the corroded beams. The proposed model had acceptable results when compared with the experimental results for both corroded and uncorroded beams as illustrated in **Figure 2-28 (c)**. The mechanical behaviour of the corroded reinforced concrete beams changed due to the corrosion-induced loss of bond between the concrete and reinforcement.




a) Dimensions of the beam

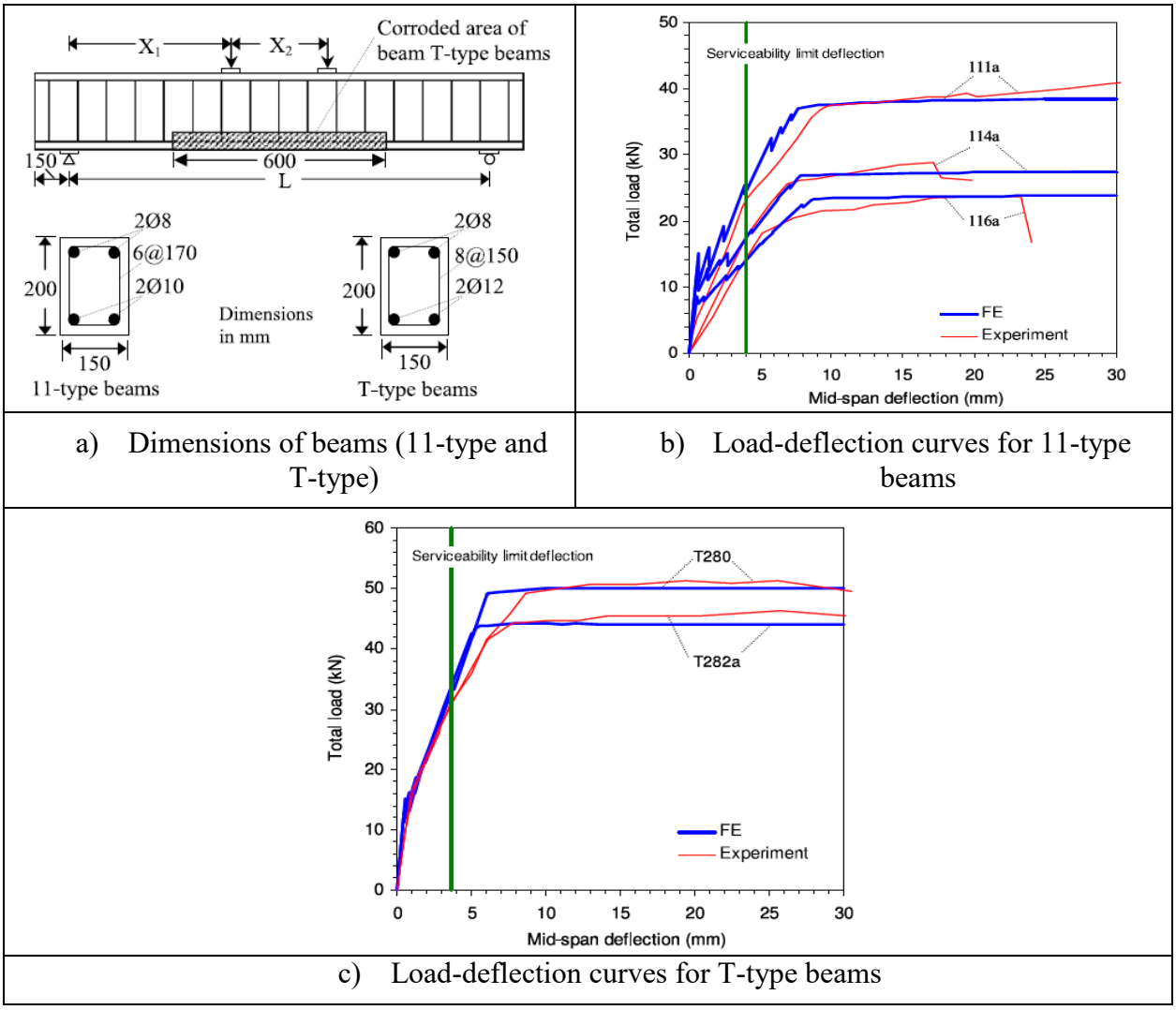
b) Variation of transfer length due to corrosion

c) Comparison between expriemental and model results for corroded and uncorroded beams

Figure 2-28 Beam dimensions and results from Francois et al. (2006)

Kallias and Rafiq (2010) investigated the effect of corrosion on reinforced concrete beams using the non-linear finite element package DIANA. Four-node plane-stress elements were used to model the concrete. All the steel reinforcement was modelled using truss elements with an elasto-perfectly plastic approach. In addition, 2D interface elements were used to model the bond between the tensile steel bars and concrete. The finite element model was validated using two experimental studies of reinforced concrete beams (11-type beams and T-type beams) with different geometry and reinforcement details, as illustrated in **Figure 2-29 (a)**. The corrosion process was accelerated on either the entire reinforcement cage or the tensile reinforcement and stirrups located in the mid-600 mm of the beams. **Figure 2-29 (b)** and **Figure 2-29 (c)** present that the finite element model results had good prediction in terms of load-deflection when compared with the experimental results. The obtained results highlighted the mass loss of the steel bars as one of the main causes to reduce the strength and bending stiffness of the corroded reinforced concrete beams. Furthermore, the compressive strength of the concrete had only a slight effect on the predicted

load-deflection behaviour of either uncorroded or corroded beams. The increase of bond deterioration between concrete and steel bars led to an increase in the crack widths.




a) Dimensions of beams (11-type and T-type)

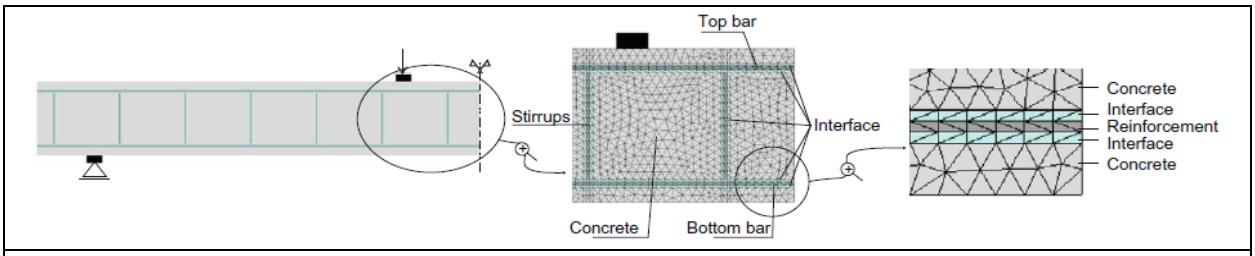
b) Load-deflection curves for 11-type beams

c) Load-deflection curves for T-type beams

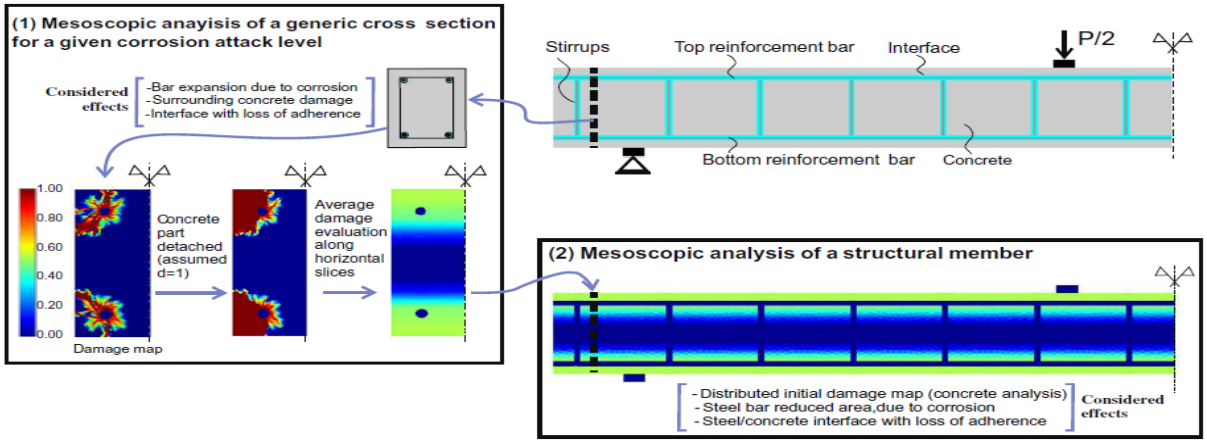
Figure 2-29 Beam dimensions and results from Kallias and Rafiq (2010)

Sánchez et al. (2010) utilized a finite element approach to simulate the deterioration of corroded reinforced concrete beams. The concrete was modeled using a continuum strong discontinuity approach (CSDA), and the steel reinforcement was modelled using an elasto-plastic constitutive relation. In addition, the steel-concrete interface was simulated using contact linear triangle elements. A 2D mesoscopic model was applied to predict the residual load carrying capacity of the corroded reinforced cocnrete beams, with beam components (concrete, steel and steel-concrete interface) as shown in **Figure 2-30 (a)**. **Figure 2-30 (b)** illustrates the methodology of linking

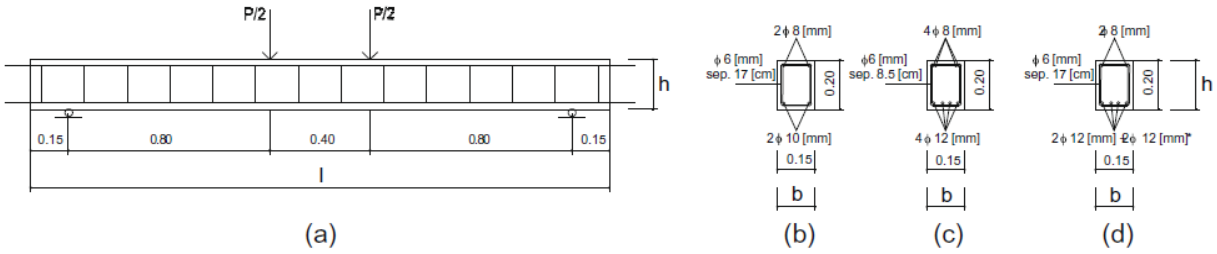
cross-sectional damage to the structural member (beam) model in the finite element software. The performance of the finite element model was validated using experimental studies of three corroded reinforced concrete beams with different dimensions as illustrated in **Figure 2-30 (c)**. The corrosion process was applied on the entire reinforcement of the beams. **Figure 2-30 (d)** and **Figure 2-30 (e)** show the load-deflection curves of the numerical model when compared with the experimental studies of the corroded beams (beams 11-4 and 31-3). The results show that the finite element model can simulate the majority of the corrosion mechanisms such as steel bars expansion, damage/cracking in the concrete, yielding in the steel bars, bond stress degradation at the interface and steel cross-section reduction.



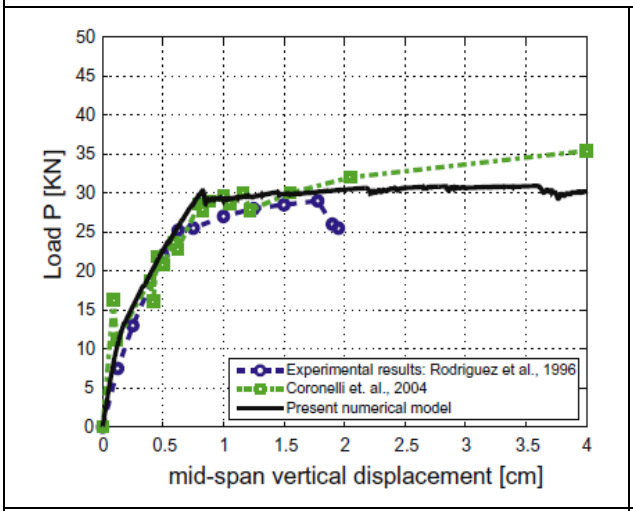

a) Mesoscopic 2D model for longitudinal section of the beam



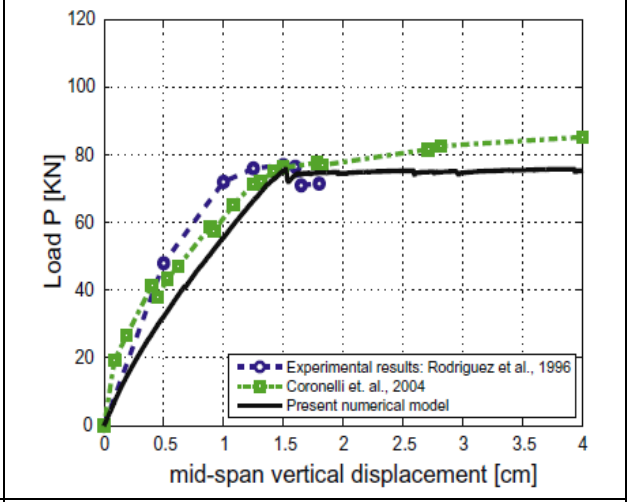

b) The strategy scheme of linking cross-sectional and structural member (beam) models




c) The geometry of the beams




d) Load-deflection curves for beam 11-4



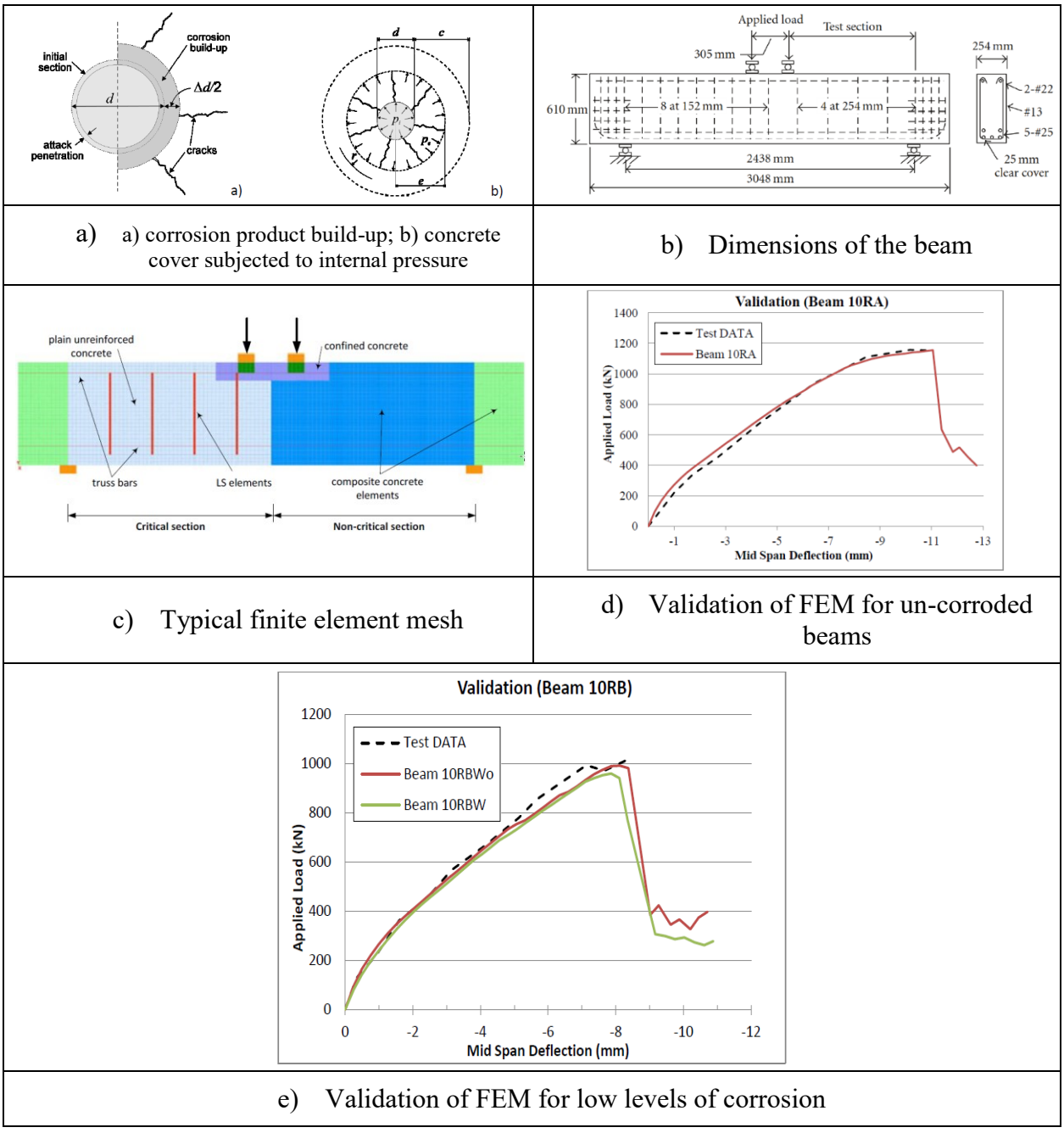

e) Load-deflection curves for beam 31-3

Figure 2-30 Beam dimensions and results from Sanchez et al., (2010)

Bernard (2013) presented the methodology of using finite element modelling to simulate the shear resistance of corroded reinforced beams. A 2D nonlinear finite element software (VecTor2) was used for the simulation. Plain concrete was modelled with 4-node rectangular plane-stress elements. Shear reinforcement (stirrups) was modelled as smeared across concrete elements for non-critical sections and as truss elements for critical sections where corrosion was simulated. The longitudinal reinforcement was modelled using 2-node truss elements with one degree of freedom per node. Perfect bond was used for all steel reinforcement during the modelling. Corrosion damage was introduced into the model by reducing the cross-sectional area of the stirrups and by inducing cracks in the concrete surrounding the stirrups through pre-strains to simulate corrosion product build-up, as given by **Eq. (2-7)** and illustrated in **Figure 2-31 (a)**. The model was validated using experimental data from reinforced concrete beams, with dimensions and a typical finite element shown in **Figure 2-31 (b)** and **Figure 2-31 (c)**, respectively. The load-deflection curve of the finite element model for an un-corroded beam had a good agreement with the experimental results in terms of stiffness and the maximum strength and deflection as presented in **Figure 2-31 (d)**. The modelled beams with and without pre-straining had also reasonable results in terms of their behaviour when compared with the experimental beam with a mass loss of 13.2% as illustrated in **Figure 2-31 (e)**. Finally, at high levels of corrosion the induced cracks using pre-straining became more effective in terms of reproducing the induced damage at failure.

$$\varepsilon_{corr} = \frac{d' - d}{d + 2c} \tag{2-7}$$

where: $\varepsilon_{corr}$ = pre-strain, $d'$ = expanded diameter, $d$ = original diameter, $c$ = concrete cover.




a) a) corrosion product build-up; b) concrete cover subjected to internal pressure

b) Dimensions of the beam

c) Typical finite element mesh

d) Validation of FEM for un-corroded beams

e) Validation of FEM for low levels of corrosion

Figure 2-31 Beam dimensions and results from Bernard (2013)

Table 2-4 Summary of the studies on corrosion modeling

| Focus | Authors | No. of beams | Beam dimensions | | | $f'_c$ (MPa) | Longitudinal reinforcement | | Stirrups | | Concrete cover (mm) | Salt (%) | Mass loss (%) | Corrosion location | Corrosion method, | $\mu A/cm^2$ or current (A) | Corrosion duration (days) | Test type |
|---|---|---|---|---|---|---|---|---|---|---|---|---|---|---|---|---|---|---|
| | | | B (mm) | H (mm) | L (mm) | | Top | Bottom | Size (mm) | S* (mm) | | | | | | | | |
| Flexure | Coronelli and Gambarova (2004) | 7 | 150 | 200 | 2000 | 34 – 50 | 2,4-8 | 2,4-10,12 | 6 | 85, 170 | - | - | - | - | - | - | - | - |
| | Francois et al (2006) | 2 | 150 | 280 | 3000 | 63 | 2-8 | 2-16 | 8 | 220 | 40 | - | - | - | N* | - | 6205 | 3PB* |
| | Dekoster et al (2003) | 2 | 150, 200 | 280, 250 | 2800, 2000 | 65.3, 70.1 | - | 12, 13 | - | - | - | - | - | B*FL* | N* | - | - | 4PB* |
| | Kallias and Rafiq (2010) | 2 | 150 | 200 | 2000, 1800 | 25 - 50 | 2-8 | 2-10, 12 | 6, 8 | 170, 150 | - | - | 11.1 – 39.16 | (Whole beams), (B*ML*, Stirrups) | Acc* | 100, 350 | - | 4PB* |
| | Sanchez et al (2010) | 8 | 150 | 200 | 2000 | 34 - 50 | 2,4-8 | 2,4-10,12 | 6 | 85, 170 | - | - | - | Whole beams | Acc* | 100 | - | 4PB* |
| Shear | Bernard (2013) | 4 | 254 | 610 | 3048 | 33.1 | 2-22 | 5-25 | 13 | 152, 254 | 25 | - | 13,23, 26 | Stirrups | Acc* | - | - | 4PB* |

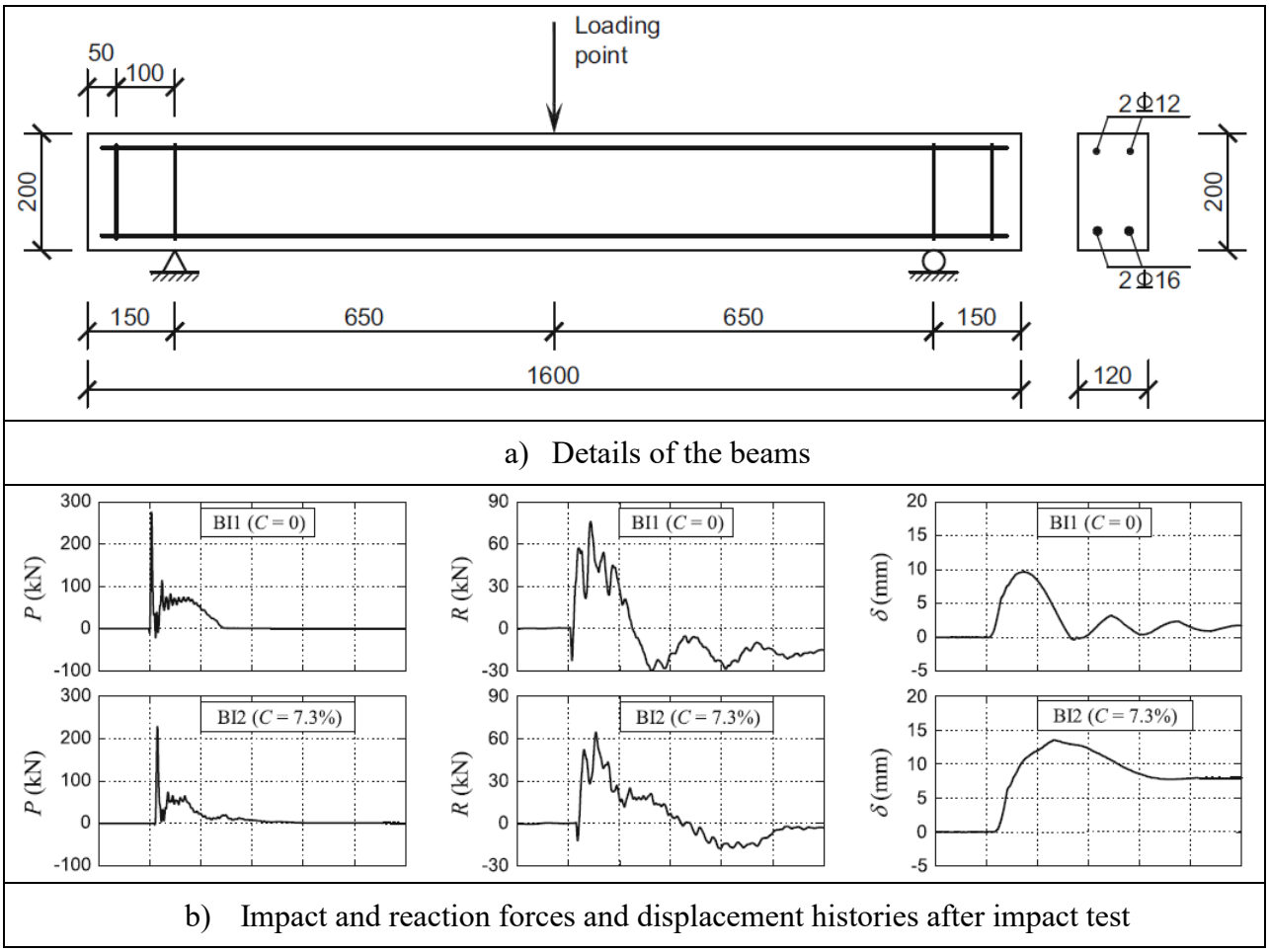
S*: Spacing. T*: Top. B*: Bottom. FL*: Full length. ML*: Mid length. Acc*: Accelerated corrosion process. 3PB*: Three-point bending test. 4PB*: Four-point bending test. N*: Natural corrosion.

## 2.4 Previous Studies on the Behaviour of Corroded Reinforced Concrete Beams Tested under Impact Test and Blast Loading

This section covers previous studies that have investigated the flexural behaviour of corroded reinforced concrete beams tested under impact, and other studies that examined structural performance under blast loading.

### 2.4.1 Impact Test

Dai et al. (2016) examined the behaviour of corroded reinforced concrete beams under impact loading. The reinforced concrete beams were built without stirrups. In total, eight reinforced concrete beams were built with dimensions of 120×200×1,600 mm as presented in **Figure 2-32 (a)**. The corrosion process was applied on the entire length of the top and bottom reinforcing steel bars. All the reinforced concrete beams were tested using a falling-weight impact and three-point bending tests. From the results, it was observed that the failure mode of the reinforced concrete beams was governed by shear. In addition, at high corrosion rates (up to 18% steel mass loss) the maximum impact force and reaction force were reduced in the reinforced concrete beams as illustrated in **Figure 2-32 (b)**. The energy dissipation capacity of the reinforced concrete beams under impact loading was also negatively affected by corrosion.



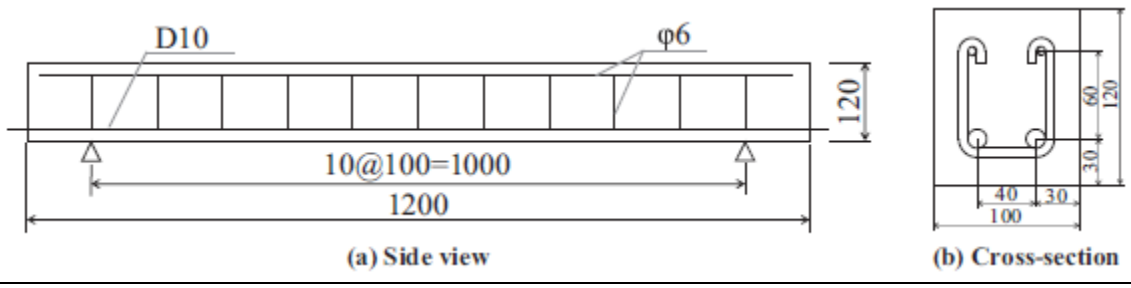

a) Details of the beams

b) Impact and reaction forces and displacement histories after impact test

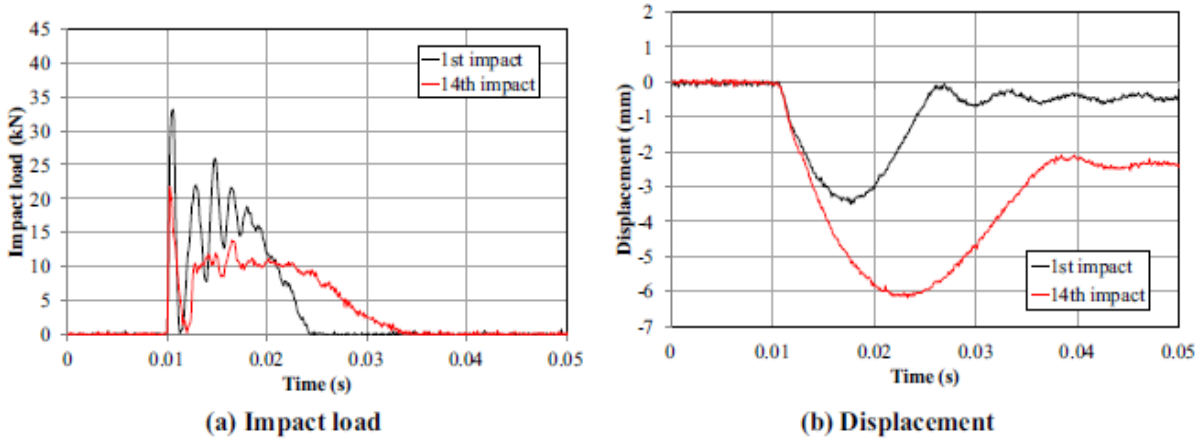
Figure 2-32 Beam dimensions and results from Dai et al. (2016)

Tamai et al. (2020) studied the effects of different levels of corrosion on the flexural response of RC beams using quasi-static and falling-weight impact load tests. Eighteen beams were constructed with dimensions of 100×120×1,200 mm as shown in **Figure 2-33 (a)**. The corrosion was applied on the tensile reinforcement using a current of 700 mA, while the contact points between the stirrups and tensile bars were insulated. The beams were tested in three-point bending using static or falling-weight impact setups. The obtained results showed that the stiffness and maximum strength of the corroded RC beams were reduced when static testing was applied. Under single impact loading, the corrosion degree had minor effects on the initial peak load and maximum amplitude of the response waveform; however, the second wave was reduced, with an increase in its duration. In addition, the maximum displacements and damage in the beams increased when the corrosion level increased (especially beyond 10%). This result can be observed when the

corrosion level reaches 12.8% in **Figure 2-33 (b)**. Under repeated impacts, the impact resistances of the corroded beams were 59% and 15% of that of the sound beam when the corrosion level reached 5.3% and 12.9%, respectively. Compared to static loading, the impact resistance was more significantly affected as the corrosion degree increased.




a) Dimensions and reinforcement layout of the beams




b) Beam impact response at corrosion level of 12.8%

Figure 2-33 Beam dimensions and results from Tamai et al. (2020)

### 2.4.2 Blast Loading

To the knowledge of the author no experimental research exists on the blast performance of corrosion-damaged RC structures. However, Yalciner (2014) presented an analytical study which examined the effect of blast loads on the performance of corroded and uncorroded reinforced concrete buildings. A corrosion rate of 0.4 $\mu$A/cm$^2$ was considered in the analysis. Three major corrosion effects were considered, including: loss of bar cross-sectional area, reduction in concrete strength and reduction in bond. The stress-strain relationship of concrete was modeled using the Kent and Park model, while the steel reinforcement was modeled using Mander's model. Reduction in concrete strength was taken into account using a model developed by Yalciner et al.

(2012). The model considers the effect of corrosion on volumetric expansion, which increases the member width. The increase in member width is calculated as follows:

$$b_f - b_0 = n_{bars}\left(\frac{4\pi\, d_s(t)}{(1-v_c)/\left(\frac{a}{b}\right)^{\sqrt{\alpha}} + (1+v_c)\left(\frac{b}{a}\right)^{\sqrt{\alpha}}} - \frac{2\pi b f_t}{E_{ef}}\right) \quad (2\text{-}8)$$

where: $b_f$ = Increased width by corrosion. $b_0$ = Original width, $n_{bars}$ = Number of the bars in the top layer, $d_s(t)$ = Thickness of corrosion product form, $v_c$ = Poisson's ration of concrete, $f_t$= Tensile strength of concrete, $E_{ef}$ = Effective elastic modulus of concrete ($a = (d_b + 2d_0)/2$), $d_b$= Diameter of reinforcement bars, $d_0$ = Thickness of the annular layer of concrete pores, $b$ = The outer radii of the thick wall cylinder ($b = S/2$), $S$ = Rebar spacing. Once the corrosion rate is known, the model can be used to reduce the concrete strength.

The ultimate bond strength of uncorroded and corroded reinforcing bars was also considered using the following relationships proposed by Yalciner et al. (2012):

For uncorroded: $\tau_{bu} = -2.7143 + 0.3621 f'_c + 2.3296\left(\frac{c}{D}\right)$ (MPa) (2-9)

For corroded: $\tau_{bu} = e^{(0.01572 f'_c + 0.22957\left(\frac{c}{D}\right) + 0.13946 C_L + 1.75913)}$ (MPa) (2-10)

where: $f'_c$ = Concrete compressive strength, $c$ = Concrete cover depth, $D$ = Diameter of steel bar.

The calculated bond strengths were then used to predict bar slippage using the model developed by Alsiwat and Saatcioglu (1992).

The reduced concrete strength, loss in bar cross-sectional area, reduced bond strength and slip rotations were then used to modify the moment-curvature relationships and used to define the member force-deformation relationships using a plastic-hinge model defined in FEMA-356.

Different blast load scenarios were considered, with four different explosion standoff distances of 6, 9, 12 and 24 m. While the damage of the structure was reduced as the explosion distance was increased, corrosion-induced damage such as increase in crack widths and reduction of steel cross-sectional area had major impacts on the blast performance of the corroded structural members, leading to premature yielding of steel reinforcement and reduced energy absorption capacity.

## 2.5 Research Gap

Based on the literature review, extensive studies have been conducted over the past 50-60 years to study the problem of reinforcement corrosion on the quasi-static shear and flexural responses of reinforcement concrete beams. However, most of the studies have focused on specimens with corrosion concentrated at mid-span or over the entire length of the longitudinal reinforcement of RC beams. Limited research has investigated extensively the effect of corrosion location, in particular that concentrated in the anchorage regions of reinforced concrete beams. Compared to flexural tests, studies focussed on shear response are also relatively more limited. Thus, there is a need to conduct research examining the influence of the corrosion process at different locations of the reinforced concrete beams (full length, mid length, ends length and stirrups).

Compared to research under static loads, the literature on the effect of reinforcement corrosion on the response of flexural members subjected to dynamic loading is scarce, with no published experimental research on the blast performance of corrosion-damaged RC members. Thus, there is a need for this research to better understand the effect of extreme blast loading on the flexural and shear behaviours of corroded reinforced concrete beams. Moreover, there is need to study the influence of parameters such as corrosion mass loss % and corrosion location on the dynamic response of such beams.

Previous research demonstrates the ability of finite element modelling to predict the static load response of corrosion damaged beams. However, given the limited parameters studied in most experiments, FE simulations should be used to conduct further parametric studies related to influential parameters that affect the structural response of corrosion-damaged RC beams. Recent studies also demonstrate the ability of nonlinear FE modelling to predict the impact and blast response of RC beams; however, research is needed to examine the ability of FE modelling to provide reliable predictions of the blast response of corrosion-damaged RC structures. There also a need for further research on the ability of single-degree-of-freedom (SDOF) analysis to predict the blast response of corrosion-damaged RC structure.

# Chapter 3: Experimental Program

## 3.1 Chapter Overview

This chapter presents the details of the experimental program in which twenty-four reinforced concrete beams were built and tested under static and blast loads. The beams, which had different reinforcement details, were subjected to an accelerated corrosion regime to different corrosion levels and locations in their longitudinal or transverse steel reinforcement. This chapter summarizes the following details related to the test program: the specimen design, material properties, construction procedure, experimental setups, and testing procedure.

## 3.2 Beams Geometry

A total of twenty-four reinforced concrete beams were built and tested in this research program. Eighteen beams were subjected to an accelerated corrosion process on their longitudinal tension steel reinforcement (full length, middle length and ends length) or on their transverse shear reinforcement to achieve a targeted steel mass loss of 15% and 30%. Ten beams were tested statically under four-point bending test, while fourteen beams were tested dynamically under blast loading using the University of Ottawa shock tube. The beams design details are shown in **Figure 3-1** and **Table 3-1**.

In all cases, the beams had dimensions of 125×250×2,440 mm and were tested under simply-supported conditions with a clear span of 2,232 mm between the supports with a constant moment region of 750 mm and shear spans of 741 mm. All the beams were reinforced with 2-10M (top) compression bars; however, there were variations in the amounts of tension steel reinforcement, with three sets of beams each consisting of 2-10M, 2-15M and 2-25M, respectively. The 10M and 15M steel bars were provided with a 90-degree hook at their ends, while the 25M bars were kept straight. The transverse reinforcement consisted of U-shaped stirrups made from 6.3-mm wire spaced at 100 mm throughout the full length of the beam. The clear concrete cover under the stirrups was 40 mm for all the beams.

The beams were classified into three groups (10M, 15M and 25M groups) based on the longitudinal steel bars size. **Table 3-1** presents the details for the beams of each group, including the beam ID, steel reinforcement details, corrosion location, target mass loss and loading type.

The specimen nomenclature follows the following logic: CB or B refers to control beam or corroded beam, respectively; FC, MC and SC refers to corrosion of the longitudinal tension steel over the full length, mid-length (central 750 mm) or shear spans (end 741 mm regions), respectively, while EMC refers to extreme mid-length corrosion; SHC refers to corrosion in the shear/transverse stirrups; 10M, 15M and 25M refers to the bar size in the tension region; and, ##% refers to the percentage of actual corrosion in terms of mass loss. CR used in the nomenclature of some beams indicates that the cover was removed (i.e., the beam was built without cover) prior to the corrosion process.

For example: CB-10M-0% is the control beam constructed with 2-10M tension bars without corrosion (0% mass loss), while B-FC-10M-13% is the companion beam with full corrosion over the entire length of the 10M tension bars with an actual mass loss of 13%. In comparison, B-MC-10M-13% has corrosion in the mid-span only with a mass loss of 13%, while B-SC-10M-11% has corrosion at the ends of the 10M steel bars with an actual mass loss of 11%. Similarly, B-EMC-10M-22% is a beam with extreme corrosion in the mid-span region with a mass loss of 22% in the 10M tension bars. B-CR-MC-15M-4% is a beam built with 2-15M bars but without cover and 4% corrosion in the mid-span region. Finally, B-SHC-25M-10% is a beam with 2-25M bars and corroded shear reinforcement with 10% mass loss in the stirrups.

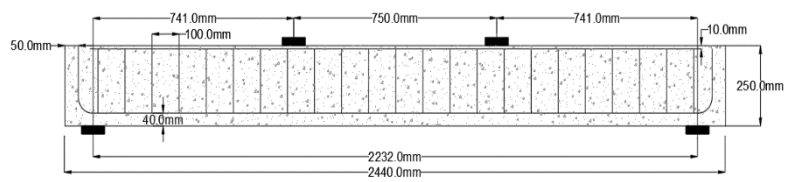
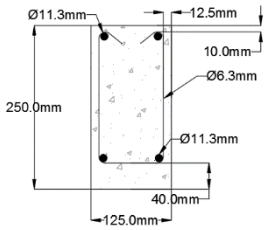
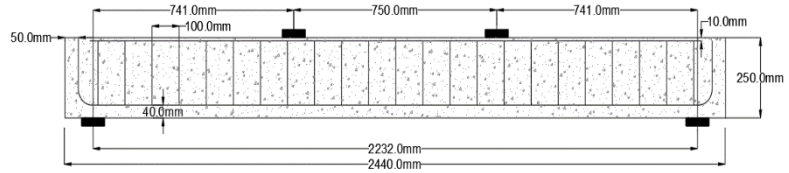
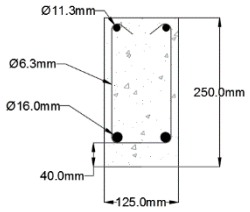
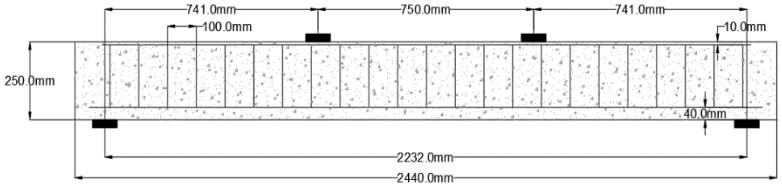
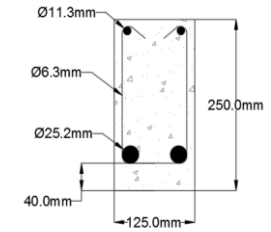
| Steel reinforcement details and geometry | Cross-section |
|---|---|
|  |  |
| a) 10M beams | |
|  |  |
| b) 15M beams | |
|  |  |
| c) 25M beams | |

Figure 3-1 The geometry of the beams with reinforcement details

Table 3-1 Main properties of the beams

| Groups | Beam ID | Top | Longitudinal reinforcement | | | Stirrups | | Corrosion location | Mass loss % (T) | Mass loss % (A) | Test type |
|---|---|---|---|---|---|---|---|---|---|---|---|
| | | | $\rho_t$(%) | Bottom | $\rho_b$(%) | Size (mm) | s*(mm) | | | | |
| 10M | CB-10M-0% | 2-10M | 1 | 2-10M | 1 | 6.3 | 100 | - | 0 | 0 | S/D |
| | B-FC-10M-13% | 2-10M | 1 | 2-10M | 1 | 6.3 | 100 | Full length | 15 | 13 | S |
| | B-MC-10M-13% | 2-10M | 1 | 2-10M | 1 | 6.3 | 100 | Middle length (central 750 mm) | 15 | 13 | S |
| | B-SC-10M-11% | 2-10M | 1 | 2-10M | 1 | 6.3 | 100 | Ends spans (2x 741 mm) | 15 | 11 | S |
| | B-MC-10M-14% | 2-10M | 1 | 2-10M | 1 | 6.3 | 100 | Middle length (central 750 mm) | 30 | 14 | S |
| | B-MC-10M-11% | 2-10M | 1 | 2-10M | 1 | 6.3 | 100 | Middle length (central 750 mm) | 15 | 11 | D |
| | B-MC-10M-15% | 2-10M | 1 | 2-10M | 1 | 6.3 | 100 | Middle length (central 750 mm) | 30 | 15 | D |
| | B-SC-10M-7% | 2-10M | 1 | 2-10M | 1 | 6.3 | 100 | Ends spans (2x 741 mm) | 15 | 7 | D |
| | B-FC-10M-12% | 2-10M | 1 | 2-10M | 1 | 6.3 | 100 | Full length | 15 | 12 | D |
| | B-EMC-10M-22% | 2-10M | 1 | 2-10M | 1 | 6.3 | 100 | Middle length (central 750 mm) | 30 | 22 | D |
| | B-CR-MC-10M-5% | 2-10M | 1 | 2-10M | 1 | 6.3 | 100 | Middle length (central 750 mm) | 30 | 5 | D |
| 15M | CB-15M-0% | 2-10M | 1 | 2-15M | 1.6 | 6.3 | 100 | - | 0 | 0 | S/D |
| | B-MC-15M-10% | 2-10M | 1 | 2-15M | 1.6 | 6.3 | 100 | Middle length (central 750 mm) | 30 | 10 | S |
| | B-MC-15M-12% | 2-10M | 1 | 2-15M | 1.6 | 6.3 | 100 | Middle length (750 mm) | 30 | 12 | D |
| | B-EMC-15M-17% | 2-10M | 1 | 2-15M | 1.6 | 6.3 | 100 | Middle length (central 750 mm) | 30 | 17 | D |
| | B-CR-MC-15M-4% | 2-10M | 1 | 2-15M | 1.6 | 6.3 | 100 | Middle length (central 750 mm) | 30 | 4 | D |
| 25M | CB-25M-0% | 2-10M | 1 | 2-25M | 4 | 6.3 | 100 | - | 0 | 0 | S/D |
| | B-SHC-25M-10% | 2-10M | 1 | 2-25M | 4 | 6.3 | 100 | Stirrups (full span) | 15 | 10 | S |
| | B-SHC-25M-12% | 2-10M | 1 | 2-25M | 4 | 6.3 | 100 | Stirrups (full span) | 30 | 12 | S |
| | B-SHC-25M-11% | 2-10M | 1 | 2-25M | 4 | 6.3 | 100 | Stirrups (full span) | 15 | 11 | D |
| | B-SHC-25M-12% | 2-10M | 1 | 2-25M | 4 | 6.3 | 100 | Stirrups (full span) | 30 | 12 | D |

Note: s* = Stirrups spacing in mm. S = Static test. D = Dynamic test. T = Target mass loss. A = Actual mass loss.

### 3.2.1 10M Group

This group included a total of twelve (12) beams, which were doubly-reinforced with 2-10M bars each for the tension and (top) compression reinforcement. Transverse reinforcement consisted of U-shaped stirrups made from 6.3-mm wires spaced at 100 mm throughout the full beam length. The group included 2 control beams and ten beams with different corrosion characteristics classified based on the location of the corrosion on the tensile steel bars (full length, mid length and ends length) and the % of mass loss, which varied between 5% and 22%. Beam B-CR-MC-10M-5% also had its cover removed over the central region before application of the corrosion regime. Five beams were tested under static four-point bending with the other seven beams tested under blast loading.

### 3.2.2 15M Group

The second beam group included six (6) specimens, which were reinforced with 2-15M longitudinal bars in tension and 2-10M longitudinal bars in compression (top). U-shaped stirrups made from 6.3-mm wire were spaced at 100 mm throughout the full beam length. The set included two control beams without corrosion and four companion beams with different levels of mid-length corrosion, which varied between 4% and 17% of steel mass loss. Similar to the previous group, one beam was designed to have both reinforcement corrosion and cover loss over the central beam region (B-CR-MC-15M-4%). This set included two beams tested under static loading and four beams tested under dynamic blast loading.

### 3.2.3 25M Group

The third and final test group consisted of six (6) reinforced concrete beams, which were constructed with 2-25M longitudinal bars in tension and 2-10M bars in compression (top). Transverse reinforcement consisted of “minimum” U-shaped stirrups made from 6.3-mm wire spaced at 100 mm throughout the full length of the specimens. The longitudinal steel and stirrup design was selected to ensure a shear-to-flexural resistance ratio near 1.0 to study the effect of corrosion in more shear-dominant beams. The beam classification was related to the amount of corrosion on the stirrups based on % mass loss of 10-12% (four beams), with two control beams without corrosion. Three beams were tested statically and the remaining three beams were tested under blast loading.

## 3.3 Materials

This section provides the details of the materials used in this research in terms of concrete mix design and steel reinforcement stress-strain relationships. The properties of the concrete in terms of fresh and hardened states are provided in Section 3.4.

### 3.3.1 Concrete Mix

The same concrete mix design was used for all beams and consisted of water, general use (GU) Portland cement, fine aggregates (concrete sand), coarse aggregate with a maximum size of 19 mm and 3% salt (NaCl), which was added as a percentage of the cement weight. The quantities of the different mix components are listed in **Table 3-2**.

Table 3-2 Concrete mix components

| **Mix components** | **Quantities** |
|---|---|
| Water | 199 kg/m$^3$ |
| GU Cement | 410 kg/m$^3$ |
| Coarse aggregate | 1099 kg/m$^3$ |
| Fine aggregate | 609 kg/m$^3$ |
| Salt | 12.3 kg/m$^3$ |

### 3.3.2 Steel Reinforcement Bars

Four types of steel reinforcement were used in this research. The 10M bars with diameter of 11.3 mm and cross-sectional area of 100 $mm^2$ were used as compression (top) bars in all beams, and as tension steel in the "10M group" specimens. The 15M bars with diameter of 16 mm and cross-sectional area of 200 $mm^2$ were used as tension reinforcement in the second group of specimens, while the 25M bars with diameter of 25.2 mm and cross-sectional area of 500 $mm^2$ were used in the third group. In all cases, smooth steel wire with a diameter of 6.3 mm and cross-sectional area of 32 $mm^2$ was used as transverse reinforcement.

Testing of the 10M, 15M and 6-mm steel coupon samples was conducted using a GALDABINI SUN 60 Universal Floor Standing Testing Machine as illustrated in **Figure 3-2**. The 25M steel bar was not tested due to the limitation in capacity of the testing machine. The properties of the tested steel bar types are summarized in **Table 3-3**, including bar diameter and area, yield strain and strength, ultimate strain and strength and strain at rupture. In addition, the stress-strain curves for the three bar types and their comparison are shown in **Figure 3-3**.




Figure 3-2 GALDABINI SUN 60 Universal Floor Standing Testing Machine, Ottawa University

Table 3-3 Physical and average mechanical properties of steel bars

| Steel type | $d_b$ (mm) | $A_b$ ($mm^2$) | Yield | | Ultimate | | Rupture |
|---|---|---|---|---|---|---|---|
| | | | $\varepsilon_{ey}$ | $f_y$ (MPa) | $\varepsilon_{eu}$ | $f_u$ (MPa) | $\varepsilon_{er}$ |
| 6.3 | 6.3 | 32 | 0.0042 | 533.69 | 0.046 | 617.75 | 0.058 |
| 10M | 11.3 | 100 | 0.0023 | 507.61 | 0.115 | 658.90 | 0.136 |
| 15M | 16 | 200 | 0.0029 | 478.81 | 0.103 | 653.30 | 0.115 |

$d_b$ = Steel bar diameter. $A_b$ = Steel bar area. $\varepsilon_{ey}$ = Yielding strain. $f_y$ = Yielding stress. $\varepsilon_{eu}$ = Ultimate strain. $f_u$ = Ultimate stress. $\varepsilon_{er}$ = Rupture strain

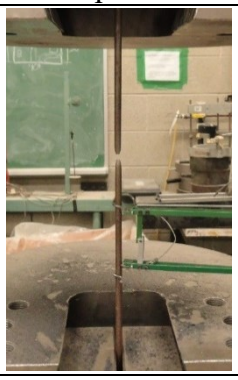
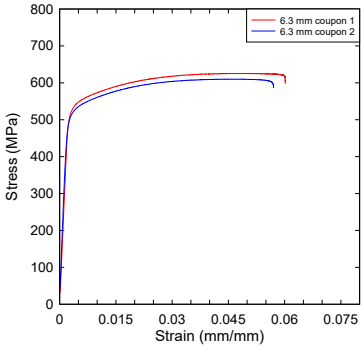
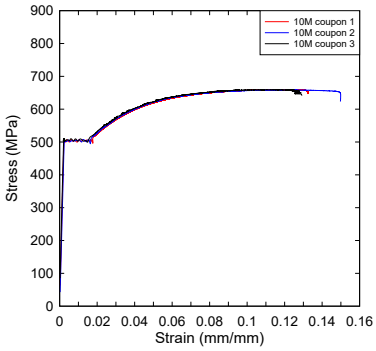
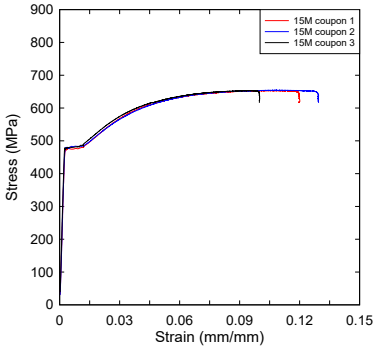
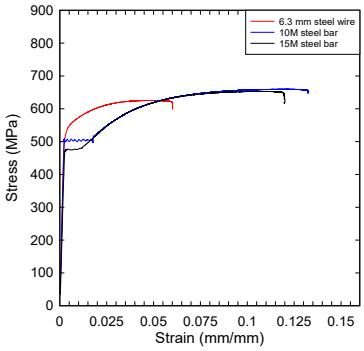
| Coupon test | Stress-strain curves |
| --- | --- |
|  |  |
| a) 6.3-mm steel wire | |
|  |  |
| b) 10M steel bar | |
|  |  |
| c) 15M steel bar | |
|  | |
| d) Comparison between steel bars | |

Figure 3-3 Stress-strain curves for each steel bar

## 3.4 Construction Procedure

All the twenty-four reinforced concrete beams were built at the University of Ottawa Structures Laboratory. This procedure included: preparing the wood formwork of the beams, bending the steel bars, painting the steel bars with epoxy, building the steel bar cages, installing strain gauges, installing electrical wires for the accelerated corrosion process, casting of the concrete and curing.

### 3.4.1 Preparation

The wood formwork that was used to cast the beams was built from plywood and each form was suitable for seven beams. Each formwork had as base a plywood sheet of 4'× 8'×1/2". The interior and sides of the form were built using plywood sheets of 4'× 8'×3/4", which was cut according to the height of the beams as illustrated in **Figure 3-4**. In addition, the sides of the formwork were supported by two wood studs with dimensions of 2" × 4" × 8'.

The steel cages of all the beams were built with 2-10M longitudinal straight steel bars in the compression zone. In the tension zone, the beams were reinforced with three different types of longitudinal steel bars (10M, 15M and 25M). The 10M and 15M steel bars were bent at their ends with 90-degree hooks, while the 25M steel bars were kept straight. The tensile reinforcement was coated using Plasti Dip (epoxy) coating at different locations (ends and mid-length) as presented in **Figure 3-5 (a)** and **(b)**. For the beams with corroded shear reinforcement, the longitudinal reinforcement in compression and tension zones was isolated using electrical tape to prevent corrosion as shown in **Figure 3-5 (c)**.

Transverse reinforcement consisted of U-shaped (open) stirrups made from 6.3-mm wires which were bent manually as shown in **Figure 3-6 (a)**. These stirrups were spaced at 100 mm throughout the full length of the specimens. In the 10M and 15M groups, the stirrups were isolated using electrical tape to target corrosion in the tension reinforcement and avoid corrosion in the stirrups, as shown in **Figure 3-6 (b)**. **Figure 3-7** shows the different steel cages after construction.

Strain gauges were installed at the mid-span of the tensile reinforcement using the following procedure: 1) the mid-span region of two tension steel bars was prepared (made smooth) using a manual grinder as shown in **Figure 3-8 (a)**; 2) strain gauges were placed at these locations, as shown in **Figure 3-8 (b)**; and, 3) the strain gauges were protected using electrical tape, as shown

in **Figure 3-8 (c)**. Two types of strain gauges were used; 120-Ω gauges were installed on the beams to be tested statically, while the 350-Ω type was used for the beams tested dynamically.

Electrical wires were installed in some steel cages to ensure the accelerated corrosion process. This was done by placing the electrical wire in the desire location of corrosion on the tensile steel bar, and this wire was fixed using stainless steel clamps as illustrated in **Figure 3-9 (a)**. For corroded shear reinforcement, all the stirrups were connected with 6.3-mm wire using welding, and this wire was connected directly to the power supply using an electrical wire as shown in **Figure 3-9 (b)**.

Prior to casting, the formwork was oiled to allow easy removal of the beams after casting and to make this form reusable. Plastic chairs with 40-mm height were placed inside the formwork after oiling to ensure the desired concrete cover. Finally, steel cages were placed inside the formwork prior to concrete casting.

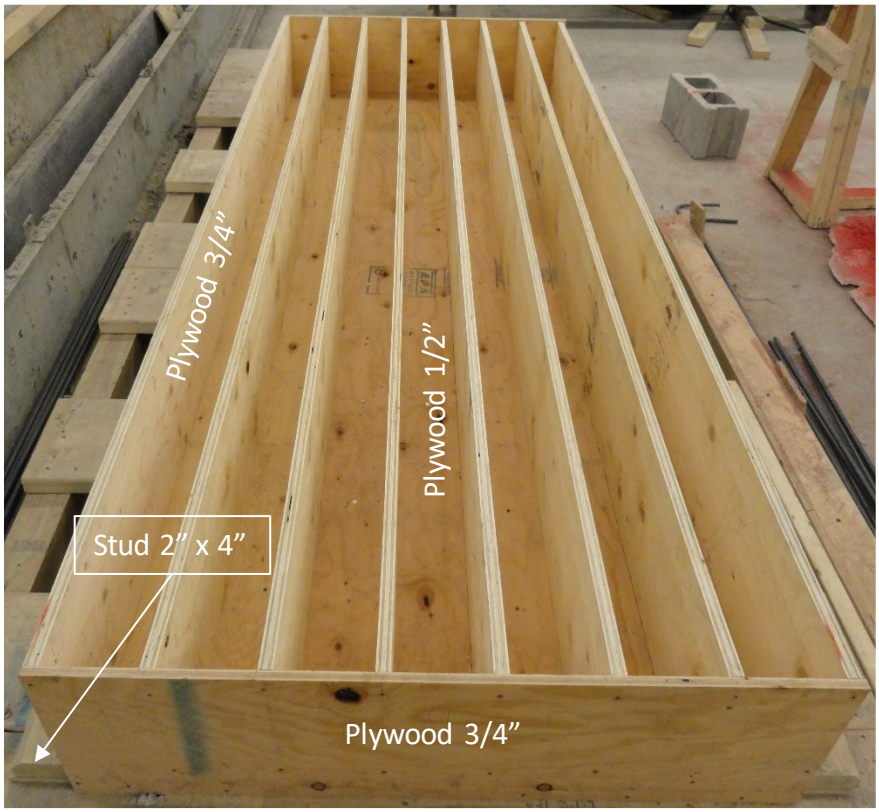
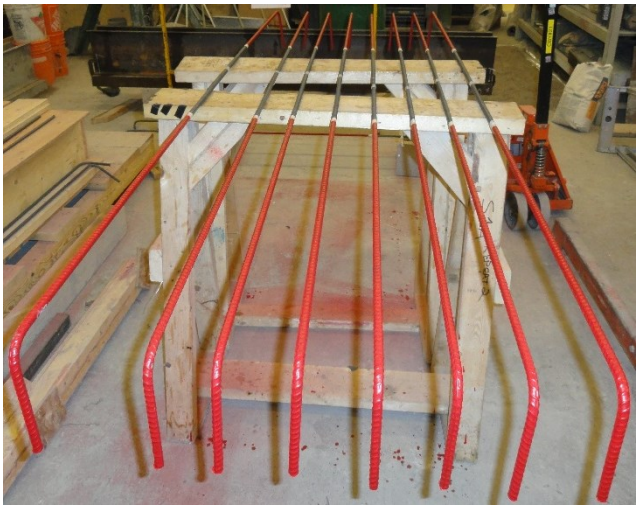



Figure 3-4 Formwork of the beams



a) Epoxy-coating on the longitudinal reinforcement ends



b) Epoxy-coating on the longitudinal reinforcement mid length

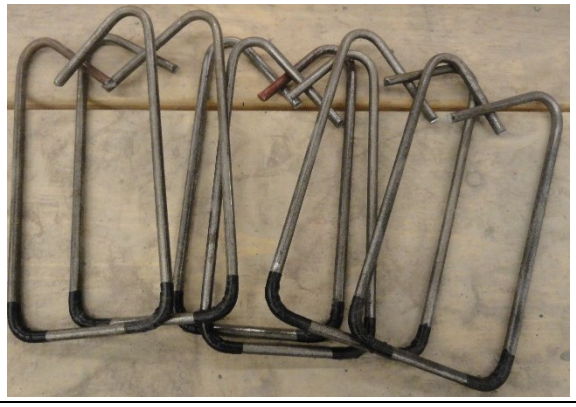


c) Isolated steel bars in tension and compression zones

Figure 3-5 Forming steel cages



a) Uninsulated stirrups



b) Insulated stirrups

Figure 3-6 U-shaped stirrups



a) 10M steel cage



b) 15M steel cage

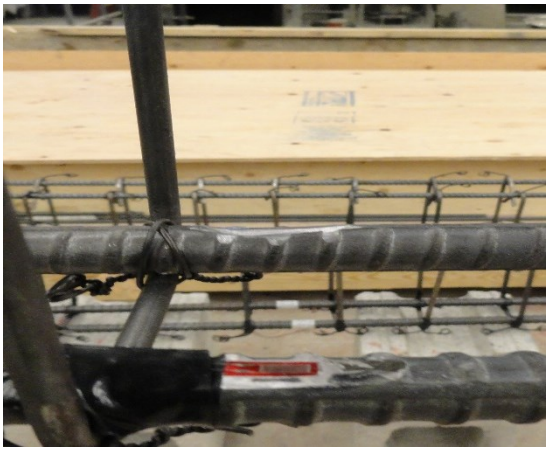


c) 25M steel cage

Figure 3-7 Steel cages of the beams



a) Grinding



b) Placing strain gauge

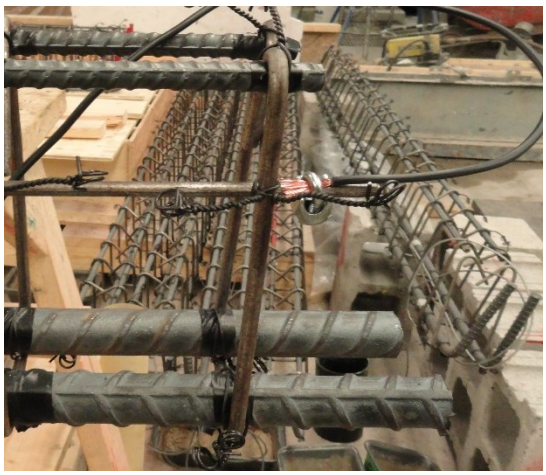


c) Covering the strain gauges

Figure 3-8 Strain gauges application steps



a) Electrical wire on tensile bar



b) Electrical wire on stirrups

Figure 3-9 Placing electrical wires at different locations on the beams

### 3.4.2 Mixing and Curing

A 420-volt electric pan-mixer with capacity of 225 L located in the University of Ottawa Structures Laboratory was used to mix the concrete of the beams, as shown in **Figure 3-10**. After mixing, the concrete was poured in layers inside the formwork, and it was vibrated to ensure uniform concrete distribution between the steel bars. The remaining concrete for each batch was used to cast concrete cylinders. The concrete surface in all beams was leveled to ensure the beams had correct dimensions. After casting, the beams were covered with plastic sheets to ensure proper moisture conditions. The following day, all the cast beams were removed from the formwork and cured using wet burlap and plastic sheets over a period of seven days. After this period, the burlap and plastic sheets were removed and the beams were cured in ambient air until testing.



Figure 3-10 Concrete mixer

### 3.4.3 Concrete Properties at Fresh State

A standard slump test (ASTM C143/C143M "Standard Test Method for Slump of Hydraulic-Cement concrete") was used to obtain the fresh state properties of the concrete mix for all beams. This test consisted of pouring the fresh concrete mix in three layers inside the metal cone. Each layer was rodded twenty-five times until the cone was filled. After leveling, the metal cone was

carefully removed and the slump was measured. **Table 3-4** summarizes the slump test values for each beam. **Figure 3-11** shows a sample photo of the slump test procedure.

Table 3-4 Concrete properties at fresh state

| Groups | Beam ID | Concrete type | Test type | Slump (mm) |
|---|---|---|---|---|
| 10M | CB-10M-0% | NC | S | 91 |
| | CB-10M-0% | NC | D | 90 |
| | B-FC-10M-13% | NC | S | 91 |
| | B-MC-10M-13% | NC | S | 91 |
| | B-SC-10M-11% | NC | S | 100 |
| | B-MC-10M-14% | NC | S | 90 |
| | B-MC-10M-11% | NC | D | 91 |
| | B-MC-10M-15% | NC | D | 101 |
| | B-SC-10M-7% | NC | D | 92 |
| | B-FC-10M-12% | NC | D | 100 |
| | B-EMC-10M-22% | NC | D | 98 |
| | B-CR-MC-10M-5% | NC | D | 100 |
| 15M | CB-15M-0% | NC | S | 96 |
| | CB-15M-0% | NC | D | 91 |
| | B-MC-15M-10% | NC | S | 85 |
| | B-MC-15M-12% | NC | D | 92 |
| | B-EMC-15M-17% | NC | D | 100 |
| | B-CR-MC-15M-4% | NC | D | 96 |
| 25M | CB-25M-0% | NC | S | 94 |
| | CB-25M-0% | NC | D | 90 |
| | B-SHC-25M-10% | NC | S | 88 |
| | B-SHC-25M-12% | NC | S | 99 |
| | B-SHC-25M-11% | NC | D | 97 |
| | B-SHC-25M-12% | NC | D | 94 |

NC: Normal concrete, S: Static test, D: Dynamic test.



Figure 3-11 Sample of slump test

### 3.4.4 Concrete Properties at Hardened State

Three concrete cylinders with dimensions of 100 mm × 200 mm were casted for each concrete batch. After end grinding, the cylinder samples were tested in compression using a 1,000-kN PILOT CONTROL machine to obtain the compressive strength, as shown in **Figure 3-12**. **Table 3-5** summarizes the concrete compressive strength for each beam, where the results represent the average from three cylinders on the day of beam testing. In some cases, a dual LVDT setup was used to obtain the entire stress-strain relationship. **Figure 3-13** shows a sample concrete stress-strain curve for normal-strength concrete, and **Figure 3-14** shows a typical concrete cylinder after testing.




Figure 3-12 Cylinder compressive testing machine

Table 3-5 Concrete compressive strength (cylinders) for each beam

| Groups | Beam ID | Concrete type | Beam test type | Compressive strength (MPa) |
|---|---|---|---|---|
| | | | | Average at testing day |
| 10M | CB-10M-0% | NC | S | 34.4 |
| | CB-10M-0% | NC | D | 49.5 |
| | B-FC-10M-13% | NC | S | 46.9 |
| | B-MC-10M-13% | NC | S | 40.6 |
| | B-SC-10M-11% | NC | S | 42.3 |
| | B-MC-10M-14% | NC | S | 38.4 |
| | B-MC-10M-11% | NC | D | 42.1 |
| | B-MC-10M-15% | NC | D | 31.3 |
| | B-SC-10M-7% | NC | D | 36.9 |
| | B-FC-10M-12% | NC | D | 40.6 |
| | B-EMC-10M-22% | NC | D | 32.9 |
| | B-CR-MC-10M-5% | NC | D | 43.2 |
| 15M | CB-15M-0% | NC | S | 47.4 |
| | CB-15M-0% | NC | D | 44.5 |
| | B-MC-15M-10% | NC | S | 43.7 |
| | B-MC-15M-12% | NC | D | 40.7 |
| | B-EMC-15M-17% | NC | D | 39.6 |
| | B-CR-MC-15M-4% | NC | D | 44.5 |
| 25M | CB-25M-0% | NC | S | 46.4 |
| | CB-25M-0% | NC | D | 34.8 |
| | B-SHC-25M-10% | NC | S | 42.8 |
| | B-SHC-25M-12% | NC | S | 41.8 |
| | B-SHC-25M-11% | NC | D | 38.6 |
| | B-SHC-25M-12% | NC | D | 34.4 |

NC: Normal concrete, S: Static test, D: Dynamic test.

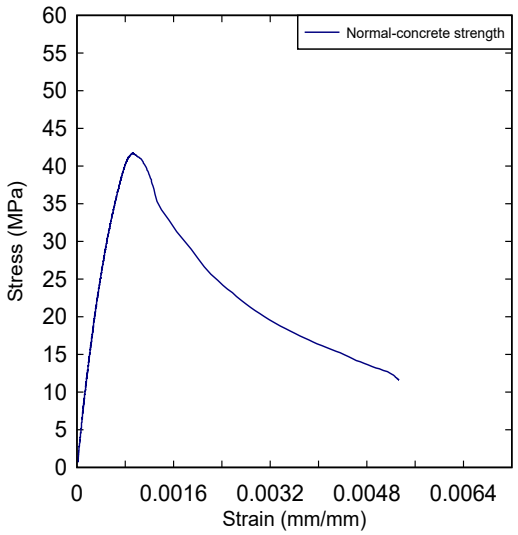



Figure 3-13 Stress-strain curve for concrete

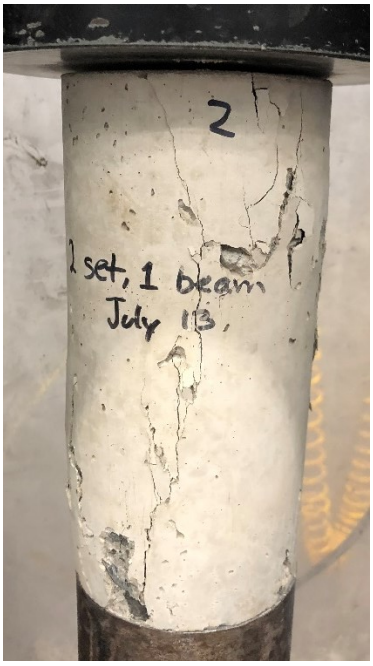



Figure 3-14 Concrete cylinder after testing

### 3.5 Corrosion Acceleration Process

In this research corrosion was accelerated using an impressed current technique. The acceleration corrosion procedure started by placing the beams in a wooden form/tank, which was sealed with three layers of plastic sheets and filled with normal tap water, as shown in **Figure 3-15**. The depth of water in the tank was approximately 110 mm. Wet sponges were then placed on the top of each beam, and stainless steel plates, which acted as cathodes, were placed on top of the wet sponges at the location of intended corrosion. In addition, blocks (loads) were placed on top of the stainless steel plates to ensure full contact between the stainless steel plates and wet sponges. All the beams were connected to a power supply, as illustrated in **Figure 3-16,** at a selected current level to reach the target mass loss specified in **Table 3-1**. The reinforcement to be corroded (either tensile reinforcement or stirrups) was connected to a positive terminal of the power supply to act as anode, whilst the stainless steel plates were connected to the negative terminal of the power supply to act as a cathode. The beams were covered with plastic sheets during the accelerated corrosion regime to keep the concrete cover moist. The current impressed on each beam was calculated from applying Faraday's law to the desired reinforcement mass loss, i.e.,

$$m_s = \frac{M}{zF} \cdot I_{corr} \cdot t \tag{3-1}$$

where $m_s$ is the mass loss (g), $M$ is the metal molar mass (55.85 g/mol for iron), $z$ is the valence of the ion formed as a result of iron oxidation (i.e., $z = 2$ for $Fe \rightarrow Fe^{2+} + 2e^{-}$), $F$ is Faraday's constant ($F$ = 96,485 C/mol), $I_{corr}$ is the corrosion current (A), and $t$ is the time elapsed since corrosion started (s).. The applied current depended on the location of corrosion and the size of steel bars as tabulated in **Table 3-1**. **Table 3-6** summarizes the applied currents and corresponding corrosion rates with the duration of application for each beam obtained from **Eq. (3-1)**. **Figure 3-17** illustrates a typical beam after the corrosion process.



Figure 3-15 Beams inside the tank

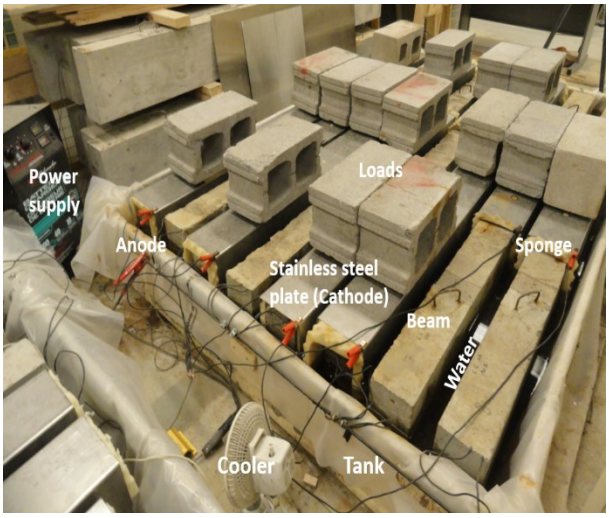



Figure 3-16 Corrosion setup components



Figure 3-17 Typical beam after corrosion process

Table 3-6 Applied current and corrosion rates with duration of application

| Groups | Beam ID | Current (A) | Corrosion rate ($\mu A/cm^2$) | Duration (days) |
|---|---|---|---|---|
| 10M | B-FC-10M-13% | 0.42 | 225 | 66 |
| | B-MC-10M-13% | 0.23 | 439 | 30 |
| | B-SC-10M-11% | 0.23 | 349 | 43 |
| | B-MC-10M-14% | 0.18 | 345 | 77 |
| | B-MC-10M-11% | 0.19 | 366 | 37 |
| | B-MC-10M-15% | 0.2 | 412 | 66 |
| | B-SC-10M-7% | 0.26 | 400 | 39 |
| | B-FC-10M-12% | 0.52 | 287 | 54 |
| | B-EMC-10M-22% | 0.16 | 295 | 111 |
| | B-CR-MC-10M-5% | 0.08 | 148 | 132 |
| 15M | B-MC-15M-10% | 0.27 | 359 | 111 |
| | B-MC-15M-12% | 0.27 | 348 | 115 |
| | B-EMC-15M-17% | 0.17 | 232 | 216 |
| | B-CR-MC-15M-4% | 0.11 | 143 | 148 |
| 25M | B-SHC-25M-10% | 0.44 | 166 | 43 |
| | B-SHC-25M-12% | 0.55 | 208 | 67 |
| | B-SHC-25M-11% | 0.49 | 186 | 44 |
| | B-SHC-25M-12% | 0.59 | 222 | 66 |

### 3.6 Experimental Tests Setup

This section describes the experimental test steps that were used in the quasi-static and dynamic beam tests.

#### 3.6.1 Static Loading Test

The setup shown in **Figure 3-18** was used to test all beams under quasi-static four-point bending. The beams were simply supported over a span of 2,232 mm, with a constant moment region of 750 mm and two equal shear-spans of 741 mm. A manually operated hydraulic jack was used to apply the loading which was then transferred to the specimens as two point loads using a steel spreader beam. The load was recorded using a load-cell placed below the hydraulic jack, with displacement at mid-span captured using a cable displacement transducer. Strains in the reinforcing bars were monitored using strain gauges, which were applied on the tension steel at mid-span. Loading of the beams began under load-control with 10-kN incremental loading until signs of yielding were detected. Upon yielding, loading continued under displacement-control with 5-mm increments until failure of the specimens (concrete crushing or shear collapse).

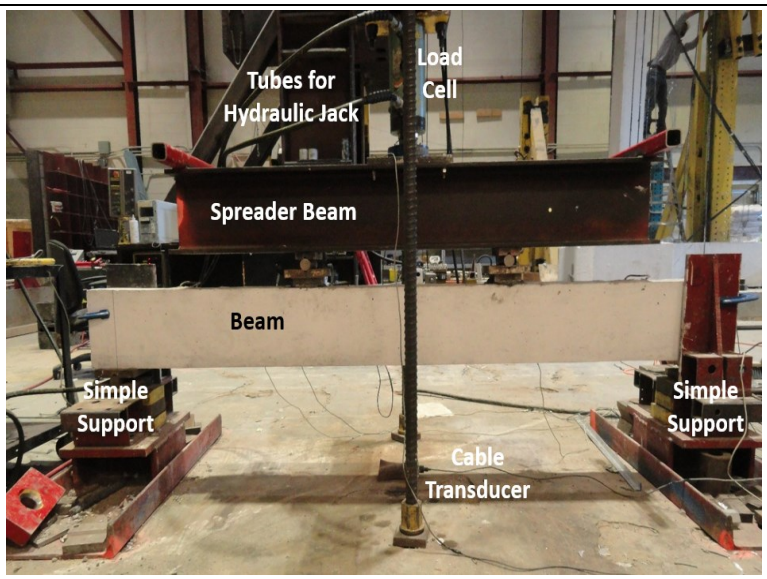
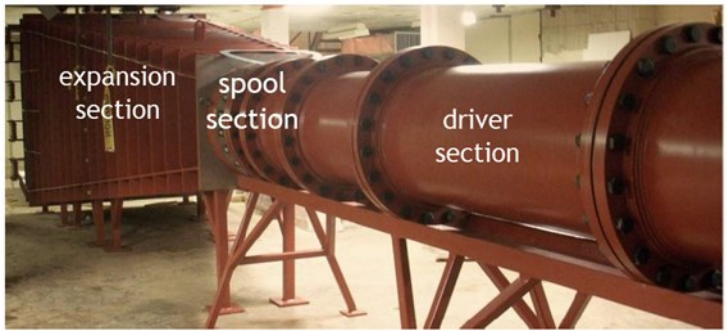



Figure 3-18 Static load test setup

### 3.6.2 Blast Loading Test (Dynamic)

#### 3.6.2.1 Shock Tube

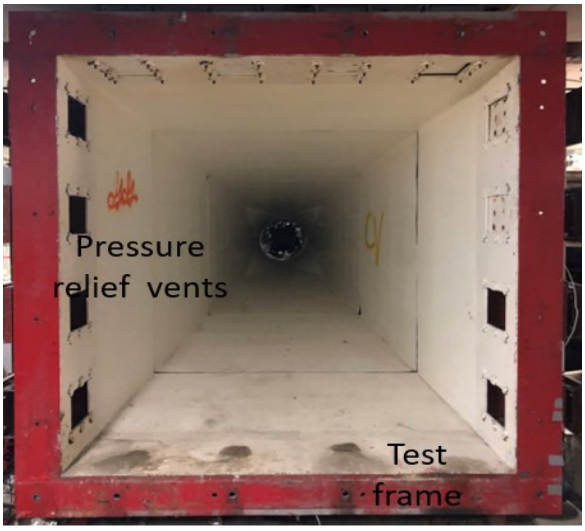
Blast testing was conducted using the shock-tube facility at the University of Ottawa. **Figure 3-19** illustrates the main components of the shock-tube which included: a variable length driver section, a spool section, an expansion section and a rigid-end test frame. The driver section generates the blast energy, while the firing of the shockwave was controlled using the double-diaphragm spool section. The rigid-end test frame had a square opening with dimensions of 2 m × 2 m where test specimens (beams) can be attached. In this research, a load-transfer device was used to collect the blast energy and transfer it onto the specimens at two points with a four-point loading setup, which was consistent with the static tests. A typical beam before testing with the blast test setup is shown in **Figure 3-20**.







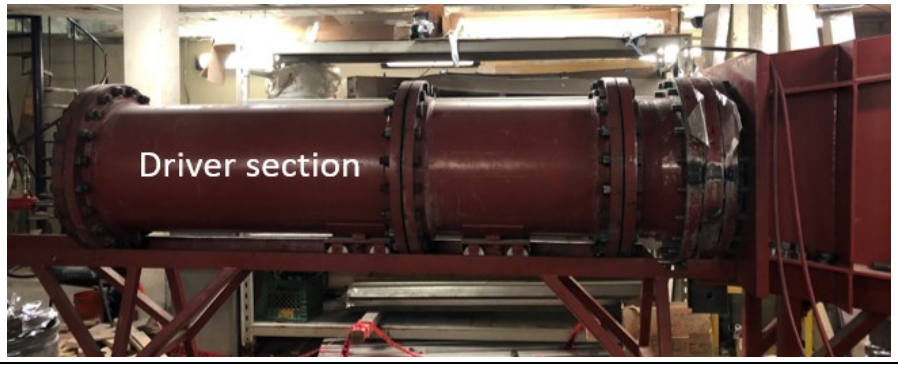
a) Shock-tube (full veiw)




b) Test frame




c) Expansion section




d) Driver section

Figure 3-19 Shock-tube



Figure 3-20 Typical beam with blast test setup

### 3.6.2.2 Lateral Load Transfer Device

A load transfer device (LTD) was used to collect the shockwave pressure at the shock-tube opening and redirect it onto the beam specimens, since they are not planar and do not cover the entire opening of the shock-tube. The LTD resulted in the application of blast loading under four-point bending, which closely matched the loading configuration used in the static testing. The LTD consisted of two side-by side rigid steel panels (2,032 mm × 1,000 mm) covering the 2 m × 2 m rigid end test frame square opening, and two I-steel load transfer beams (160 mm × 165 mm × 1,200 mm) which applied the loading as two point loads. To allow for free lateral movement of the middle portion of the LTD, sliding hinges were provided near the top and bottom supports. **Figure 3-21** presents the lateral load transfer device in detail.

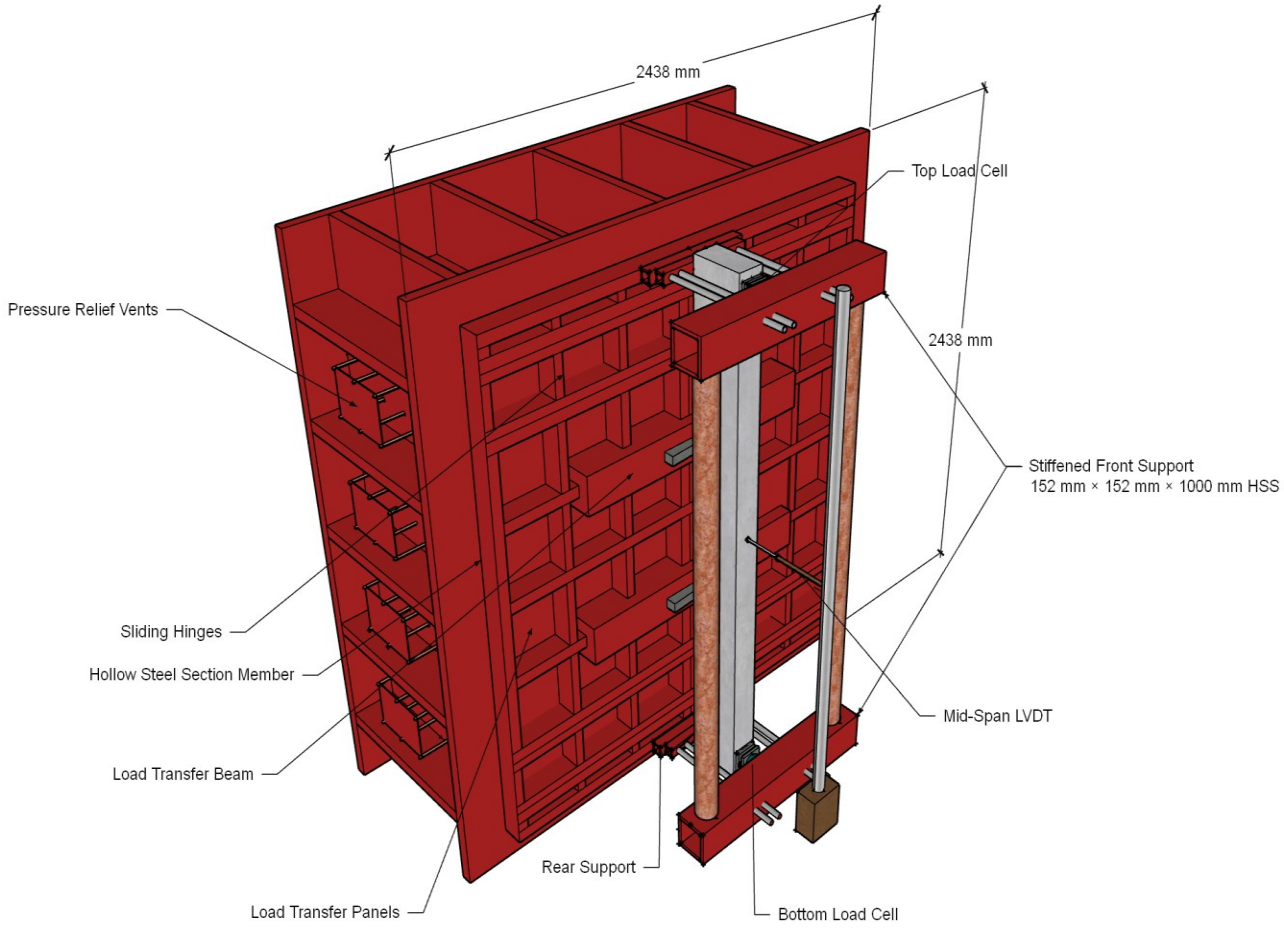



Figure 3-21 Isotropic view of lateral load transfer device (reproduced from Bastami, 2019)

### 3.6.2.3 Supports

The blast loading test had the same load configuration as the static loading and similar simply-supported boundary conditions, which were implemented using the front and rear supports at the top and bottom beam reaction locations. The front supports consisted of square HSS sections with dimensions of 152 × 152 × 1,000 mm welded to a circular load cell and tightened using four 19-mm diameter threaded-steel rods. The rear supports consisted of two square HSS sections with dimensions of 51 × 51 × 500 mm and 51 × 51 × 440 mm, respectively, which were welded to the LTD. The support details are illustrated in **Figure 3-22**.

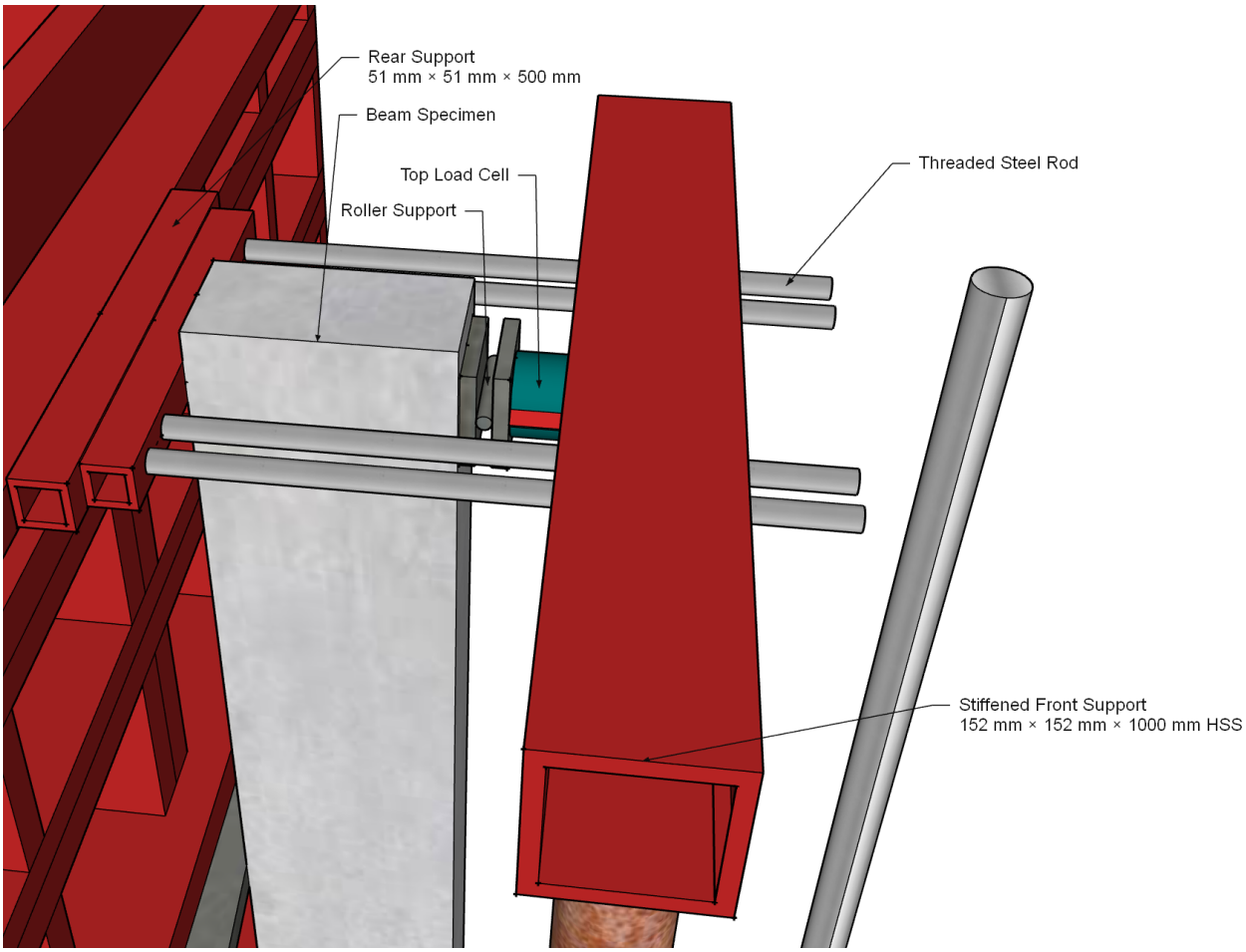



Figure 3-22 Support details (reproduced from Bastami, 2019)

#### 3.6.2.4 Data Acquisition System

The data for each test was collected using a Yokogawa SL1000 High-Speed Data Acquisition Unit. The data included strains, displacements, pressure readings and support reactions during the test. The system had a capacity of recording 100,000 data samples per second.

#### 3.6.2.5 Pressure Sensors

Two PCB Piezotronics Model #112A22 piezoelectric pressure sensors were used to record the complete blast shock wave pressure time history during each blast test. The two sensors were located at the bottom and side of the end frame section of the shock-tube.

#### 3.6.2.6 Strain Gauges

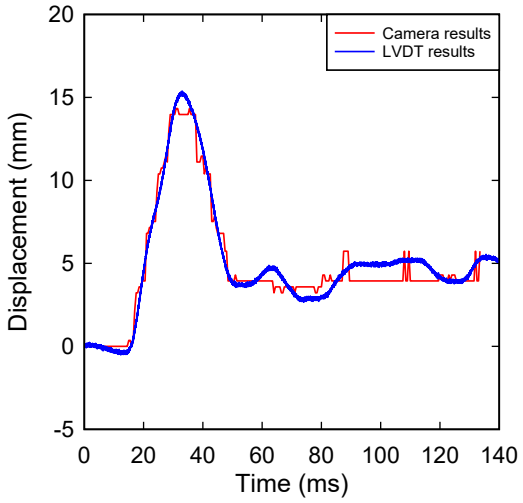
The strains in the steel reinforcement were measured using two 350-Ω strain gauges with a length of 6 mm (FLA-6-350-11), which were installed at the mid-span of the tensile steel bars.

#### 3.6.2.7 Linear Variable Displacement Transducer (LVDT)

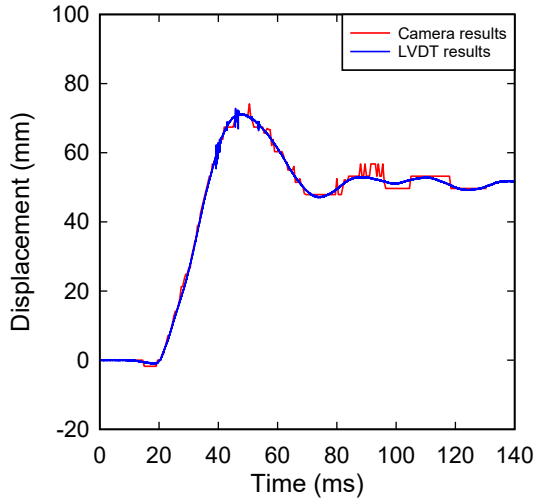
One LVDT was used to record the displacement time history of the beams during testing. The LVDT was placed at the mid-span of the beams.

#### 3.6.2.8 High-Speed Video Cameras

The instrumentation during the blast load tests also included two high-speed cameras (AOS Technology X-PRI), which were located at the front and side of the beams. These two cameras had the capability of recording the response of the beams at a frame rate of 2,000 frames per second. In addition to capturing the video response, the software and cameras were capable of capturing displacements, especially for those shots where the failure was expected to be brittle. **Figure 3-23** compares displacement time histories obtained using the cameras and LVDT; it is obvious that the cameras provided reliable and accurate results.




a) Control beam in the 10M group after the first shot (17 psi)




b) Mid corrosion beam with 12% mass loss in the 15M group after the second shot (70 psi)

Figure 3-23 Camera validation

### 3.6.2.9 Testing Procedure

The beams in this study were tested by applying different blast pressures, which were selected based on the expected moment resistance and corrosion/deterioration properties. In all cases, the driver was kept constant at 9 ft (2,743 mm), while the driver pressure was increased from 17 psi to 90 psi based on the beam test group.

The blast sequence for the 10M, 15M and 25M group beams was as follows:

- 10M group beams: most beams were tested at driver pressures of 17 psi and 50 psi, except one beam with corrosion at the ends, which was tested with an additional intermediate 35-psi shot.
- 15M group beams: most beams were tested at driver pressures of 17 psi and 70 psi, except for two beams, which were tested under a single blast of 70 psi only.
- 25M group beams: all beams were tested under one blast of 90 psi.

In general, the intention of applying an initial 17-psi shot was to test the beams under elastic or near-yield conditions. The remaining shots (50 psi, 70 psi and 90 psi) were applied on the beams to cause damage up to failure. **Figure 3-24** shows an example of typical blast shots for each group

of beams. **Table 3-7** summarizes the shockwave properties for each blast in terms of peak reflected pressure ($P_r$), positive phase duration ($t_d$) and reflected impulse ($I_r$), as measured under the positive phase of the pressure time histories.

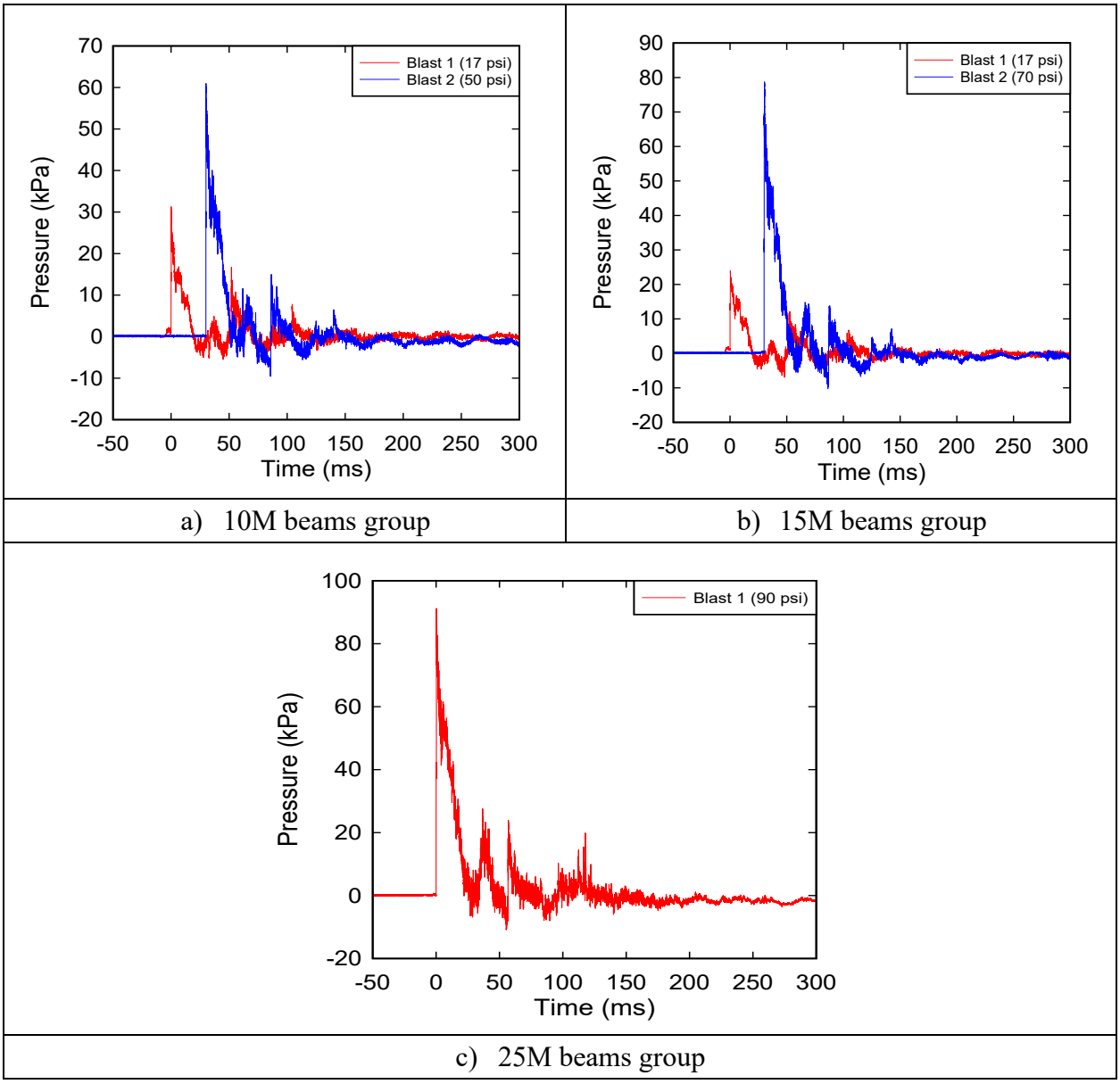



Figure 3-24 Typical blast shots for each group of beams

Table 3-7 Blast shots properties

| Blast ID | Driver pressure kPa (psi) | Driver length mm (ft) | Average reflected pressure ($P_r$) kPa | Average reflected impulse ($I_r$) kPa-msec | Average Positive Phase Duration, $t_d$ msec |
|---|---|---|---|---|---|
| Blast 1 (10M) | 117 (17) | 2743 (9) | 28.86 | 248.74 | 18.84 |
| Blast 2 (10M) | 345 (50) | 2743 (9) | 60.62 | 544.30 | 21.11 |
| Blast 1 (15M) | 117 (17) | 2743 (9) | 26.45 | 249.42 | 18.84 |
| Blast 2 (15M) | 483 (70) | 2743 (9) | 78.87 | 721.29 | 22.14 |
| Blast 1 (25M) | 621 (90) | 2743 (9) | 94.37 | 918.67 | 23.63 |

### 3.7 Mass Loss Measurement

After static and blast testing, the corroded beams were broken using either a jack hammer or a manual sledge hammer as shown in **Figure 3-25**. The corroded steel bar at the target corrosion location was then cut using a grinder. The steel bar was then cut into smaller pieces with approximate lengths of 100 mm as shown in **Figure 3-26**. These pieces were cleaned by following ASTM G1-03 (2011). The cleaning process was done in the Environmental Civil Engineering Laboratory at the University of Ottawa. The procedure of cleaning included the following steps: 1) preparing the cleaning tools and materials, which included a small plastic container, plastic brush, glass container, 500 mL of hydrochloric acid, 500 mL of water and 3.5 g of hexamethylene tetramine as shown in **Figure 3-27**; 2) filling the plastic container with 500 mL of water and 500 mL of hydrochloric acid using the glass beaker; 3) adding 3.5 g of hexamethylene tetramine to the water mixture; 4) mixing the solution using a plastic brush; 5) putting the small pieces of corroded steel bar inside the container and leaving them for 10 minutes before cleaning; 6) cleaning each small piece of corroded steel with the brush and water as shown in **Figure 3-28**; 7) weighting each small piece of corroded steel bar using the balance; and, 8) calculating the mass loss for each small piece of corroded bar by subtracting the original weight from the new weight after corrosion. **Figure 3-29** shows a corroded steel bar after cleaning.



Figure 3-25 Breaking the beams



Figure 3-26 Corroded steel bar before cleaning



Figure 3-27 Tools and materials for steel bar cleaning



Figure 3-28 Cleaning process



Figure 3-29 Corroded steel bar after cleaning

# Chapter 4: Experimental Results: Details Results from the Static Tests

## 4.1 Introduction

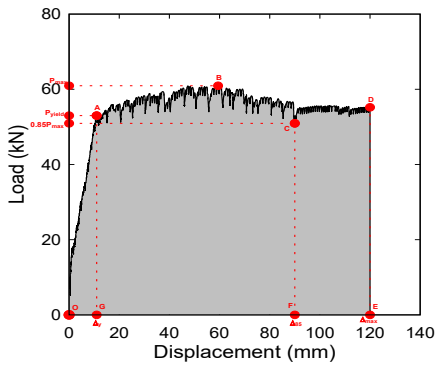
This chapter presents the detailed experimental results of the ten beams which were tested in the experimental program under static loading. The following data was collected for each beam:

- The load-deflection response;
- The load vs tensile strain in the longitudinal steel reinforcement (when available);
- The maximum flexural and shear crack-widths as a function of load or displacement, and;
- Photographs at key load stages.

In addition, the following key parameters are extracted from the static load-deflection curves:

- The load and displacement at yielding ($P_y$, $\Delta_y$);
- The beam stiffness after cracking (K)
- The maximum load ($P_{max}$)
- The post-peak displacement corresponding to 85% of $P_{max}$ ($\Delta_{85}$)
- The maximum displacement at failure or end of testing ($\Delta_{max}$)
- The ductility (in terms of $\Delta_{85}/\Delta_y$ and $\Delta_{max}/\Delta_y$)
- The toughness $Au_{85}$ and $Au_{max}$ (defined as the area under the load-deflection curve until $\Delta_{85}$ and $\Delta_{max}$) and the failure mechanism.

A visual representation of the different variables is shown in **Figure 4-1**.

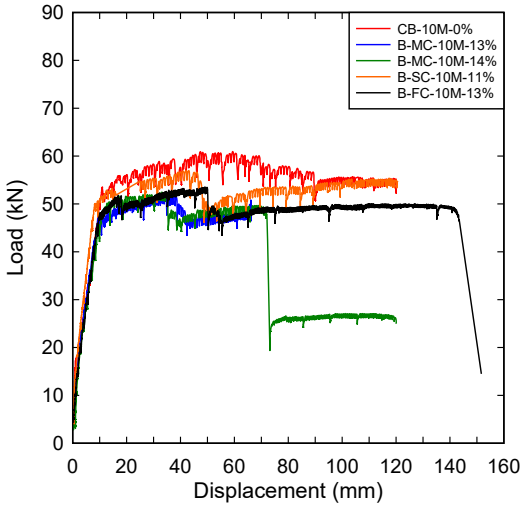



- A: load corresponding to yielding of specimen;
- B: maximum load revisited by the specimen;
- C: load corresponding to 85% of the peak load;
- D: failure of specimen;
- E: displacement at failure;
- F: displacement corresponding to when load reached 85% of peak load;
- G: displacement at yield;
- $A_{OABCF}$ or $A_{OABCDE}$ toughness or area under the curve (shaded in grey).

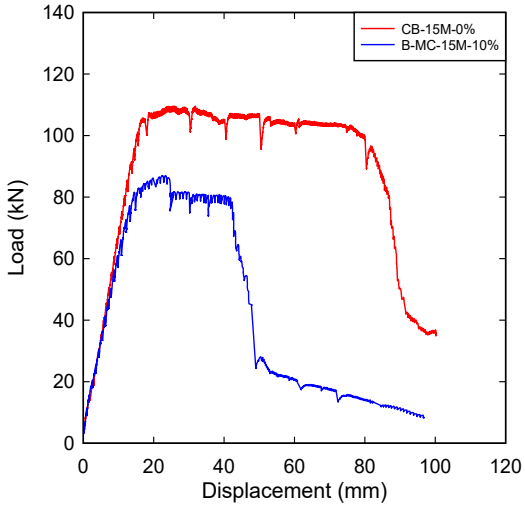
Figure 4-1 Key static test load-deflection parameters

## 4.2 Summary of Results

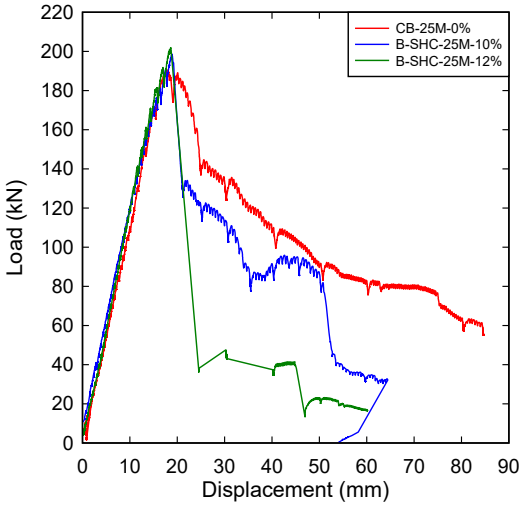
A total of ten (10) reinforced concrete beams were tested, including five (5) beams in the 10M group, two (2) beams in the 15M group and three (3) beams in the 25M group. The results for all beams in terms of load-deflection response are presented in **Figure** 4-2 and **Table** 4-1. **Section 4.3** presents the detailed results of all beams, beginning with the control beam and followed by the corroded specimens in each of the 10M, 15M and 25M groups. The **next chapter** provides a comparison and discussion of these results.




a) 10M group




b) 15M group




c) 25M group

Figure 4-2 Experimental results for all beams in the 10M, 15M and 25M groups

Table 4-1 Key load-deflection results for all beams

| Beam ID | Load (kN) | | Displacement (mm) | | | Stiffness K (N/mm) | Ductility | | Toughness (kN-mm) | | Failure Mechanism |
|---|---|---|---|---|---|---|---|---|---|---|---|
| | $P_y$ | $P_{max}$ | $\Delta_y$ | $\Delta_{85}$ | $\Delta_{max}$ | | $\left(\frac{\Delta_{85}}{\Delta_y}\right)$ | $\left(\frac{\Delta_{max}}{\Delta_y}\right)$ | $Au_{85}$ | $Au_{max}$ | |
| CB-10M-0% | 54 | 61 | 11 | 90 | 120 | 4,836 | 8 | 11 | 4,881 | 6,525 | Concrete crushing |
| B-MC-10M-13% | 48 | 52 | 10 | 42 | 66 | 4,638 | 4 | 6 | 1,896 | 3,323 | Flexural failure |
| B-MC-10M-14% | 49 | 53 | 11 | 35 | 71 | 4,366 | 3 | 6 | 1,562 | 4,605 | Rebar rupture |
| B-SC-10M-11% | 50 | 57 | 8 | 49 | 121 | 5,981 | 6 | 14 | 2,444 | 6,247 | Flexural failure |
| B-FC-10M-13% | 48 | 53 | 10 | 54 | 140 | 4,767 | 5 | 14 | 2,532 | 7,154 | Rebar rupture |
| CB-15M-0% | 106 | 110 | 17 | 51 | 82 | 6,136 | 3 | 5 | 4,544 | 8,817 | Concrete crushing |
| B-MC-15M-10% | 82 | 87 | 14 | 25 | 42 | 5,639 | 2 | 3 | 1,506 | 4,079 | Flexural failure |
| CB-25M-0% | - | 190 | - | 25 | 84 | - | - | - | 3,017 | 8,635 | Shear failure |
| B-SHC-25M-10% | - | 198 | - | 19 | 64 | - | - | - | 2,462 | 6,000 | Shear failure |
| B-SHC-25M-12% | - | 202 | - | 19 | 60 | - | - | - | 2,715 | 3,873 | Shear failure |

## 4.3 Detailed Experimental Results

### 4.3.1 10M Group

The 10M group included five beams which were doubly-reinforced with 2-10M bars in tension and compression (top bars). In all cases, transverse reinforcement consisted of U-shaped stirrups made from 6.3-mm wire spaced at 100 mm throughout the beam span. Corrosion was applied on the 10M tension bars at different locations including: middle span, end spans and full span.

#### 4.3.1.1 10M: Control (0% mass loss) (CB-10M-0%)

Beam CB-10M-0% serves as the reference (control) beam in the 10M group. The results in terms of the load-deflection response, tensile strain readings, and maximum crack-widths (in flexure and shear) are presented in **Figure** 4-3 and **Figure** 4-4 . **Figure** 4-5 shows key load stages in the beam response. A summary of key load and displacement results is provided in **Table** 4-2.

The yield strength for this beam occurred at a load of 54 kN and a displacement of 11 mm. The maximum load of 61 kN was recorded at a displacement of 59.4 mm. The displacement at the end of testing reached 120 mm (limitation of the testing device) with the beam showing a residual capacity of 55 kN. The failure displacement based on 0.85Pmax ($\Delta_{85}$) was 90 mm. This beam experienced a ductile flexure failure with significant yielding of the longitudinal bars in tension prior to crushing of the concrete. Failure was associated with crushing of the concrete in the compression zone in the mid-span region.

Table 4-2 : Key results: CB-10M-0%

| Load (kN) | | Displacement (mm) | | | Stiffness K (N/mm) | Ductility | | Toughness (kN-mm) | | Failure Mechanism |
|---|---|---|---|---|---|---|---|---|---|---|
| $P_y$ | $P_{max}$ | $\Delta_y$ | $\Delta_{85}$ | $\Delta_{max}$ | | $\left(\frac{\Delta_{85}}{\Delta_y}\right)$ | $\left(\frac{\Delta_{max}}{\Delta_y}\right)$ | $Au_{85}$ | $Au_{max}$ | |
| 54 | 61 | 11 | 90 | 120 | 4,836 | 8 | 11 | 4,881 | 6,525 | Concrete crushing |

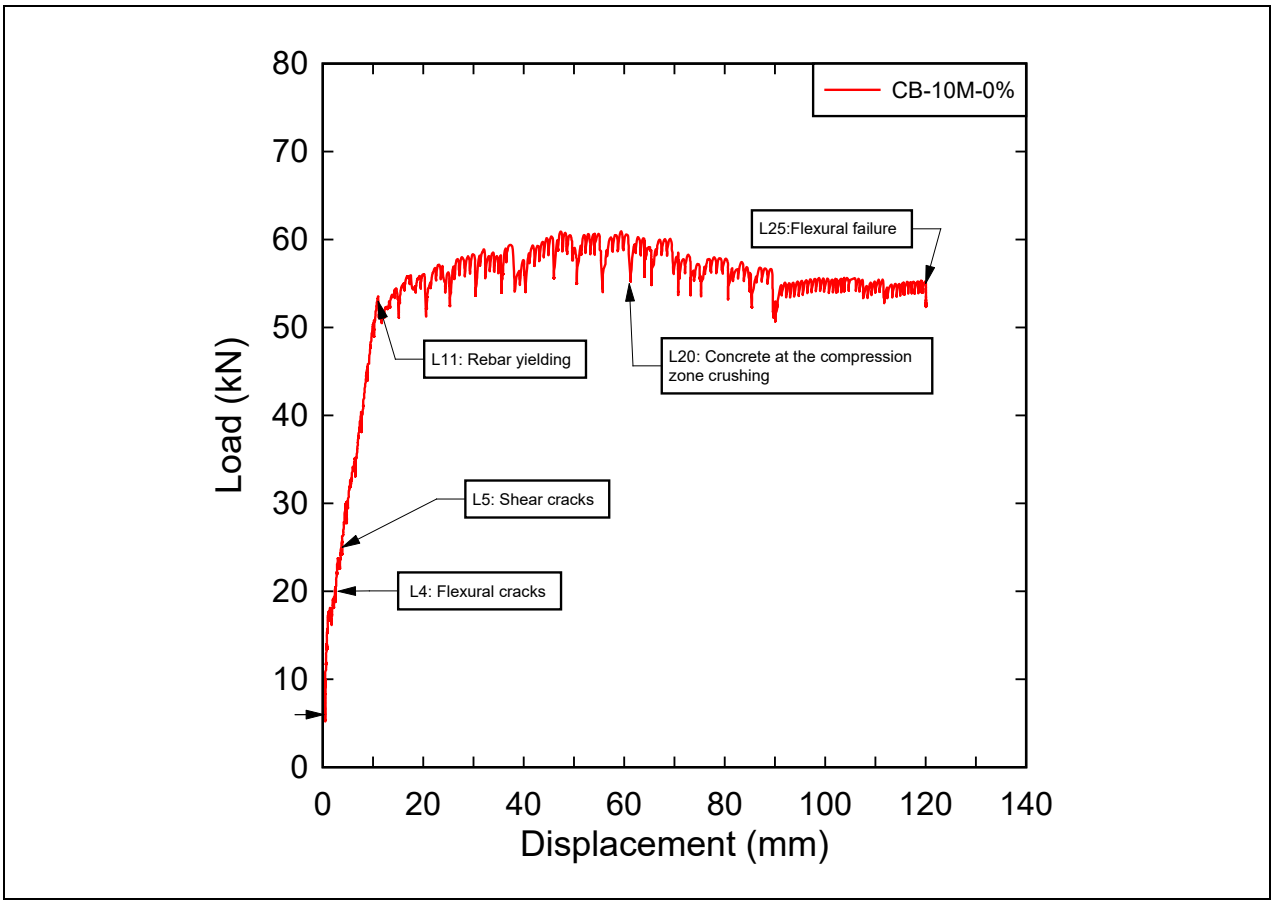
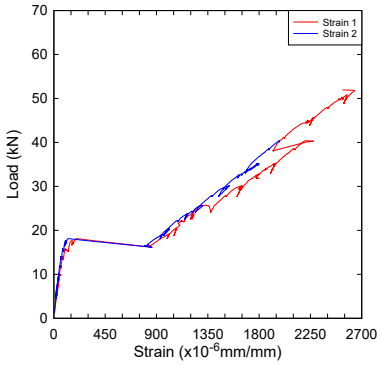
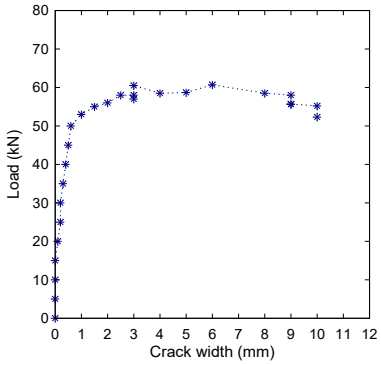


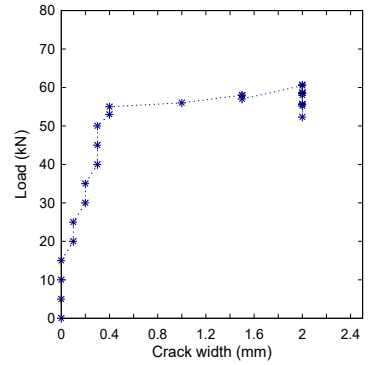

Figure 4-3 Experimental results: Load-displacement response (CB-10M-0%)




a) Tensile strain in bars




b) Maximum flexural cracks width




c) Maximum shear cracks width

Figure 4-4 Experimental results: strains and crack widths (CB-10M-0%)

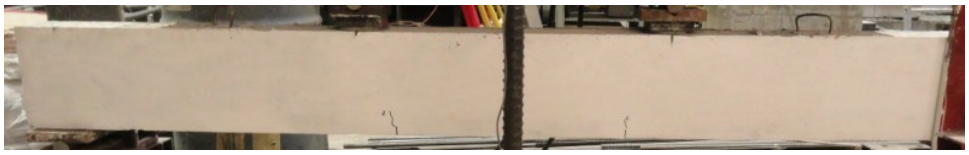
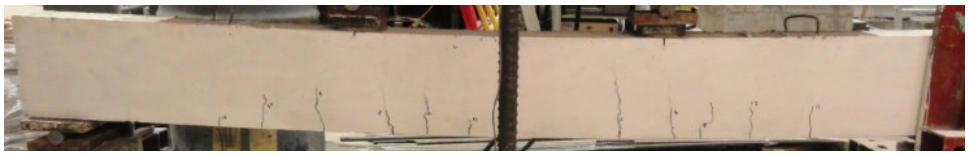
<table>
<tr><th colspan="3">Experimental Parameters</th><th>Description</th></tr>
<tr><td>Load Stage</td><td>Load (kN)</td><td>Mid-Span Deflection (mm)</td><td rowspan="3">First hairline cracks appear in the flexural zone</td></tr>
<tr><td>4</td><td>20</td><td>2.5</td></tr>
<tr><td colspan="3">  </td></tr>
<tr><td>Load Stage</td><td>Load (kN)</td><td>Mid-Span Deflection (mm)</td><td rowspan="3">First hairline cracks appear in the shear zone</td></tr>
<tr><td>5</td><td>25</td><td>3.6</td></tr>
<tr><td colspan="3">  </td></tr>
<tr><td>Load Stage</td><td>Load (kN)</td><td>Mid-Span Deflection (mm)</td><td rowspan="3">Steel reinforcement yielding</td></tr>
<tr><td>11</td><td>53.5</td><td>11</td></tr>
<tr><td colspan="3">  </td></tr>
<tr><td>Load Stage</td><td>Load (kN)</td><td>Mid-Span Deflection (mm)</td><td rowspan="3">Concrete at the compression zone started crushing</td></tr>
<tr><td>20</td><td>55.2</td><td>61.3</td></tr>
<tr><td colspan="3">  </td></tr>
<tr><td>Load Stage</td><td>Load (kN)</td><td>Mid-Span Deflection (mm)</td><td rowspan="3">Concrete crushed at the compression zone and failed in flexure</td></tr>
<tr><td>26</td><td>55</td><td>120</td></tr>
<tr><td colspan="3">  </td></tr>
</table>

Figure 4-5 Main events during testing (CB-10M-0%)

#### 4.3.1.2 10M: Mid-span corrosion – 13% mass loss (B-MC-10M-13%)

The second beam in the 10M group was subjected to corrosion over a length of 750 mm in the mid-span region. The target mass loss was 15%. After testing, the actual average mass loss was determined to be 13%. Considering all extracted samples, the maximum mass loss was 17% as shown in **Figure** 4-6.

**Figure** 4-7 shows the condition of the beam prior to testing. It was observed that the corrosion resulted in staining of the concrete surface and cracking over the length of the beam. The cracks were mainly horizontal near the tension and compression steel reinforcement.

The test results in terms of load-deflection response and maximum crack-widths are presented in **Figure** 4-8 and **Figure** 4-9. The important events are shown in **Figure** 4-10. A summary of key results is presented in **Table** 4-3.

The beam showed a yield strength of 48 kN at a displacement of 10 mm. The maximum load reached 52 kN at a displacement of 34 mm. The final displacement for this test was 66 mm with the beam showing a residual capacity of 46.68 kN (it was noted that the test was stopped due to the malfunction of the loading device). The failure displacement corresponding to $0.85P_{max}$ ($\Delta_{85}$) occurred at 42 mm. Although the beam did not show a brittle failure, the corrosion of the steel reinforcement led to reductions in the maximum load, stiffness, ductility and toughness when compared to the control beam. In addition, the corrosion process increased the crack widths which resulted in more severe (and random) cracking at equivalent load stages. The beam experienced significant crushing/spalling of the top cover concrete cover in the mid-span compression zone with the development of very large cracks in the tension zone.

Table 4-3 : Key results: B-MC-10M-13%

| Load (kN) | | Displacement (mm) | | | Stiffness K (N/mm) | Ductility | | Toughness (kN-mm) | | Failure Mechanism |
|---|---|---|---|---|---|---|---|---|---|---|
| $P_y$ | $P_{max}$ | $\Delta_y$ | $\Delta_{85}$ | $\Delta_{max}$ | | $\left(\frac{\Delta_{85}}{\Delta_y}\right)$ | $\left(\frac{\Delta_{max}}{\Delta_y}\right)$ | $Au_{85}$ | $Au_{max}$ | |
| 48 | 52.1 | 10.4 | 42.4 | 66 | 4,638 | 4.1 | 6.4 | 1,896 | 3,323 | Flexural failure |

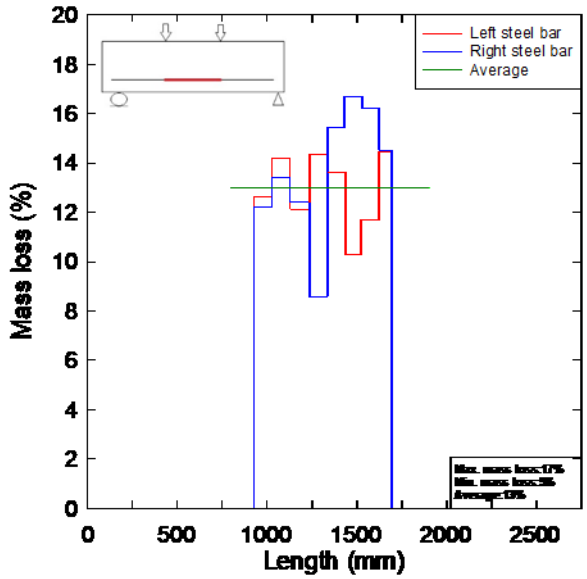



Figure 4-6 Mass loss distribution along the middle length of the tensile bars (B-MC-10M-13%)



Figure 4-7 Cracking in the beam before testing (B-MC-10M-13%)

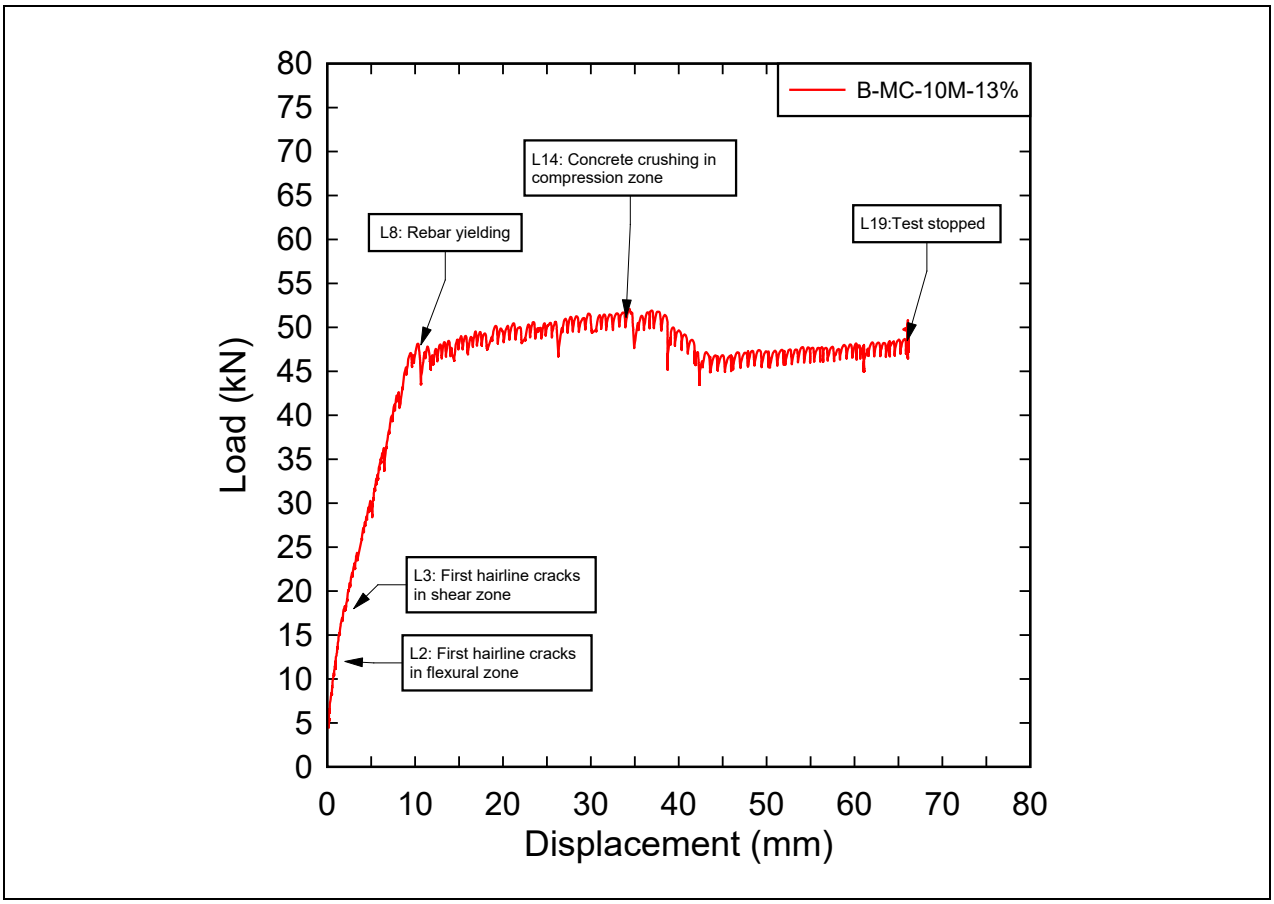
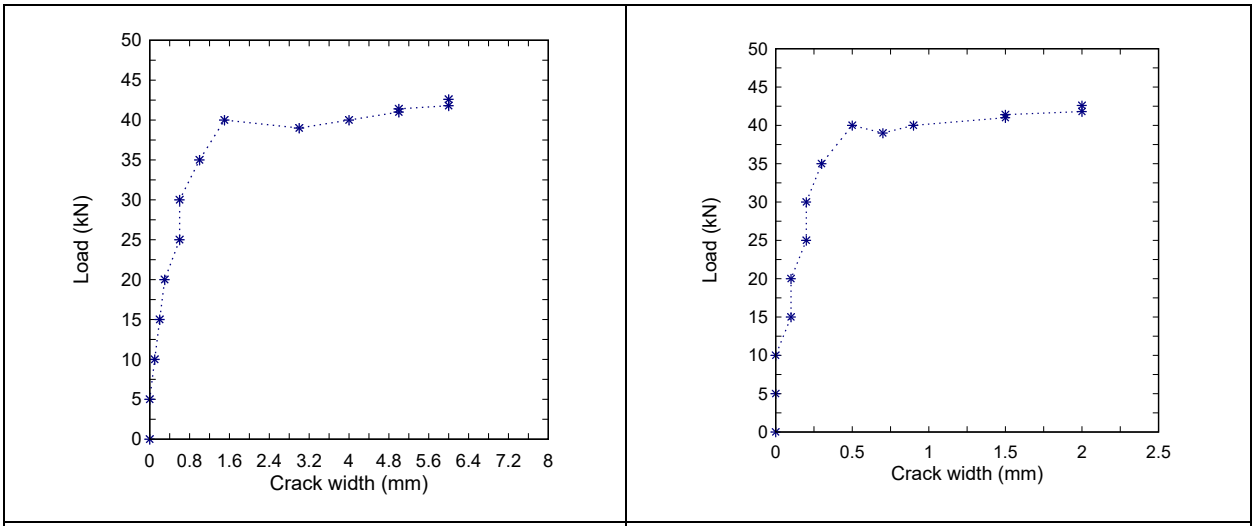



Figure 4-8 Experimental results: load-displacement response (B-FC-10M-13%)




a) Maximum flexural cracks | b) Maximum shear cracks

Figure 4-9 Experimental results: crack widths (B-MC-10M-13%)

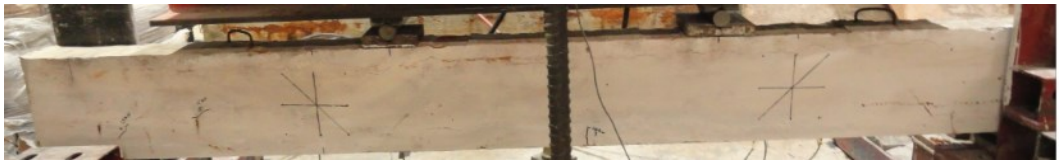
<table>
<tr><th colspan="3">Experimental Parameters</th><th>Description</th></tr>
<tr><td>Load Stage</td><td>Load (kN)</td><td>Mid-Span Deflection (mm)</td><td rowspan="3">First hairline cracks appear in the flexural and shear zones</td></tr>
<tr><td>2,3</td><td>12, 18</td><td>0.95, 2</td></tr>
<tr><td colspan="3">  </td></tr>
<tr><td>Load Stage</td><td>Load (kN)</td><td>Mid-Span Deflection (mm)</td><td rowspan="3">Steel reinforcement yielding</td></tr>
<tr><td>8</td><td>48</td><td>10.3</td></tr>
<tr><td colspan="3">  </td></tr>
<tr><td>Load Stage</td><td>Load (kN)</td><td>Mid-Span Deflection (mm)</td><td rowspan="3">Cracks widths increased at the tension zone and concrete starts crushing at compression zone</td></tr>
<tr><td>14</td><td>51.1</td><td>34</td></tr>
<tr><td colspan="3">  </td></tr>
<tr><td>Load Stage</td><td>Load (kN)</td><td>Mid-Span Deflection (mm)</td><td rowspan="3">Top concrete cover spalls with large cracks in the tension zone (test stopped)</td></tr>
<tr><td>19</td><td>48.5</td><td>66</td></tr>
<tr><td colspan="3">  </td></tr>
</table>

Figure 4-10 Main events during testing (B-MC-10M-13%)

#### 4.3.1.3 10M: Mid-span corrosion – 14% mass loss (B-MC-10M-14%)

The third beam in the 10M group was subjected to corrosion over its mid-span region over a length of 750 mm. The target mass loss for the 10M reinforcement was 30%. After testing, the actual average mass loss on the bars was determined to be 14%; however, the mass loss in some of the extracted bar samples reached 23% and 20% as shown in **Figure** 4-11.

Prior to beam testing, the beam showed signs of corrosion-induced cracking and damage over its length, with the main type of cracks corresponding to horizontal cracking at the level of the longitudinal bars in the tension and compression zones as shown in **Figure** 4-12.

The results in terms of load-deflection response and maximum crack-widths responses are presented in **Figure** 4-13 and **Figure** 4-14, respectively. In addition, the main events during testing are shown in **Figure** 4-15. Results for this beam are also summarized in **Table** 4-4.

This beam reached a yield strength of 49 kN at a displacement of 11 mm. The maximum load was 53 kN and occurred at a displacement of 33 mm. Considering the 85% drop in load capacity, the beam reached 0.85Pmax (45 kN) at a displacement $\Delta_{85}$ = 35 mm. A more sudden drop in load occurred at a displacement of 71 mm due to rupture of the 10M reinforcement. As a result, the beam showed lower ductility and a more brittle failure mode when compared to the control specimen. In addition, the beam also showed reductions in maximum load, stiffness and overall toughness when compared to the control specimen. The corrosion also affected the cracking process both in terms of crack widths (larger flexural cracks at equivalent stages) and crack patterns, with a more random crack distribution as shown in **Figure** 4-15. In addition to the more sudden bar rupture failure, concrete damage in terms of crushing and spalling was also more significant in the corroded beam as shown in **Figure** 4-16.

Table 4-4 : Key results: B-MC-10M-14%

| Load (kN) | | Displacement (mm) | | | Stiffness K (N/mm) | Ductility | | Toughness (kN-mm) | | Failure Mechanism |
|---|---|---|---|---|---|---|---|---|---|---|
| $P_y$ | $P_{max}$ | $\Delta_y$ | $\Delta_{85}$ | $\Delta_{max}$ | | $\left(\frac{\Delta_{85}}{\Delta_y}\right)$ | $\left(\frac{\Delta_{max}}{\Delta_y}\right)$ | $Au_{85}$ | $Au_{max}$ | |
| 49 | 53 | 11 | 35 | 71 | 4,366 | 3.1 | 6.3 | 1,562 | 4,605 | Rebar rupture |

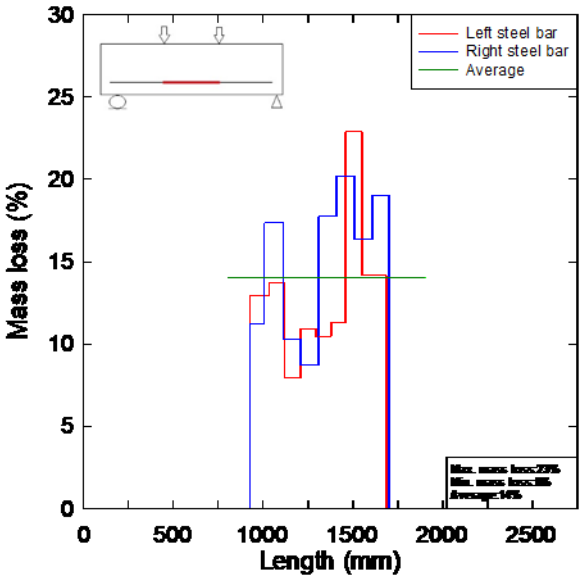



Figure 4-11 Mass loss distribution along the middle length of the tensile bars (B-MC-10M-14%)

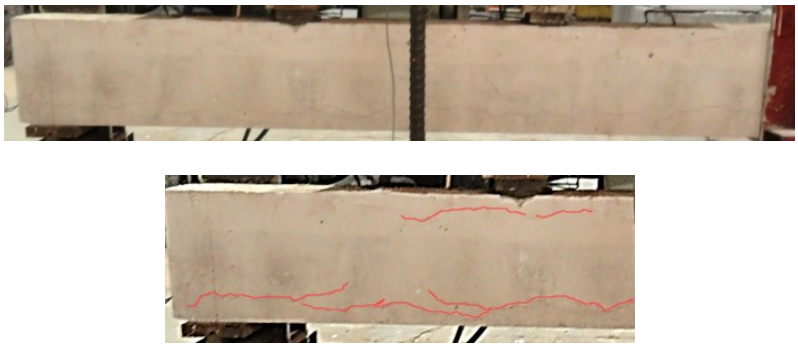


Figure 4-12 Cracking in the beam before testing: B-MC-10M-14%

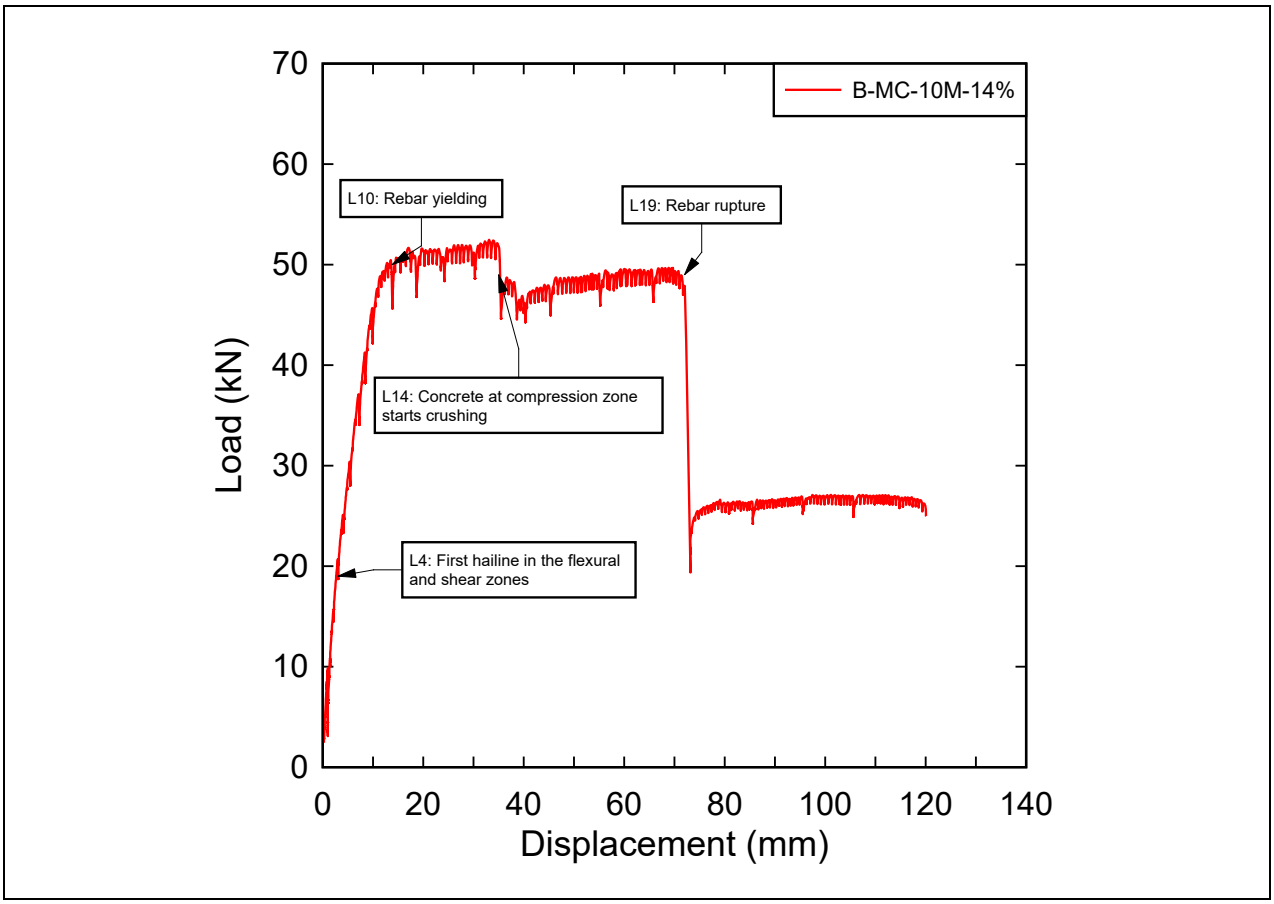
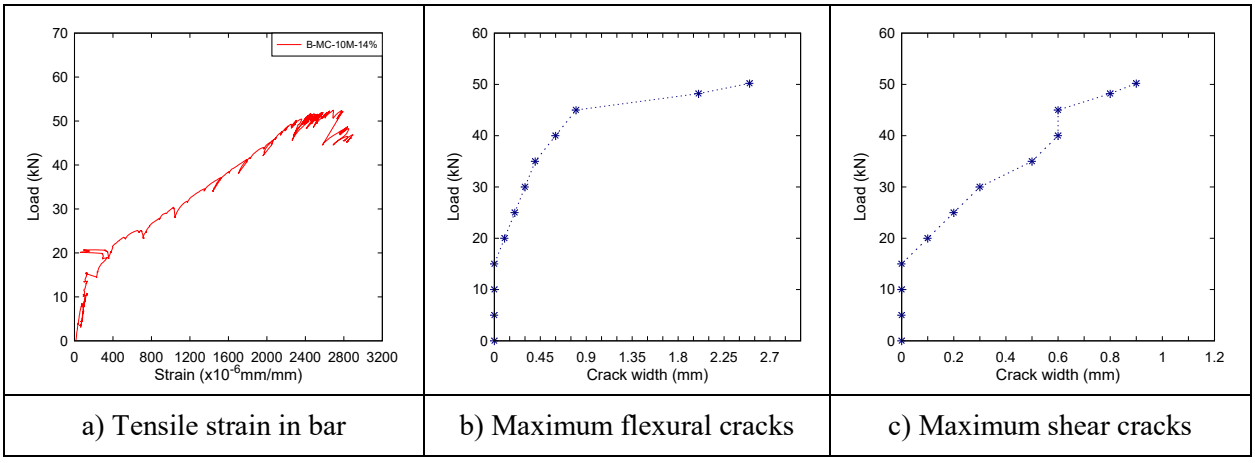



Figure 4-13 Experimental results: load-displacement response (B-MC-10M-14%)




a) Tensile strain in bar | b) Maximum flexural cracks | c) Maximum shear cracks

Figure 4-14 Experimental results: crack widths (B-MC-10M-14%)

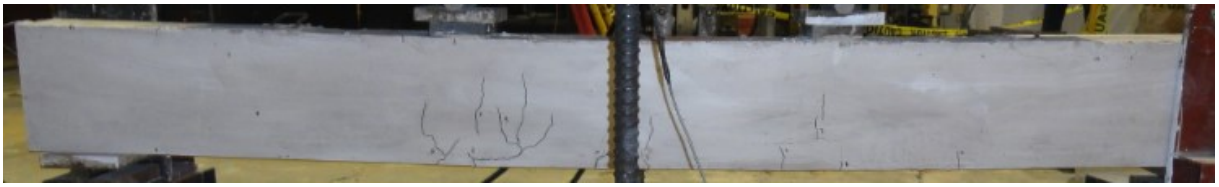
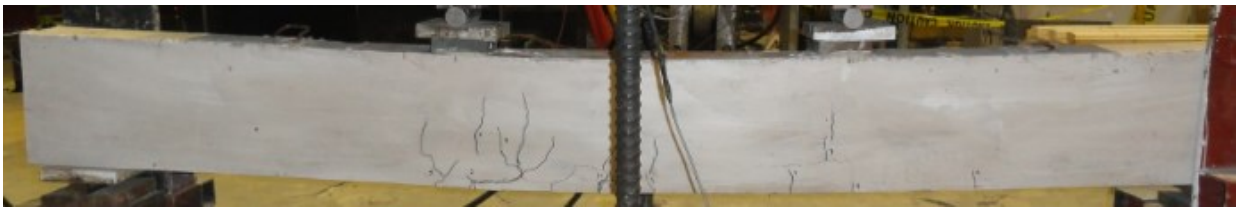
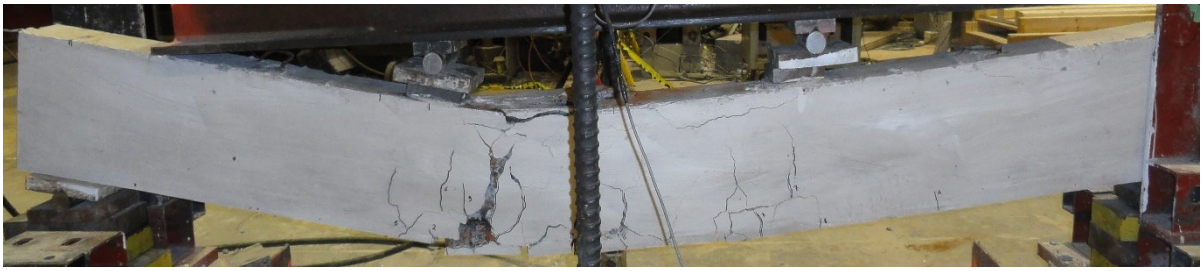
<table>
<tr><th colspan="3">Experimental Parameters</th><th>Description</th></tr>
<tr><td>Load Stage</td><td>Load (kN)</td><td>Mid-Span Deflection (mm)</td><td rowspan="3">First hairline cracks appear in the flexural and shear zones</td></tr>
<tr><td>4</td><td>19</td><td>3</td></tr>
<tr><td colspan="3">  </td></tr>
<tr><td>Load Stage</td><td>Load (kN)</td><td>Mid-Span Deflection (mm)</td><td rowspan="3">Steel reinforcement yielding</td></tr>
<tr><td>10</td><td>49</td><td>11.1</td></tr>
<tr><td colspan="3">  </td></tr>
<tr><td>Load Stage</td><td>Load (kN)</td><td>Mid-Span Deflection (mm)</td><td rowspan="3">Concrete starts crushing at compression zone</td></tr>
<tr><td>13</td><td>49</td><td>35</td></tr>
<tr><td colspan="3">  </td></tr>
<tr><td>Load Stage</td><td>Load (kN)</td><td>Mid-Span Deflection (mm)</td><td rowspan="3">Concrete crushed at compression zone and rebar rupture at the tension zone</td></tr>
<tr><td>22</td><td>24.5</td><td>120</td></tr>
<tr><td colspan="3">  </td></tr>
</table>

Figure 4-15 Main events during testing (B-MC-10M-14%)




Figure 4-16 Bar rupture and concrete damage at the end of testing (B-MC-10M-14%)

#### 4.3.1.4 10M: End/Side corrosion – 11% mass loss (B-SC-10M-11%)

The fourth beam in the 10M group was subjected to corrosion of the steel reinforcement in both shear regions. The target mass loss was 15% for both ends. After testing, the actual average mass loss was determined to be 11%, although the mass loss of the individual extracted bar samples reached 16-17% at some locations (see **Figure** 4-17).

**Figure** 4-18 shows the condition of the beam prior to testing. It was observed that the corrosion led to staining of the concrete surface and concrete cracking, with the formation of horizontal cracks at the level of the longitudinal steel reinforcement. The cracking was more significant in the end shear spans.

The results in terms of load-deflection response and maximum crack-widths are presented in **Figure** 4-19 and **Figure** 4-20, respectively. The main events during testing are shown in **Figure** 4-21. **Table** 4-5 summarizes the key results from the test.

The yield strength of the beam occurred at a load of 50 kN and a displacement of 8 mm, while the maximum strength reached 57 kN at a displacement of 43.5 mm. The displacement at the end of testing was 121 mm with the beam maintaining a residual capacity of 55 kN. The displacement corresponding to 0.85Pmax ($\Delta_{85}$) was 49 mm. The beam showed reduced peak strength, ductility and toughness when compared with the control specimen. The corrosion process also led to an increase in crack widths at equivalent load stages with more random cracking. As shown in **Figure** 4-21, the beam experienced failure of the cover concrete cover in the compression zone with the development of large crack widths in the tension zone at failure.

Table 4-5 : Key results: B-SC-10M-11%

| Load (kN) | | Displacement (mm) | | | Stiffness K (N/mm) | Ductility | | Toughness (kN-mm) | | Failure Mechanism |
|---|---|---|---|---|---|---|---|---|---|---|
| $P_y$ | $P_{max}$ | $\Delta_y$ | $\Delta_{85}$ | $\Delta_{max}$ | | $\left(\frac{\Delta_{85}}{\Delta_y}\right)$ | $\left(\frac{\Delta_{max}}{\Delta_y}\right)$ | $Au_{85}$ | $Au_{max}$ | |
| 50 | 57 | 8.3 | 49 | 121 | 5,981 | 6 | 14.4 | 2,444 | 6,247 | Flexural failure |

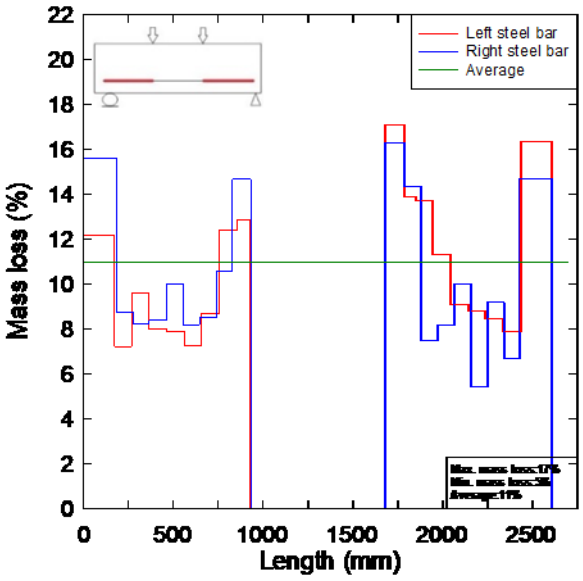



Figure 4-17 Mass loss distribution along the ends length of the tensile bars (B-SC-10M-11%)



Figure 4-18 Cracking in the beam before testing (B-SC-10M-11%)

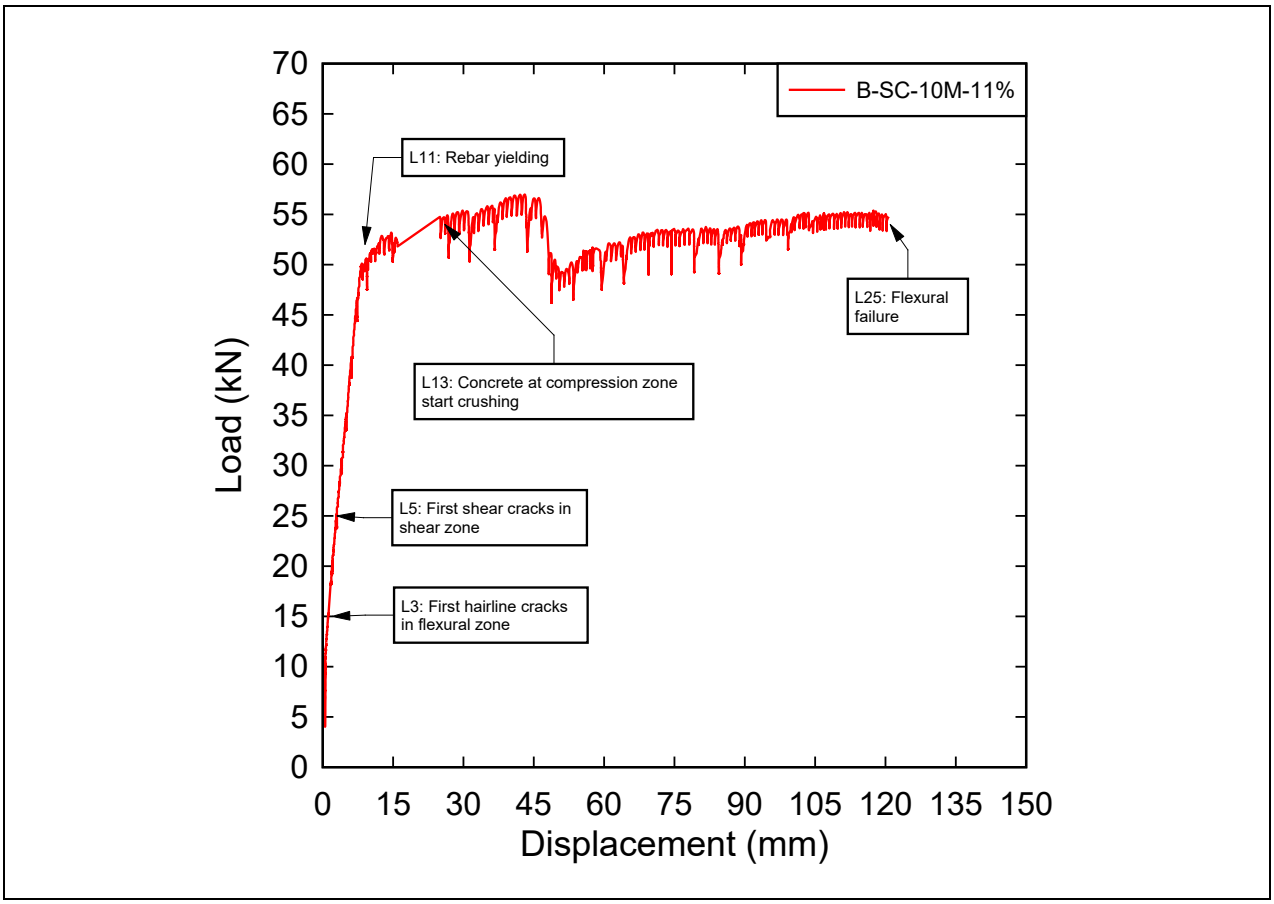
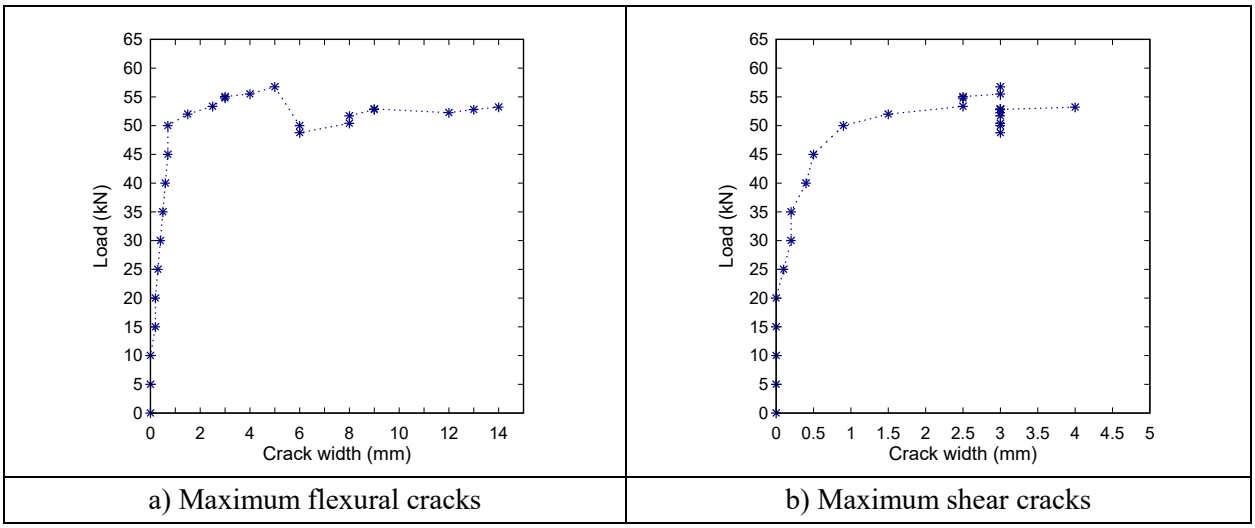



Figure 4-19 Experimental results: load-displacement response (B-SC-10M-11%)




a) Maximum flexural cracks

b) Maximum shear cracks

Figure 4-20 Experimental results: crack widths (B-SC-10M-11%)

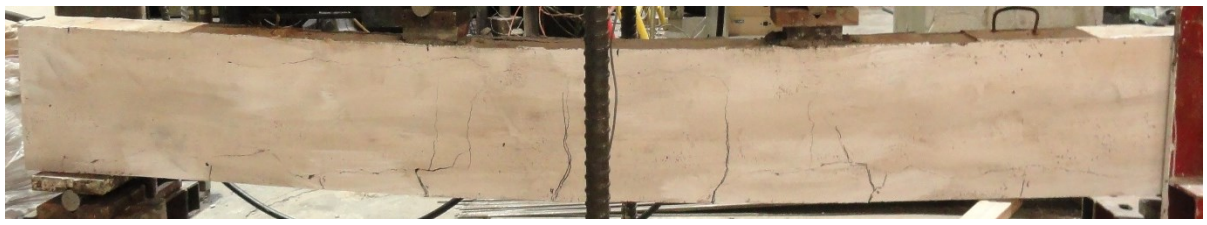
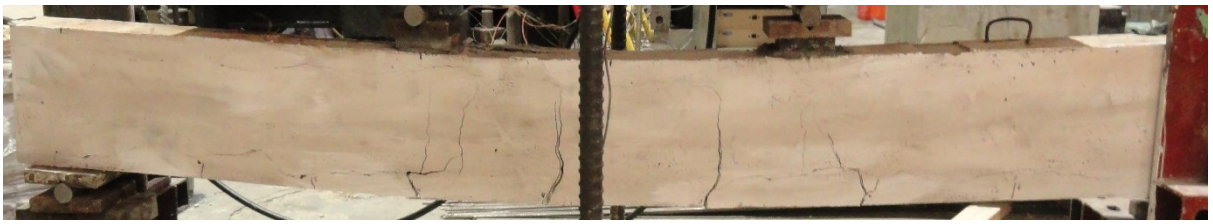
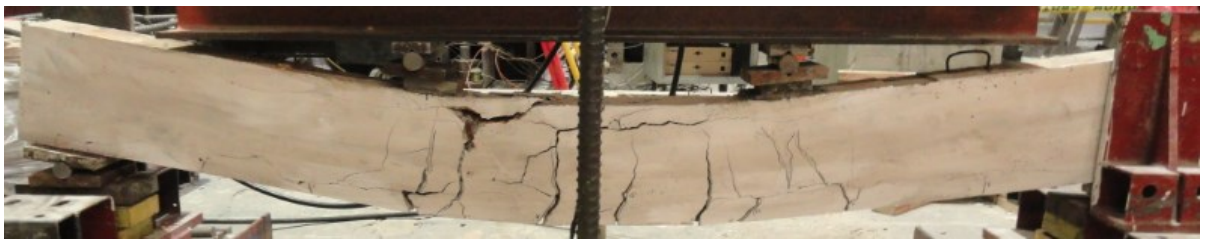
<table>
<tr><th colspan="3">Experimental Parameters</th><th>Description</th></tr>
<tr><td>Load Stage</td><td>Load (kN)</td><td>Mid-Span Deflection (mm)</td><td rowspan="3">First hairline cracks appear in the flexural zone</td></tr>
<tr><td>3</td><td>15</td><td>1.2</td></tr>
<tr><td colspan="3">  </td></tr>
<tr><td>Load Stage</td><td>Load (kN)</td><td>Mid-Span Deflection (mm)</td><td rowspan="3">First hairline cracks appear in the shear zone</td></tr>
<tr><td>5</td><td>25</td><td>3</td></tr>
<tr><td colspan="3">  </td></tr>
<tr><td>Load Stage</td><td>Load (kN)</td><td>Mid-Span Deflection (mm)</td><td rowspan="3">Steel reinforcement yielding</td></tr>
<tr><td>11</td><td>50</td><td>8.3</td></tr>
<tr><td colspan="3">  </td></tr>
<tr><td>Load Stage</td><td>Load (kN)</td><td>Mid-Span Deflection (mm)</td><td rowspan="3">Concrete at the compression zone starts crushing</td></tr>
<tr><td>13</td><td>55</td><td>26</td></tr>
<tr><td colspan="3">  </td></tr>
<tr><td>Load Stage</td><td>Load (kN)</td><td>Mid-Span Deflection (mm)</td><td rowspan="3">Concrete spalled at the compression zone with large cracks in the tension zone</td></tr>
<tr><td>25</td><td>54.5</td><td>121</td></tr>
<tr><td colspan="3">  </td></tr>
</table>

Figure 4-21 Main events during testing (B-SC-10M-11%)

#### 4.3.1.5 10M: Full length Corrosion - 13% mass loss (B-FC-10M-13%)

The final beam in the 10M group was subjected to corrosion of the tension steel reinforcement over the entire beam length. The target mass loss for the 10M bars was 15%. After testing, the actual average mass loss on the bars was determined to be 13%. Considering all extracted bar samples, the maximum and minimum mass loss values were 27% and 6%, respectively (see **Figure** 4-22).

The condition of the beam prior to testing is shown in **Figure** 4-23. The beam showed corrosion-induced cracking and damage over its entire length, with horizontal cracks at the level of the longitudinal bars in the tension zone.

The results in terms of load-deflection response and crack widths are presented in **Figure** 4-24 and **Figure** 4-25, respectively, while the main events at different load stages are shown in **Figure** 4-26. **Table** 4-6 provides a summary of the key test results.

The yield strength of 48 kN occurred at a displacement of 10 mm, while the maximum load of 53 kN was recorded at a displacement of 50 mm. The displacement corresponding to 85% drop in load capacity ($0.85P_{max}$ = 45 kN) occurred at a displacement of 54 mm. Prior to failure, the cover in the mid-span tension region began to show signs of spalling, with debonding at the level of the tension steel bars. Eventually the beam experienced a sudden drop in load capacity at a displacement of 140 mm due to rupture of the tension steel bars. In addition to the brittle failure, the beam also showed a reduction in maximum load, stiffness, ductility and toughness when compared with the control specimen.

**Figure** 4-27 shows a close-up of the beam damage which was associated with beam collapse and spalling of the concrete cover over the mid-span region.

Table 4-6 : Key results: B-FC-10M-13%

| Load (kN) | | Displacement (mm) | | | Stiffness K (N/mm) | Ductility | | Toughness (kN-mm) | | Failure Mechanism |
|---|---|---|---|---|---|---|---|---|---|---|
| $P_y$ | $P_{max}$ | $\Delta_y$ | $\Delta_{85}$ | $\Delta_{max}$ | | $\left(\frac{\Delta_{85}}{\Delta_y}\right)$ | $\left(\frac{\Delta_{max}}{\Delta_y}\right)$ | $Au_{85}$ | $Au_{max}$ | |
| 48 | 53 | 10 | 54 | 140 | 4,767 | 5.4 | 14 | 2,532 | 7,154 | Rebar rupture |

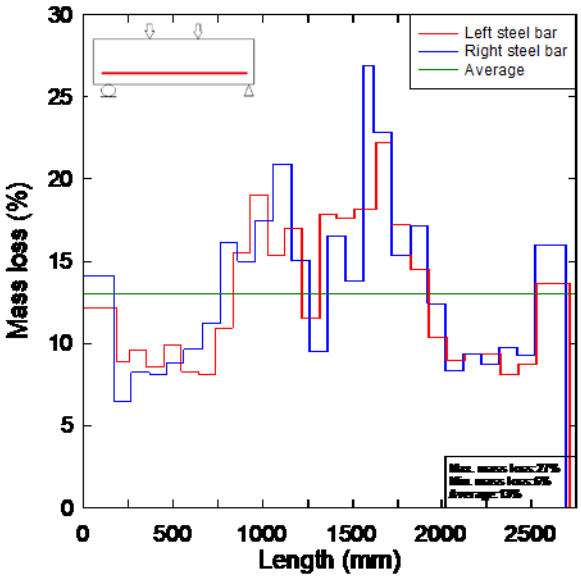



Figure 4-22 Mass loss distribution along the entire length of the tensile bars (B-FC-10M-13%)

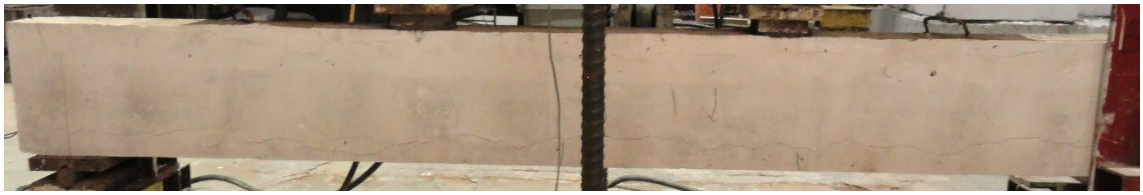


Figure 4-23 Cracking in the beam before testing (B-FC-10M-13%)

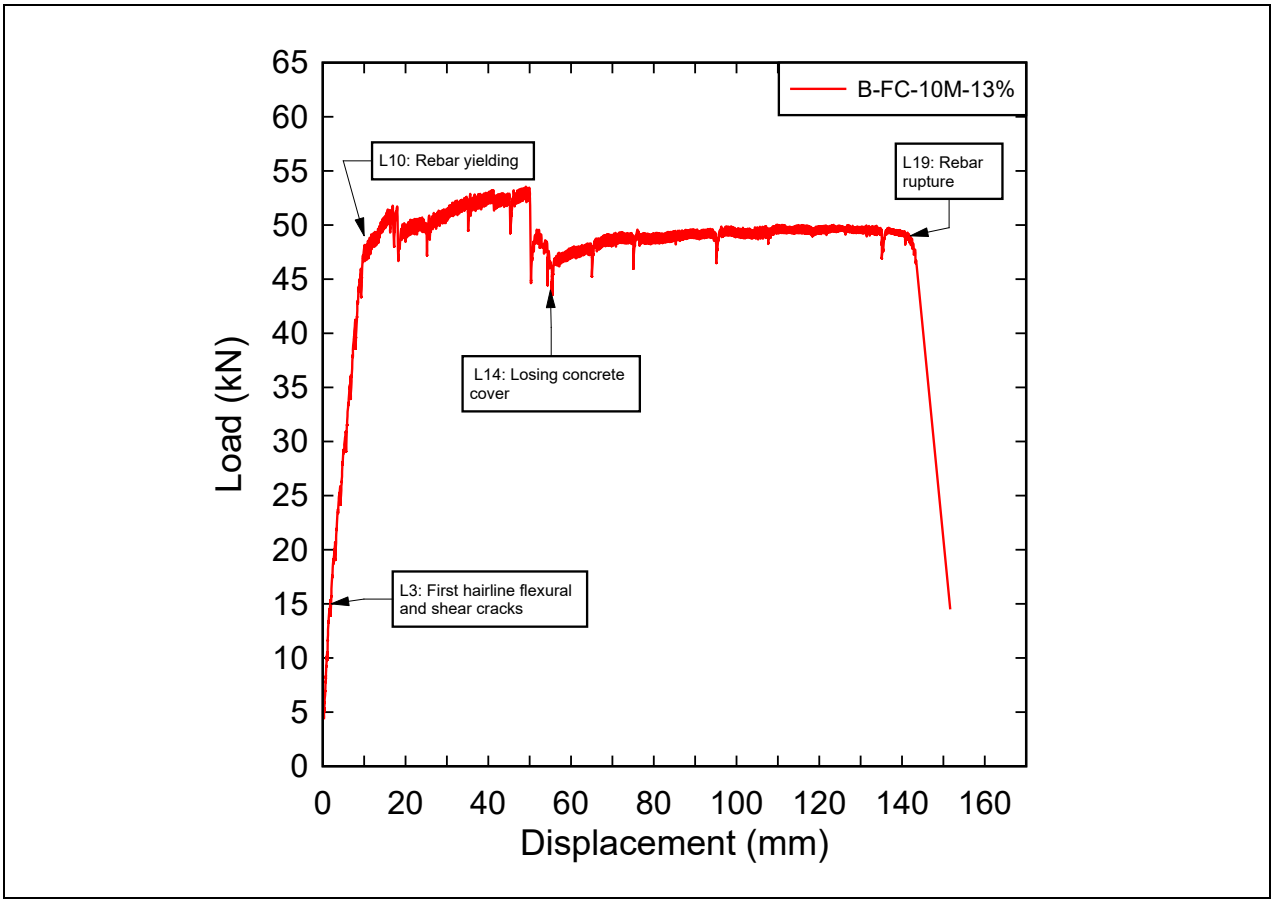
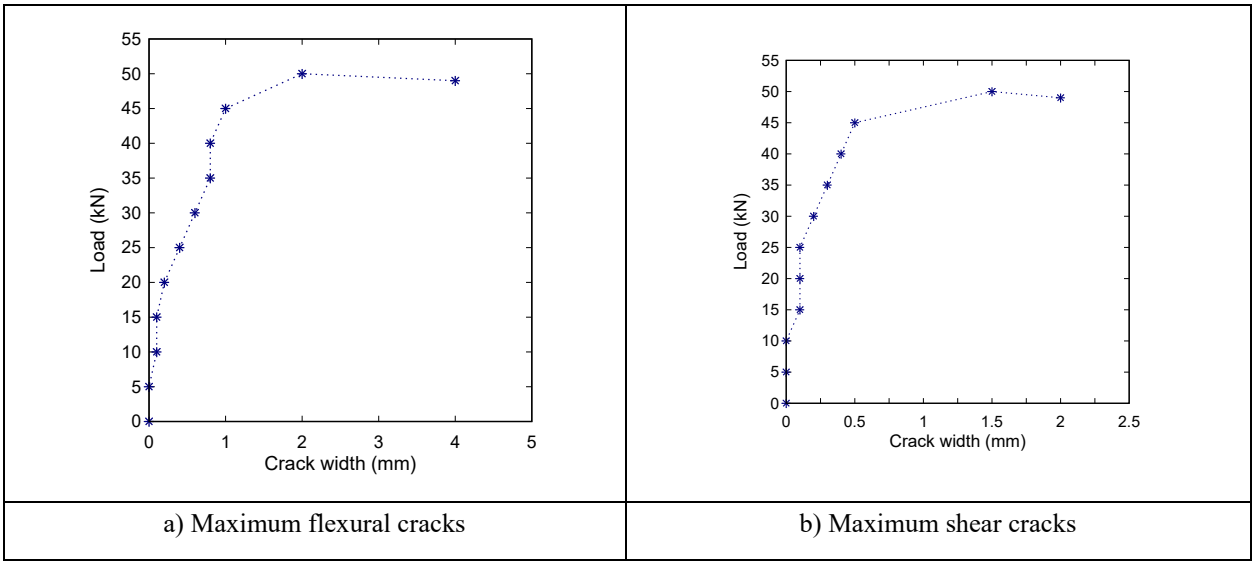



Figure 4-24 Experimental results: load-displacement response (B-FC-10M-13%)




a) Maximum flexural cracks

b) Maximum shear cracks

Figure 4-25 Experimental results: crack widths (B-FC-10M-13%)

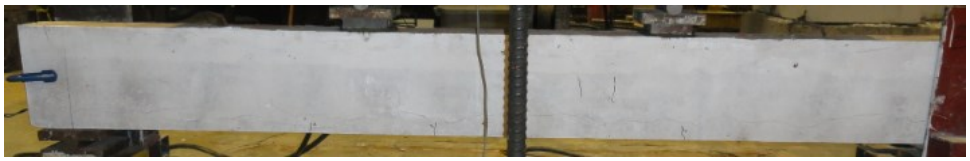
<table>
<tr><th colspan="3">Experimental Parameters</th><th>Description</th></tr>
<tr><td>Load Stage</td><td>Load (kN)</td><td>Mid-Span Deflection (mm)</td><td rowspan="3">First hairline cracks appear in the flexural and shear zones</td></tr>
<tr><td>2</td><td>15</td><td>1.1</td></tr>
<tr><td colspan="3">  </td></tr>
<tr><td>Load Stage</td><td>Load (kN)</td><td>Mid-Span Deflection (mm)</td><td rowspan="3">Steel reinforcement yielding</td></tr>
<tr><td>10</td><td>48.15</td><td>10.1</td></tr>
<tr><td colspan="3">  </td></tr>
<tr><td>Load Stage</td><td>Load (kN)</td><td>Mid-Span Deflection (mm)</td><td rowspan="3">Losing bond between concrete cover and reinforcement and concrete starts crushing at compression zone</td></tr>
<tr><td>14</td><td>44</td><td>55.3</td></tr>
<tr><td colspan="3">  </td></tr>
<tr><td>Load Stage</td><td>Load (kN)</td><td>Mid-Span Deflection (mm)</td><td rowspan="3">Beam splits into two with severe spalling on the concrete cover and rebar rupture in the tension zone</td></tr>
<tr><td>19</td><td>14.5</td><td>152</td></tr>
<tr><td colspan="3">  </td></tr>
</table>

Figure 4-26 Main events during testing (B-FC-10M-13%)

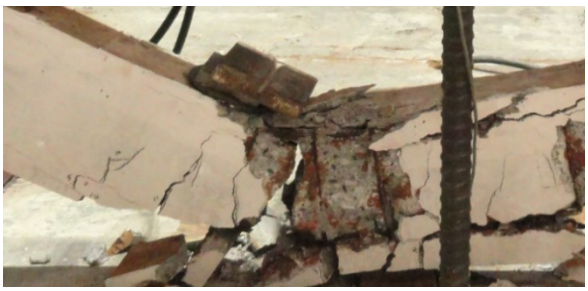


Figure 4-27 Beam collapse with severe spalling and bar rupture (B-FC-10M-13%)

### 4.3.2 15M group

This group consists of two beams which were doubly-reinforced with 2-15M bars in tension and 2-10M in compression (as top bars). In all cases, transverse reinforcement consisted of U-shaped stirrups made from 6.3-mm wire spaced at 100 mm throughout the full beam span. Corrosion was applied on the 15M bars over the mid-span region for one of the beams.

#### 4.3.2.1 15M: Control (0% mass loss) (CB-15M-0%)

Beam CB-15M-0% was the first beam tested in the 15M group and serves as the reference beam in this group. The test results in terms of load-deflection response, tensile strains, and maximum flexural and shear crack-widths are presented in **Figure** 4-28 and **Figure** 4-29. Furthermore, main events during testing are shown in **Figure** 4-30. **Table** 4-7 summarizes the test results.

The test results show that the yield strength of this specimen occurred at a load of 106 kN at a displacement of 17 mm, while the maximum load of 110 kN was recorded at a displacement of 31.8 mm. The failure displacement based on $0.85P_{max}$ ($\Delta_{85}$) was 51 mm. The beam showed a sudden drop in capacity due to concrete crushing with a final displacement of 82 mm. This specimen experienced a ductile flexure failure with significant yielding of the longitudinal bars prior to crushing of the concrete in the compression zone. This failure was also associated to severe buckling of the top longitudinal bars in the mid-span compression zone (see **Figure** 4-30).

Table 4-7 : Key results: CB-15M-0%

| Load (kN) | | Displacement (mm) | | | Stiffness K (N/mm) | Ductility | | Toughness (kN-mm) | | Failure Mechanism |
|---|---|---|---|---|---|---|---|---|---|---|
| $P_y$ | $P_{max}$ | $\Delta_y$ | $\Delta_{85}$ | $\Delta_{max}$ | | $\left(\frac{\Delta_{85}}{\Delta_y}\right)$ | $\left(\frac{\Delta_{max}}{\Delta_y}\right)$ | $Au_{85}$ | $Au_{max}$ | |
| 106 | 110 | 17.2 | 50.5 | 82 | 6,136 | 3 | 5 | 4,544 | 8,817 | Severe concrete crushing and buckling |

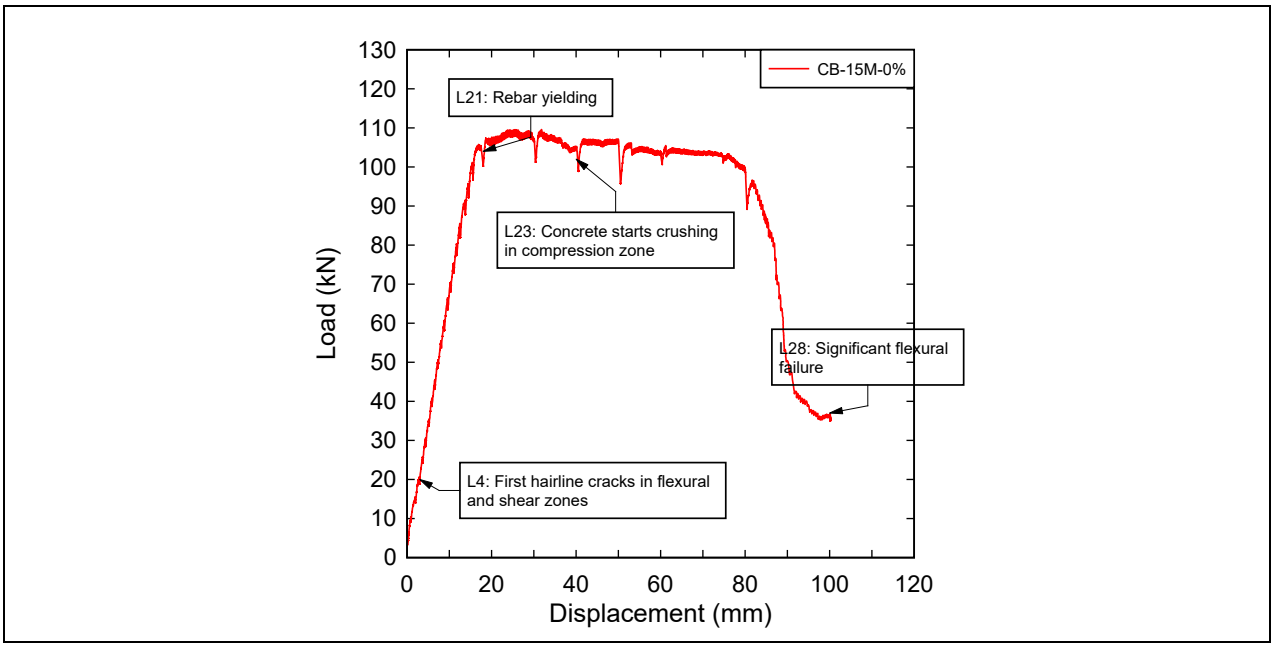
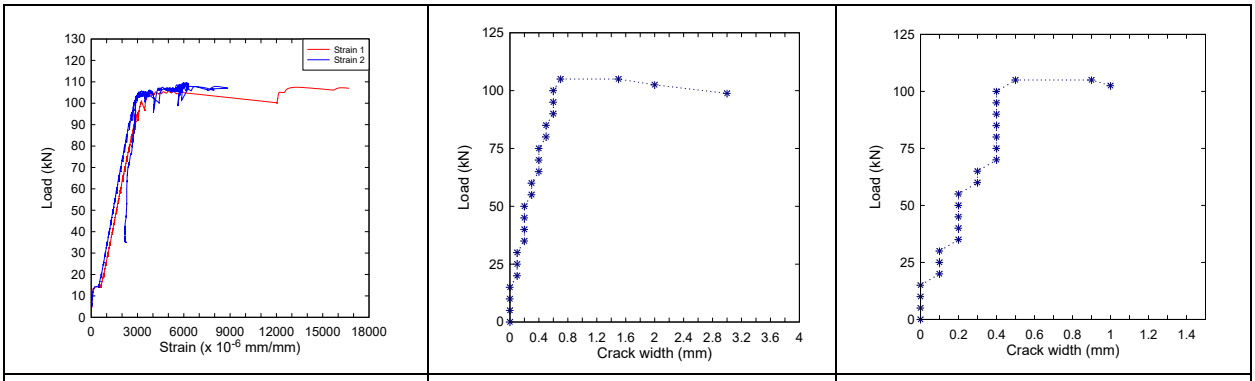



Figure 4-28 Experimental results: load-displacement response (CB-15M-0%)




| a) Tensile strain in bars | b) Max. flexural crack width | c) Maximum shear crack width |
|---|---|---|

Figure 4-29 Experimental results: strains and crack widths (CB-15M-0%)

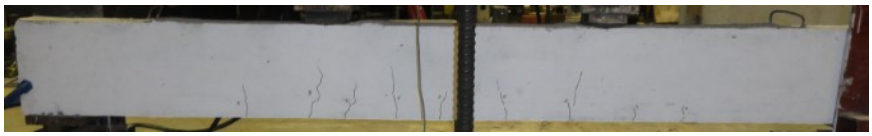
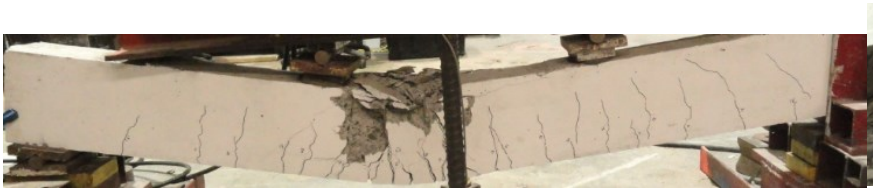
<table>
<tr><th colspan="3">Experimental Parameters</th><th>Description</th></tr>
<tr><td>Load Stage</td><td>Load (kN)</td><td>Mid-Span Deflection (mm)</td><td rowspan="3">First hairline cracks appear in the flexural and shear zones</td></tr>
<tr><td>4</td><td>20</td><td>3</td></tr>
<tr><td colspan="3">  </td></tr>
<tr><td>Load Stage</td><td>Load (kN)</td><td>Mid-Span Deflection (mm)</td><td rowspan="3">Rebar yielding</td></tr>
<tr><td>21</td><td>106</td><td>17.2</td></tr>
<tr><td colspan="3">  </td></tr>
<tr><td>Load Stage</td><td>Load (kN)</td><td>Mid-Span Deflection (mm)</td><td rowspan="3">Concrete starts crushing in compression zone</td></tr>
<tr><td>23</td><td>102.4</td><td>40.3</td></tr>
<tr><td colspan="3">  </td></tr>
<tr><td>Load Stage</td><td>Load (kN)</td><td>Mid-Span Deflection (mm)</td><td rowspan="3">Significant flexural failure associated with crushing of concrete and buckling of the longitudinal bars in the compression zone</td></tr>
<tr><td>28</td><td>37</td><td>100</td></tr>
<tr><td colspan="3">   </td></tr>
</table>

Figure 4-30 Main events during testing (CB-15M-0%)

#### 4.3.2.2 15M: Mid-span corrosion – 10% mass loss (B-MC-15M-10%)

The second beam in the 15M group was subjected to corrosion of the 15M bars over 750 mm in the mid-span region. The target mass loss was 30%. After testing the actual average mass loss was found to be 10%. Considering all extracted bar samples, the maximum mass loss did not exceed 13% (see **Figure** 4-31).

**Figure** 4-32 shows the condition of the beam prior to testing. The beam showed signs of staining and concrete cracking over its length. The main types of cracking were horizontal at the level of the tension and compression longitudinal reinforcing bars. These effects were mainly concentrated in the mid-span constant moment region.

The results in terms of load-deflection response, tensile strain measurements and maximum crack-width response are shown in **Figure** 4-33 and **Figure** 4-34, respectively. The main events during testing are presented in **Figure** 4-35. **Table** 4-8 provides a summary of the key results from the test.

The beam reached its yield strength of 82 kN at a displacement of 14.4 mm. The maximum strength of 87 kN occurred at a displacement of 23 mm. The displacement based on $0.85P_{max}$ ($\Delta_{85}$) was 25 mm. A major drop in load occurred at a displacement of 42 mm due to the effects of corrosion. In addition to the more brittle failure, the beam showed reductions in maximum load, stiffness, ductility and toughness when compared to the control specimen.

The corrosion of the steel reinforcement affected the cracking process in terms of crack widths and cracking patterns, with more random crack distribution as shown in **Figure** 4-35.

**Figure** 4-36 shows that the flexure failure was associated with severe buckling of the longitudinal bars in the compression zone and severe spalling of the concrete cover.

Table 4-8 : Key results: B-MC-15M-10%

| Load (kN) | | Displacement (mm) | | | Stiffness K (N/mm) | Ductility | | Toughness (kN-mm) | | Failure Mechanism |
|---|---|---|---|---|---|---|---|---|---|---|
| $P_y$ | $P_{max}$ | $\Delta_y$ | $\Delta_{85}$ | $\Delta_{max}$ | | $\left(\frac{\Delta_{85}}{\Delta_y}\right)$ | $\left(\frac{\Delta_{max}}{\Delta_y}\right)$ | $Au_{85}$ | $Au_{max}$ | |
| 82 | 87 | 14.4 | 25 | 42 | 5,639 | 1.7 | 3 | 1,506 | 4,079 | Significant buckling and spalling |

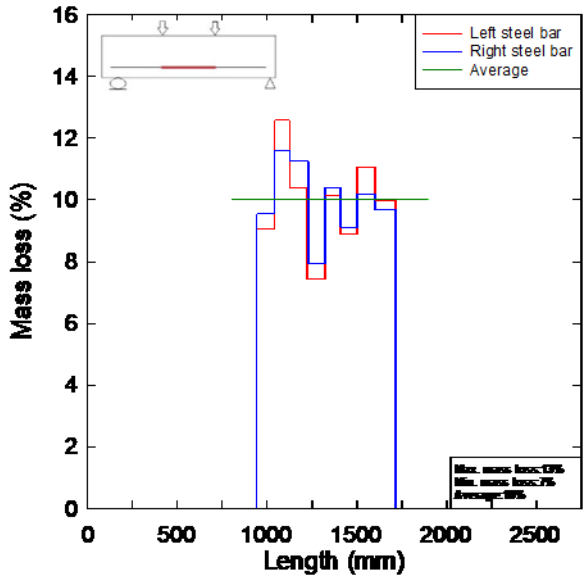



Figure 4-31 Mass loss distribution along the middle length of the tensile bars (B-MC-15M-10%)



Figure 4-32 Cracking patterns of the beam before testing (B-MC-15M-10%)

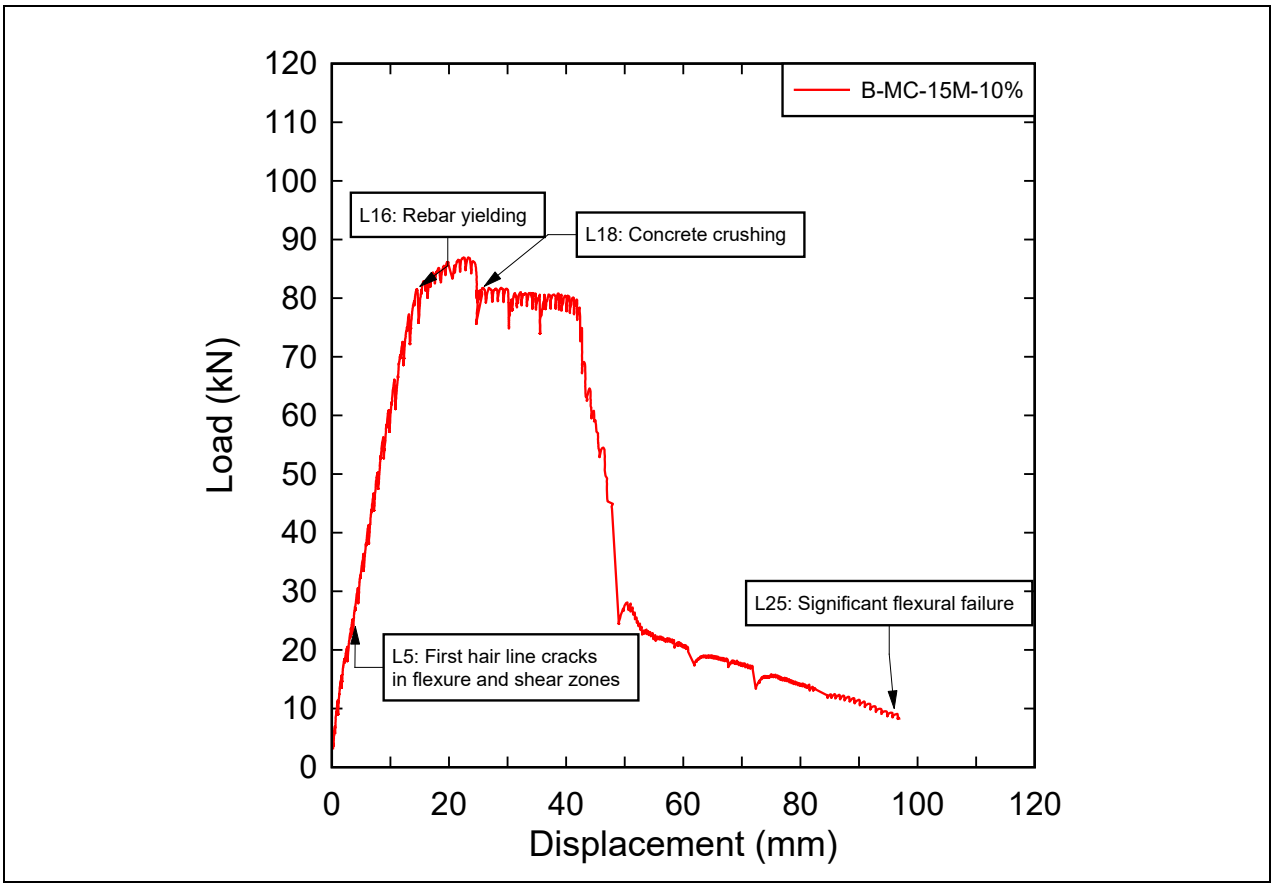
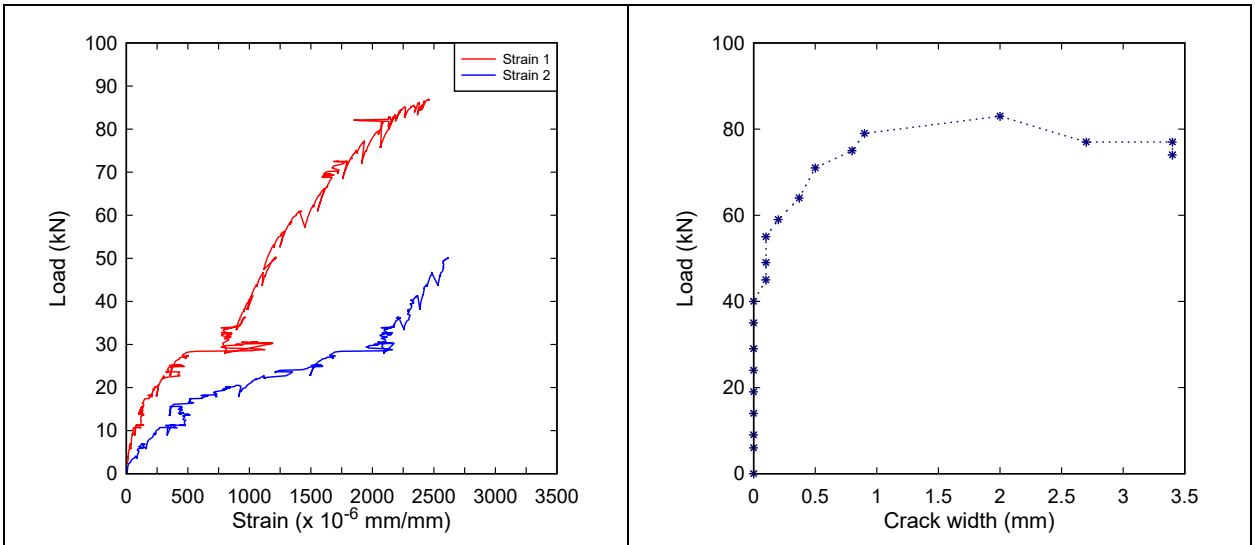



Figure 4-33 Experimental results: load-displacement response (B-MC-15M-10%)




a) Tensile strain in bars

b) Maximum flexural cracks

Figure 4-34 Experimental results: strains and crack widths (B-MC-15M-10%)

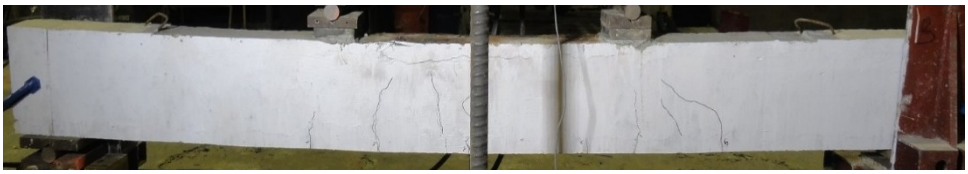
<table>
<tr><th colspan="3">Experimental Parameters</th><th>Description</th></tr>
<tr><td>Load Stage</td><td>Load (kN)</td><td>Mid-Span Deflection (mm)</td><td rowspan="3">First hairline cracks appear in the flexural and shear zones</td></tr>
<tr><td>5</td><td>24</td><td>3.5</td></tr>
<tr><td colspan="3">  </td></tr>
<tr><td>Load Stage</td><td>Load (kN)</td><td>Mid-Span Deflection (mm)</td><td rowspan="3">Rebar yielding</td></tr>
<tr><td>16</td><td>81.5</td><td>14.5</td></tr>
<tr><td colspan="3">  </td></tr>
<tr><td>Load Stage</td><td>Load (kN)</td><td>Mid-Span Deflection (mm)</td><td rowspan="3">Concrete starts crushing in the compression zone</td></tr>
<tr><td>18</td><td>79</td><td>25.6</td></tr>
<tr><td colspan="3">  </td></tr>
<tr><td>Load Stage</td><td>Load (kN)</td><td>Mid-Span Deflection (mm)</td><td rowspan="3">Significant flexural failure associated with buckling of longitudinal bars in the compression zone, with severe spalling of cover concrete</td></tr>
<tr><td>25</td><td>8</td><td>97</td></tr>
<tr><td colspan="3">  </td></tr>
</table>

Figure 4-35 The main events through loading stages (B-MC-15M-10%)



Figure 4-36 Severe buckling and spalling (B-MC-15M-10%)

### 4.3.3 25M Group

The 25M group included three beams which were built with 2-25M bars in tension and 2-10M bars in compression (as top bars). The increased tensile steel ratio was intended to increase the shear demands in this beam series. In all cases, transverse reinforcement consisted of U-shaped stirrups made from 6.3-mm wire spaced at 100 mm throughout the full beam span, which corresponds to the minimum required by the CSA A23.3-14 standard (i.e., s = d/2). The corrosion process in this series was on the transverse reinforcement throughout their spans.

#### 4.3.3.1 25M: Control – 0% mass loss (CB-25M-0%)

Beam CB-25M-0% was the reference beam in the 25M group. The test results in terms of load-deflection response, strains, and crack-widths are presented in **Figure** 4-37 and **Figure** 4-38, respectively. **Figure** 4-39 shows the main events during the test. Key results are summarized in **Table** 4-9.

The results show that this beam reached a maximum load of 190 kN at a displacement of 18 mm. Soon after reaching the peak load, the beam showed a steady drop in load-carrying capacity, reaching an ultimate displacement of 84 mm at the end of testing, with a residual load of 61 kN. Considering $0.85P_{max}$, the failure displacement $\Delta_{85}$ was 25 mm. Although the tension steel just reached yielding, this specimen experienced a gradual shear failure, with concrete crushing and diagonal shear cracking in the right shear span. This failure was also associated with buckling of the top longitudinal bars in the compression zone in the shear-span region, as shown in **Figure** 4-40.

Table 4-9 : Key results: CB-25M-0%

| Load (kN) | | Displacement (mm) | | | Stiffness K (N/mm) | Ductility | | Toughness (kN-mm) | | Failure Mechanism |
|---|---|---|---|---|---|---|---|---|---|---|
| $P_y$ | $P_{max}$ | $\Delta_y$ | $\Delta_{85}$ | $\Delta_{max}$ | | $\left(\frac{\Delta_{85}}{\Delta_y}\right)$ | $\left(\frac{\Delta_{max}}{\Delta_y}\right)$ | $Au_{85}$ | $Au_{max}$ | |
| - | 190 | - | 25 | 84 | - | - | - | 3,017 | 8,635 | Shear failure |

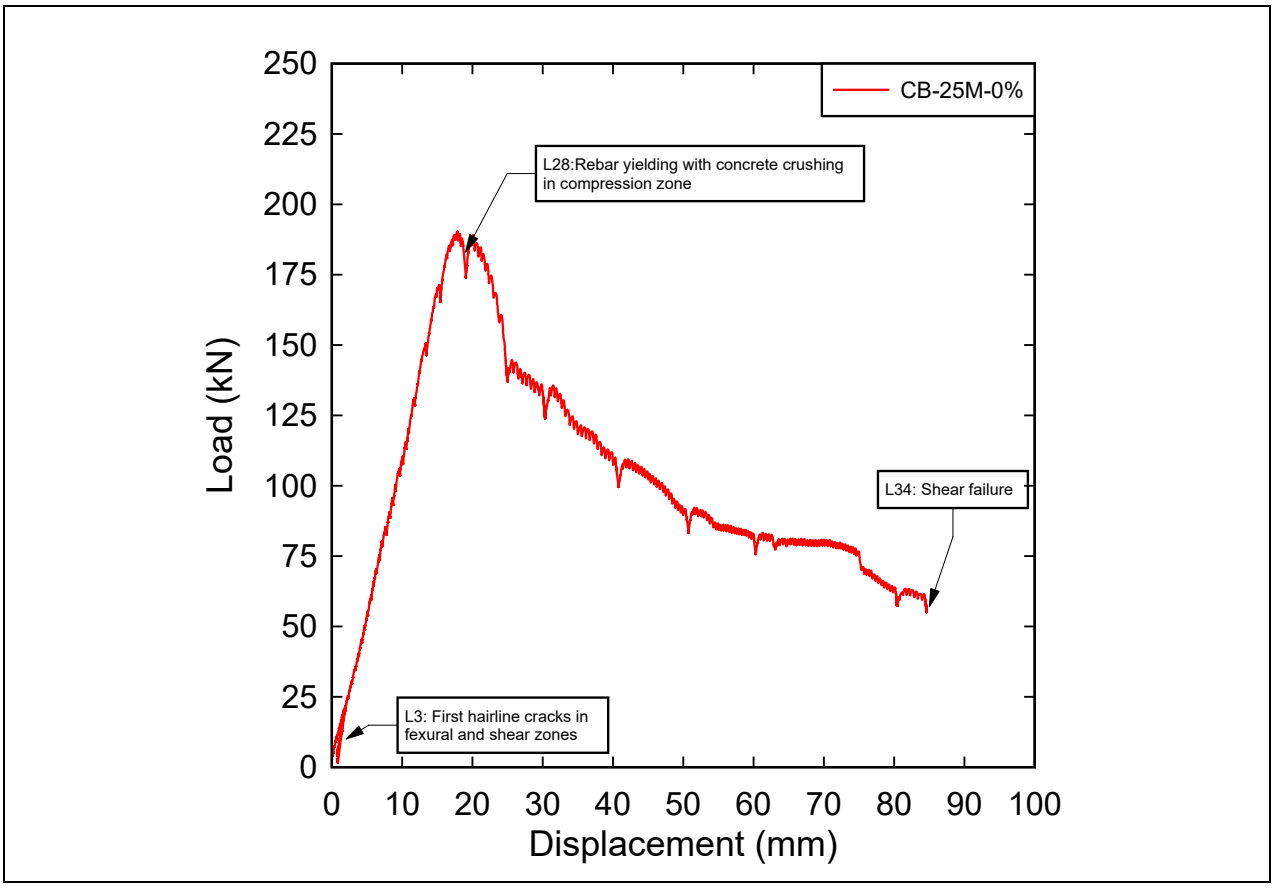
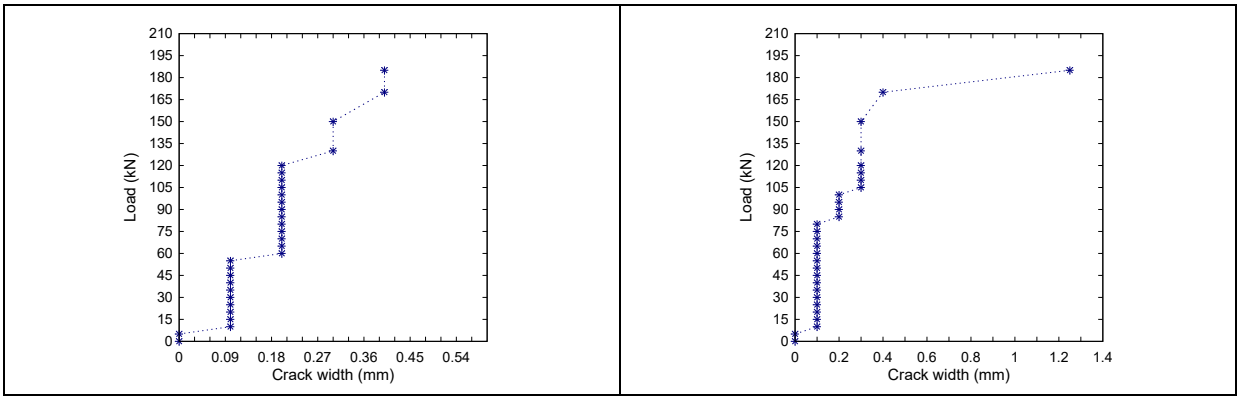



Figure 4-37 Experimental results: load-displacement response (CB-25M-0%)




a) Maximum flexural cracks | b) Maximum shear cracks

Figure 4-38 Experimental results: crack widths (CB-25M-0%)

<table>
<tr><th colspan="3">Experimental Parameters</th><th>Description</th></tr>
<tr><td>Load Stage</td><td>Load (kN)</td><td>Mid-Span Deflection (mm)</td><td rowspan="3">First hairline cracks appear in the flexural and shear zones</td></tr>
<tr><td>4</td><td>20</td><td>1.9</td></tr>
<tr><td colspan="3">  </td></tr>
<tr><td>Load Stage</td><td>Load (kN)</td><td>Mid-Span Deflection (mm)</td><td rowspan="3">Rebar yielded suddenly associated with significant shear cracks and concrete crushing in compression zone</td></tr>
<tr><td>28</td><td>183.3</td><td>18.8</td></tr>
<tr><td colspan="3">  </td></tr>
<tr><td>Load Stage</td><td>Load (kN)</td><td>Mid-Span Deflection (mm)</td><td rowspan="3">Significant shear failure associated with significant buckling of longitudinal bars in compression zone</td></tr>
<tr><td>34</td><td>57.2</td><td>84.5</td></tr>
<tr><td colspan="3">  </td></tr>
</table>

Figure 4-39 The main events during testing (CB-25M-0%)



Figure 4-40 Buckling of top bars in shear span region (CB-25M-0%)

#### 4.3.3.2 25M: Shear corrosion – 10% mass loss (B-SHC-25M-10%)

Beam B-SHC-25M-10% had the same properties as the control beam, but was subjected to corrosion of the U-shaped stirrups throughout its span. The corrosion process aimed for a mass loss of 15% in the stirrups. The actual average mass loss was 10%, with a maximum mass loss not exceeding 17% over the length of the extracted stirrups as shown in **Figure** 4-41.

Before testing, the beam showed clear signs of corrosion in terms of staining of the concrete surface and cracking over its length and depth, particularly at the stirrup locations as shown in **Figure** 4-42. The primary cracks before testing consisted of vertical cracks coinciding with the location of the stirrups.

**Figure** 4-43 and **Figure** 4-44 show the results in terms of load-deflection response, tensile strains and maximum crack-widths, respectively. Key events during testing are presented **Figure** 4-45. A summary of results is provided in **Table** 4-10.

The maximum capacity of this beam reached 198 kN at a displacement of 19 mm, which was slightly higher than that of the control specimen. Shortly after reaching its peak strength, the load dropped suddenly to 125 kN, after which the beam showed a more gradual decrease in capacity. The displacement at the end of the test was 64 mm. Compared to the control, the beam showed lower toughness (area under the load-deflection curve). Furthermore, the corrosion process increased the cracks widths during the test and resulted in a more random cracking pattern. The shear failure was associated with concrete crushing at the point load location and buckling of the top longitudinal reinforcement in the compression zone in the right shear-span region (see **Figure** 4-46). Moreover, the beam showed loss of the side concrete in the failure region.

Table 4-10 : Key results: B-SHC-25M-10%

| Load (kN) | | Displacement (mm) | | | Stiffness K (N/mm) | Ductility | | Toughness (kN-mm) | | Failure Mechanism |
|---|---|---|---|---|---|---|---|---|---|---|
| $P_y$ | $P_{max}$ | $\Delta_y$ | $\Delta_{85}$ | $\Delta_{max}$ | | $\left(\frac{\Delta_{85}}{\Delta_y}\right)$ | $\left(\frac{\Delta_{max}}{\Delta_y}\right)$ | $Au_{85}$ | $Au_{max}$ | |
| - | 198 | - | 19 | 64 | - | - | - | 2,462 | 6,000 | Shear failure |

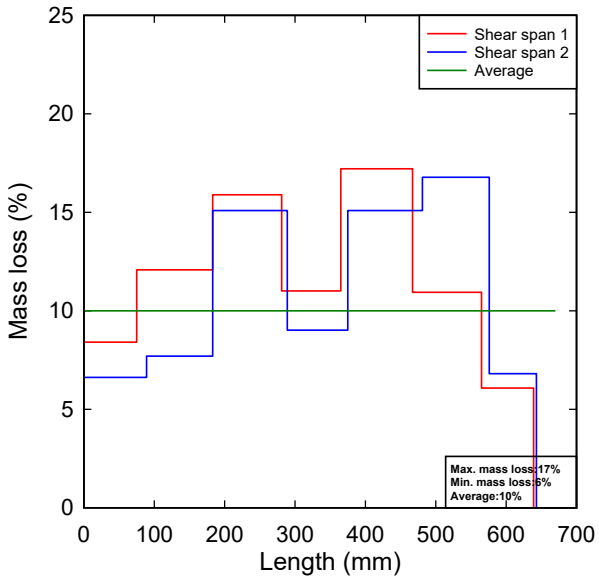



Figure 4-41 Mass loss distribution along the stirrups in shear span (B-SHC-25M-10%)

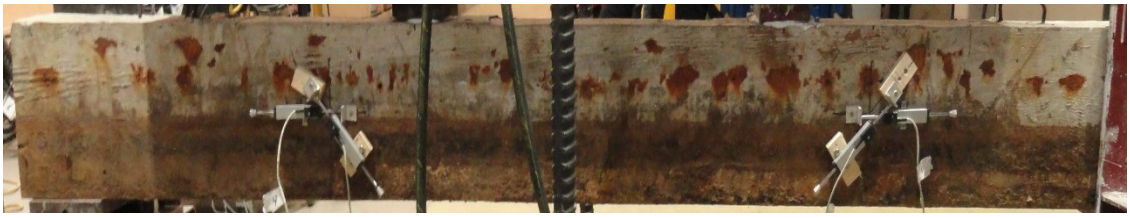


Figure 4-42 Cracking in the beam before testing (B-SHC-25M-10%)

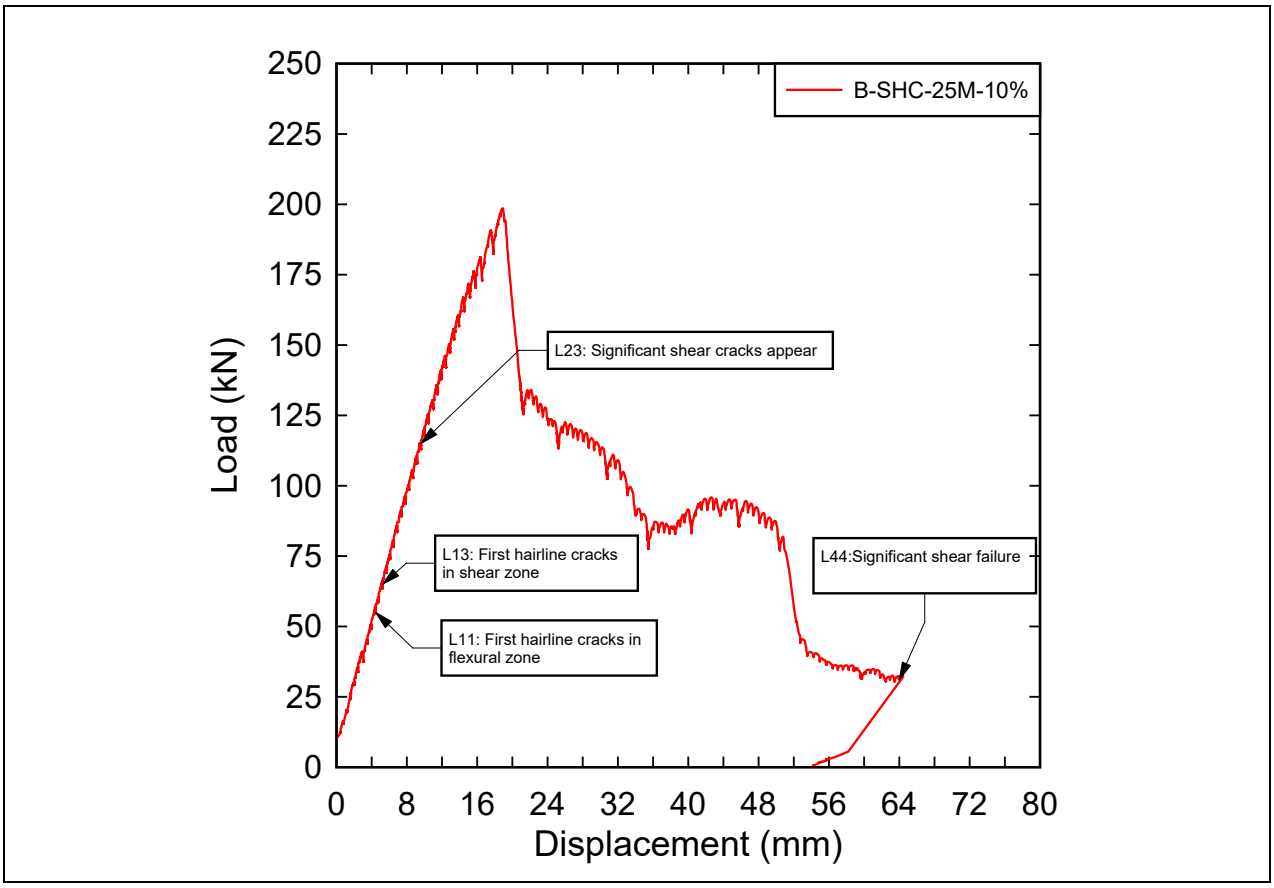
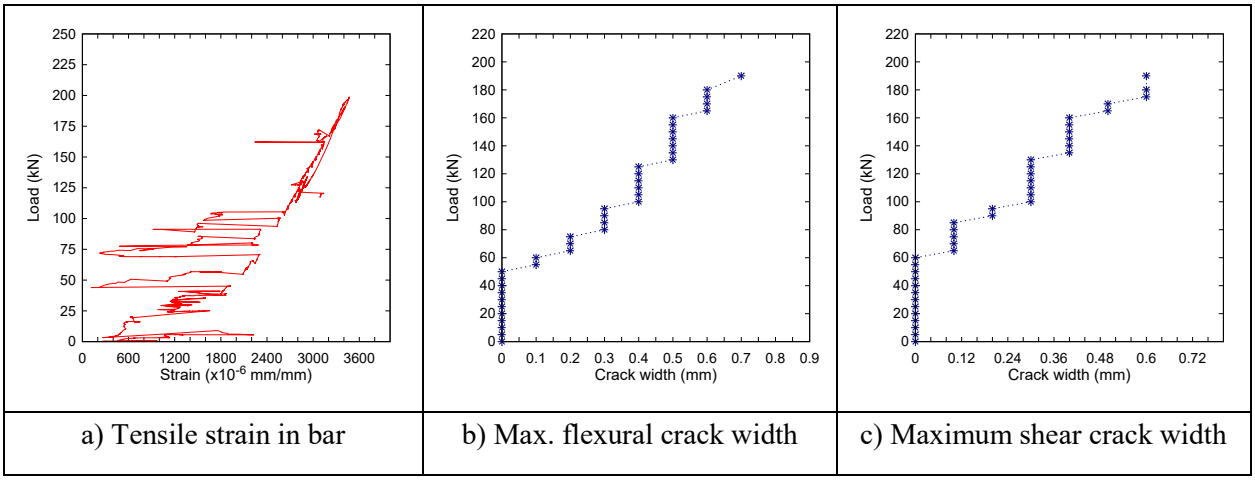



Figure 4-43 Experimental results: load-displacement response (B-SHC-25M-10%)




a) Tensile strain in bar | b) Max. flexural crack width | c) Maximum shear crack width

Figure 4-44 Experimental results: strains and crack widths (B-SHC-25M-10%)

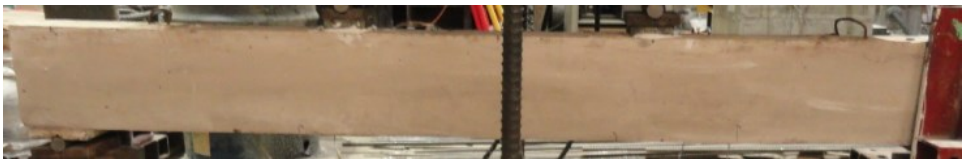
<table>
<tr><th colspan="3">Experimental Parameters</th><th>Description</th></tr>
<tr><td>Load Stage</td><td>Load (kN)</td><td>Mid-Span Deflection (mm)</td><td rowspan="3">First hairline cracks appear in the flexural zone</td></tr>
<tr><td>11</td><td>55</td><td>4.4</td></tr>
<tr><td colspan="3">  </td></tr>
<tr><td>Load Stage</td><td>Load (kN)</td><td>Mid-Span Deflection (mm)</td><td rowspan="3">First hairline cracks appear in the shear zone</td></tr>
<tr><td>13</td><td>65</td><td>5.2</td></tr>
<tr><td colspan="3">  </td></tr>
<tr><td>Load Stage</td><td>Load (kN)</td><td>Mid-Span Deflection (mm)</td><td rowspan="3">Significant shear cracks appear and concrete starts crushing in compression zone</td></tr>
<tr><td>23</td><td>115</td><td>9.6</td></tr>
<tr><td colspan="3">  </td></tr>
<tr><td>Load Stage</td><td>Load (kN)</td><td>Mid-Span Deflection (mm)</td><td rowspan="3">Significant shear failure associated with significant buckling of longitudinal bars in compression zone</td></tr>
<tr><td>44</td><td>32.1</td><td>64.3</td></tr>
<tr><td colspan="3">  </td></tr>
</table>

Figure 4-45 Main events during testing (B-SHC-25M-10%)



Figure 4-46 Buckling of the longitudinal bars and loss of side cover (B-SHC-25M-10%)

#### 4.3.3.3 25M: Shear corrosion – 12% mass loss (B-SHC-25M-12%)

The final beam in the 25M group had the same properties as the control specimen, but was subjected to corrosion of the U-shaped stirrups throughout the beam span. The corrosion process aimed at producing a mass loss of 30% in the stirrups. The actual average mass loss was 12%, which was lower than the 30% target, with a maximum mass loss not exceeding 22% at any one location over the length of the extracted stirrups as shown in **Figure** 4-47.

Prior to beam testing, the beam showed clear signs of corrosion in terms of staining and concrete cracking over its length and depth, particularly at the stirrup locations as shown in **Figure** 4-48. The cracks before testing consisted of horizontal cracks at the locations of the longitudinal bars in tension and compression and also, vertical cracks at the stirrups.

The results in terms of load-deflection response, tensile strain measurement and maximum crack-widths responses are presented in **Figure** 4-49 and **Figure** 4-50, respectively. In addition, the main events during testing are shown in **Figure** 4-51. Key results are also summarized in **Table** 4-11.

The beam reached a maximum capacity of 202 kN at a displacement of 19 mm. After its peak strength, the load dropped suddenly with a residual strength of 37 kN. The final displacement at the end of testing was 60 mm. In addition to the more brittle shear failure, the beam showed lower toughness (area under the load-deflection curve) when compared to the control. Moreover, the corrosion process increased the cracks widths during the test and resulted in a more random cracking pattern. Similar to the previous beam, the shear failure was associated with concrete crushing at the point load location and buckling of the top longitudinal reinforcement in the compression zone in the right shear-span region. Moreover, in addition to the diagonal cracking, the beam experienced loss of the side concrete cover in this region. As shown in **Figure** 4-52, the damage was also associated with rupture of the corroded transverse reinforcement.

Table 4-11 : Key results: B-SHC-25M-12%

| Load (kN) | | Displacement (mm) | | | Stiffness K (N/mm) | Ductility | | Toughness (kN-mm) | | Failure Mechanism |
|---|---|---|---|---|---|---|---|---|---|---|
| $P_y$ | $P_{max}$ | $\Delta_y$ | $\Delta_{85}$ | $\Delta_{max}$ | | $\left(\frac{\Delta_{85}}{\Delta_y}\right)$ | $\left(\frac{\Delta_{max}}{\Delta_y}\right)$ | $Au_{85}$ | $Au_{max}$ | |
| - | 202 | - | 19 | 60 | - | - | - | 2,715 | 3,873 | Shear failure |

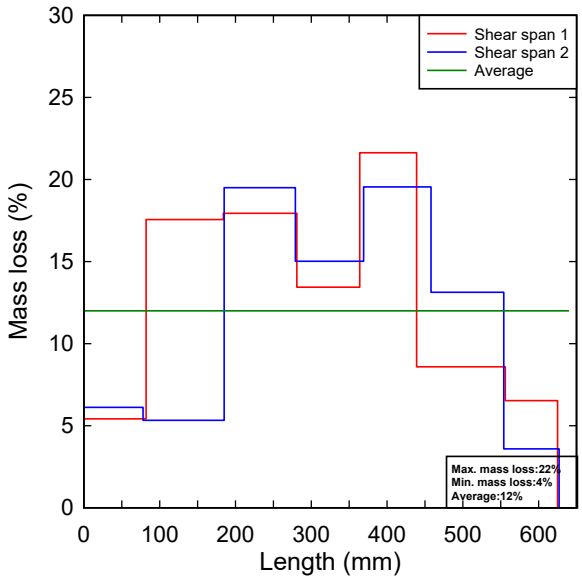



Figure 4-47 Mass loss distribution along the stirrups in shear span (B-SHC-25M-12%)



Figure 4-48 Corrosion-induced cracking in the beam before testing (B-SHC-25M-12%)

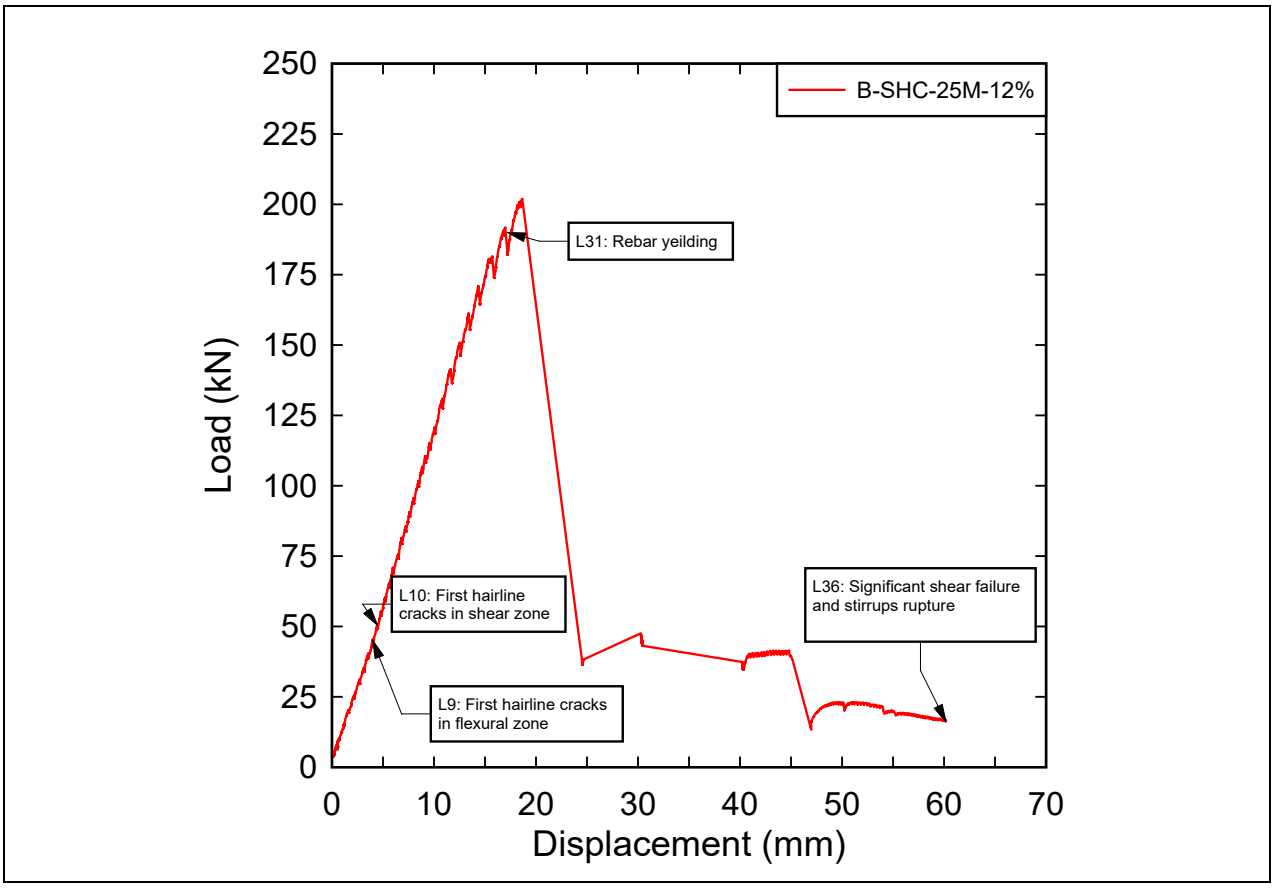
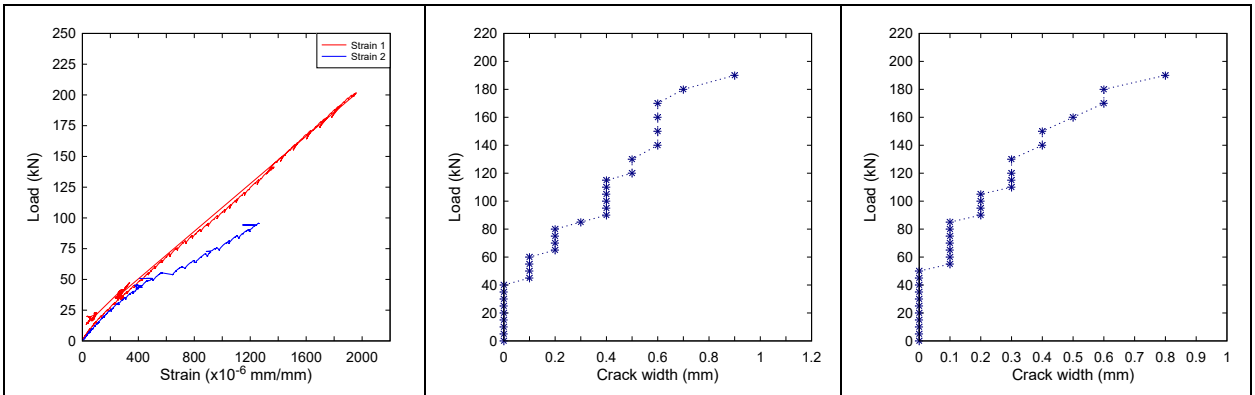



Figure 4-49 Experimental results: load-displacement response (B-SHC-25M-10%)




a) Tensile strain in bars | b) Maximum flexural crack width | c) Maximum shear crack width

Figure 4-50 Experimental results: strains and crack widths (B-SHC-25M-12%)

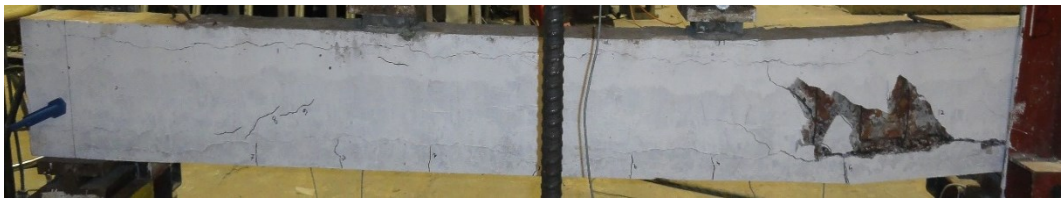
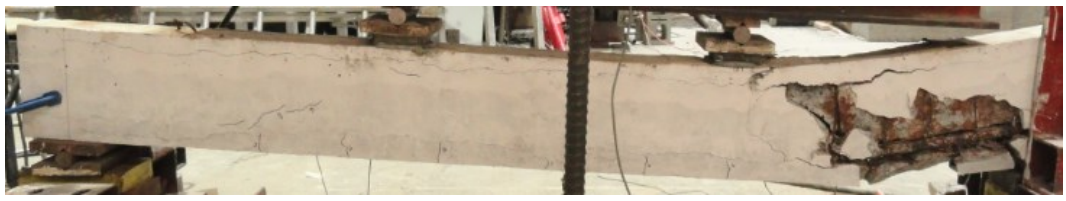
<table>
<tr><th colspan="3">Experimental Parameters</th><th>Description</th></tr>
<tr><td>Load Stage</td><td>Load (kN)</td><td>Mid-Span Deflection (mm)</td><td rowspan="3">First hairline cracks appear in the flexural zone</td></tr>
<tr><td>9</td><td>45</td><td>4</td></tr>
<tr><td colspan="3">  </td></tr>
<tr><td>Load Stage</td><td>Load (kN)</td><td>Mid-Span Deflection (mm)</td><td rowspan="3">First hairline cracks appear in the shear zone</td></tr>
<tr><td>10</td><td>50</td><td>4</td></tr>
<tr><td colspan="3">  </td></tr>
<tr><td>Load Stage</td><td>Load (kN)</td><td>Mid-Span Deflection (mm)</td><td rowspan="3">Rebar yielding with significant shear cracks appear</td></tr>
<tr><td>31</td><td>190</td><td>17</td></tr>
<tr><td colspan="3">  </td></tr>
<tr><td>Load Stage</td><td>Load (kN)</td><td>Mid-Span Deflection (mm)</td><td rowspan="3">Load drops suddenly with spalling of the concrete cover</td></tr>
<tr><td>32</td><td>37</td><td>25</td></tr>
<tr><td colspan="3">  </td></tr>
<tr><td>Load Stage</td><td>Load (kN)</td><td>Mid-Span Deflection (mm)</td><td rowspan="3">Significant shear failure associated with rupture of stirrups and crushing of concrete cover</td></tr>
<tr><td>36</td><td>16</td><td>60</td></tr>
<tr><td colspan="3">  </td></tr>
</table>

Figure 4-51 Main events during testing (B-SHC-25M-12%)



Figure 4-52 Rupture of stirrups and severe concrete damage (B-SHC-25M-12%)

# Chapter 5: Discussion of Static Results

## 5.1 Chapter Overview

This chapter discusses the effects of test parameters on the reinforced concrete beams tested statically under four-point bending. These parameters were examined by comparing the maximum strength, maximum displacement, stiffness, ductility, toughness, and failure mode of the beams.

The parameters discussed in the following sections include:

- Effect of mid-span corrosion:
    - 10M group: CB-10M-0% vs B-MC-10M-14% vs B-MC-10M-13%
    - 15M group: CB-15M-0% vs B-MC-15M-10%

- Effect of end-span corrosion:
    - 10M group: CB-10M-0% vs B-SC-10M-11%

- Effect of full-span corrosion:
    - 10M group: CB-10M-0% vs B-FC-10M-13%

- Effect of corrosion location (mid, end and full span):
    - 10M group: B-MC-10M-13% vs B-SC-10M-11% vs B-FC-10M-13%

- Effect of shear corrosion and mass loss in stirrups:
    - 25M group: CB-25M-0% vs B-SHC-25M-10% vs B-SHC-25M-12%

## 5.2 Effects of mid-span corrosion

### 5.2.1 10M group: CB-10M-0% vs B-MC-10M-14% and B-MC-10M-13%

The results of beams CB-10M-0%, B-MC-10M-14% and B-MC-10M-13% were compared to examine the effect of corrosion of the tension steel in the mid-span region on the flexural response of the beams in the 10M group. All beams had identical design properties, which included 2-10M bars in tension and compression with U-shaped stirrups at 100 mm throughout the span. Beams B-MC-10M-14% and B-MC-10M-13% were subjected to corrosion of the 10M tension bars over the central 750-mm mid-span region, with an actual average mass loss of 14% and 13%, respectively. **Figure 5-1** compares the beam load-deflection responses, while photos of the beams at failure are shown in **Figure 5-2**. **Figure 5-3** compares key response parameters in a bar chart format.

It was observed that the corrosion affected all aspects of beam flexural behaviour under static loading. Examining the effect on strength, the maximum and yield strengths of beam B-MC-10M-14% showed reductions of 13% and 9%, respectively, when compared to beam CB-10M-0%. The reduction in strength can be explained by the reduction in tension reinforcement area due to corrosion. The corroded beam also showed a reduction of 10% in stiffness. Similar reductions in strength and stiffness were observed in beam B-MC-10M-13%.

Testing of beam B-MC-10M-13% was ended early; however, the ductility and failure mode can be compared for the remaining two beams. Beam B-MC-10M-14% showed a reduction of 41% in maximum displacement when compared to the control beam, with a sudden drop in capacity at $\Delta$ = 71 mm due to rupture of the 10M tension bars. In comparison beam CB-10M-0% continued to carry significant load up to the end of testing at $\Delta$ = 120 mm.

Considering $0.85P_{max}$, the ductility ($\Delta_{85}/\Delta_y$) and toughness ($A_{u85}$) of beam B-MC-10M-14% decreased by 63% and 68%, respectively, when compared to CB-10M-0%. Both beams failed in flexure, with significant yielding of the tension steel reinforcement; however, the failure of B-MC-10M-14% was more brittle and was associated with sudden rupture of the 10M bars in the mid-span region and more significant spalling of the cover concrete, as shown in **Figure 5-2**.

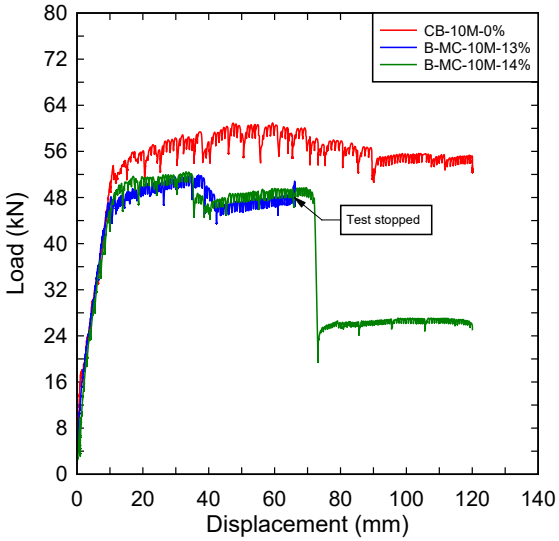



Figure 5-1 Load-deflection comparison: effect of mid-span corrosion (10M group)

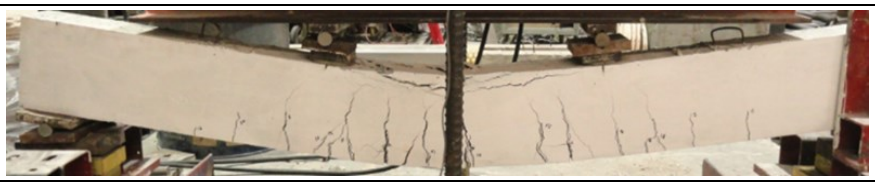
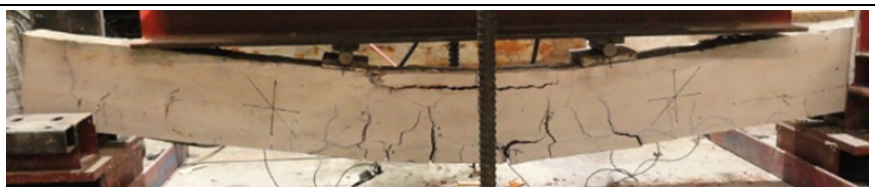
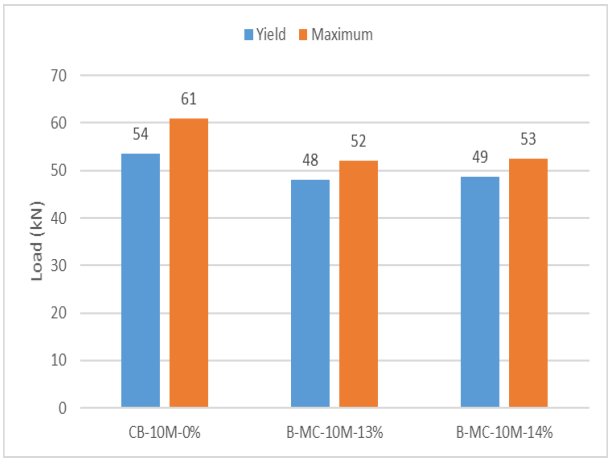
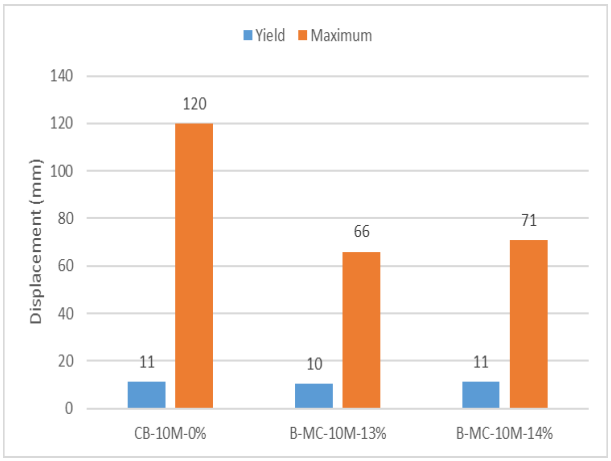
| CB-10M-0% |
| --- |
|  |
| B-MC-10M-13% |
|  |
| B-MC-10M-14% (front and back) |
|  |

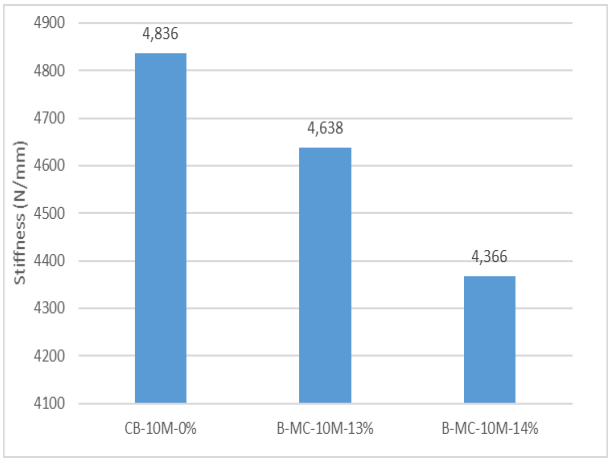
Figure 5-2 Failure mode comparison: effect of mid-span corrosion (10M group)



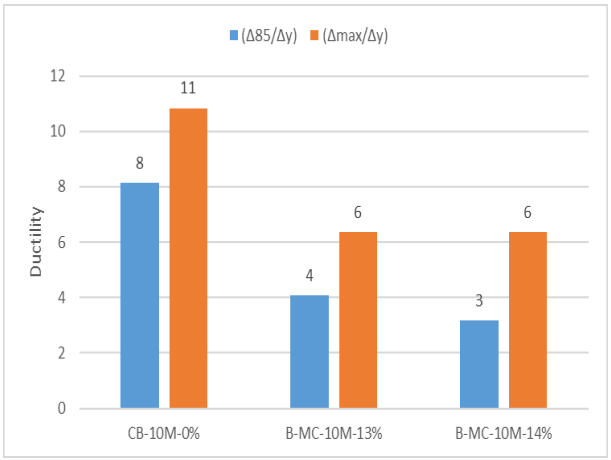

a) Load resistance



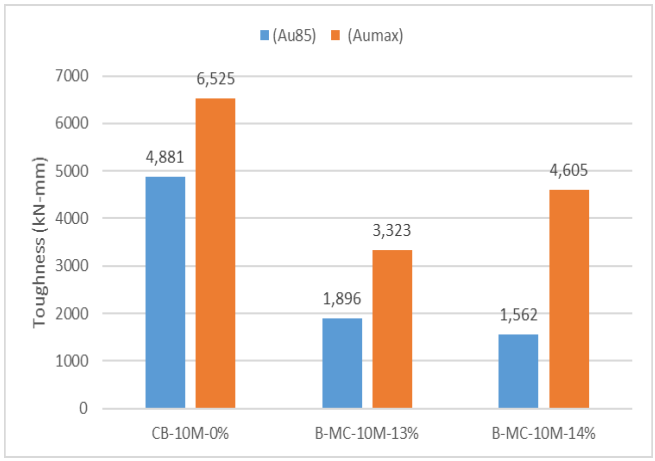

b) Displacement




c) Stiffness




d) Ductility




e) Toughness

Figure 5-3 Comparison of key results: effect of mid-span corrosion (10M group)

### 5.2.2 15M group: CB-15M-0% vs B-MC-15M-10%

The results of beams CB-15M-0% and B-MC-15M-10% were compared to examine the influence of corrosion on the flexural response of the beams in the 15M group. Both beams were constructed with identical design properties, which included 2-15M bars in tension and 2-10M bars in compression, with U-shaped stirrups at 100 mm spacing throughout the beam span. Beam B-MC-15M-10% was subjected to corrosion of the 15M tension bars over a length of 750-mm in the mid-span region, with an actual average mass loss of 10%. **Figure 5-4** shows a comparison of the beam load-deflection responses, and **Figure 5-5** presents photos of the beams at failure. Comparison of key response parameters is shown in **Figure 5-6**.

Examining **Figure 5-4**, it was observed that beam B-MC-15M-10% showed reductions of 21%, 23% and 8% in maximum strength, yield strength and stiffness when compared to beam CB-15M-0%. Beam B-MC-15M-10% showed a significant and sudden drop in load capacity at $\Delta = 42$ mm. As a result, the displacement $\Delta_{85}$, ductility ($\Delta_{max}/\Delta_y$) and toughness ($Au_{max}$) decreased by 51%, 40% and 54%, respectively, when compared to the control beam. Both beams failed in flexure with significant yielding of the tension steel; however, the failure mode of beam B-MC-15M-10% was associated with more sudden crushing of concrete, buckling of the longitudinal bars and severe spalling of the cover concrete in the mid-span of the beam.

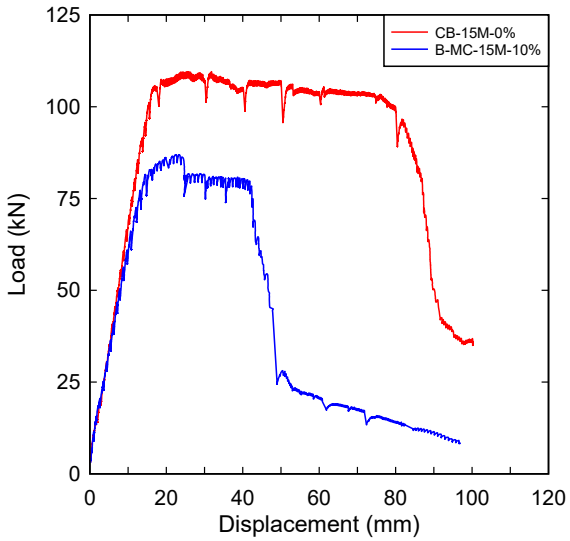
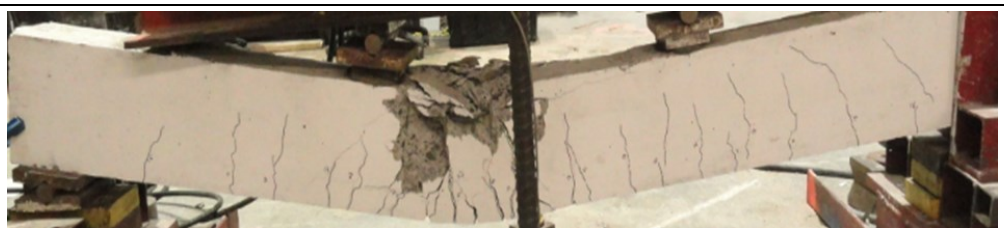



Figure 5-4 Load-deflection comparison: effect of mid-span corrosion (15M group)

CB-15M-0%



B-MC-15M-10% (front)



B-MC-15M-10% (back)



Figure 5-5 Failure mode comparison: effect of mid-span corrosion (15M group)

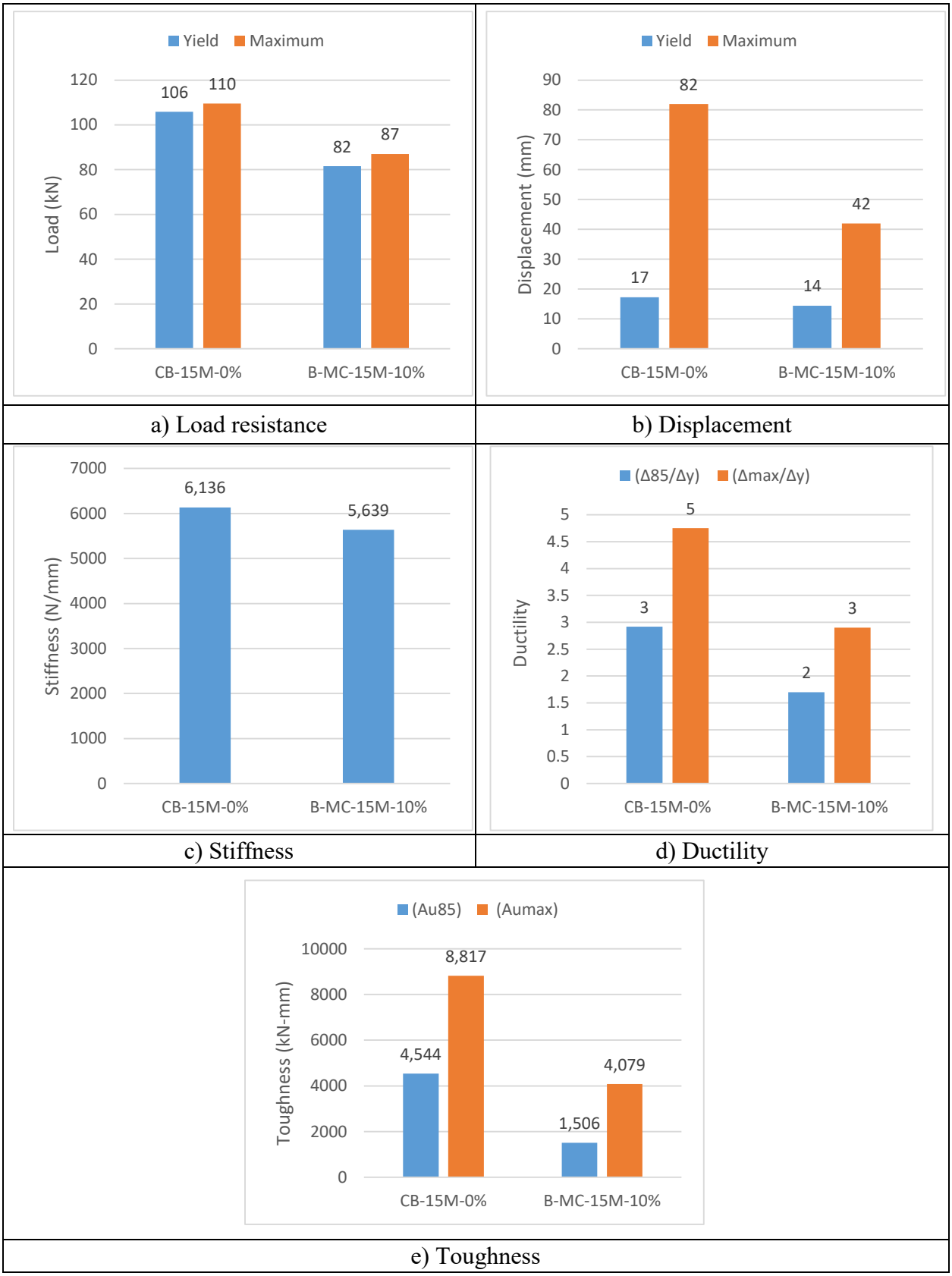



Figure 5-6 Comparison of key results: effect of mid-span corrosion (15M group)

## 5.3 Effects of corrosion in the end span region

### 5.3.1 10M group: CB-10M-0% vs B-SC-10M-11%

The results of beams CB-10M-0% and B-SC-10M-11% were compared to examine the effect of corrosion in the end-span regions on the flexural response of the beams in the 10M group. Both beams were doubly reinforced with 2-10M bars in tension and compression with U-shaped stirrups at 100 mm throughout their span. However, the end spans of the bottom 10M bars in beam B-SC-10M-11% were corroded over a length of 1,850 mm, with an actual average mass loss of 11%.

**Figure 5-7** compares the beam load-deflection responses, while photos of the beams at failure are shown in **Figure 5-8**. **Figure 5-9** shows a comparison of key response parameters.

**Figure 5-7** shows that unlike the mid-span case, the corrosion of the bar end spans had minor effect on the flexural response under static loading. Nonetheless beam B-SC-10M-11% showed slight reductions in yield strength, maximum strength and maximum displacement when compared to CB-10M-0% due to bond slippage in the shear-span. Conversely, the corroded beam showed a higher stiffness with an increase of 24%, when compared to the control beam. The corrosion effects were more noticeable when examining the ductility ($\Delta_{85}/\Delta_y$) and toughness ($A_{u85}$), where beam B-SC-10M-11% showed reductions of 25% and 50%, respectively, when compared to CB-10M-0%. As shown in **Figure 5-8**, both beams failed in flexure with significant yielding of the tension steel; however, beam CB-10M-0% showed more gradual crushing of concrete in the mid-span region. Crushing in beam B-SC-10M-11% was relatively more sudden with a clear increase in flexural crack widths in the mid-span region. Nonetheless, the overall structural responses of both beams were quite similar.

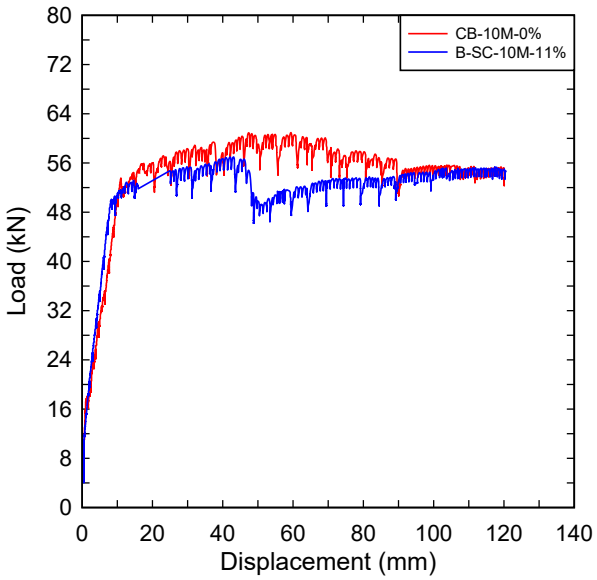



Figure 5-7 Load-deflection comparison: effect of end-span corrosion (10M group)

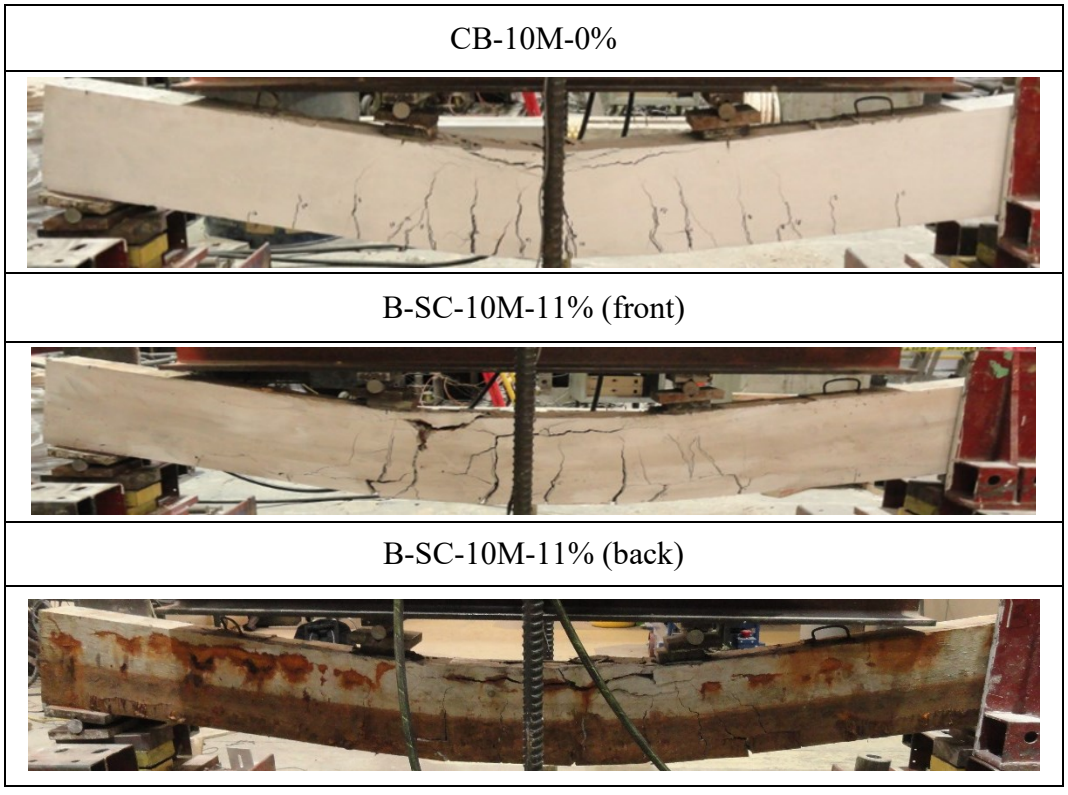
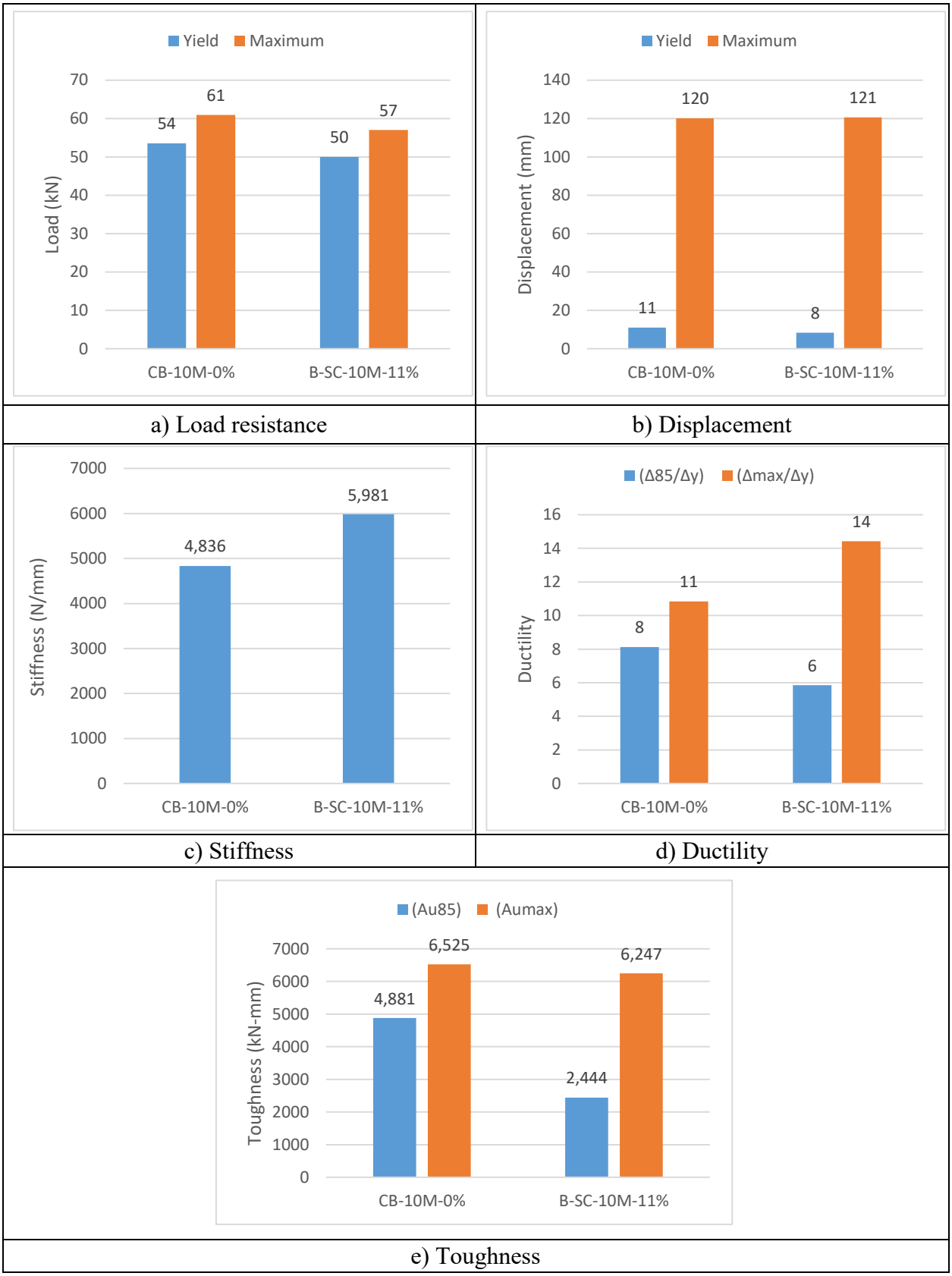



Figure 5-8 Failure mode comparison: effect of end-span corrosion (10M group)




a) Load resistance

b) Displacement

c) Stiffness

d) Ductility

e) Toughness

Figure 5-9 Test results comparison: effect of end-span corrosion (10M group)

## 5.4 Effects of corrosion over the full span

### 5.4.1 10M group: CB-10M-0% vs B-FC-10M-13%

The results of beams CB-10M-0% and B-FC-10M-13% were compared to investigate the effect of full-span corrosion on flexural response. Both beams were identical, except that beam B-FC-10M-13% was subjected to corrosion of the 10M tension bars over the entire length, with an actual average mass loss of 11%.

The comparison of beam load-deflection responses is shown in **Figure 5-10**, while **Figure 5-11** presents the beams photos at failure. Key response parameters are shown in **Figure 5-12**.

Examining **Figure 5-10**, the corrosion affected all aspects of beam flexural behaviour under static loading. The stiffness was only slightly reduced by 1.4%; however, beam B-FC-10M-13% showed reductions of 13% and 11% in maximum and yield strengths, respectively, when compared to CB-10M-0%. Considering the $\Delta_{85}$ displacement, the ductility ($\Delta_{85}/\Delta_y$) and toughness ($A_{u85}$) were also reduced by 38% and 48%, respectively, when comparing B-FC-10M-13% to CB-10M-0%. The overall toughness ($A_{umax}$) of B-FC-10M-13% showed an increase of 9% since the test was continued for a longer period in order to observe the rupture of the steel reinforcement (as a result the final displacement and area under the load-deflection curve were larger for the corroded beam).

As shown in **Figure 5-11**, both beams failed in flexure, with significant yielding of the tension steel reinforcement and gradual crushing of concrete in the mid-span compression region. However, the failure of beam B-FC-10M-13% was associated with sudden bar rupture, severe spalling and collapse of the beam at the end of testing.

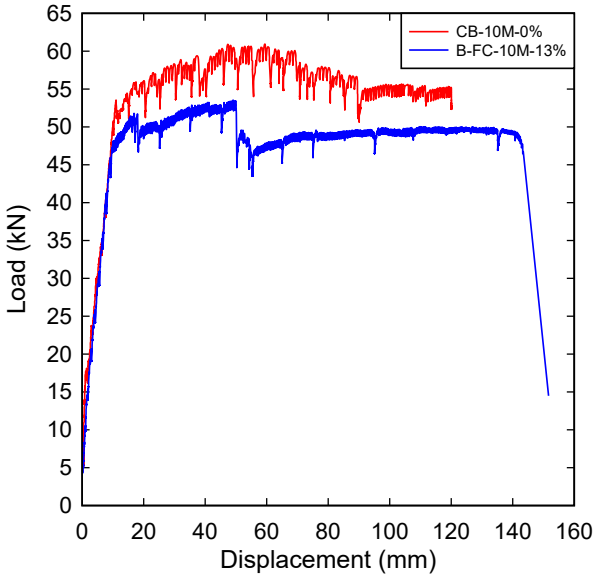



Figure 5-10 Load-deflection comparison: effect of full-span corrosion (10M group)

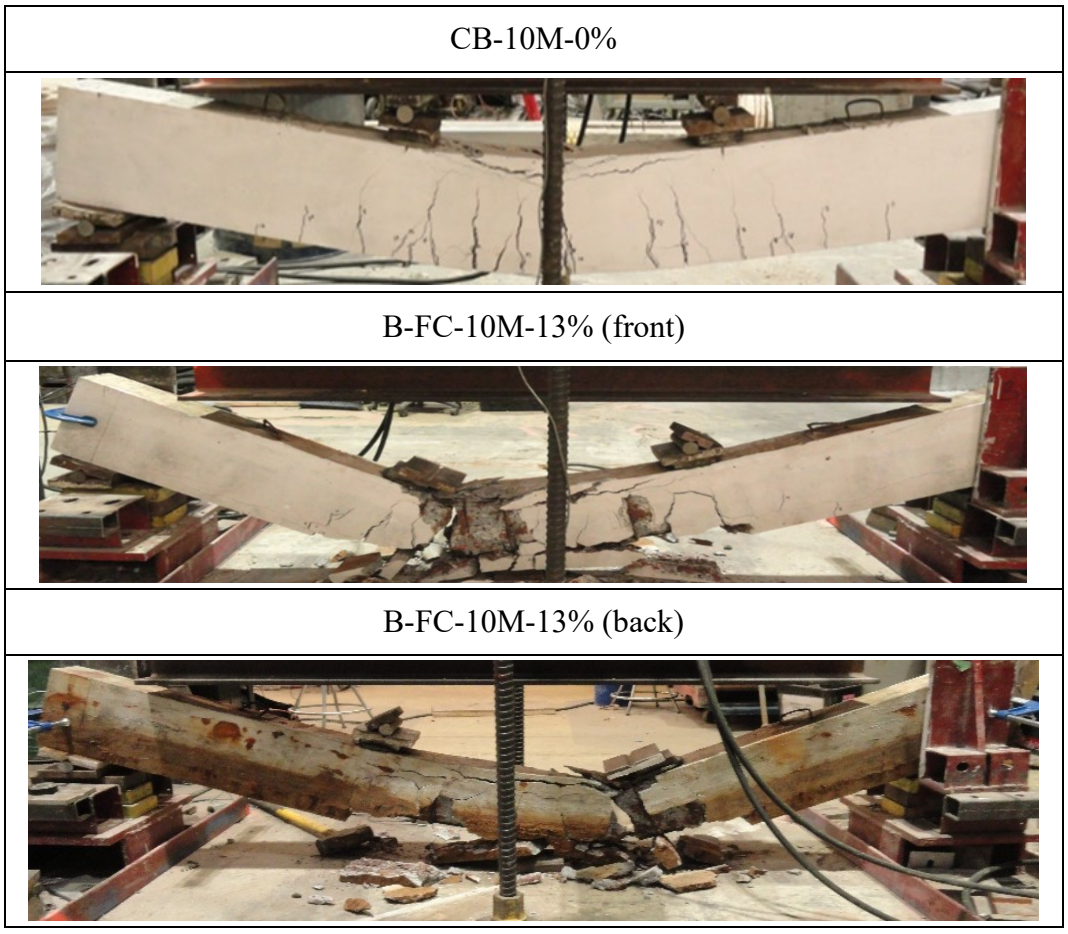
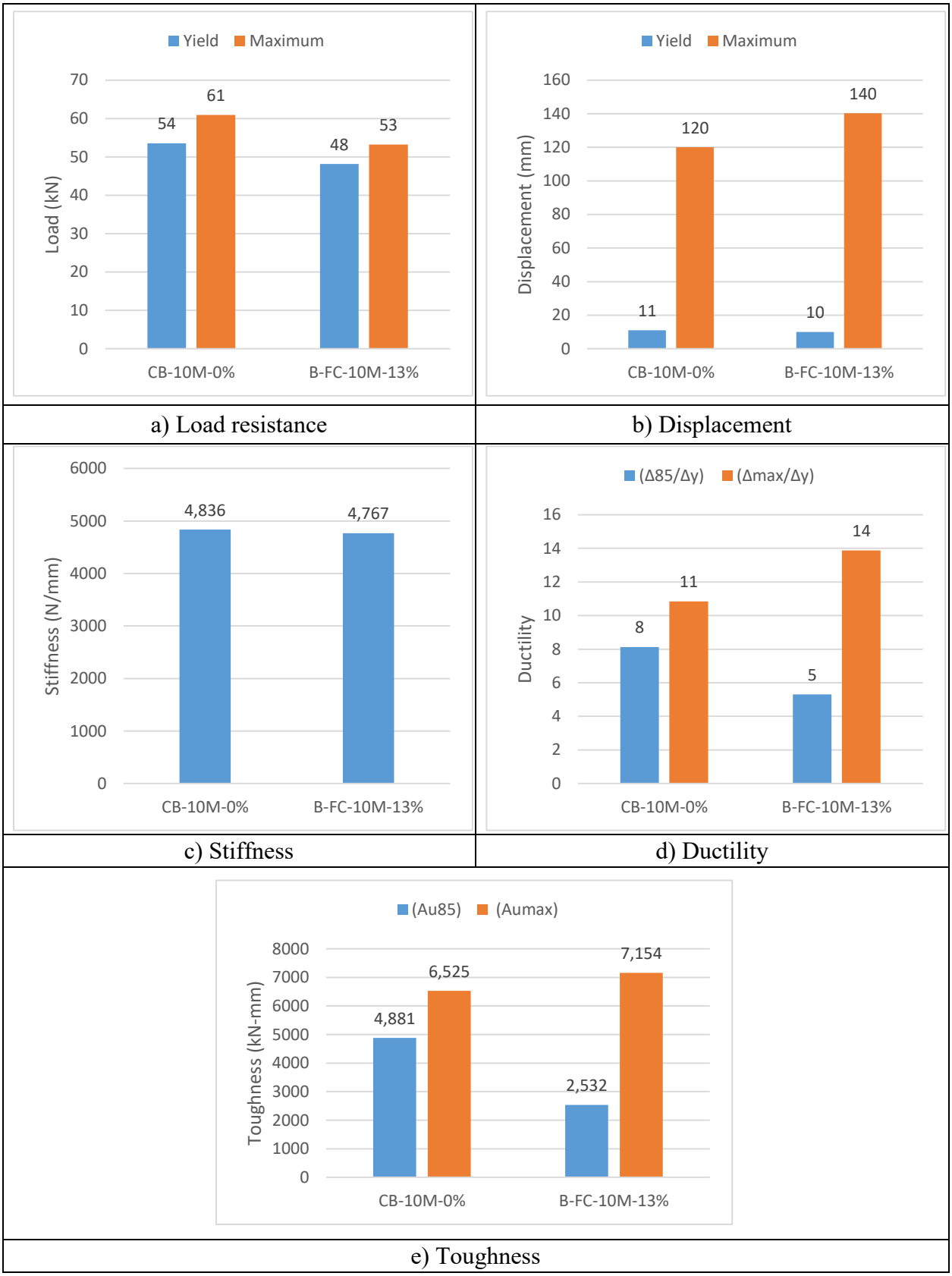



Figure 5-11 Failure mode comparison: effect of full-span corrosion (10M group)




a) Load resistance

b) Displacement

c) Stiffness

d) Ductility

e) Toughness

Figure 5-12 Test results comparison: effect of full-span corrosion (10M group)

## 5.5 Effect of corrosion location (mid, end and full span corrosion)

### 5.5.1 10M group: B-MC-10M-14% vs B-SC-10M-11% vs B-FC-10M-13%

The results of beams B-MC-10M-14%, B-SC-10M-11% and B-FC-10M-13% were compared to inspect the effect of the extent of corrosion (or corrosion location) on the flexural response of the beams in the 10M group. All beams had similar properties and masses losses (14%, 11% and 13%); however, the bottom 10M bars were subjected to corrosion over different locations: mid-span only, end-span only and full-span.

**Figure 5-13** compares the load-deflection responses of the beams. Photos at failure are shown in **Figure 5-14**. **Figure 5-15** compares key response parameters in bar chart format.

It was observed that the extent of corrosion was an influential parameter that affected the load-deflection response and failure mode of the beams. Examining the effect on strength, the greatest reductions in maximum and yield strengths were observed for beams B-MC-10M-14% and B-FC-10M-13% when compared to the control CB-10-0% beam. Conversely the beam with end corrosion (B-SC-10M-11%) showed only a slight decrease in beam capacity at yield and maximum strength. Indeed, this beam showed a similar load-deflection response when compared to the control specimen. Comparing the ductility and toughness at $\Delta_{85}$, all corroded beams showed reductions in ductility and toughness when compared to the control specimen; however, the greatest decrease in $\Delta_{85}/\Delta_y$ and $A_{u85}$ were observed for beam B-MC-10M-14%.

Examining the effect of corrosion on failure mode, all corroded specimens showed more significant damage in terms of the extent of concrete crushing and increase in crack widths when compared to the control specimen. However, failure was most severe and sudden in beam B-MC-10M-14%, which suffered bar rupture failure at $\Delta$ = 71 mm. Beam B-FC-10M-13% also experienced bar rupture, but at a much larger mid-span displacement ($\Delta$ > 140 mm). Nonetheless, both specimens showed more severe damage (cracking, crushing, spalling of cover concrete) in the mid-span region when compared to the control beam.

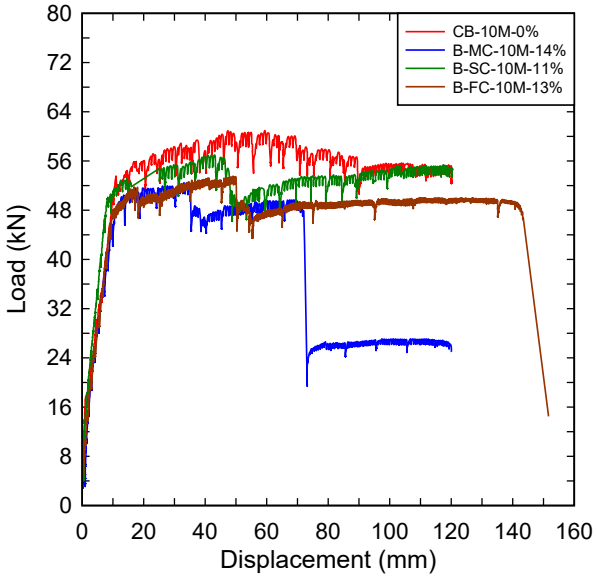



Figure 5-13 Load-deflection comparison: effect of corrosion location (10M group)

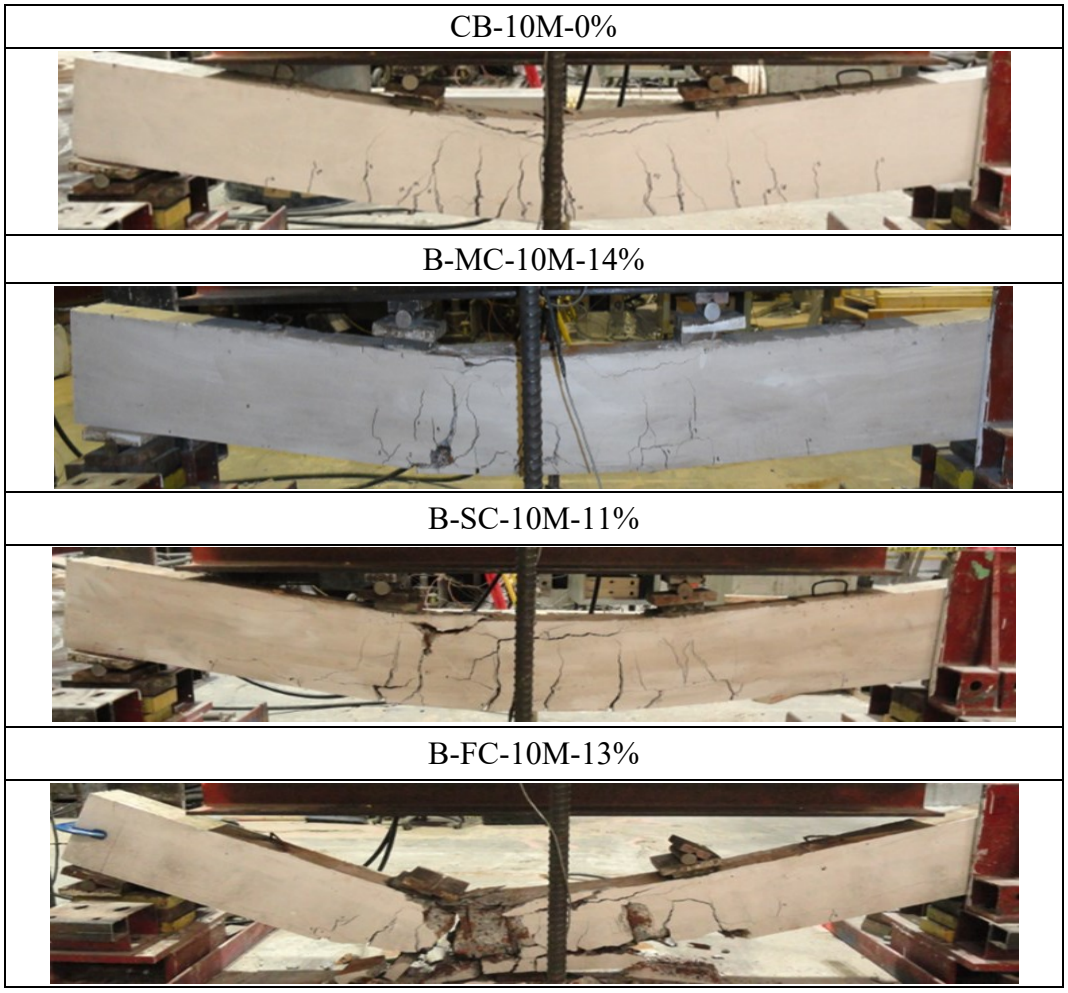
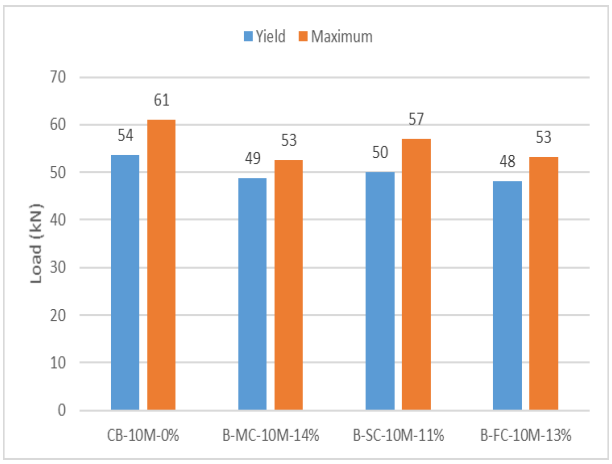
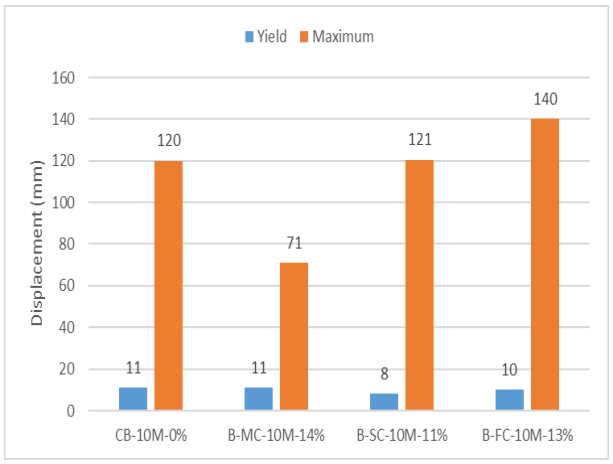


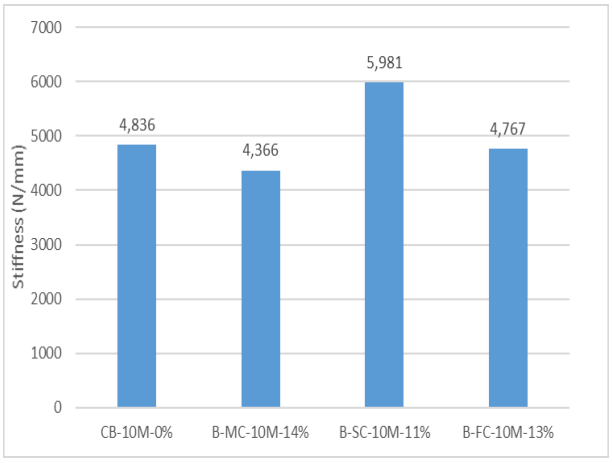

Figure 5-14 Failure mode comparison: effect of corrosion location (10M group)



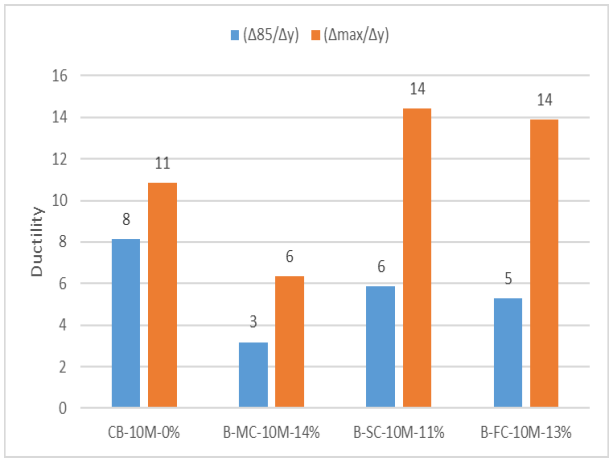

a) Load resistance



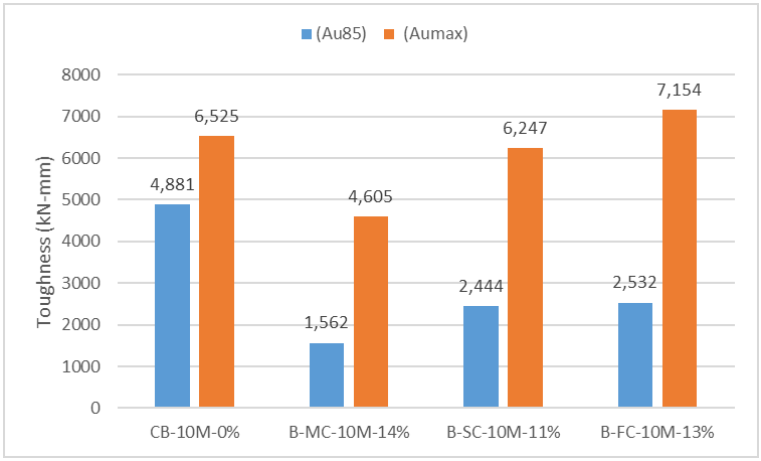

b) Displacement




c) Stiffness




d) Ductility




e) Toughness

Figure 5-15 Test results comparison: 10M group (effect of corrosion location)

## 5.6 Effects of corrosion in the shear reinforcement

### 5.6.1 25M group: CB-25M-0% vs B-SHC-25M-12% and B-SHC-25M-10%

The results of beams CB-25M-0% vs B-SHC-25M-12% and B-SHC-25M-10% were compared to examine the effect of corrosion on the shear-flexure response of the beams in the 25M group. All beams had identical design properties which consisted of 2-25M bars in tension, 2-10M bars in compression and provision of minimum U-shaped stirrups at 100 mm spacing throughout the beam span. However, the stirrups in beams B-SHC-25M-12% and B-SHC-25M-10% were subjected to corrosion. The actual average mass loss of the stirrups was determined to be 12% and 10% for beams B-SHC-25M-12% and B-SHC-25M-10%, respectively. **Figure 5-16** compares the beam load-deflection responses, while photos of the beams at failure are shown in **Figure 5-17**. **Figure 5-18** compares key response parameters in bar chart format.

It was observed that all three beams reached yielding prior to failure and therefore showed similar maximum capacities. In fact, the maximum strength of beam CB-25M-0% reached 190 kN, which was slightly lower than beam B-SHC-25M-12% ($P_{max}$ = 198 kN). Beam B-SHC-25M-10% showed an even higher capacity of 202 kN, which can possibly be explained by variations in material properties (e.g., actual yield strengths of the 25M bars) in each beam. Likewise, both beams showed similar stiffness in their ascending branch. The effect of corrosion of the transverse reinforcement was more evident when comparing the failure modes and post-peak beam responses. Considering the $0.85P_{max}$ criteria, all three beams showed similar $\Delta_{85}$ displacement; however, a much more sudden and steep drop in load occurred in beam B-SHC-25M-12%. As a result, the failure was more brittle in B-SHC-25M-12%, which showed a reduction of 55% in toughness when computed up to $\Delta_{max}$ (3,873 vs 8,635 kN-mm). The failure was more gradual in B-SHC-25M-10%; however, its toughness (6,000 kN-mm) was also reduced when compared to the control specimen. All three beams experienced shear failure, with diagonal shear cracking, which was also associated with concrete crushing and buckling of the longitudinal bars near the point load location. However, damage in beam B-SHC-25M-12% occurred more suddenly and resulted in severe spalling of the side concrete cover with rupture of the stirrups, as shown in **Figure 5-17**. Damage was also extensive in B-SHC-25M-10%; however, rupture of the stirrups did not occur at the critical location.

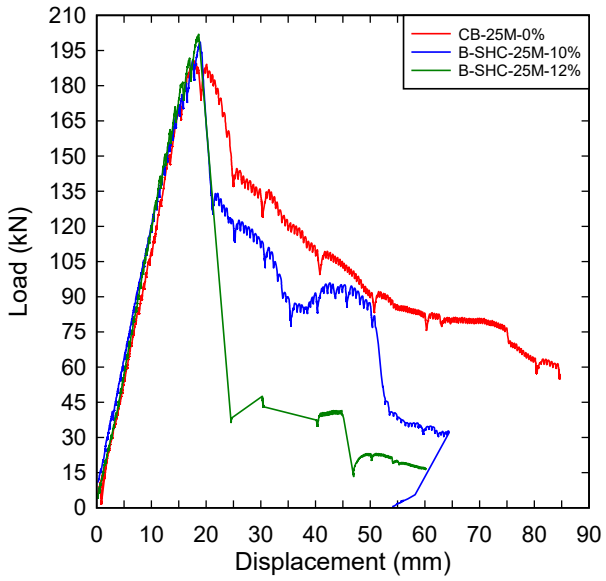



Figure 5-16 Load-deflection comparison: effect of corrosion in stirrups (25M group)

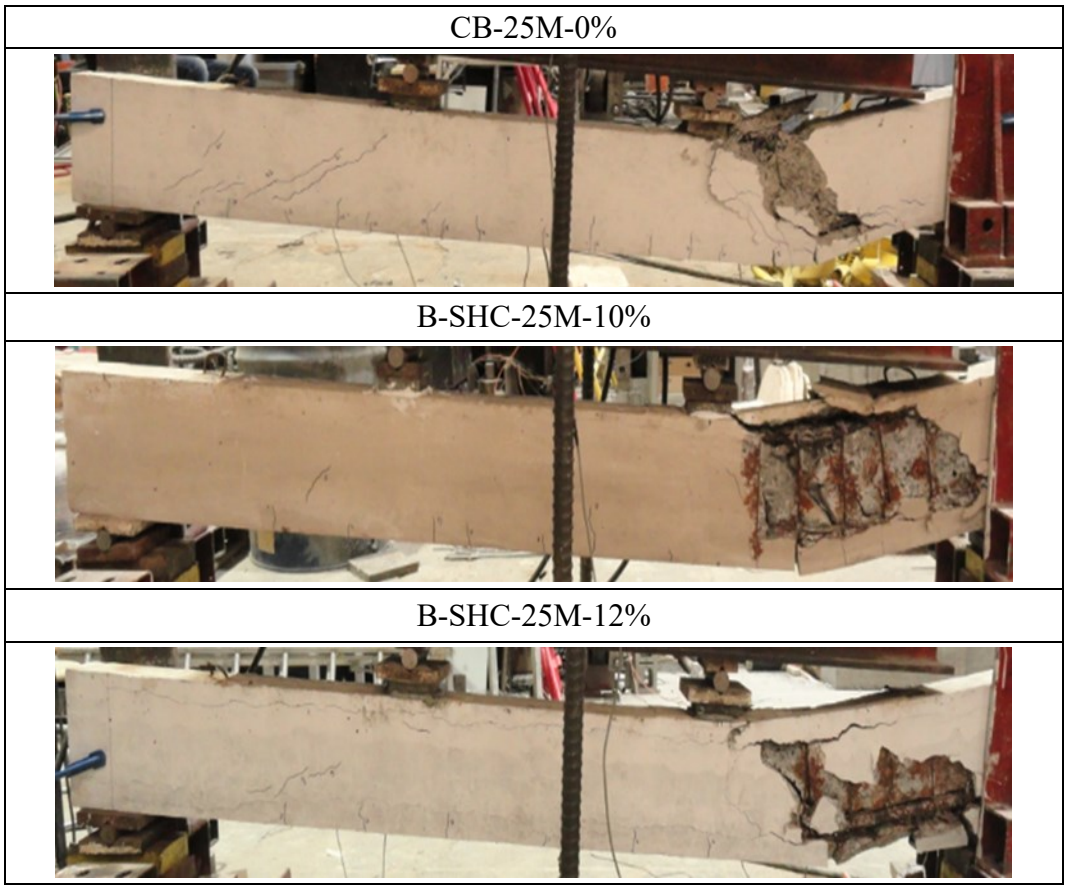
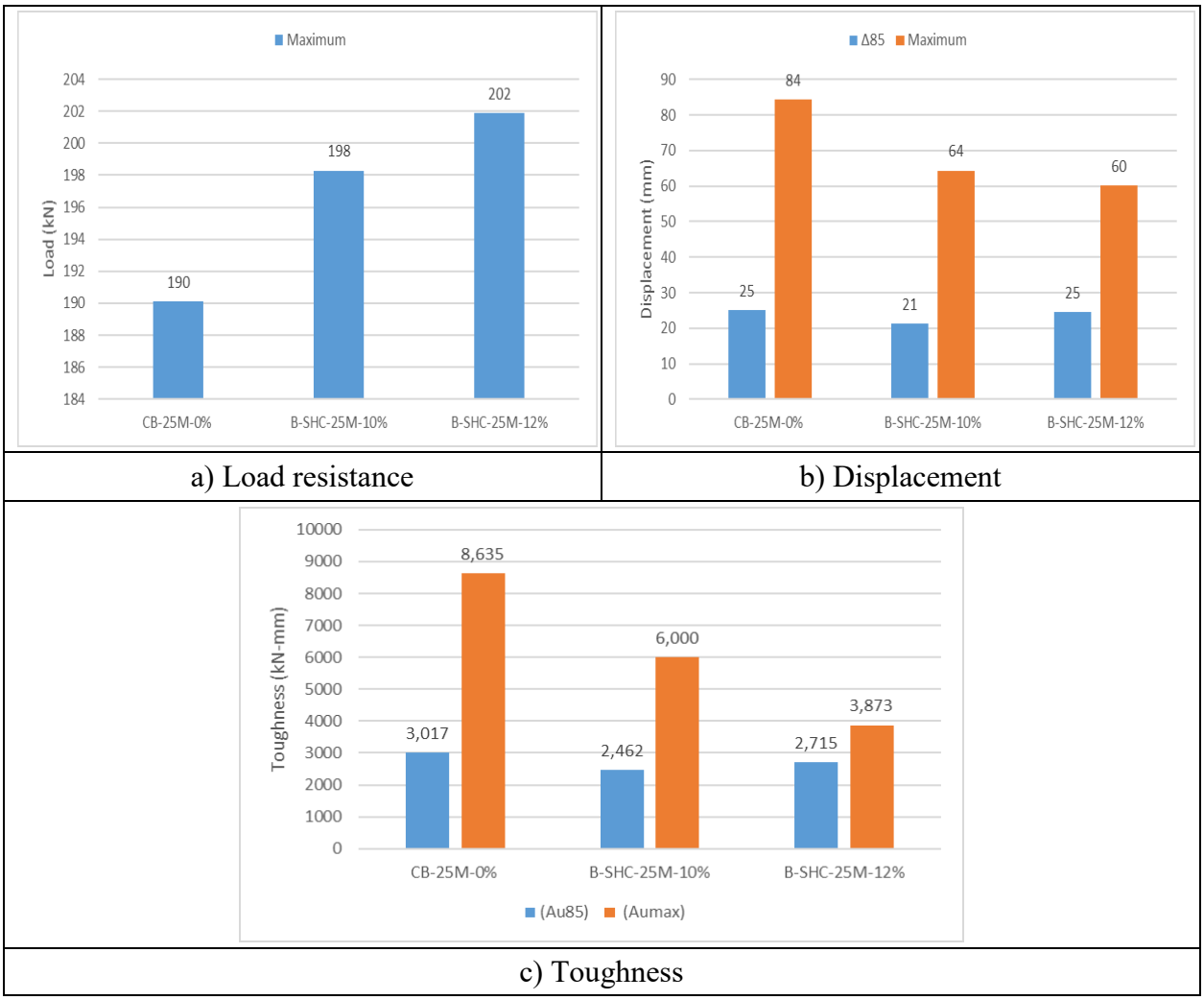



Figure 5-17 Failure mode comparison: effect of corrosion in stirrups (25M group)




a) Load resistance

b) Displacement

c) Toughness

Figure 5-18 Test results comparison: 25M group (effect of corrosion mass loss in stirrups)

# Chapter 6: Dynamic Experimental Results

## 6.1 Chapter Overview

This chapter summarizes the experimental results from the blast testing program. The results from the blast tests are presented in terms of blast shockwave properties, specimen response in terms of mid-span displacements, damage progression, steel reinforcement strains and dynamic reactions. Where applicable, results from post-blast residual static testing of the beams are also summarized.

## 6.2 Summary of the Results

A total of fourteen (14) reinforced concrete beams were tested under shock-tube induced blast loading, including seven (7) beams in the 10M group, four (4) beams in the 15M group and three (3) beams in the 25M group.

The results for all beams are presented in **Table 6-1** and include: ($P_d$) driver pressure, peak reflected pressure ($P_r$), positive phase duration ($t_d$), reflected impulse ($I_r$) for each blast, along with the specimen response in terms of maximum and residual mid-span displacements ($\Delta_{max}$ and $\Delta_{res}$), maximum support rotation ($\theta_{max}$), and observed damage. **Figure 6-1** presents a photographic record of the beams at the end of blast testing.

In addition to the above, the experimentally recorded maximum support rotations are also compared with the expected damage levels in the CSA S850 standard as shown in **Table 6-2**.

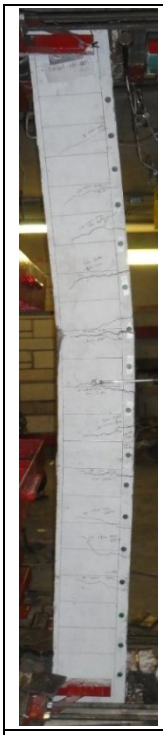
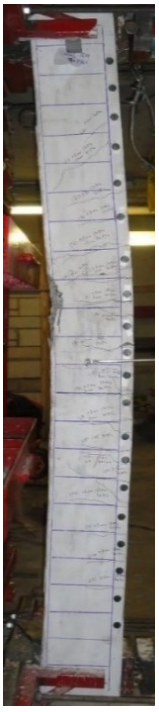
Table 6-1 Blast test results for all beams

| Beams | Shockwave properties | | | | Displacements | | Support rotation | |
|---|---|---|---|---|---|---|---|---|
| ID | $P_d$ (psi) | $P_r$ (kPa) | $I_r$ (kPa-ms) | $t_d$ (ms) | $\Delta_{max}$ (mm) | $\Delta_{res}$ (mm) | $\theta_{max}$ (°) | CSA S850 Damage State |
| CB-10M-0% | 17 | 31.3 | 250 | 18.5 | 15.4 | 4.3 | 0.72 | Superficial |
| | 50 | 61.0 | 550 | 20.8 | 72.6 | 52.0 | 3.40 | Moderate |
| B-MC-10M-11% | 17 | 27.3 | 257 | 19.3 | 18.0 | 7.0 | 0.84 | Superficial |
| | 50 | 64.3 | 547 | 22.4 | 86.3 | 64.3 | 4.10 | Heavy |
| B-MC-10M-15% | 17 | 27.8 | 249 | 19.3 | 15.6 | 5.4 | 0.72 | Superficial |
| | 50 | 59.3 | 529 | 21.0 | 107.0 | 43.4 | 4.90 | Heavy |
| B-EMC-10M-22% | 50 | 61.0 | 541 | 21.0 | 217.3 | 181.4 | 10.10 | Hazardous/ Blowout |
| B-SC-10M-7% | 17 | 29.2 | 239 | 18.5 | 20.4 | 6.6 | 0.95 | Superficial |
| | 35 | 48.5 | 356 | 19.3 | 33.0 | 15.0 | 1.60 | Moderate |
| | 50 | 61.5 | 555 | 21.6 | 70.1 | 45.2 | 3.30 | Moderate |
| B-FC-10M-12% | 50 | 52.0 | 540 | 21.0 | 83.7 | 61.7 | 4.00 | Heavy |
| B-CR-MC-10M-5% | 50 | 65.6 | 548 | 21.0 | 79.0 | 57.0 | 3.70 | Moderate |
| | | | | | | | | |
| CB-15M-0% | 17 | 24.0 | 248 | 19.3 | 10.6 | 3.2 | 0.50 | Superficial |
| | 70 | 78.8 | 734 | 22.4 | 70.6 | 50.5 | 3.30 | Moderate |
| B-MC-15M-12% | 17 | 29.0 | 251 | 18.5 | 11.0 | 2.0 | 0.50 | Superficial |
| | 70 | 80.0 | 703 | 22.4 | 71.2 | 51.0 | 3.40 | Moderate |
| B-EMC-15M-17% | 70 | 80.1 | 729 | 22.4 | 169.0 | 149.2 | 8.00 | Hazardous |
| B-CR-MC-15M-4% | 70 | 77.0 | 720 | 21.6 | 76.0 | 54.0 | 3.60 | Moderate |
| | | | | | | | | |
| CB-25M-0% | 90 | 91.4 | 927 | 23.2 | 46.0 | 22.4 | 2.20 | Moderate |
| B-SHC-25M-11% | 90 | 96.7 | 903 | 23.2 | 92.6 | 68.5 | 4.40 | Heavy |
| B-SHC-25M-12% | 90 | 95.2 | 926 | 24.7 | 45.5 | 32.0 | 2.20 | Moderate |

**Note**: $P_d$ = driver pressure, $P_r$ = peak reflected pressure, $t_d$ = positive phase duration, $I_r$ = reflected impulse (area under the positive phase of the pressure-time history); $\Delta_{max}$ = maximum mid-span displacement; $\Delta_{res}$ = residual mid-span displacement; $\theta_{max}$ = maximum support rotation.

Table 6-2 CSA S850 damage levels (reproduced from the CSA S850 Standard)

| Angle (support rotation) | | Response Limit | Expected Damage Level |
|---|---|---|---|
| Single-reinforced beam | Double-reinforced beam | | |
| $\theta < 1°$ | $\theta < 1°$ | <B1 | Superficial |
| $1° \leq \theta < 2°$ | $1° \leq \theta < 4°$ | B2-B1 | Moderate |
| $2° \leq \theta < 5°$ | $4° \leq \theta < 6°$ | B3-B2 | Heavy |
| $5° \leq \theta < 10°$ | $6° \leq \theta < 10°$ | B4-B3 | Hazardous |
| $\theta \geq 10°$ | $\theta \geq 10°$ | ≥B4 | Blowout |

| | | | | | | |
|---|---|---|---|---|---|---|
|  |  |  |  |  |  |  |
| CB-10M-0% | B-MC-10M-11% | B-FC-10M-12% | B-SC-10M-7% | B-MC-10M-15% | B-EMC-10M-22% | B-CR-MC-10M-5% |
| **a) 10M beams group (after 50 psi shot)** | | | | | | |
|  |  |  |  | | | |
| CB-15M-0% | B-MC-15M-12% | B-EMC-15M-17% | B-CR-MC-15M-4% | | | |
| **b) 15M beams group (after 70 psi shot)** | | | | | | |



| CB-25M-0% | B-SHC-25M-11% | B-SHC-25M-12% |
|---|---|---|
| **c) 25M beams group (after 90 psi shot)** | | |

Figure 6-1 Photos of the beams at the end of blast testing

## 6.3 Detailed Experimental Results

### 6.3.1 10M Group

The 10M group included seven beams which were tested under shock-tube blast loads. The beams were doubly-reinforced with 2-10M bars in tension and compression (as top bars), and they were provided with U-shaped stirrups made from 6.3-mm wire, which were uniformly spaced at 100 mm throughout the beam span.

#### 6.3.1.1 10M: Control (0% mass loss) (CB-10M-0%)

Beam CB-10M-0% was the first beam tested under blast loading and was the reference beam in the 10M group. No corrosion was applied prior to testing. The beam was subjected to two blasts at driver pressures of 17 and 50 psi. The key results that include the properties of shockwaves and displacements at these blasts are shown in **Table 6-3**. Complete reflected pressure, reflected impulse and mid-span displacement time histories are shown in **Figure 6-2**. Photos that show damage after each blast are provided in **Figure 6-3**. The dynamic resistance results and measured strains in the tension steel are shown in **Figure 6-4**.

Blast 1 (17 psi) was the first shot applied on this specimen and resulted in the formation of hairline flexural cracks in the constant moment region and the formation of inclined flexural-shear cracks in the shear spans. The maximum and residual displacements were recorded as 15.4 mm and 4.3 mm, respectively, while the maximum strain reached 0.00367 mm/mm indicating steel yielding. The support rotation ($\theta_{max}$) was 0.72°, which corresponds to *superficial* damage.

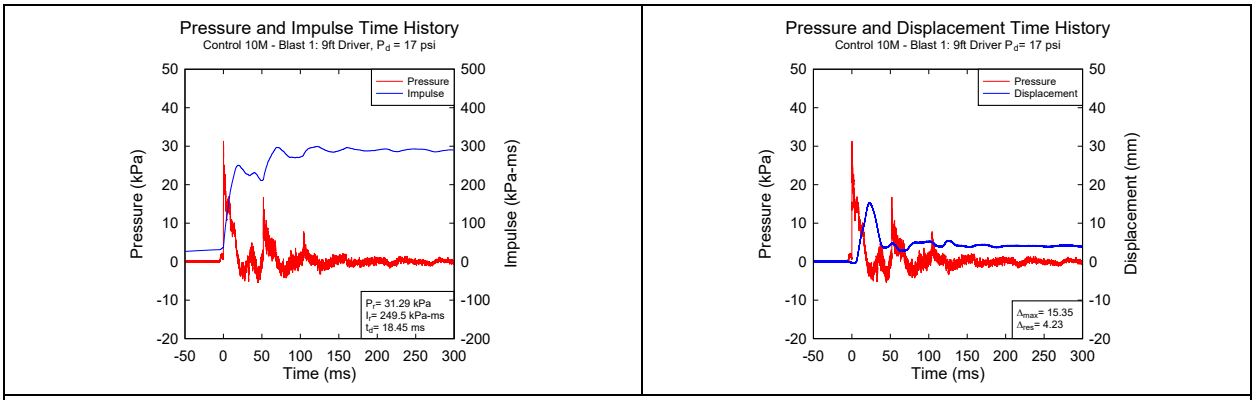
Blast 2 (50 psi) resulted in the extension of existing flexural cracks and increased crack widths in the constant moment region. The width of the most severe crack reached 6 mm and was located near the beam mid-span. The maximum and residual displacements reached 72.6 mm and 52 mm, respectively, with a maximum support rotation of $\theta_{max}$ = 3.4°, which corresponds to *moderate* damage. The maximum strain in the tension bars reached 0.024 mm/mm, indicating the tension steel reinforcement was well into the inelastic range. Despite the relatively large support rotation and noticeable residual displacement, the beam only showed minor crushing in the mid-span compression zone, with no significant cover spalling.

Since the beam had limited damage, it was again tested under quasi-static four-point bending to assess its residual capacity, and the results are presented in **Figure 6-5**. The cumulative residual

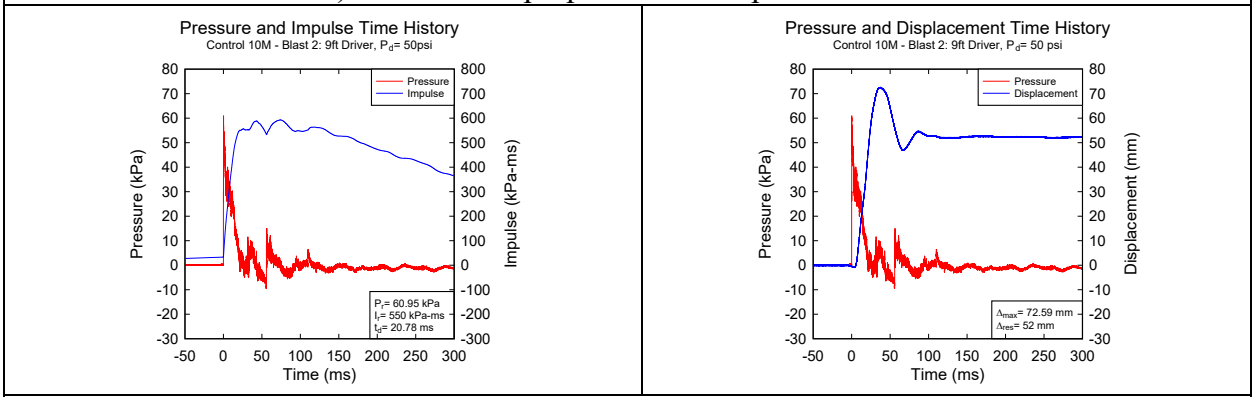
displacement during the blast test was 56 mm, which was the starting point of the test. It was observed that the beam followed a similar trend when compared to the companion undamaged beam, which was tested under static loads only. The blast-damaged beam reached a maximum residual capacity of $P_{max}^r$ = 57 kN, which was only slightly below the undamaged peak capacity of $P_{max}$ = 61 kN. The beam also showed an ability to carry sustained loads, reaching a displacement $\Delta_{max}^r$ =131 mm, with a residual load of $P_{end}^r$ = 56 kN at the end of testing. The ductile flexural failure was associated with concrete crushing of the top cover in the mid-span region.

Table 6-3 Key blast test results: CB-10M-0%

| **Beams** | **Shockwave properties** | | | | **Displacement** | | **$\theta_{max}$** | **Response limit and expected damage** | |
|---|---|---|---|---|---|---|---|---|---|
| **ID** | **$P_d$** | **$P_r$** | **$I_r$** | **$t_p$** | **$\Delta_{max}$** | **$\Delta_{res}$** | | | |
| | **(psi)** | **(kPa)** | **(kPa-ms)** | **(ms)** | **(mm)** | **(mm)** | **(°)** | | |
| CB-10M-0% | 17 | 31.3 | 250 | 18.5 | 15.4 | 4.3 | 0.72 | <B1 | Superficial |
| | 50 | 61.0 | 550 | 20.8 | 72.6 | 52.0 | 3.40 | B1-B2 | Moderate |

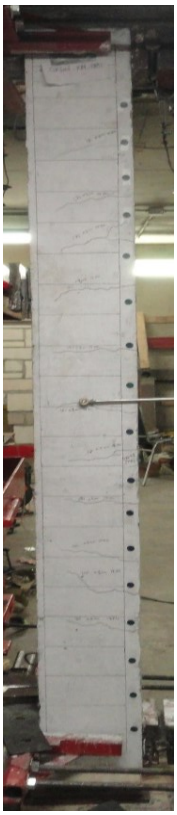



a) Shockwaves properties and displacement for Blast 1




b) Shockwaves properties and displacement for Blast 2

Figure 6-2 Reflected pressure, impulse and mid-span displacement histories (CB-10M-0%)



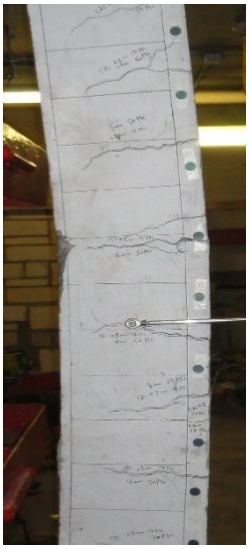
a) Blast 1



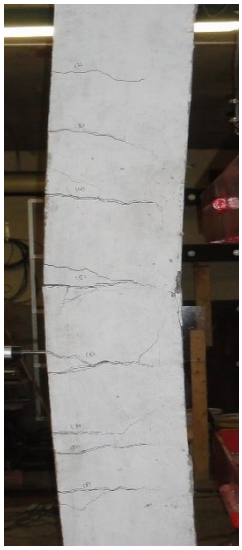
b) Blast 2



c) High-speed camera showing Blast 2 fragments



d) Mid-span cracking (one side) (Blast 2)



e) Mid-span cracking (other side) (Blast 2)



f) Mid-span cracking (tension face) (Blast 2)

Figure 6-3 Beam damage after the blast shots (CB-10M-0%)

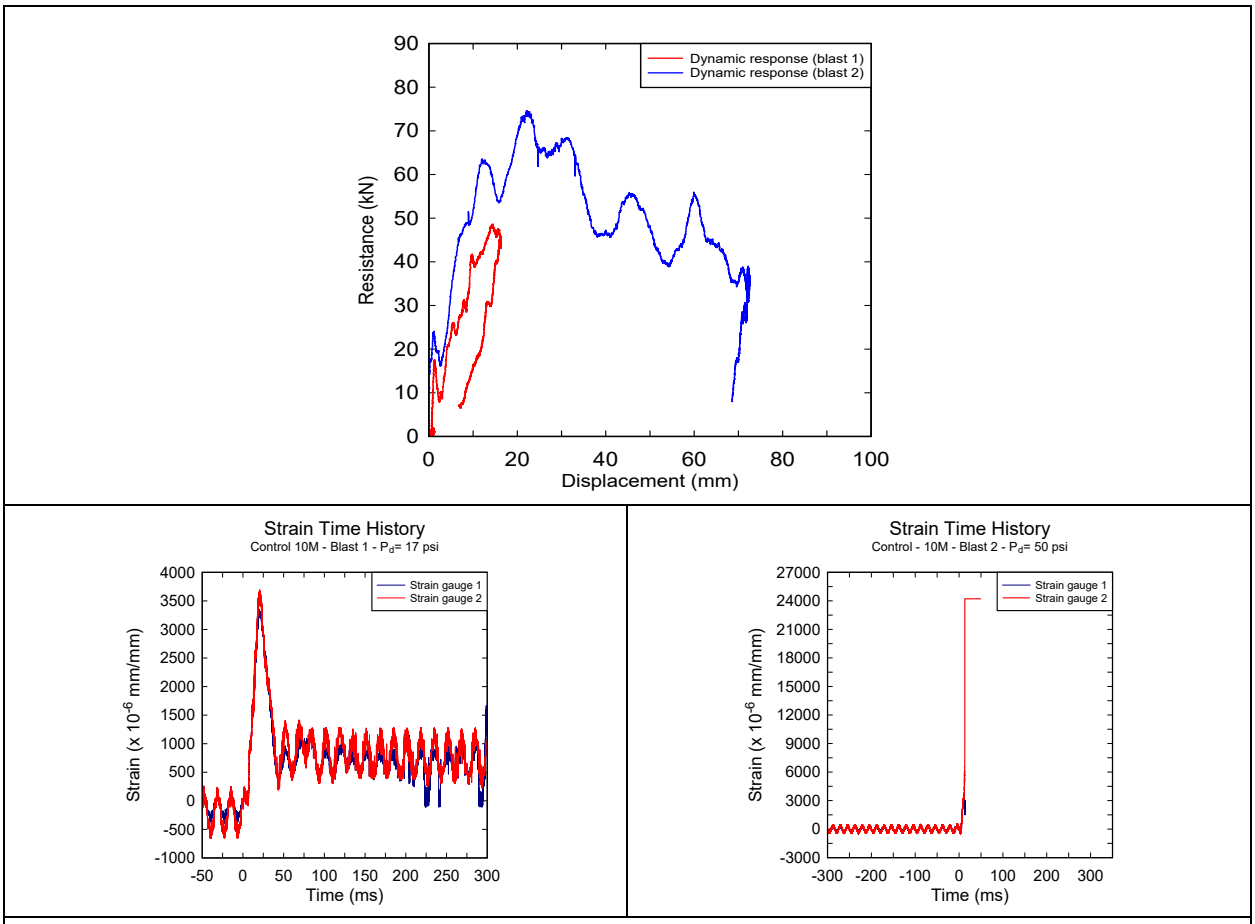
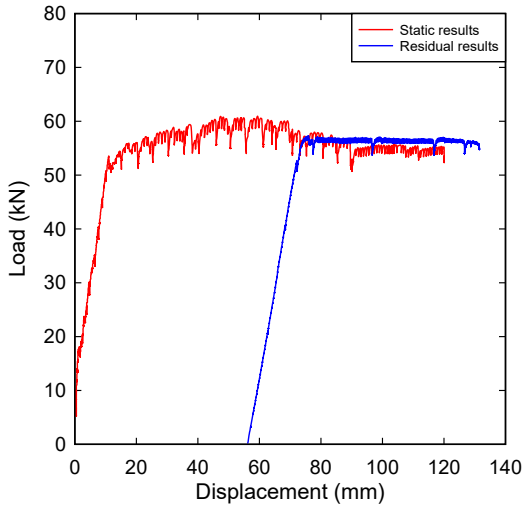
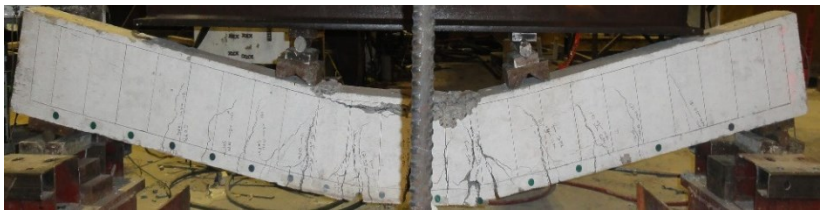



Figure 6-4 Blast load resistance and strain time history curves (CB-10M-0%)




| Residual test results | |
|---|---|
| ΣΔ res (mm) | 56 |
| $P_{max}^{r}$ (kN) | 57 |
| $D_{max}^{r}$ (mm) | 131 |
| $P_{end}^{r}$ (kN) | 56 |

a) Load- deflection curve and results for residual test

| Before the residual test | Comments |
|---|---|
|  | Cracks distributed on the entire length of the beam.<br>Some large cracks in the mid-span region. |
| After the residual test | Comments |
|  | Concrete crushing in the compression zone at the mid-region.<br>Severe cracks in the moment region. |

b) Photos of the beam before and after the residual test

Figure 6-5 Residual test results (CB-10M-0%)

#### 6.3.1.2 10M: Mid-span corrosion-11% mass loss (B-MC-10M-11%)

The second beam in the 10M group was subjected to corrosion over a length of 750 mm in the mid-span region. The aimed mass loss for the 10M longitudinal reinforcement in the tension zone was 15%. After testing, the actual average mass loss on the 10M bars was determined to be 11%. Examining all extracted bar samples, the largest mass loss reached 16% (see **Figure 6-6**).

Prior to testing, signs of cracking and damage were observed over the beam length due to the effects of corrosion. The main cracks type was horizontal cracking at the level of the longitudinal bars in the tension and compression zones, as shown in **Figure 6-7**.

This specimen was subjected to two blasts at driver pressures of 17 and 50 psi. The key data from these tests are summarized in **Table 6-4**. The pressure, impulse and displacement histories are presented in **Figure 6-8**, while the damage after each test is shown in **Figure 6-9**. The resistance curve as obtained from the dynamic reactions is plotted in **Figure 6-10**.

Blast 1 (17 psi) resulted in maximum and residual displacements of 18 mm and 7 mm, respectively. Similar to the previous beam, the blast resulted in the formation of hairline flexural and flexural-shear cracks. The support rotation remained below 1°, corresponding to *superficial* damage.

Blast 2 (50 psi) resulted in failure of the specimen in flexure, with significant spalling of the concrete cover in the mid-span tension region due to the effects of corrosion. Also, significant crushing occurred in the compression face at the mid-span of the beam. The high-speed video showed the formation of significant blast fragments at failure. The maximum displacement and residual displacement reached 86.30 mm and 64.30 mm, respectively. The maximum support rotation was 4.1°, which corresponds to *heavy* damage. Because of the significant failure, no residual static test was conducted on this beam.

Table 6-4 Key results: B-MC-10M-11%

| Beam ID | Shockwave properties | | | | Displacement | | $\theta_{max}$ | Response limit and expected damage | |
|---|---|---|---|---|---|---|---|---|---|
| | $P_d$ (psi) | $P_r$ (kPa) | $I_r$ (kPa-ms) | $t_p$ (ms) | $\Delta_{max}$ (mm) | $\Delta_{res}$ (mm) | (°) | | |
| B-MC-10M-11% | 17 | 27.3 | 257 | 19.3 | 18.0 | 7.0 | 0.84 | <B1 | Superficial |
| | 50 | 64.3 | 547 | 22.4 | 86.3 | 64.3 | 4.10 | B3-B2 | Heavy |

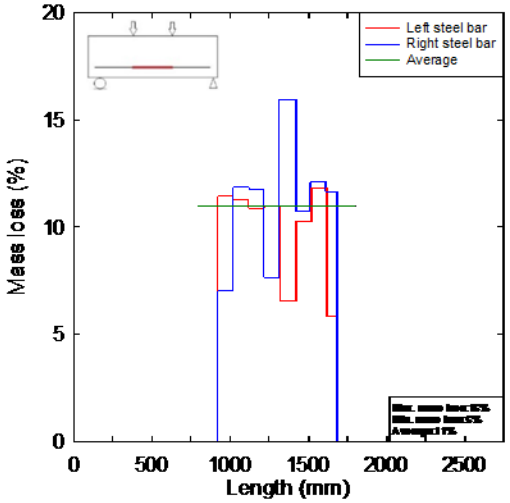
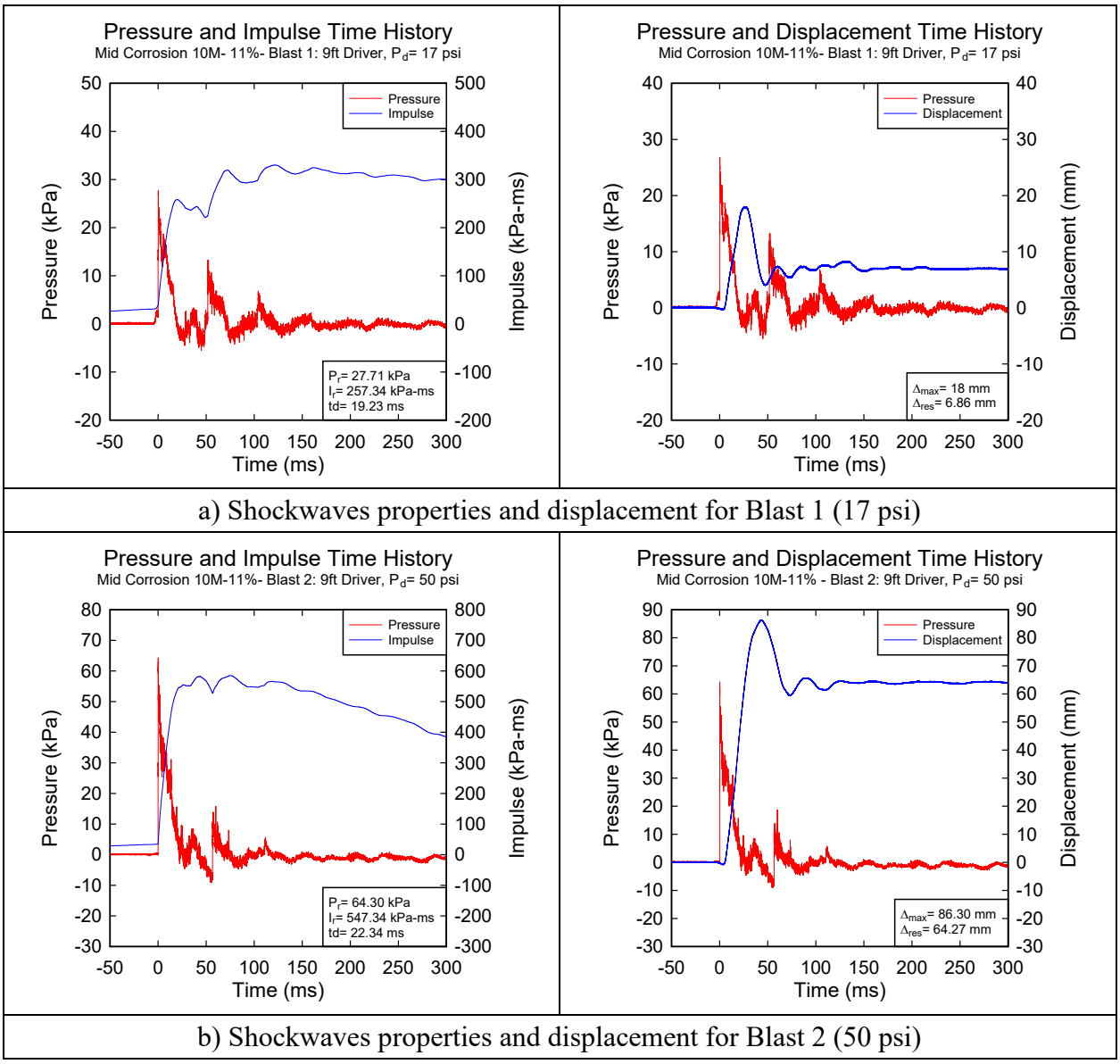



Figure 6-6 Mass loss distribution along the middle length of the tensile bars (B-MC-10M-11%)



Figure 6-7 Cracking in the beam before testing (B-MC-10M-11%)




a) Shockwaves properties and displacement for Blast 1 (17 psi)

b) Shockwaves properties and displacement for Blast 2 (50 psi)

Figure 6-8 Reflected pressure, impulse and mid-span displacement histories (B-MC-10M-11%)

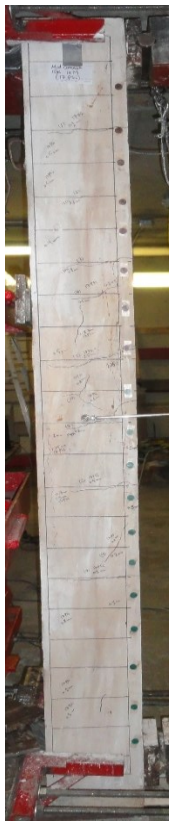
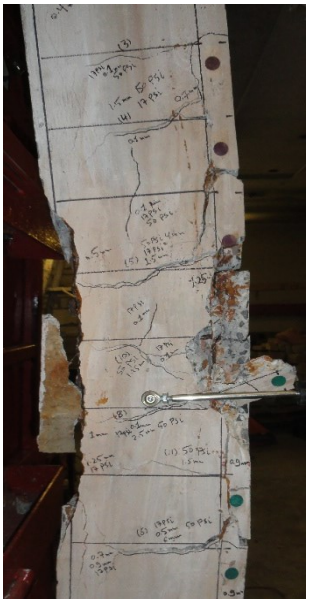
| | | |
|---|---|---|
|  |  |  |
| a) Blast 1 (17 psi) | b) Blast 2 (50 psi) | c) High-speed camera showing (Blast 2) fragments |
|  |  |  |
| d) Significant concrete spalling in mid-region (one side) (Blast 2) | e) Significant concrete spalling in mid-region (other side) (Blast 2) | f) Significant concrete spalling and cracks in mid-region (tension face) (Blast 2) |

Figure 6-9 Beam damage after testing (B-MC-10M-11%)

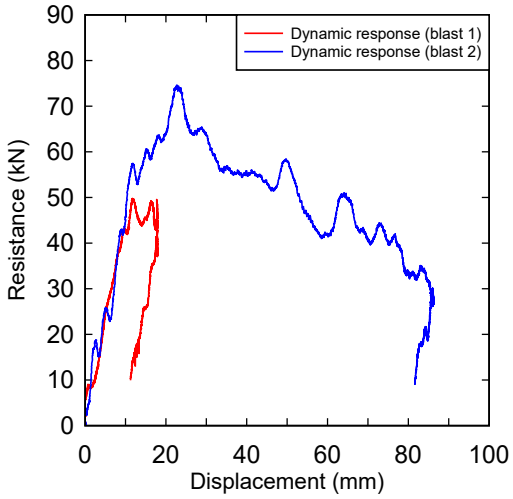



Figure 6-10 Blast load resistance curves (B-MC-10M-11%)

#### 6.3.1.3 10M: Mid-span corrosion-15% mass loss (B-MC-10M-15%)

The third beam in the 10M group was subjected to corrosion over a length of 750 mm in the mid-span region. The intended mass loss for the 10M longitudinal reinforcement in the tension zone was 30%; however, after testing, the actual average mass loss on the 10M bars was determined to be 15%. The measured mass loss on the extracted bar samples was lower than 30% over the entire 750 mm length; however, some portions reached 18% and 19%, as shown in **Figure 6-11**.

Before testing the beam showed signs of cracking and damage over its length due to the effects of corrosion, with the main type of cracks corresponding to horizontal cracking at the level of the longitudinal bars in the tension and compression zones, as shown in **Figure 6-12**.

This specimen was subjected to two blasts at driver pressures of 17 and 50 psi. **Table 6-5** summarizes the key data from these tests including the shockwaves properties and beam response in terms of displacements and damage. The pressure, impulse and mid-span displacement histories for each blast are presented in **Figure 6-13**, while the damage after each test is shown in **Figure 6-14**. The dynamic resistance and strain time history curves are illustrated in **Figure 6-15**.

Blast 1 (17 psi) resulted in maximum and residual displacements of 15.6 mm and 5.4 mm, respectively, which were similar to the control specimen. The strain in the tension 10M bars reached a maximum value of 0.010 mm/mm, which indicates yielding. Similar to the previous beams, the blast resulted in the formation of hairline flexural and flexural-shear cracks. The support rotation remained below 1°, corresponding to *superficial* damage. However, additional damage in terms of slight crushing and loss of side cover was observed when compared to the control specimen.

Blast 2 (50 psi) resulted in complete failure of the specimen in flexure, with severe spalling of the concrete cover in the mid-span tension region and rupture of the main tension reinforcement due to the effects of corrosion. Important crushing also occurred on the compression face at mid-span. The high-speed video showed the formation of significant blast fragments at failure. The recorded maximum and residual displacements were 107.0 mm and 43.4 mm, respectively, which were larger than those of the control beam. The strain in the tension steel reached a maximum reading of 0.019 mm/mm before it failed. The maximum support rotation was 4.9°, which corresponds to

*heavy* damage. Since bar rupture occurred, no residual static testing was conducted on this specimen.

Table 6-5 Key results (B-MC-10M-15%)

| Beams | Shockwave properties | | | | Displacement | | $\theta_{max}$ | Response limit and expected damage | |
|---|---|---|---|---|---|---|---|---|---|
| ID | $P_d$ | $P_r$ | $I_r$ | $t_p$ | $\Delta_{max}$ | $\Delta_{res}$ | | | |
| | (psi) | (kPa) | (kPa-ms) | (ms) | (mm) | (mm) | (°) | | |
| B-MC-10M-15% | 17 | 27.8 | 249 | 19.3 | 15.6 | 5.4 | 0.72 | <B1 | Superficial |
| | 50 | 59.3 | 529 | 21.0 | 107.0 | 43.4 | 4.90 | B3-B2 | Heavy |

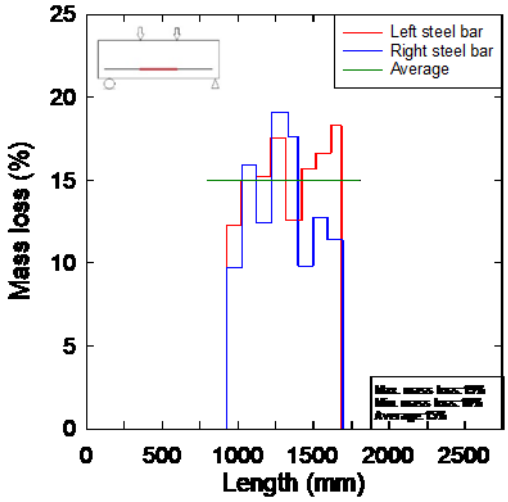
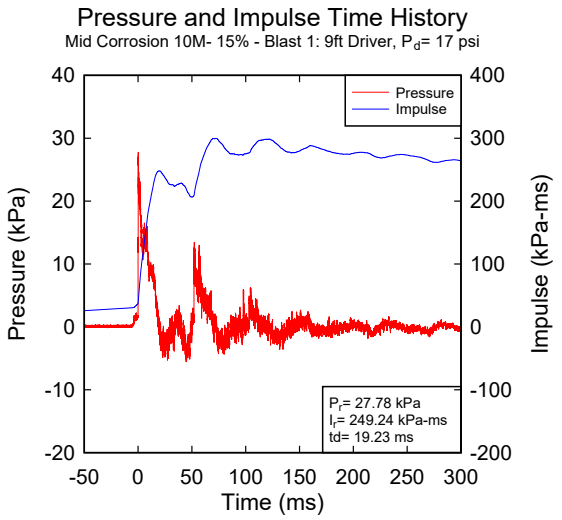
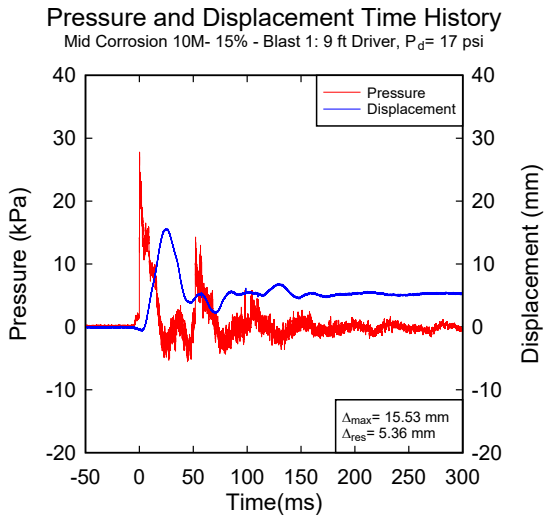



Figure 6-11 Mass loss distribution along the middle length of the tensile bars (B-MC-10M-15%)

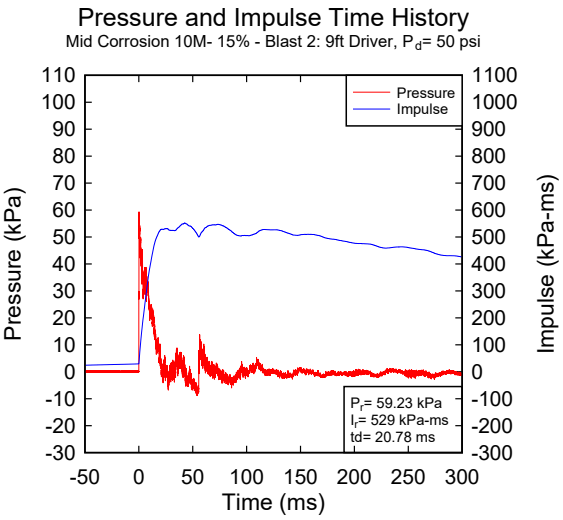


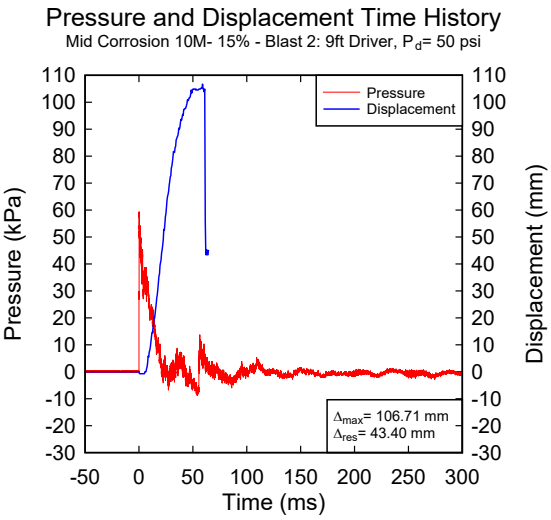
Figure 6-12 Beam cracking before testing (B-MC-10M-15%)




a) Shockwaves properties and displacement for Blast 1




b) Shockwaves properties and displacement for Blast 2

Figure 6-13 Reflected pressure, impulse and mid-span histories (B-MC-10M-15%)

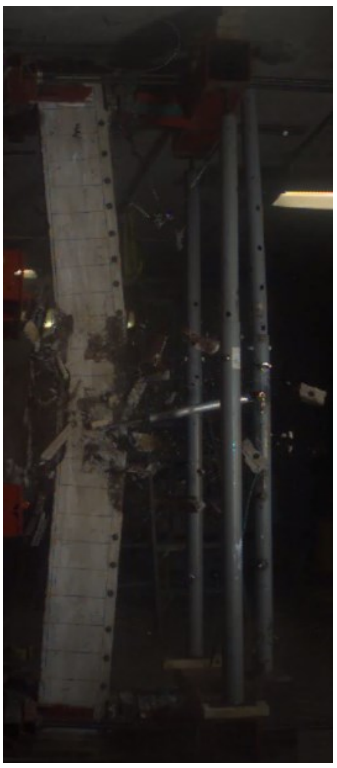
| | | |
|---|---|---|
|  |  |  |
| a) Blast 1 (17 psi) | b) Blast 2 (50 psi) | c) High-speed camera showing (Blast 2) fragments |
|  |  |  |
| d) Severe concrete spalling in mid-region (one side) (Blast 2) | e) Severe concrete spalling in mid-region (other side) (Blast 2) | f) Severe concrete spalling and bar rupture in mid-region (tension face) (Blast 2) |

Figure 6-14 Beam damage after testing (B-MC-10M-15%)

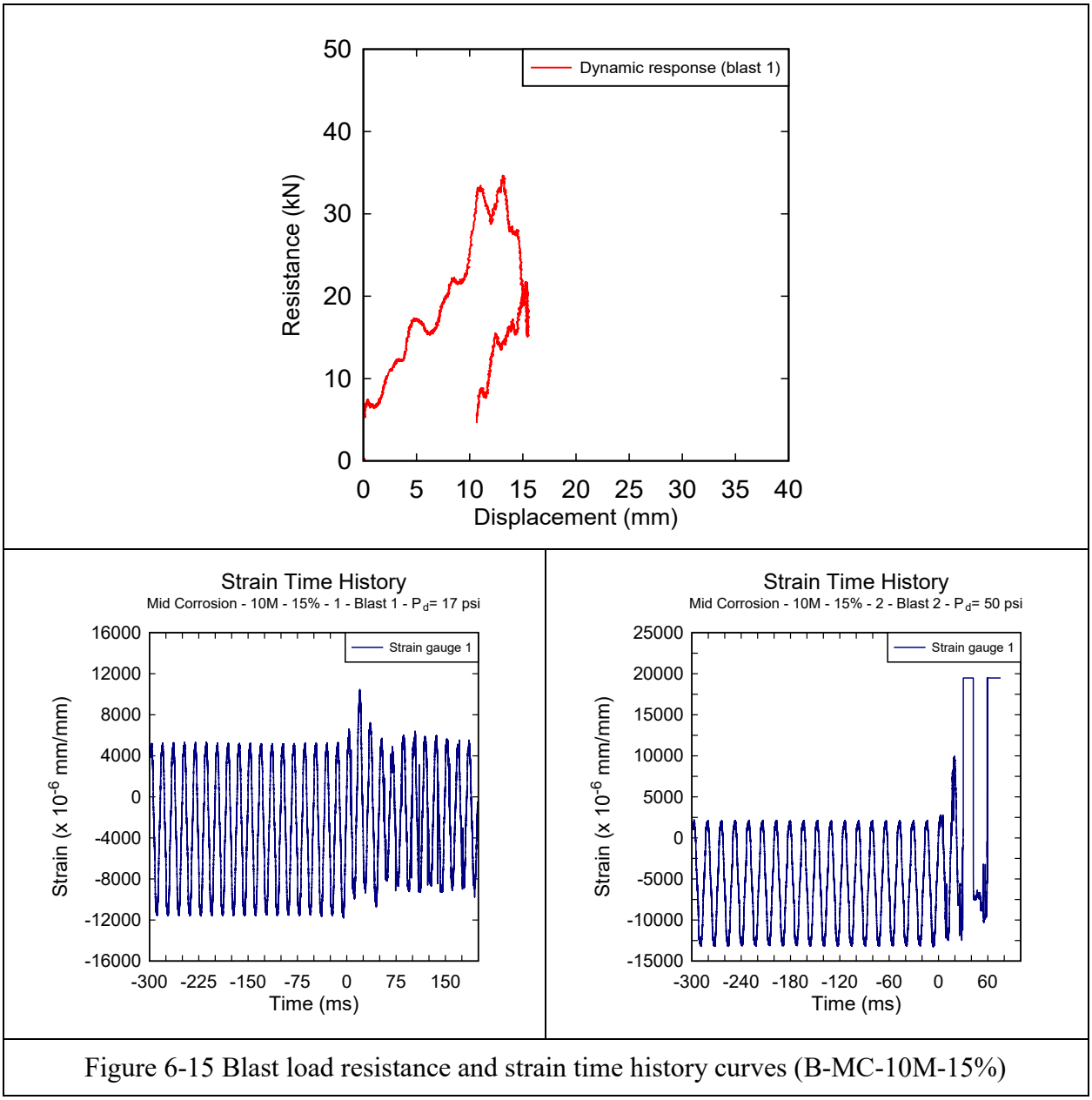



Figure 6-15 Blast load resistance and strain time history curves (B-MC-10M-15%)

#### 6.3.1.4 10M: Full length corrosion-12% mass loss (B-FC-10M-12%)

The next beam in the 10M group was subjected to corrosion of the tension reinforcement over the entire beam length. The target mass loss for the 10M bars in the tension zone was 15%; however, the actual average mass loss was found to be 12%. Examining all extracted samples, the maximum mass loss exceeded 15% in some portions as shown in **Figure 6-16**.

Before testing the beam showed clear signs of corrosion staining and cracking over its length and depth. The cracks were horizontal and mainly concentrated at the level of the longitudinal reinforcement in the tension and compression regions as shown in **Figure 6-17**.

This specimen was subjected to two blasts at driver pressures of 17 and 50 psi; however, the results of blast 1 (17 psi) were not recorded properly due to a malfunction in the data acquisition system. **Table 6-6** summarizes the key results, and the reflected pressure, impulse and mid-span displacement histories are presented in **Figure 6-18**. Beam damage at the end of testing is shown in **Figure 6-19**, while the results from the residual static test are shown in **Figure 6-20**.

Blast 1 (17 psi) resulted in the formation of hairline flexural and flexural-shear cracks. No displacement data was recorded during the test. Blast 2 (50 psi) resulted in flexure damage, with concrete crushing in the mid-span zone and significant cracking on the tension face. The high-speed video showed the formation of some blast fragments at failure. The displacement reached a maximum of 83.70 mm, while the residual displacement reached 61.70 mm. The maximum support rotation was $\theta_{max} = 4^{\circ}$, which corresponds to *Heavy* damage.

Since the beam had limited damage, its residual capacity was examined under static four-point bending. The starting point of the test was 68.60 mm, which corresponded to the cumulative residual displacement during the blast test. The results of the test are shown in **Figure 6-20**. It was observed that the beam followed the same trend observed in the undamaged companion specimen which was tested under static loads only. The maximum residual capacity of the blast-damaged beam was 50 kN at a displacement of 88 mm. This maximum displacement sustained by the beam was 110 mm with a residual load of 49 kN just prior to failure. The beam failed in flexure due to rupture of corroded tensile bars with crushing of the concrete in the compression zone.

Table 6-6 Key results (B-FC-10M-12%)

| Beams | Shockwave properties | | | | Displacement | | $\theta_{max}$ | Response limit and expected damage | |
|---|---|---|---|---|---|---|---|---|---|
| ID | $P_d$ | $P_r$ | $I_r$ | $t_p$ | $\Delta_{max}$ | $\Delta_{res}$ | | | |
| | (psi) | (kPa) | (kPa-ms) | (ms) | (mm) | (mm) | (°) | | |
| B-FC-10M-12% | 50 | 52.0 | 540 | 21.0 | 83.7 | 61.7 | 4.00 | B3-B2 | Heavy |

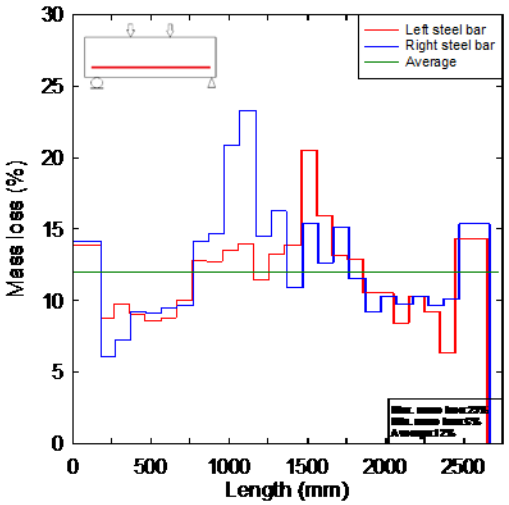
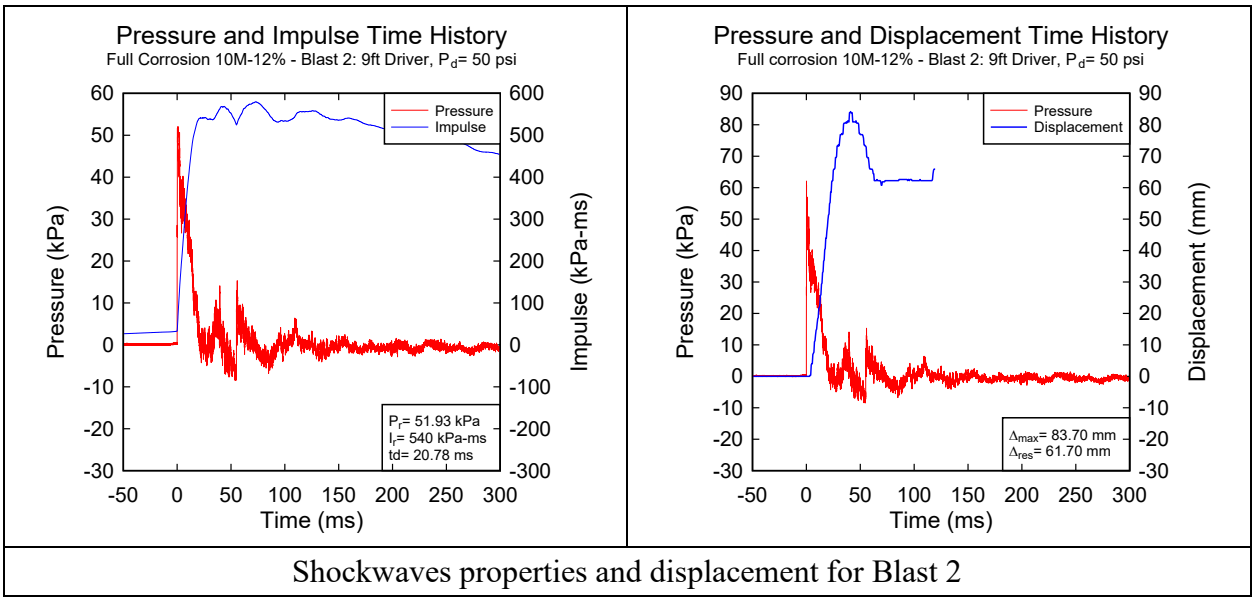



Figure 6-16 Mass loss distribution along the entire length of the tensile bars (B-FC-10M-12%)



Figure 6-17 Beam cracks before testing (B-FC-10M-12%)




Shockwaves properties and displacement for Blast 2

Figure 6-18 Reflected pressure, impulse and mid-span displacement histories (B-FC-10M-12%)

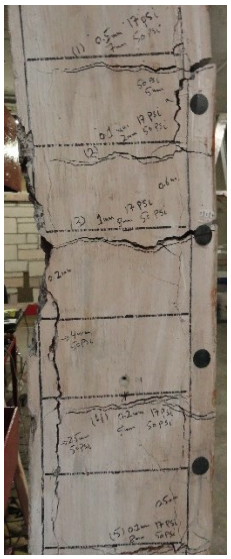
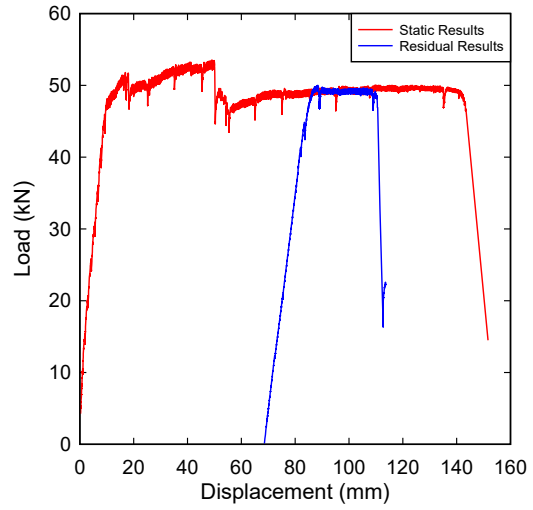
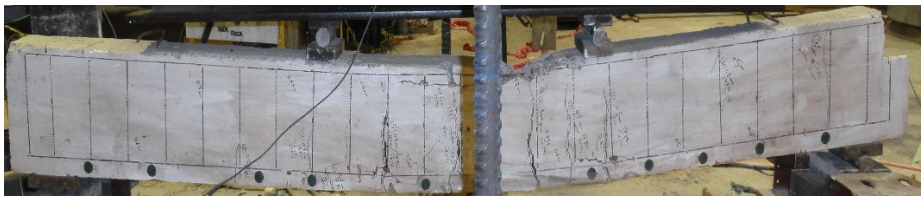
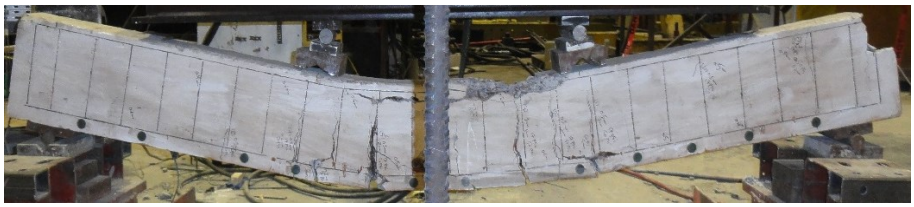
| | | |
|---|---|---|
|  |  |  |
| a) Blast 1(17 psi) | b) Blast 2 (50 psi) | c) High-speed camera showing (Blast 2) fragments |
|  |  |  |
| d) Significant concrete crushing in mid-region (one side) (Blast 2) | e) Significant concrete crushing in mid-region (other side) (Blast 2) | f) Significant cracks in mid-region (tension face) (Blast 2) |

Figure 6-19 Beam damage after testing (B-FC-10M-12%)




| Residual test results | |
|---|---|
| ΣΔ res (mm) | 68.60 |
| $P_{max}^{r}$ (kN) | 50 |
| $D_{max}^{r}$ (mm) | 110 |
| $P_{end}^{r}$ (kN) | 48.77 |

a) Load- deflection curve and results for residual test

| Before the residual test | Comments |
|---|---|
|  | Initial crushing and cracking prior to residual static test. |
| **After the residual test** | **Comments** |
|  | Concrete crushing and severe cracks in the mid-span zone.<br><br>Rupture of the 10M bars in the tension zone. |

b) Photos of the beam before and after the residual test

Figure 6-20 Residual test results (B-FC-10M-12%)

#### 6.3.1.5 10M: End/side corrosion-7% mass loss (B-SC-10M-7%)

The next beam in the 10M group was subjected to corrosion of the 10M tension reinforcement at both shear regions. The target mass loss for the 10M bars was 15%. After testing, the actual average mass loss was determined to be 7%; however, after examining all extracted samples, the maximum mass loss reached 11% and 12% in some portions (see **Figure 6-21**).

Prior to testing, the beam had horizontal cracking at the level of the longitudinal bars in the tension and compression zones. Some corrosion stains were also observed over the beam length (refer to **Figure 6-22**).

This beam was tested under blast loads at three driver pressures of 17, 35 and 50 psi. The 35 psi shot was applied since this beam was the first to be tested in the research program. The key data including the shockwave properties and beam response is summarized in **Table 6-7**. **Figure 6-23** shows the reflected pressure, impulse and mid-span displacement histories for each blast. The beam damage progression is presented in **Figure 6-24**. The results from the residual static test are shown in **Figure 6-25**.

Blast 1 (17 psi) resulted in the formation of hairline flexural cracks in the mid-span region and the formation of horizontal hairline cracks at the level of the tensile bars in the shear-span region. The maximum and residual displacements were recorded as 20.4 mm and 7 mm, respectively, with a maximum support rotation of 1°, which corresponds to *superficial* damage.

Blast 2 (35 psi) resulted in the extension of the existing cracks and increase in crack widths in the mid-span and shear-span regions. The maximum and residual displacements reached 33 mm and 15 mm, respectively.

Blast 3 (50 psi) resulted in significant flexural cracks in the constant moment region, and concrete cover spalling on the tension face in the top shear-span just above the point load location. The width of the most severe crack reached 5 mm and was located in the mid-span region. The recorded maximum and residual displacements reached 70 mm and 45 mm, respectively, with a maximum support rotation of 3.3°, which corresponds to *moderate* damage.

Since the beam had limited damage, it was tested under quasi-static four-point bending to assess its residual capacity (see **Figure 6-25**). The initial point of the test was 65.80 mm, which was the

cumulative residual displacement during the blast test. The maximum residual capacity reached 61.30 kN at a displacement of 83 mm, which was higher than the maximum resistance of the undamaged companion beam which was tested under static loads only. The beam showed an ability to carry sustained loads, reaching a displacement of 136 mm with a residual load of 55 kN. The flexural damage at the end of testing was associated with concrete crushing in the mid-span region.

Table 6-7 Key results (B-SC-10M-7%)

| **Beams** | **Shockwave properties** | | | | **Displacement** | | $\theta_{max}$ | **Response limit and expected damage** | |
|---|---|---|---|---|---|---|---|---|---|
| **ID** | $P_d$ | $P_r$ | $I_r$ | $t_p$ | $\Delta_{max}$ | $\Delta_{res}$ | | | |
| | **(psi)** | **(kPa)** | **(kPa-ms)** | **(ms)** | **(mm)** | **(mm)** | **(º)** | | |
| B-SC-10M-7% | 17 | 29.2 | 239 | 18.5 | 20.4 | 7.0 | 0.95 | <B1 | Superficial |
| | 35 | 48.5 | 356 | 19.3 | 33.0 | 15.0 | 1.60 | B2-B1 | Moderate |
| | 50 | 61.5 | 555 | 21.6 | 70.0 | 45.0 | 3.30 | B2-B1 | Moderate |

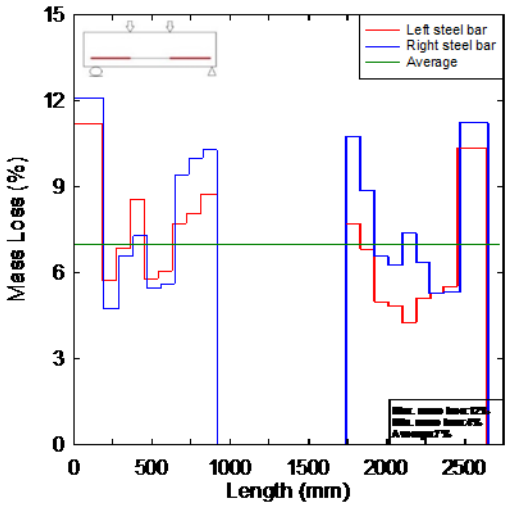
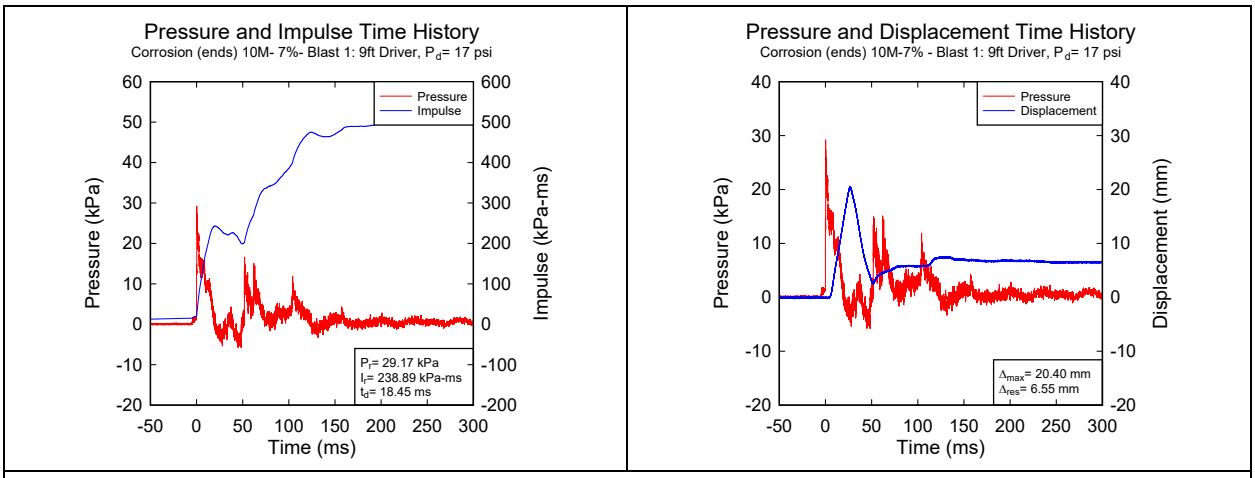


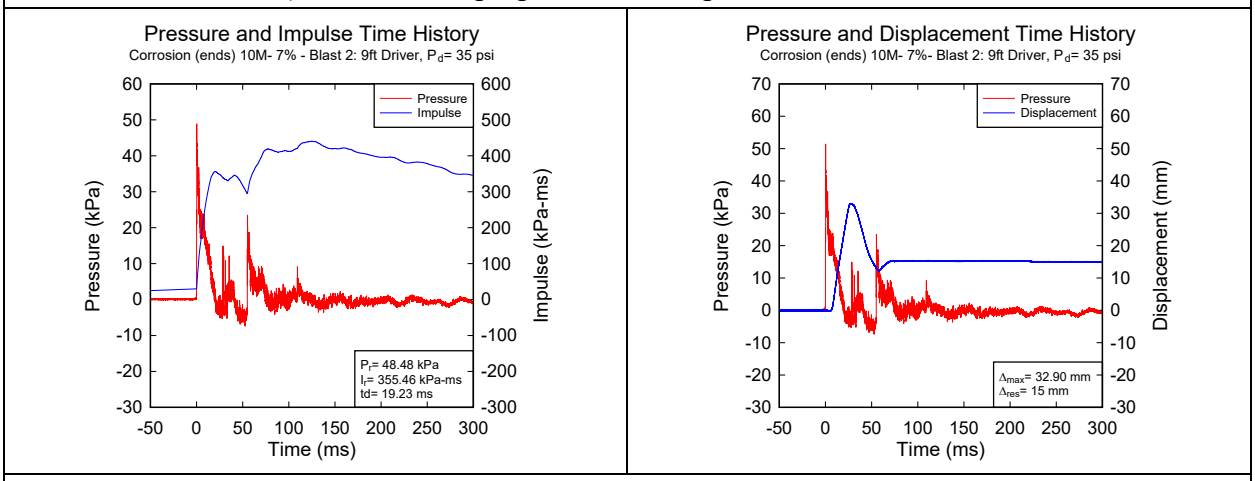

Figure 6-21 Mass loss distribution along the ends length of the tensile bars (B-SC-10M-7%)



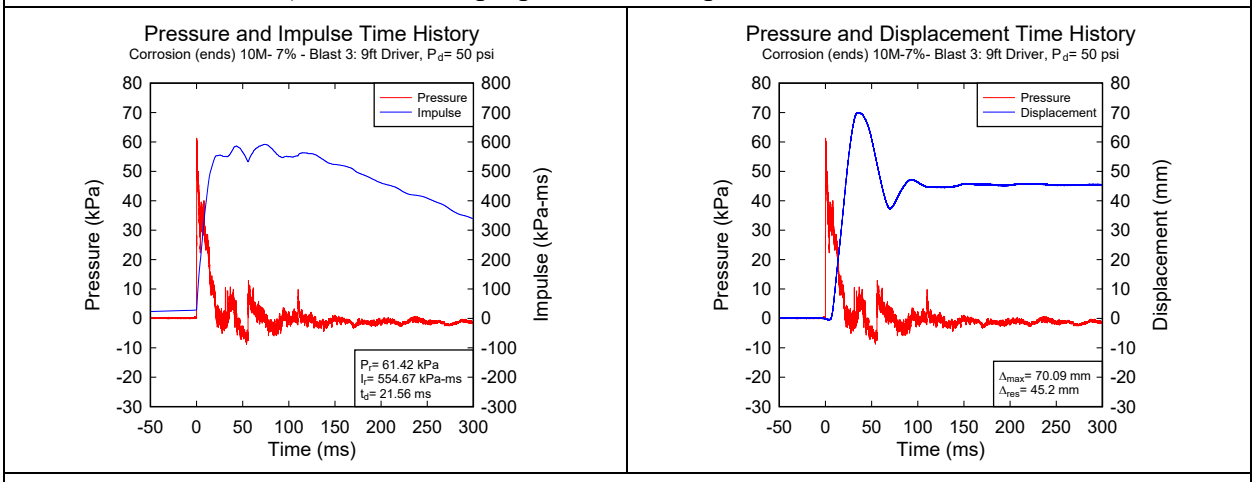
Figure 6-22 Cracking in the beam before testing (B-SC-10M-7%)




a) Shockwaves properties and displacement for Blast 1




b) Shockwaves properties and displacement for Blast 2




c) Shockwaves properties and displacement for Blast 3

Figure 6-23 Reflected pressure, impulse and mid-span displacement histories (B-SC-10M-7%)



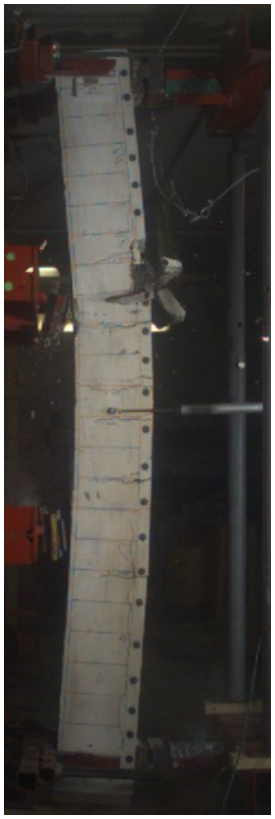
a) Blast 1 (17 psi)



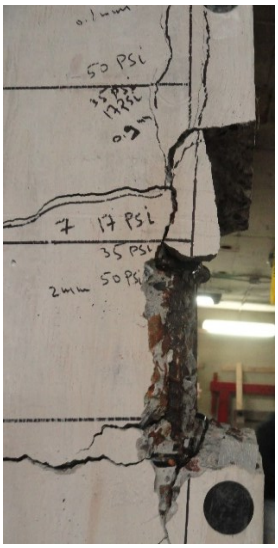
b) Blast 2 (35 psi)



c) Blast 3 (50 psi)



d) High-speed camera showing (Blast 3) fragments




e) Cover spalling in the top shear-span and cracks (one side) (Blast 3)

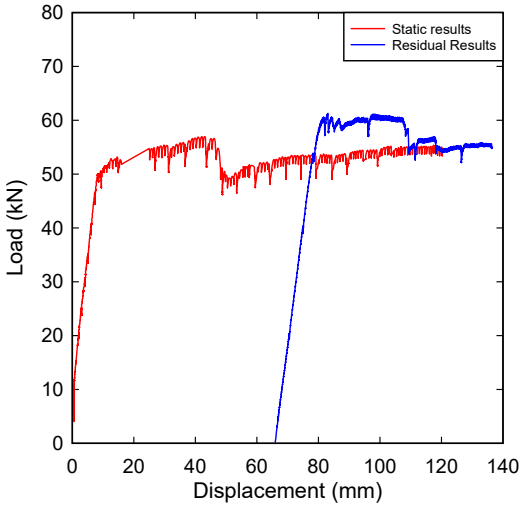



f) Cover spalling in the top shear-span and cracks (other side) (Blast 3)



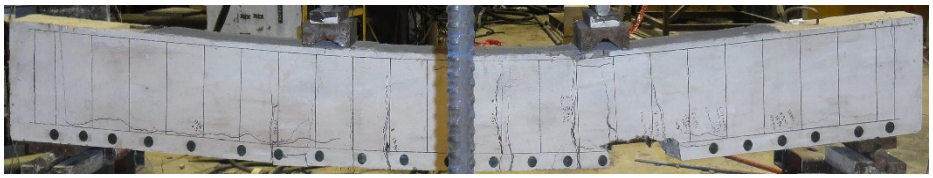
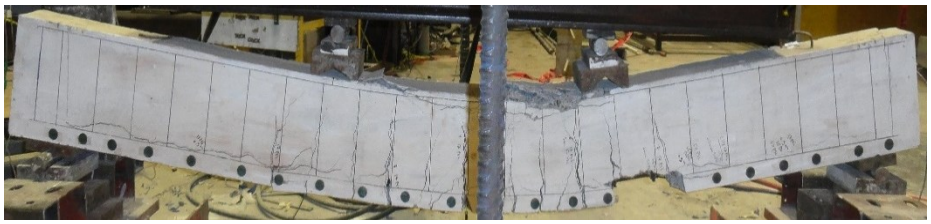
e) Cover spalling in top shear-span and cracks (tension face) (Blast 3)

Figure 6-24 Beam damage after testing (B-SC-10M-7%)




| Residual test results | |
|---|---|
| ΣΔ res (mm) | 65.80 |
| $P_{max}^{r}$ (kN) | 61.30 |
| $D_{max}^{r}$ (mm) | 136.30 |
| $P_{end}^{r}$ (kN) | 55.38 |

a) Load-deflection curve and summary of residual test results

| Before the residual test | Comments |
|---|---|
|  | Significant cracks in the mid-span.<br>Concrete spalling in the tension-region. |
| After the residual test | Comments |
|  | Concrete crushing in the compression zone. |

b) Photos of the beam before and after the residual test

Figure 6-25 Residual test results (B-SC-10M-7%)

#### 6.3.1.6 10M: Mid-span corrosion- 22% extreme mass loss (B-EMC-10M-22%)

The next beam in the 10M group was subjected to "extreme" corrosion over a length of 750 mm in the mid-span zone. The aimed mass loss was 30% on the longitudinal bars in the tension zone, but the actual average mass loss was determined to be 22%, even though one portion of the extracted bar samples exceeded the mass loss of 30% (see **Figure 6-26**).

The observed cracks before testing were horizontal and located at the level of the longitudinal bars in the tension and compression zones. Concrete staining due to the corrosion was also observed in the mid-span region as shown in **Figure 6-27**.

This beam was subjected to a single blast at a driver pressure of 50 psi. The key data from this test is summarized in **Table 6-8**, while the results in terms of reflected pressure, impulse and mid-span displacement histories are shown in **Figure 6-28**. The beam damage after the blast test is presented in **Figure 6-29**, whereas **Figure 6-30** shows the reinforcement strain time history.

Blast 1 (50 psi) resulted in complete failure of the beam in flexure, with severe spalling of the concrete cover mainly in the mid-span zone and rupture of the two tension reinforcing bars due to the effects of corrosion, which resulted in the beam nearly splitting into two portions (see **Figure 6-29**). The maximum and the residual displacements were recorded at 217.3 mm and 181.4 mm, respectively, which were much larger than those of the control specimen. The maximum strain in the tensile bars reached 0.025 mm/mm prior to failure. The maximum support rotation reached 10.1°, which corresponds to *blowout* damage.

Table 6-8 Key results (B-EMC-10M-22%)

| **Beams** | **Shockwave properties** | | | | **Displacement** | | $\theta_{max}$ | **Response limit and expected damage** | |
|---|---|---|---|---|---|---|---|---|---|
| **ID** | $P_d$ | $P_r$ | $I_r$ | $t_p$ | $\Delta_{max}$ | $\Delta_{res}$ | | | |
| | **(psi)** | **(kPa)** | **(kPa-ms)** | **(ms)** | **(mm)** | **(mm)** | **Degree** | | |
| B-EMC-10M-22% | 50 | 61.0 | 541 | 21.0 | 217.3 | 181.4 | 10.10 | ≥B4 | Blowout |

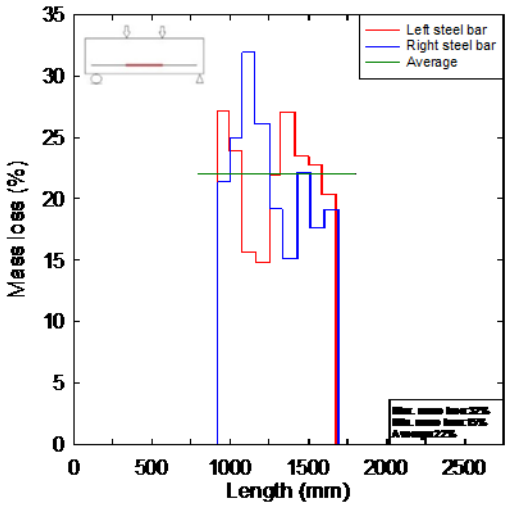



Figure 6-26 Mass loss distribution along the middle length of the tensile bars (B-EMC-10M-22%)



Figure 6-27 Corrosion-induced cracking in the beam before testing (B-EMC-10M-22%)

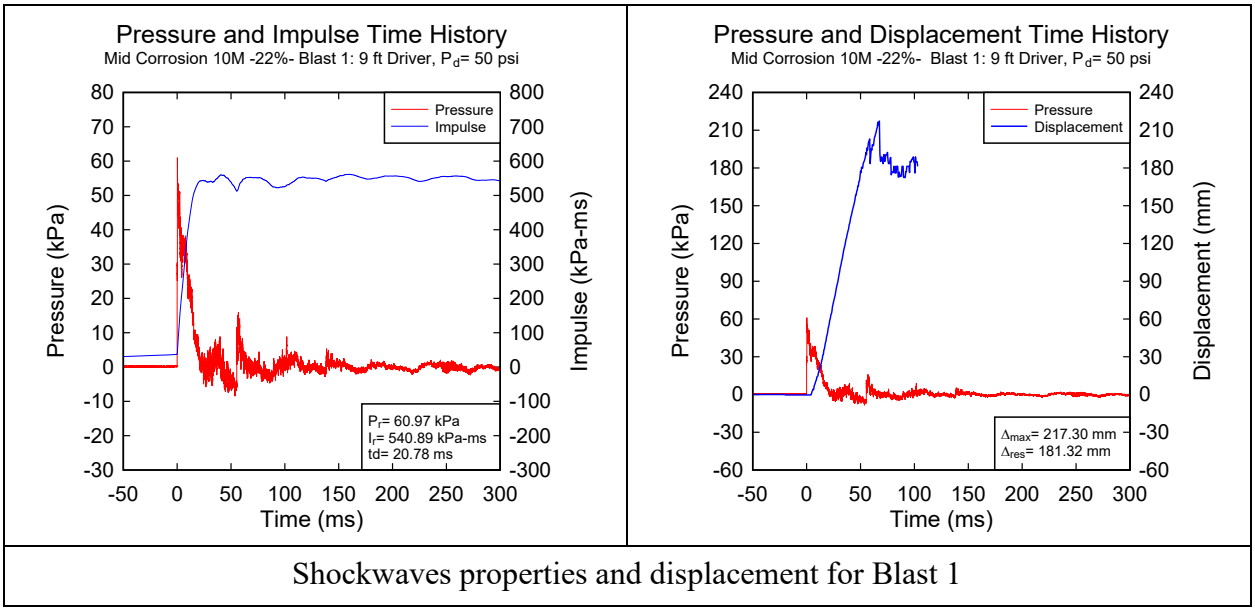


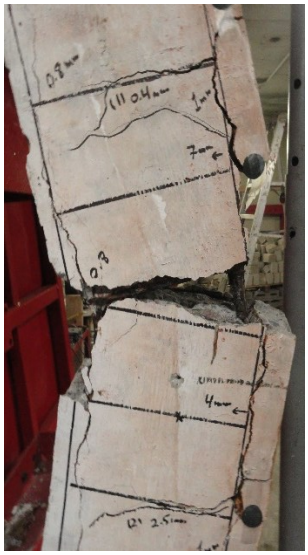

Figure 6-28 Reflected pressure, impulse and mid-span displacement histories (B-EMC-10M-22%)



a) Blast 1 (50 psi)



b) High-speed camera showing Blast 1 fragments



c) Bars rupture and beam splitting in mid-span zone (one side) (Blast 1)



d) Bars rupture and beam splitting in mid-span zone (other side) (Blast 1)



e) Bars rupture and beam splitting in mid-span zone (tension face) (Blast 1)

Figure 6-29 Beam damage after testing (B-EMC-10M-22%)

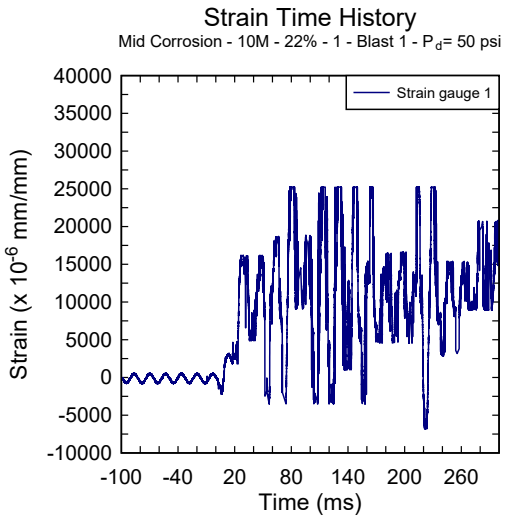



Figure 6-30 Strain time history in the tension 10M bars (B-EMC-10M-22%)

#### 6.3.1.7 10M: cover-removal with mid-span corrosion – 5% mass loss (B-CR-MC-10M-5%)

The last beam in the 10M group was subjected to the combined effects of concrete cover removal and mid-span corrosion. The concrete cover was first removed, and then the 10M tension reinforcement was subjected to corrosion over a length of 750 mm in the mid-span region. The intended mass loss for the 10M longitudinal bars in the tension region was 30%; however, after testing, the actual average mass loss was measured to be only 5%. Considering all extracted bar samples, the maximum mass loss did not exceed 6% (see **Figure 6-31**).

Before testing the beam showed limited signs of damage with the exception of some corrosion spots on the concrete cover and rusting of the tensile bars at mid-span as shown **Figure 6-32**.

Similar to the previous beam, this specimen was subjected to a single blast at a 50 psi driver pressure. **Table 6-9** provides a summary of the key data, whereas **Figure 6-33** shows the reflected pressure, impulse and mid-span displacement histories for this test. Photos of the beam damage after testing are shown in **Figure 6-34**.

Blast 1 (50 psi) resulted in significant flexural cracks, which were mainly distributed in the mid-span region and resulted in concrete crushing in the compression zone. Additional minor cracks were observed in the shear regions. The most significant crack width reached 4 mm and was located in the mid-span zone. The maximum and residual displacements were recorded as 79 mm and 57 mm, respectively, with a maximum support rotation of 3.7°, which corresponds to *moderate* damage.

Table 6-9 Key results (B-CR-MC-10M-5%)

| **Beams** | **Shockwave properties** | | | | **Displacement** | | $\theta_{max}$ | **Response limit and expected damage** | |
|---|---|---|---|---|---|---|---|---|---|
| **ID** | $P_d$ | $P_r$ | $I_r$ | $t_p$ | $\Delta_{max}$ | $\Delta_{res}$ | | | |
| | **(psi)** | **(kPa)** | **(kPa-ms)** | **(ms)** | **(mm)** | **(mm)** | **Degree** | | |
| B-CR-MC-10M-5% | 50 | 65.6 | 548 | 21.0 | 79.0 | 57.0 | 3.70 | B2-B1 | Moderate |

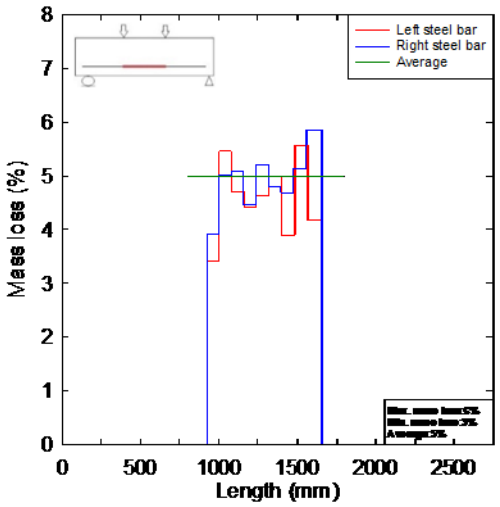
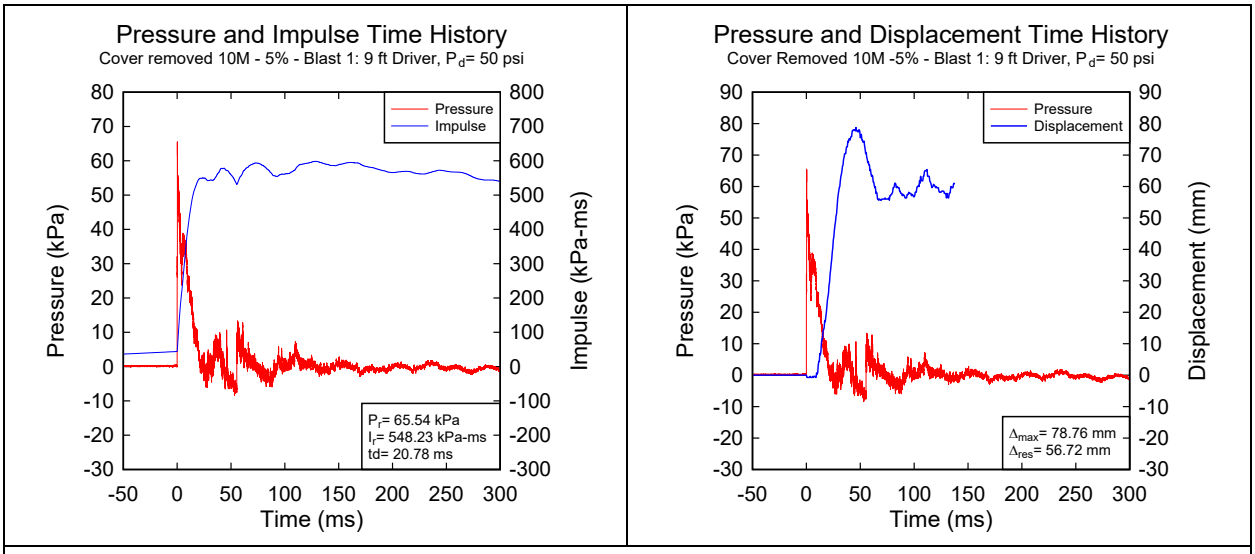



Figure 6-31 Mass loss distribution along the middle length of the tensile bars (B-CR-MC-10M-5%)



Figure 6-32 The condition of the beam before testing (B-CR-MC-10M-5%)




Shockwaves properties and displacement for Blast 1

Figure 6-33 Reflected pressure, impulse and mid-span displacement histories (B-CR-MC-10M-5%)



a) Blast 1 (50 psi)



b) High-speed camera showing Blast 1 fragments



c) Concrete crushing in compression zone and some cracks in the mid-span (one side) (Blast 1)



d) Concrete crushing in compression zone and some cracks in the mid-span (other side) (Blast 1)



e) Corroded bars at the mid-span (tension face) (Blast 1)

Figure 6-34 Beam damage after testing (B-CR-MC-10M-5%)

### 6.3.2 15M Group

The 15M group included four beams which were tested under shock-tube blast loads. The beams were doubly-reinforced with 2-10M bars in tension and 2-15M bars in compression (as top bars), and they were provided with U-shaped stirrups made from 6.3-mm wire which were uniformly spaced at 100 mm throughout the beam span.

#### 6.3.2.1 15M: Control (0% mass loss) (CB-15M-0%)

Beam CB-15M-0% was the first beam tested under blast loading in the 15M group and was the control specimen in this group. Before testing, no corrosion was applied. The beam was subjected to two blasts at driver pressures of 17 and 70 psi. **Table 6-10** shows the key results that include the properties of the shockwaves and displacements at these blasts. **Figure 6-35** presents the complete reflected pressure, reflected impulse and mid-span displacements time histories. Photos that show damage after each blast are provided in **Figure 6-36**. The dynamic resistance results (as obtained from the support load cells) and measured strains in the tension steel are shown in **Figure 6-37**.

Blast 1 (17 psi) resulted in the formation of hairline flexural cracks in the constant moment region and the formation of inclined flexural-shear cracks in the shear spans. The maximum and residual displacements reached 10.6 mm and 3.2 mm, respectively, while the maximum strain recorded as 0.00206 mm/mm indicating the steel was near yielding. The support rotation ($\theta_{max}$) reached 0.5°, which corresponds to *superficial* damage.

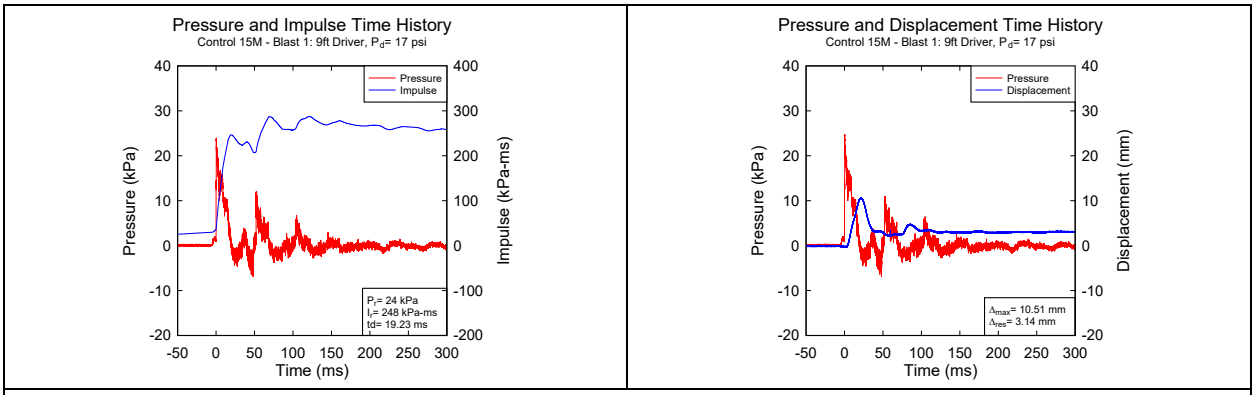
Blast 2 (70 psi) resulted in the extension of existing flexural cracks and increased crack widths in the mid-span region. The most severe crack width reached 4 mm and was located in the mid-span of the beam. The maximum and residual displacements were recorded as 70.6 mm and 50.5 mm, respectively, with a maximum support rotation of $\theta_{max}$ = 3.3°, which corresponds to *moderate* damage. The maximum strain in the tension bars reached 0.024 mm/mm, indicating the tension steel reinforcement was well into the inelastic range. Despite the relatively large support rotation and noticeable residual displacement, the beam only showed minor crushing in the mid-span compression zone, with no significant cover spalling.

After testing, the beam was tested under quasi-static four-point bending to evaluate its residual capacity, and the results are presented in **Figure 6-38**. The starting point of the test was at 53.56

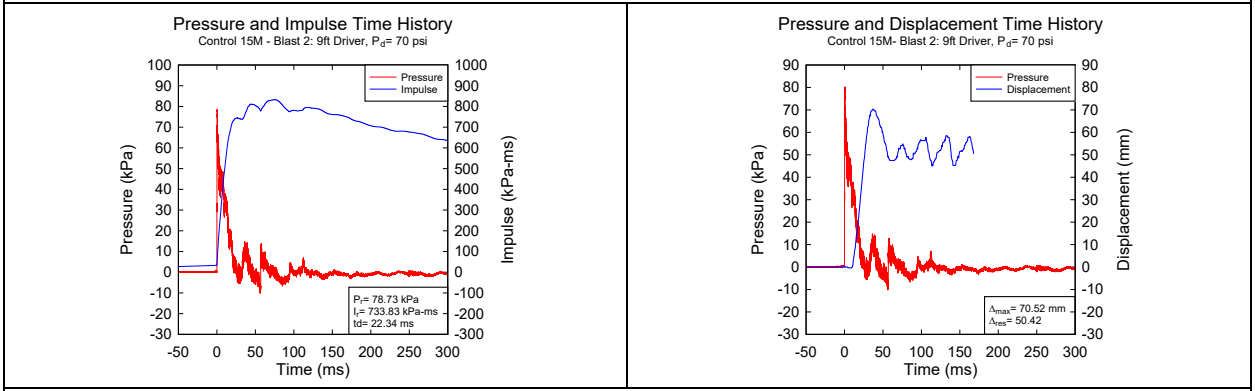
mm, which is the cumulative residual displacement during the blast test. It was observed that the beam followed a similar trend when compared to the companion undamaged beam which was tested under static loads only. The blast-damaged beam reached a maximum residual capacity of $P_{max}^{r}$ = 102.50 kN, which was slightly below the undamaged peak capacity of $P_{max}$ = 110 kN. The beam also showed an ability to carry sustained loads, reaching a displacement $\Delta_{max}^{r}$ =103 mm, with a residual load of $P_{end}^{r}$ = 98 kN at the end of testing. The flexural failure at the end of the test was associated with concrete crushing and buckling of the longitudinal bars in the compression region at the beam mid-span.

Table 6-10 Key results (CB-15M-0%)

| Beams | Shockwave properties | | | | Displacement | | $\theta_{max}$ | Response limit and expected damage | |
|---|---|---|---|---|---|---|---|---|---|
| ID | $P_d$ (psi) | $P_r$ (kPa) | $I_r$ (kPa-ms) | $t_p$ (ms) | $\Delta_{max}$ (mm) | $\Delta_{res}$ (mm) | (°) | | |
| CB-15M-0% | 17 | 24.0 | 248 | 19.3 | 10.6 | 3.2 | 0.50 | <B1 | Superficial |
| | 70 | 78.8 | 734 | 22.4 | 70.6 | 50.5 | 3.30 | B1-B2 | Moderate |




a) Shockwaves properties and displacement for Blast 1




b) Shockwaves properties and displacement for Blast 2

Figure 6-35 Reflected pressure, impulse and mid-span displacement histories (CB-15M-0%)

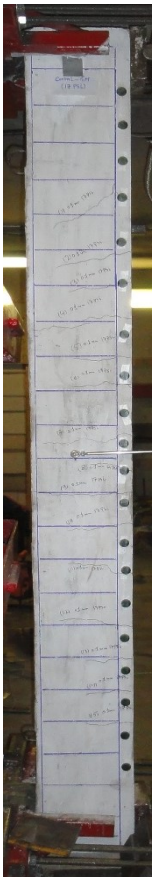
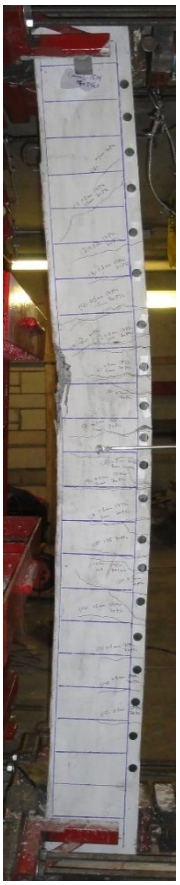
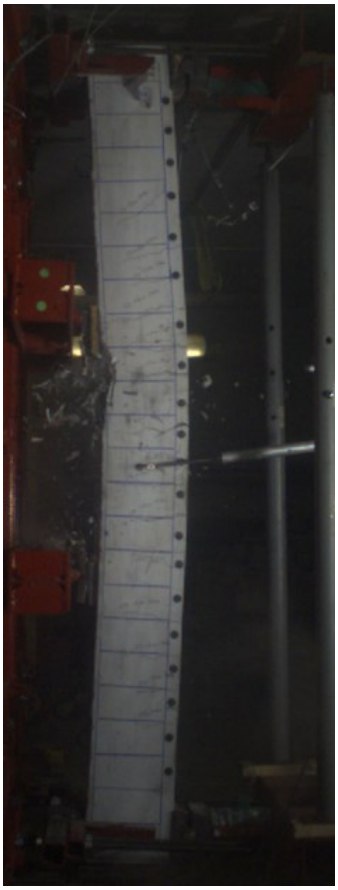
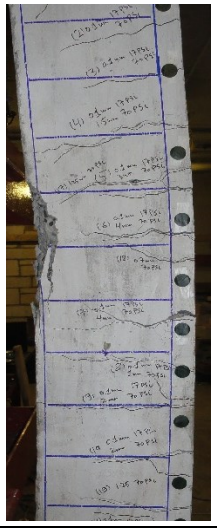
| | | |
|---|---|---|
|  |  |  |
| a) Blast 1 (17 psi) | b) Blast 2 (70 psi) | c) High-speed camera showing Blast 2 fragments |
|  |  |  |
| d) Mid-span cracks with slight concrete crushing (one side) (Blast 2) | e) Mid-span cracks with slight concrete crushing (other side) (Blast 2) | f) Mid-span cracks in tension face (tension face) (Blast 2) |

Figure 6-36 The beam damage after testing (CB-15M-0%)

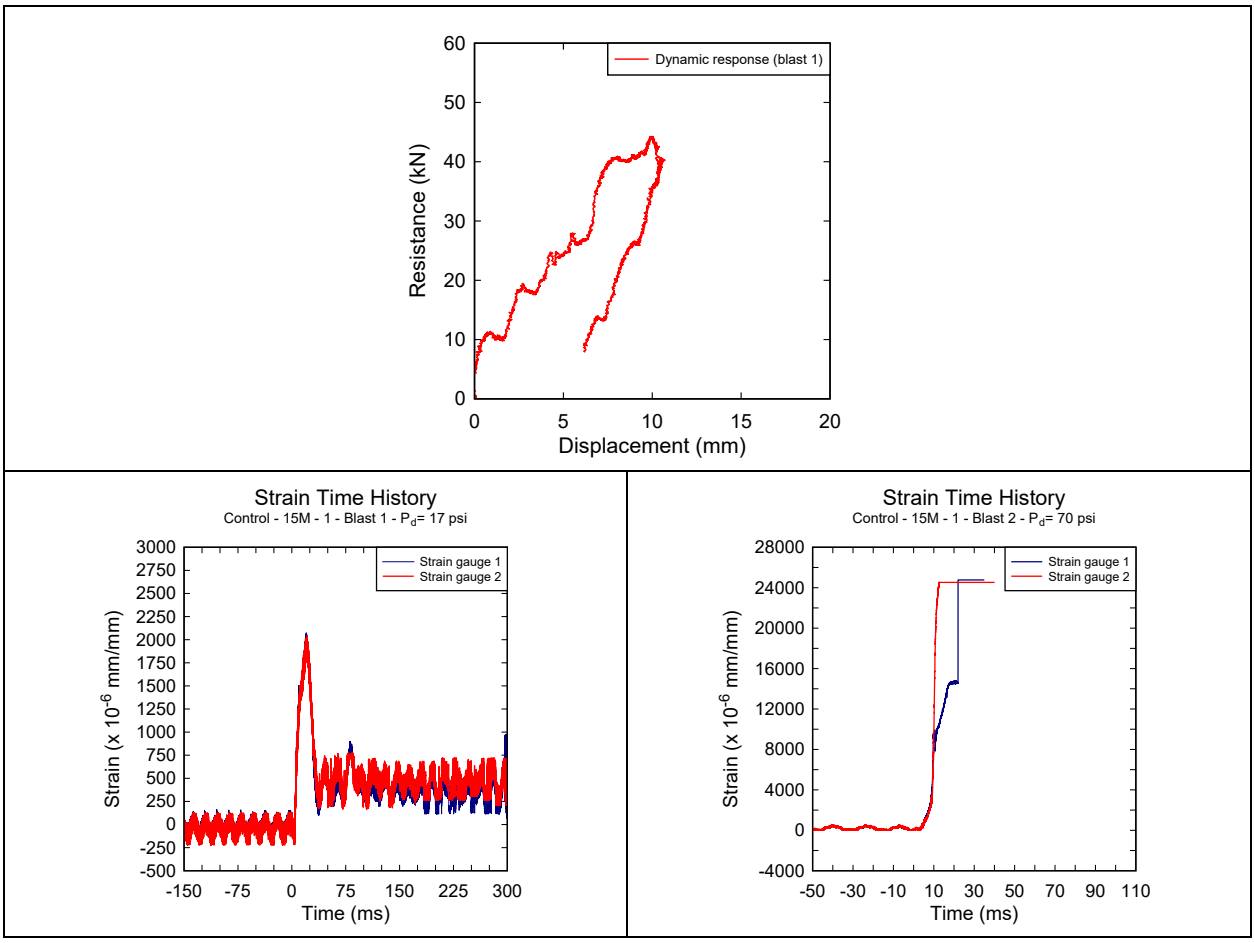
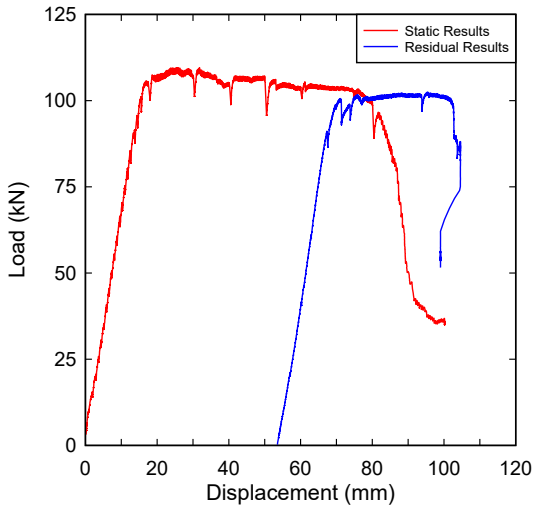



Figure 6-37 Blast load resistance and strain time history curves (CB-15M-0%)




| Residual test results | |
|---|---|
| ΣΔ res (mm) | 53.56 |
| $P_{max}^{r}$ (kN) | 102.50 |
| $D_{max}^{r}$ (mm) | 102.70 |
| $P_{end}^{r}$ (kN) | 98 |

a) Load- deflection curve and results for residual test

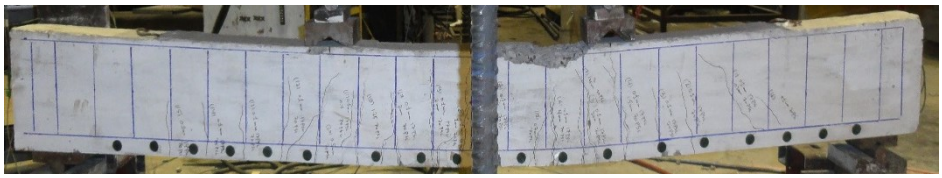
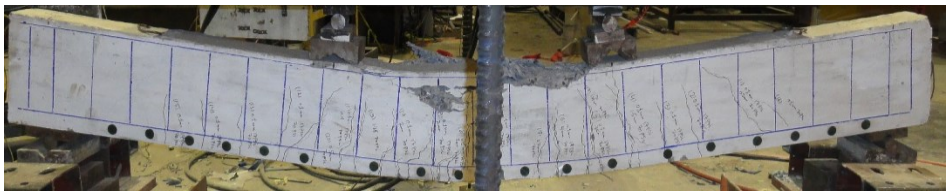
| Before the residual test | Comments |
|---|---|
|  | Flexural and shear cracks distributed over the length of the beam.<br>Slight concrete crushing in the mid-span at compression zone. |
| After the residual test | Comments |
|  | Concrete crushing in the compression zone associated with buckling of the top longitudinal reinforcement. |
| b) Photos of the beam before and after the residual test | |

Figure 6-38 Residual test results (CB-15M-0%)

#### 6.3.2.2 15M: Mid-span corrosion – 12% mass loss (B-MC-15M-12%)

The second beam in the 15M group was similar to the reference specimen in terms of design properties; however, it was subjected to corrosion over a length of 750 mm in the mid-span region. The target mass loss was 30% for the 15M longitudinal bars in the tension zone; nonetheless, the actual average mass loss was found to be 12%. The maximum mass loss reached 19% in one portion of the extracted bar samples (see **Figure 6-39**).

Prior to beam testing, the observed cracking consisted of horizontal cracks in the mid-span region at the level of the tension and compression longitudinal bars, and there were signs of corrosion stains on the concrete surface as shown in **Figure 6-40**.

Similar to the reference specimen, this beam was subjected to two blast loads at 17 and 70 psi driver pressures. **Table 6-11** summarizes the properties of the shockwaves and beam response in terms of displacements. The reflected pressure, impulse and mid-span displacements histories for each blast are shown in **Figure 6-41**. The damage in the beam during the tests is shown in **Figure 6-42**. **Figure 6-43** shows the dynamic resistance curve, as obtained from the support load cells, and the strain time history curves for the instrumented 15M bars.

Blast 1 (17 psi) resulted in maximum and residual displacements of 11 mm and 2 mm, respectively, which were similar to the control specimen. The strain in the tension 15M bars reached the maximum value of 0.0013 mm/mm, which indicates the bars were still in the elastic range. Similar to the previous beam, the blast resulted in the formation of hairline flexural and flexural-shear cracks. The support rotation remained below 1°, corresponding to *superficial* damage.

Blast 2 (70 psi) resulted in failure of the specimen in flexure, with severe spalling of the concrete cover in the mid-span in tension and crushing of the top concrete cover in compression. The high-speed video showed the formation of significant blast fragments at failure. The recorded maximum and residual displacements were 71.2 mm and 51 mm, respectively. The strain in the tension steel reached a maximum reading of 0.025 mm/mm before it failed. The maximum support rotation was 3.4°, which corresponds to *moderate* damage. Due to the severe failure, no residual static test was conducted on this specimen.

Table 6-11 Key results (B-MC-15M-12%)

| Beams | Shockwave properties | | | | Displacement | | $\theta_{max}$ | Response limit and expected damage | |
|---|---|---|---|---|---|---|---|---|---|
| ID | $P_d$ | $P_r$ | $I_r$ | $t_p$ | $\Delta_{max}$ | $\Delta_{res}$ | | | |
| | (psi) | (kPa) | (kPa-ms) | (ms) | (mm) | (mm) | (°) | | |
| B-MC-15M-12% | 17 | 29 | 251 | 18.5 | 11 | 2 | 0.5 | <B1 | Superficial |
| | 70 | 80 | 703 | 22.4 | 71.2 | 51 | 3.4 | B2-B1 | Moderate |

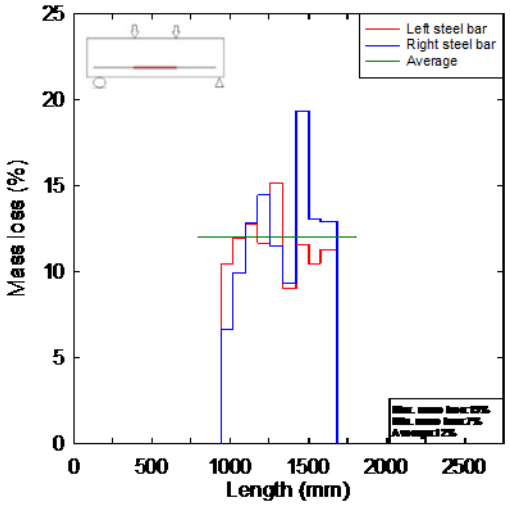
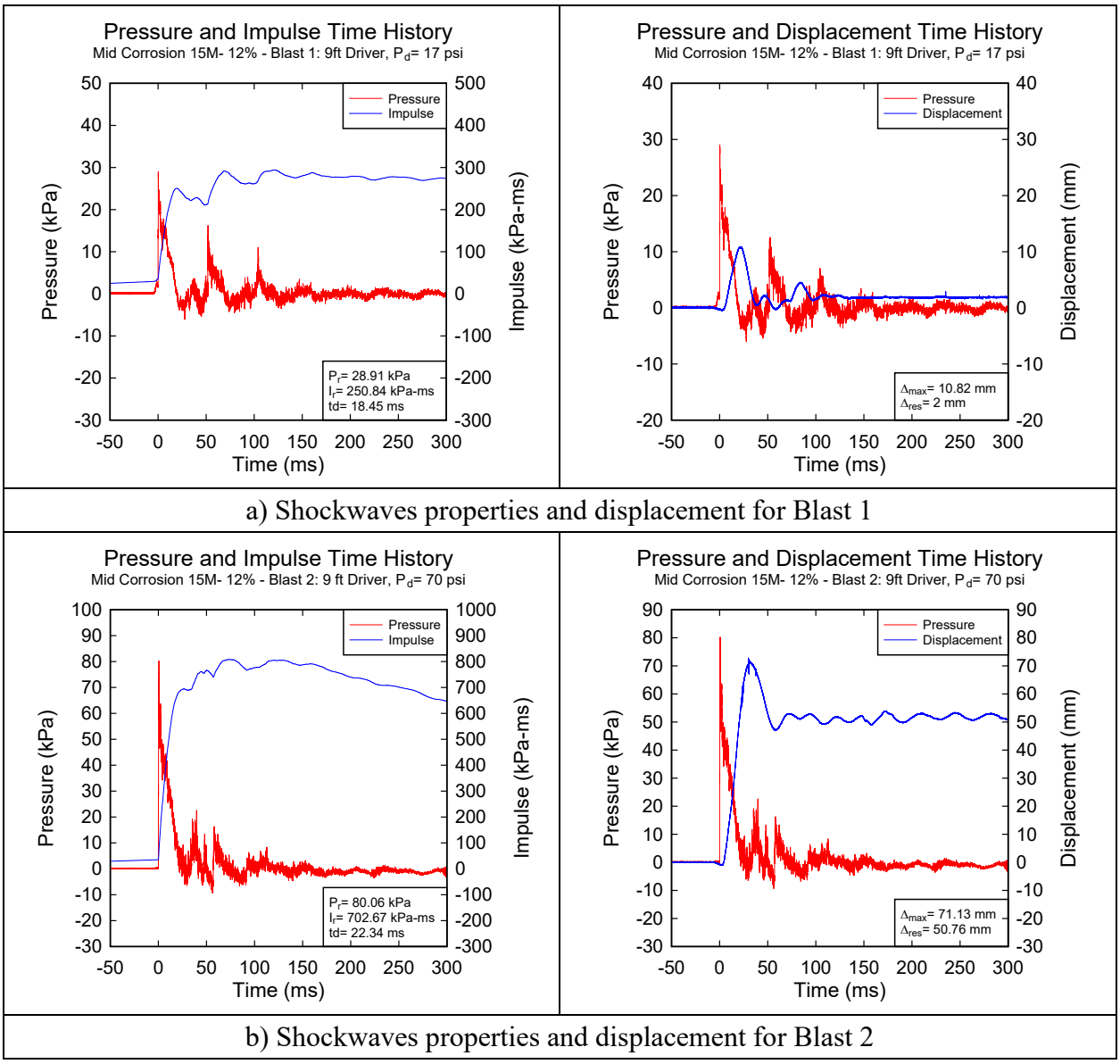



Figure 6-39 Mass loss distribution along the middle length of the tensile bars (B-MC-15M-12%)



Figure 6-40 The condition of the beam before testing (B-MC-15M-12%)




a) Shockwaves properties and displacement for Blast 1

b) Shockwaves properties and displacement for Blast 2

Figure 6-41 Reflected pressure, impulse and mid-span displacement histories (B-MC-15M-12%)

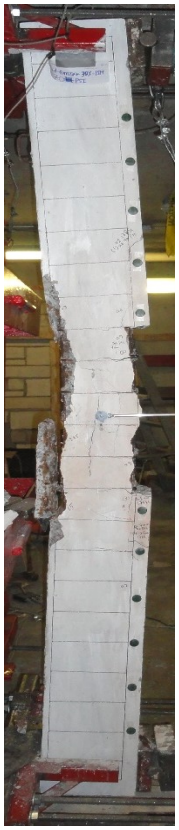
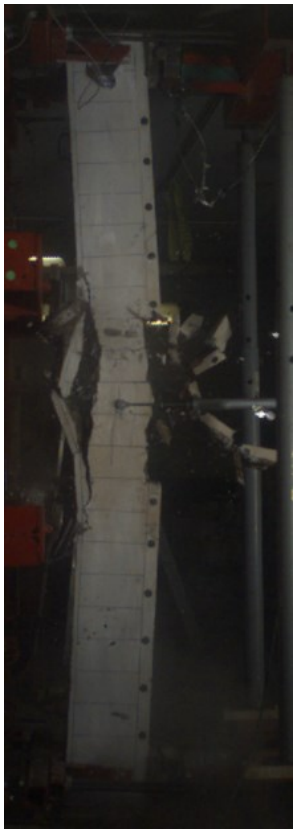
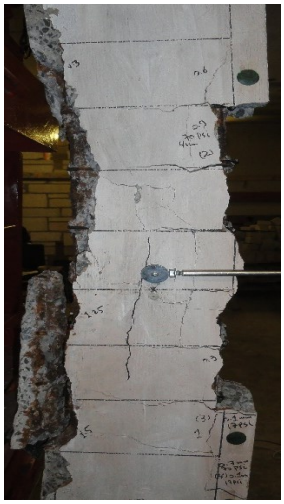
| | | |
|---|---|---|
|  |  |  |
| a) Blast 1 (17 psi) | b) Blast 2 (70 psi) | c) High-speed camera showing Blast 2 fragments |
|  |  |  |
| d) Severe concrete spalling and crushing in mid-zone (one side) (Blast 2) | e) Severe concrete spalling and crushing in mid-zone (other side) (Blast 2) | e) Severe concrete spalling (tension face) (Blast 2) |

Figure 6-42 Photos of the beam damage after testing (B-MC-15M-12%)

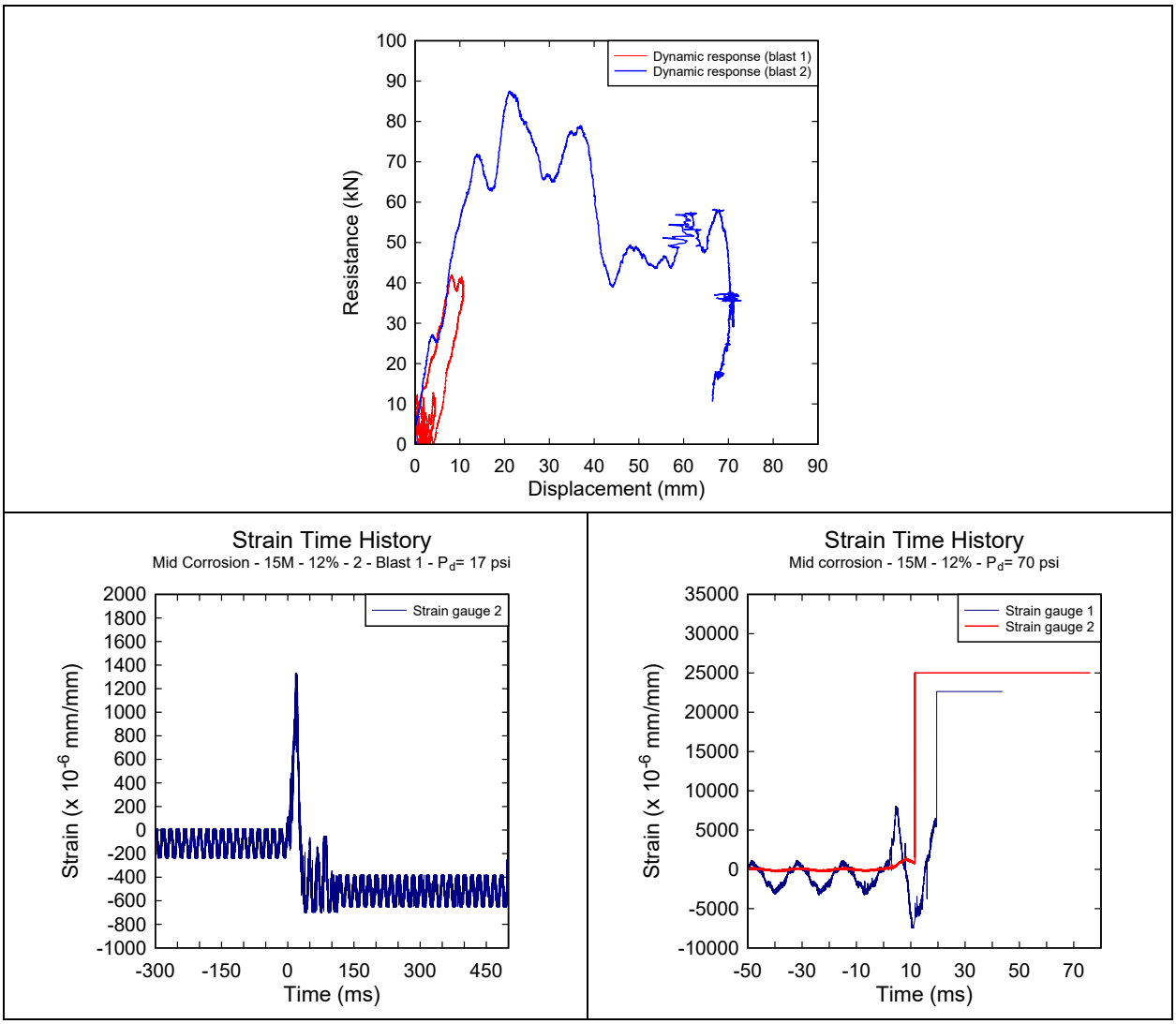



Figure 6-43 Blast load resistance curve and strain time history curves (B-MC-15M-12%)

#### 6.3.2.3 15M: Mid-span corrosion – 17% extreme mass loss (B-EMC-15M-17%)

Beam B-EMC-15M-17% was constructed with similar design properties as the control specimen, but it was subjected to corrosion of the 15M bars over a length of 750 mm in the mid-span region. The intended mass loss for the 15M longitudinal reinforcement in the tension zone was 30%; however, after testing, the actual average mass loss was measured to be 17%. Despite this, the mass loss reached 29% and 28% in some portions of the extracted bar samples (see **Figure 6-44**).

The observed cracks before testing were horizontal cracks mainly distributed at the level of the longitudinal bars in the tension and compression zones, with associated corrosion stains on the concrete surface in the mid-span region as shown in **Figure 6-45**.

This beam was subjected to a single blast at a 70 psi driver pressure. The key results are summarized in **Table 6-12**, while the complete reflected pressure, impulse and mid-span displacement time histories are shown in **Figure 6-46**. The damage of the beam after the test is presented in **Figure 6-47**, whereas **Figure 6-48** shows the strain time history curve for the instrumented 15M bars.

Blast 1 (70 psi) resulted in complete failure of the beam in flexure, with severe spalling of the concrete cover in the mid-span region and rupture of the two main 15M tension bars due to the effects of corrosion, which resulted in the beam nearly splitting in two (see **Figure 6-47**). The maximum and residual displacements reached 169.0 mm and 149.2 mm, respectively, which were much larger than those of the control specimen. The maximum strain in tensile bars reached 0.022 mm/mm, with maximum support rotation of 8°, which corresponds to *hazardous* damage.

Table 6-12 Key results (B-EMC-15M-17%)

| **Beams** | **Shockwave properties** | | | | **Displacement** | | $\theta_{max}$ | **Response limit and expected damage** | |
|---|---|---|---|---|---|---|---|---|---|
| **ID** | $P_d$ | $P_r$ | $I_r$ | $t_p$ | $\Delta_{max}$ | $\Delta_{res}$ | | | |
| | **(psi)** | **(kPa)** | **(kPa-ms)** | **(ms)** | **(mm)** | **(mm)** | **Degree** | | |
| B-EMC-15M-17% | 70 | 80.1 | 729 | 22.4 | 169.0 | 149.2 | 8.00 | B4-B3 | Hazardous |

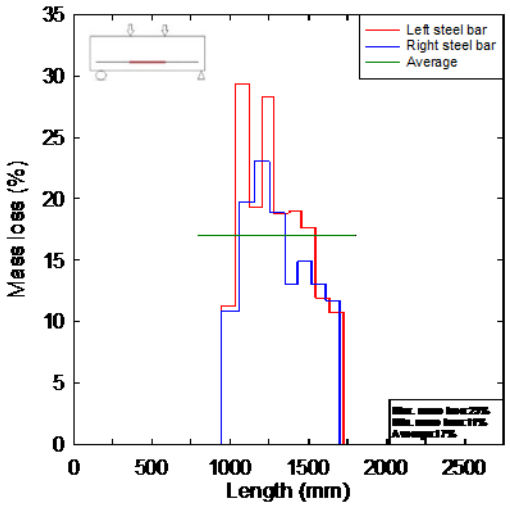



Figure 6-44 Mass loss distribution along the middle length of the tensile bars (B-EMC-15M-17%)



Figure 6-45 Condition of the beam before testing (B-EMC-15M-17%)

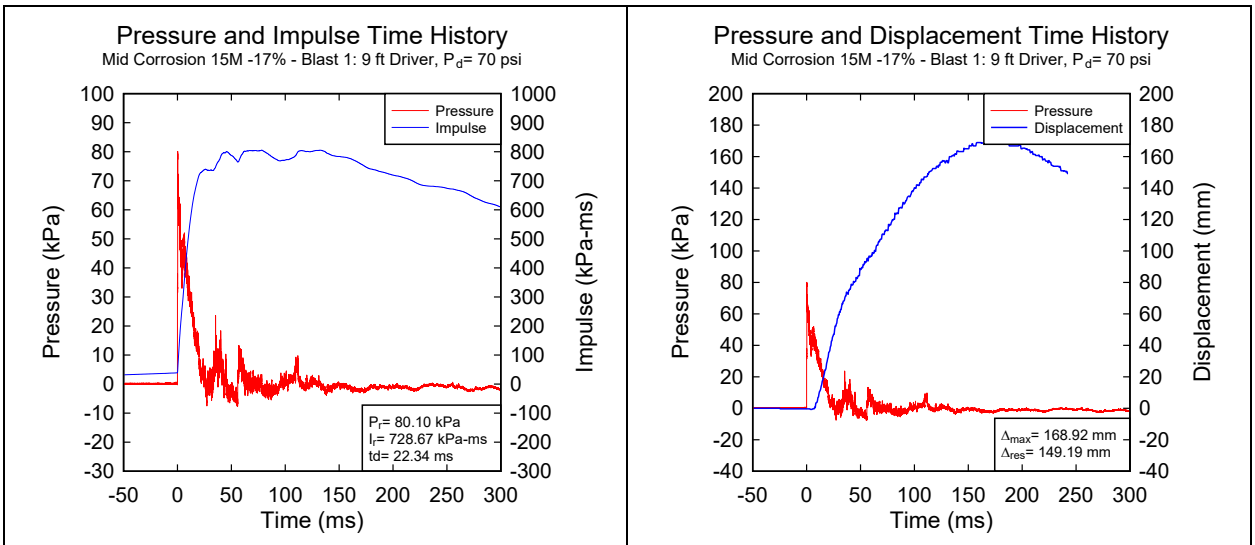



Figure 6-46 Reflected pressure, impulse and mid-span displacement (B-EMC-15M-17%)



a) Blast 1



b) High-speed camera showing Blast 1 fragments



c) Bars rupture and beam splitting with severe spalling in mid-zone (one side) (Blast 1)



d) Bars rupture and beam splitting with severe spalling in mid-zone (other side) (Blast 1)



c) Bars rupture and beam splitting with severe spalling in mid-zone (tension face) (Blast 1)

Figure 6-47 The condition of the beam after testing (B-EMC-15M-17%)

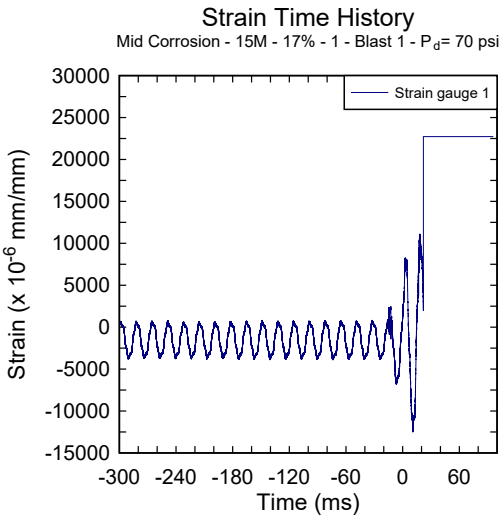



Figure 6-48 Strain time history curve (B-EMC-15M-17%)

#### 6.3.2.4 15M: Cover-removal with mid-span corrosion - 4% mass loss (B-CR-MC-15M-4%)

The last beam in the 15M group had similar design properties as the control specimen; however, it was subjected to combined cover removal and corrosion. The concrete cover in the mid-span zone was first removed, and the exposed tension 15M bars were then subjected to corrosion over a length of 750 mm in the mid-span region. The aimed mass loss was 30% for the 15M longitudinal bars in the tension region; however, the actual average mass loss was determined to be 4%. The actual obtained mass loss was much lower than 30%, and the maximum mass loss did not exceed 7% in any one portion of the extracted bar samples (see **Figure 6-49**).

Prior to beam testing, the beam showed no signs of corrosion-induced damage, except that some corrosion spots were observed on the concrete surface, with rusting of the exposed tensile bars in the mid-span region as presented in **Figure 6-50**.

Similar to the previous beam, this specimen was subjected to a single blast at a driver pressure of 70 psi. **Table 6-13** summarizes the key data, while the reflected pressure, impulse and mid-span displacement time histories are illustrated in **Figure 6-51**. The damage of the beam at the end of the test is shown in **Figure 6-52**.

Blast 1 (70 psi) resulted in significant flexural cracks distributed in the mid-span region and associated with significant concrete crushing in the compression region. The maximum crack width reached 2 mm in the mid-span region. Some minor cracks were also observed in the shear span regions. The maximum and residual displacements reached 76 mm and 54 mm, respectively, with a maximum support rotation of 3.6°, which corresponds to *moderate* damage.

Table 6-13 Key results (B-CR-MC-15M-5%)

| **Beams** | **Shockwave properties** | | | | **Displacement** | | $\theta_{max}$ | **Response limit and expected damage** | |
|---|---|---|---|---|---|---|---|---|---|
| **ID** | $P_d$ | $P_r$ | $I_r$ | $t_p$ | $\Delta_{max}$ | $\Delta_{res}$ | | | |
| | **(psi)** | **(kPa)** | **(kPa-ms)** | **(ms)** | **(mm)** | **(mm)** | **Degree** | | |
| B-CR-MC-15M-4% | 70 | 77.0 | 720 | 21.6 | 76.0 | 54.0 | 3.60 | B2-B1 | Moderate |

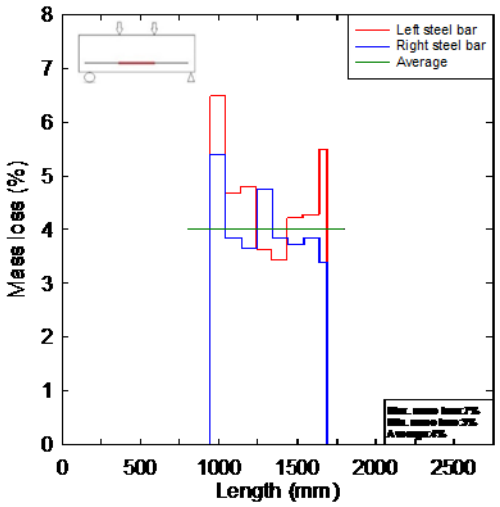



Figure 6-49 Mass loss distribution along the middle length of the tensile bars (B-CR-MC-15M-4%)

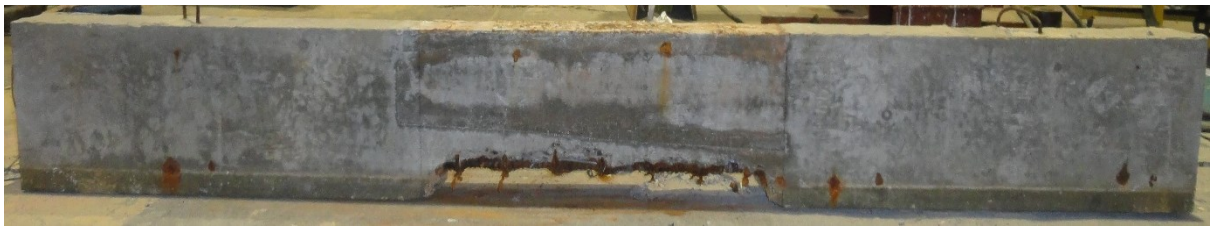


Figure 6-50 The condition of the beam before testing (B-CR-MC-15M-4%)

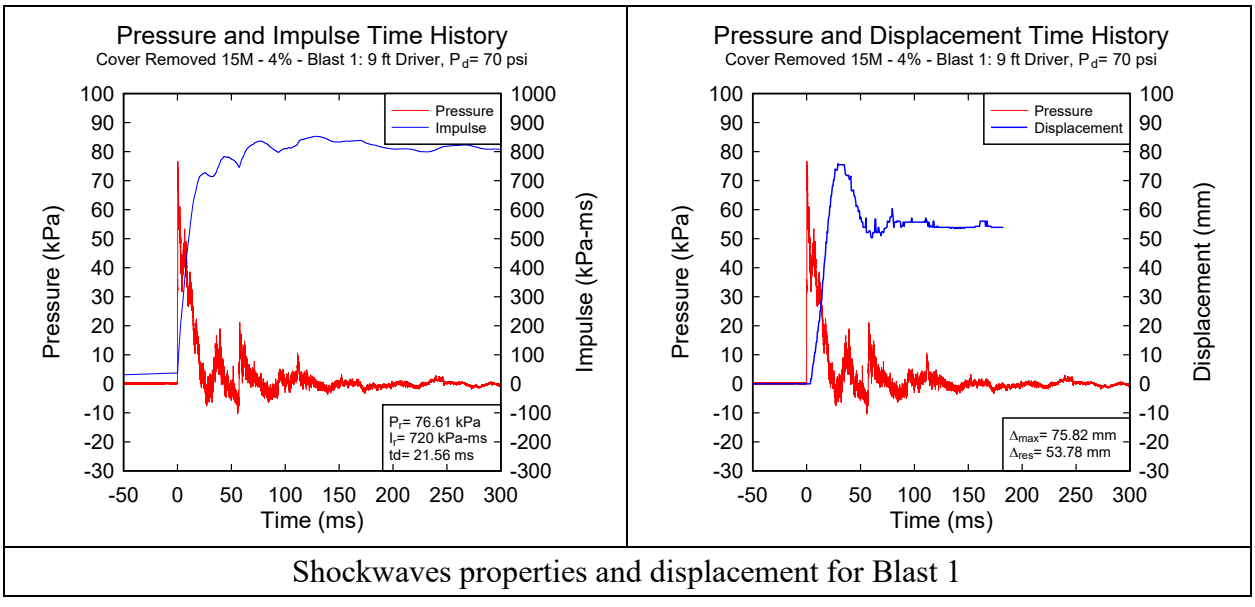
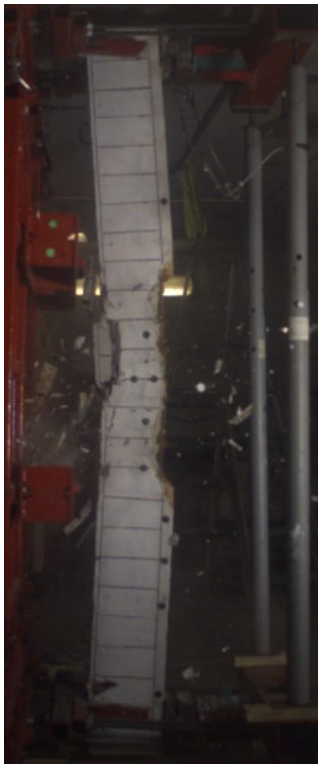



Figure 6-51 Reflected pressure, impulse and mid-span displacement histories (B-CR-MC-15M-4%)



a) Blast 1



b) High-speed camera showing Blast 1 fragments



c) Concrete spalling in compression zone and some cracks in the mid-span (one side) (Blast 1)



d) Concrete spalling in compression zone and some cracks in the mid-span (other side) (Blast 1)



e) Corroded exposed reinforcement at the mid-span (tension face) (Blast 1)

Figure 6-52 Beam damage after testing (B-CR-MC-15M-4%)

### 6.3.3 25M Group

The 25M group included three beams which were built with 2-25M bars in tension and 2-10M bars in compression (as top bars). The increased tensile steel ratio was intended to increase the shear demands in this beam series. In all cases, transverse reinforcement consisted of U-shaped stirrups made from 6.3-mm wire spaced at 100 mm throughout the full beam span, which corresponded to the minimum required by the CSA A23.3-14 standard (i.e., s = d/2). The corrosion process in this series was applied on the transverse reinforcement throughout their spans.

#### 6.3.3.1 25M: Control (0% mass loss) (CB-25M-0%)

Beam CB-25M-0% was the first beam tested under blast loading in this series and serves as the reference beam in the 25M group. No corrosion was applied on this specimen, and the beam was subjected to a single blast at 90 psi driver pressure. The results for this test in terms of reflected pressure, impulse and mid-span displacement histories are presented in **Figure 6-53**, while key data is summarized in **Table 6-14**. In addition, plots of the dynamic resistance and tension steel strains are presented in **Figure 6-54**. The damage at the end of testing is shown in **Figure 6-55**.

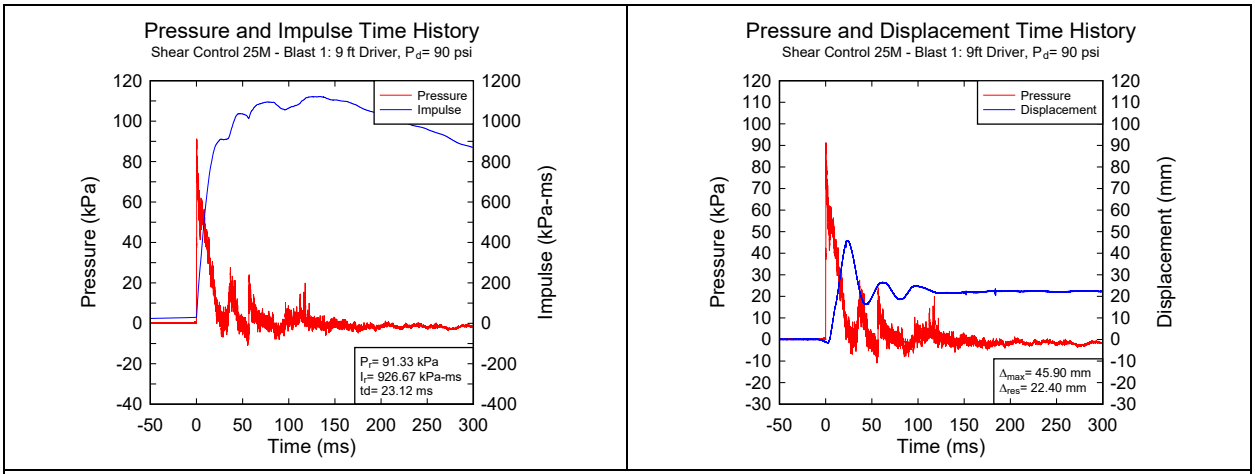
Blast 1 (90 psi) was intended to cause significant damage in the specimen and resulted in concrete crushing in the mid-span compression zone. Moreover, significant cracks were formed over the entire beam length, with the formation of significant diagonal cracking in the shear regions. Unlike the companion beam, which was tested under static loading, this beam failed in flexure. The change in failure mode can partly be explained by the beam's similar flexural/shear capacities, and the effect of dynamic loading on increasing beam shear resistance. The maximum and residual displacements recorded during the test were 46 mm and 22.40 mm, respectively. The maximum strain of the 25M tension reinforcement recorded at 0.0031 mm/mm, which indicates yielding. The maximum support rotation was 2.2º, which corresponds to *moderate* damage.

Since the beam damage was limited, its residual capacity was assessed under static four-point bending (see **Figure 6-56**). Considering the initial residual displacement of 22.4 mm, the beam reached a maximum residual capacity of 127 kN at a displacement of 40 mm, which was well below the maximum resistance of the undamaged beam, but close to the trend of the reference beam load-deflection curve at a similar displacement. Testing continued until the beam reached 89 mm with a remaining load capacity of 23 kN. Unlike the undamaged beam, failure occurred in

flexure due to crushing of the concrete in the mid-span compression zone. The beam also showed significant loss of concrete side cover at failure.

Table 6-14 Key results (CB-25M-0%)

| Beams | Shockwave properties | | | | Displacement | | $\theta_{max}$ | Response limit and expected damage | |
|---|---|---|---|---|---|---|---|---|---|
| ID | $P_d$ | $P_r$ | $I_r$ | $t_p$ | $\Delta_{max}$ | $\Delta_{res}$ | | | |
| | (psi) | (kPa) | (kPa-ms) | (ms) | (mm) | (mm) | (°) | | |
| CB-25M-0% | 90 | 91.4 | 927 | 23.2 | 46.0 | 22.4 | 2.20 | B2-B1 | Moderate |




Shockwaves properties and displacement for Blast 1

Figure 6-53 Reflected pressure, impulse and mid-span displacement (CB-25M-0%)

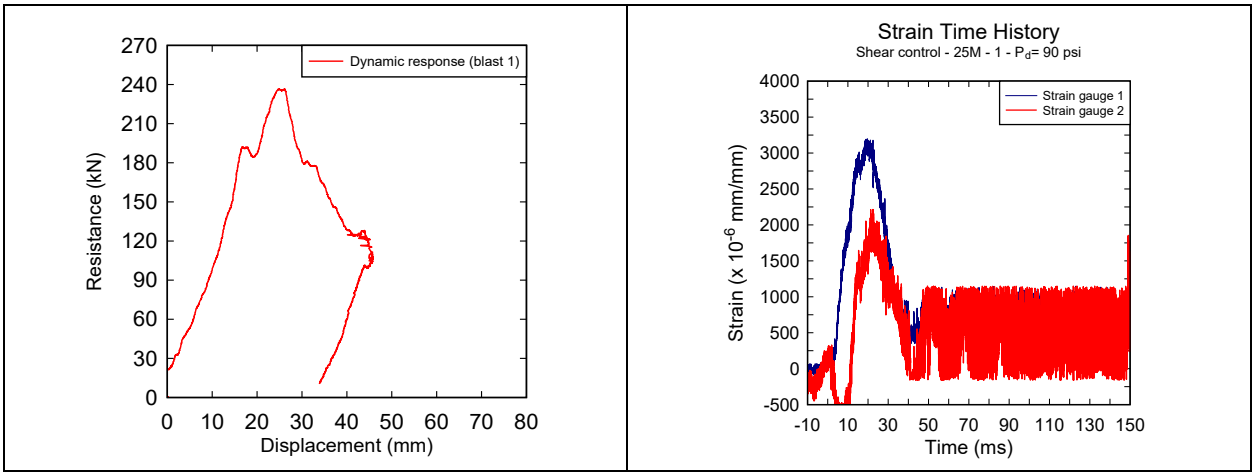



Figure 6-54 Blast load resistance and strain time history curves (CB-25M-0%)



a) Blast 1



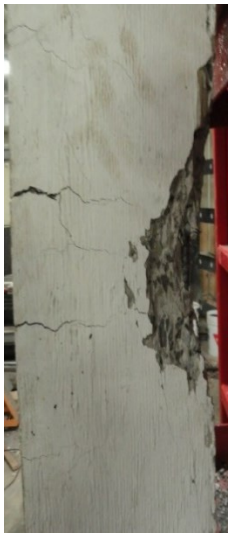
b) High-speed camera showing Blast 1 fragments



c) Concrete crushing in compression zone and some cracks in the mid-span (one side) (Blast 1)

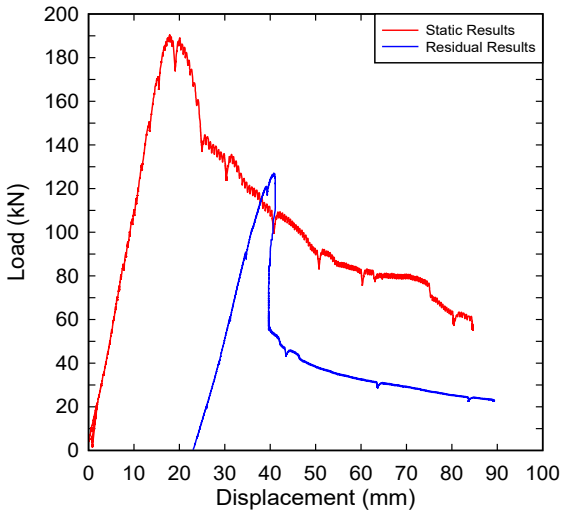


d) Cracks in the tension zone at the mid-span (tension face) (Blast 1)



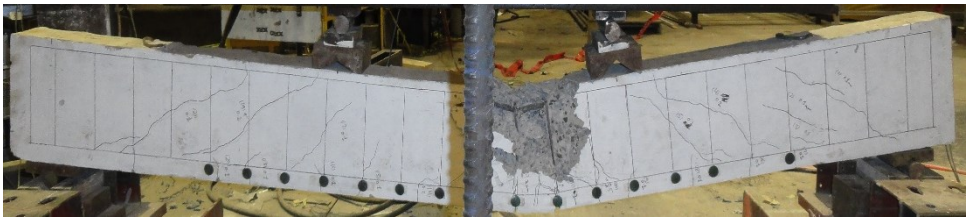
e) Concrete crushing in compression zone and some cracks in the mid-span (other side) (Blast 1)

Figure 6-55 The condition of the beam after the blast test (CB-25M-0%)




| Residual test results | |
|---|---|
| ΣΔ res (mm) | 22.40 |
| $P_{max}^{r}$ (kN) | 127 |
| $D_{max}^{r}$ (mm) | 89 |
| $P_{end}^{r}$ (kN) | 23 |

a) Load-deflection curve and summary of residual test results

| Before the residual test | Comments |
|---|---|
|  | Concrete crushed in the mid-span.<br>Flexural and shear cracks over the beam span. |
| After the residual test | Comments |
|  | Severe concrete crushing and buckling of the top longitudinal bars.<br>Side cover spalling in the mid-span region. |

b) Photos of the beam before and after the residual test

Figure 6-56 The residual test results (CB-25M-0%)

#### 6.3.3.2 25M: shear corrosion – 11% mass loss (B-SHC-25M-11%)

Beam B-SHC-25M-12% had similar design properties as the reference specimen in the 25M group; however, it was subjected to corrosion of the transverse reinforcement throughout its span. The targeted mass loss on the stirrups was 15%; however, after testing, the actual average mass loss was found to be 11%. The mass loss reached 17% and 15% on some portions of the extracted bar samples as presented in **Figure 6-57**. Before testing, the specimen showed clear signs of corrosion in the form of staining of the concrete cover at the stirrup locations as shown in **Figure 6-58**.

Similar to the reference beam, this specimen was tested under a single blast load at a driver pressure of 90 psi. The key data from this test is presented in **Table 6-15**. **Figure 6-59** shows the results in terms of reflected pressure, impulse and displacement time histories. Beam damage at the end of testing is shown in **Figure 6-60**. The dynamic reaction and strain data are presented in **Figure 6-61**.

Similar to the control specimen, Blast 1 (90 psi) resulted in the failure of the beam in flexure. Nonetheless, the failure was severe and associated with severe concrete crushing and spalling in the mid-span region. Significant buckling of the longitudinal bars was also noticeable in the compression region. Additional flexural and diagonal cracks were also observed in the mid-span and shear-span regions, respectively. The data showed that the beam reached maximum and residual displacements at 92.6 mm and 68.50 mm, respectively, during the test. The maximum strain reading on the tension reinforcement was 0.0049 mm/mm, which indicates possible steel yielding. The maximum support rotation reached 4.4°, which corresponds to *heavy* damage. Due to the brittle failure, no residual testing was conducted on this specimen.

Table 6-15 Key results (B-SHC-25M-11%)

| **Beams** | **Shockwave properties** | | | | **Displacement** | | $\theta_{max}$ | **Response limit and expected damage** | |
|---|---|---|---|---|---|---|---|---|---|
| **ID** | $P_d$ | $P_r$ | $I_r$ | $t_p$ | $\Delta_{max}$ | $\Delta_{res}$ | | | |
| | **(psi)** | **(kPa)** | **(kPa-ms)** | **(ms)** | **(mm)** | **(mm)** | **Degree** | | |
| B-SHC-25M-11% | 90 | 96.7 | 903 | 23.2 | 92.6 | 68.5 | 4.40 | B3-B2 | Heavy |

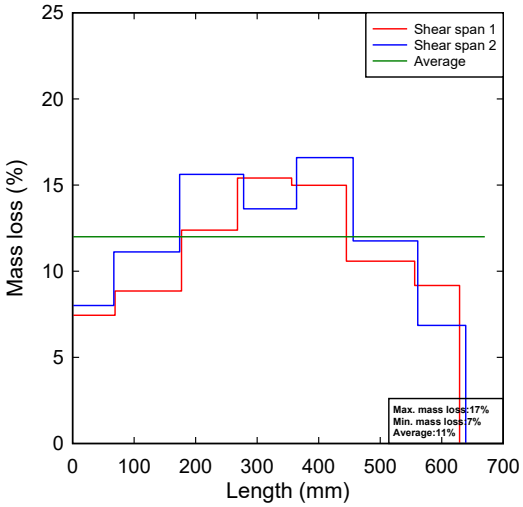
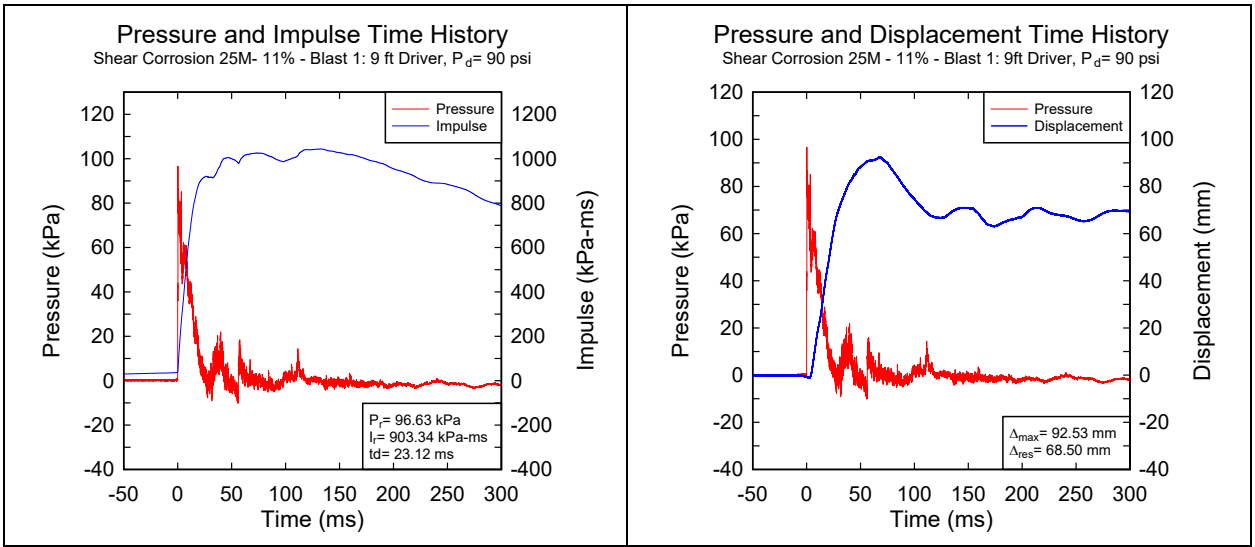



Figure 6-57 Mass loss distribution along the stirrups in the shear span (B-SHC-25M-11%)



Figure 6-58 The beam before testing (B-SHC-25M-11%)




Shockwaves properties and displacement for Blast 1

Figure 6-59 Reflected pressure, impulse and mid-span displacement (B-SHC-25M-11%)

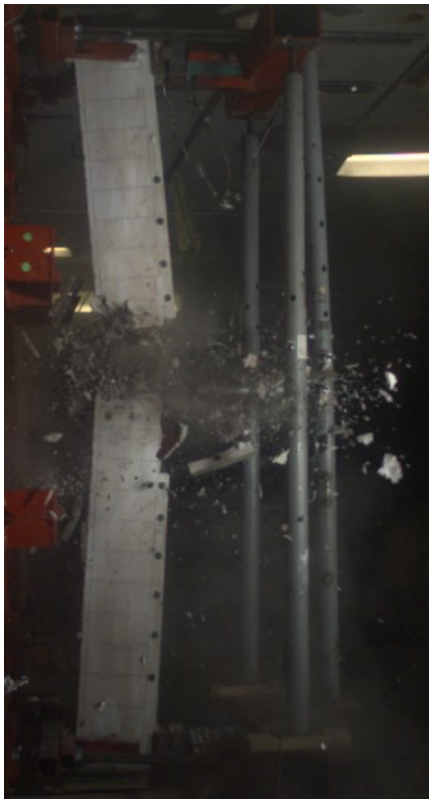
<table>
<tr><td>  </td><td colspan="2">  </td></tr>
<tr><td>a) Blast 1 (90 psi)</td><td colspan="2">b) High-speed camera showing Blast 1 fragments</td></tr>
<tr><td>  </td><td>  </td><td>  </td></tr>
<tr><td>c) Severe crushing and spalling at mid-span (side)</td><td>d) Severe crushing, spalling, and bar buckling in the mid-span (compression face)</td><td>e) Severe crushing and spalling at mid-span (tension face)</td></tr>
</table>

Figure 6-60 Damage in the beam after testing (B-SHC-25M-11%)

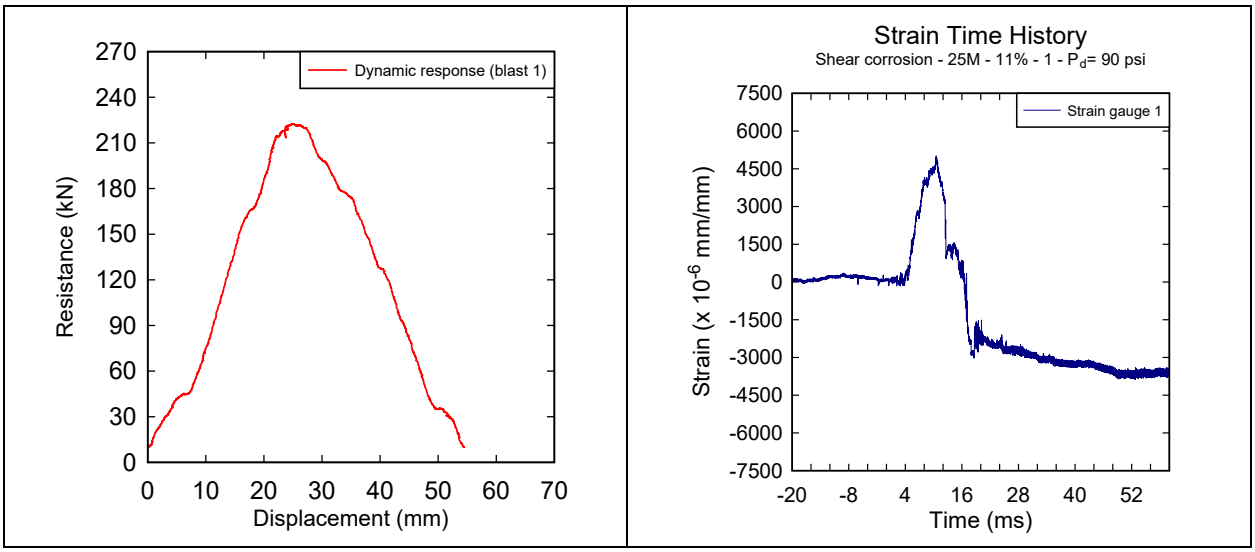



Figure 6-61 Blast load resistance and strain time history curves (B-SHC-25M-11%)

#### 6.3.3.3 25M: shear corrosion – 12% mass loss (B-SHC-25M-12%)

The final beam in the 25M group had the same properties as the control specimen, but it was subjected to corrosion of the transverse reinforcement throughout its span. The intended mass loss on the stirrups was 30%; however, the actual average mass loss was measured to be 12%, with the maximum mass loss not exceeding 17% at any one location as shown in **Figure 6-62**. Prior to testing, the beam showed clear signs of corrosion at the stirrup locations as shown in **Figure 6-63**.

Similar to the control, this beam was tested under a single blast load corresponding to a 90 psi driver pressure. The results for this test in terms of reflected pressure, impulse and displacement time histories are shown in **Figure 6-64**, while key data is presented in **Table 6-16**. Damage at the end of testing is shown in **Figure 6-65**, while the dynamic reaction and strain data are presented in **Figure 6-66**.

Unlike the previous two specimens, Blast 1 (90 psi) resulted in failure of the beam in shear, which indicated that the corrosion had a more important effect on the shear resistance of this beam. The shear failure occurred in the bottom shear span and was associated with diagonal cracking and severe spalling of the concrete cover both at the side and tension faces in the shear span. Additionally, the beam showed signs of crushing at mid-span, with significant flexural and diagonal cracking in the central mid-span and top shear span regions, respectively. The data indicated that the beam experienced maximum and residual displacements of 45.5 mm and 32.0 mm, respectively, during the test. The maximum strain reading on the tension reinforcement reached 0.0031 mm/mm, which indicates possible steel yielding. The maximum support rotation reached 2.2°, which corresponds to *moderate* damage; however, the beam failed severely in shear. Due to the brittle failure of this beam, no residual testing was conducted on this specimen.

Table 6-16 Key results (B-SHC-25M-12%)

| **Beams** | **Shockwave properties** | | | | **Displacement** | | $\theta_{max}$ | **Response limit and expected damage** | |
|---|---|---|---|---|---|---|---|---|---|
| **ID** | $P_d$ | $P_r$ | $I_r$ | $t_p$ | $\Delta_{max}$ | $\Delta_{res}$ | | | |
| | **(psi)** | **(kPa)** | **(kPa-ms)** | **(ms)** | **(mm)** | **(mm)** | **Degree** | | |
| B-SHC-25M-12% | 90 | 95.2 | 926 | 24.7 | 45.5 | 32.0 | 2.20 | B2-B1 | Moderate |

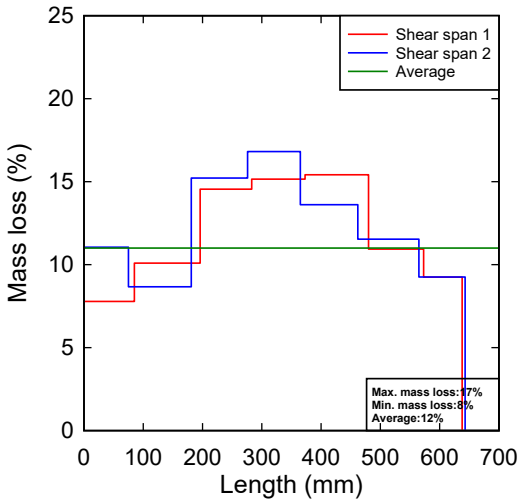
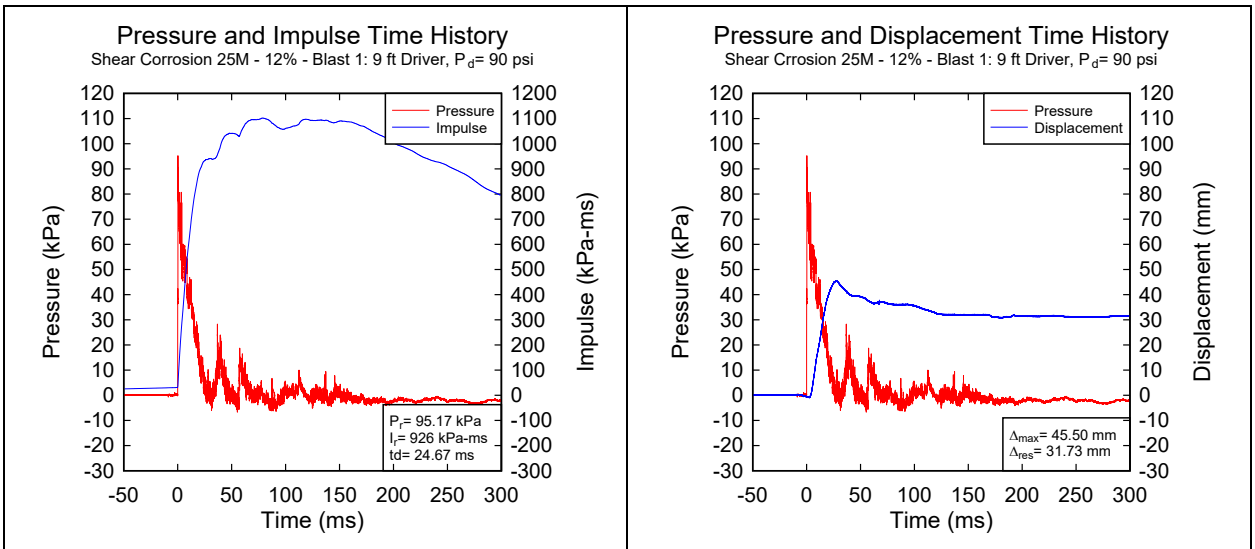



Figure 6-62 Mass loss distribution along the stirrups in the shear span (B-SHC-25M-12%)



Figure 6-63 The condition of the beam before testing (B-SHC-25M-12%)




Shockwaves properties and displacement for Blast 1

Figure 6-64 Reflected pressure, impulse and mid-span displacement (B-SHC-25M-12%)

<table>
<tr><td colspan="2">  </td><td>  </td></tr>
<tr><td colspan="2">a) Blast 1</td><td>b) High-speed camera showing Blast 1 fragments</td></tr>
<tr><td>  </td><td>  </td><td>  </td></tr>
<tr><td>c) Severe spalling and cracks in the shear zone (one side) (Blast 1)</td><td>d) Severe spalling and cracks in the shear zone (tension face) (Blast 1)</td><td>e) Severe spalling and cracks in the shear zone (other side) (Blast 1)</td></tr>
</table>

Figure 6-65 The damage of the beam after the test (B-SHC-25M-12%)

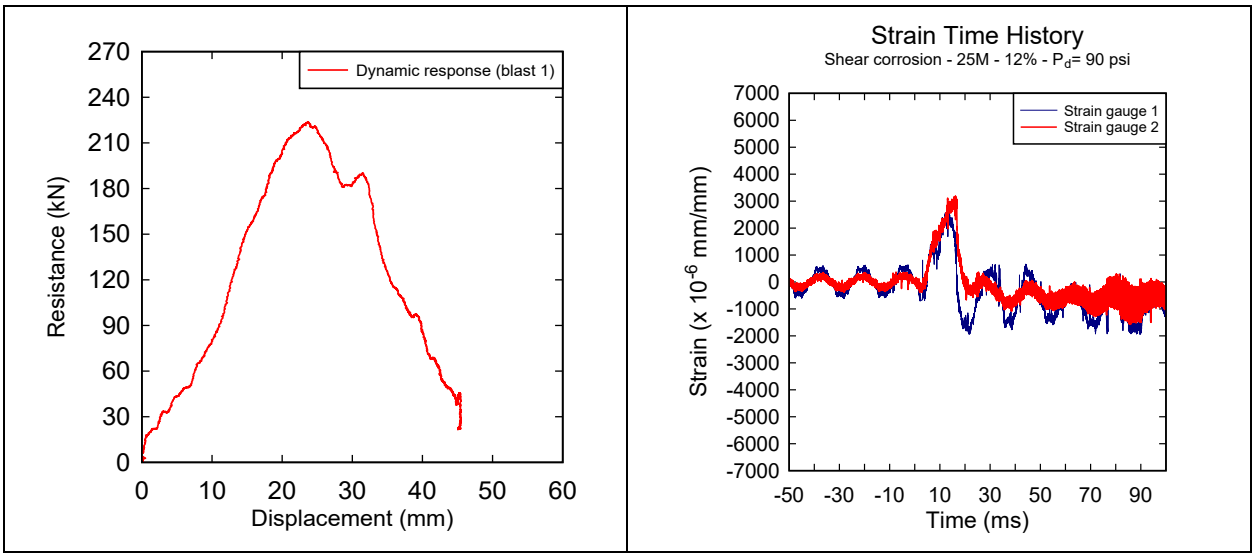



Figure 6-66 Blast load resistance and strain time history curves (B-SHC-25M-12%)

# Chapter 7: Discussion of Blast Results

## 7.1 Chapter Overview

This chapter presents the effects of the test's variables on the behaviour of the reinforced concrete beams, which were tested dynamically under blast loads. The test's variables were evaluated by comparing various parameters, including: the maximum and residual mid-span displacements, support rotations, blast load capacities, failure mode and damage in the beams. The following test's variables are discussed in more detail in the following sections:

- **Effect of mid-span corrosion:**
  - 10M group: CB-10M-0% vs B-MC-10M-11% vs B-MC-10M-15% vs B-EMC-10M-22%
  - 15M group: CB-15M-0% vs B-MC-15M-12% vs B-EMC-15M-17%
- **Effect of end-span corrosion:**
  - 10M group: CB-10M-0% vs B-SC-10M-7%
- **Effect of full-span corrosion:**
  - 10M group: CB-10M-0% vs B-FC-10M-12%
- **Effect of corrosion locations (mid, ends and full span):**
  - 10M group: CB-10M-0% vs B-MC-10M-11% vs B-SC-10M-7% vs B-FC-10M-12%
- **Effect of mid-span corrosion combined with cover-removal/loss:**
  - 10M group: CB-10M-0% vs B-CR-MC-10M-5%
  - 15M group: CB-15M-0% vs B-CR-MC-10M-4%
- **Effect of shear corrosion:**
  - 25M group: CB-25M-0% vs B-SHC-25M-12% vs B-SHC-25M-11%

## 7.2 Effect of mid-span corrosion

### 7.2.1 10M group: CB-10M-0% vs B-MC-10M-11% vs B-MC-10M-15% vs B-EMC-10M-22%

Beams CB-10M-0%, B-MC-10M-11%, B-MC-10M-15% and B-EMC-10M-22% were compared to examine the effects of mid-span corrosion and various levels of corrosion on the blast response in the 10M group. All beams were constructed using identical design properties, which consisted of 2-10M bars in tension/compression and had U-shaped stirrups at 100-mm spacing throughout the beam span. However, the tension 10M bars in beams B-MC-10M-11%, B-MC-10M-15% and B-EMC-10M-22% had varying levels of corrosion in the mid-span region, corresponding to average mass losses of 11%, 15% and 22%, respectively.

The control specimen (CB-10M-0%) and the beams with intermediate corrosion (11% and 15% mass loss) were subjected to two blasts at driver pressures of 17 and 50 psi. Beam B-EMC-10M-22%, which had heavy/extreme corrosion (22% average mass loss), was subjected to a single blast load at a driver pressure of 50 psi. **Figure 7-1** shows a comparison of displacements for all beams after each blast, while **Table 7-1** provides a summary of the key results in terms of support rotations and failure mode. Photos of the beams after each blast are presented in **Figure 7-2**. **Figure 7-3** shows images of damage and fragmentation of the beams at failure.

By examining Blast 1 (17 psi) it was observed that the control beam and beams with intermediate corrosion showed similar maximum displacements. Beam B-MC-10M-11% showed a slightly higher maximum deformation (18 mm) when compared to its two companions (~16 mm). The larger displacement can partly be explained by the relatively larger impulse applied on B-MC-10M-11% when compared to its companions ($I_r$ = 257 vs 250 kPa-ms). Both corroded beams showed larger residual deformations when compared to CB-10M-0%, with increases of 29% and 66% for beams B-MC-10M-15% and B-MC-10M-11%, respectively. All beams showed maximum support rotations of less than 1°, which qualifies as *superficial* damage. Indeed, the three beams showed similar cracking patterns and limited damage; however, some initial signs of side cover spalling and concrete crushing were observed in beam B-MC-10M-15% and B-MC-10M-11%.

Blast 2 (50 psi) was meant to test the beams in the inelastic range and therefore the effects of corrosion were clearer. Examining the deformations in **Figure 7-1**, the maximum displacements in beams B-MC-10M-11%, B-MC-10M-15% and B-EMC-10M-22% were increased by 19%, 47%

and 199% when compared to the control CB-10M-0% specimen. The maximum support rotations also increased from 3.4° in the control (*superficial* damage) to 4.1°, 4.9° (*heavy* damage) and 10.1° (*hazardous/blowout* damage) in the corroded specimens with 11%, 15% and 22% average mass loss, respectively. The residual displacements were also affected with increases of 24% and 249% for beams B-MC-10M-11% and B-EMC-10M-22%, respectively, when compared to CB-10M-0%.

While the three specimens showed a flexural dominant response, the damage and failure mode became more severe as the amount of corrosion was increased (see **Figure 7-2**). Indeed, greater concrete damage in terms of crushing and spalling was observed when comparing beams B-MC-10M-11% (11% mass loss) and CB-10M-0% (control). As the mass loss was increased further to 15%, failure in beam B-MC-10M-15% was associated with more severe cover spalling on the tension face, more significant crushing on the compression face, and rupture of the main 10M tension reinforcement. Moreover, inspection of the high-speed video showed the corroded specimen developed significant blast fragments at failure. At 22% mass loss, beam B-EMC-10M-22% experienced a severe *blowout* failure, with significant concrete damage and fracture of the 10M tension reinforcement. In comparison the control beam survived this blast with moderate damage and showed significant residual load-carrying capacity as discussed in **Chapter 6**.

In summary, the results showed that corrosion of the tension reinforcement in the mid-span region affected all aspects of blast response and resulted in increased displacements and damage. The effects became more significant as the mass loss was increased, with a change in failure mode and loss of residual capacity as the average mass loss became ≥ to 15%. The mass loss of 22% was particularly detrimental to blast resistance and resulted in severe blowout failure.

Table 7-1 Key results: effect of mid-span corrosion and mass loss

| Beam ID | Blast ID (psi) | $I_r$ (kPa-ms) | Displacement (mm) | | Support rotation | | Failure mode |
|---|---|---|---|---|---|---|---|
| | | | $d_{max}$ | $d_{res}$ | $\theta_{max}$ | CSA S850 damage | |
| CB-10M-0% | 17 | 250 | 15.4 | 4.3 | 0.72 | Superficial | **Flexural failure:** light concrete crushing and extensive cracks |
| | 50 | 550 | 72.6 | 52.0 | 3.40 | Moderate | |
| B-MC-10M-11% | 17 | 257 | 18.0 | 7.0 | 0.84 | Superficial | **Flexural failure:** significant concrete crushing and spalling |
| | 50 | 547 | 86.3 | 64.3 | 4.10 | Heavy | |
| B-MC-10M-15% | 17 | 249 | 15.6 | 5.4 | 0.72 | Superficial | **Flexural failure:** severe concrete crushing and spalling, with rupture of the 10M bars |
| | 50 | 529 | 107.0 | 43.4 | 4.90 | Heavy | |
| B-EMC-10M-22% | 50 | 541 | 217.3 | 181.4 | 10.10 | Hazardous | **Blowout failure**: Concrete damage/ Rebar rupture |

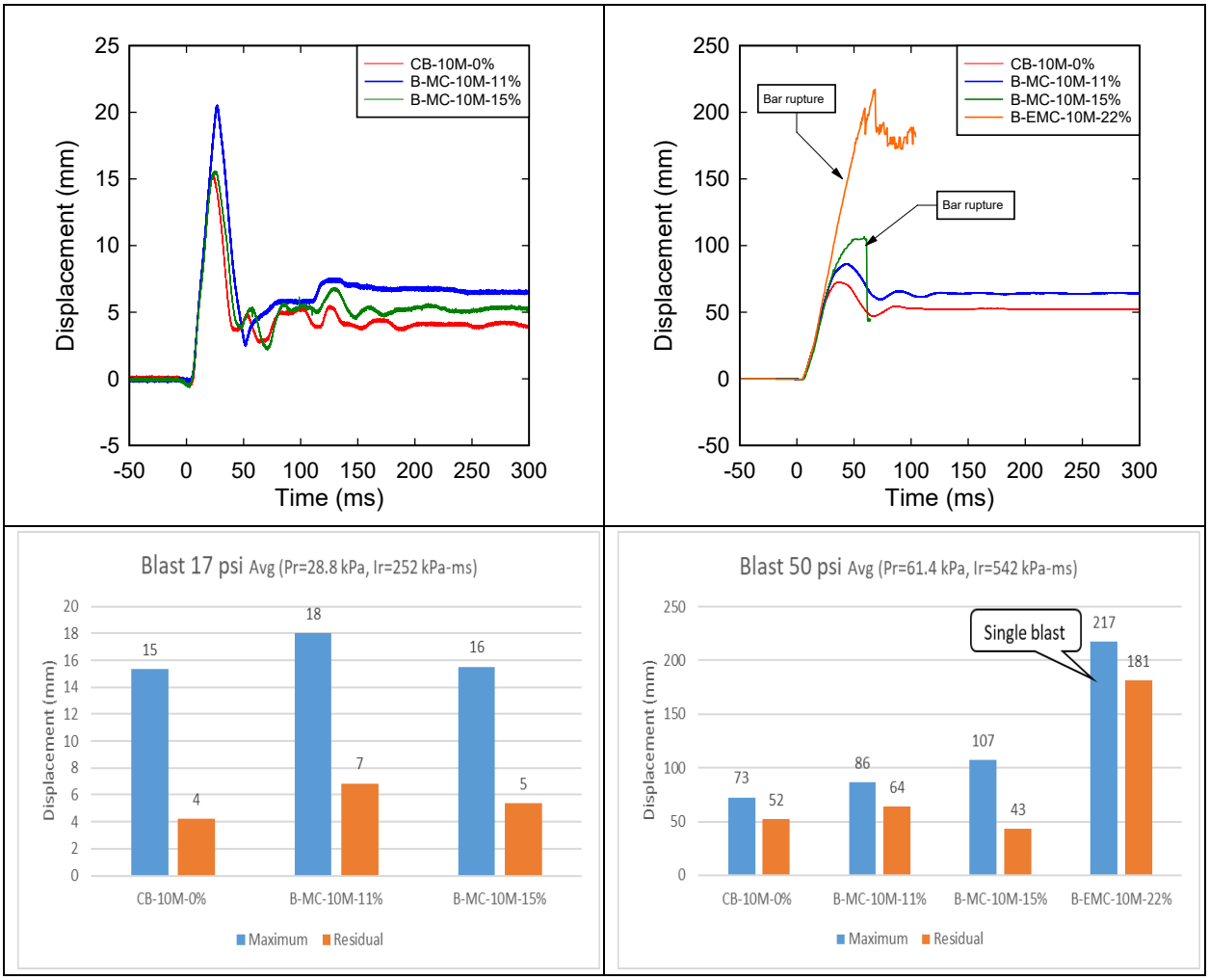



Figure 7-1 Displacements for blast 1-2: effect of mid-span corrosion (10M group)

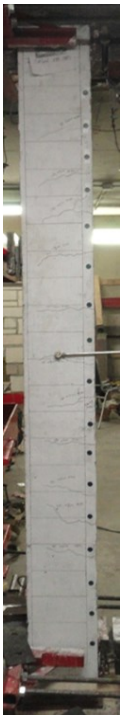
| | | | |
|---|---|---|---|
|  |  |  | B-EMC-10M-22%<br>No test |
| CB-10M-0%<br>($P_d$ = 17 psi): 1st shot | B-MC-10M-11%<br>($P_d$ = 17 psi): 1st shot | B-MC-10M-15%<br>($P_d$ = 17 psi): 1st shot | |
|  |  |  |  |
| CB-10M-0%<br>($P_d$ = 50 psi): 2nd shot | B-MC-10M-11%<br>($P_d$ = 50 psi): 2nd shot | B-MC-10M-15%<br>($P_d$ = 50 psi): 2nd shot | B-EMC-10M-22%<br>($P_d$ = 50 psi): Single shot |

Figure 7-2 Failure mode: effect of mid-span corrosion (10M group)



| B-MC-10M-11% | B-MC-10M-15% | B-EMC-10M-22% |
|---|---|---|

Figure 7-3 Damage and fragmentation at failure: effect of mid-span corrosion (10M group)

### 7.2.2 15M group: CB-15M-0% vs B-MC-15M-12% vs B-EMC-15M-17%

Beams CB-15M-0%, B-MC-15M-12% and B-EMC-15M-17% were compared to examine the effects of mid-span corrosion and various levels of corrosion on the blast response in the 15M group. All beams were constructed using identical design properties, which consisted of 2-15M/2-10M bars in tension/compression and had U-shaped stirrups at 100-mm spacing throughout the beam span. However, the tension 15M bars in beams B-MC-15M-12% and B-EMC-15M-17% were subjected to corrosion over the central mid-span region, with actual average mass losses of 12% and 17%, respectively.

The control specimen (CB-15M-0%) and beam B-MC-15M-12% were subjected to two blasts at driver pressures of 17 and 70 psi. Beam B-EMC-10M-17%, which had heavy/extreme corrosion (17% mass loss), was subjected to a single blast load at a driver pressure of 70 psi. **Figure 7-4** compares the displacements for all beams after the 70 psi blast, whereas beam damage at the end of testing is shown in **Figure 7-5**. **Figure 7-6** illustrates the fragmentation of the beams at failure. **Table 7-2** provides a summary of the key results.

The 17-psi shot tested beams CB-15M-0% and B-MC-15M-12% within the elastic range. Both beams experienced similar maximum displacements (10.6 and 11mm) with *superficial* damage. The 70 psi shot brought all beams into the inelastic range. Although beams CB-15M-0% and B-MC-15M-12% showed similar maximum and residual displacements (~ 71 mm and 51 mm, respectively), with support rotations of 3.3$^{o}$ and 3.4$^{o}$, the corroded specimen experienced greater damage in terms of concrete crushing and cover spalling over the central mid-span region, with the development of significant blast fragments at failure. The increased level of corrosion in B-EMC-10M-17% led to severe increases of 140% and 195% in maximum and residual displacements, respectively, when compared to beams CB-15M-0% and B-MC-15M-12%. In addition, the maximum support rotation of B-EMC-10M-17% reached 8$^{o}$, with *hazardous* damage. The severe failure in this beam was associated with concrete crushing and spalling of the concrete cover in the mid-span zone and rupture of the corroded 15M bars on the tension face, which led to the beam nearly splitting in two as shown in **Figure 7-5**. Although spalling and crushing were also significant in beam B-MC-15M-12%, the lower intensity of corrosion did not result in bar fracture.

In conclusion, at a moderate level of corrosion (12% mass loss) blast damage was increased; however, displacements were not affected. An increased level of corrosion (17% mass loss) affected all aspects of blast response and led to hazardous failure under blast loading.

Table 7-2 Key results: effect of mid-span corrosion (15M group)

| Beam ID | Blast ID (psi) | $I_r$ (kPa-ms) | Displacement (mm) | | Support rotation | | Failure mode |
|---|---|---|---|---|---|---|---|
| | | | $d_{max}$ | $d_{res}$ | $\theta_{max}$ | CSA S850 damage | |
| CB-15M-0% | 17 | 248 | 10.6 | 3.2 | 0.50 | Superficial | **Flexural failure:** concrete crushing and extensive cracks |
| | 70 | 734 | 70.6 | 50.5 | 3.30 | Moderate | |
| B-MC-15M-12% | 17 | 251 | 11.0 | 2.0 | 0.50 | Superficial | **Flexural failure:** severe concrete crushing and spalling |
| | 70 | 703 | 71.2 | 51.0 | 3.40 | Moderate | |
| B-EMC-15M-17% | 70 | 729 | 169.0 | 149.2 | 8.00 | Hazardous | **Hazardous failure**: severe concrete damage & bar fracture |

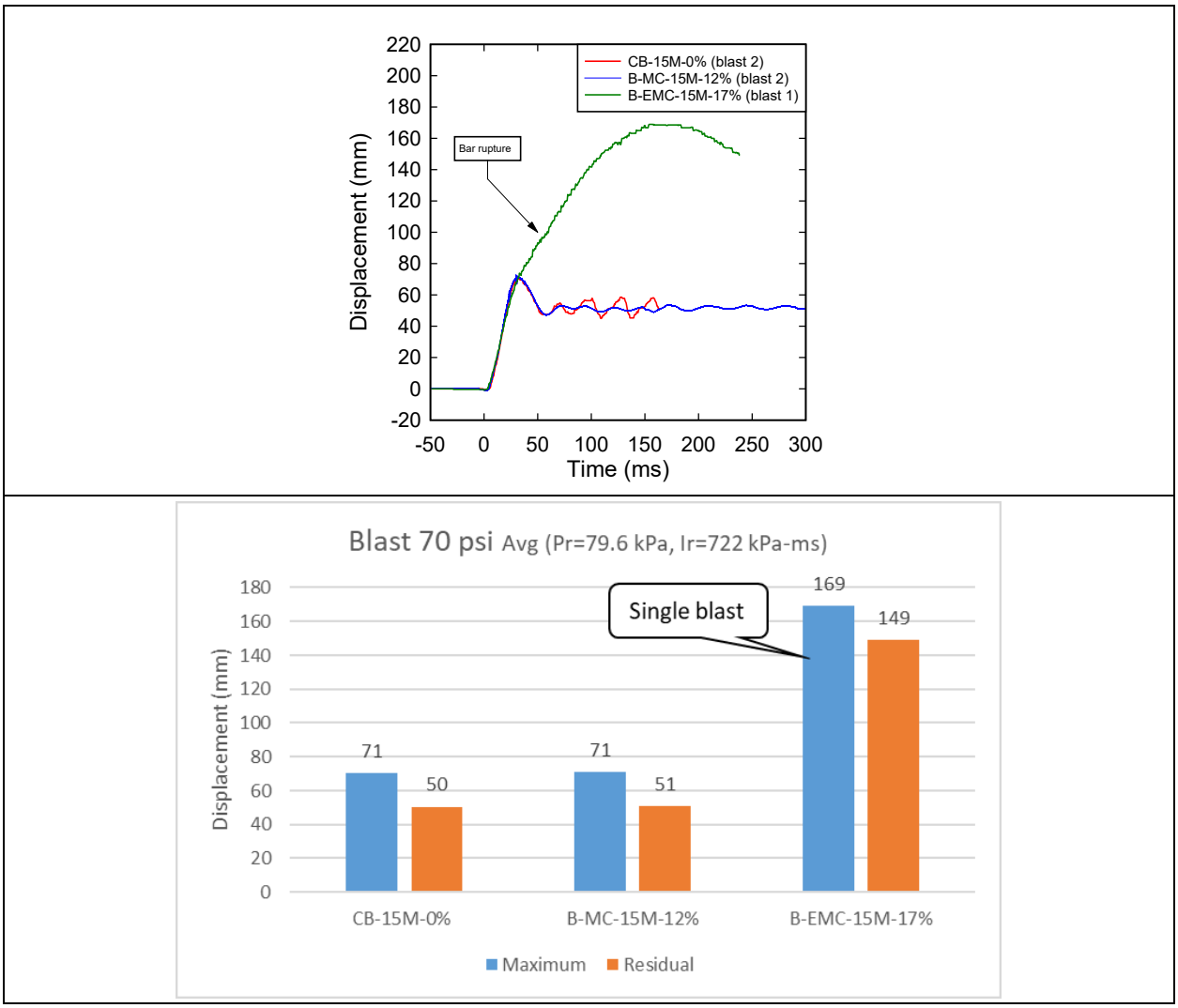
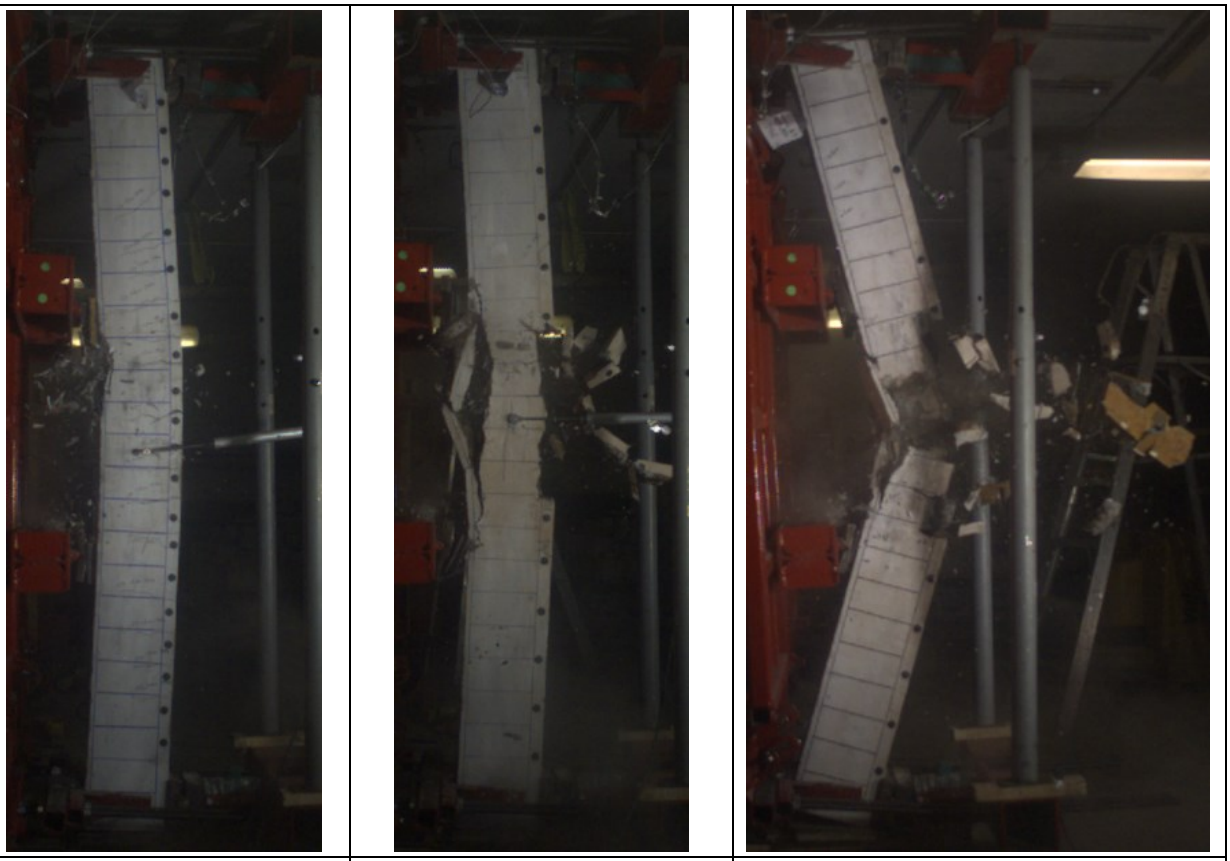



Figure 7-4 Displacements: effect of mid-span corrosion (15M group)



| CB-15M-0% ($P_d$ = 70 psi): 2nd shot | B-MC-15M-12% ($P_d$ = 70 psi): 2nd shot | B-EMC-15M-17% ($P_d$ = 70 psi): Single shot |
|---|---|---|

Figure 7-5 Failure mode and damage: effect of mid-span corrosion (15M group)



| CB-15M-0% | B-MC-15M-12% | B-EMC-15M-17% |
|---|---|---|

Figure 7-6 Fragmentation at failure: effect of mid-span corrosion (15M group)

## 7.3 Effect of end-span corrosion

### 7.3.1 10M group: CB-10M-0% vs B-SC-10M-7%

The performance of beams CB-10M-0% vs B-SC-10M-7% was compared to investigate the effect of end-span corrosion on the blast response of the beams in the 10M group. Both beams were constructed using identical design properties, which consisted of 2-10M bars in tension/compression and had U-shaped stirrups at 100-mm spacing throughout the beam span. However, the tension 10M bars in beam B-SC-10M-7% were subjected to corrosion in the end spans, with an actual average mass loss of 7%.

Both beams were subjected to blasts at driver pressures of 17 and 50 psi. The displacement of the beams is compared in **Figure 7-7**, while **Table 7-3** summarizes the key results. **Figure 7-8** presents the damage of the beams after each blast.

Examining the results after the 17-psi shot, the maximum and residual displacements of beam B-SC-10M-7% were respectively 33% and 53% higher when compared to CB-10M-0%. However, the maximum support rotation in both beams was less than 1°, which corresponds to *superficial* damage according to CSA S850. Both beams showed similar cracking patterns and limited damage after this test.

Both beams showed similar displacements at the 50-psi shot, with slightly lower maximum and permanent deformations in beam B-SC-10M-7%. Both beams showed similar maximum support rotation of less than 4°, which corresponds to *moderate* damage. Furthermore, both beams experienced flexure failure and similar cracking patterns; however, beam B-SC-10M-7% displayed larger crack widths and experienced concrete cover spalling on the tension face in the top shear-span region (see **Figure 7-8**). In conclusion, the combined effects of low intensity corrosion, which was only concentrated at the ends of the beam, had minor effect on the beam blast performance.

**Figure 7-9** shows the dynamic resistance curves for the beams based on the load-cell recordings. It was observed that both beams had similar pre-peak and post-peak behaviours; however, the maximum dynamic load and stiffness of beam B-SC-10M-7% showed a relative increase when compared to beam CB-10M-0%, which provided further evidence of the limited effects of corrosion in this comparison set.

Table 7-3 Key results: effect of end-span corrosion (10M group)

| Beam ID | Blast ID (psi) | $I_r$ (kPa-ms) | Displacement (mm) | | Support rotation | | Failure mode |
|---|---|---|---|---|---|---|---|
| | | | $d_{max}$ | $d_{res}$ | $\theta_{max}$ | CSA S850 damage | |
| CB-10M-0% | 17 | 250 | 15.4 | 4.3 | 0.72 | Superficial | **Flexural failure:** light concrete crushing and extensive cracks |
| | 50 | 550 | 72.6 | 52.0 | 3.40 | Moderate | |
| B-SC-10M-7% | 17 | 239 | 20.4 | 6.6 | 0.95 | Superficial | **Flexural failure:** light concrete crushing and spalling |
| | 50 | 555 | 70.1 | 45.2 | 3.30 | Moderate | |

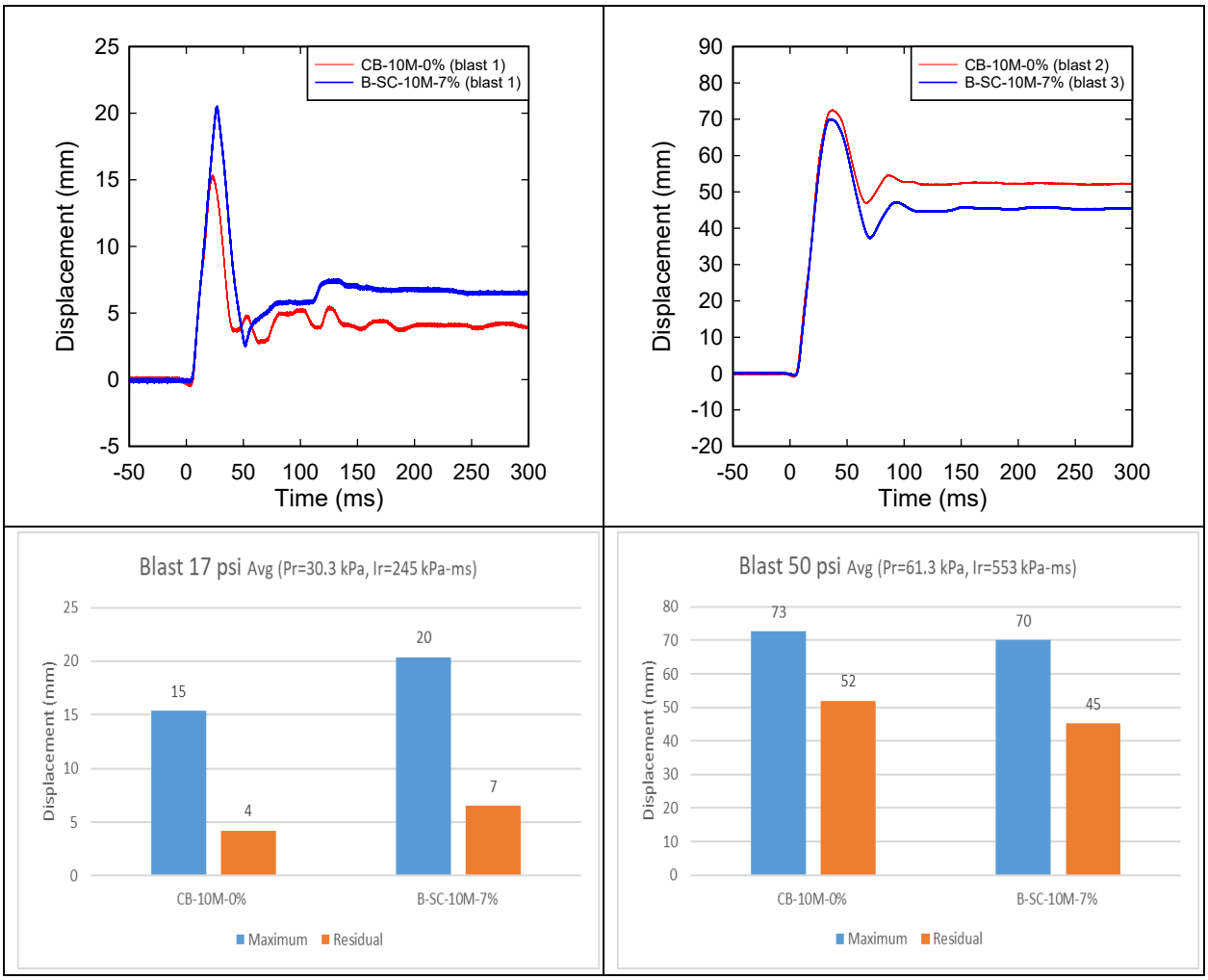
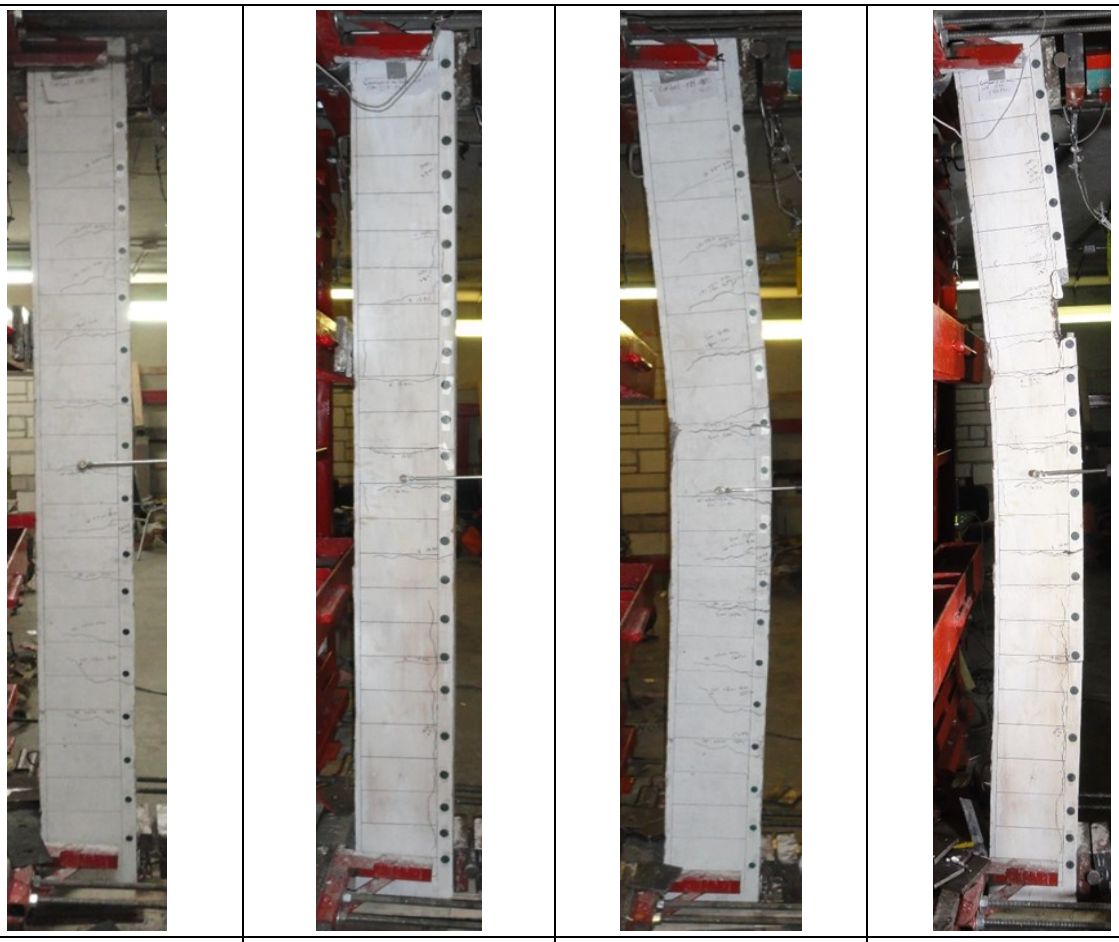



Figure 7-7 Displacements: effect of end-span corrosion with 7% mass loss (10M group)



| CB-10M-0% ($P_d$ = 17 psi): 1st shot | B-SC-10M-7% ($P_d$ = 17 psi): 1st shot | CB-10M-0% ($P_d$ = 50 psi): 2nd shot | B-SC-10M-7% ($P_d$ = 50 psi): 3rd shot |
|---|---|---|---|

Figure 7-8 Failure mode: effect of end-span corrosion with 7% mass loss (10M group)

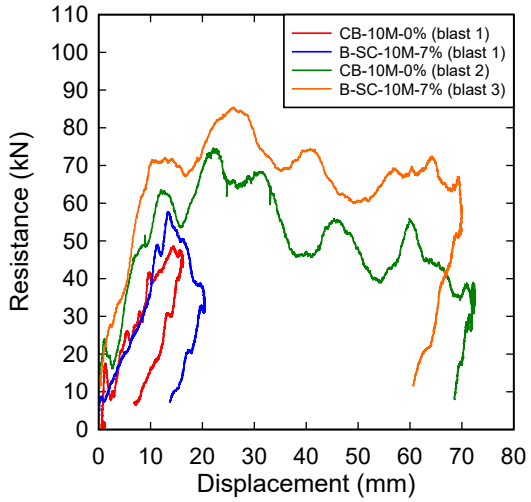



Figure 7-9 Dynamic reactions: effect of end-span corrosion with 7% mass loss (10M group)

## 7.4 Effect of full-span corrosion

### 7.4.1 10M group: CB-10M-0% vs B-FC-10M-12%

The results of beams CB-10M-0% and B-FC-10M-12% were compared to examine the effect of corrosion over the full beam span on the blast response of the beams in the 10M group. These beams were constructed with identical properties, which consisted of 2-10M bars in tension and compression and had U-shaped stirrups spaced at 100-mm throughout their span. However, the tension 10M bars in beam B-FC-10M-12% was subjected to corrosion over its entire length, with an actual average mass loss of 12%.

Beam CB-10M-0% was subjected to two blasts at driver pressures of 17 and 50 psi, while B-FC-10M-12% was subjected to a single shot at 50 psi. **Figure 7-10** shows a comparison of the beams displacements at the common test shot, and **Figure 7-11** compares the damage in the beams at the end of testing. A summary of the key data is shown in **Table 7-4**.

Examining the results at the 50-psi shot, the maximum and residual displacements of beam B-FC-10M-12% showed respectively increases of 13% and 16% when compared to beam CB-10M-0% due to the effects of corrosion of the 10M tensile bars (see **Table 7-4** and **Figure 7-10**). The maximum support rotation increased from 3.4° in the control (*moderate* damage) to 4°, which corresponds to *heavy* damage in the corroded beam. Both beams experienced a flexural failure, with similar cracking patterns; however, beam B-FC-10M-12% showed more significant concrete crushing in the compression face at mid-span and more significant cracks in the tension face (see **Figure 7-11**).

In summary, the application of corrosion corresponding to an average of 12% mass loss over the entire beam length resulted in moderate effects on the beam response under blast loading.

Table 7-4 Key results: effect of full span corrosion at 12% mass loss (10M group)

| Beam ID | Blast ID (psi) | $I_r$ (kPa-ms) | Displacement (mm) | | Support rotation | | Failure mode |
|---|---|---|---|---|---|---|---|
| | | | $d_{max}$ | $d_{res}$ | $\theta_{max}$ | CSA S850 damage | |
| CB-10M-0% | 50 | 550 | 72.6 | 52.0 | 3.40 | Moderate | **Flexural failure:** light concrete crushing and extensive cracks |
| B-FC-10M-12% | 50 | 540 | 83.7 | 61.7 | 4.00 | Heavy | **Flexural failure:** significant concrete crushing and cracks |

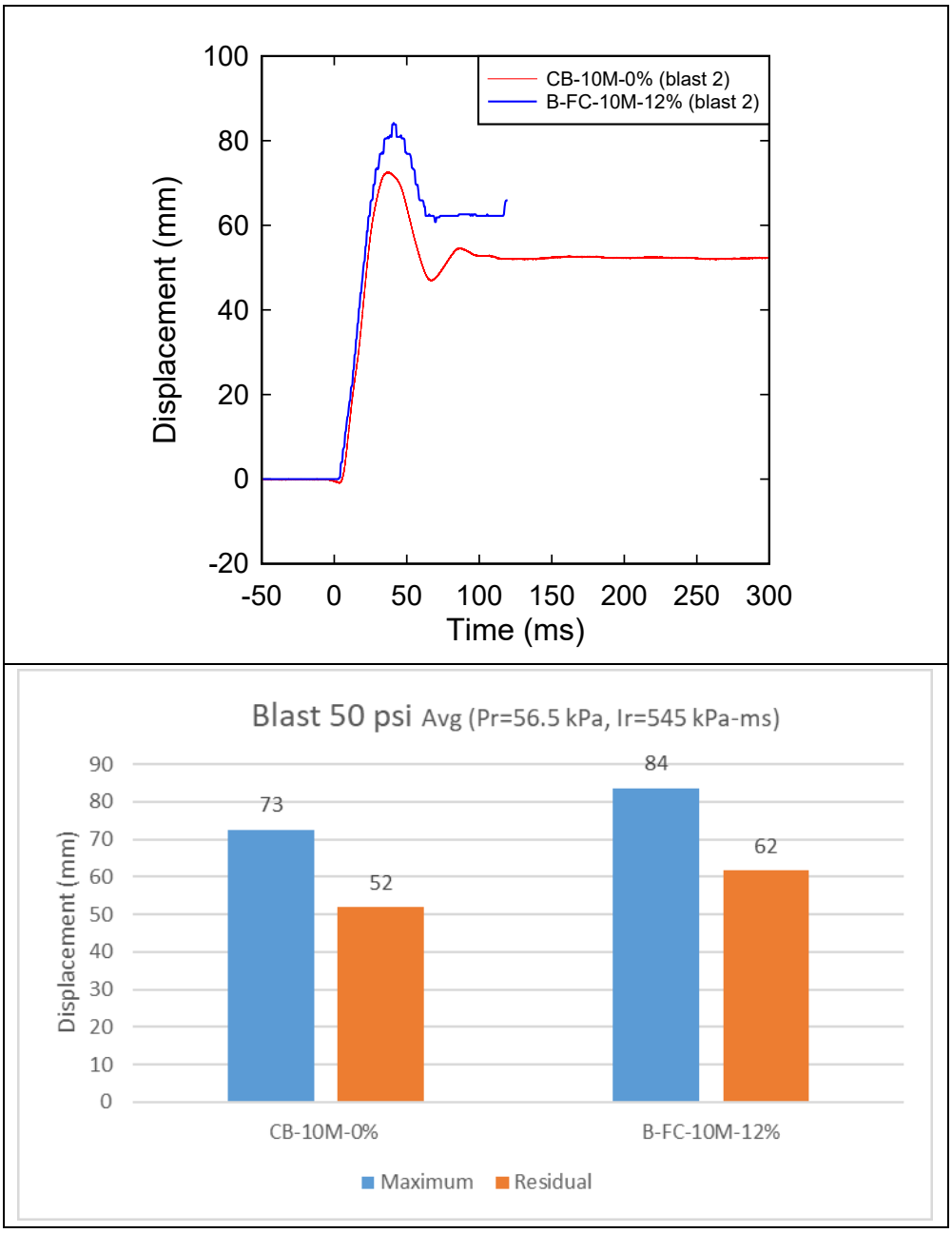



Figure 7-10 Displacements: effect of full span corrosion at 12% mass (10M group)



| CB-10M-0% ($P_d$ = 50 psi): 2nd shot | B-FC-10M-12% ($P_d$ = 50 psi): 2nd shot |
|---|---|

Figure 7-11 Failure mode: effect of full span corrosion at 12% mass loss (10M group)

## 7.5 Effect of corrosion location (mid, end and full span)

### 7.5.1 10M group: B-MC-10M-11% vs B-SC-10M-7% vs B-FC-10M-12%

The results from beams B-MC-10M-11%, B-SC-10M-7% and B-FC-10M-12% in the 10M group were examined to study the effects of corrosion location on the blast response in the 10M group. The three beams were identical in terms of design as discussed in the previous sections; however, each beam was subjected to corrosion at different locations corresponding to the mid-span, the end-spans only and the full span, with actual average mass losses of 11%, 7% and 12%, respectively.

The comparison was made for the 50 psi shot, which was common to the three beams. **Figure 7-12** shows the comparison of displacements at this blast, while the damage for each beam is shown in **Figure 7-13**. **Table 7-5** provides a summary of the key results from this test.

Examining the results at the 50-psi blast, the highest maximum and residual displacements occurred in beam B-MC-10M-11% when compared to the two other beams. Keeping in mind the difference in mass loss (11% vs 7%), the increases in maximum and residual deformations were respectively 23% and 42% for the MC beam (mid-span corrosion) when compared to the SC beam (end-span corrosion). The corresponding maximum support rotations were 4.1° and 3.4°, respectively, which represents *heavy* and *moderate* damage. Examining the failure photos, beam B-MC-10M-11% showed more significant crushing and spalling at mid-span, which generated significant blast fragments at failure. Damage at mid-span was better controlled in B-SC-10M-7%, while spalling shifts from mid-span to the top shear span (see **Figure 7-13**).

Comparing B-MC-10M-11% and B-FC-10M-12%, the MC and FC specimens showed very similar maximum displacements (86 vs 84 mm), residual displacements (64 vs 62 mm) and support rotations (4.1° and 4°) corresponding to *heavy* damage. Both beams experienced similar failure modes; however, relatively more significant damage in terms of crushing and spalling occurred in B-MC-10M-11% (see **Figure 7-13**).

In summary, the results seem to indicate that corrosion at mid-span is more critical in terms of the effect on maximum/residual deformations and damage when compared to corrosion at the end spans only. Moreover, corrosion in the mid-span and full-span regions resulted in similar blast

response in terms of displacements; however, damage was greater in the case of MC type corrosion.

Table 7-5 Key results: effect of corrosion location in the 10M group

| Beam ID | Blast ID (psi) | $I_r$ (kPa-ms) | Displacement (mm) | | Support rotation | | Failure mode |
|---|---|---|---|---|---|---|---|
| | | | $d_{max}$ | $d_{res}$ | $\theta_{max}$ | CSA S850 damage | |
| CB-10M-0% | 50 | 550 | 72.6 | 52.0 | 3.40 | Moderate | **Flexural failure:** light concrete crushing and extensive cracks |
| B-MC-10M-11% | 50 | 547 | 86.3 | 64.3 | 4.10 | Heavy | **Flexural failure:** significant concrete crushing and spalling |
| B-SC-10M-7% | 50 | 555 | 70.1 | 45.2 | 3.30 | Moderate | **Flexural failure:** light concrete crushing and spalling |
| B-FC-10M-12% | 50 | 540 | 83.7 | 61.7 | 4.00 | Heavy | **Flexural failure:** significant concrete crushing and cracks |

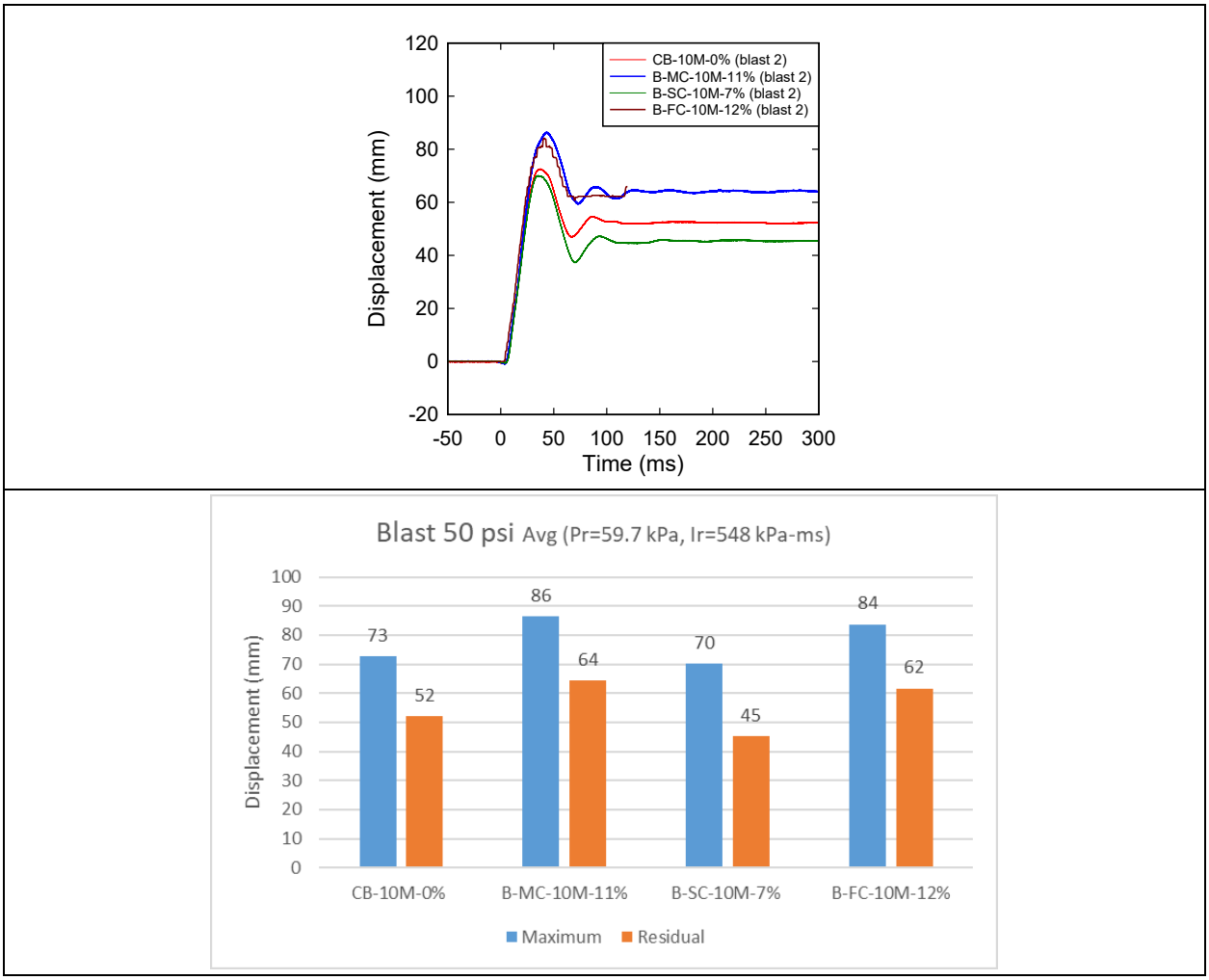



Figure 7-12 Displacements: effect of corrosion locations in the 10M group



| CB-10M-0% ($P_d$ = 50 psi): 2nd shot | B-MC-10M-11% ($P_d$ = 50 psi): 2nd shot | B-SC-10M-7% ($P_d$ = 50 psi): 2nd shot | B-FC-10M-12% ($P_d$ = 50 psi): 2nd shot |
|---|---|---|---|

Figure 7-13 Failure mode: effect of corrosion locations in the 10M group

## 7.6 Effect of cover-removal with mid-span corrosion

### 7.6.1 10M group: CB-10M-0% vs B-CR-MC-10M-5%

The results of beams CB-10M-0% and B-CR-MC-10M-5% were compared to evaluate the effects of corrosion in combination with concrete cover-removal on the blast response of the beams in the 10M group. Both beams had the same 10M-group design properties, with the exception that beam B-CR-MC-10M-5% was subjected to corrosion after removal of the concrete cover in the mid-span region over a length of 750 mm. The subsequent corrosion resulted in an actual average mass loss of 5%. Both beams were subjected to a common blast at a driver pressure of 50 psi. **Figure 7-14** provides a comparison of the beam displacements, while **Figure 7-15** shows the damage in the beams at the end of testing. **Table 7-6** summarizes additional key results from these tests.

Evaluating the results at the 50 psi shot, beam B-CR-MC-10M-5% showed maximum and residual displacements of 79 mm and 57 mm, respectively, which were 9% and 10% higher when compared to beam CB-10M-0%. The maximum support rotation for both beams did not exceed 4°, corresponding to *moderate* damage. Both beams failed in flexure; however, beam B-CR-MC-10M-5% showed more concrete crushing/damage in the mid-span compression region (see **Figure 7-15**).

Given the low amount of corrosion which did not exceed 5% in terms of average mass loss, it can be concluded that the cover loss had only limited effects on the blast response in this set. Therefore, it can be concluded that corrosion of the actual reinforcement is more critical than mere exposure of the bars due to cover loss.

Table 7-6 Key results: effect of corrosion and cover-removal in the mid-span

| Beam ID | Blast ID (psi) | $I_r$ (kPa-ms) | Displacement (mm) | | Support rotation | | Failure mode |
|---|---|---|---|---|---|---|---|
| | | | $d_{max}$ | $d_{res}$ | $\theta_{max}$ | CSA S850 damage | |
| CB-10M-0% | 50 | 550 | 72.6 | 52.0 | 3.40 | Moderate | **Flexural failure:** light concrete crushing and extensive cracks |
| B-CR-MC-10M-5% | 50 | 548 | 79.0 | 57.0 | 3.70 | Moderate | **Flexural failure:** significant concrete crushing and extensive cracks |

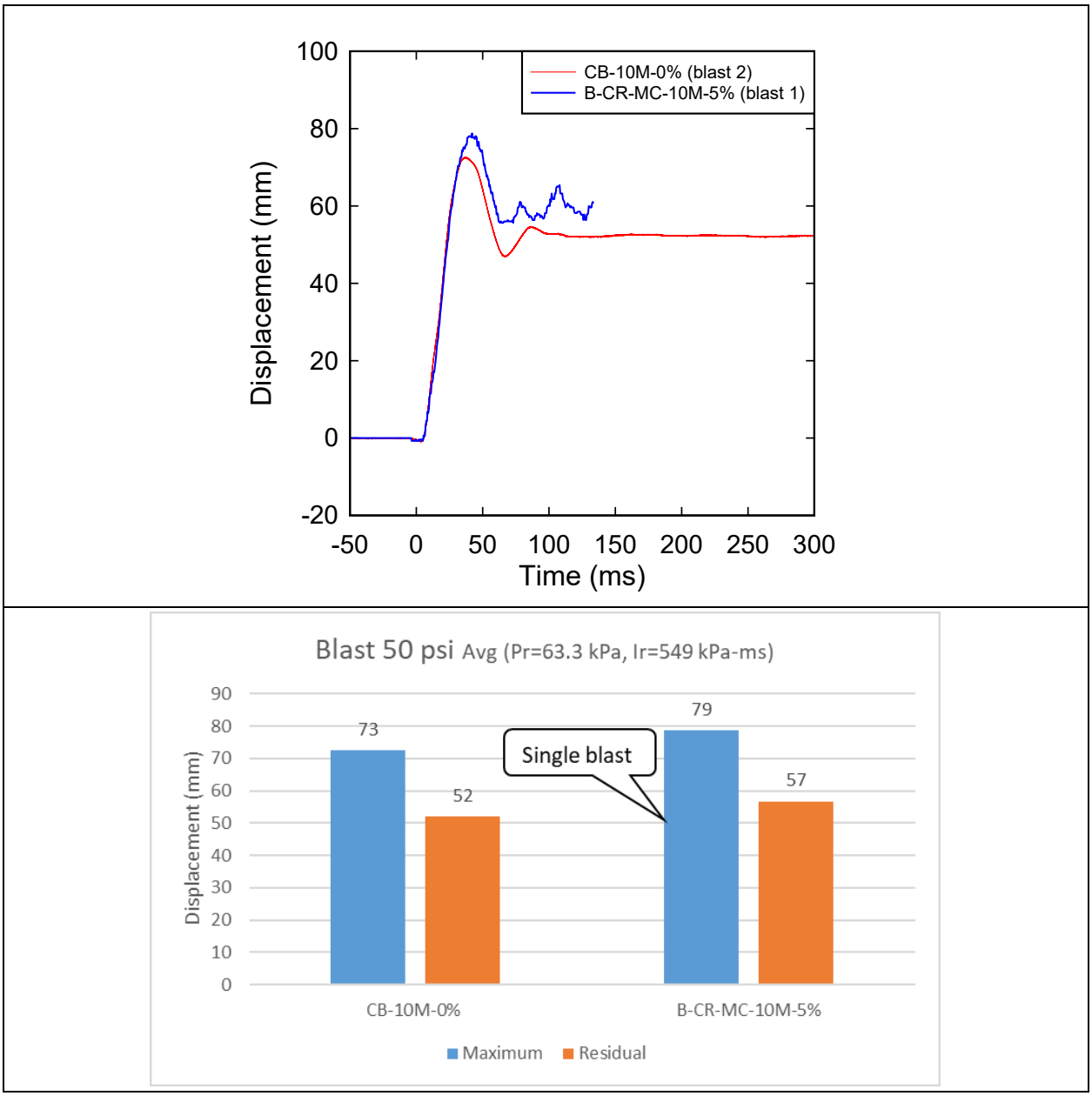
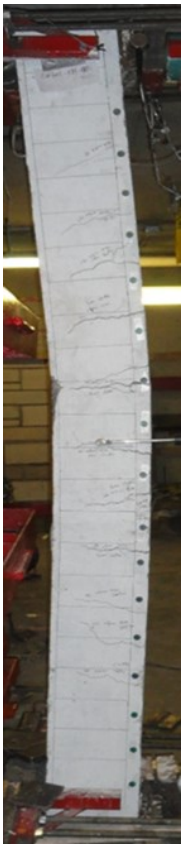
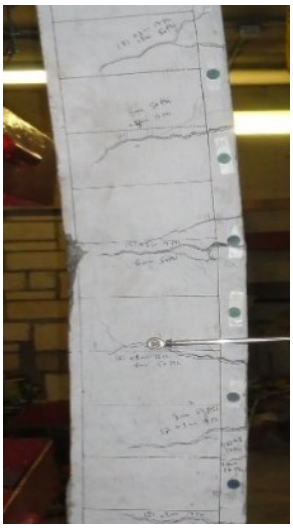



Figure 7-14 Displacements: effect of corrosion and cover-removal in the mid-span (10M group)



| CB-10M-0% ($P_d$ = 50 psi): 2nd shot | B-CR-MC-10M-5% ($P_d$ = 50 psi): 1st shot |
|---|---|

Figure 7-15 Failure mode: effect of corrosion and cover-removal in the mid-span (10M group)

### 7.6.2 15M group: CB-15M-0% vs B-CR-MC-15M-4%

The effects of combined corrosion and cover loss on the blast response were examined in the 15M group by comparing the results of beams CB-15M-0% and B-CR-MC-15M-4%. Both beams had similar design properties; however, B-CR-MC-15M-4% was subjected to corrosion after removal of the concrete cover in the mid-span region, with an actual average mass loss of 4% in the 15M reinforcement. Both beams were subjected to a common blast at a 70 psi driver pressure. The displacement comparison is shown in **Figure 7-16**, while damage in the beams at the end of testing is presented in **Figure 7-17**. **Table 7-7** summarizes the key results from this test.

Examining the results at the 70 psi shot, the maximum and residual displacements of beam B-CR-MC-15M-4% increased by 8% and 7%, respectively, when compared to beam CB-15M-0%. Both beams showed similar maximum support rotations of less than 4°, which corresponds to *moderate* damage. Both beams experienced similar flexural failures; however, beam B-CR-MC-15M-4% showed noticeably more concrete crushing and damage in the mid-span zone when compared to beam CB-15M-0% (see **Figure 7-17**). This beam also showed more significant blast fragments at failure.

In general, the results from this series and previous series indicates that the removal of the concrete cover in the mid-span region does not have a significant impact on the blast behaviour of beams with low amounts of reinforcement corrosion as long as reinforcement anchorage is not compromised.

Table 7-7 Key results: effect of corrosion and cover-removal in the mid-span (15M group)

| Beam ID | Blast ID (psi) | $I_r$ (kPa-ms) | Displacement (mm) | | Support rotation | | Failure mode |
|---|---|---|---|---|---|---|---|
| | | | $d_{max}$ | $d_{res}$ | $\theta_{max}$ | CSA S850 damage | |
| CB-15M-0% | 70 | 734 | 70.6 | 50.5 | 3.30 | Moderate | **Flexural failure**: concrete crushing and extensive cracks |
| B-CR-MC-15M-4% | 70 | 720 | 76.0 | 54.0 | 3.60 | Moderate | **Flexural failure**: significant concrete crushing and cracks |

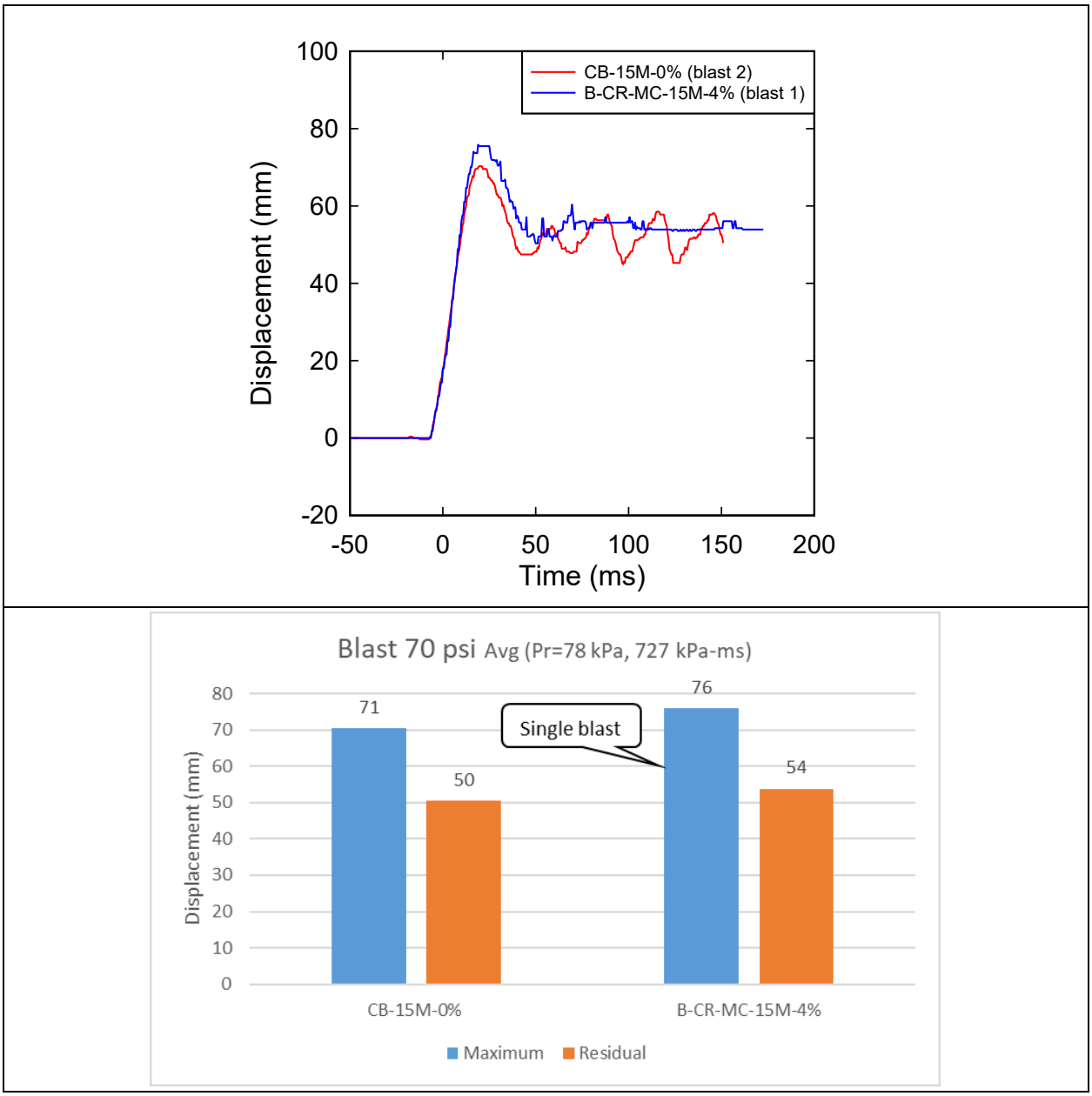
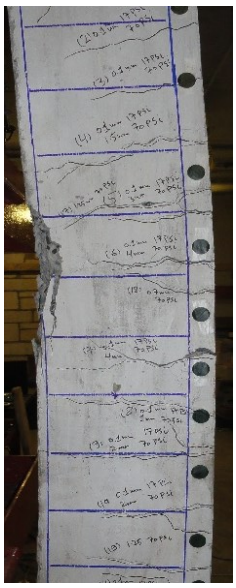



Figure 7-16 Displacements: effect of corrosion and cover-removal in the mid-span (15M group)



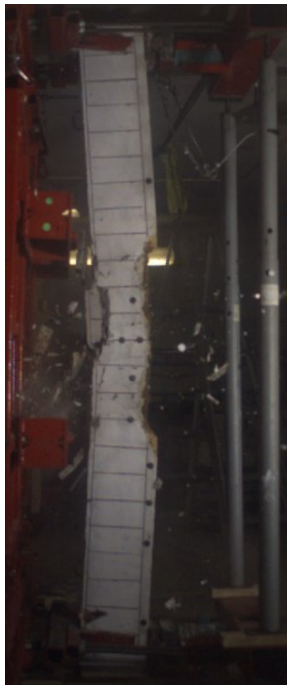


CB-15M-0%
($P_d$ = 70 psi): 2nd shot





B-CR-MC-15M-4%
($P_d$ = 70 psi): 1st shot



Blast fragments in beam B-CR-MC-15M-4% at failure

Figure 7-17 Failure mode: effect of corrosion and cover-removed at mid-span (15M group )

## 7.7 Effect of shear-span corrosion

### 7.7.1 25M group: CB-25M-0% vs B-SHC-25M-11% vs B-SHC-25M-12%

The results of beams CB-25M-0%, B-SHC-25M-11% and B-SHC-25M-12% were compared to examine the effect of corrosion of the transverse reinforcement in the 25M group. All beams had identical design properties, which consisted of 2-25M bars in tension, 2-10M bars in compression and provision of minimum U-shaped stirrups. However, the stirrups in beams B-SHC-25M-11% and B-SHC-25M-12% were subjected to corrosion throughout the beam span, with actual average mass loss of 11% and 12%, respectively. All beams were subjected to a single blast corresponding to a driver pressure of 90 psi. **Figure 7-18** compares the beam displacements after this blast, while **Figure 7-19** compares the damage at the end of testing. A summary of key data is presented in **Table 7-8**. Beginning with the two beams which failed in flexure, beam B-SHC-25M-11% showed significant increases of 101% and 206% in maximum and residual displacements, respectively, when compared to beam CB-25M-0% due to the more severe flexural failure. The maximum support rotation of beam B-SHC-25M-11% reached 4.4°, which corresponds to *heavy* damage, compared to 2.2° (*moderate* damage) in beam CB-25M-0%. Indeed, the failure photos and high speed video showed more significant concrete crushing, side and tension cover spalling, and blast fragments for beam SHC-25M-11%. The failure in beam CB-25M-0% was in flexure; however, the damage was more controlled.

Beam B-SHC-25M-12% recorded similar maximum displacement when compared to CB-25M-0% due to the difference in failure mode. Unlike CB-25M-0% (control) and B-SHC-25M-11% which failed in flexure, beam B-SHC-25M-12% experienced a brittle shear failure in its bottom shear span. Failure was associated with diagonal shear cracking and significant spalling of the concrete cover on the side and tension faces in the shear failure region as shown in **Figure 7-19**.

Examining the dynamic resistance curves in **Figure 7-20**, all beams showed similar pre-peak and post-peak behaviours; however, the stiffness and maximum dynamic capacities of beams B-SHC-25M-11% and B-SHC-25M-12% were slightly reduced when compared to beam CB-25M-0%.

In summary, it can be concluded that the corrosion of the transverse reinforcement affects beam blast performance in terms of damage and failure mode. However, given the variability in the test results, further research is recommended.

Table 7-8 Key results: effect of shear corrosion in the 25M group

| Beam ID | Blast ID (psi) | $I_r$ (kPa-ms) | Displacement (mm) | | Support rotation | | Failure mode |
|---|---|---|---|---|---|---|---|
| | | | $d_{max}$ | $d_{res}$ | $\theta_{max}$ | CSA S850 damage | |
| CB-25M-0% | 90 | 927 | 46.0 | 22.4 | 2.20 | Moderate | **Flexural failure**: significant concrete crushing and extensive cracks |
| B-SHC-25M-11% | 90 | 903 | 92.6 | 68.5 | 4.40 | Heavy | **Flexural failure**: severe concrete crushing and spalling |
| B-SHC-25M-12% | 90 | 926 | 45.5 | 32.0 | 2.20 | Moderate | **Shear failure**: severe spalling and extensive cracks |

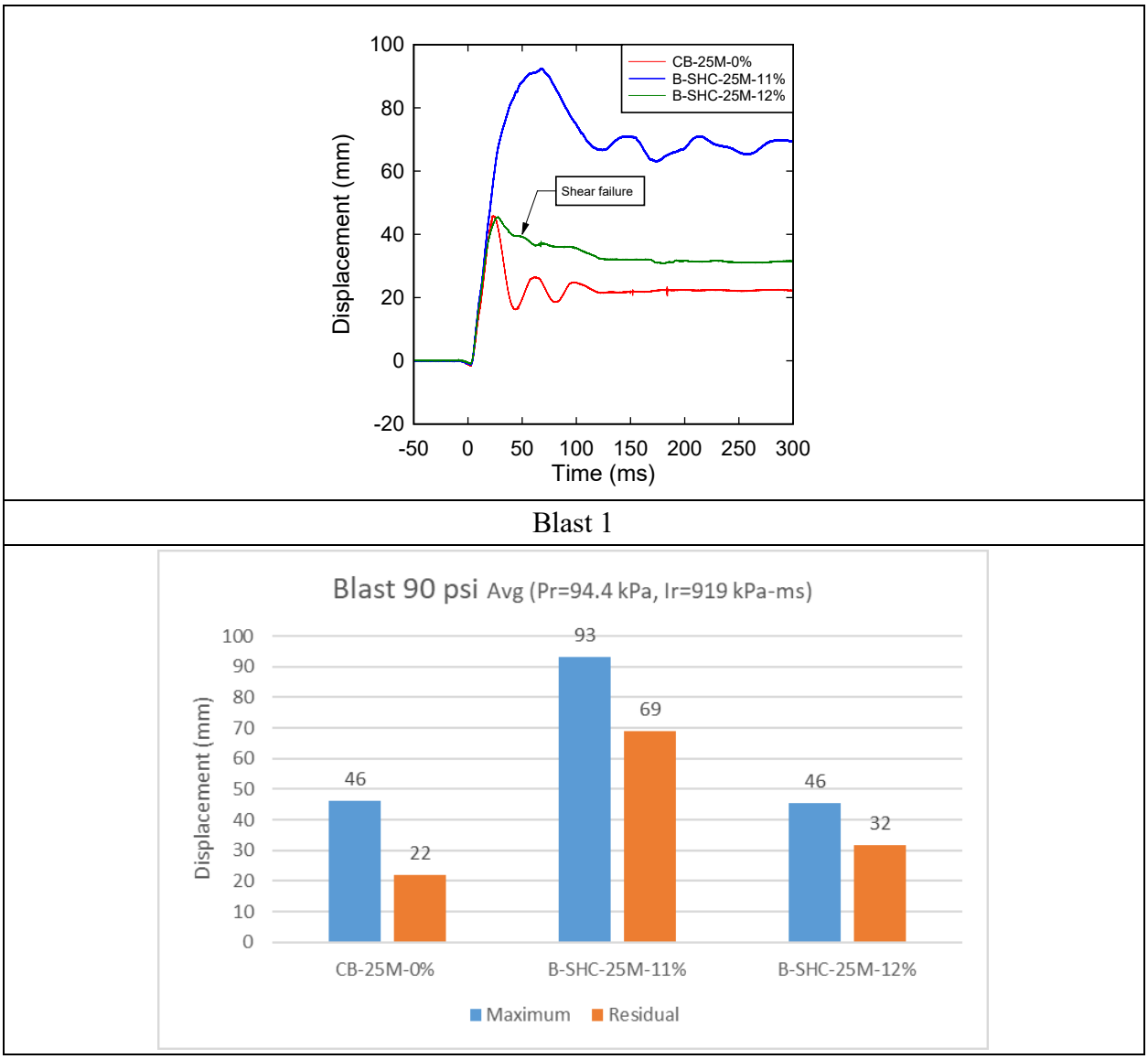



Figure 7-18 Displacements: effect of shear corrosion in the 25M group

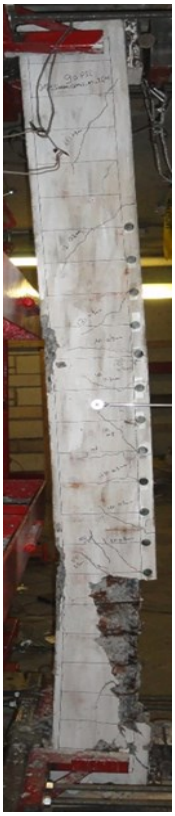
| | | |
|---|---|---|
|  |  |  |
| CB-25M-0%<br>($P_d$ = 90 psi) | B-SHC-25M-11%<br>($P_d$ = 90 psi) | B-SHC-25M-12%<br>($P_d$ = 90 psi) |

Figure 7-19 Failure mode: effect of shear corrosion in the 25M group

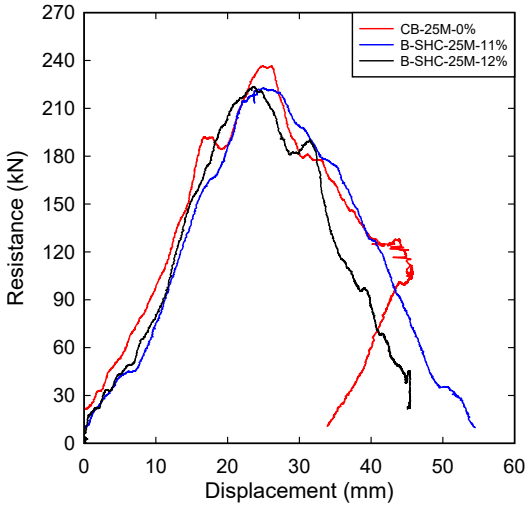



Figure 7-20 Dynamic reactions: effect of shear corrosion in the 25M group

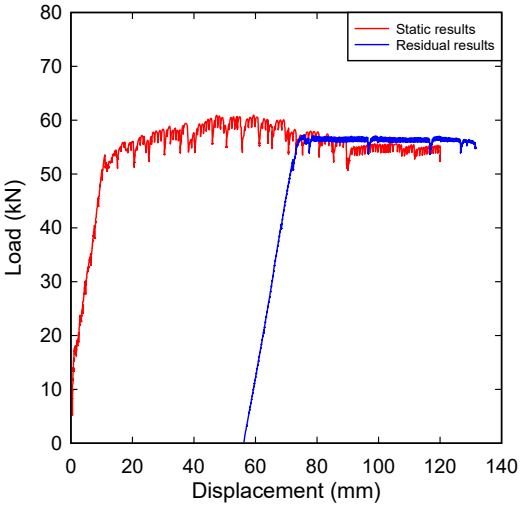
## 7.8 Effects of corrosion on residual static capacity

Most of the corroded beams in this study failed in a brittle manner under blast loading, without any residual capacity. However, beams B-SC-10M-7% (10M bars, end-span corrosion, average mass loss of 7%) and B-FC-10M-12% (10M bars, full length corrosion, average mass loss of 12%) survived their final blast tests with limited damage and were subsequently tested under four-point static loads to assess their residual capacity. This section compares the residual results of these two beams with that of the control CB-10M-0% specimen.

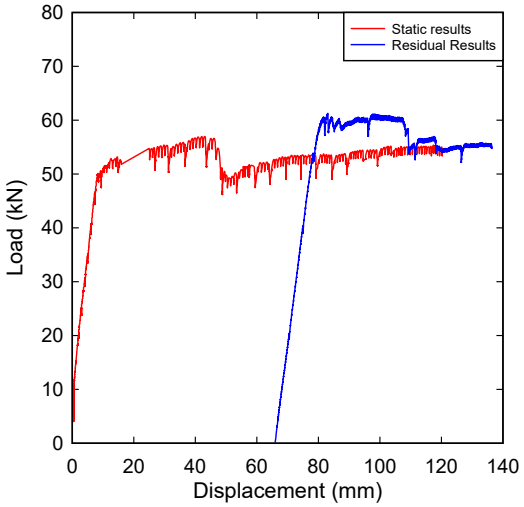
### 7.8.1 CB-10M-0% vs B-SC-10M-7%

Beam B-SC-10M-7% was tested under blast loads at driver pressures of 17, 35 and 50 psi. After blast testing, its residual strength was studied under static loading. **Figure 7-21 (b)** shows that the beam had a residual capacity of 61.30 kN, which was higher than the peak resistance of the companion beam tested under static loads only. The beam showed an ability to carry sustained loads, reaching a displacement of 136 mm with a final residual load of 55 kN.

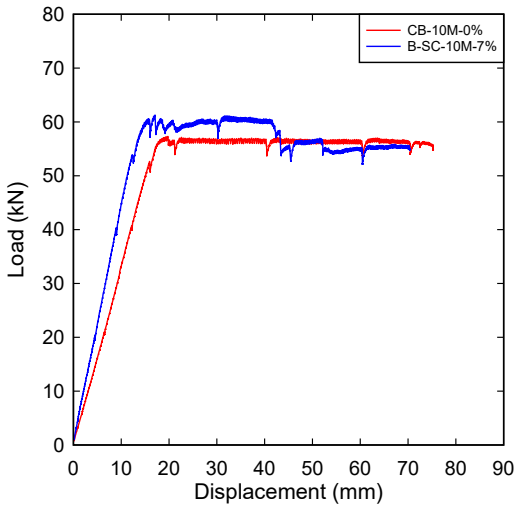
**Figure 7-21 (c)** compares the residual load-deflection curves of beams B-SC-10M-7% and CB-10M-0% (control). It was observed that the maximum strength, yield strength and stiffness of beam B-SC-10M-7% were not decreased when compared with beam CB-10M-0% (in fact the corroded specimen showed slight increases when compared to the control). Moreover, both beams showed similar maximum displacement and the same flexural failure mode as shown in **Figure 7-22**. The results confirmed that the combined effects of low intensity corrosion, which was only concentrated in the ends of the beam, had limited effects on the post-blast residual performance of beam B-SC-10M-7%.




a) CB-10M-0%: Residual vs static only




b) B-SC-10M-7%: Residual vs static only




c) CB-10M-0% vs B-SC-10M-7%: Residual

Figure 7-21 Residual test results: effect of end-span corrosion with 7% mass loss

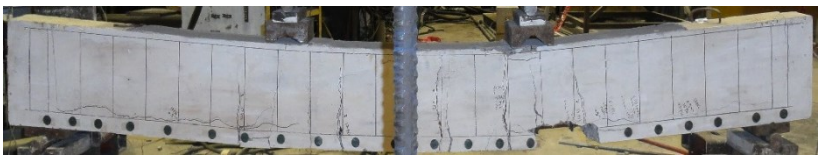
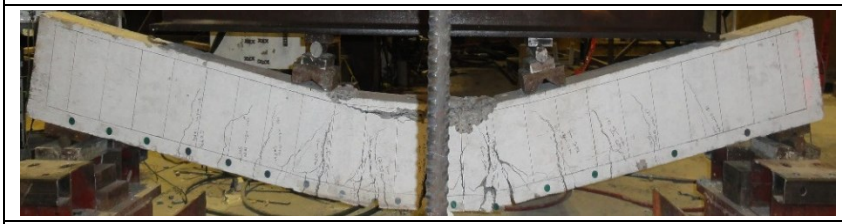
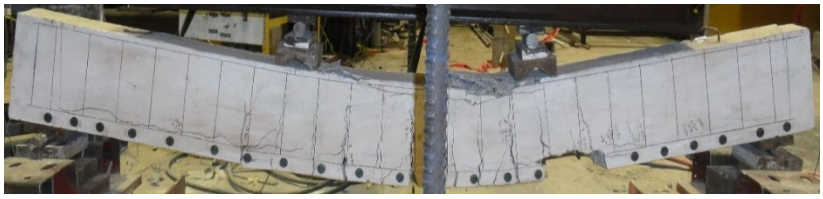
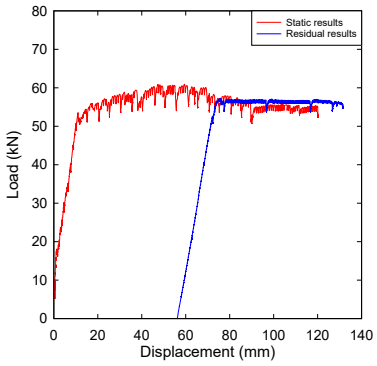
| Before the residual test | Comments |
|---|---|
| CB-10M-0% | |
|  | Cracks distributed on the entire length of the beam.<br>Some large cracks in the mid-span region. |
| B-SC-10M-7% | |
|  | Significant cracks in the mid-span.<br>Concrete spalling in the tension- region. |
| After the residual test | Comments |
| CB-10M-0% | |
|  | Concrete crushing in the compression zone at the mid-region.<br>Severe cracks in the moment region. |
| B-SC-10M-7% | |
|  | Concrete crushing in the compression zone. |

Figure 7-22 Photos of the beams (CB-10M-0% and B-SC-10M-7%) before and after the residual test

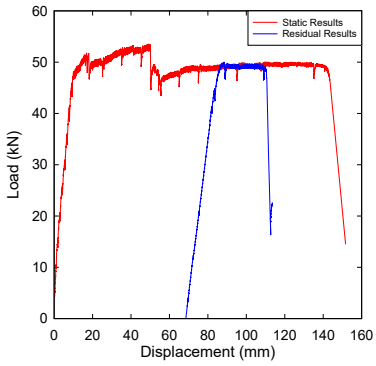
### 7.8.2 CB-10M-0% vs B-FC-10M-12%

Beam B-FC-10M-12% was tested under blast loads at driver pressures of 17 and 50 psi. After blast testing, its residual strength was studied under static loading. **Figure 7-23 (b)** shows that the beam had a residual capacity of 50 kN, which matched the expected residual strength observed in the companion beam tested under static loads only. However, the blast-damaged beam failed at an earlier displacement due rupture of the tension steel reinforcement.

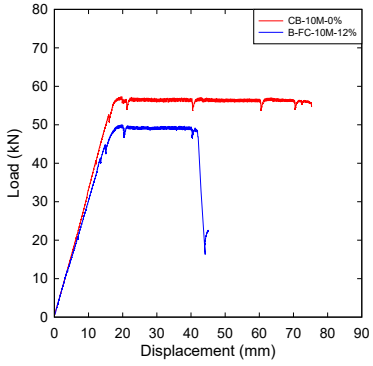
The effect of corrosion was observed by comparing the residual test results for beams B-FC-10M-12% and CB-10M-0% (control). **Figure 7-23 (c)** shows that the maximum strength and ductility of beam B-FC-10M-12% decreased when compared to CB-10M-0%. Importantly, beam B-FC-10M-12% experienced a sudden/brittle failure in flexure associated with bar rupture, whereas beam CB-10M-0% continued to carry loads with a behavior which was similar to the reference beam tested under static loading only, as presented in **Figure 7-24**. The results showed that this corrosion case had an important effect on the post-blast residual performance of the beams.




a) CB-10M-0%: Residual vs static only




b) B-FC-10M-12%: Residual vs static only




c) CB-10M-0% vs B-FC-10M-12%: Residual

Figure 7-23 Residual test results: effect of full-span corrosion at 12% mass loss

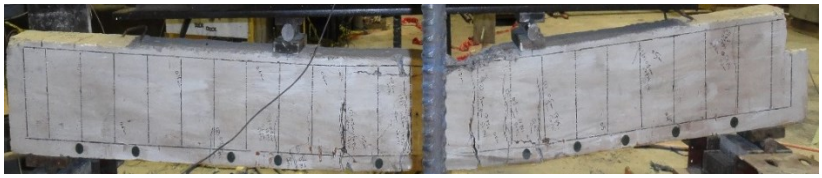
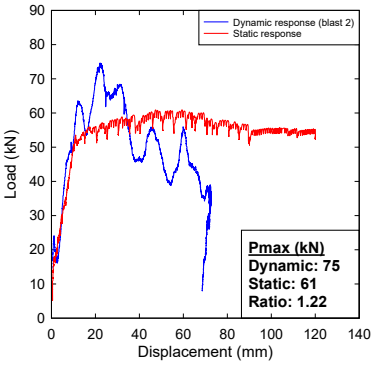
| Before the residual test | Comments |
|---|---|
| CB-10M-0% | |
|  | Cracks distributed on the entire length of the beam.<br>Some large cracks in the mid-span region. |
| B-FC-10M-12% | |
|  | Initial crushing and cracking prior to residual static test. |
| After the residual test | Comments |
| CB-10M-0% | |
|  | Concrete crushing in the compression zone at the mid-region.<br>Severe cracks in the moment region. |
| B-FC-10M-12% | |
|  | Concrete crushing and severe cracks in the mid-span zone.<br>Rupture of the 10M bars in the tension zone. |

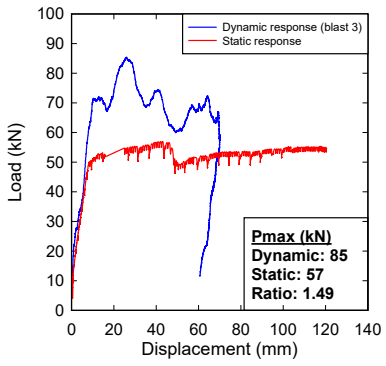
Figure 7-24 Photos of the beams (CB-10M-0% and B-FC-10M-12%) before and after the residual test

### 7.9 Static vs Dynamic resistance

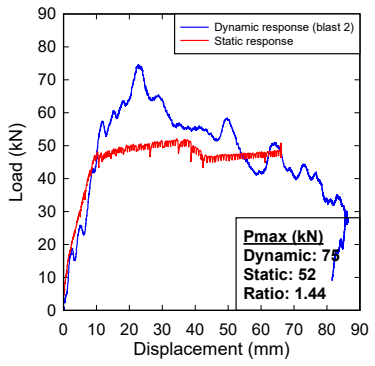
This section provides a comparison of the resistance curves of the beams under static and dynamic blast loading. **Figure 7-25** shows the results for beams CB-10M-0%, B-SC-10M-7% and B-MC-10M-11% (10M series), and CB-25M-0%, B-SHC-25M-11% and B-SHC-25M-12% (25M series). The dynamic resistance results were obtained by summing the support reactions recorded by the load-cells during testing. It was observed that static and dynamic resistance curves generally followed similar trends in terms of load-displacement response. The maximum loads under dynamic and static loading, and their ratio ($P^{D}_{max}$ / $P^{S}_{max}$) were reported in the plots. In general, the obtained maximum loads from dynamic blast loading were higher than the maximum loads in static loading for all the beams; this increase can be clarified by the effects of high strain-rate on the concrete and steel bars which led to increase their strengths. The average of dynamic to static strengths ratio for all the beams was determined to be 1.26, which was within the range according to Magnusson et al. (2010). Comparing the individual sets, the average load ratios were 1.38 and 1.15 for the 10M and 25M series, respectively. The results showed that both the flexural and shear dominant beams showed an increase in resistance under dynamic loading. The results also confirmed that the increase in strength also occurred in the corrosion-damaged beams, which would seem to indicate that strain-rate effects were not negated by the steel corrosion.



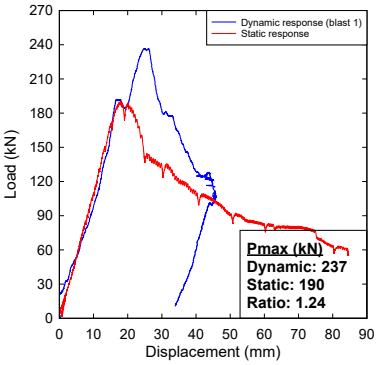

a) Control (10M): CB-10M-0%



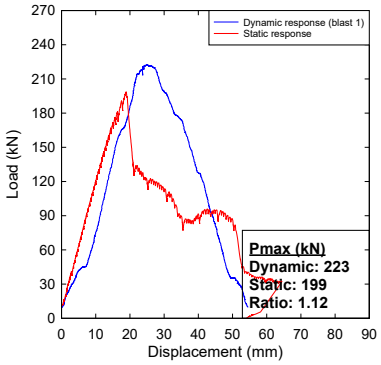

b) End-span corrosion (10M): B-SC-10M-7%



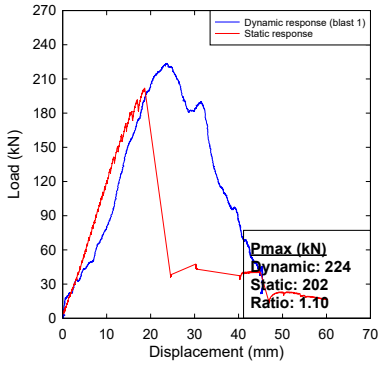

c) Mid-corrosion (10M): B-MC-10M-11%




d) Control (25M): CB-25M-0%




e) Shear corrosion 11%: B-SHC-25M-11%




f) Shear corrosion 12%: B-SHC-25M-11%

Figure 7-25 Comparison of static vs dynamic resistance

# Chapter 8: Finite Element Analysis of Corrosion-Damaged Beams Under Static Loading

## 8.1 Chapter Overview

This chapter presents the first phase of the numerical research program, which aims at predicting the response of the tested beams under static loading. Finite element models of the control and corroded beams were developed using 2D nonlinear finite element software (VecTor2). The effects of corrosion were considered by reducing the steel cross-sectional area, modifying the steel stress-strain relationship, and modelling corrosion-induced cracking in the concrete. The chapter presents a description of the FE models, a summary of the FE results considering different modelling features, and a comparison between the predicted and experimental results.

## 8.2 Numerical Methodology

Two-dimensional nonlinear finite element (FE) software (VecTor2) was used to predict the flexural and shear responses of the un-corroded (control) and corroded beams under static four-point bending.

To account for symmetry, half of the simply-supported beams was modelled in VecTor2 as shown in **Figure 8-1**. Concrete was modelled using 4-node rectangular plane-stress elements with 2 degrees of freedom per node, with a mesh size of 10 mm x 10 mm for the flexure-governed beams (10M and 15M groups) (see **Figure 8-1 (a)** and **Figure 8-1 (b)**). A slightly larger mesh of 20 mm x 20 mm was used for the shear-governed beams (25M group) (see **Figure 8-1 (c)**). The FE meshing was selected based on a preliminary sensitivity analysis while also considering the recommendations in other VecTor2 studies. Longitudinal steel reinforcement was modelled with 2-node truss bar elements, while transverse reinforcement was either smeared in the concrete elements (for the 10M/15M beams) or modelled using discrete 2-node truss elements (in the 25M group). Steel plates were placed at the supports and under the load points to distribute the load and avoid stress concentrations. The analysis was run under displacement control by applying an increasing displacement at the loading point. In all cases, the steel bars were assumed to be perfectly bonded to the concrete.

The constitutive models used in the FE analysis for the beams in the 10M/15M and 25M groups are listed in **Table 8-1** and **Table 8-2,** respectively. The pre-peak and post-peak response of

concrete in compression was modelled using the Popovics (NSC: normal-strength concrete) and Popovics/Mander models, respectively. The steel reinforcement was modeled using a trilinear elastic-hardening curve. Concrete properties (tensile strength, modulus of elasticity and concrete peak strain) were calculated according to the equations provided in the VecTor2 manual (Wong et al., 2013), except for the compressive strength ($f_c'$), which was determined from the cylinder tests. When $f_c'$ was over 40 MPa, the modulus of elasticity ($E_c$) was calculated using **Equation 8-1**. The maximum crack width was fixed at 2 mm for the flexure-governed beams (10M and 15M groups) (see **Table 8-1**), but it was fixed at 5 mm for the shear-governed beams (25M group) (see **Table 8-2**); these values were chosen after conducting a sensitivity analysis. In general, the remaining concrete modelling parameters were kept the same as the defaults.

$$E_c = 3320 \sqrt{f'_c} + 6900 \quad (8\text{-}1)$$

where: $E_c$ (MPa) = modulus of elasticity, $f_c'$ (MPa) = compression strength.

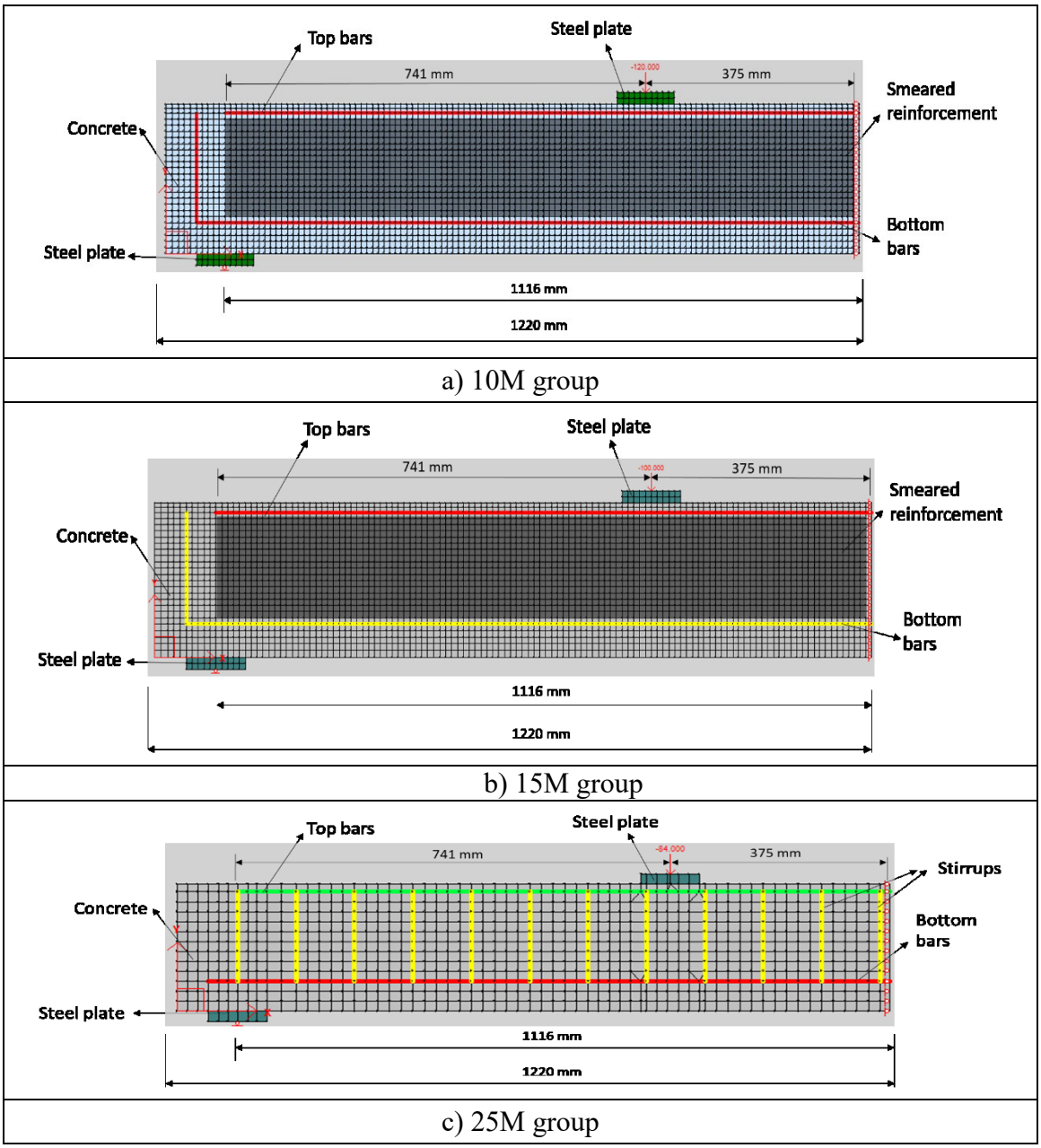



Figure 8-1 Typical finite element meshes for 10M, 15M and 25M groups

Table 8-1 Constitutive models used in FE analysis for 10M and 15M groups

| **Concrete Constitutive Models** | | | |
|---|---|---|---|
| **Compression Pre-Peak** | Popovics (NSC) | **Dilation** | Variable – Isotropic |
| **Compression Post-Peak** | Popovics / Mander | **Cracking Criterion** | Mohr-Coulomb (Stress) |
| **Compression Softening** | Vecchio 1992-A (e1/e2-Form) | **Crack Stress Calc** | Basic (DSFM/MCFT) |
| **Tension Stiffening** | Modified Bentz 2003 | **Crack Width Check** | 2 mm Max Crack Width |
| **Tension Softening** | Bilinear | **Crack Slip Calc** | Walraven |
| **FRC Tension** | SDEM-Monotonic | **Creep and Relaxation** | Not Considered |
| **Confined Strength** | Kupfer / Richart | **Hysteretic Response** | Nonlinear w / Plastic Offsets |
| **Reinforcement Models** | | | |
| **Hysteretic Response** | Bauschinger Effect (Seckin) | **Buckling** | Akkaya 2012 (Modified Dhakal-Maekawa) |
| **Dowel Action** | Tassios (Crack Slip) | **Concrete Bond** | Perfect Bond |

Table 8-2 Constitutive models used in FE analysis for 25M group

| **Concrete Constitutive Models** | | | |
|---|---|---|---|
| **Compression Pre-Peak** | Popovics (NSC) | **Dilation** | Variable – Isotropic |
| **Compression Post-Peak** | Popovics / Mander | **Cracking Criterion** | Mohr-Coulomb (Stress) |
| **Compression Softening** | Vecchio 1992-A (e1/e2-Form) | **Crack Stress Calc** | Basic (DSFM/MCFT) |
| **Tension Stiffening** | Modified Bentz 2003 | **Crack Width Check** | 5 mm Max Crack Width |
| **Tension Softening** | Bilinear | **Crack Slip Calc** | Walraven |
| **FRC Tension** | SDEM-Monotonic | **Creep and Relaxation** | Not Considered |
| **Confined Strength** | Kupfer / Richart | **Hysteretic Response** | Nonlinear w / Plastic Offsets |
| **Reinforcement Models** | | | |
| **Hysteretic Response** | Bauschinger Effect (Seckin) | **Buckling** | Akkaya 2012 (Modified Dhakal-Maekawa) |
| **Dowel Action** | Tassios (Crack Slip) | **Concrete Bond** | Perfect Bond |

### 8.2.1 Reduction of steel bar area

Corrosion was simulated by reducing the cross-sectional area of the steel reinforcement based on the measured mass loss. Mass loss was calculated experimentally (ASTM G1) by measuring the weight of the steel bars before and after the corrosion process using the following equation:

$$\text{Mass loss } \% = \frac{(w_{ori} - w_{corr})}{w_{ori}} \tag{8-2}$$

where: $w_{ori}$ = original weight of the steel bar, $w_{corr}$ = weight of steel bar after corrosion.

The reduced bar diameter, and thickness reduction, were then determined using the following equations:

$$\frac{d_b^2 - d_{corr}^2}{d_b^2} = \text{mass loss } \% \tag{8-3}$$

$$d_{corr} = d_b - ax(t) \tag{8-4}$$

where: $d_{corr}$ (mm) = diameter of corroded steel bar, $d_b$ (mm) = diameter of un-corroded steel bar, $a$ = 2 for uniform corrosion, $x(t)$ = the corrosion penetration depth, which was assumed to be uniform around the bar perimeter as shown in **Figure 8-2**.

The reduced area of the corroded steel bar was then calculated using the following equation:

$$A_{s(red)} = A_s - A_{s(corr)} \tag{8-5}$$

where: $A_{s(red)}$ (mm$^2$) = reduction in steel bar area, $A_s$ (mm$^2$) = original steel bar area, $A_{s(corr)}$ (mm$^2$) = corroded steel bar area.

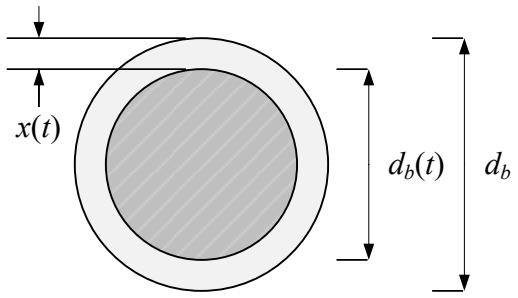



Figure 8-2 Uniform corrosion

### 8.2.2 Modified and unmodified stress-strain of corroded and un-corroded steel bars

The stress-strain properties of the un-corroded steel bars were assigned based on the data from the steel tension coupon tests. To account for the effects of corrosion on the steel stress-strain response, these properties were then modified using **Equations 8-6** to **8-8** as recommended in the "LIFECON DELIVERABLE D 3.2: Service Life Models Report" (Lay et al. 2003). The stress-strain responses of the un-corroded and corroded steel bars were then predicted using the model presented in **Equations 8-9** to **8-11** (Wong et al., 2013). **Figure 8-3** illustrates the stress-strain curves for the un-corroded and corroded steel bars (10M, 15M and 6.3 mm). **Figure 8-4** shows how the discrete and smeared steel reinforcement properties were defined in VecTor2.

$$f_y = (1 - \alpha_y * A_{corr}) * f_{y0} \quad (8\text{-}6)$$

$$f_u = (1 - \alpha_u * A_{corr}) * f_{u0} \quad (8\text{-}7)$$

$$\lambda = (1 - \alpha_1 * A_{corr}) * \lambda_0 \quad (8\text{-}8)$$

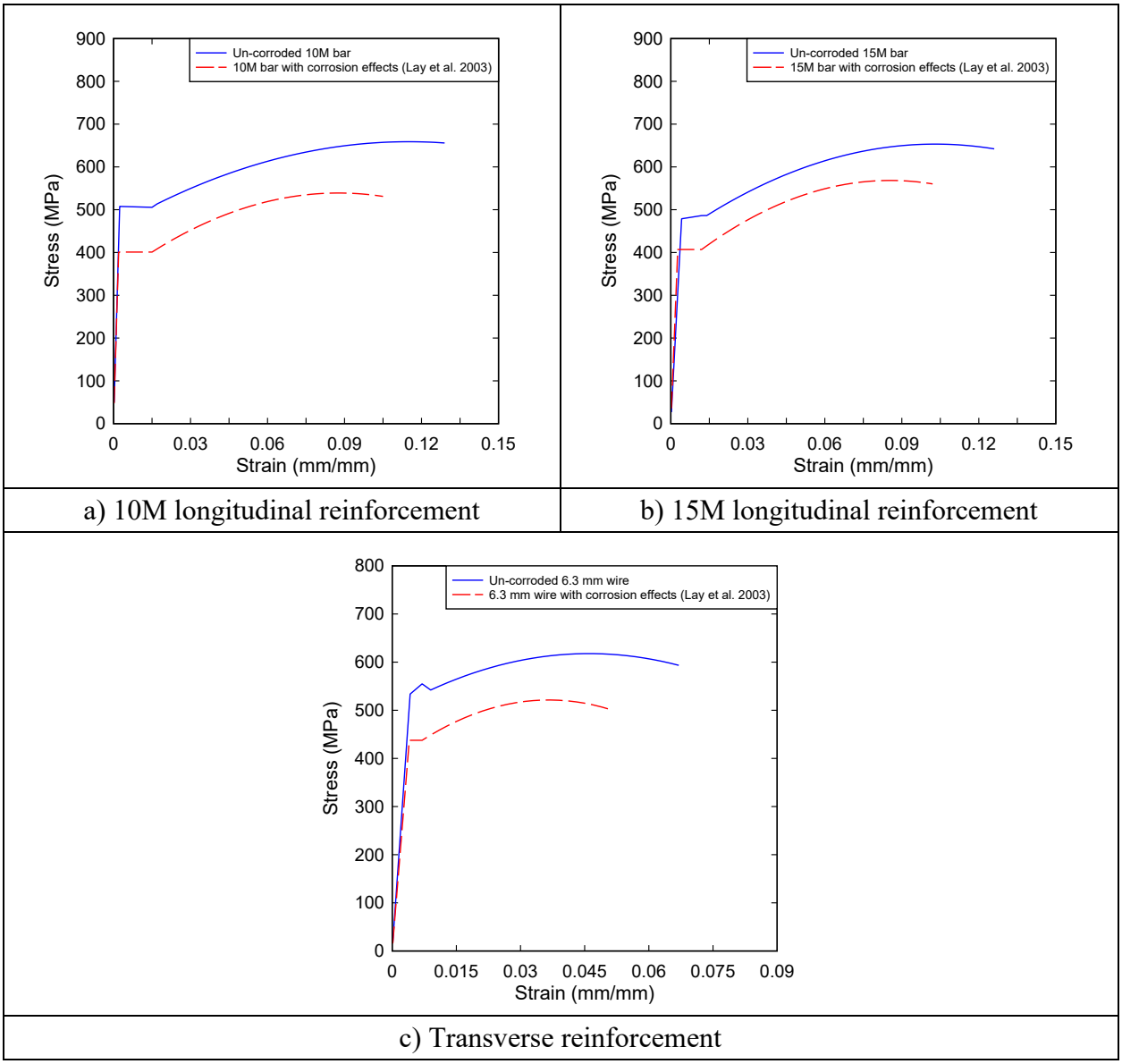
where: $f_y$ and $f_u$ (MPa) = yield and ultimate stresses in the corroded state; $f_{y0}$, $f_{u0}$ and $\lambda_0$ (MPa) = yield stress, ultimate stress and ultimate strain in the un-corroded state; $\lambda$ = ultimate strain in the corroded state; $\alpha_y$, $\alpha_u$ and $\alpha_1$ = regression coefficients ($\alpha_y = 0.015$, $\alpha_u = 0.013$ and $\alpha_1 = 0.017$; these values were selected based on the recommendations in Andrade et al. (1991)).

$$f_s = E_s \varepsilon_s \qquad \text{for } \varepsilon_s \le \varepsilon_y \quad (8\text{-}9)$$

$$f_s = f_y \qquad \text{for } \varepsilon_y < \varepsilon_s \le \varepsilon_{sh} \quad (8\text{-}10)$$

$$f_s = f_u + \left(f_y - f_u\right)\left(\frac{\varepsilon_u - \varepsilon_s}{\varepsilon_u - \varepsilon_{sh}}\right)^4 \qquad \text{for } \varepsilon_{sh} < \varepsilon_s \le \varepsilon_u \quad (8\text{-}11)$$

where: $f_s$ (MPa) = steel stress; $f_y$ and $f_u$ (MPa) = yield and ultimate stresses; $\varepsilon_s$ = steel strain; $\varepsilon_y$, $\varepsilon_{sh}$ and $\varepsilon_u$ = yield, hardening and ultimate strains of steel reinforcement, respectively.

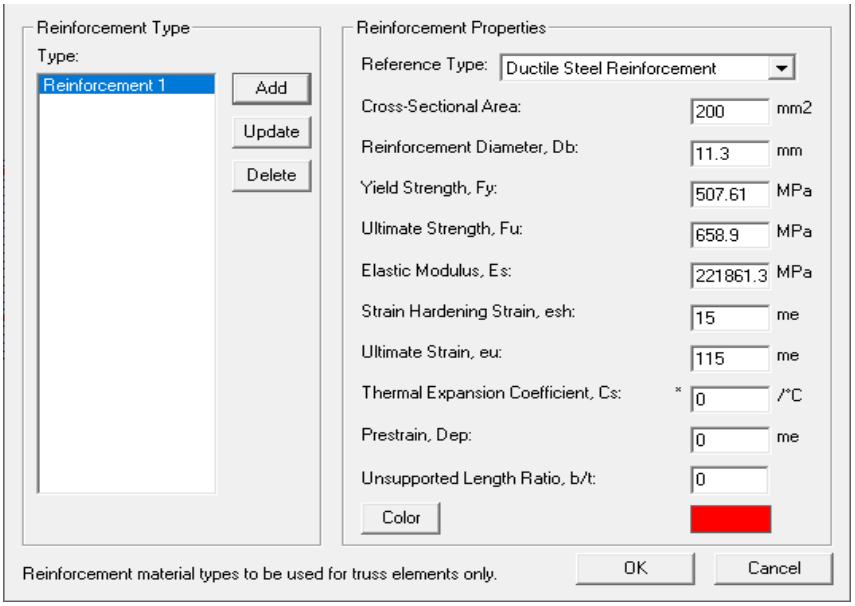



a) 10M longitudinal reinforcement

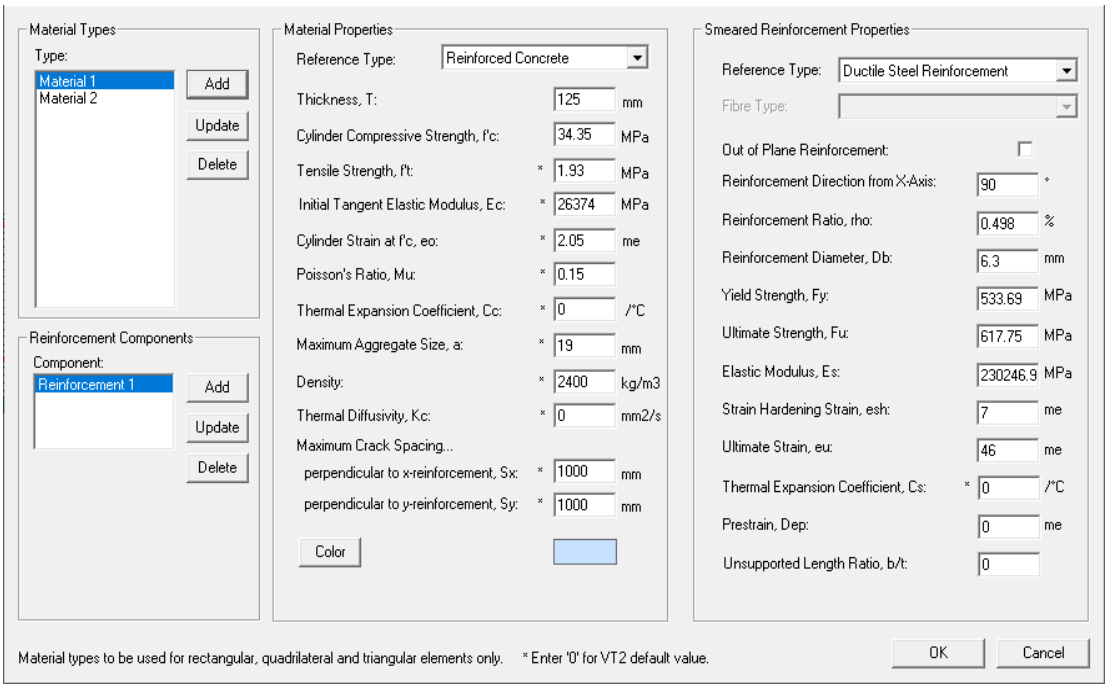
b) 15M longitudinal reinforcement

c) Transverse reinforcement

Figure 8-3 Stress-strain curves for un-corroded and corroded steel bars (10M, 15M and 6.3 mm)




a) Longitudinal steel reinforcement properties




b) Smeared reinforcement properties

Figure 8-4 Defining steel reinforcement properties in VecTor2

### 8.2.3 Corrosion-induced cracking

Concrete damage caused by the build-up of corrosion products around the steel reinforcement was also considered in the FE model. Corrosion-induced cracking was simulated using the analogy of a thick-wall cylinder subjected to internal pressure and introduced in the FE model in the form of equivalent strains. Prior to loading, compressive pre-strains perpendicular to the corroded steel bars were applied in the concrete elements near the reinforcement to simulate expansion caused by the build-up of corrosion by-products. The pre-strained concrete was then released before loading to induce tensile stresses in the surrounding concrete elements. The amount of pre-strain was calculated based on the percentage of corrosion attack and associated volume build-up of corrosion using **Equations 8-12** to **8-15**. The applied pre-strains were distributed over the influenced surrounding concrete elements, i.e., within the thick wall cylinder representing the affected concrete cover as shown in **Figure 8-5** (Bernard, 2013). The pre-strain values for the different corroded beams are listed in **Table 8-3**, and the locations of the applied pre-strains are illustrated in **Figure 8-6**.

The total expanded area resulting from the corrosion products build-up was determined by using the following expression:

$$A_{s(exp)} = \mu A_{s(red)} + \frac{\pi\,(d_b - 2x)^2}{4} \tag{8-12}$$

where: $A_{s(exp)}$ ($mm^2$) = total expanded area of corroded steel bar, $\mu$ = ratio of steel-to-corrosion product density (which can vary between 2-4), $A_{s(red)}$ ($mm^2$) = reduction of steel bar area, $d_b$ (mm)= original diameter of steel bar, and $x$ (mm) = the penetration of corrosion. **Equation 8-12** assumes uniform corrosion around the reinforcing steel bar. In the current study, $\mu$ was taken as 2 (Bernard, 2013).

The expanded diameter was then calculated as:

$$d_{exp} = \sqrt{\frac{4\,A_{S(exp)}}{\pi}} \tag{8-13}$$

where: $d_{exp}$ (mm) = expanded diameter of corroded steel bar, $A_{s(exp)}$ ($mm^2$) = total expanded area of corroded steel bar. The strain induced in the thick wall cylinder, applied perpendicular to the corroded longitudinal reinforcement, was then calculated from:

$$\varepsilon = \frac{(d_{exp} - d_b)}{(d_b + (2 \times c))} \quad (8\text{-}14)$$

where: $\varepsilon$ (millistrain) = corrosion-induced strain in the reinforcement, $d_{exp}$ (mm) = diameter of steel bars expanded, $d_b$ (mm) = original diameter of steel bars, $c$ (mm) = concrete cover.

The same procedure was used to calculate the corrosion-induced strain in a single leg of stirrup. However, in the 2D FE model both legs in the stirrup were assumed to be corroding at the same rate and level, and therefore the compressive pre-strain was adjusted by averaging the strains in each leg over the width of the beam as follows (see **Figure 8-5**):

$$\varepsilon_{avg} = ( \varepsilon_1 + \varepsilon_2 ) \times \left( \frac{2( d_b + 2c)}{b} \right) \quad (8\text{-}15)$$

where: $\varepsilon_{avg}$ (millistrain) = average of corrosion-induced strains for both legs of the stirrup, $\varepsilon_1$ (millistrain) = corrosion-induced strain for the first leg of the stirrup, $\varepsilon_2$ (millistrain) = corrosion-induced strain for the second leg of the stirrup, $d_b$ (mm) = original diameter of the stirrup, $c$ (mm) = concrete cover, $b$ (mm) = beam width.

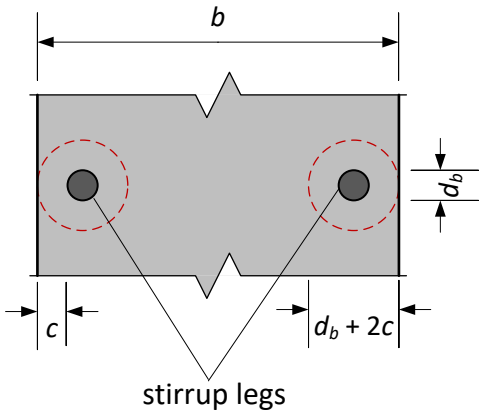
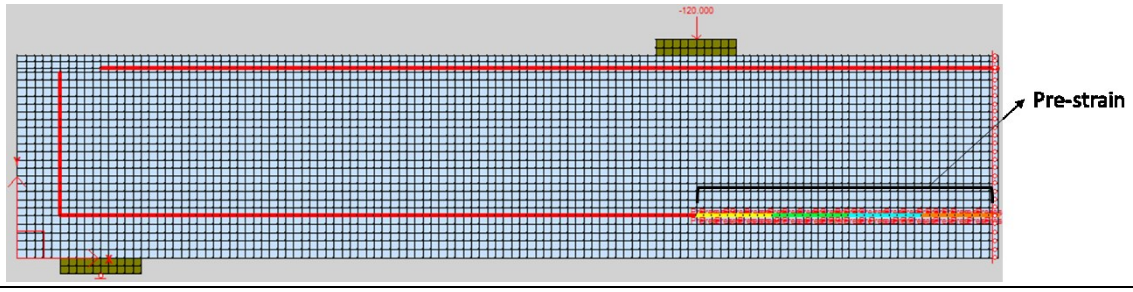
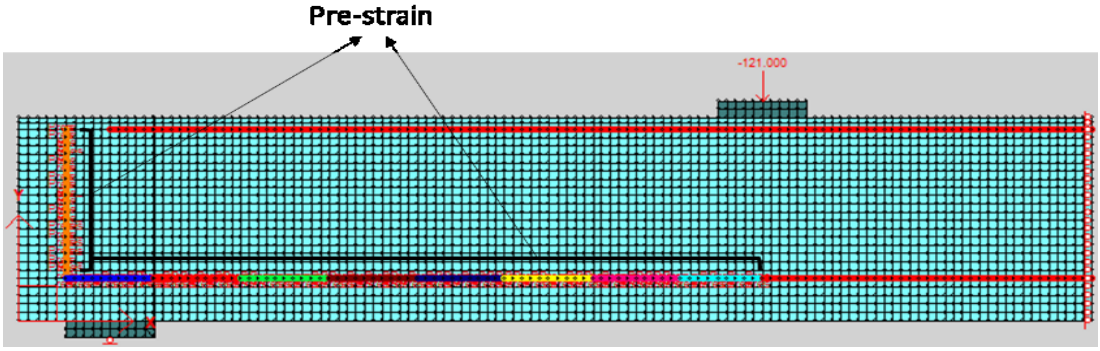


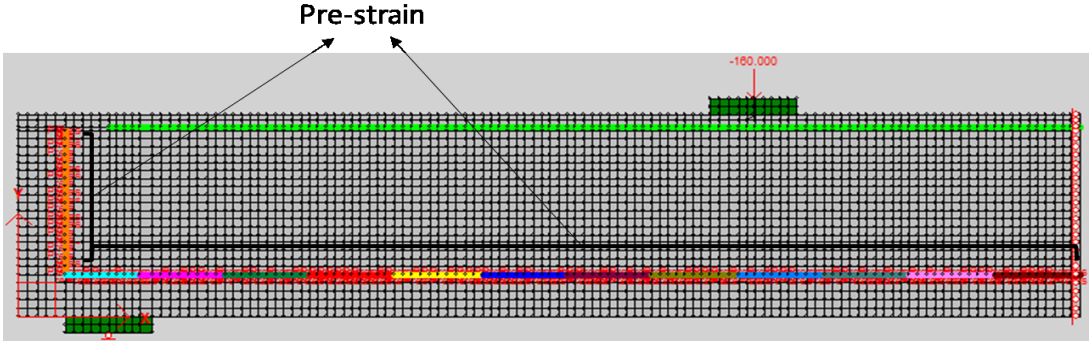

Figure 8-5 Applying corrosion-induced strains on stirrups in RC beam (adapted from Bernard, 2013)



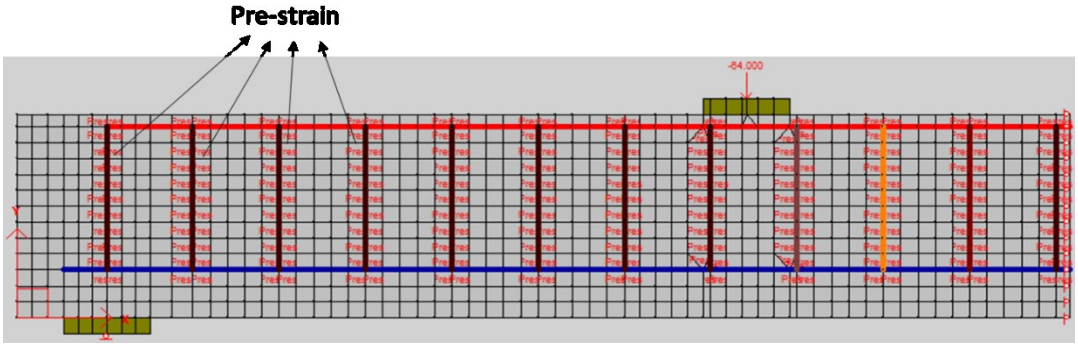

a) Beams with mid-span corrosion




b) Beams with corrosion at the ends




c) Beams with full-length corrosion




d) Beams with shear reinforcement corrosion

Figure 8-6 Locations of applied equivalent pre-strains for various beam types

Table 8-3 Equivalent pre-strains with corresponding mass loss

| Beam ID | $M_{loss}$ (%) | Location of pre-strain | μ | b (mm) | c (mm) | $A_s$ ($mm^2$) | $d_b$ (mm) | $A_{s(exp)}$ ($mm^2$) | $d_{exp}$ (mm) | ε (millistrain) |
|---|---|---|---|---|---|---|---|---|---|---|
| B-MC-10M-13% | 13 | Longitudinal (middle) | 2 | 125 | 40 | 100.23 | 11.3 | 112.84 | 11.98 | 7.55 |
| B-MC-10M-14% | 14 | Longitudinal (middle) | 2 | 125 | 40 | 100.23 | 11.3 | 113.77 | 12.03 | 8.00 |
| B-SC-10M-11% | 11 | Longitudinal (ends) | 2 | 125 | 40 | 100.23 | 11.3 | 110.95 | 11.88 | 6.45 |
| B-FC-10M-13% | 13 | Longitudinal (full-length) | 2 | 125 | 40 | 100.23 | 11.3 | 112.84 | 11.98 | 7.55 |
| B-MC-15M-10% | 10 | Longitudinal (middle) | 2 | 125 | 40 | 200.96 | 16 | 220.55 | 16.76 | 7.93 |
| B-SHC-25M-10% | 10 | Transverse (stirrups) | 2 | 125 | 12.5 | 31.15 | 6.3 | 34.19 | 6.59 | 9.59 |
| B-SHC-25M-12% | 12 | Transverse (stirrups) | 2 | 125 | 12.5 | 31.15 | 6.3 | 34.78 | 6.65 | 11.41 |

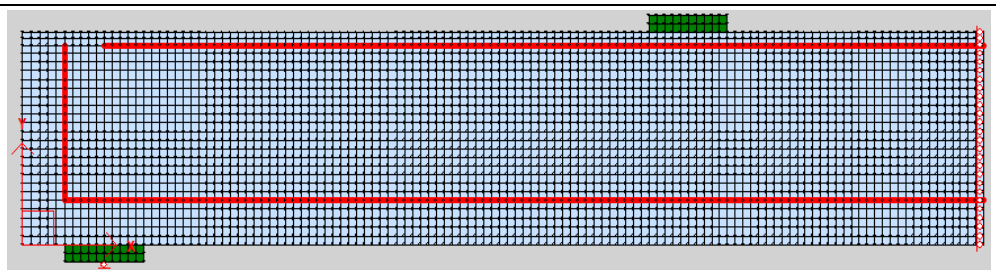
b = Beam width; c = Concrete cover; $A_s$ = Original steel bar area; $d_b$ = Original diameter of steel bar; $A_{s(exp)}$ = Total expanded area of corroded steel bar; $d_{exp}$ = Diameter of steel bars expanded; ε = Corrosion-induced equivalent pre-strain in the concrete.

### 8.3 Mesh Size Sensitivity

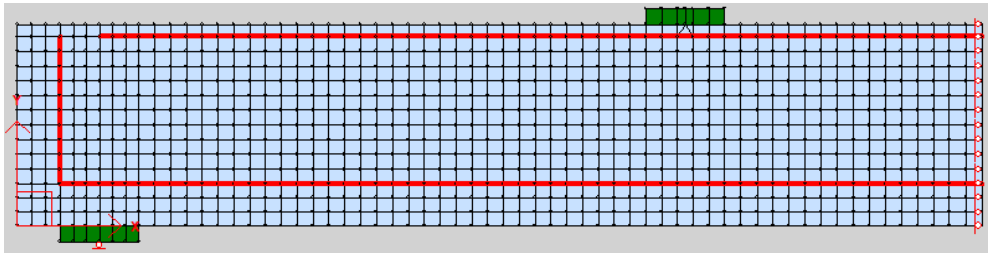
The optimal mesh size was selected based on a mesh sensitivity analysis. The accuracy of the FE model was examined by gradually decreasing the mesh size and comparing the ultimate loads in the models and experiments. For the flexure-governed beams, four mesh sizes of 40 mm, 30 mm, 20 mm, and 10 mm were considered as shown in **Figure 8-7**. The analysis was conducted on the control (un-corroded) 10M beam. The first mesh (40 mm) resulted in 344 elements and an ultimate load of 66.7 kN; the second mesh (30 mm) resulted in 676 elements and an ultimate load of 64.6 kN; the third mesh (20 mm) had 1,007 elements with a maximum load of 62.6 kN; and the final mesh (10 mm) resulted in 3,337 elements and an ultimate load of 61.6 kN. As shown in **Figure 8-8**, the ultimate load of the un-corroded 10M beam was found to converge at 10 mm; this mesh also resulted in the best approximation when comparing the experimental and FE load-deflection curves.

For the shear-governed beams, three mesh sizes were examined: 20 mm, 30 mm, and 40 mm, with 1,064, 579 and 495 elements, respectively, as shown in **Figure 8-9**. Considering the control 25M

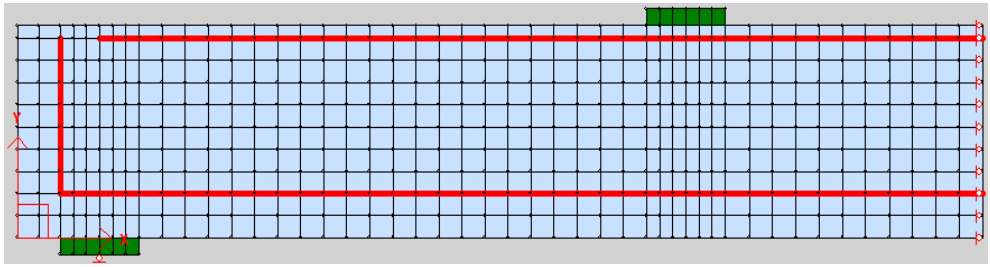
beam, the ultimate strengths for the 20-mm, 30-mm and 40-mm mesh cases were 197.7 kN, 199.8 kN and 199.6 kN, respectively. While no clear trend was observed when comparing the maximum strengths, the different meshes result in distinct load-deflection responses as shown in **Figure 8-10**. Based on this analysis, the 20-mm mesh size was deemed to be the most suitable as it provided the most reasonable numerical result when compared with the experimental load-deflection response.



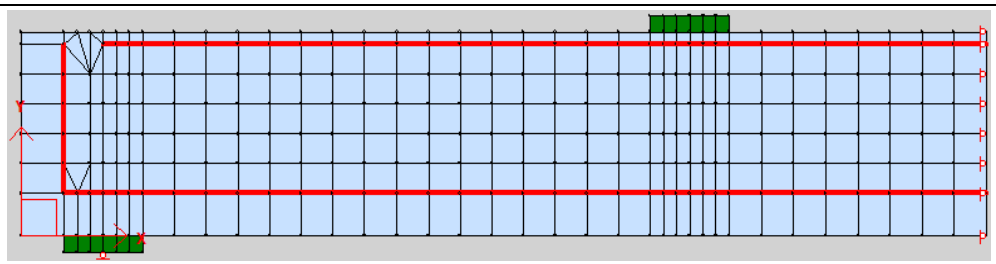
a) 10 mm mesh



b) 20 mm mesh

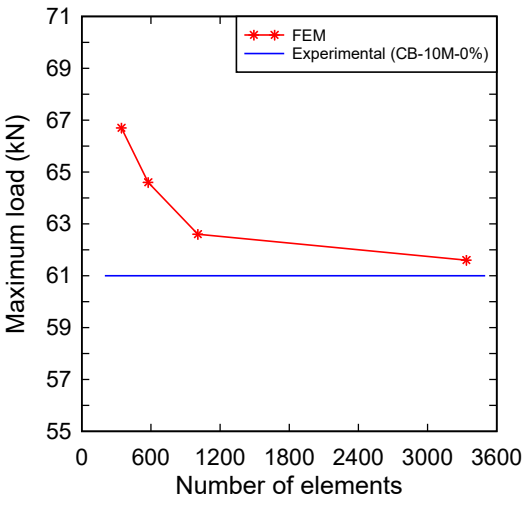


c) 30 mm mesh

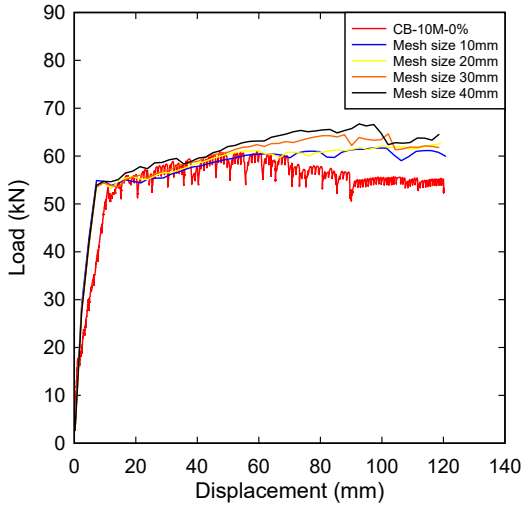


d) 40 mm mesh

Figure 8-7 Mesh sizes considered in the analysis of beam CB-10-0% (flexure-dominant)

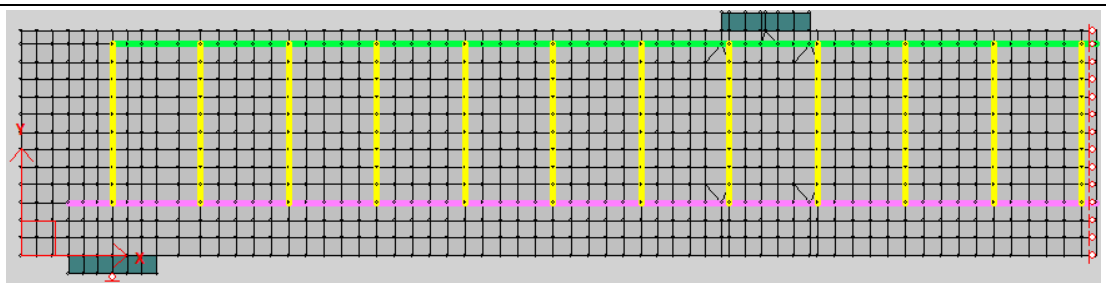



a) Max. load vs No. of elements

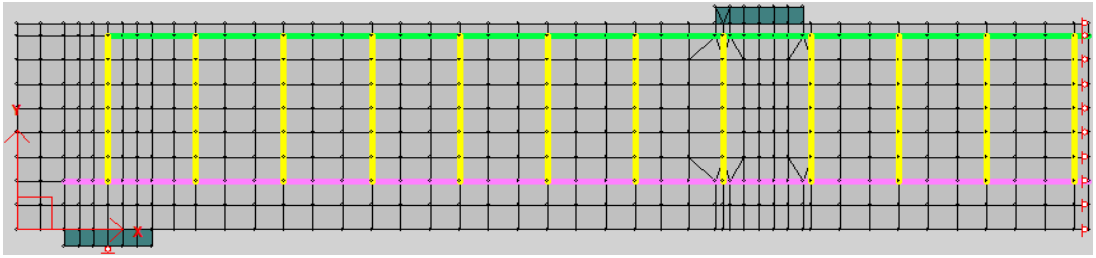



b) Load-deflection response

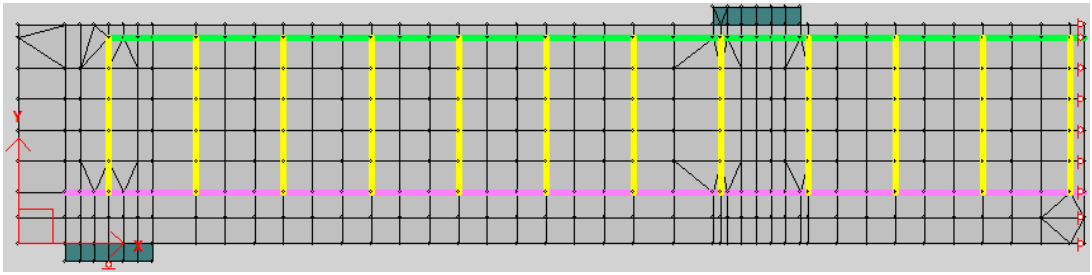
Figure 8-8 Mesh size sensitivity in beam CB-10M-0%



a) 20 mm



b) 30 mm



c) 40 mm

Figure 8-9 Mesh sizes considered in the analysis of beam CB-25M-0% (shear-dominant)

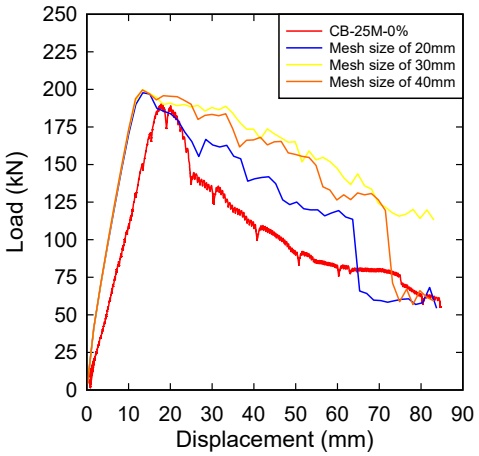
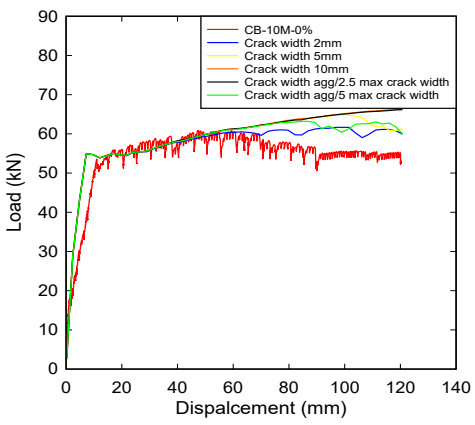



Figure 8-10 Experimental vs simulated load-deflection curves for beam CB-25M-0%

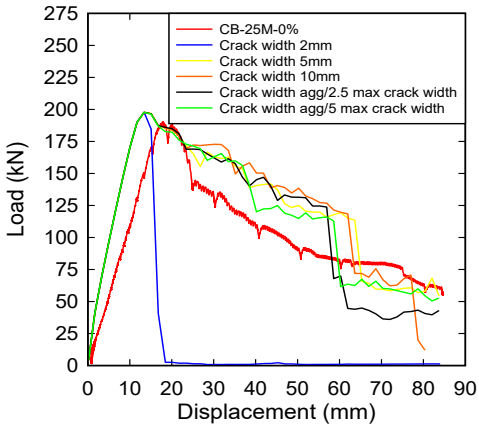
## 8.4 Crack width sensitivity

A sensitivity analysis was also conducted to select the most appropriate crack width parameter in the FE models, as shown in **Figure 8-11**. This crack width is a limit defined in VecTor2 above, which average compressive stresses are reduced. This was implemented to model the inability of concrete to transmit compressive stresses across large cracks. As noted by Bernard (2013), the selection of crack width limit can significantly affect the strength and deformation capacities of the beam model. Moreover, this limit should not be omitted in order for aggregates to properly interlock and transfer stresses at a crack, and therefore should be adjusted based on the reinforcement arrangement (Bernard, 2013). By default, VecTor2 sets the crack width limit to a conservative value of agg/10, where agg is the maximum aggregate size (i.e., for the default aggregate size of 10 mm, the crack width limit is set to 1 mm). In the current study, different crack width limits were considered, including: 2 mm, 5 mm, 10 mm, agg/2.5, and agg/5, with agg = 19 mm for the concrete used in this study. For the flexure-governed beams (CB-10M-0%), a maximum crack width of 2 mm resulted in the most acceptable results as shown in **Figure 8-11 (a)**. While all cases showed similar stiffness, yield load and maximum load, the 2-mm case resulted in the best approximation of post-peak response and ductility. Setting the crack width limit at 2 mm was considered conservative since crack widths beyond this value were expected in RC beams (Bernard, 2013). Bernard (2013) suggested a crack width limit of 10 mm (or half the aggregate size) to engage aggregate interlock in the shear resistance mechanism. In the current analysis, a maximum crack width of 5 mm was found to be the most appropriate for the shear-governed beams

(CB-25M-0%) when considering the pre-peak and post-peak responses as illustrated in **Figure 8-11 (b)**.




a) CB-10M-%




b) CB-25M-0%

Figure 8-11 Crack width sensitivity: results for beams CB-10M-0% and CB-25M-0%

## 8.5 Sensitivity of different corrosion modeling features on the FE model results

The effects of corrosion were considered using several modeling features including reduction in steel bar cross-sectional area (Ared), modification of stress-strain response (SS), and introducing corrosion-induced cracking using applied pre-strains (PS). To better study the effects of these features and their combination, several analysis cases were considered in the FE models as shown in **Table 8-4**. According to the sensitivity analysis, it was found that case 4 was generally most suitable for the corroded beams as will be discussed in the following sections.

Table 8-4 FE analysis cases considering different corrosion modelling features

| Case # | ID | Reduction in steel bar area (Ared) | Stress-strain modifications (SS) | Pre-strain (concrete damage) (PS) |
|---|---|---|---|---|
| **Case 1** | No effect | | | |
| **Case 2a** | (Ared) | x | | |
| **Case 2b** | (SS) | | x | |
| **Case 2c** | (PS) | | | x |
| **Case 3** | (Ared+SS+PS) | x | x | x |
| **Case 4** | (SS+PS) | | x | x |

## 8.6 Numerical Results

### 8.6.1 Flexure-governed beams

Finite element modelling was first conducted to predict the responses of the flexure-dominant beams in the 10M and 15M series. The analysis included seven beams with different corrosion scenarios (controls, mid-corrosion, end-corrosion, and full-corrosion).

#### 8.6.1.1 Control Beams (0% mass loss): CB-10M-0% and CB-15M-0%

Beams CB-10M-0% and CB-15M-0% were control specimens which were built with 2-10M and 2-15M tension bars, respectively. The beams were modelled without the effects of corrosion.

Analysis of both beams was conducted using a 10×10 mm mesh. Truss bar elements were used to model the longitudinal reinforcement, while the stirrups were smeared in the concrete elements (refer to **Figure 8-14 (a)** and **Figure 8-15 (a)**). **Table 8-5** presents a summary of the FE and experimental results. The load-deflection responses are compared in **Figure 8-12**, while **Figure 8-13** provides a comparison of the experimental and simulated cracking patterns. **Figure 8-14** and **Figure 8-15** provide a summary of steel reinforcement and concrete stresses from the FE models.

In general, the FE models resulted in good predictions of the load-deflection response for both beams. Considering beam CB-10M-0%, the FE model resulted in yield ($P_y$) and ultimate loads ($P_{max}$) of 55 kN and 62 kN, respectively, with numerical-to-experimental ratios of $\frac{P_{y_{FE}}}{P_y}$ = 1.01, $\frac{P_{max_{FE}}}{P_{max}}$ = 1.01. However, the stiffness was over-estimated as shown in **Figure 8-12 (a)**. The maximum displacement ($\Delta_{max}$) was well predicted, with the beam showing an ability to carry load at the end of the simulation, which matches the experimental result.

For beam CB-15M-0%, the FE model resulted in a yield and ultimate strengths of 99 kN and 109 kN, with corresponding ratios of $\frac{P_{y_{FE}}}{P_y}$ = 0.93 and $\frac{P_{max_{FE}}}{P_{max}}$ = 0.99. However, the stiffness was over-estimated as shown in **Figure 8-12 (b)**. The maximum displacement was slightly over-estimated with a $\frac{\Delta_{max_{FE}}}{\Delta_{max}}$ = 1.18; however, the simulation showed the same sudden drop in load. In general, the FE load-deflection response showd a good match with the experimental result.

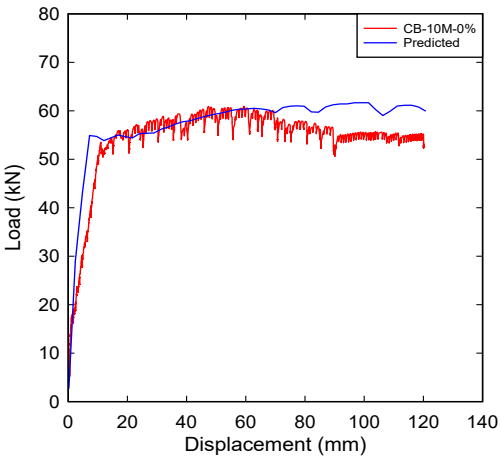
Examining **Figure 8-13**, it was observed that the FE cracking patterns, and failure modes match well with the experiments for both beams. The steel and concrete stresses profiles in **Figure 8-14** and **Figure 8-15** further demonstrate that failure occurred after significant yielding of the tension steel reinforcement, with crushing of the concrete in the top cover region. The results for the 10M beam showed that the tension steel reached maximum stresses of 615 MPa at the point of maximum load, indicating that the steel was in the strain hardening range. The maximum compressive stresses in the concrete reached $f_c'$ (35 MPa) at maximum load which indicates crushing. Similar effects was observed for the beam with 15M bars. The maximum strains at the tension bar level reached 44 mm/m and 27 mm/m in beams CB-10M-0% and CB-15M-0% at the end of testing, which were below the ultimate strain of the steel reinforcement ($\varepsilon_u$ = 100 mm/m).

Table 8-5 Experimental and simulation results for CB-10M-0% and CB-15M-0%

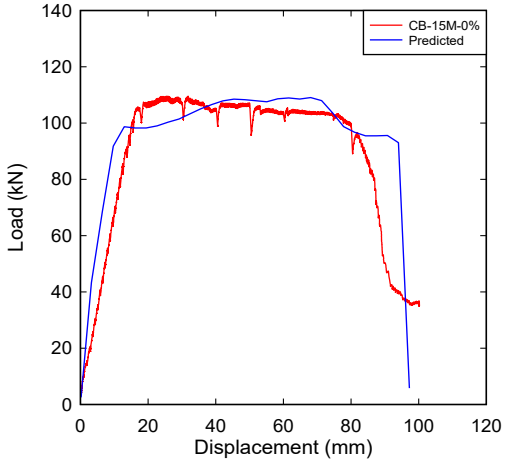
| Beam ID | Load (kN) | | | | $\frac{P_{max_{FE}}}{P_{max}}$ | $\frac{P_{y_{FE}}}{P_y}$ | Displ.(mm) | | $\frac{\Delta_{max_{FE}}}{\Delta_{max}}$ | Predicted failure mode |
|---|---|---|---|---|---|---|---|---|---|---|
| | Exp. | | FE | | | | Exp. | FE | | |
| | $P_{max}$ | $P_y$ | $P_{max_{FE}}$ | $P_{y_{FE}}$ | | | $\Delta_{max}$ | $\Delta_{maxFE}$ | | |
| CB-10M-0% | 61 | 54 | 62 | 55 | 1.01 | 1.01 | 120 | 120 | 1.00 | Flexural failure with steel yielding and concrete crushing |
| CB-15M-0% | 110 | 106 | 109 | 99 | 0.99 | 0.93 | 82 | 94 | 1.14 | Flexural failure with steel yielding and concrete crushing |
| Average<br>(S.D.)<br>(C.V.) | - | - | - | - | 1.00<br>(0.01)<br>(1.00) | 0.97<br>(0.04)<br>(4.12) | - | - | 1.07<br>(0.07)<br>(6.54) | - |

$P_{max}$, $P_y$ and $\Delta_{max}$: experimental ultimate strength, yield strength and maximum displacement;

$P_{max(FE)}$, $P_{y(FE)}$, $\Delta_{max(FE)}$: numerical ultimate strength, yield strength and maximum displacement.




a) CB-10M-0%




b) CB-15M-0%

Figure 8-12 Load-deflection curves: 10M and 15M controls

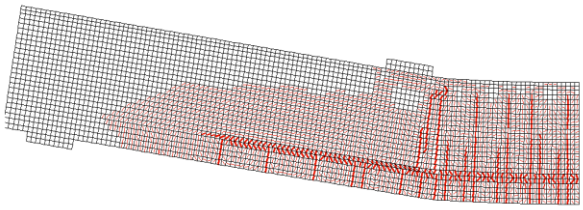
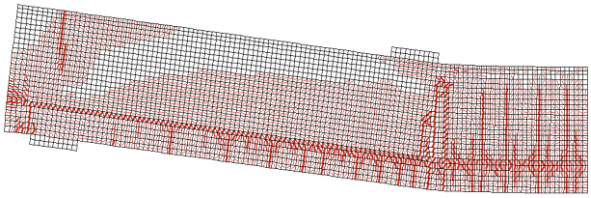
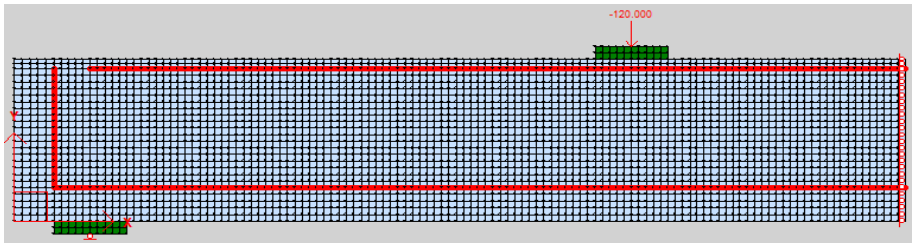
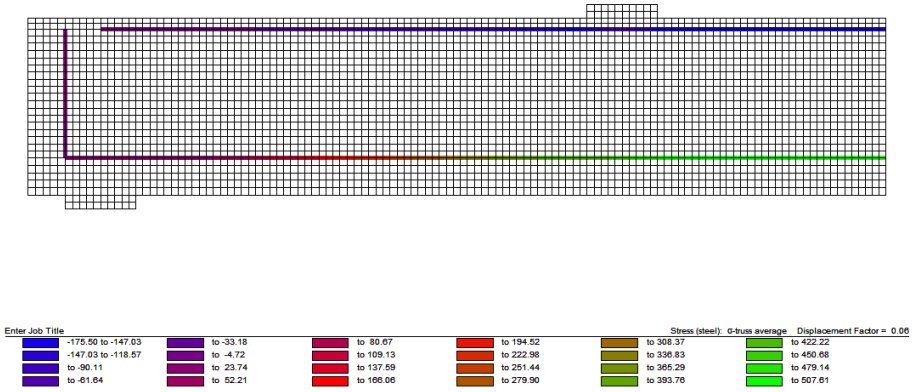
| Experimental | Simulation |
|---|---|
|  |  |
| a) CB-10M-0% | |
|  |  |
| b) CB-15M-0% | |

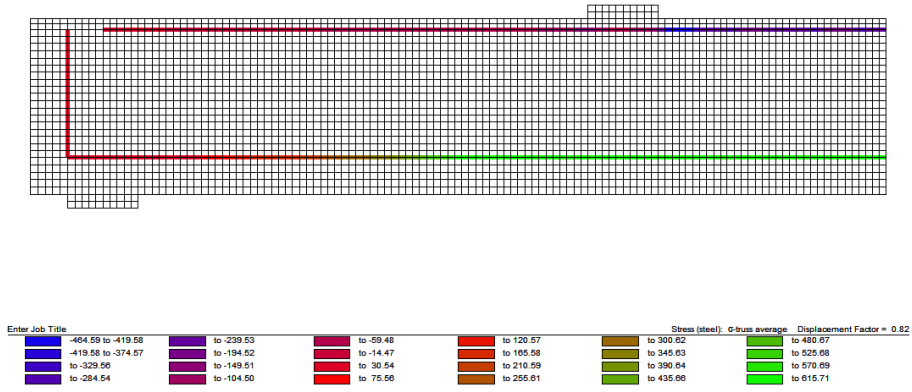
Figure 8-13 Failure mode and cracking patters (experimental vs simulation)



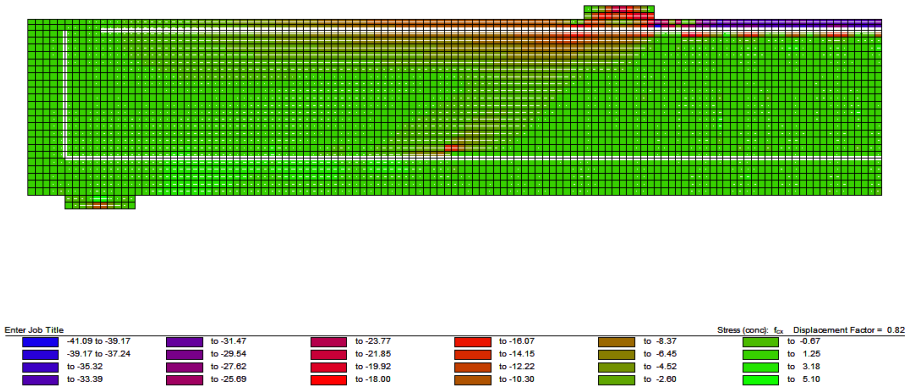

a) Finite element layout




b) Stress distribution in steel at yielding

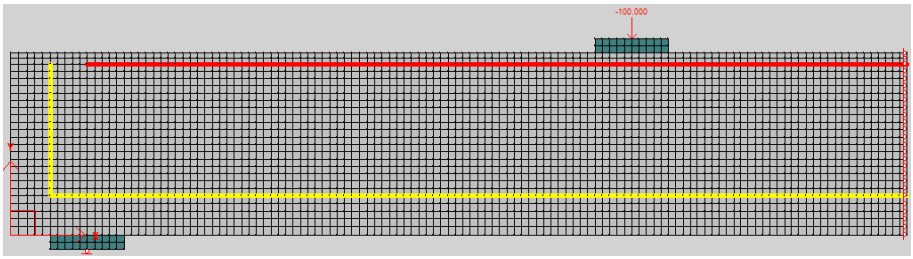



c) Stress distribution in steel at peak load

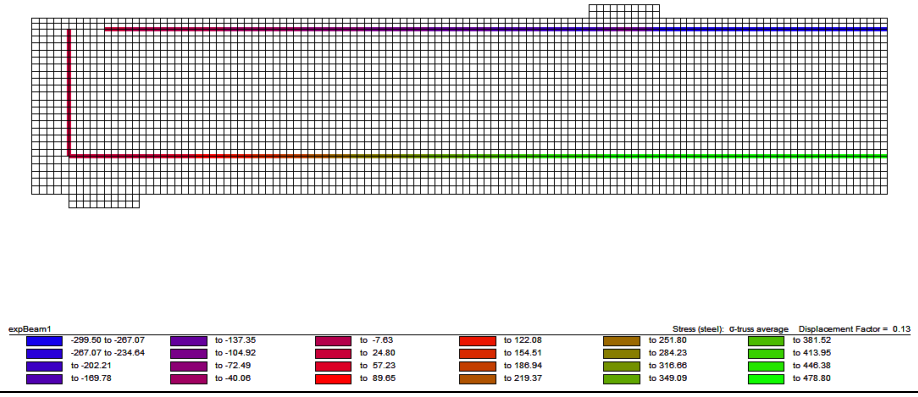



d) Stress distribution in concrete at peak load

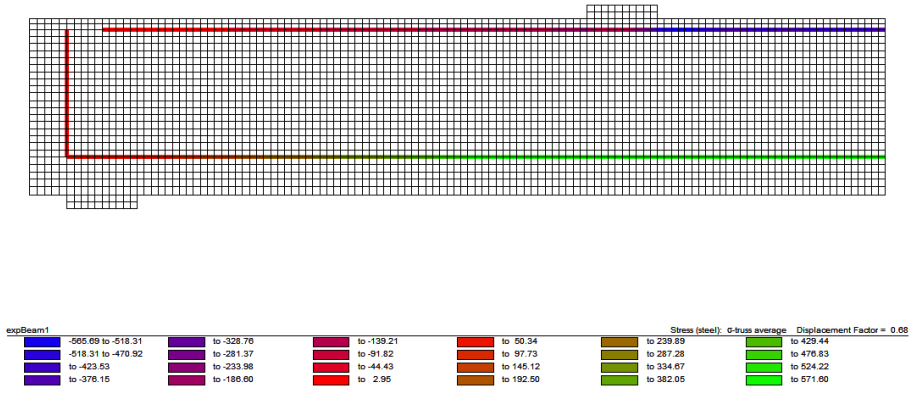
Figure 8-14 Finite element results of beam (CB-10M-0%)



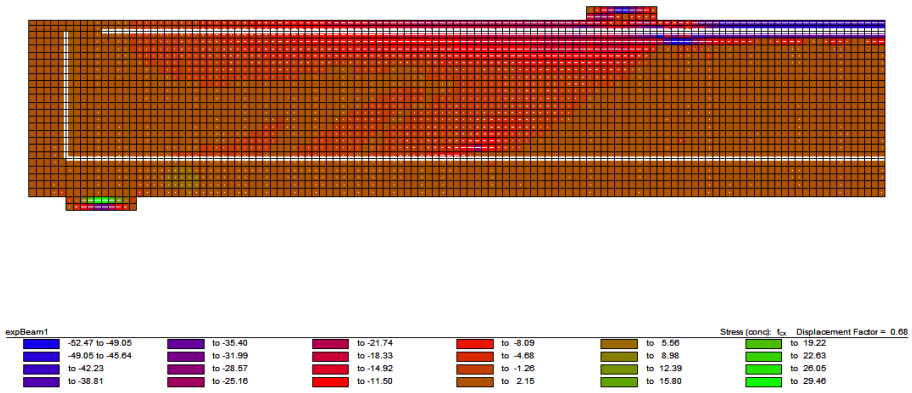

a) Finite element layout




b) Stress distribution in steel at yielding




c) Stress distribution in steel at peak load




d) Stress distribution in concrete at peak load

Figure 8-15 Finite element results of beam (CB-15M-0%)

#### 8.6.1.2 Mid corrosion: B-MC-10M-13%, B-MC-10M-14% and B-MC-15M-10%

This section presents the FE results of beams B-MC-10M-13%, B-MC-10M-14% and B-MC-15M-10%, which were subjected to mid-span corrosion. The FE models used a 10×10 mm mesh, with truss bar elements and smeared reinforcement for the longitudinal and transverse reinforcement, respectively. Corrosion damage was modelled by reducing the steel area, modifying the steel stress-strain properties, and inducing cracking in the concrete elements surrounding the mid-span longitudinal bars over a length of 750 mm (refer to **Figure 8-18 (a)**, **Figure 8-19 (a)**, and **Figure 8-20 (a)**).

Various analysis cases were considered as listed in **Table 8-4**, including case 1: without corrosion effects, cases 2a-2b-2c, which considered each modelling feature separately (Ared, SS or PS only), and cases 3 and 4, which combined different features (Ared + SS + PS or SS + PS). **Figure 8-16** and **Table 8-6** compare the FE and experimental results for all cases. **Figure 8-17** provides a comparison of cracking patterns (case 4), while **Figure 8-18** to **Figure 8-20** provide a summary of steel reinforcement and concrete stresses from the FE models (case 4).

By comparing the load-deflection responses in **Figure 8-16**, it was observed that the results were more sensitive to the reduction in bar area or modification of steel stress-strain properties, compared to the introduction of initial pre-strains. In general, case 4 produced the most suitable results, while case 3 resultd in over-estimation of corrosion effects.

For B-MC-10M-13%, case 2a (Ared), case 2b (SS) and case 4 (SS+PS) showed good agreement with the test results, when comparing yield strength, ultimate strength, maximum displacement, and failure mode, since both the reduction in bar area and modified stress-strain properties considered the effects of mass loss. Case 4, which incorporated stress-strain modification and concrete-induced cracking, resulted in prediction ratios of $\frac{P_{y_{FE}}}{P_y} = 1.00$, $\frac{P_{max_{FE}}}{P_{max}} = 1.01$ and $\frac{\Delta_{max_{FE}}}{\Delta_{max}} = 0.97$. Conversely, case 3 (which combines all features) showed an under-estimation of beam response. Likewise, the response of the corroded beams was over-estimated by case 1 (no corrosion) and case 2c (PS only) (see **Figure 8-16 (a)** and **Table 8-6**). As shown in **Figure 8-17 (a)**, the case 4 FE model resulted in good prediction of cracking patterns and flexural failure mode. **Figure 8-18 (c)** shows that the maximum stress in the steel reinforcement reached 521 MPa at peak load, just below the ultimate tensile stress in the corroded steel bar model ($f_u$ = 547 MPa).

Examination of the strain data showd the development of high strains at the crack locations, with a maximum tensile strain of 41 mm/m in the 10M steel bars (the strains are significant but below $\varepsilon_u$ = 90 mm/m used in the steel model). The maximum stress in the concrete reached above $f_c'$ (40 MPa) at the peak load, which indicates concrete crushing and matches with the experimental failure mode.

A similar trend was observed for beam B-MC-10M-14%; reasonable agreement was obtained for cases 2a, 2b and 4, while cases 1/2c resulted in over-estimation of the response parameters (see **Figure 8-16 (b)** and **Table 8-6**). Case 3 showed a reasonable prediction of maximum strength and ductility, with higher stiffness and lower yield strength when compared to the test result (see **Figure 8-16 (b)** and **Table 8-6**). Case 2a, case 2b, case 3 and case 4 showed that the beam failed in flexure with a sudden drop in load due to rupture of the tension bars, which matches the experimental result (see **Figure 8-17 (b)**); conversely, bar rupture did not occur in cases 1 and 2c. **Figure 8-19 (c)** shows the maximum stress in the tension steel reinforcement at peak load reached the ultimate stress used in the steel model ($f_u$ = 539 MPa). Inspection of the strain data showed the development of large tensile strains (above 70 mm/m) where bar rupture occurred. The recorded stress in the tension steel reinforcement was lost at the end of testing, which further confirms the bar rupture failure.

Same cases were also considered for beam B-MC-15M-10%; however, the post-peak response was generally over-estimated in the FE models. As such, case 5, which incorporated case 4 features and an elasto-plastic steel tension model, was also considered in the analysis. With this modification, case 5 resulted in the following prediction ratios: $\frac{P_{y_{FE}}}{P_y}$ = 1.07, $\frac{P_{max_{FE}}}{P_{max}}$ = 1.01 and $\frac{\Delta_{max_{FE}}}{\Delta_{max}}$ = 1.11. Reasonable results for yield strength were obtained for cases 2a, 2b and 4, while this result was over-estimated by cases 1/2c and under-estimated by case 3. In general cases 1-4 resulted in over-prediction of ductility, while a more accurate result was obtained for case 5. At peak load, the maximum stress in the tension steel reached 478 MPa, which matches the yield stress used in the elastic-plastic steel model for this beam (see **Figure 8-20 (c)**). Significant localized cracking was observed in the FE model. The maximum stress in the concrete reacheed $f_c'$ (44 MPa) at peak load, which indicates concrete crushing and matches with the experimental failure mode (see **Figure 8-20 (d)** and **Figure 8-17 (c)**).

Table 8-6 Experimental and simulation results for beams with mid corrosion

| Beam ID | Case ID | Load (kN) | | | | $\frac{P_{max_{FE}}}{P_{max}}$ | $\frac{P_{y_{FE}}}{P_y}$ | Displ.(mm) | | $\frac{\Delta_{max_{FE}}}{\Delta_{max}}$ | Predicted failure mode |
|---|---|---|---|---|---|---|---|---|---|---|---|
| | | Exp. | | FE | | | | Exp. | FE | | |
| | | $P_{max}$ | $P_y$ | $P_{maxFE}$ | $P_{yFE}$ | | | $\Delta_{max}$ | $\Delta_{maxFE}$ | | |
| B-MC-10M-13% | Case 1 | 52 | 48 | 61 | 56 | 1.17 | 1.17 | 66 | 64 | 0.97 | Flexural failure with steel yielding, significant cracks in tension zone, and crushing at beam mid-span |
| | Case 2a | | | 55 | 50 | 1.05 | 1.04 | | 64 | 0.97 | |
| | Case 2b | | | 54 | 48 | 1.03 | 1.00 | | 64 | 0.97 | |
| | Case 2c | | | 61 | 56 | 1.17 | 1.17 | | 64 | 0.97 | |
| | Case 3 | | | 47 | 42 | 0.90 | 0.90 | | 64 | 0.97 | |
| | Case 4 | | | 53 | 48 | 1.01 | 1.00 | | 64 | 0.97 | |
| B-MC-10M-14% | Case 1 | 53 | 49 | 62 | 55 | 1.17 | 1.12 | 71 | 118 | 1.66 | Flexural failure associated with bar rupture in tension zone |
| | Case 2a | | | 56 | 48 | 1.05 | 0.98 | | 89 | 1.25 | |
| | Case 2b | | | 55 | 45 | 1.04 | 0.92 | | 106 | 1.49 | |
| | Case 2c | | | 62 | 55 | 1.17 | 1.12 | | 121 | 1.70 | |
| | Case 3 | | | 47 | 40 | 0.89 | 0.82 | | 75 | 1.05 | |
| | Case 4 | | | 54 | 45 | 1.02 | 0.92 | | 106 | 1.49 | |
| B-MC-15M-10% | Case 1 | 87 | 82 | 109 | 98 | 1.25 | 1.19 | 42 | 85 | 2.02 | Flexural failure with steel yielding, significant cracks in tension zone, and crushing at beam mid-span |
| | Case 2a | | | 107 | 88 | 1.23 | 1.07 | | 94 | 2.23 | |
| | Case 2b | | | 106 | 84 | 1.21 | 1.02 | | 91 | 2.17 | |
| | Case 2c | | | 108 | 98 | 1.24 | 1.19 | | 90 | 2.14 | |
| | Case 3 | | | 95 | 76 | 1.09 | 0.93 | | 81 | 1.92 | |
| | Case 4 | | | 102 | 84 | 1.17 | 1.02 | | 78 | 1.85 | |
| | Case 5 | | | 88 | 88 | 1.01 | 1.07 | | 47 | 1.11 | |

| All beams | Case ID | $\frac{P_{max_{FE}}}{P_{max}}$ | | $\frac{P_{y_{FE}}}{P_y}$ | | $\frac{\Delta_{max_{FE}}}{\Delta_{max}}$ | |
|---|---|---|---|---|---|---|---|
| | | Avg. | S.D. (C.V) | Avg. | S.D. (C.V) | Avg. | S.D. (C.V) |
| Statistical data | Case 1 | 1.19 | 0.04 (3.36) | 1.16 | 0.03 (2.58) | 1.55 | 0.43 (27.74) |
| | Case 2a | 1.11 | 0.08 (7.20) | 1.03 | 0.04 (3.88) | 1.48 | 0.54 (36.48) |
| | Case 2b | 1.09 | 0.08 (7.33) | 0.98 | 0.04 (4.08) | 1.54 | 0.49 (31.81) |
| | Case 2c | 1.19 | 0.03 (2.52) | 1.16 | 0.03 (2.58) | 1.60 | 0.48 (30.00) |
| | Case 3 | 0.96 | 0.09 (9.37) | 0.88 | 0.04 (4.54) | 1.31 | 0.43 (32.82) |
| | Case 4 | 1.67 | 0.07 (4.19) | 0.98 | 0.04 (4.08) | 1.43 | 0.36 (25.17) |

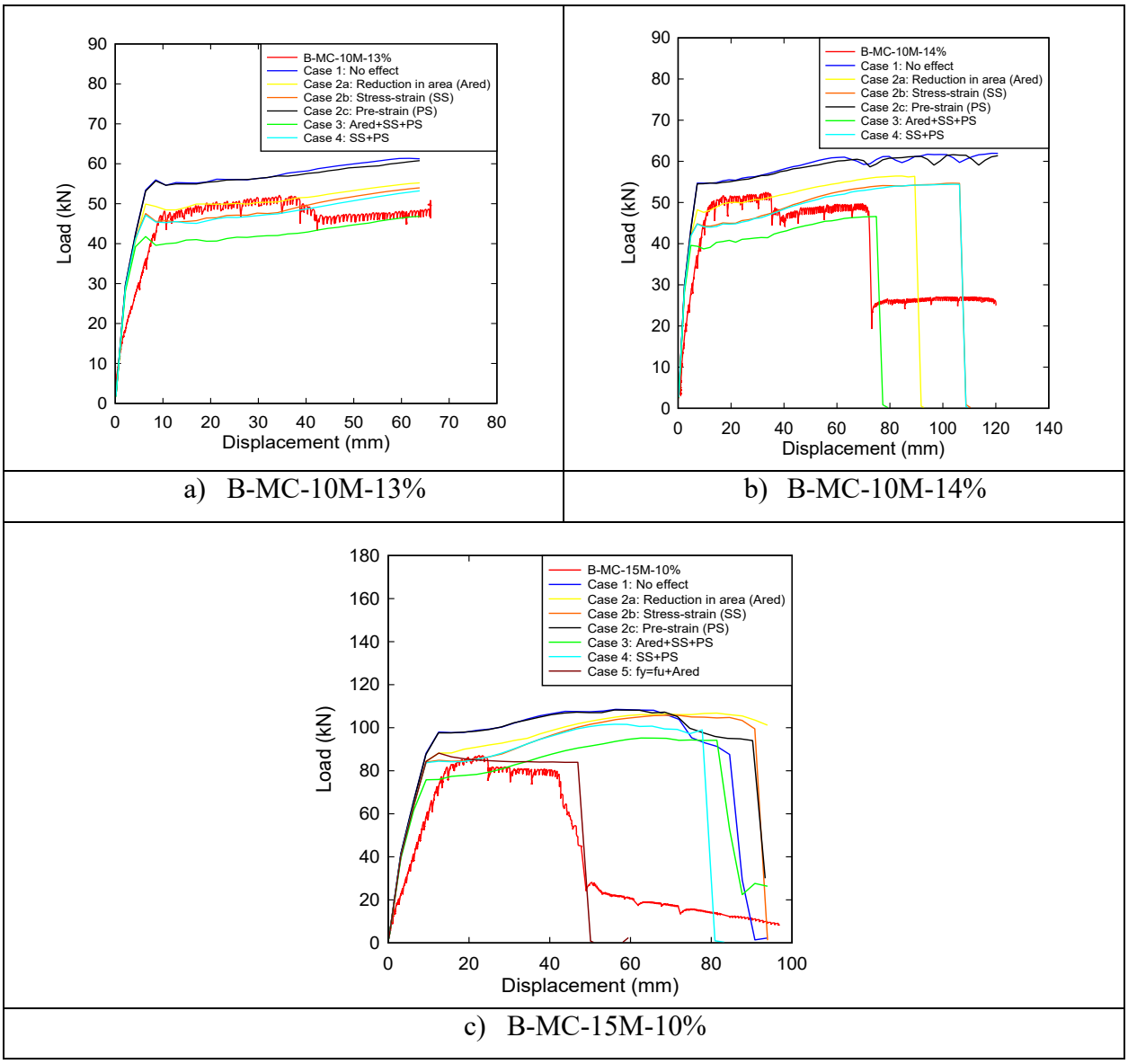



Figure 8-16 Load-deflection responses for three beams with mid-corrosion

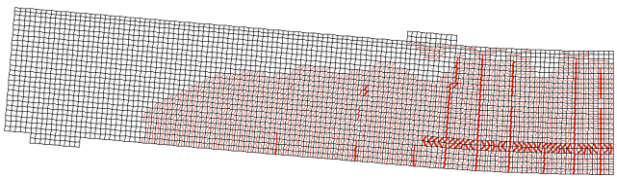
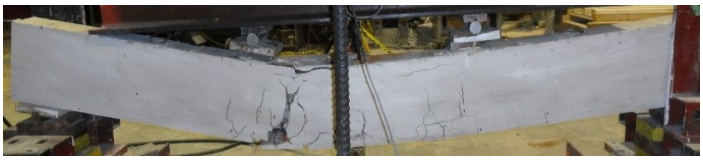
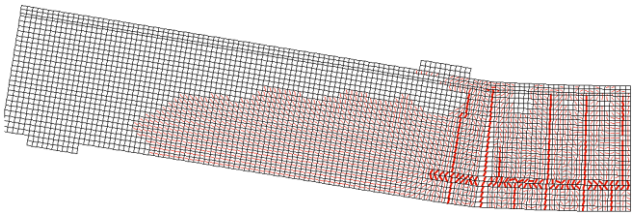
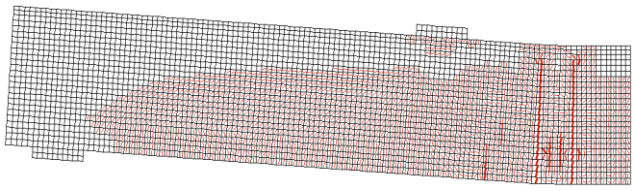
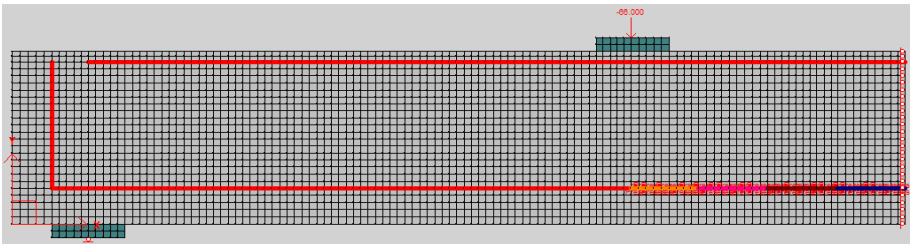
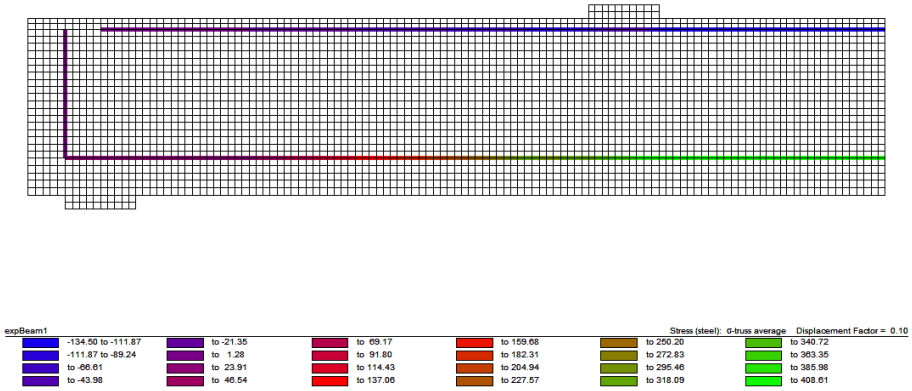
| Experimental | Simulation |
| --- | --- |
|  |  |
| a) B-MC-10M-13% (case 4) | |
|  |  |
| b) B-MC-10M-14% (case 4) | |
|  |  |
| c) B-MC-15M-10% (case 5) | |

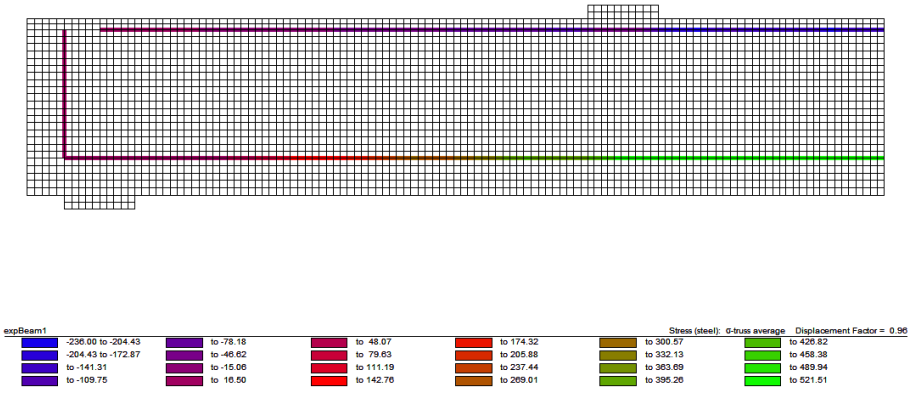
Figure 8-17 Failure mode and crack patterns (experimental vs simulation)



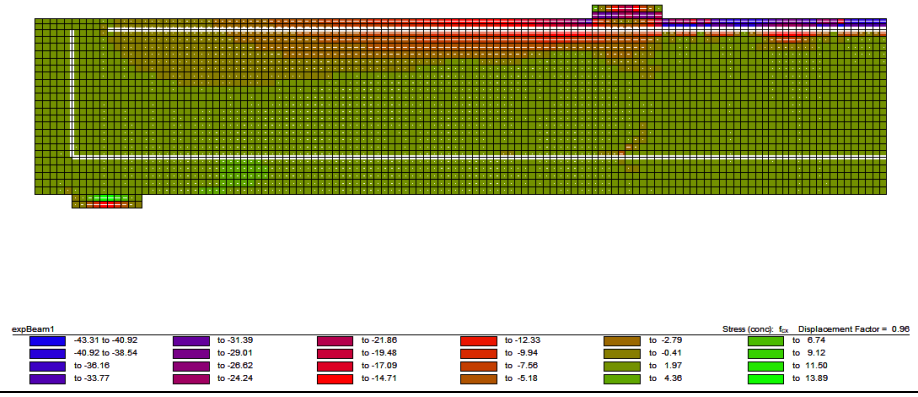

a) Finite element mesh




b) Stress distribution in steel at yielding

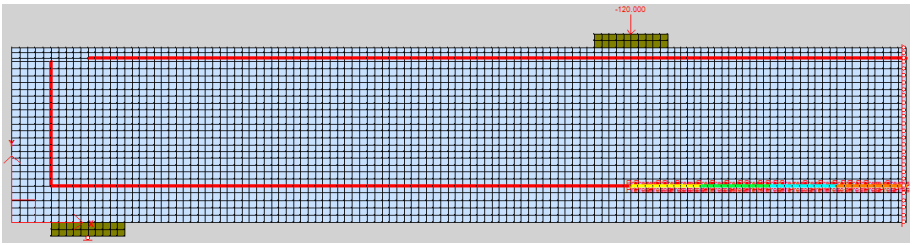



c) Stress distribution in steel at peak load

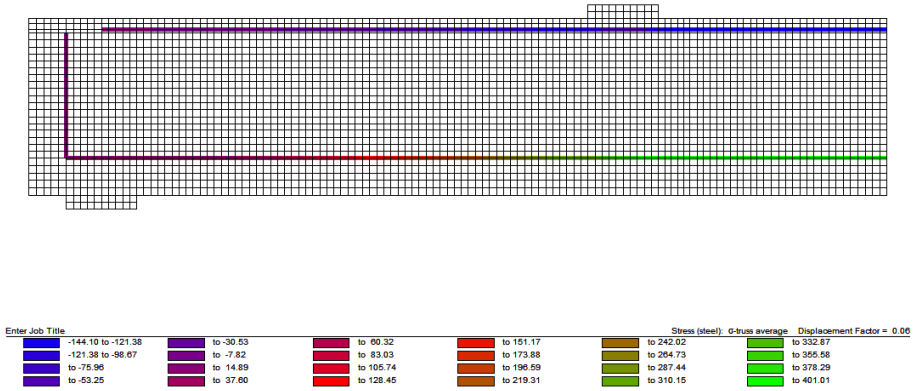



d) Stress distribution in concrete at peak load

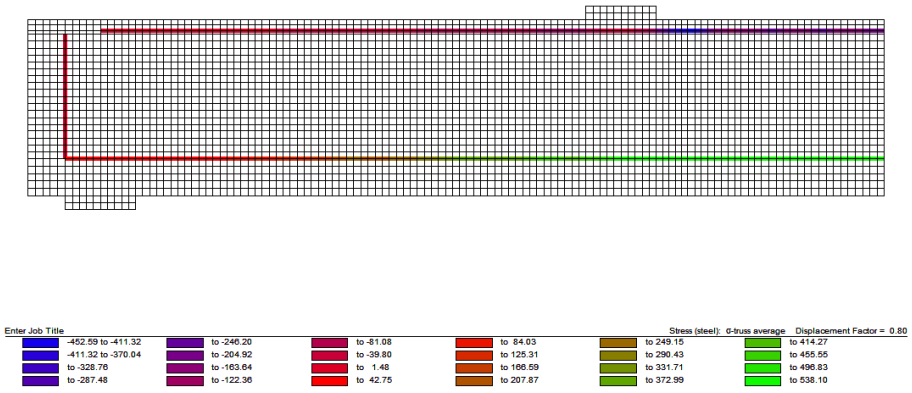
Figure 8-18 Finite elements results of (B-MC-10M-13%) (case 4)



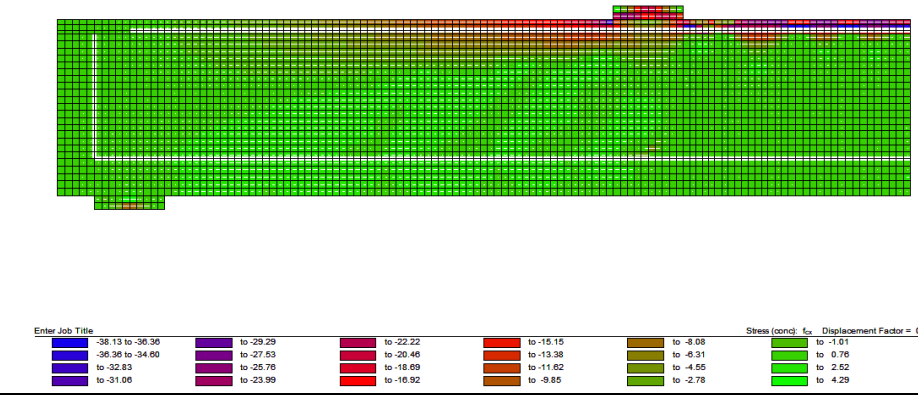

a) Finite element mesh




b) Stress distribution in steel at yielding

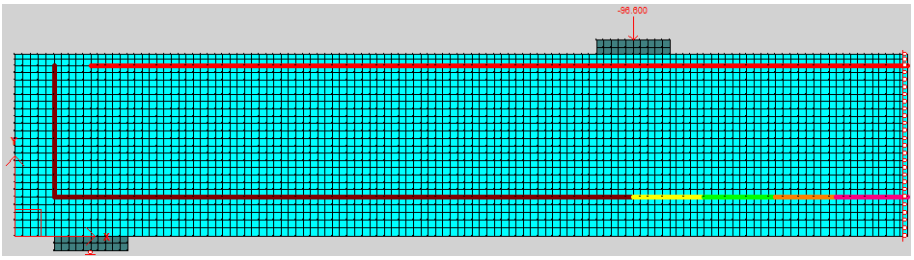



c) Stress distribution in steel at peak load

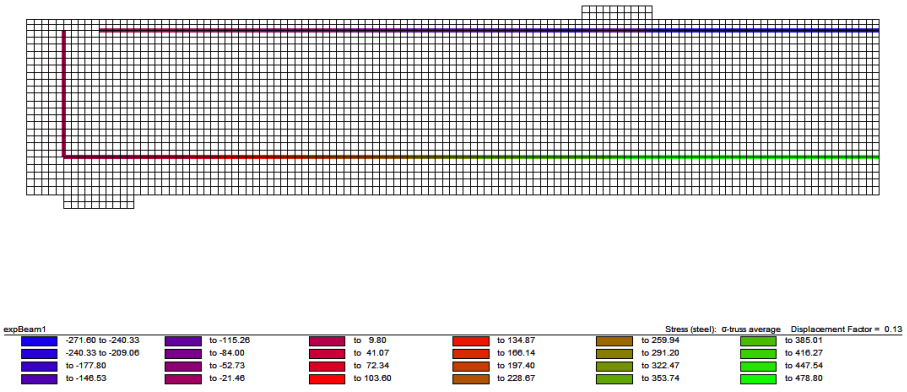



d) Stress distribution in concrete at peak load

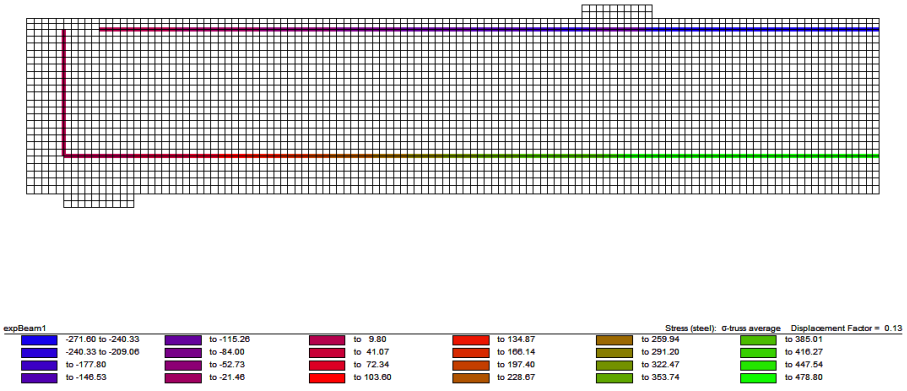
Figure 8-19 Finite element results of beam (B-MC-10M-14%) (case 4)



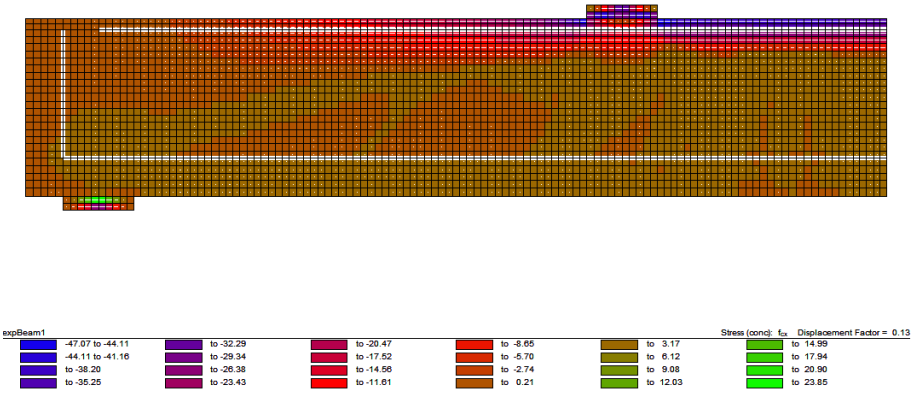

a) Finite element mesh




b) Stress distribution in steel at yielding




c) Stress distribution in steel at peak load




d) Stress distribution in concrete at peak load

Figure 8-20 Finite element results of beam (B-MC-15M-10%) (case 5)

#### 8.6.1.3 Corrosion at the ends (B-SC-10M-11%)

Beam B-SC-10M-11% was subjected to corrosion at its ends, with a measured average mass loss of 11%. The FE model considered the same modelling features presented in the previous section, except that corrosion effects were introduced at both beam ends only (refer to **Figure 8-23 (a)**). **Figure 8-21** and **Table 8-7** present a comparison of the FE and experimental results for this beam, while the cracking patterns, and steel and concrete stresses are shown in **Figure 8-22** and **Figure 8-23**, respectively.

When considering the different analysis cases, case 4 (SS + PS) resulted in the best approximation of the experimental load-deflection response, as illustrated in **Figure 8-21**. Similar results were obtained for cases 2a and 2b, while cases 1 and 2c resulted in over-estimation of the beam response. Case 3 resulted in an under-estimation of maximum strength but a reasonable prediction of yield strength. In general, all cases resulted in over-estimation of the beam stiffness.

**Figure 8-22** shows that the case 4 FE model resulted in a reasonable prediction of cracking patterns and flexural failure mode, including the damage near underneath the loading point. The maximum steel stress reached 555 MPa at the peak load (slightly below $f_u$ = 565 MPa). The steel strain at the end of the simulation was 45 mm/m, below the ultimate strain of 93 mm/m in the steel model. **Figure 8-23 (d)** shows that the concrete stress reached 37 MPa at peak load, which is near the peak stress $f_c'$ = 42 MPa. The model predicted concrete crushing in the compression region, with significant cracks in the tension region, which matches the experimental result (see **Figure 8-22)**.

Table 8-7 Experimental and simulation results of beam B-SC-10M-11%

| Beam ID | Case ID | Load (kN) | | | | $\frac{P_{max_{FE}}}{P_{max}}$ | $\frac{P_{y_{FE}}}{P_y}$ | Displ.(mm) | | $\frac{\Delta_{max_{FE}}}{\Delta_{max}}$ | Predicted failure mode |
|---|---|---|---|---|---|---|---|---|---|---|---|
| | | Exp. | | FE | | | | Exp. | FE | | |
| | | $P_{max}$ | $P_y$ | $P_{maxFE}$ | $P_{yFE}$ | | | $\Delta_{max}$ | $\Delta_{maxFE}$ | | |
| B-SC-10M-11% | Case 1 | 57 | 50 | 63 | 60 | 1.10 | 1.20 | 121 | 110 | 0.91 | Flexural failure with steel yielding, significant cracks in tension zone and concrete crushing in compression |
| | Case 2a | | | 58 | 57 | 1.01 | 1.14 | | 110 | 0.91 | |
| | Case 2b | | | 57 | 57 | 1.00 | 1.14 | | 110 | 0.91 | |
| | Case 2c | | | 61 | 60 | 1.07 | 1.20 | | 110 | 0.91 | |
| | Case 3 | | | 52 | 49 | 0.91 | 0.98 | | 110 | 0.91 | |
| | Case 4 | | | 56 | 56 | 0.98 | 1.12 | | 110 | 0.91 | |

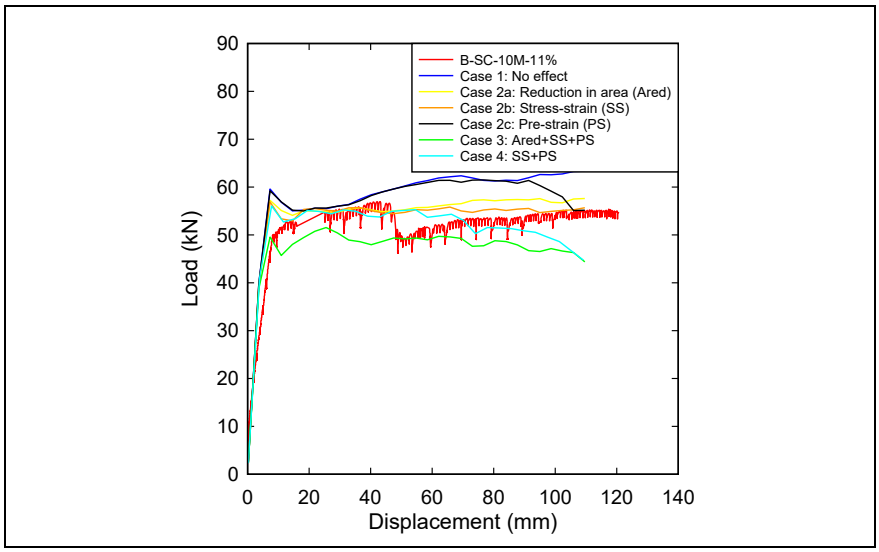



Figure 8-21 Load-deflection responses of B-SC-10M-11%

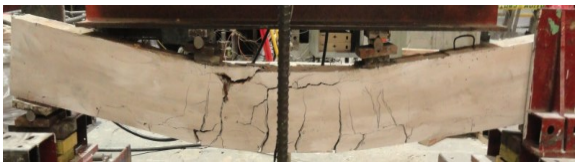
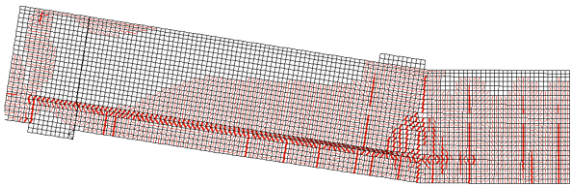
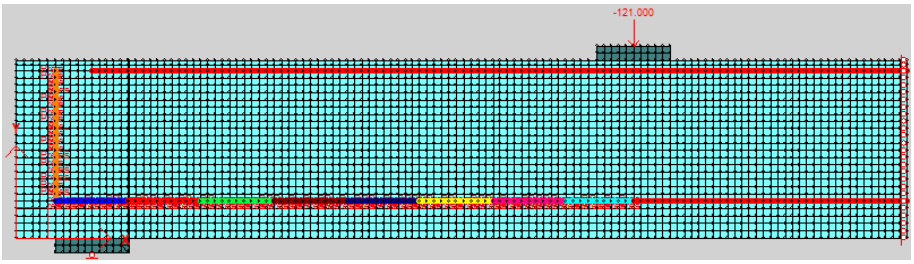
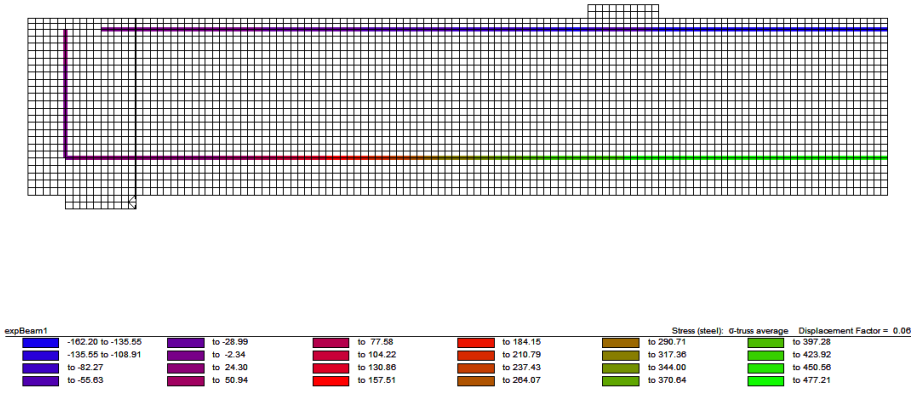
| Experimental | Simulation |
|---|---|
|  |  |

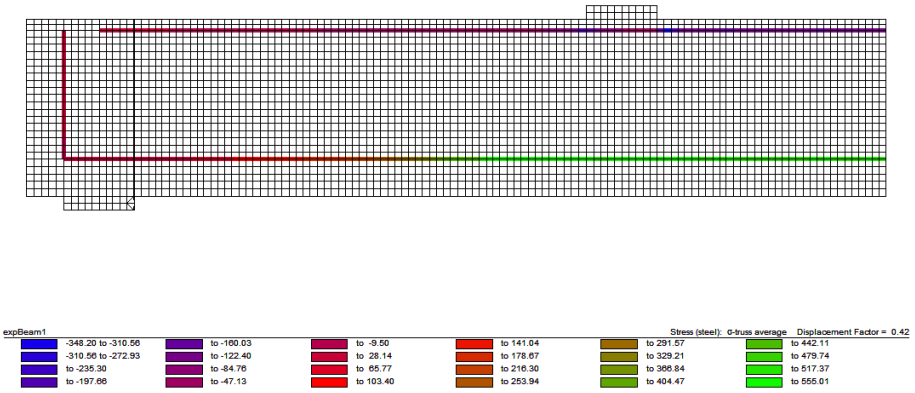
Figure 8-22 Experimental failure mode vs simulation of B-SC-10M-11% (case 4)



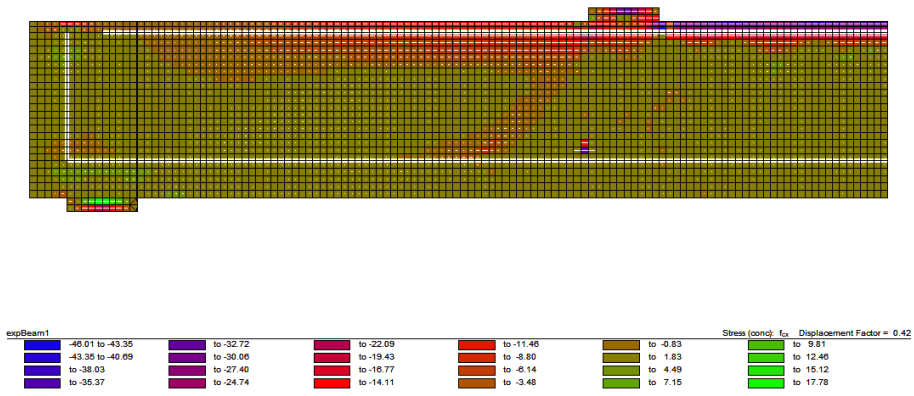

a) Finite element mesh




b) Stress distribution in steel at yielding




c) Stress distribution in steel at peak load




d) Stress distribution in concrete at the peak load

Figure 8-23 Finite elements results of beam B-SC-10M-11% (case 4)

#### 8.6.1.4 Full corrosion (B-FC-10M-13%)

The final beam in the flexure series was subjected to corrosion of the tension reinforcement over the entire beam length, with an average mass loss of 13%. The FE model for beam B-FC-10M-13% used the same modelling features as previous beams; however, the corroded bar properties and corrosion induced-cracking in the concrete elements were introduced over the entire tension bar length (see **Figure 8-26 (a)**). The FE results for this beam are presented in **Figure 8-24** and **Table 8-8**. Cracking patterns, and stresses in the reinforcing steel and concrete are presented in **Figure 8-25** and **Figure 8-26**, respectively.

Consistent with the previous beams, case 4 (SS + PS) resulted in the most reasonable prediction of the load-deflection response (**Figure 8-24**), with predictions ratios of 1.0, 0.95, and 1.06 for yield strength, ultimate load and maximum displacement (see **Table 8-8**). Similar results were once again obtained for cases 2a and 2b, which respectively considered area reduction and stress-strain modification separately. Likewise, cases 1 and 2c, which did not consider these features, resulted in an over-estimation of load parameters. Finally, case 3, which combined all features, resulted in an over-estimation of corrosion effects, with under-estimation of yield strength, maximum strength, and ductility. Consistent with the previous beams, the stiffness was generally over-estimated in all FE models.

**Figure 8-25** shows that case 4 predicted a flexure failure which was associated with severe cracking and rupture of tensile steel bars in the mid-span region, matching the experimental failure mode. **Figure 8-26 (c)** shows that the maximum stress in the steel at peak load reached 539 MPa, slightly below the ultimate stress of 548 MPa used in the steel model. A maximum strain of 54 mm/m was recorded at the level of the tension bars at the mid-span at the end of the simulation. On the other hand, the stress in the concrete reached $f_c'$ = 47 MPa at the peak load, which indicates concrete crushing in the mid-span of the beam (see **Figure 8-26 (d)** and **Figure 8-25**).

Table 8-8 Experimental and simulation results of beam B-FC-10M-13%

| Beam ID | Case ID | Load (kN) | | | | $\frac{P_{max_{FE}}}{P_{max}}$ | $\frac{P_{y_{FE}}}{P_y}$ | Displ.(mm) | | $\frac{\Delta_{max_{FE}}}{\Delta_{max}}$ | Predicted failure mode |
|---|---|---|---|---|---|---|---|---|---|---|---|
| | | Exp. | | FE | | | | Exp. | FE | | |
| | | $P_{max}$ | $P_y$ | $P_{maxFE}$ | $P_{yFE}$ | | | $\Delta_{max}$ | $\Delta_{maxFE}$ | | |
| B-FC-10M-13% | Case 1 | 57 | 48 | 65 | 58 | 1.14 | 1.2 | 140 | 154 | 1.1 | Flexural failure associated with rebar rupture in tension zone |
| | Case 2a | | | 55 | 49 | 0.96 | 1.02 | | 149 | 1.06 | |
| | Case 2b | | | 55 | 48 | 0.96 | 1 | | 138 | 0.99 | |
| | Case 2c | | | 62 | 58 | 1.08 | 1.2 | | 133 | 0.95 | |
| | Case 3 | | | 46 | 44 | 0.8 | 0.92 | | 128 | 0.91 | |
| | Case 4 | | | 54 | 48 | 0.95 | 1 | | 149 | 1.06 | |

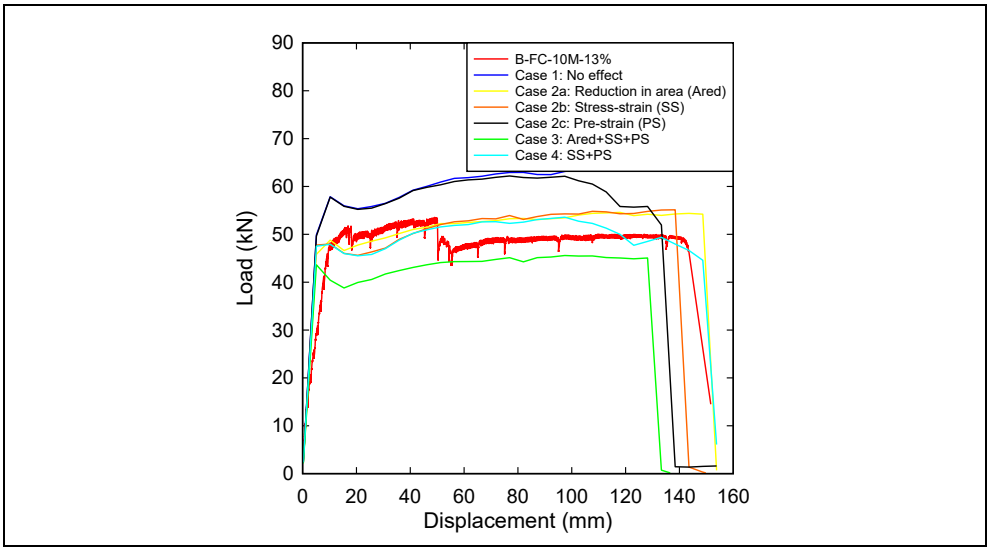



Figure 8-24 Load-deflection responses of beam B-FC-10M-13%

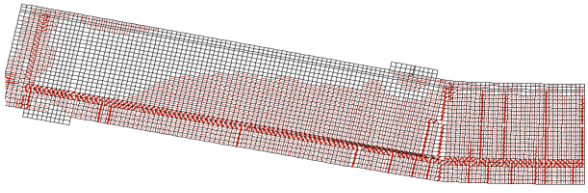
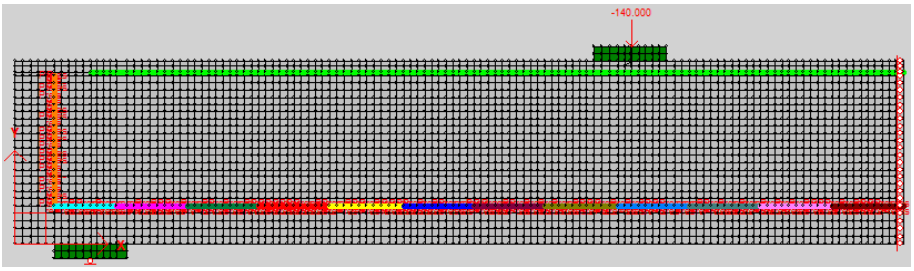
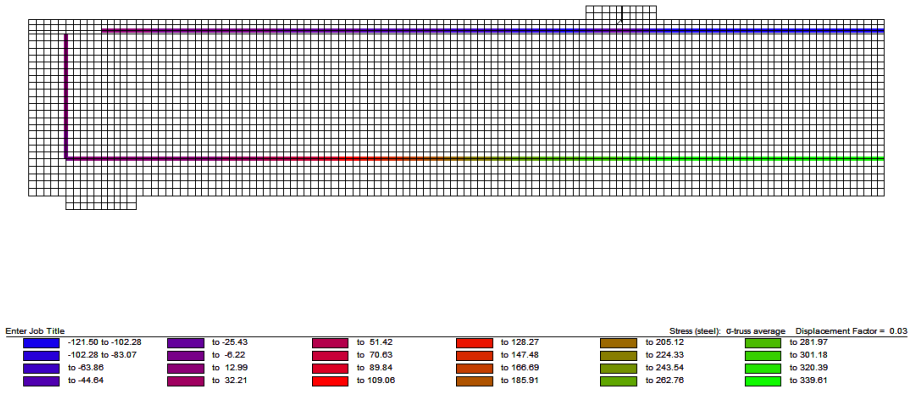
| Experimental | Simulation |
|---|---|
|  |  |

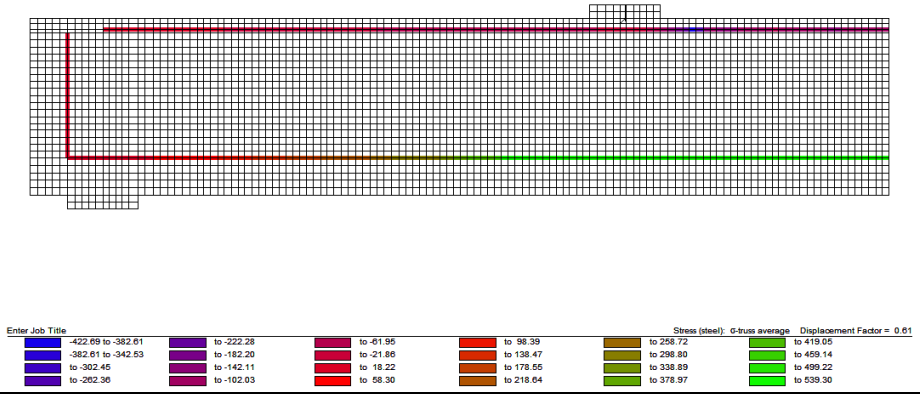
Figure 8-25 Experimental failure mode vs simulation for beam B-FC-10M-13% (case 4)



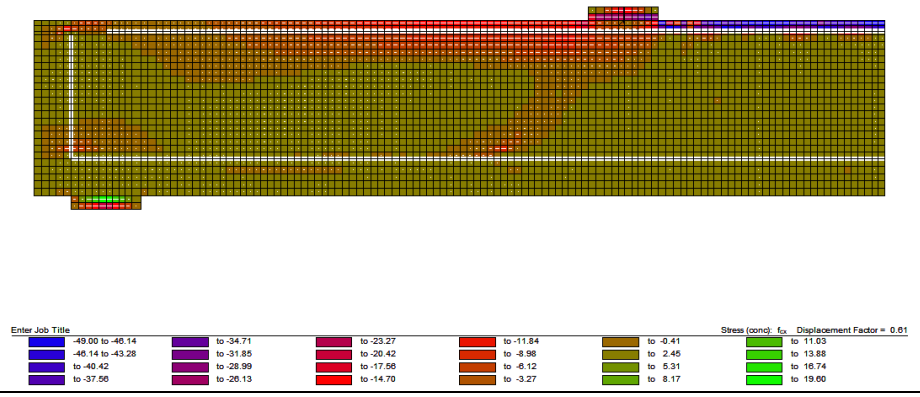

a) Finite element mesh




b) Stress distribution in steel at yielding




c) Stress distribution in steel at peak load




d) Stress distribution in concrete at peak load

Figure 8-26 Finite element results of beam B-FC-10M-13% (case 4)

### 8.6.2 Shear-governed beams

This section presents the finite element modelling results for the "shear-governed" beams in the 25M group. This set included one control beam and two corroded specimens with different mass loss %. Unlike the previous set, the FE models used a 20×20 mm mesh, with truss bar elements for both the longitudinal (25M) and transverse (6.3 mm) reinforcement.

#### 8.6.2.1 Control shear beam (CB-25M-0%)

Beam CB-25M-0% was the first beam in the 25M group and was analyzed without considering the effects of corrosion. The FE model is shown in **Figure 8-29 (a)**, while a comparison of the FE and experimental results is presented in **Figure 8-27** and **Table 8-9**. **Figure 8-28** shows a comparison of experimental and FE cracking patterns, while **Figure 8-29** provides finite element results in terms of concrete and steel reinforcement stresses.

Examination of the FE results showed that the beam reached a maximum strength of 198 kN and a load-deflection response which was acceptable when compared to the experimental results (see **Figure 8-27** and **Table 8-9**); however, the failure mode in the numerical mode corresponded to severe concrete crushing, rather than shear failure (see **Figure 8-28**). Beam CB-25M-0% was designed with a flexure-to-shear capacity of nearly 1.0. In addition, the large tension steel ratio resulted in over-reinforced conditions, which can explain the difference in failure mode. In addition to concrete crushing at mid-span, the FE model showed significant diagonal cracking and damage along the bar length in the shear span. The concrete reached a maximum stress above 40 MPa due to the crushing, while the maximum stress in the transverse reinforcement reached 551 MPa, which indicates the stirrups reached yielding (see **Figure 8-29**).

Table 8-9 Experimental and simulation results of beam CB-25M-0%

| Beam ID | Load (kN) | | | | $\frac{P_{max_{FE}}}{P_{max}}$ | $\frac{P_{y_{FE}}}{P_y}$ | Displ.(mm) | | $\frac{\Delta_{max_{FE}}}{\Delta_{max}}$ | Predicted failure mode |
|---|---|---|---|---|---|---|---|---|---|---|
| | Exp. | | FE | | | | Exp. | FE | | |
| | $P_{max}$ | $P_y$ | $P_{maxFE}$ | $P_{yFE}$ | | | $\Delta_{max}$ | $\Delta_{maxFE}$ | | |
| CB-25M-0% | 190 | - | 198 | - | 1.04 | - | 84 | 84 | 1.00 | Flexural failure associated with severe concrete crushing at mid-span |

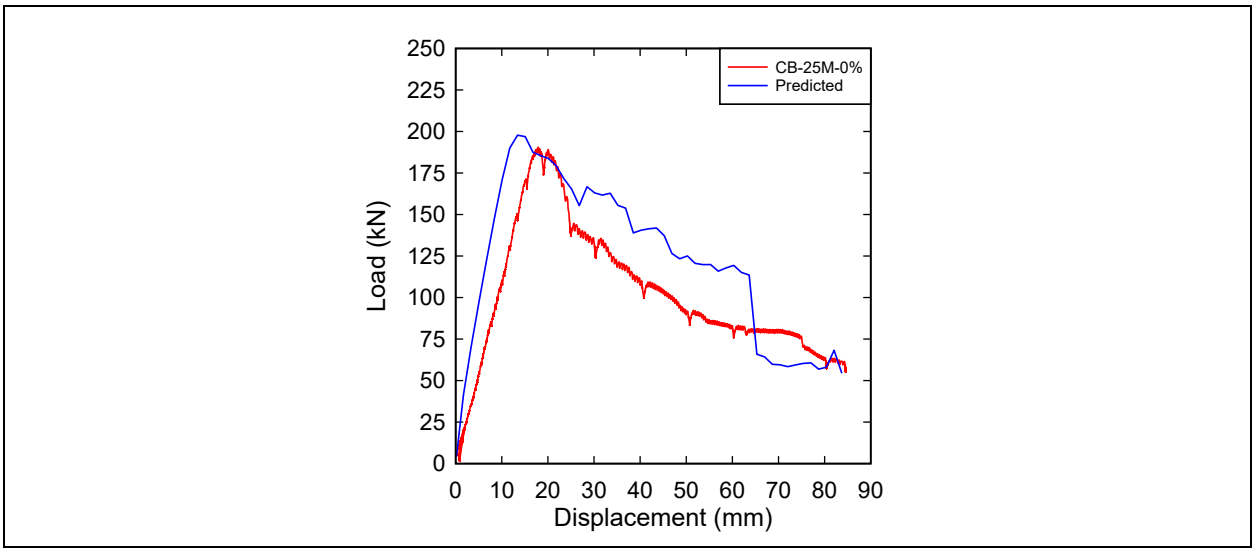



Figure 8-27 Experimental and simulation load-deflection responses for CB-25M-0%

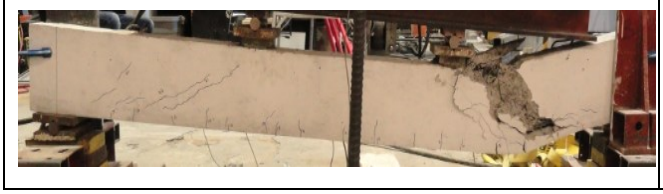
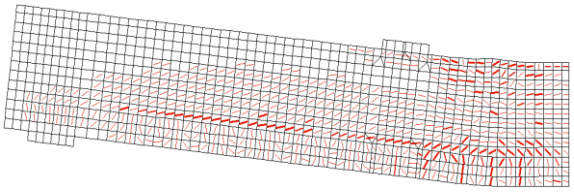
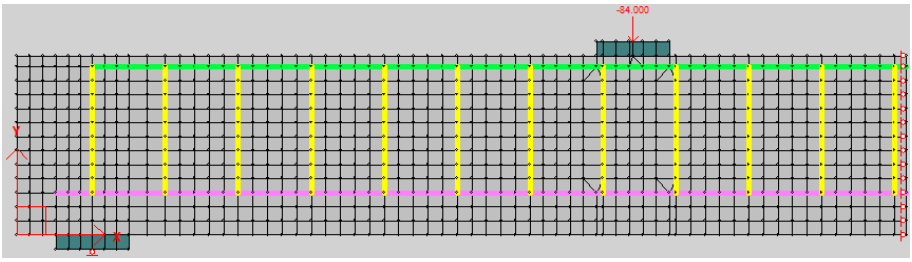
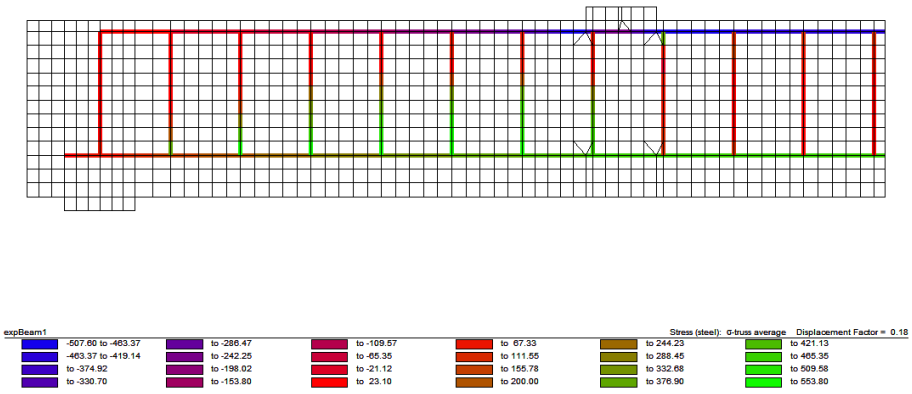
| Experimental | Simulation |
|---|---|
|  |  |

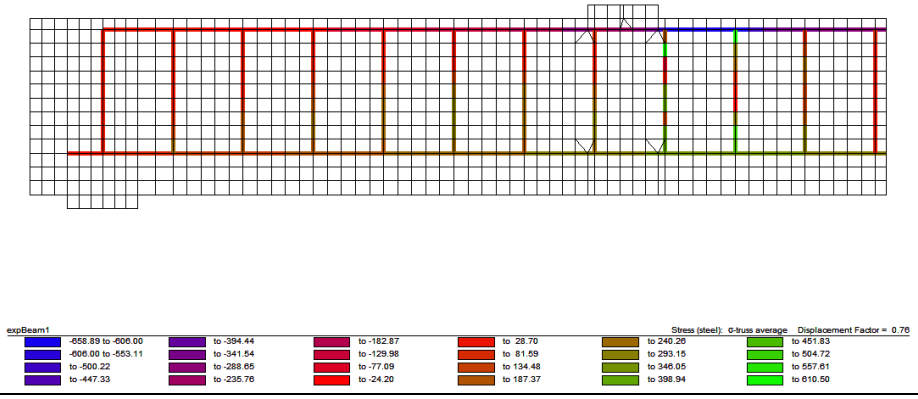
Figure 8-28 Experimental failure mode vs simulation for beam CB-25M-0%



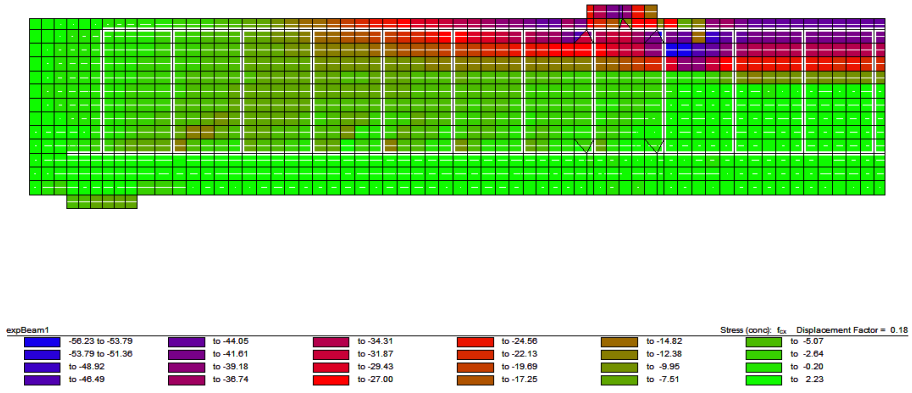

a) Finite element mesh




b) Stress distribution in steel at peak load




c) Stress distribution in steel at the point of load drop




d) Stress distribution in concrete at peak load

Figure 8-29 Finite element results of beam CB-25M-0%

#### 8.6.2.2 Shear corrosion beams (B-SHC-25M-10%) and (B-SHC-25M-12%)

This last section presents the FE results for the 25M beams with corroded shear reinforcement. The same FE model was used; however, corrosion effects were applied on the stirrups over the entire beam span by reducing their bar area and modifying their steel properties based on 10% and 12% mass loss, respectively, while corrosion-induced cracking was simulated by applying pre-strains on the transverse reinforcement as shown in **Figure 8-32 (a)** and **Figure 8-33 (a)**.

Comparison of the experimental and simulation results are shown in **Table 8-10** and **Figure 8-30**. **Figure 8-31**, **Figure 8-32** and **Figure 8-33** present damage profiles, and concrete and steel reinforcement stresses obtained from the FE models. Various simulation cases were considered (cases 1 to 4 as listed in **Table 8-4**).

In general, cases 1, 2a and 2b resulted in peak load ratios of nearly 1.0 when considering both beams (see **Table 8-10**). Lower average peak load ratios of 0.87 and 0.86 were obtained for cases 2c and 4, which considered steel stress-strain modification without and with applied pre-strain, respectively. Case 3 which combined all modelling features results in under-estimation of peak capacity, especially in the case of beam B-SHC-25M-12% (load ratio = 0.78).

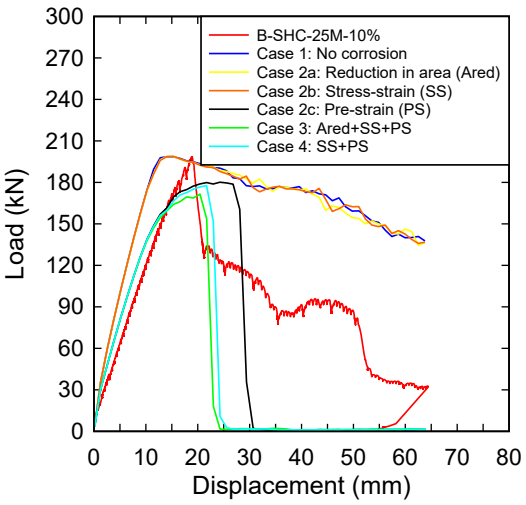
Considering the general trend of the ascending and descending load-deflection responses (**Figure 8-30**), optimal results were obtained for case 4, while the post-peak response was over-estimated in cases 1 and 2a. It was also interesting to note that the cases which considered pre-strain (cases 2c, 3 and 4) resulted in better estimation of beam stiffness.

The predicted failure mode was shear failure for both beams; however, a more sudden loss in load capacity was observed for cases 2c, 3 and 4 (see **Figure 8-30**). Large concrete stresses were observed in both the mid-span and shear-spans regions for both beams B-SHC-25M-10% and B-SHC-25M-12% in the case 4 simulation, which matches the damage observed in the experiments (see **Figure 8-32 (d)** and **Figure 8-33 (d)**). The maximum stresses in the stirrups were found to be 495 MPa and 460 MPa, respectively, which exceed the yield stress in the steel models.

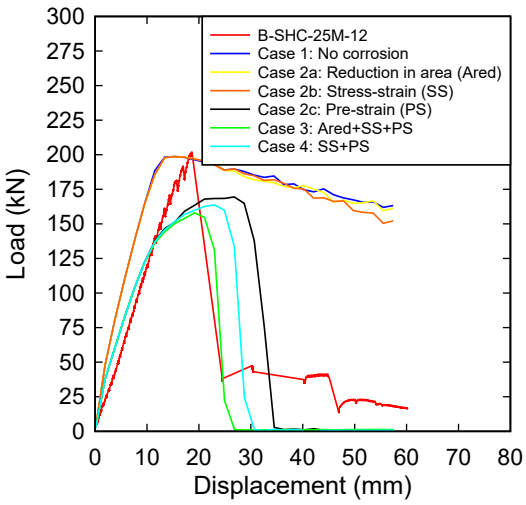
Table 8-10 Summary of the experimental and simulation results of beams with corroded stirrups

| Beam ID | Case ID | Load (kN) | | | | $\frac{P_{max_{FE}}}{P_{max}}$ | $\frac{P_{y_{FE}}}{P_y}$ | Displ.(mm) | | $\frac{\Delta_{max_{FE}}}{\Delta_{max}}$ | Predicted failure mode |
|---|---|---|---|---|---|---|---|---|---|---|---|
| | | Exp. | | FE | | | | Exp. | FE | | |
| | | $P_{max}$ | $P_y$ | $P_{maxFE}$ | $P_{yFE}$ | | | $\Delta_{max}$ | $\Delta_{maxFE}$ | | |
| B-SHC-25M-10% | Case 1 | 198 | - | 199 | - | 1.00 | - | 64 | 64 | 1.00 | Shear failure with significant cracking in shear zone |
| | Case 2a | | | 199 | - | 1.00 | - | | 64 | 1.00 | |
| | Case 2b | | | 199 | - | 1.00 | - | | 64 | 1.00 | |
| | Case 2c | | | 180 | - | 0.90 | - | | 28 | 0.44 | |
| | Case 3 | | | 172 | - | 0.87 | - | | 22 | 0.34 | |
| | Case 4 | | | 178 | - | 0.90 | - | | 23 | 0.36 | |
| B-SHC-25M-12% | Case 1 | 202 | - | 199 | - | 0.98 | - | 60 | 57 | 0.95 | Shear failure associated with severe cracking in shear zone |
| | Case 2a | | | 199 | - | 0.98 | - | | 57 | 0.95 | |
| | Case 2b | | | 199 | - | 0.98 | - | | 57 | 0.95 | |
| | Case 2c | | | 169 | - | 0.84 | - | | 31 | 0.52 | |
| | Case 3 | | | 158 | - | 0.78 | - | | 23 | 0.38 | |
| | Case 4 | | | 164 | - | 0.81 | - | | 27 | 0.45 | |

| All beams | Case ID | $\frac{P_{max_{FE}}}{P_{max}}$ | | $\frac{\Delta_{max_{FE}}}{\Delta_{max}}$ | |
|---|---|---|---|---|---|
| | | Avg. | S.D. (C.V) | Avg. | S.D. (C.V) |
| Statistical data | Case 1 | 0.99 | 0.01 (1.01) | 0.97 | 0.02 (2.06) |
| | Case 2a | 0.99 | 0.01 (1.01) | 0.97 | 0.02 (2.06_ |
| | Case 2b | 0.99 | 0.01 (1.01) | 0.97 | 0.02 (2.06) |
| | Case 2c | 0.87 | 0.03 (3.40) | 0.48 | 0.04 (8.33) |
| | Case 3 | 0.83 | 0.04 (4.81) | 0.36 | 0.02 (5.55) |
| | Case 4 | 0.86 | 0.04 (4.65) | 0.40 | 0.04 (10.00) |




a) B-SHC-25M-10%




b) B-SHC-25M-12%

Figure 8-30 Experimental and simulation responses of beams with corroded stirrups

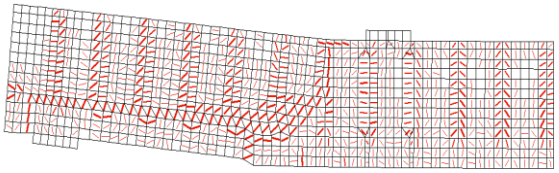
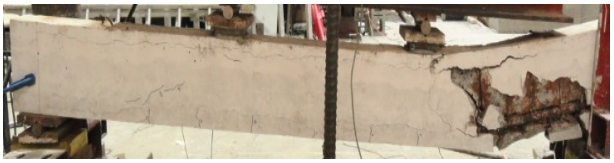
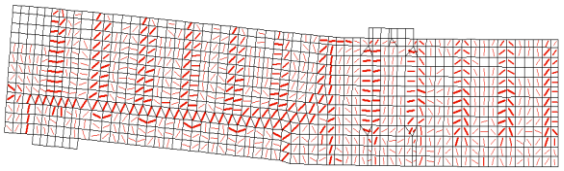
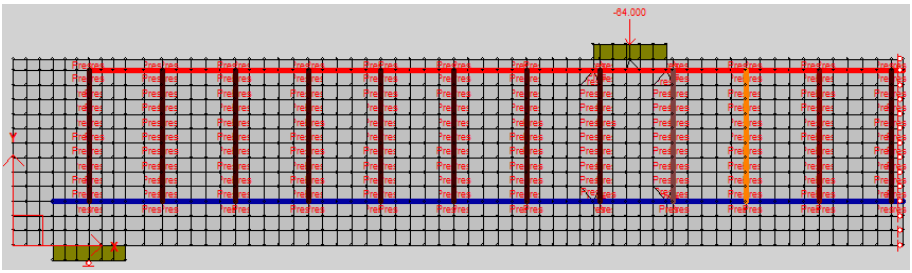
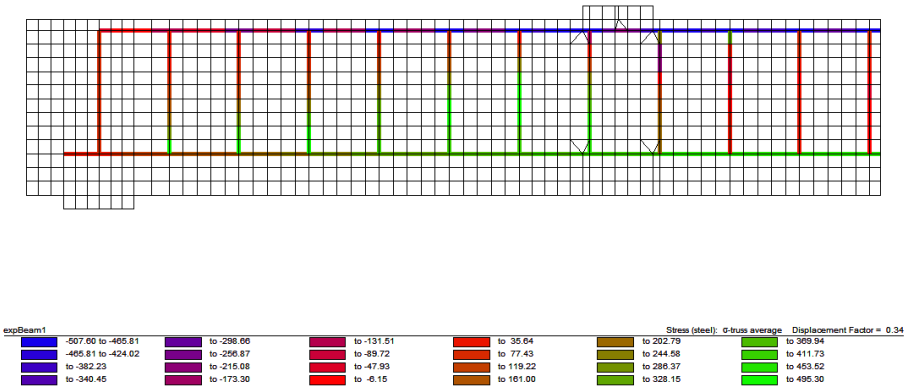
| Experimental | Simulation |
|---|---|
|  |  |
| a) B-SHC-25M-10% (case 4) | |
|  |  |
| b) B-SHC-25M-12% (case 4) | |

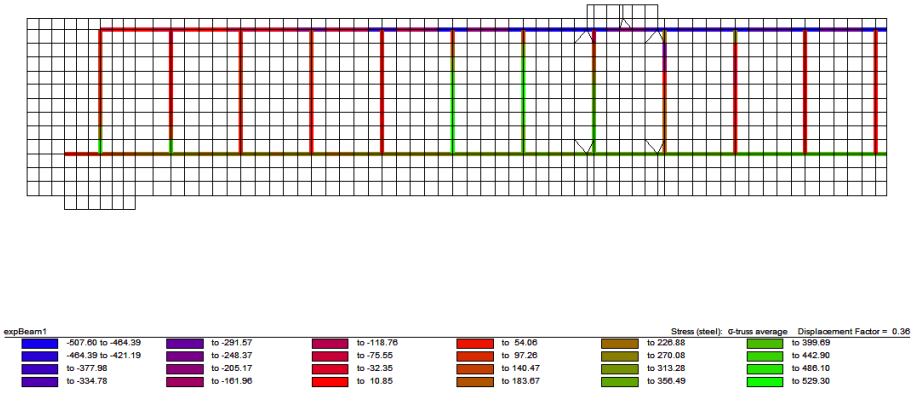
Figure 8-31 Failure mode comparison between experimental and simulation beams (case 4)



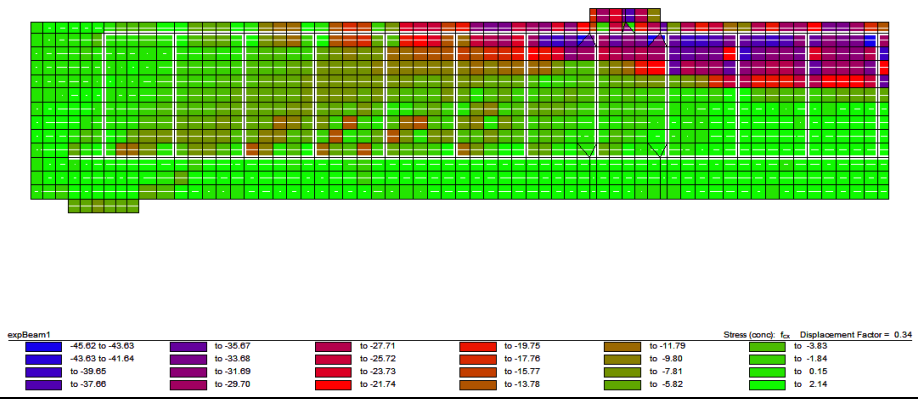

a) Finite element mesh




b) Stress distribution in steel at peak load

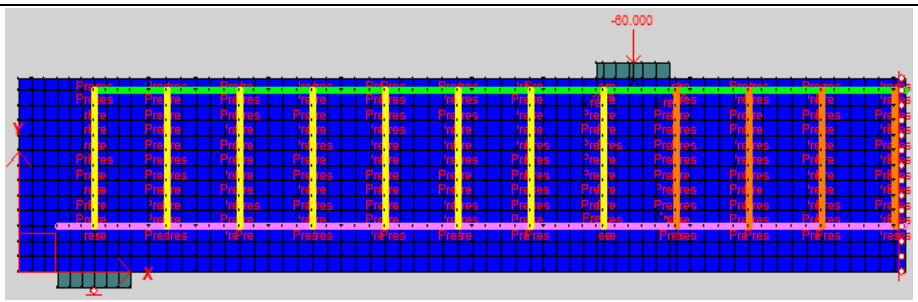



c) Stress distribution in steel at the point of load drop

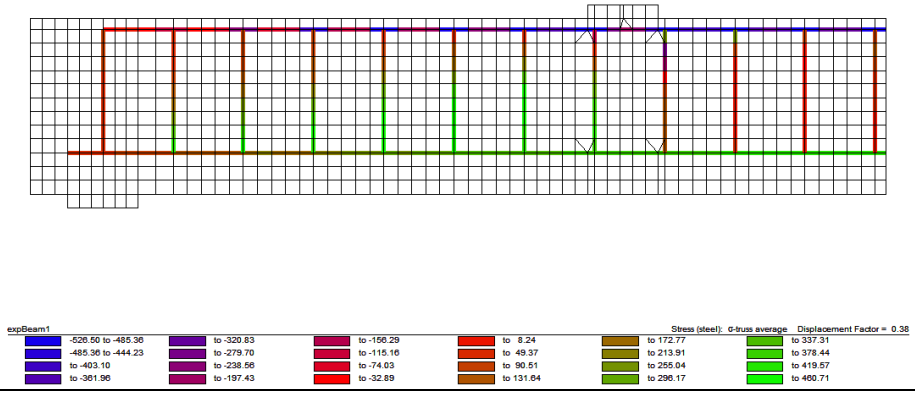



d) Stress distribution in concrete at peak load

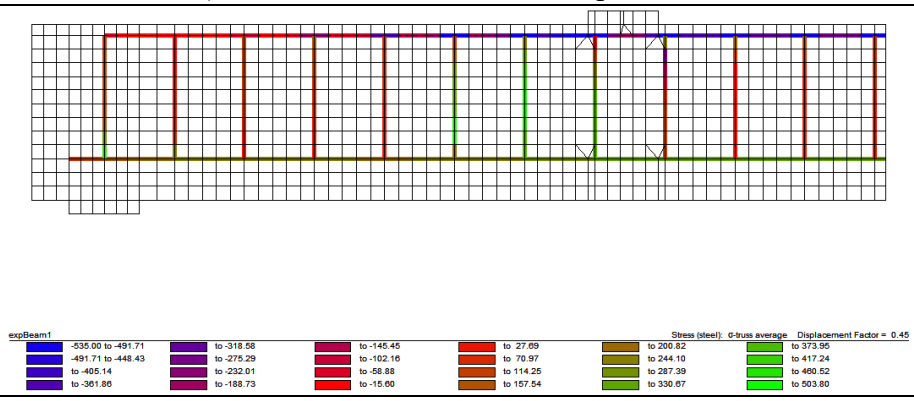
Figure 8-32 Finite element results of beam B-SHC-25M-10% (case 4)



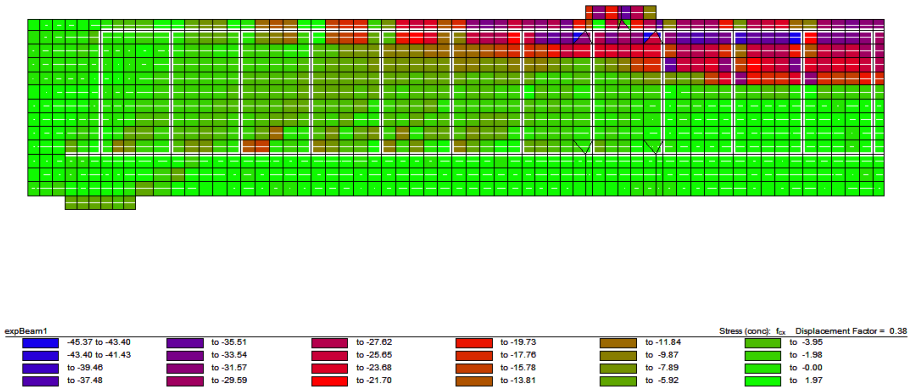

a) Finite element mesh




b) Stress distribution in steel at peak load




c) Stress distribution in steel at the point of load drop




d) Stress distribution in concrete at peak load

Figure 8-33 Finite element results of beam B-SHC-25M-12% (case 4)

# Chapter 9: SDOF Analysis of Corrosion-Damaged Beams under Blast Loading

## 9.1 Chapter Overview

This chapter covers the second phase of the numerical research programme, which includes the single degree of freedom (SDOF) analysis approach. The goal of this method is to predict the maximum displacement response of the test beams (both control and corroded) when blast loading is applied. The 2D nonlinear finite element (FE) programme VecTor2 (Wong et al., 2013) was used to develop dynamic resistance curves after applying dynamic increase factors (DIF) to the material properties of the beams. The RCBlast software (Jacques, 2014) was then used to predict the dynamic responses of the beams. This chapter also covers the SDOF approach procedure, a summary of the SDOF approach results, and a comparison of predicted and experimental results.

## 9.2 Procedure of SDOF Analysis Approach

The main purpose of using the SDOF approach is to predict the maximum displacements of tested beams when they are subjected to blast loading. Two-dimensional nonlinear FE programVecTor2 was used to develop the dynamic resistance function of each beam (R(t)). The FE analysis considered corrosion effects by modifying the steel stress-strain relationship and modelling corrosion-induced concrete cracking in the concrete. The same FE approach used in the static analysis was implemented here, except that DIF factors were applied to material properties to account for strain-rate effects. Three DIF cases were used to predict the dynamic resistance curve of the beams: 1- No DIF applied, 2- DIF taken from the UFC design criteria (UFC-3-340-02, 2008) for the case of bending stresses in the far design range (see **Table 9-1**), 3- DIF taken from Saatcioglu et al. (2011) model, with the DIF for concrete and reinforcing bars given as:

$$\text{1- Plain Concrete: DIF} = \begin{cases} 0.03\ln(\dot{\varepsilon}) + 1.30 \geq 1.0 & for\ \dot{\varepsilon} < 30\ s^{-1} \\ 0.55\ln(\dot{\varepsilon}) - 0.47 & for\ \dot{\varepsilon} \geq 30\ s^{-1} \end{cases} \quad (9\text{-}1)$$

In the simulations, the strain rate $\dot{\varepsilon}$ was assumed to be 1.0 $s^{-1}$, resulting in a DIF of 1.30.

2- Steel reinforcement: a- At yield ($DIF_y$) = $0.034\ln(\dot{\varepsilon}) + 1.30 \geq 1.0$

$$\text{b- At ultimate } (DIF_u) = 0.0101\ln(\dot{\varepsilon}) + 1.10 \geq 1.0 \quad (9\text{-}2)$$

The strain rate ($\dot{\varepsilon}$) was assumed to be 1 $s^{-1}$ at yield and ultimate, resulting in $DIF_y$ and $DIF_u$ of 1.30 and 1.10, respectively. This strain rate was selected based on strain data from the instrumented steel reinforcement during the shock-tube tests, and the recommendations in previous shock-tube studies (Li et al., 2018; Algassem et al., 2019; and Jacques E., 2016).

SDOF analysis was used to predict the dynamic responses of the beams by solving the equation of motion in Eq. (9-3) using software RCBlast:

$$K_{LM}m\ddot{u}(t) + R\big(u(t)\big) = AP_r(t) \tag{9-3}$$

where: $K_{LM}$ = load-mass transformation factor, which is used to transform the real structure into the equivalent SDOF system taking into account the beam loading and boundary conditions (taken as 0.6 and 0.56 before and after yield, respectively); m = mass of the system consisting of the weight of the beam and LTD (taken as 450 kg); $u(t)$ and ü(t) = beam mid-span displacement and acceleration, respectively; R(u(t)) = beam resistance function; and, APr(t) = loading function, where A is the impacted area of the LTD (taken as 3.4 $m^2$) and Pr(t) is an idealized triangular pressure-time history, having the same reflected pressure and impulse observed in the experiments. **Figure 9-1** shows the RCBlast software interface after the SDOF analysis is completed. The output showed the resistance function which was developed in VecTor2 (top left), $K_{LM}$ factors before and after yielding (top left), idealized pressure time history (top right) and displacement time history result (bottom window).

Table 9-1 Dynamic increase factors for reinforced concrete design (UFC-3-340-02, 2008)

| Type of stress | Far design range | | | Close-in design range | | |
|---|---|---|---|---|---|---|
| | Reinforcing bars | | Concrete | Reinforcing bars | | Concrete |
| | $f_{dy}/f_y$ | $f_{du}/f_u$ | $f'_{dc}/f'_c$ | $f_{dy}/f_y$ | $f_{du}/f_u$ | $f'_{dc}/f'_c$ |
| Bending | 1.17 | 1.05 | 1.19 | 1.23 | 1.05 | 1.25 |
| Diagonal tension | 1.00 | - | 1.00 | 1.10 | 1.00 | 1.00 |
| Direct shear | 1.10 | 1.00 | 1.10 | 1.10 | 1.00 | 1.10 |
| Bond | 1.17 | 1.05 | 1.00 | 1.23 | 1.05 | 1.00 |
| Compression | 1.10 | - | 1.12 | 1.13 | - | 1.16 |

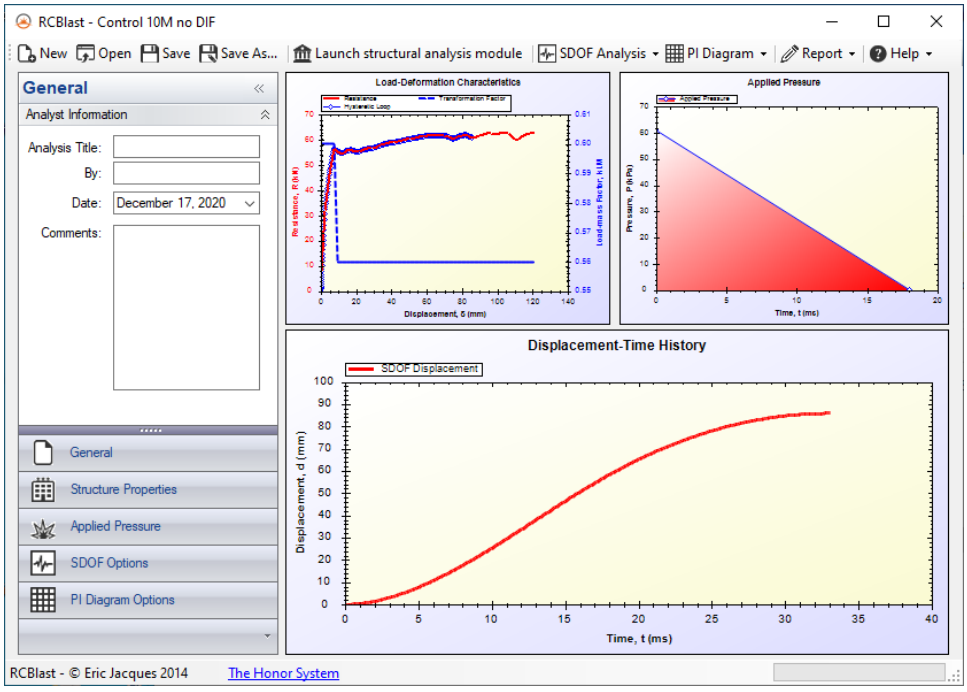



Figure 9-1 RCBlast software interface after analysis

## 9.3 Corrosion inducing-cracking

Corrosion inducing-cracking was simulated similarly as in the static analysis; however, the applied pre-strain was different since it is directly dependent on the actual steel mass loss due to corrosion. As a result, **Table 9-2** presents the applied pre-strain for beams tested under blast-loading.

Table 9-2 Equivalent pre-strains with corresponding mass loss

| Beam ID | $M_{loss}$ (%) | μ | b (mm) | c (mm) | $A_s$ ($mm^2$) | $d_b$ (mm) | $A_{s(exp)}$ ($mm^2$) | $d_{exp}$ (mm) | ε (millistrain) |
|---|---|---|---|---|---|---|---|---|---|
| B-MC-10M-11% | 11% | 2 | 125 | 40 | 100.23 | 11.3 | 110.95 | 11.88 | 6.45 |
| B-SC-10M-7% | 7% | 2 | 125 | 40 | 100.23 | 11.3 | 107.13 | 11.68 | 4.18 |
| B-FC-10M-12% | 12% | 2 | 125 | 40 | 100.23 | 11.3 | 111.90 | 11.93 | 7.00 |
| B-MC-10M-15% | 15% | 2 | 125 | 40 | 100.23 | 11.3 | 114.70 | 12.08 | 8.63 |
| B-EMC-10M-22% | 22% | 2 | 125 | 40 | 100.23 | 11.3 | 121.07 | 12.41 | 12.25 |
| B-CR-MC-10M-5% | 5% | 2 | 125 | 40 | 100.23 | 11.3 | 105.18 | 11.57 | 3.01 |
| B-MC-15M-12% | 12% | 2 | 125 | 40 | 200.96 | 16 | 224.35 | 16.90 | 9.43 |
| B-CR-MC-15M-4% | 4% | 2 | 125 | 40 | 200.96 | 16 | 208.91 | 16.31 | 3.26 |
| B-EMC-15M-17% | 17% | 2 | 125 | 40 | 200.96 | 16 | 233.67 | 17.25 | 13.05 |
| B-SHC-25M-12% | 12% | 2 | 125 | 12.5 | 31.15 | 6.3 | 34.78 | 6.65 | 11.41 |
| B-SHC-25M-11% | 11% | 2 | 125 | 12.5 | 31.15 | 6.3 | 34.48 | 6.62 | 10.50 |

b = Beam width; c = Concrete cover; $A_s$ = Original steel bar area; $d_b$ = Original diameter of steel bar; $A_{s(exp)}$ = Total expanded area of corroded steel bar; $d_{exp}$ = Diameter of steel bars expanded; ε = Corrosion-induced pre-strain in the concrete near the reinforcement.

## 9.4 SDOF approach results

### 9.4.1 Flexure-governed beams

SDOF analysis was first applied on the flexure-governed beams in the 10M and 15M series to predict the maximum displacement using the RCBlast software. This analysis included eleven beams with different scenarios of corrosion (control, mid-corrosion, cover-removed-mid corrosion, end-corrosion and full-corrosion).

#### 9.4.1.1 Control beams (0% mass loss): CB-10M-0% and CB-15M-0%

Beams CB-10M-0% and CB-15M-0% were the control specimens which were constructed with 2-10M and 2-15M tension bars, respectively. The beams were modelled without the effects of corrosion. Both beams were analyzed using a 10×10 mm mesh in the VecTor2 FE program. The longitudinal reinforcement was simulated as truss elements, whereas the stirrups were smeared in the concrete elements (refer to **Figure 9-2 (a)** and **Figure 9-2 (b)**). To account for strain-rate effects, three DIF cases were considered: Case 1: No DIF (no dynamic increase factor), Case 2: Design DIF (UFC design criteria), and Case 3: Saatcioglu DIF.

The experimental and SDOF results are summarized in **Table 9-3**. The beam resistance function obtained from VecTor2, the displacement time history comparison between the SDOF analysis and experimental results, and the load-deformation response using Saatcioglu DIF for both beams are illustrated in **Figure 9-3** and **Figure 9-4**. It was observed that the load-deflection responses of both beams in **Figure 9-3 (a)** and **Figure 9-4 (a)** showed lower maximum strength and yield strength for case1 than for cases 2 and 3 due to the effect of the dynamic increase factor. Case 3 showed larger maximum and yield strength when compared to Case 2 due to the larger dynamic increase factors in the Saatcioglu model.

For beam CB-10M-0%, the maximum displacements after the first and second shots (17 psi and 50 psi) were well predicted for cases 2 and 3, as shown in **Figure 9-3 (b)** and **(d)**, respectively. The SDOF analysis resulted in maximum displacements at shots 1-2 of 15.9 mm and 74.2 mm, respectively, for case 2, and of 14.9 mm and 67.4 mm for case 3 after the first and second shots, respectively. The analytical-to-experimental displacement ratios $\frac{\delta_{anls}}{\delta_{exp}}$ were 1.03 and 1.02 for Case 2 and 0.96 and 0.93 for Case 3 for the first and second shots, respectively (**Table 9-3)**. The SDOF

analysis over-estimated the mid-span displacement by 17% and 18% for both shots respectively when no DIF was considered, as shown in **Table 9-3** and **Figure 9-3 (c)** and **Figure 9-3 (e)**. **Figure 9-3 (b)** shows that the beam response for Case 3 reached the yield point as expected after the first shot of 17 psi, whereas **Figure 9-3 (d)** shows that the beam was in the post-yield range but still had capacity for more loading after the second shot of 50 psi.

For specimen CB-15M-0%, the SDOF analysis predicted well the maximum displacement for the three cases after the first shot, with prediction ratios of $\frac{\delta_{anls}}{\delta_{exp}}$ = 0.97, 0.94 and 0.92, respectively, whereas the maximum displacement was over-estimated by 14% for case 1 and was underestimated for cases 2 and 3 after the second shot, as shown in **Table 9-3** and **Figure 9-4 (c)** and **Figure 9-4 (e)**. The best prediction was obtained for Case 2, with a $\frac{\delta_{anls}}{\delta_{exp}}$ ratio of 0.97. The load-deformation behaviour of the beam for Case 3 showed that the beam had not reached the yield region after the first shot, whereas it reached its ultimate displacement after the second shot, as shown in **Figure 9-4 (b)** and **Figure 9-4 (d),** respectively.

**Table 9-4** summarizes the analytical-to-experimental displacement ratios for both control beams and for each of the DIF cases. The results of the SDOF analysis provided predictions within 10% of the experimental results with COV of 5% or lower when the DIF was included. The results were closer to the experimental values when DIFs were applied to the material properties in the analysis, with the best predictions obtained using the design DIF model (average $\frac{\delta_{anls}}{\delta_{exp}}$ ratio = 0.98).

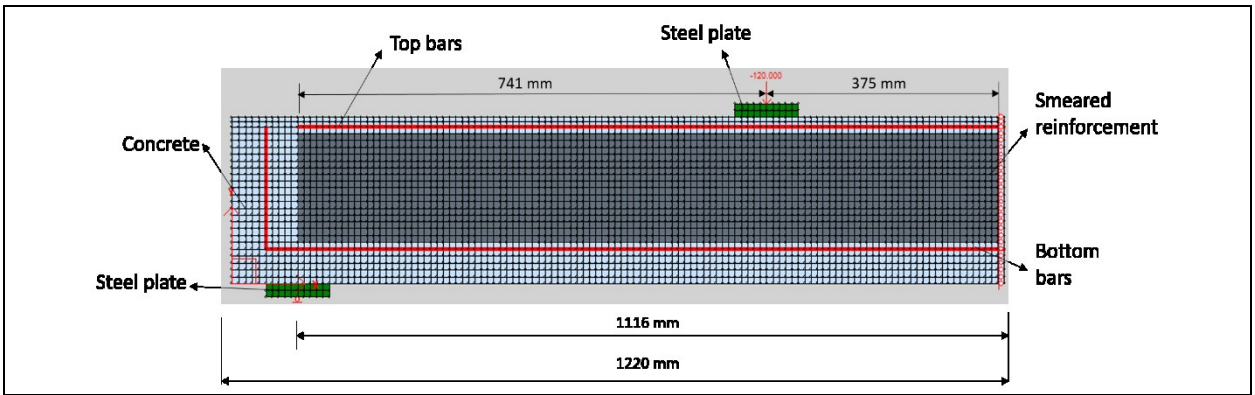
Table 9-3 Idealized blast properties and analysis results

| Beam ID | Shot # | Idealized shockwave properties | | | Maximum mid-span displacement | | | | | | |
|---|---|---|---|---|---|---|---|---|---|---|---|
| | | | | | | Analysis (SDOF) | | | | | |
| | | $P_r$ (kPa) | $I_r$ (kPa·msec) | $t_d$ (msec) | $\delta_{exp}$ (mm) | $\delta_{anls}$ (mm) No DIF | $\delta_{anls}$ (mm) design DIF | $\delta_{anls}$ (mm) Saatcioglu DIF | $\delta_{anls}/\delta_{exp}$ No DIF | $\delta_{anls}/\delta_{exp}$ design DIF | $\delta_{anls}/\delta_{exp}$ Saatcioglu DIF |
| CB-10M-0% | 1 | 31.3 | 250 | 15.9 | 15.4 | 18.0 | 15.9 | 14.9 | 1.17 | 1.03 | 0.96 |
| | 2 | 61.0 | 550 | 18.0 | 72.6 | 85.8 | 74.2 | 67.4 | 1.18 | 1.02 | 0.93 |
| CB-15M-0% | 1 | 24.0 | 248 | 20.7 | 10.6 | 10.3 | 9.9 | 9.7 | 0.97 | 0.94 | 0.92 |
| | 2 | 78.8 | 734 | 18.6 | 70.6 | 80.9 | 68.9 | 62.4 | 1.14 | 0.97 | 0.88 |

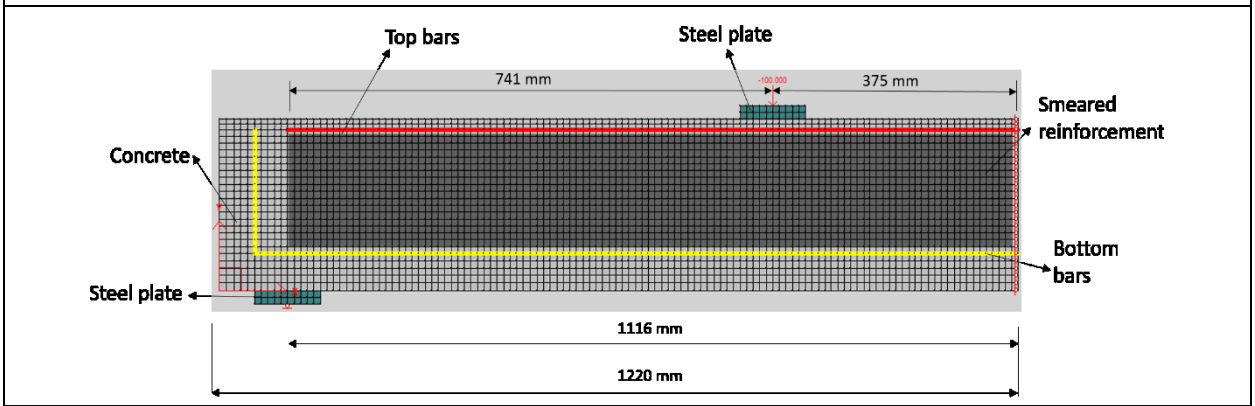
$P_r$ =reflected pressure; $I_r$ = reflected impulse; $t_d$ = positive phase duration; $\delta_{exp}$ = experimental mid-span displacement; $\delta_{anls}$ = analytical mid-span displacement.

Table 9-4 Summary of analysis results for control beams

| All beams | Shot # | $\delta_{anls}/\delta_{exp}$ | | | | | |
|---|---|---|---|---|---|---|---|
| | | No DIF | | Design DIF | | Saatcioglu DIF | |
| | | Avg. | S.D. (COV) | Avg. | S.D. (COV) | Avg. | S.D. (COV) |
| Statistical data | 1 | 1.07 | 0.14 (13.2) | 0.98 | 0.06 (6.1) | 0.94 | 0.02 (2.1) |
| | 2 | 1.16 | 0.02 (1.7) | 0.99 | 0.03 (3.0) | 0.90 | 0.03 (3.3) |
| | Avg | 1.11 | 0.06 (5.4) | 0.98 | 0.007 (0.7) | 0.92 | 0.02 (2.1) |

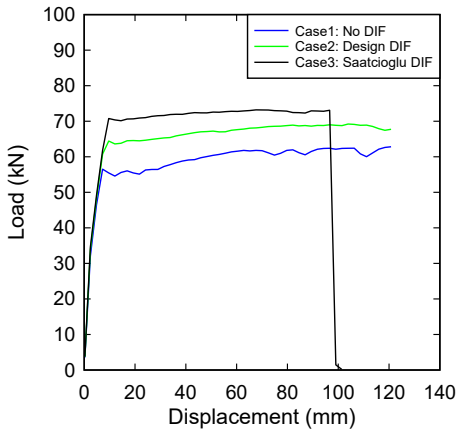



a- CB-10M-0%

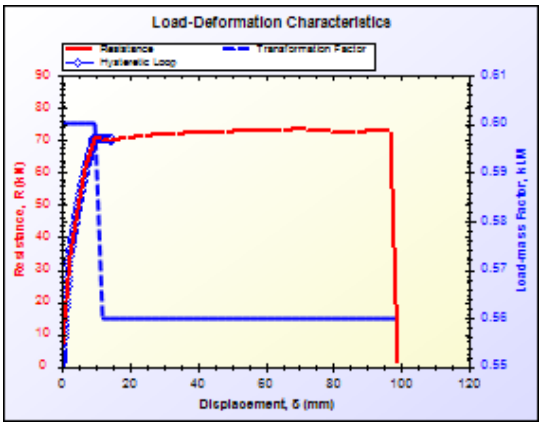



b- CB-15M-0%

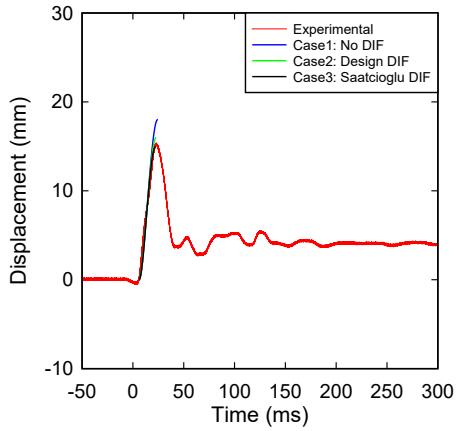
Figure 9-2 FE model



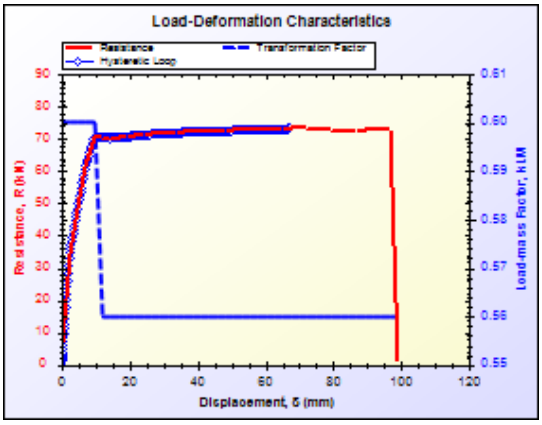

a- Resistance function



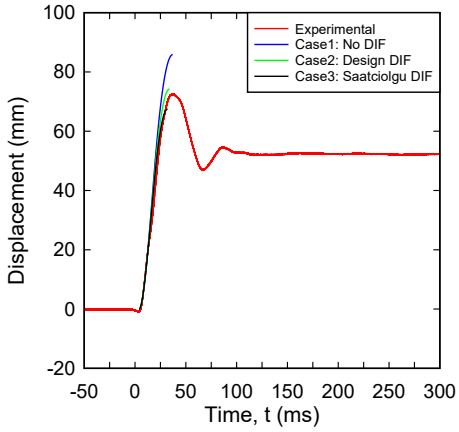

b- Load-deformation (Saatcioglu DIF, 17 psi)




c- Displacement-time history (17 psi)

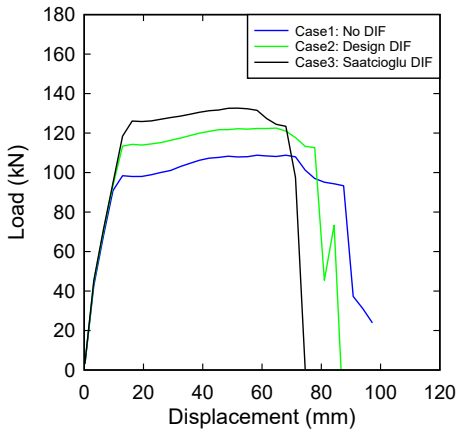



d- Load-deformation (Saatcioglu DIF, 50 psi)

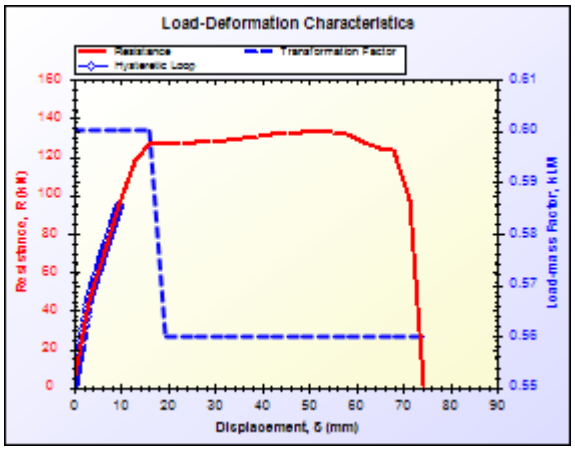



e- Displacement-time history (50 psi)

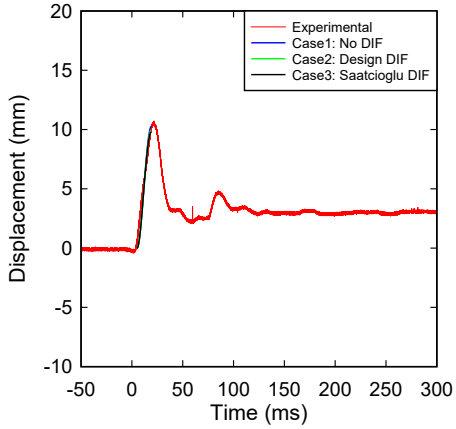
Figure 9-3 Predicted (SDOF) vs experimental displacements (CB-10M-0%)



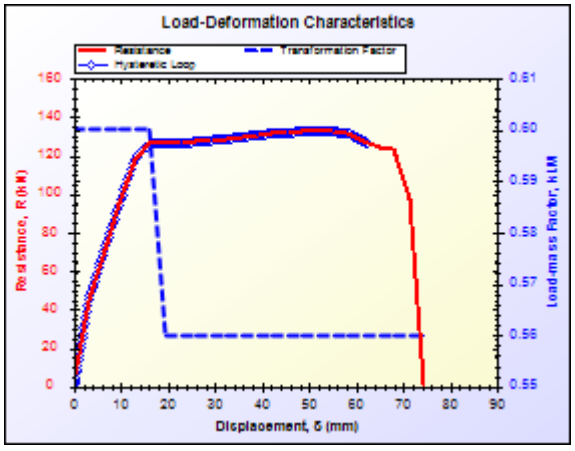

a- Resistance function



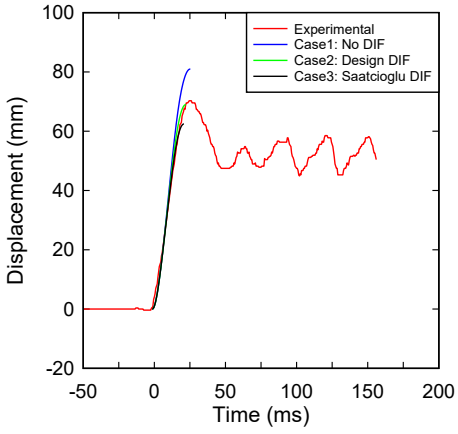

b- Load-deformation (Saatcioglu DIF, 17 psi)




c- Displacement-time history (17 psi)




d- Load-deformation (Saatcioglu DIF, 70 psi)




e- Displacement-time history (70 psi)

Figure 9-4 Predicted (SDOF) vs experimental displacements (CB-15M-0%)

#### 9.4.1.2 Specimens undergoing corrosion at mid-span

This section presents the SDOF analysis results of beams, which were undergoing tension reinforcement corrosion at mid-span. These beams include specimens B-MC-10M-11%, B-MC-10M-15%, B-EMC-10M-22%, B-MC-15M-12%, and B-EMC-15M-17%. In addition, the results for beams B-CR-MC-10M-5% and B-CR-MC-15M-4%, whose concrete cover was removed before applying accelerated corrosion over a partial length of 750 mm at mid-span, were also included. The FE models used a 10×10 mm mesh in this analysis, with truss bar elements and smeared reinforcement for the longitudinal and transverse reinforcement, respectively. Corrosion-induced damage in each beam was modeled by modifying the steel stress-strain properties and inducing cracking in the concrete elements surrounding the longitudinal bars over a length of 750 mm at mid-span (refer to **Figure 9-5**). The experimental and the SDOF analysis results are summarized in **Table 9-5**, with a summary of the results tabulated in **Table 9-6**. The resistance function obtained from the FE simulation, the displacement-time history comparison between the SDOF analysis and experimental results, and the load-deformation response using Saatcioglu DIF for each beam are shown in **Figure 9-6** to **Figure 9-12**.

From observing the resistance functions obtained from the FE analysis, it was noted that using cases 2 and 3 with DIF applied to the material properties resulted in higher capacities for each beam compared to case 1 with no DIF, as illustrated in **Figure 9-6 (a)** to **Figure 9-12 (a)**. The ductility was similar for the three DIF cases in all beams, with the exception of specimens B-MC-15M-12% and B-EMC-15M-17%. Using case 3 in the FE analysis of beam B-MC-15M-12% resulted in higher ductility than in cases 1 and 2, as shown in **Figure 9-10 (a)**, whereas the ductility of beam B-EMC-15M-17% obtained using case 3 fallen in between cases 1 and 2, as presented in **Figure 9-12 (a)**.

The trend of the predicted maximum displacement for B-MC-10M-11% showed good agreement with the experimental data for the three DIF cases after applying the first shot, as observed in **Figure 9-6 (c)** and **Table 9-5**. The maximum displacement after the second shot reached 82.2 mm for case 3 (see **Figure 9-6 (e)**), with a prediction ratio of $\frac{\delta_{anls}}{\delta_{exp}} = 0.95$ as reported in **Table 9-5**. In comparison, cases 1-2 predicted failure (i.e., ultimate displacement exceeded). The load-deformation response after applying the first shot in **Figure 9-6 (b)** showed the beam exceeded the yield point, whereas the beam nearly reached the ultimate displacement after the second shot,

as shown in **Figure 9-6 (d)**. The results from shot 2 were consistent with the severe failure observed in the experiments.

The prediction of the maximum mid-span displacement for B-MC-10M-15% was high for cases 1 and 2, with values reaching 22.2 mm and 19.0 mm, respectively; however the prediction for case3 was acceptable with the $\frac{\delta_{anls}}{\delta_{exp}}$ ratio of 1.12 after the first shot (**Figure 9-7 (c)**). The SDOF results for the second shot underestimated the maximum displacement for all cases, with ratios of $\frac{\delta_{anls}}{\delta_{exp}}$ = 0.93, 0.84 and 0.76, for cases 1, 2 and 3, respectively, as presented in **Table 9-5** and **Figure 9-7 (e)**. The load-deformation in **Figure 9-7 (b)** shows the beam had reached yielding after the first shot, whereas **Figure 9-7 (d)** demonstrates that the beam was well into the post-yield range, but did not reach the ultimate displacement after the second shot.

The SDOF analysis for DIF case 3 of beam B-EMC-10M-22% predicted failure with a maximum mid-span displacement which exceeds the ultimate displacement in the resistance curve, as shown in **Table 9-5** and **Figure 9-8 (c)**. **Figure 9-8 (b)** shows that the beam completely failed which matches the observation in the experiments. Failures (ultimate displacement exceeded) wre also predicted for cases 1-2.

For Beam B-CR-MC-10M-5%, the maximum displacement from the SDOF analysis reached 75.7 mm with a prediction ratio of $\frac{\delta_{anls}}{\delta_{exp}}$ = 0.95 for case 3, which was an acceptable prediction when compared to the experimental result, as shown in **Table 9-5** and **Figure 9-9 (c)**. The load-deformation in **Figure 9-9 (b)** shows that the beam nearly reached the ultimate displacement. Failures (ultimate displacement exceeded) were predicted for cases 1-2.

The predicted maximum displacement after the first shot for B-MC-15M-12% was 12.9 mm, 12.2 mm and 11.9 mm, for DIF cases 1, 2 and 3, respectively, with numerical-to-experimental ratios of $\frac{\delta_{anls}}{\delta_{exp}}$ = 1.17, 1.11 and 1.08, respectively, as illustrated in **Figure 9-10 (c)**. After the second shot, the prediction ratios reached 1.08 and 1 for DIF cases 2 and 3, respectively, as shown in **Table 9-5** and **Figure 9-10 (e)**, whereas the simulation predicted failure occurs under case 1. This beam reached the yield point after the first shot (**Figure 9-10 (b)**), while the load-deformation result after the second shot showed that the beam still has deformation capacity as presented in **Figure 9-10 (d)**.

For beam B-CR-MC-15M-4%, the predicted displacement was acceptable for DIF cases 2 and 3 with prediction ratios of 0.92 and 0.84, respectively, as illustrated in **Table 9-5** and **Figure 9-11 (c)**, whereas failure was predicted for case 1. **Figure 9-11 (b)** shows that this beam approximately reached the ultimate displacement after a 70 psi shot under case 3.

The predicted results of B-EMC-15M-17% (single shot at 70 psi) underestimated the displacement for the three DIF cases with displacements of 99.8 mm, 89.0 mm and 82.4 mm and corresponding ratios of $\frac{\delta_{anls}}{\delta_{exp}}$ = 0.59, 0.52 and 0.49 for cases 1, 2 and 3, respectively, as seen in **Table 9-5** and **Figure 9-12 (c)**. The load-deformation result showed that the beam response was well into the post-yield range but had not yet failed as shown in **Figure 9-12 (b)**. On the other hand, the beam experienced a blow out failure in the experiment.

In general, examining all beams, the displacement predictions were unreliable for case 1 (no DIF) with predictions of failure in nearly all the simulations. Comparing cases 2 and 3, the design DIF model resulted in more accurate results, with an average $\frac{\delta_{anls}}{\delta_{exp}}$ ratio of 0.95. Case 3 generally under-estimated the final displacements with an average $\frac{\delta_{anls}}{\delta_{exp}}$ ratio of 0.90. Based on these findings, case 2 is recommended for the SDOF blast analysis of corrosion-damaged RC beams.

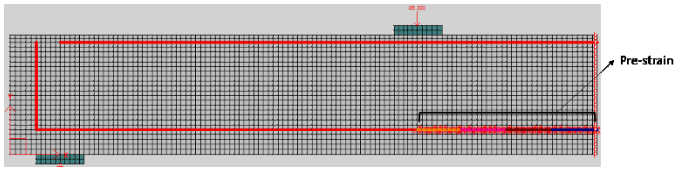
Table 9-5 Idealized blast properties and analysis results

| Beam ID | Shot # | Idealized shockwave properties | | | Maximum mid-span displacement | | | | | | |
|---|---|---|---|---|---|---|---|---|---|---|---|
| | | | | | | Analysis (SDOF) | | | | | |
| | | $P_r$ (kPa) | $I_r$ (kPa·msec) | $t_d$ (msec) | $\delta_{exp}$ (mm) | $\delta_{anls}$ (mm) No DIF | $\delta_{anls}$ (mm) design DIF | $\delta_{anls}$ (mm) Saatcioglu DIF | $\delta_{anls}/\delta_{exp}$ No DIF | $\delta_{anls}/\delta_{exp}$ design DIF | $\delta_{anls}/\delta_{exp}$ Saatcioglu DIF |
| B-MC-10M-11% | 1 | 27.3 | 257 | 18.8 | 18.0 | 20.6 | 17.6 | 16.0 | 1.14 | 0.98 | 0.89 |
| | 2 | 64.3 | 547 | 17.0 | 86.3 | -* | -* | 82.2 | - | - | 0.95 |
| B-MC-10M-15% | 1 | 27.8 | 249 | 17.9 | 15.6 | 22.2 | 19.0 | 17.6 | 1.42 | 1.22 | 1.12 |
| | 2 | 59.3 | 529 | 17.8 | 107.0 | 100.2 | 89.8 | 82.0 | 0.93 | 0.84 | 0.76 |
| B-EMC-10M-22% | 1 | 61.0 | 541 | 17.7 | 217.3 | -* | -* | -* | - | - | - |
| B-CR-MC-10M-5% | 1 | 65.6 | 548 | 16.7 | 79.0 | -* | -* | 75.7 | - | - | 0.95 |
| B-MC-15M-12% | 1 | 29.0 | 251 | 17.3 | 11.0 | 12.9 | 12.2 | 11.9 | 1.17 | 1.11 | 1.08 |
| | 2 | 80.0 | 703 | 17.5 | 71.2 | -* | 77.4 | 71.0 | - | 1.08 | 1 |
| B-CR-MC-15M-4% | 1 | 77.0 | 720 | 18.7 | 76.0 | -* | 70.2 | 64.1 | - | 0.92 | 0.84 |
| B-EMC-15M-17% | 1 | 80.1 | 729 | 18.2 | 169.0 | 99.8 | 89.0 | 82.4 | 0.59 | 0.52 | 0.49 |

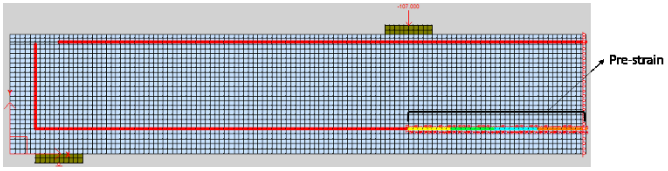
$P_r$ =reflected pressure; $I_r$ = reflected impulse; $t_d$ = positive phase duration; $\delta_{exp}$ = experimental mid-span displacement; $\delta_{anls}$ = analytical mid-span displacement. (*) = Ultimate displacement exceeded.

Table 9-6 Summary of analysis results for beams with corrosion at mid-span

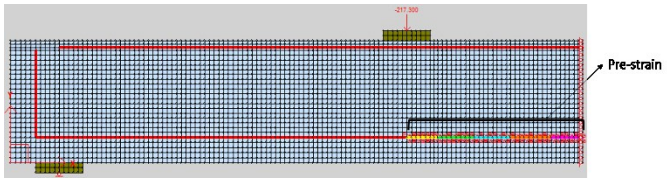
| All beams | Shot # | $\delta_{anls}/\delta_{exp}$ | | | | | |
|---|---|---|---|---|---|---|---|
| | | No DIF | | Design DIF | | Saatcioglu DIF | |
| | | Avg. | S.D. (%) | Avg. | S.D. (%) | Avg. | S.D. (%) |
| Statistical data | 1 | 1.08 | 0.34 (31.4) | 0.95 | 0.26 (27.3) | 0.83 | 0.26 (31.3) |
| | 2 | - | - | 0.96 | 0.16 (16.6) | 0.90 | 0.12 (13.3) |
| | Avg | 1.08 | 0.34 (31.4) | 0.95 | 0.007 (0.7) | 0.87 | 0.04 (4.5) |



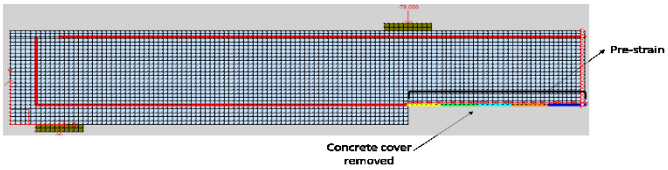

B-MC-10M-11%



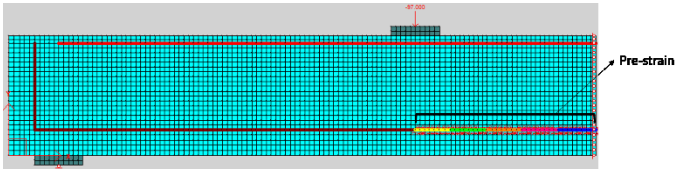

B-MC-10M-15%



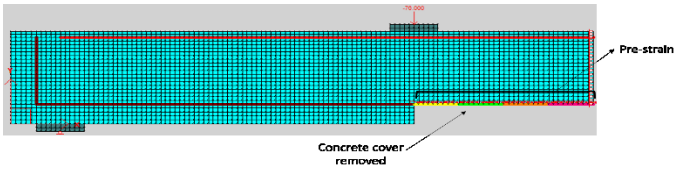

B-EMC-10M-22%



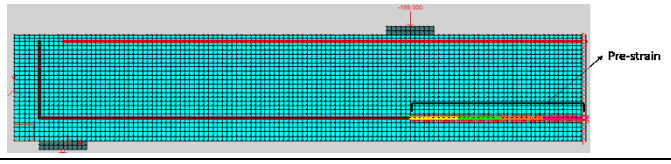

B-CR-MC-10M-5%




B-MC-15M-12%

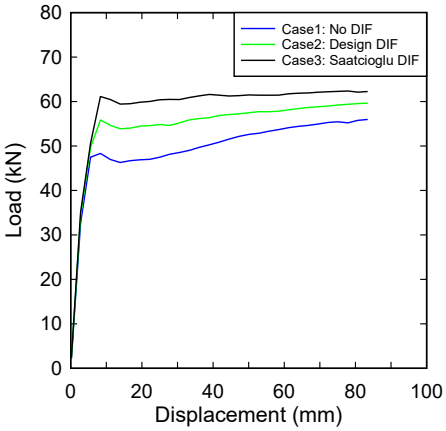



B-CR-MC-15M-4%

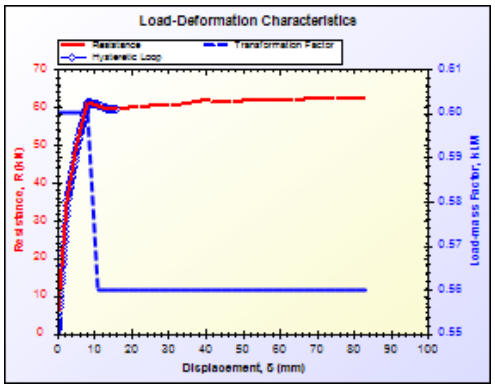



B-EMC-15M-17%

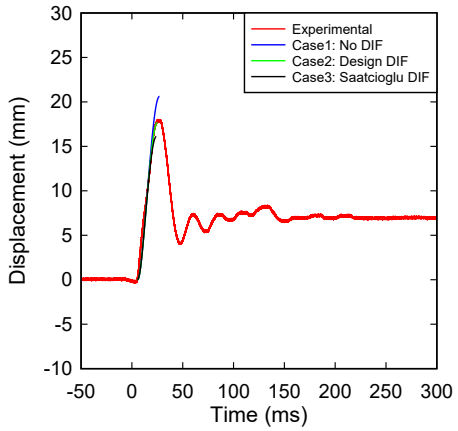
Figure 9-5 FE models for beams undergoing corrosion at mid-span



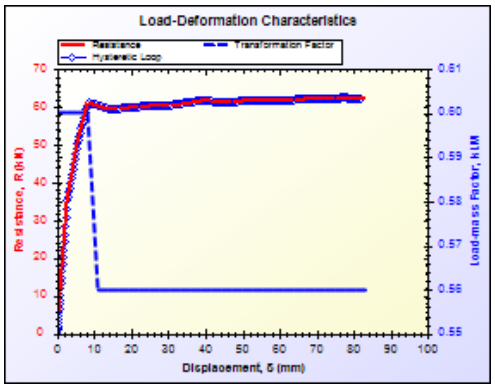

a- Resistance function



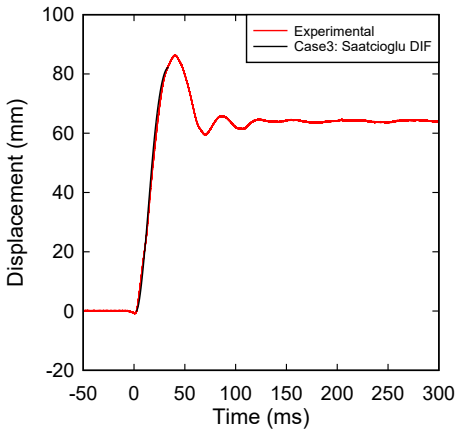

b- Load-deformation (Saatcioglu DIF, 17 psi)




c- Displacement-time history (17 psi)

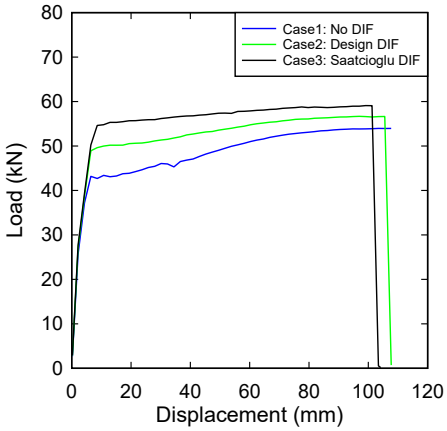



d- Load-deformation (Saatcioglu DIF, 50 psi)

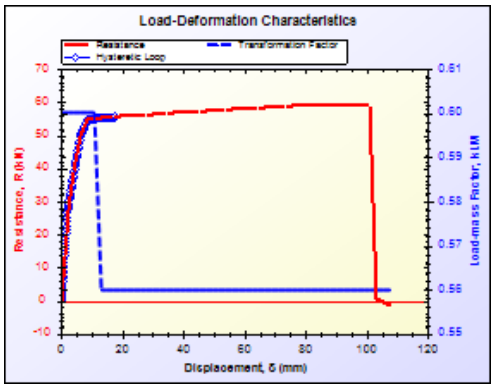



e- Displacement-time history (50 psi)

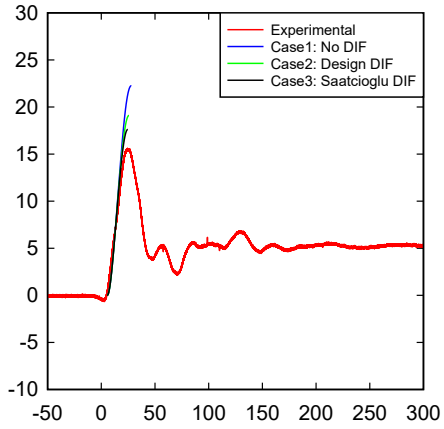
Figure 9-6 Predicted (SDOF) vs experimental displacements (B-MC-10M-11%)



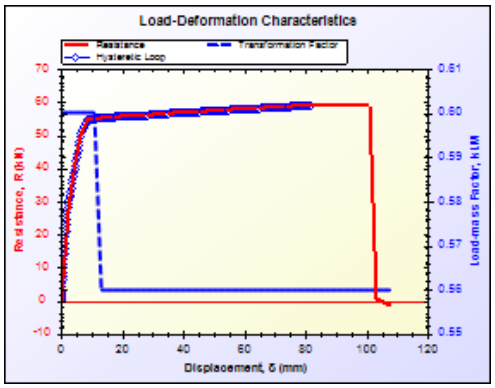

a- Resistance function



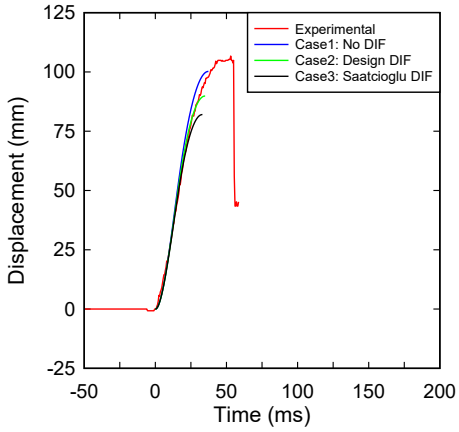

b- Load-deformation (Saatcioglu DIF, 17 psi)




c- Displacement-time history (17 psi)

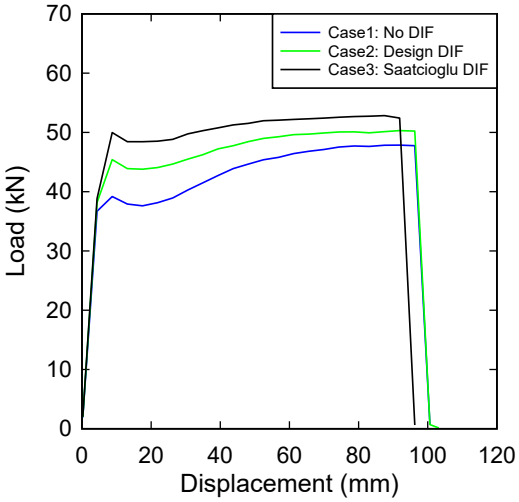



d- Load-deformation (Saatcioglu DIF, 50 psi)

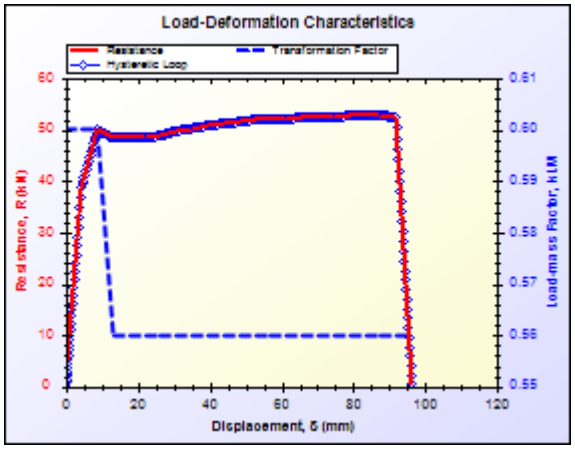



e- Displacement-time history (50 psi)

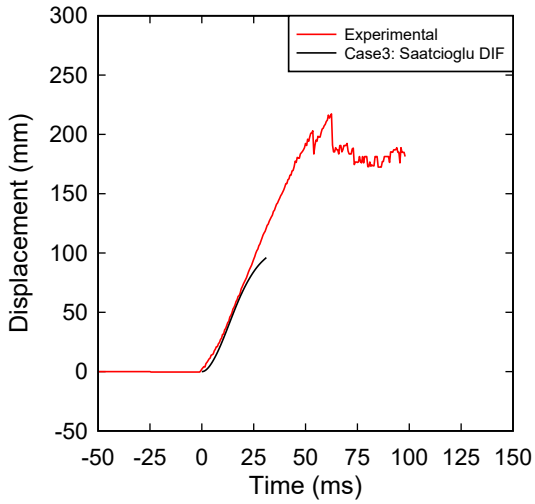
Figure 9-7 Predicted (SDOF) vs experimental displacements (B-MC-10M-15%)




a- Resistance function

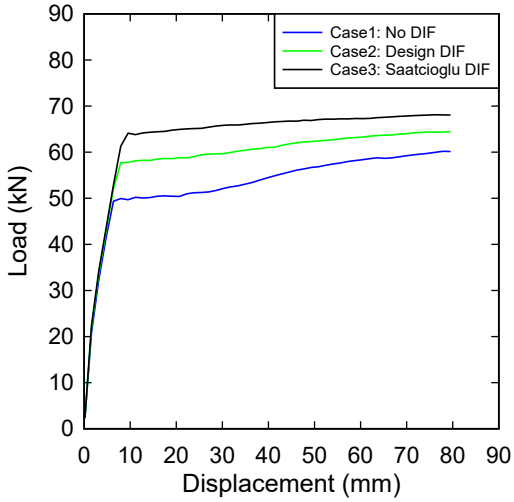



b- Load-deformation (Saatcioglu DIF, 50 psi)

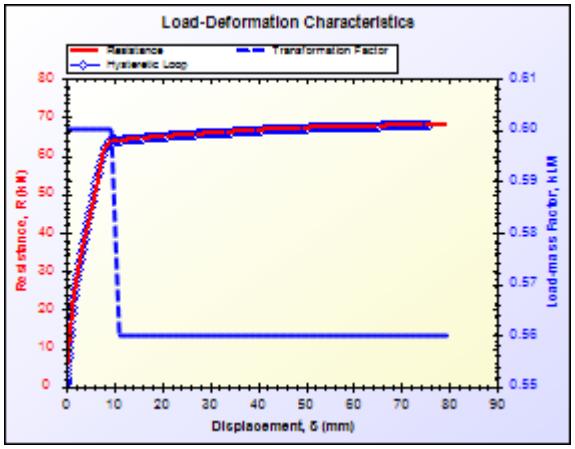



c- Displacement-time history (50 psi)

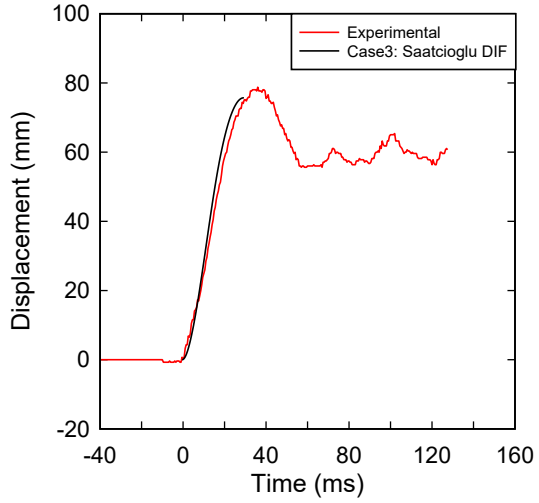
Figure 9-8 Predicted (SDOF) vs experimental displacements (B-EMC-10M-22%)




a- Resistance function

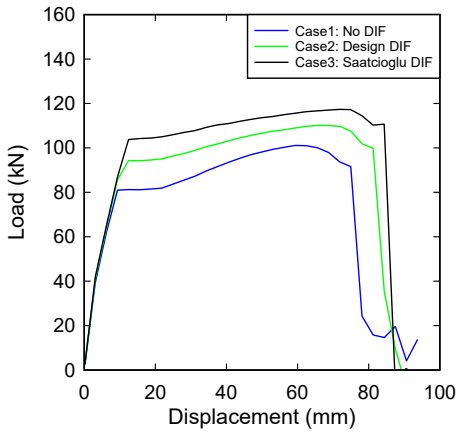



b- Load-deformation (Saatcioglu DIF, 50 psi)

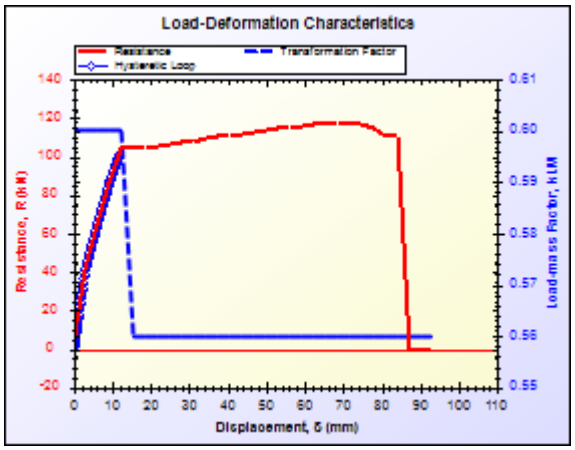



c- Displacement-time history (50 psi)

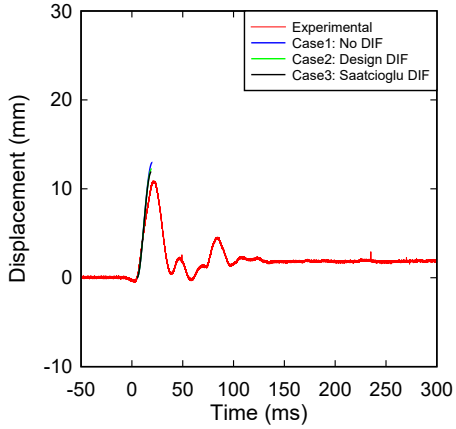
Figure 9-9 Predicted (SDOF) vs experimental displacements (B-CR-MC-10M-5%)



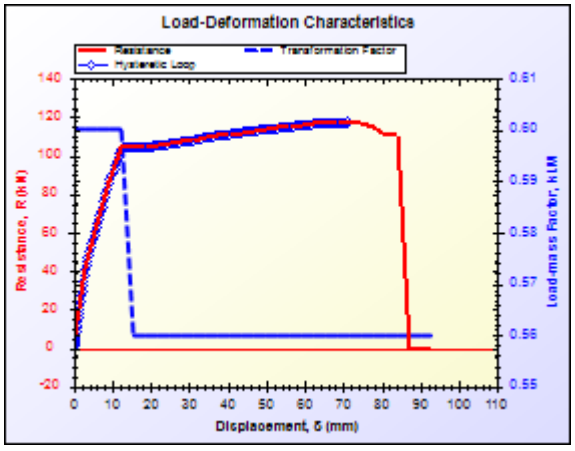

a- Resistance function



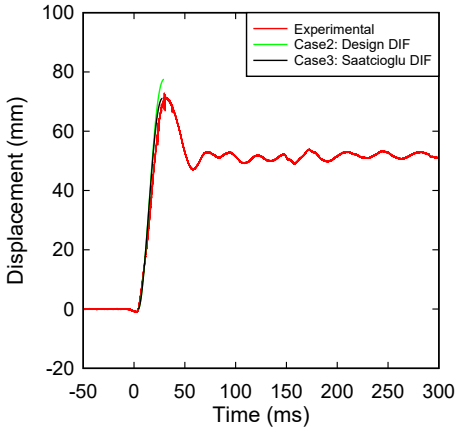

b- Load-deformation (Saatcioglu DIF, 17 psi)




c- Displacement-time history (17 psi)

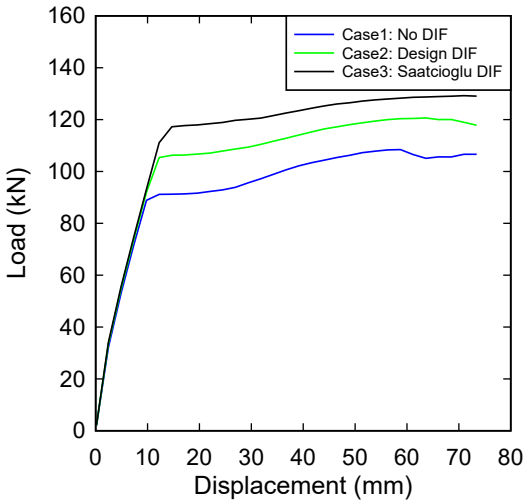



d- Load-deformation (Saatcioglu DIF, 70 psi)

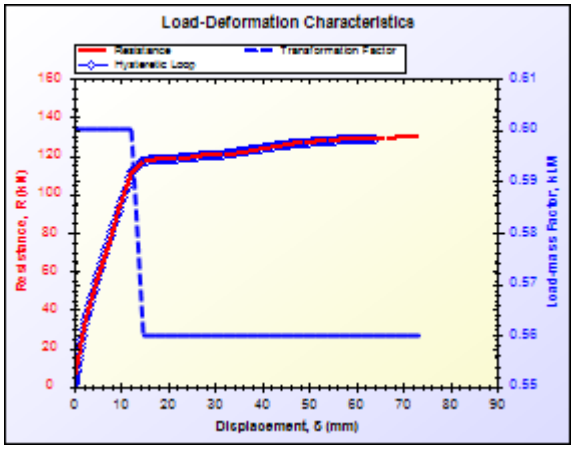



e- Displacement-time history (70 psi)

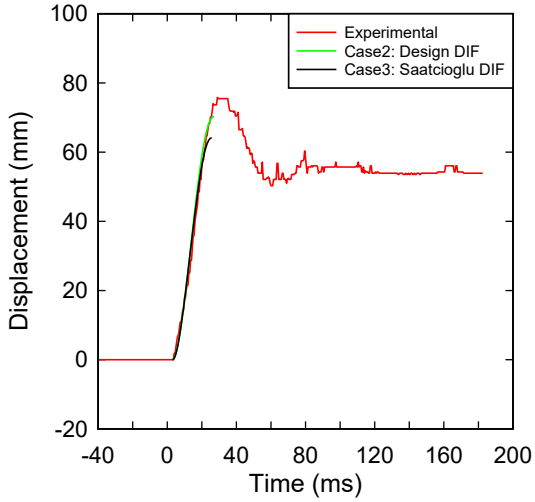
Figure 9-10 Predicted (SDOF) vs experimental displacements (B-MC-15M-12%)




a- Resistance function

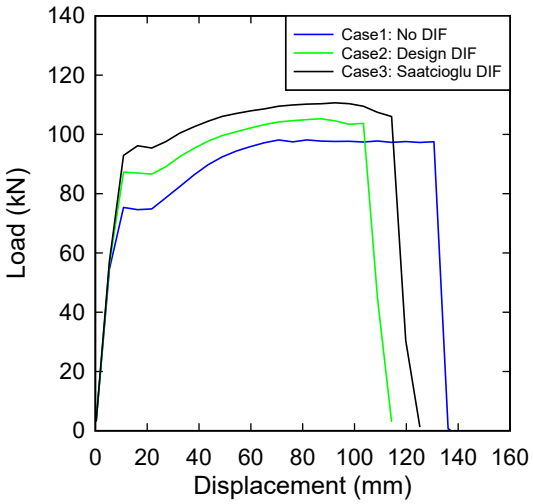



b- Load-deformation (Saatcioglu DIF, 70 psi)

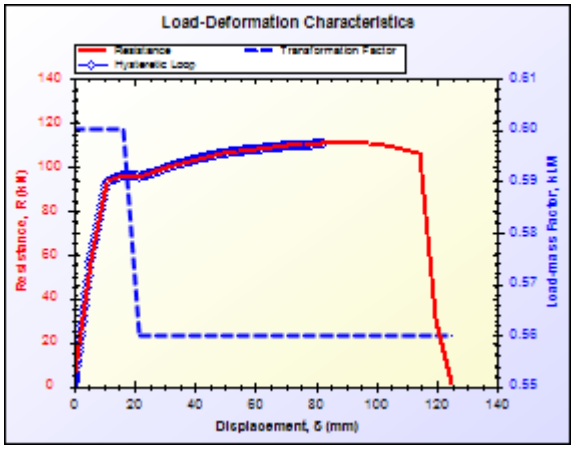



c- Displacement-time history (70 psi)

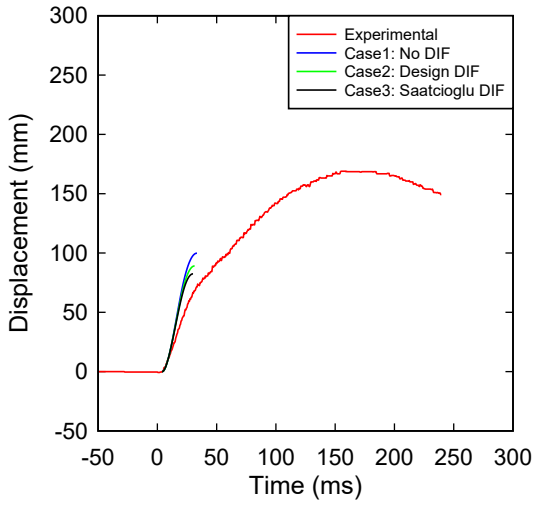
Figure 9-11 Predicted (SDOF) vs experimental displacements (B-CR-MC-15M-4%)




a- Resistance function




b- Load-deformation (Saatcioglu DIF, 70 psi)

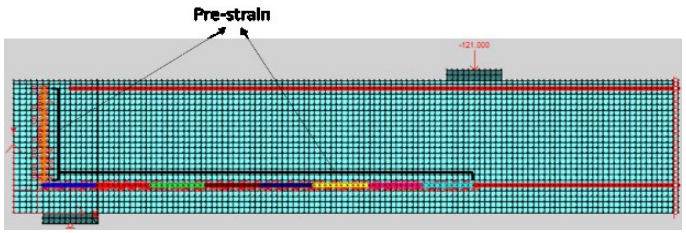



c- Displacement-time history (70 psi)

Figure 9-12 Predicted (SDOF) vs experimental displacements (B-EMC-15M-17%)

#### 9.4.1.3 Specimen undergoing corrosion at end supports

Specimen B-SC-10M-7% had its longitudinal tensile reinforcement corroded at its ends, with a measured average mass loss of 7%. As a part of the SDOF analysis, the FE model used to obtain the resistance function had the same features presented in Section 9.3.1.2, except that corrosion effects were introduced at both beam ends only (refer to **Figure 9-13**). **Figure 9-14 (a)** shows that the predicted load-deflection of this beam displayed less ductility for DIF case 3 compared to the other two DIF cases; however, it predicted a higher yield load and ultimate capacity for this DIF case.




a- B-SC-10M-7%

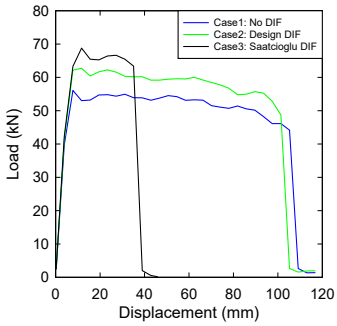
Figure 9-13 FE model of beam undergoing corrosion at the ends

The SDOF results for this beam are summarized in **Table 9-7**. Whereas the predicted displacement after the first blast shot was underestimated for the three DIF cases (**Figure 9-14 (c)**), the displacement after the second shot was overestimated for DIF cases 1 and 2 with near perfect results for case 3 (**Figure 9-14 (e)**). DIF cases 2 and 3 showed acceptable results at this shot, with prediction ratios of 1.06 and 0.99, respectively, whereas case 1 resulted in a larger displacement ratio of 1.21 (refer to **Table 9-7** and **Figure 9-14 (e)**). At shot 3, cases 1 and 2 resulted in over-estimations of the maximum displacements; however, a more accurate result was obtained for case 2 ( $\frac{\delta_{anls}}{\delta_{exp}}$ ratios of 1.41 and 1.20 for cases 1 and 2, respectively). The ultimate displacement was exceeded for case 3. The load-deformation curves for case 2 showed that the beam exceeded yielding after the first and second shots (**Figure 9-14 (b)** and **Figure 9-14 (d)**) but did not reach the ultimate displacement after shot 3 (refer to **Figure 9-14 (f)**). In contrast, the ultimate displacement was exceeded when using case 3 (refer to **Figure 9-14 (h)**).

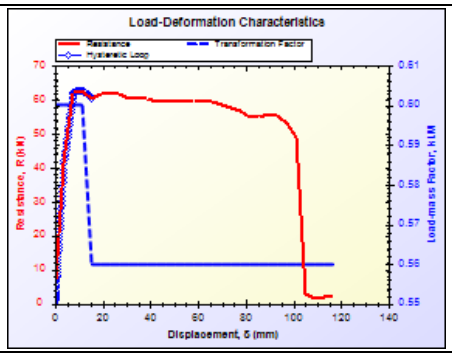
Table 9-7 Idealized blast properties and results for beam B-SC-10M-7%

| Beam ID | Shot # | Idealized shockwave properties | | | Maximum mid-span displacement | | | | | | |
|---|---|---|---|---|---|---|---|---|---|---|---|
| | | | | | | Analysis (SDOF) | | | | | |
| | | $P_r$ (kPa) | $I_r$ (kPa·msec) | $t_d$ (msec) | $\delta_{exp}$ (mm) | $\delta_{anls}$ (mm) No DIF | $\delta_{anls}$ (mm) design DIF | $\delta_{anls}$ (mm) Saatcioglu DIF | $\delta_{anls}/\delta_{exp}$ No DIF | $\delta_{anls}/\delta_{exp}$ design DIF | $\delta_{anls}/\delta_{exp}$ Saatcioglu DIF |
| B-SC-10M-7% | 1 | 29.2 | 239 | 16.3 | 20.4 | 17.6 | 15.6 | 14.8 | 0.86 | 0.76 | 0.73 |
| | 2 | 48.5 | 356 | 14.6 | 33.0 | 40.2 | 35.0 | 32.6 | 1.21 | 1.06 | 0.99 |
| | 3 | 61.5 | 555 | 18.0 | 70.1 | 99.0 | 84.7 | -* | 1.41 | 1.20 | - |

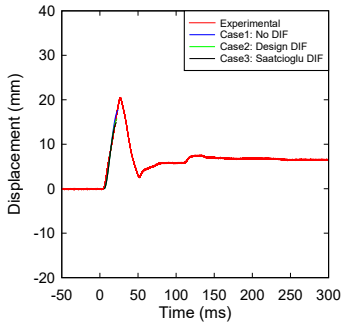
$P_r$ =reflected pressure; $I_r$ = reflected impulse; $t_d$ = positive phase duration; $\delta_{exp}$ = experimental mid-span displacement; $\delta_{anls}$ = analytical mid-span displacement; (*) = Ultimate displacement exceeded.



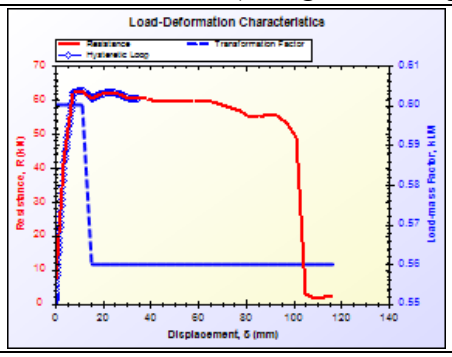

a- Resistance function



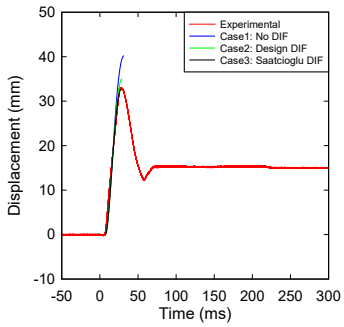

b- Load-deformation (Design DIF, 17 psi)



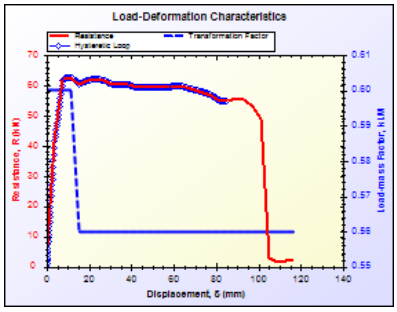

c- Displacement-time history (17 psi)



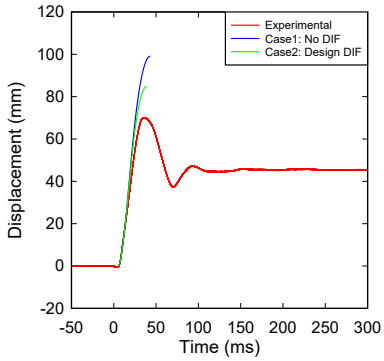

d- Load-deformation (Design DIF, 35 psi)



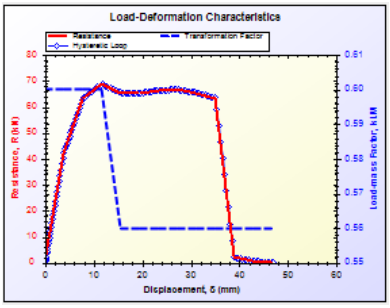

e- Displacement-time history (35 psi)




f- Load-deformation (Design DIF, 50 psi)




g- Displacement-time history (50 psi)




h- Load-deformation (Saatcioglu DIF, 50 psi)

Figure 9-14 Predicted (SDOF) vs experimental displacements (B-SC-10M-7%)

#### 9.4.1.4 Specimen undergoing corrosion along the entire span

Beam B-FC-10M-12% was subjected to corrosion of the tension reinforcement over its entire span, with an average mass loss of 12%. The FE model used to obtain the resistance function for the SDOF analysis had the same modelling features as the previous beams; however, the corroded bar properties and corrosion induced-cracking in the concrete elements were introduced over the entire span of the longitudinal tensile reinforcement (see **Figure 9-15**).

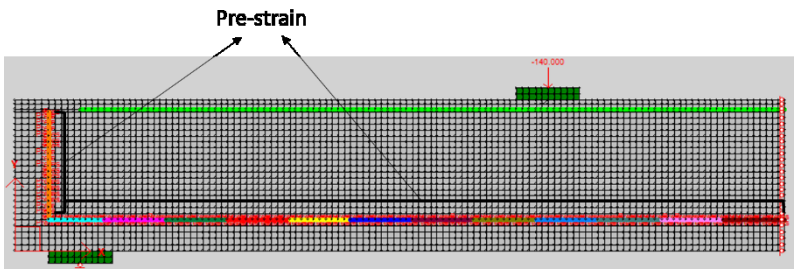
Like beam B-SC-10M-7%, whose reinforcement was corroded at the support ends, the load-deflection response of beam B-FC-10M-12% obtained from the FE analysis showed higher yield load and ultimate capacity for DIF case 3 albeit lower ductility than the other two DIF cases (see **Figure 9-16 (a)**).

From **Figure 9-16 (c)** and **Table 9-8**, it was observed that the predicted displacement of the beam was overestimated for DIF case 1 and underestimated for DIF case 3, with prediction ratios of $\frac{\delta_{anls}}{\delta_{exp}}$ = 1.15 and 0.91, respectively. The analysis of this beam using DIF case 2 resulted with the same maximum displacement of 84.0 mm observed in the experimental blast test. According to **Figure 9-16 (b)**, this beam yielded but did not reach the ultimate displacement under case 3.

Table 9-8 Idealized blast properties and results for beam B-FC-10M-12%

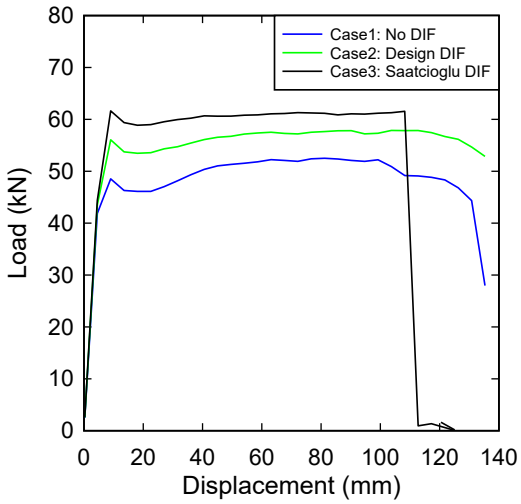
| Beam ID | Shot # | Idealized shockwave properties | | | Maximum mid-span displacement | | | | | | |
|---|---|---|---|---|---|---|---|---|---|---|---|
| | | | | | | Analysis (SDOF) | | | | | |
| | | $P_r$ (kPa) | $I_r$ (kPa·msec) | $t_d$ (msec) | $\delta_{exp}$ (mm) | $\delta_{anls}$ (mm) No DIF | $\delta_{anls}$ (mm) design DIF | $\delta_{anls}$ (mm) Saatcioglu DIF | $\delta_{anls}/\delta_{exp}$ No DIF | $\delta_{anls}/\delta_{exp}$ design DIF | $\Delta_{anls}/\delta_{exp}$ Saatcioglu DIF |
| B-SC-10M-7% | 1 | 52 | 540 | 20.7 | 83.7 | 96.5 | 84.0 | 76.3 | 1.15 | 1.00 | 0.91 |

$P_r$ =reflected pressure; $I_r$ = reflected impulse; $t_d$ = positive phase duration; $\delta_{exp}$ = experimental mid-span displacement; $\delta_{anls}$ = analytical mid-span displacement.

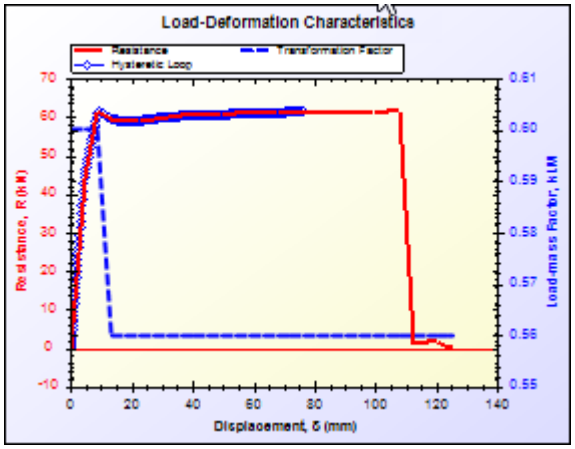



a- B-FC-10M-12%

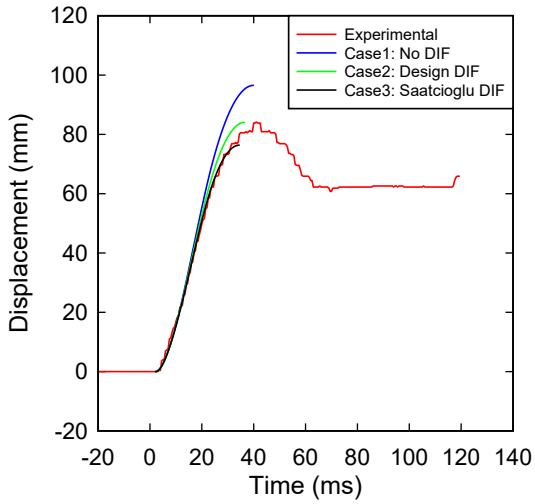
Figure 9-15 FE model of beam undergoing corrosion along its entire length




a- Resistance function




b- Load-deformation (Saatcioglu DIF, 50 psi)




c- Displacement-time history (50 psi)

Figure 9-16 Predicted (SDOF) vs experimental displacements (B-FC-10M-12%)

### 9.4.2 Shear-governed beams

The results of the SDOF analysis for the shear-dominant beams in the 25M group are presented in this section. This group included one control beam and two corroded specimens with a different mass loss %. The FE models used a 20×20 mm mesh, with truss bar elements for both the longitudinal (25M) and transverse (6.3 mm) reinforcement. Stirrups were modelled as truss elements to facilitate the input of corrosion-induced deterioration. The resistance functions obtained from the FE analysis were used in RCBlast to obtain the dynamic response of the beams.

#### 9.4.2.1 Control shear beam CB-25M-%

This beam was the first beam simulated without considering the corrosion effects in the 25M group. The FE model of this beam is shown in **Figure 9-17**. The load-deflection responses of the beam from the FE analysis for the three DIF cases are shown in **Figure 9-18 (a)**. According to **Table 9-9** and **Figure 9-18 (c)**, failure was predicted under case 1, 2 and 3 (ultimate displacement exceeded). Nonetheless, the load-deformation response under case 3 showed that the beam reached the ultimate displacement at this blast (see **Figure 9-18 (b)**).

Table 9-9 Idealized blast properties and results for control beam CB-25M-0%

| Beam ID | Shot # | Idealized shockwave properties | | | Maximum mid-span displacement | | | | | | |
|---|---|---|---|---|---|---|---|---|---|---|---|
| | | | | | | Analysis (SDOF) | | | | | |
| | | $P_r$ (kPa) | $I_r$ (kPa·msec) | $t_d$ (msec) | $\delta_{exp}$ (mm) | $\delta_{anls}$ (mm) No DIF | $\delta_{anls}$ (mm) design DIF | $\delta_{anls}$ (mm) Saatcioglu DIF | $\delta_{anls}/\delta_{exp}$ No DIF | $\delta_{anls}/\delta_{exp}$ design DIF | $\delta_{anls}/\delta_{exp}$ Saatcioglu DIF |
| CB-25M-0% | 1 | 91.4 | 927 | 20.3 | 46.0 | -* | -* | -* | - | - | - |

$P_r$ =reflected pressure; $I_r$ = reflected impulse; $t_d$ = positive phase duration; $\delta_{exp}$ = experimental mid-span displacement; $\delta_{anls}$ = analytical mid-span displacement; (*) = Ultimate displacement exceeded.

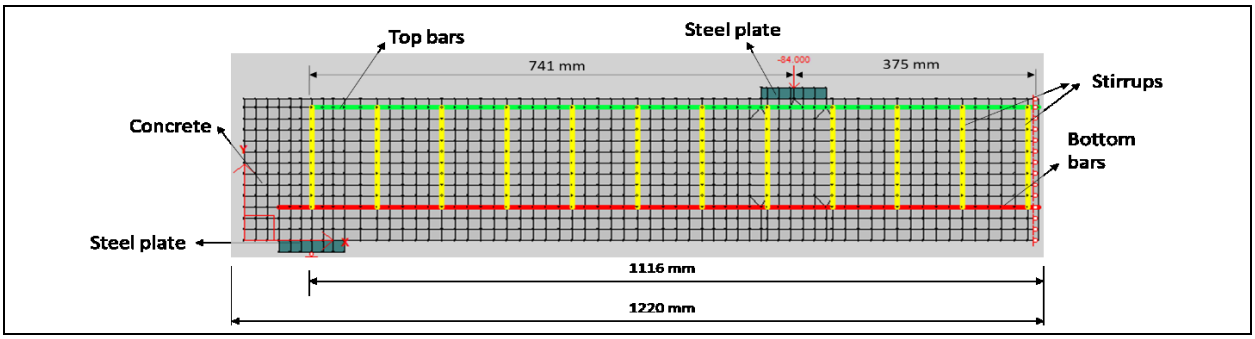
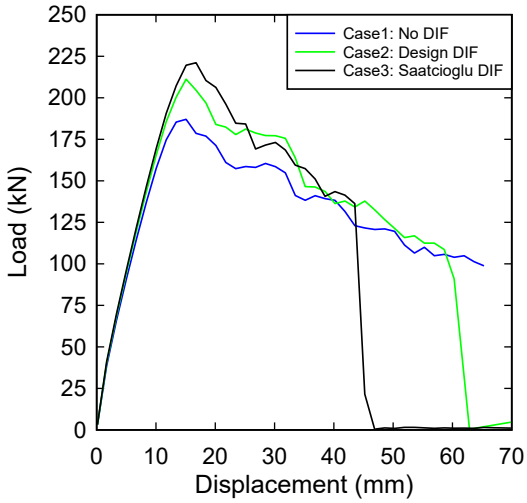
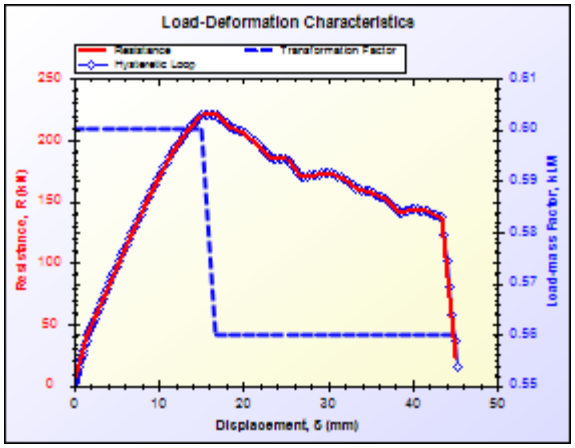


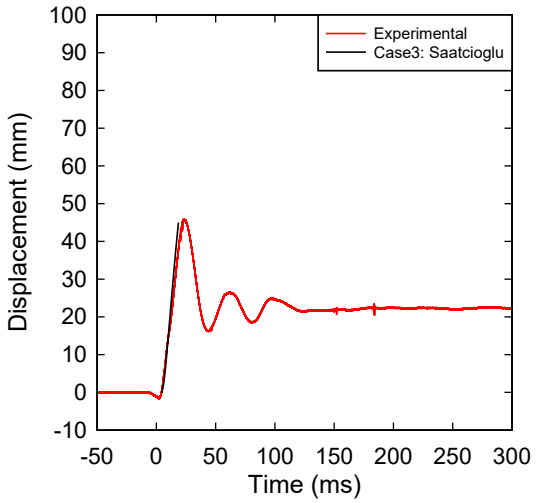

Figure 9-17 FE model of CB-25M-0%




a- Resistance function




b- Load-deformation (Saatcioglu DIF, 90 psi)




c- Displacement-time history (90 psi)

Figure 9-18 Predicted (SDOF) vs experimental displacements (CB-25M-0%)

#### 9.4.2.2 Shear corrosion beams: B-SHC-25M-11% and B-SHC-25M-12%

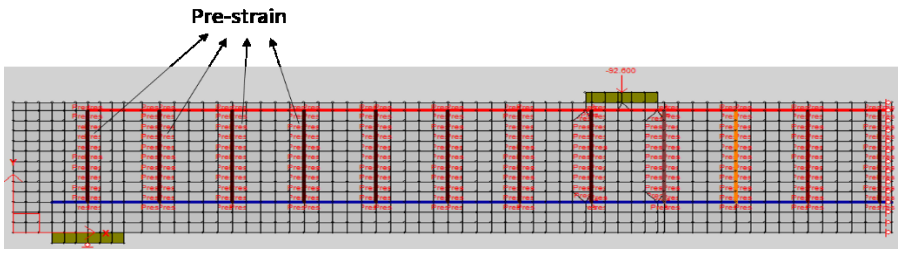
This section presents the SDOF analysis of the 25M beams with corroded shear reinforcement. The same FE model used for the control beam in this group was used; however, corrosion effects were applied on the stirrups over the entire beam span by modifying their steel properties based on 12% and 11% mass loss, while corrosion-induced cracking was simulated by applying pre-strains on the concrete elements next to the transverse reinforcement, as shown in **Figure 9-19**.

Both beams showed that the predicted resistance curve of DIF case 3 was higher than the other two DIF cases; however, the ductility of beam B-SHC-25M-12% for case 3 was higher compared to the other beam B-SHC-25M-11% (see **Figure 9-20 (a)** and **Figure 9-21 (a)**). The predicted displacement for both beams exceeded the ultimate displacement for the three DIF cases, which indicates failure (refer to **Figure 9-20 (c)** and **Figure 9-21 (c)**). This can also be confirmed when observing the load-deformation responses in **Figure 9-20 (b)** and **Figure 9-21 (b)**.

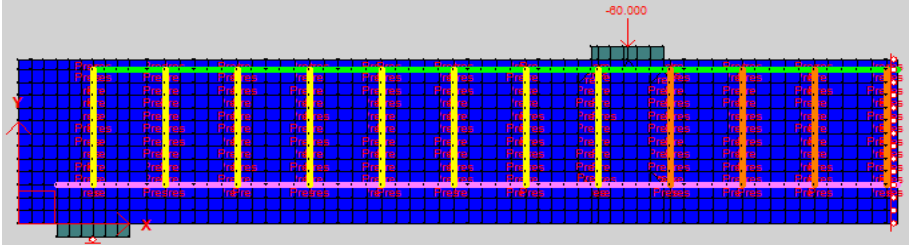
Table 9-10 Idealized blast properties and results for beams undergoing stirrup corrosion

| Beam ID | Shot # | Idealized shockwave properties | | | Maximum mid-span displacement | | | | | | |
|---|---|---|---|---|---|---|---|---|---|---|---|
| | | | | | | Analysis (SDOF) | | | | | |
| | | $P_r$ (kPa) | $I_r$ (kPa·msec) | $t_d$ (msec) | $\delta_{exp}$ (mm) | $\delta_{anls}$ (mm) No DIF | $\delta_{anls}$ (mm) design DIF | $\delta_{anls}$ (mm) Saatcioglu DIF | $\delta_{anls}/\delta_{exp}$ No DIF | $\delta_{anls}/\delta_{exp}$ design DIF | $\delta_{anls}/\delta_{exp}$ Saatcioglu DIF |
| B-SHC-25M-11% | 1 | 96.7 | 903 | 18.6 | 92.6 | -* | -* | -* | - | - | - |
| B-SHC-25M-12% | 1 | 95.2 | 926 | 19.4 | 45.5 | -* | -* | -* | - | - | - |

$P_r$ =reflected pressure; $I_r$ = reflected impulse; $t_d$ = positive phase duration; $\delta_{exp}$ = experimental mid-span displacement; $\delta_{anls}$ = analytical mid-span displacement; (*) = Ultimate displacement exceeded.

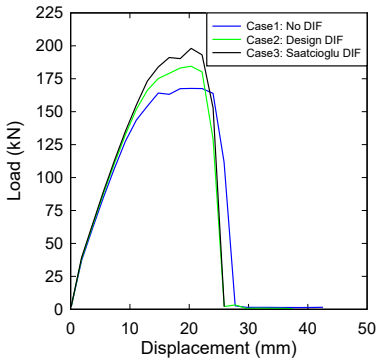



a- B-SHC-25M-11%

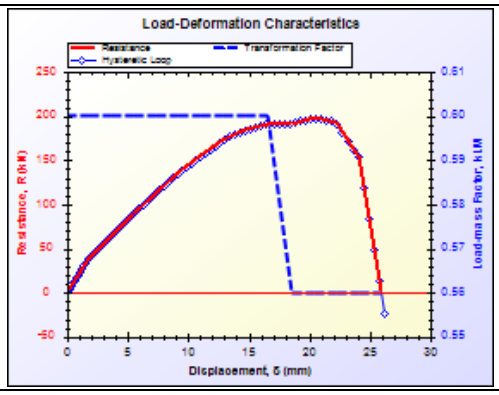


b- B-SHC-25M-12%

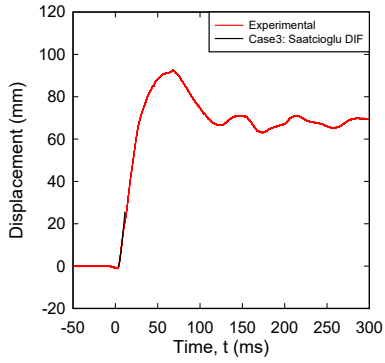
Figure 9-19 FE models of beams undergoing stirrup corrosion




a- Resistance function

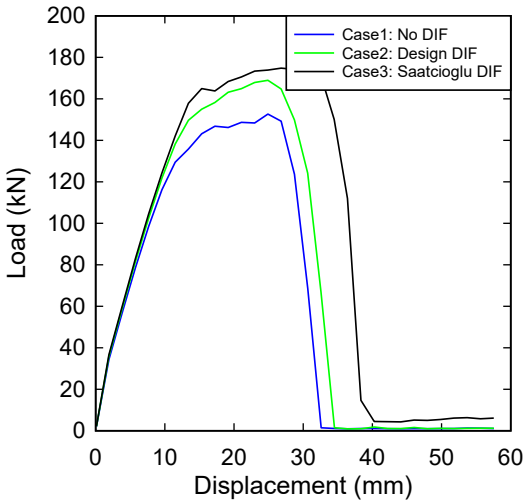



b- Load-deformation (Saatcioglu DIF, 90 psi)

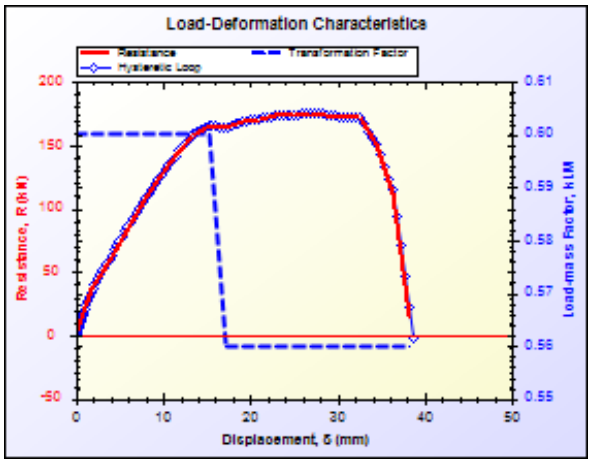



c- Displacement-time history (90 psi)

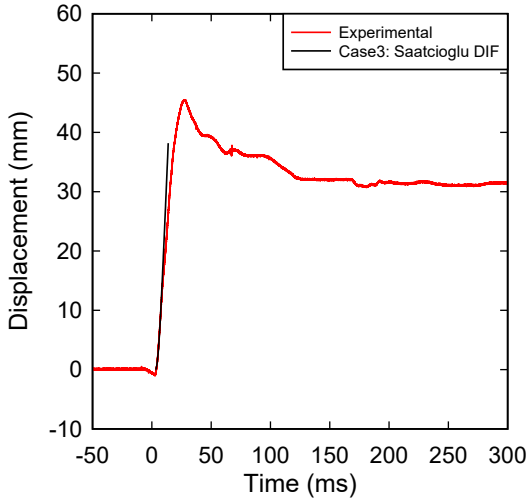
Figure 9-20 Predicted (DIF) vs experimental (B-SHC-25M-11%)




a- Resistance function




b- Load-deformation (Saatcioglu DIF, 90 psi)




c- Displacement-time history (90 psi)

Figure 9-21 Predicted (DIF) vs experimental (B-SHC-25M-12%)

# Chapter 10: Finite Element Analysis of Corrosion-Damaged Beams Under Blast-Loading

## 10.1 Chapter Overview

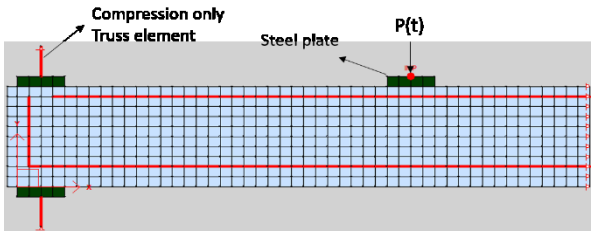
This chapter aims to present the last phase of the numerical research programme by predicting the full dynamic response of the tested beams under blast-loading. A 2D nonlinear finite element software (VecTor2) was used to develop finite element models of the control and corroded beams. The corrosion effects were considered during the analysis by modifying the steel stress-strain relationship and modelling corrosion-induced cracking in the concrete. In addition, this chapter provides a description of the FE model for each beam, a summary of the FE results, and a comparison between the predicted and experimental results.

## 10.2 Modelling Methodology

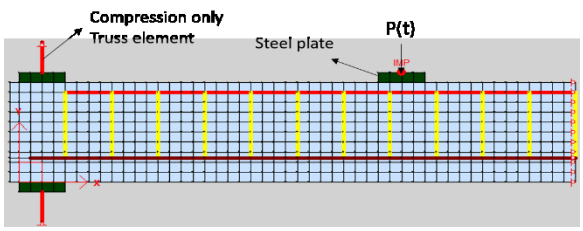
Two-dimensional nonlinear finite element (FE) software (VecTor2) was used to predict the flexural and shear responses of the un-corroded (control) and corroded beams under blast-loading. The procedure used in the FE modelling of the 10M, 15M and 25M beam groups was the same as that used in the static analysis of the beams (see Chapter 8), with some modifications as follows: 1)- The mesh size used was 25×25 mm for all the models of the beams; 2)- dynamic increase factors (DIF) for concrete and reinforcing steel were used to consider the effects of strain-rates; 3)- the boundary conditions in the shock-tube were simulated by using steel plates and compression-only truss bars; 4)- the blast load was applied using an idealized five-point curve having the same peak reflected pressure and a similar post-peak loading as the experimental ones, as shown in **Figure 10-1 (c)**; 5)- the mass of the beam and LTD was distributed to all concrete nodes as nodal masses; and, 6)- the dynamic analysis was carried out using Newmark's constant acceleration method, with a time step of 0.1 ms and with Rayleigh damping implemented in the analysis. The typical FE model for each group is illustrated in **Figure 10-1 (a)** and **(b)**.

### 10.2.1 Corrosion inducing-cracking

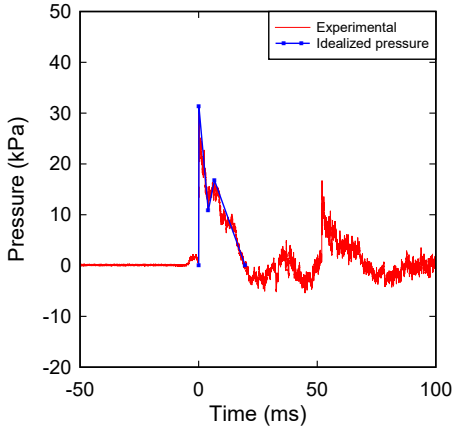
Corrosion inducing-cracking was simulated similarly as in the static analysis; however, the applied pre-strain was different since it is directly dependent on the actual steel mass loss due to corrosion. As a result, **Table 10-1** presents the applied pre-strain for beams tested under blast-loading.




a- 10M and 15M groups




b- 25M group




c- Idealized blast pressure-time history (10M group) (CB-10M-0%, 17 psi)

Figure 10-1 FE models and idealized blast pressure-time history

Table 10-1 Equivalent pre-strains with corresponding mass loss

| Beam ID | $M_{loss}$ (%) | μ | b (mm) | c (mm) | $A_s$ ($mm^2$) | $d_b$ (mm) | $A_{s(exp)}$ ($mm^2$) | $d_{exp}$ (mm) | ε (millistrain) |
|---|---|---|---|---|---|---|---|---|---|
| B-MC-10M-11% | 11% | 2 | 125 | 40 | 100.23 | 11.3 | 110.95 | 11.88 | 6.45 |
| B-SC-10M-7% | 7% | 2 | 125 | 40 | 100.23 | 11.3 | 107.13 | 11.68 | 4.18 |
| B-FC-10M-12% | 12% | 2 | 125 | 40 | 100.23 | 11.3 | 111.90 | 11.93 | 7.00 |
| B-MC-10M-15% | 15% | 2 | 125 | 40 | 100.23 | 11.3 | 114.70 | 12.08 | 8.63 |
| B-EMC-10M-22% | 22% | 2 | 125 | 40 | 100.23 | 11.3 | 121.07 | 12.41 | 12.25 |
| B-CR-MC-10M-5% | 5% | 2 | 125 | 40 | 100.23 | 11.3 | 105.18 | 11.57 | 3.01 |
| B-MC-15M-12% | 12% | 2 | 125 | 40 | 200.96 | 16 | 224.35 | 16.90 | 9.43 |
| B-CR-MC-15M-4% | 4% | 2 | 125 | 40 | 200.96 | 16 | 208.91 | 16.31 | 3.26 |
| B-EMC-15M-17% | 17% | 2 | 125 | 40 | 200.96 | 16 | 233.67 | 17.25 | 13.05 |
| B-SHC-25M-12% | 12% | 2 | 125 | 12.5 | 31.15 | 6.3 | 34.78 | 6.65 | 11.41 |
| B-SHC-25M-11% | 11% | 2 | 125 | 12.5 | 31.15 | 6.3 | 34.48 | 6.62 | 10.50 |

b = Beam width; c = Concrete cover; $A_s$ = Original steel bar area; $d_b$ = Original diameter of steel bar; $A_{s(exp)}$ = Total expanded area of corroded steel bar; $d_{exp}$ = Diameter of steel bars expanded; ε = Corrosion-induced pre-strain in concrete near the reinforcement.

### 10.3 Mesh size sensitivity

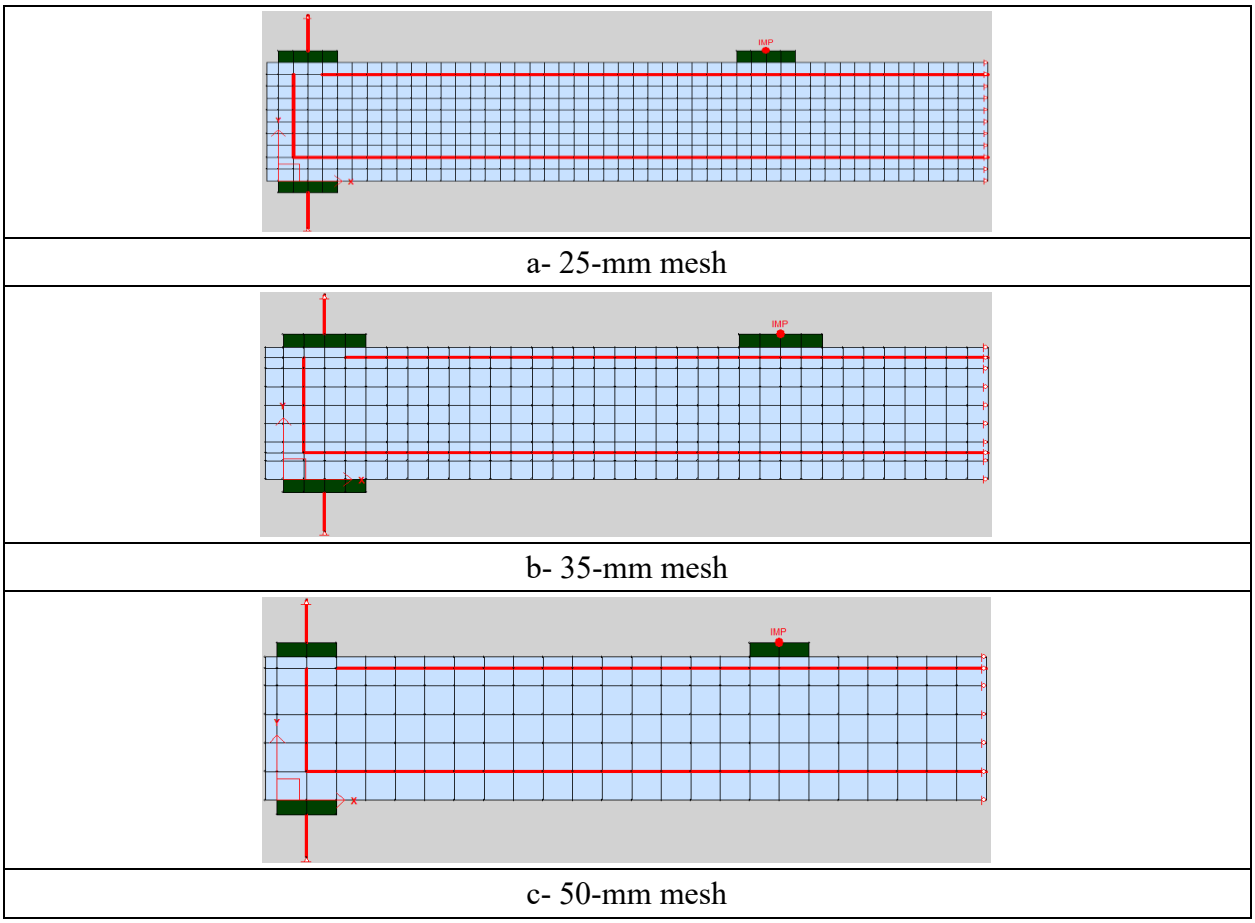
The optimal mesh size was chosen based on a mesh sensitivity analysis. The FE model accuracy was investigated by gradually increasing mesh size and comparing the numerical displacement results with the experimental ones. For flexure-governed beams, three mesh sizes of 25 mm, 35 mm and 50 mm were considered in the FE model of the control (un-corroded) 10M and 15M beams, as shown in **Figure 10-2**.

Considering CB-10M-0% and the first shot: the 25-mm mesh with 603 elements resulted in a maximum displacement of 12.5 mm; the 35-mm mesh with 399 elements resulted in a displacement of 13.3 mm; and the 50-mm mesh with 207 elements resulted in a maximum displacement of 17.8 mm (see **Figure 10-3 (a)**). The mesh sizes studied to apply the second blast shot were 25 mm and 35 mm, with maximum displacements of 59.4 mm and 75.2 mm, respectively (see **Figure 10-3 (b)**). No results could be obtained with the 50 mm mesh.

Considering CB-15M-0% and the first shot: the 25-mm mesh with 603 elements resulted in a maximum displacement of 8.7 mm; the 35-mm mesh with 399 elements resulted in a displacement of 8.7 mm; and the 50-mm mesh with 207 elements resulted in a maximum displacement of 10.0 mm (see **Figure 10-3 (c)**). The mesh sizes studied to apply the second blast shot were 25 mm, 35 mm, and 50 mm, with maximum displacements of 66.7 mm, 75.3 mm and 110.1 mm, respectively (refer to **Figure 10-3 (d)**).

The results considering both beams are shown in **Table 10-2** and **Figure 10-4**. The average numerical-to-experimental displacement ratios $\frac{\delta_{num}}{\delta_{exp}}$ for the mesh sizes of 25, 35 and 50 mm were respectively 0.85, 0.95 and 1.22 with coefficients of variation (COV) of 7.1%, 12.6% and 25.4%.

In general, the mesh size of 25 mm was deemed to have the most stable results when compared with the experimental values. Consequently, all FE models for corroded and un-corroded beams were simulated using a mesh size of 25×25 mm.



a- 25-mm mesh

b- 35-mm mesh

c- 50-mm mesh

Figure 10-2 Mesh sizes considered in the analysis of the control beams

Table 10-2 Mesh sensitivity: data analysis

| Beam ID | Shot # | Shockwave properties | | Maximum displacements | | | | Displacement ratios | | |
|---|---|---|---|---|---|---|---|---|---|---|
| | | $P_r$ (kPa) | $I_r$ (kPa·msec) | $\delta_{exp}$ (mm) | $\delta_{num}$ (mm) | | | $\delta_{num}/\delta_{exp}$ | | |
| | | | | | Mesh 25 | Mesh 35 | Mesh 50 | Mesh 25 | Mesh 35 | Mesh 50 |
| CB-10M-0% | 1 | 31.3 | 250 | 15.4 | 12.5 | 13.3 | 17.8 | 0.81 | 0.86 | 1.16 |
| | 2 | 61.0 | 550 | 72.6 | 59.4 | 75.2 | - | 0.82 | 1.03 | - |
| CB-15M-0% | 1 | 24.0 | 248 | 10.6 | 8.7 | 8.7 | 10.0 | 0.82 | 0.82 | 0.94 |
| | 2 | 78.8 | 734 | 70.6 | 66.7 | 75.3 | 110.1 | 0.95 | 1.07 | 1.56 |
| | | | | | | | Average | 0.85 | 0.95 | 1.22 |
| | | | | | | | STDEV | 0.06 | 0.12 | 0.31 |
| | | | | | | | COV | 7.1% | 12.6% | 25.4% |

Note: $P_r$ =reflected pressure; $I_r$ = reflected impulse; $\delta_{exp}$ = experimental maximum mid-span displacement; $\delta_{num}$ = numerical maximum mid-span displacement; $\delta_{num}/\delta_{exp}$ = displacement ratio.

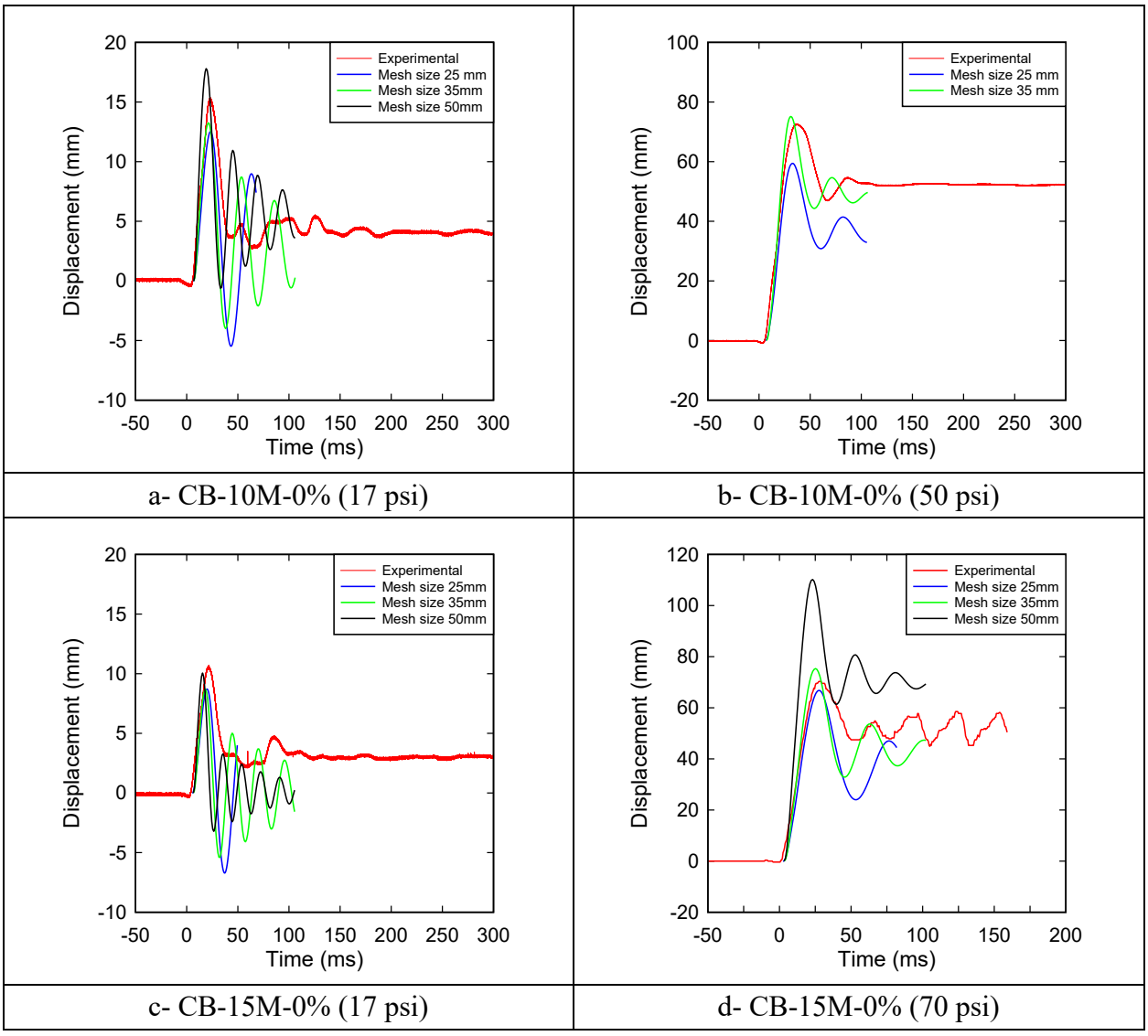
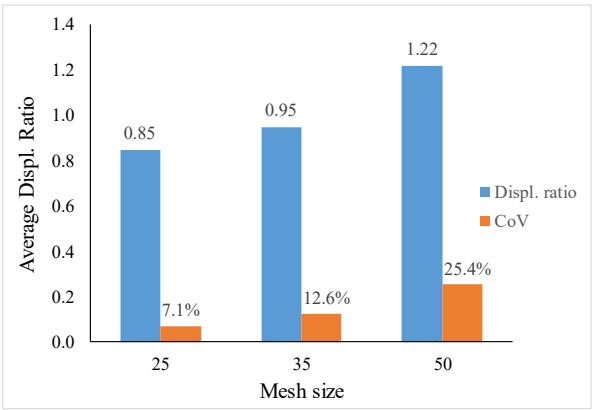
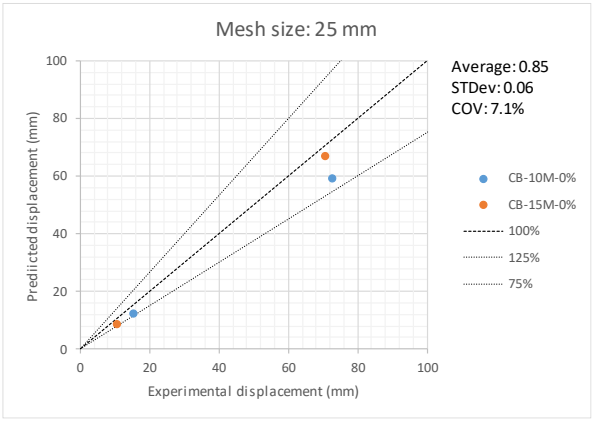


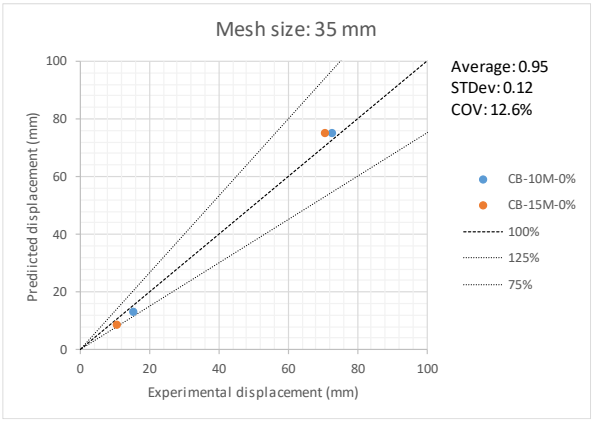

Figure 10-3 Mesh size sensitivity: displacement-time histories



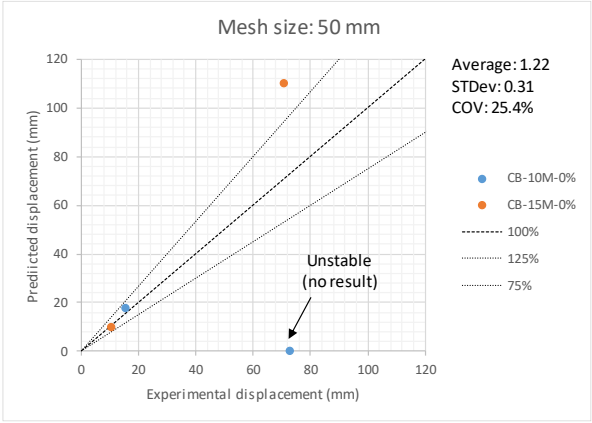

a- Average displacement ratios




b- Mesh size: 25 mm




c- Mesh size: 35 mm




d- Mesh size: 50mm

Figure 10-4 Mesh size sensitivity: average displacement ratios and comparison of displacements

## 10.4 Dynamic increase factor (DIF) sensitivity

The model used to apply a DIF to material properties was selected based on a DIF sensitivity analysis. The accuracy of the FE model was examined by applying four different options of DIF models and comparing the simulated displacements with the experimental ones:

i. Option DIF1: fib MC2010 for concrete, Malvar-Crawford for reinforcing steel,
ii. Option DIF2: fib MC2010 for concrete, CEB-FIB (1988) for reinforcing steel,
iii. Option DIF3: fib MC1990 for concrete, CEB-FIB (1988) for reinforcing steel, and
iv. Option No DIF: no DIF was applied to material properties.

A sensitivity analysis of the above 4 options was carried out by conducting FE analysis of the control (un-corroded) 10M and 15M beams, CB-10M-10% and CM-15M-0%, as well as two beams with mid-span corrosion within each series, B-MC-10M-11% and B-MC-15-12%. Sample displacement-time histories for each beam are shown in **Figure 10-5**.

The results considering all 4 beams are shown in **Table 10-3** and **Figure 10-6**. The average displacement ratios $\frac{\delta_{num}}{\delta_{exp}}$ for DIF options 1, 2, 3 and No DIF were respectively 0.87, 0.93, 0.91 and 1.07, with coefficients of variation (COV) of 9.2%, 9.7%, 9.8% and 11.2%.

Similar results were obtained for DIF options 2 and 3, whereas the displacements were generally over-estimated (with displacement ratios > 1.0) when No DIF is applied. According to **Figure 10-6 (a)**, the most suitable DIF option for the analysis is DIF2 when comparing the average experimental and numerical results. Accordingly, Option DIF2 was used for the remaining flexure-governed beams in the 10M and 15M groups and for the shear-governed beams in the 25M group.

Table 10-3 DIF sensitivity: data analysis

| Beam ID | Shot # | Shockwave properties | | Maximum displacements | | | | | Displacement ratios | | | |
|---|---|---|---|---|---|---|---|---|---|---|---|---|
| | | $P_r$ (kPa) | $I_r$ (kPa·msec) | $\delta_{exp}$ (mm) | $\delta_{num}$ (mm) | | | | $\delta_{num}/\delta_{exp}$ | | | |
| | | | | | DIF1 | DIF2 | DIF3 | No DIF | DIF1 | DIF2 | DIF3 | No DIF |
| CB-10M-0% | 1 | 31.3 | 250 | 15.4 | 12.5 | 12.7 | 12.4 | 14.6 | 0.81 | 0.82 | 0.8 | 0.94 |
| | 2 | 61.0 | 550 | 72.6 | 59.4 | 65.0 | 64.4 | 73.9 | 0.81 | 0.89 | 0.88 | 1.01 |
| CB-15M-0% | 1 | 24.0 | 248 | 10.6 | 8.7 | 8.7 | 8.5 | 9.6 | 0.82 | 0.82 | 0.80 | 0.90 |
| | 2 | 78.8 | 734 | 70.6 | 66.7 | 73.8 | 72.6 | 86.4 | 0.94 | 1.04 | 1.02 | 1.22 |
| B-MC-10M-11% | 1 | 27.3 | 257 | 18.0 | 14.3 | 15.2 | 15.4 | 18.8 | 0.79 | 0.84 | 0.85 | 1.04 |
| | 2 | 64.3 | 547 | 86.3 | - | 83.5 | 82.0 | 98.0 | - | 0.97 | 0.95 | 1.13 |
| B-MC-15M-12% | 1 | 29.0 | 251 | 11.0 | 11.0 | 11.0 | 10.8 | 12.0 | 1.00 | 1.00 | 0.98 | 1.09 |
| | 2 | 80.0 | 703 | 71.2 | 66.0 | 72.8 | 71.3 | 87.0 | 0.93 | 1.02 | 1.00 | 1.22 |
| | | | | | | | | Average | 0.87 | 0.93 | 0.91 | 1.07 |
| | | | | | | | | STDEV | 0.08 | 0.09 | 0.09 | 0.12 |
| | | | | | | | | COV | 9.2% | 9.7% | 9.8% | 11.2% |

Note: $P_r$ =reflected pressure; $I_r$ = reflected impulse; $\delta_{exp}$ = experimental maximum mid-span displacement; $\delta_{num}$ = numerical maximum mid-span displacement; $\delta_{num}/\delta_{exp}$ = displacement ratio.

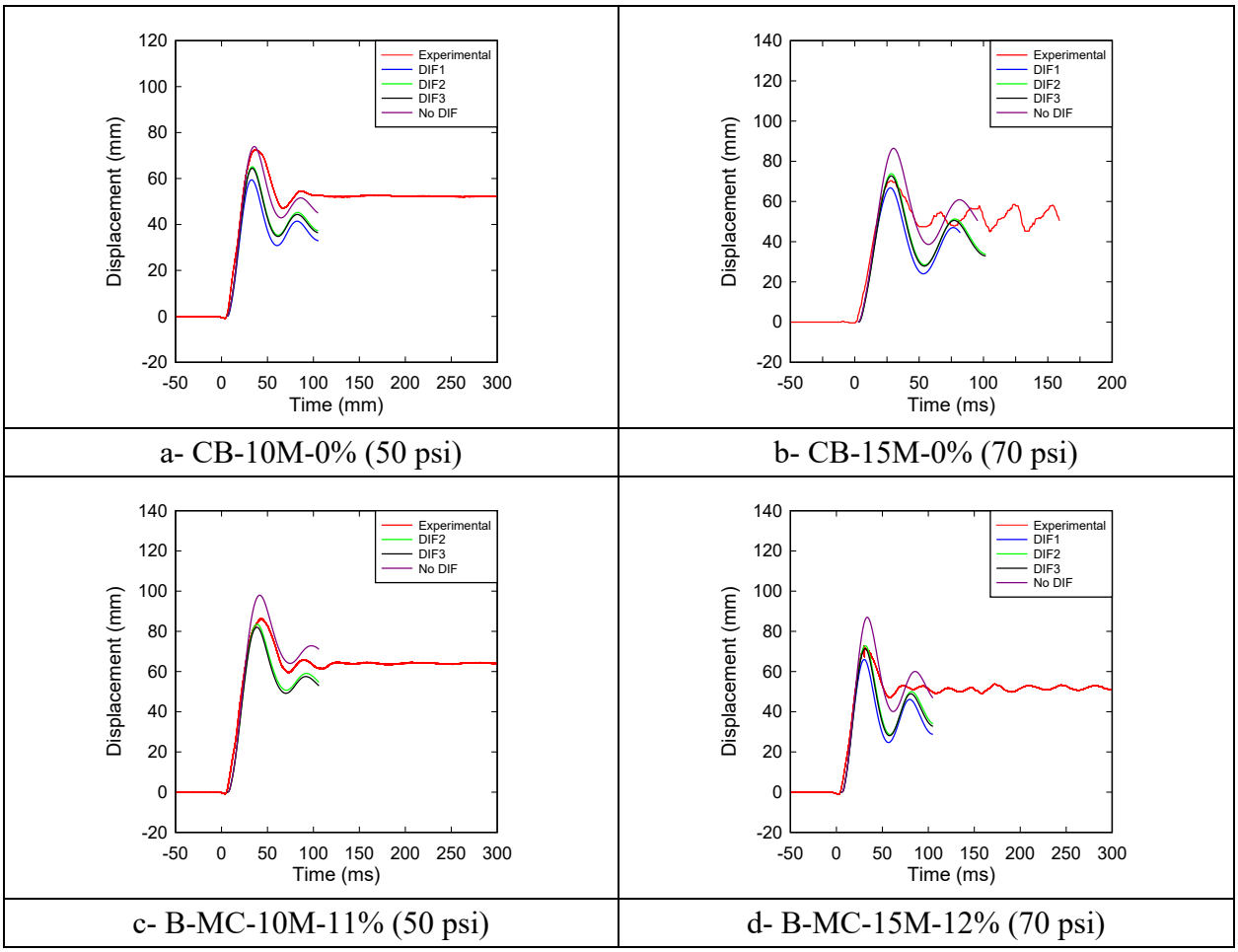
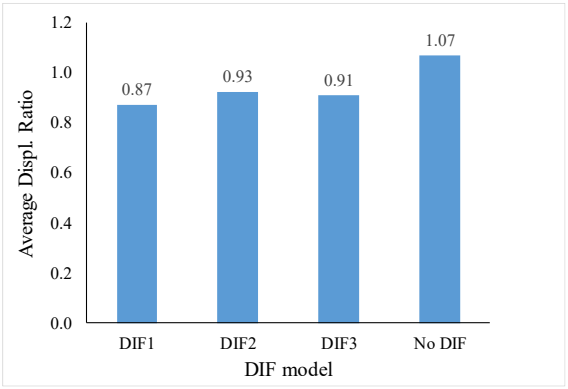
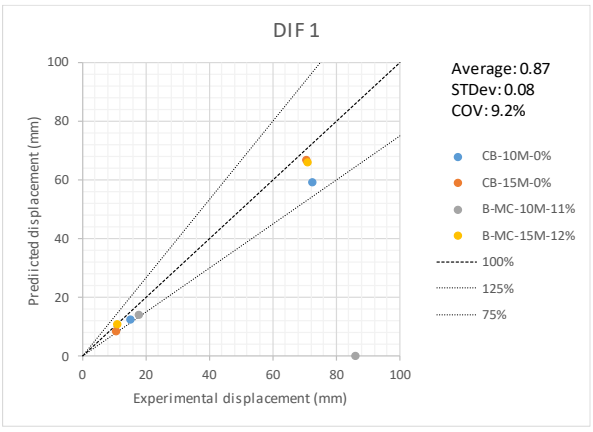


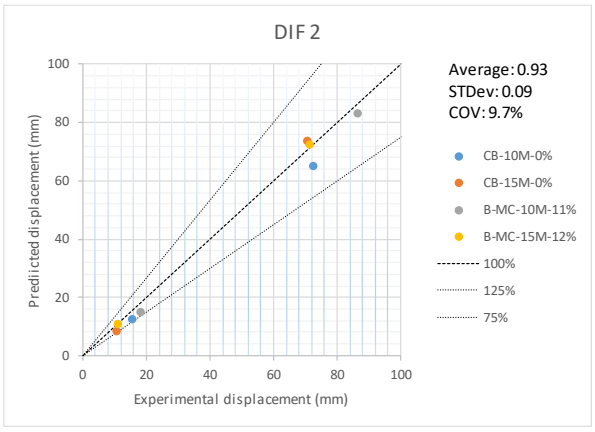

Figure 10-5 DIF sensitivity analysis: sample displacement-time histories



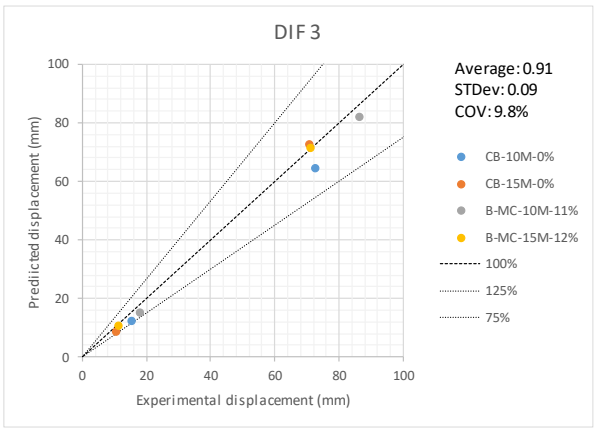

a- Average displacement ratios



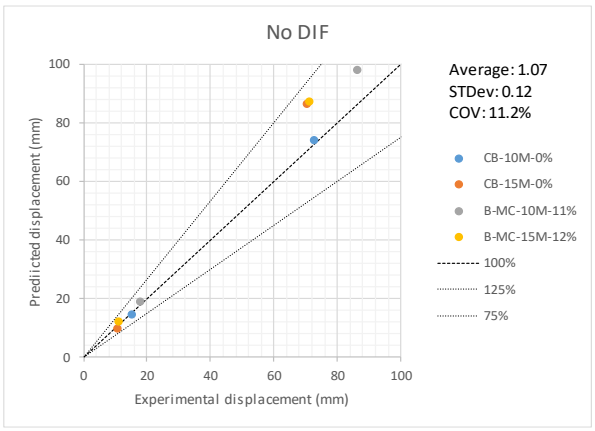

b- DIF 1




c- DIF 2




d- DIF 3




e- No DIF

Figure 10-6 DIF sensitivity: average displacement ratios and comparison of displacements

## 10.5 Damping ratio sensitivity

The damping ratio used in the FE analysis was selected after conducting a damping sensitivity analysis. Two damping cases were considered: case D1 with 1% and 5%, and case D2 with 0.5% and 0.75%, where % represents the damping ratios for the first two modes, respectively.

The FE analysis results for the control (un-corroded) 10M and 15M beams are shown in **Figure 10-7**. **Table 10-4** and **Figure 10-7 (a)** show the average displacement ratios for both cases when considering the two control beams. The average displacement ratios $\frac{\delta_{num}}{\delta_{exp}}$ for damping options D1 and D2 were 0.89 and 0.92, respectively, with coefficients of variation (COV) of 11.2% and 8.7%. Based on the results case D2 resulted in a better approximation of the experimental displacement than case D1. As a result, case D2 was selected as the most suitable damping case when analysing the control (or un-corroded) beams.

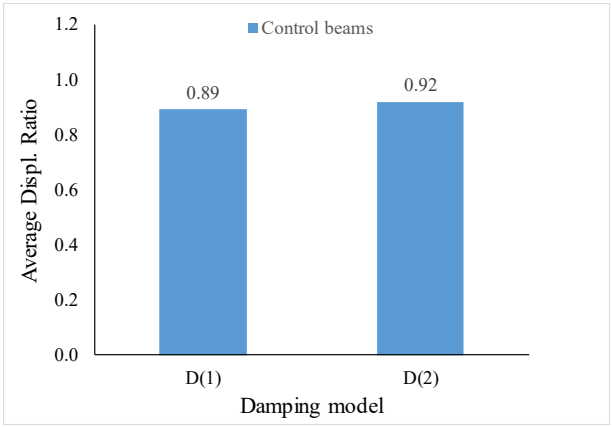
A similar analysis was conducted for a corroded beam in each of the 10M and 15M groups. The results from B-MC-10M-11% and B-MC-15-12% showed that a better estimation of the maximum displacements was obtained when using damping case D1 instead of case D2 (see **Figure 10-8**). **Table 10-4** and **Figure 10-8 (a)** show the average displacement ratios for both cases when considering the two corroded beams. The average displacement ratios $\frac{\delta_{num}}{\delta_{exp}}$ for damping options D1 and D2 were respectively 0.95 and 1.08, with coefficients of variation (COV) of 8.4% and 7.4%. As a result, case D1 was selected as the most suitable damping case to account for corrosion-induced damage in the analysis for corroded beams. As damage accumulates, the damping was increased, so increasing damping for the corroded specimens is appropriate (Saatci and Vecchio, 2009).

Table 10-4 Damping ratio sensitivity: data analysis

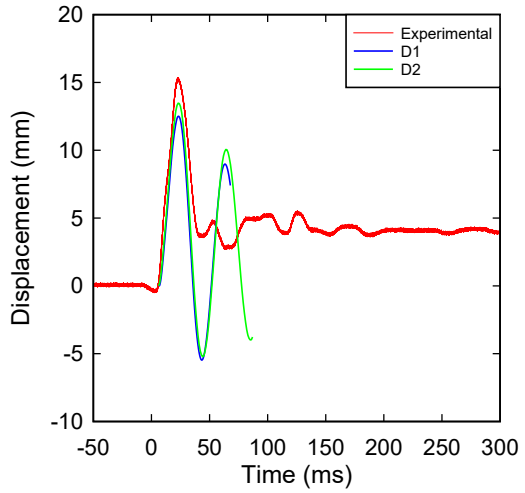
| Beam ID | Shot # | Shockwave properties | | Maximum displacements | | | Displ. Ratios | |
|---|---|---|---|---|---|---|---|---|
| | | $P_r$ (kPa) | $I_r$ (kPa·msec) | $\delta_{exp}$ (mm) | $\delta_{num}$ (mm) | | $\delta_{num}/\delta_{exp}$ | |
| | | | | | D1 | D2 | D1 | D2 |
| CB-10M-0% | 1 | 31.3 | 250 | 15.4 | 12.7 | 13.5 | 0.82 | 0.87 |
| | 2 | 61.0 | 550 | 72.6 | 65.0 | 68.7 | 0.89 | 0.94 |
| CB-15M-0% | 1 | 24.0 | 248 | 10.6 | 8.7 | 8.9 | 0.82 | 0.84 |
| | 2 | 78.8 | 734 | 70.6 | 73.8 | 73.0 | 1.04 | 1.03 |
| | | | | | | Average | 0.89 | 0.92 |
| | | | | | | STDEV | 0.10 | 0.08 |
| | | | | | | COV | 11.2% | 8.7% |

| Beam ID | Shot # | Shockwave properties | | Maximum displacements | | | Displ. Ratios | |
|---|---|---|---|---|---|---|---|---|
| | | $P_r$ (kPa) | $I_r$ (kPa·msec) | $\delta_{exp}$ (mm) | $\delta_{num}$ (mm) | | $\delta_{num}/\delta_{exp}$ | |
| | | | | | D1 | D2 | D1 | D2 |
| B-MC-10M-11% | 1 | 27.3 | 257 | 18.0 | 15.2 | 17.8 | 0.84 | 0.99 |
| | 2 | 64.3 | 547 | 86.3 | 83.5 | 96.5 | 0.97 | 1.11 |
| B-MC-15M-12% | 1 | 29.0 | 251 | 11.0 | 11.0 | 11.7 | 1.02 | 1.14 |
| | 2 | 80.0 | 703 | 71.2 | 72.8 | 81.6 | 0.98 | - |
| | | | | | | Average | 0.95 | 1.08 |
| | | | | | | STDEV | 0.08 | 0.08 |
| | | | | | | COV | 8.4% | 7.4% |

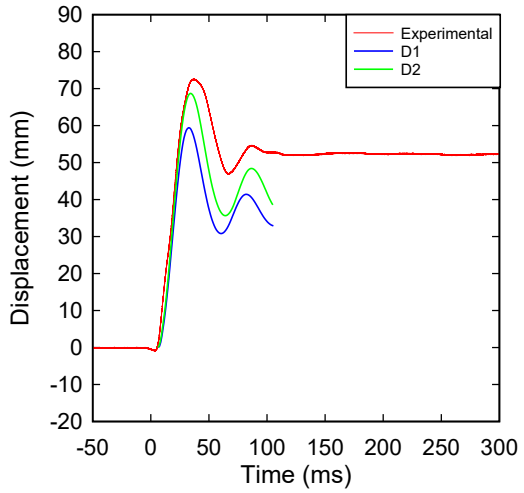
Note: $P_r$ =reflected pressure; $I_r$ = reflected impulse; $\delta_{exp}$ = experimental maximum mid-span displacement; $\delta_{num}$ = numerical maximum mid-span displacement; $\delta_{num}/\delta_{exp}$ = displacement ratio.



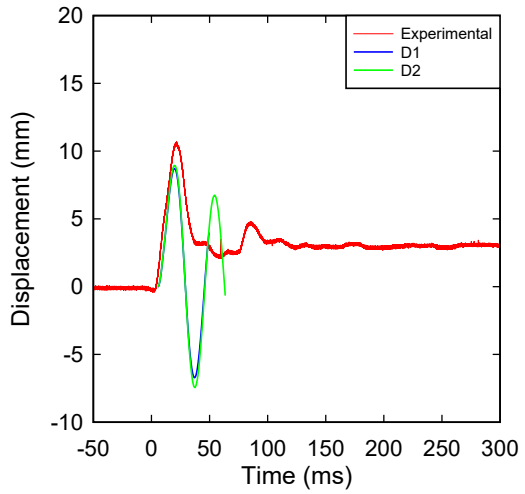

a- Average displacement ratios (control beams)



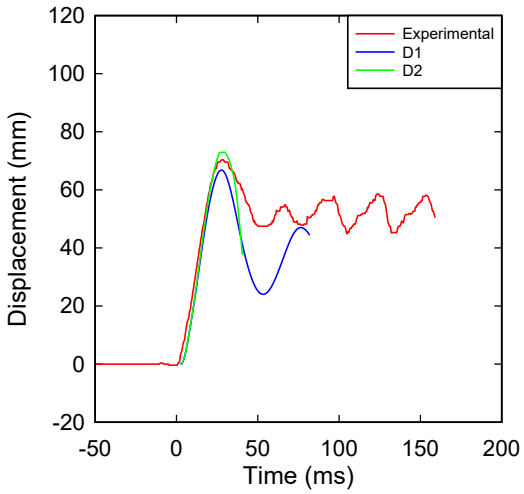

b- CB-10M-0% (17 psi)




c- CB-10M-0% (50 psi)

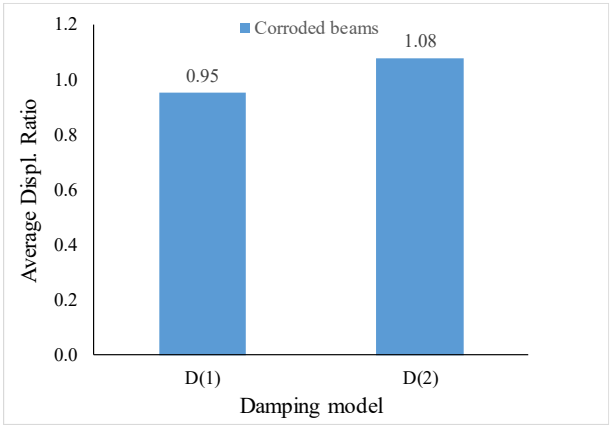



d- CB-15M-0% (17 psi)

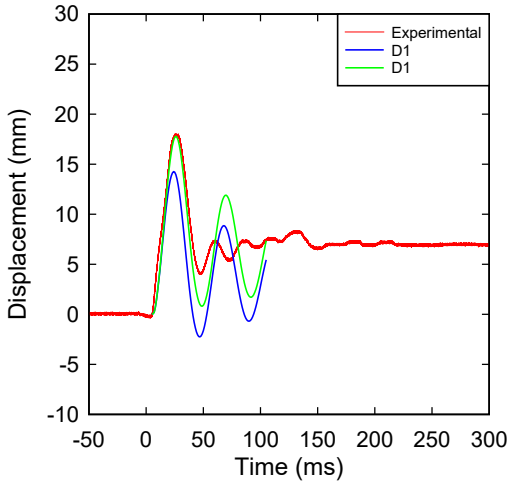



e- CB-15M-0% (70 psi)

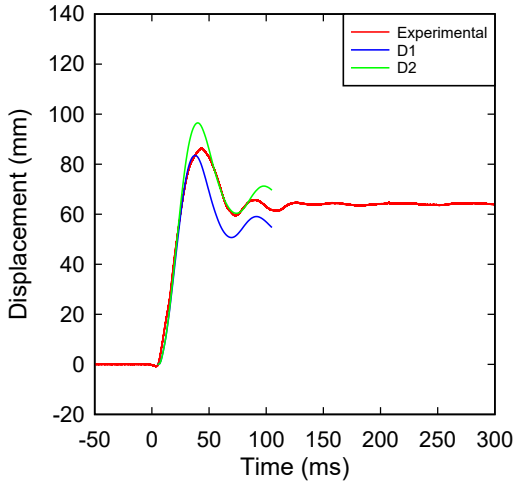
Figure 10-7 Damping ratio sensitivity for control beams: CB-10M-0% and CB-15M-0%



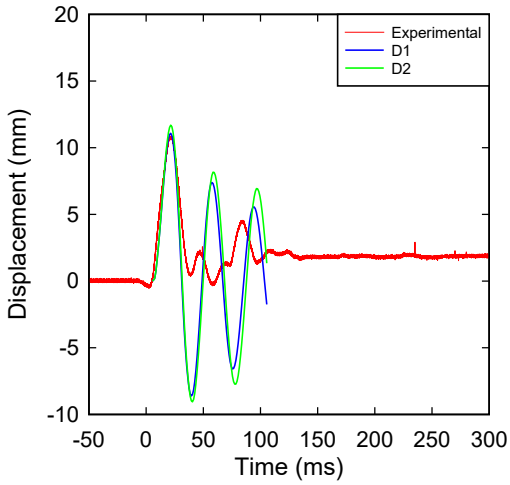

a- Average displacement ratios (corroded beams)



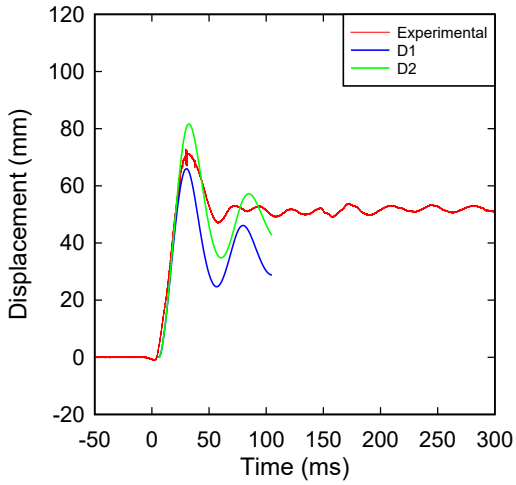

b- B-MC-10M-11% (17 psi)




c- MC-10M-11% (50 psi)




d- B-MC-15M-12% (17 psi)




e- B-MC-15M-12% (70 psi)

Figure 10-8 Damping ratio sensitivity for corroded beams: B-MC-10M-11% and B-MC-15M-12%

## 10.6 Numerical results for all beams

### 10.6.1 Flexure-governed beams

The response of the flexure-governed beams in the 10M and 15M series was predicted using the dynamic finite element procedures and parameters discussed in Sections 10.2-10.5. The FE models used a mesh with 25 mm×25 mm plane-stress concrete elements. The longitudinal reinforcement was modelled as truss bar elements, while the stirrups were smeared in the concrete elements. Eleven beams with different corrosion scenarios (control, mid-corrosion, cover-removed-mid corrosion, end-corrosion, and full-corrosion) were included in the analysis.

#### 10.6.1.1 Control beams (0% mass loss): CB-10M-0% and CB-15M-0%

Control (un-corroded) beams CB-10M-0% and CB-15M-0% were built with 2-10M and 2-15M in the tension zone, respectively. These two beams were modelled without corrosion effects as shown in **Figure 10-9**. The 4 DIF cases and 2 damping scenarios were considered for these beams.

**Figure 10-10** shows the idealized blast pressure-time history for both beams. A summary of the FE and experimental results with statistical results is presented in **Table 10-5**. A comparison of the experimental and predicted displacements is presented in **Figure 10-11**, while **Figure 10-12** provides the experimental and numerical reactions for both beams. In addition, **Figure 10-13** and **Figure 10-14** present a comparison of cracking patterns between the FE results and experimental observations.

Based on the sensitivity analysis, it was found that using a dynamic increase factor of DIF2 with damping ratios of 0.5% and 0.75% for the first two modes (D2), resulted in the most acceptable results for the control beams (see **Table 10-5** and **Figure 10-11**). For beam CB-10M-0%, the predicted maximum displacements after the first and second shots (17 psi and 50 psi) reached 13.5 mm and 68.7 mm, respectively, with prediction ratios of 0.87 and 0.94. For beam CB-15M-0%, the recorded maximum displacements were 8.9 mm and 73.1 mm after the first and second shots (17 psi and 70 psi) with prediction ratios of 0.84 and 1.03, respectively. Considering both beams the average displacement ratio for case DIF2-D2 was 0.92 with a coefficient of variation (COV) of 8.7%.

Considering the dynamic reactions, the pre and post-peak responses of the predicted dynamic reaction of beam CB-10M-0% followed the trend observed in the experiments after shot 2 (50 psi), while shot 1 (17 psi) showed higher pre and post-peak responses; however, the predicted maximum reactions were higher than the experimental results for both damping cases and both shots (see **Figure 10-12**). For beam CB-15M-0%, the FE analysis resulted in an over-estimated prediction of the pre- and post-peak responses and maximum strength of the beam after the first shot.

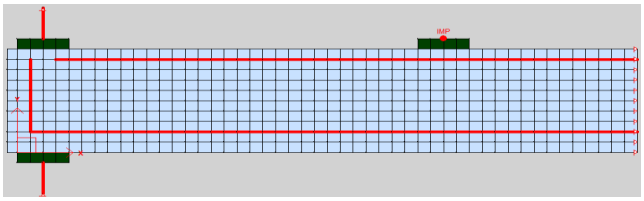
By inspecting **Figure 10-13** and **Figure 10-14**, it was observed that the FE cracking patterns and failure modes match well with the experiments for both beams.

Table 10-5 Summary of the FE results for 10M/15M control beams

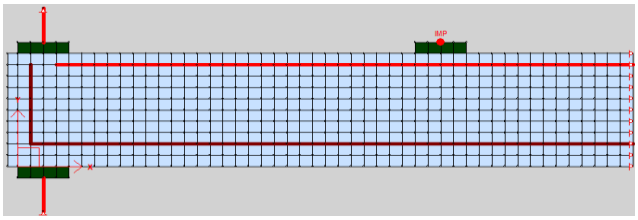
| Beam ID | Shot # | Shockwave properties | | Maximum displacements | | | | | | Displacement ratios | | | | |
|---|---|---|---|---|---|---|---|---|---|---|---|---|---|---|
| | | $P_r$ | $I_r$ | $\delta_{exp}$ | $\delta_{num}$ (mm) | | | | | $\delta_{num}/\delta_{exp}$ | | | | |
| | | (kPa) | (kPa·msec) | (mm) | DIF1-D1 | DIF2-D1 | DIF3-D1 | No DIF-D1 | DIF2-D2 | DIF1-D1 | DIF2-D1 | DIF3-D1 | No DIF-D1 | DIF2-D2 |
| CB-10M-0% | 1 | 31.3 | 250 | 15.4 | 12.5 | 12.7 | 12.45 | 14.6 | 13.5 | 0.81 | 0.82 | 0.8 | 0.94 | 0.87 |
| | 2 | 61.0 | 550 | 72.6 | 59.4 | 65.0 | 64.45 | 73.9 | 68.7 | 0.81 | 0.89 | 0.88 | 1.01 | 0.94 |
| CB-15M-0% | 1 | 24.0 | 248 | 10.6 | 8.7 | 8.7 | 8.48 | 9.6 | 8.9 | 0.82 | 0.82 | 0.80 | 0.90 | 0.84 |
| | 2 | 78.8 | 734 | 70.6 | 66.7 | 73.8 | 72.68 | 86.4 | 73.0 | 0.94 | 1.04 | 1.02 | 1.22 | 1.03 |
| | | | | | | | | | Average | 0.85 | 0.89 | 0.88 | 1.02 | 0.92 |
| | | | | | | | | | STDEV | 0.06 | 0.10 | 0.10 | 0.14 | 0.08 |
| | | | | | | | | | COV | 7.1% | 11.2% | 11.3% | 13.7% | 8.7% |

Note: $P_r$ =reflected pressure; $I_r$ = reflected impulse; $\delta_{exp}$ = experimental maximum mid-span displacement; $\delta_{num}$ = numerical maximum mid-span displacement; $\delta_{num}/\delta_{exp}$ = displacement ratio.

Note: DIF1-D1, DIF2-D1, DIF3-D1 and No DIF-D1 are run with Damping D1 (1% and 5%); DIF2-D2 = DIF2 is run with Damping D2 (0.5% and 0.75%).

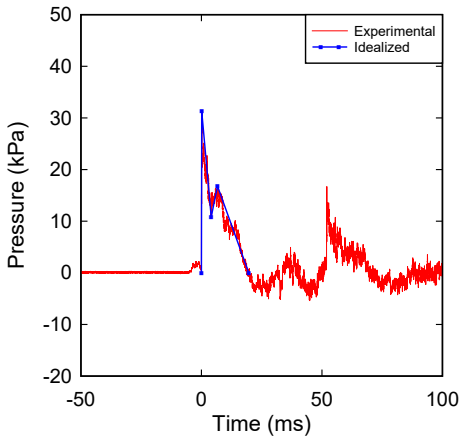


a- CB-10M-0%

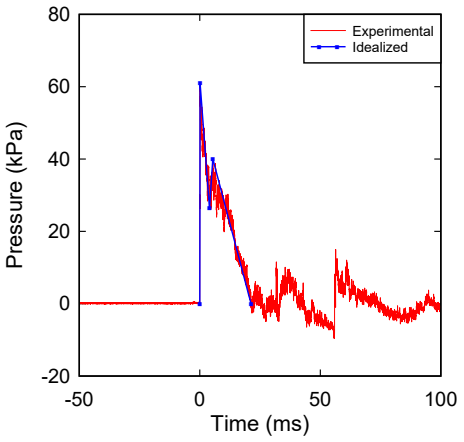


b- CB-15M-0%

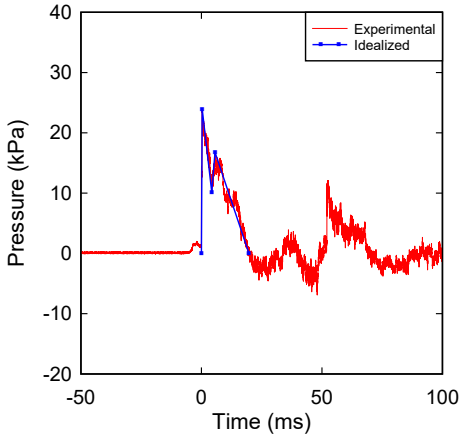
Figure 10-9 FE models of control beams



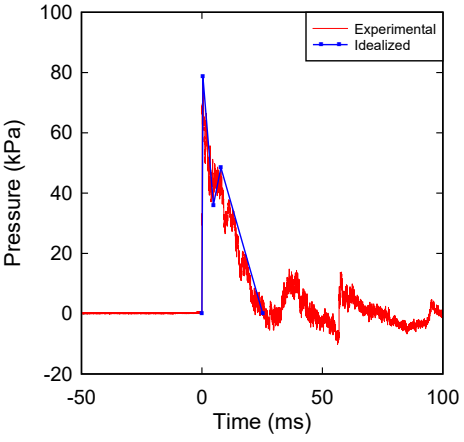

a- CB-10M-0% - 17 psi




b- CB-10M-0% - 50 psi

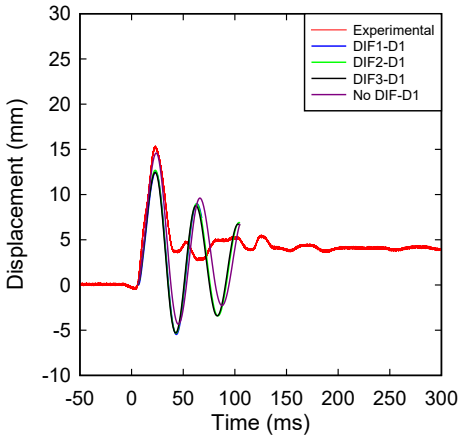



c- CB-15M-0% - 17 psi

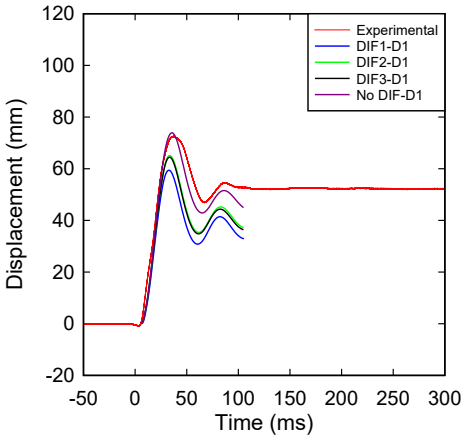



d- CB-15M-0% - 70 psi

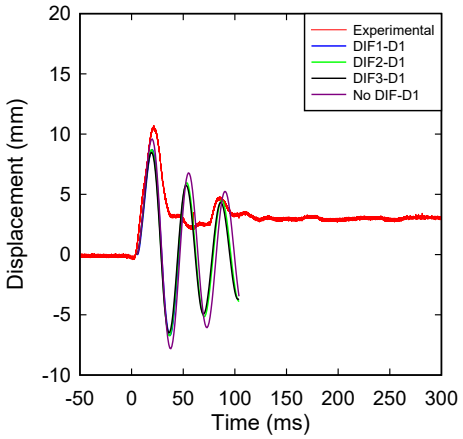
Figure 10-10 Idealized blast pressure-time history for beams CB-10M-0% and CB-15M-0%



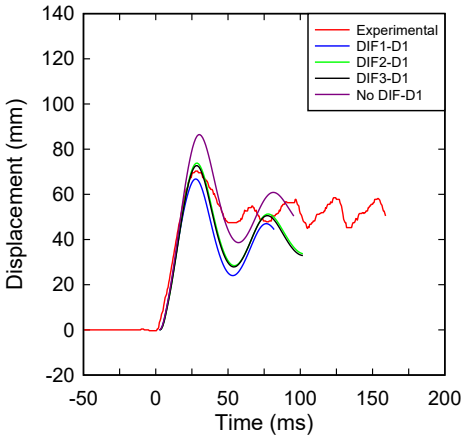

a- CB-10M-0% - 17 psi




b- CB-10M-0% - 50 psi

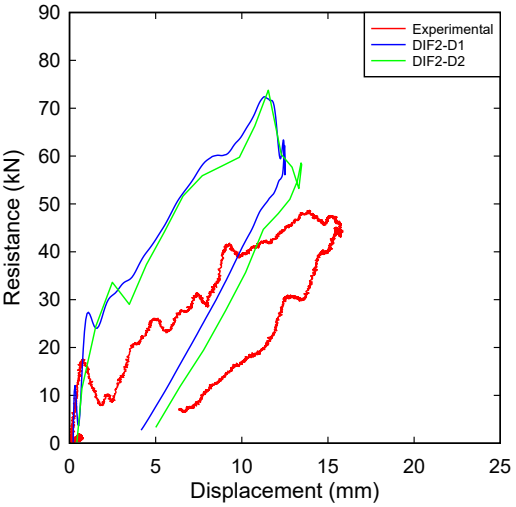



c- CB-15M-0% - 17 psi

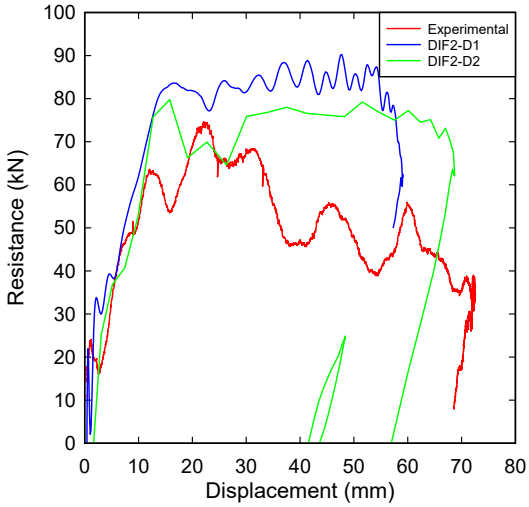



d- CB-15M-0% - 70 psi

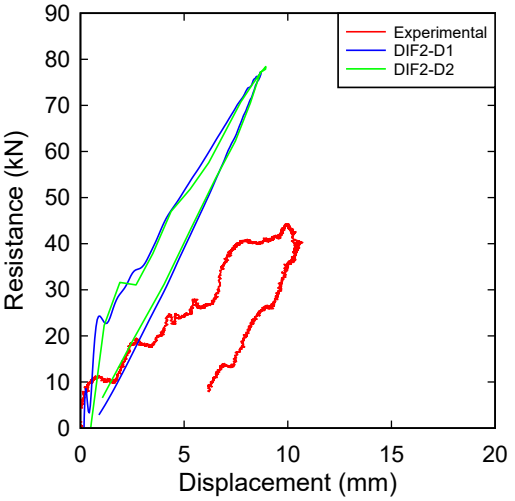
Figure 10-11 Predicted vs experimental results for beams CB-10M-0% and CB-15M-0%



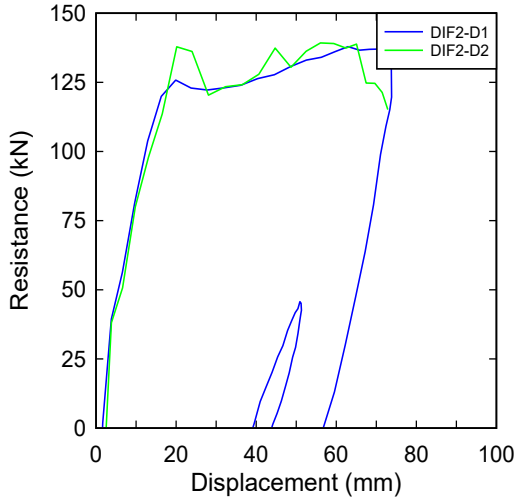

a- CB-10M-0% -17 psi




b- CB-10M-0% -50 psi




c- CB-15M-0% -17 psi




d- CB-15M-0% -70 psi
(no data captured during test)

Figure 10-12 Predicted vs experimental reactions for beams CB-10M-0% and CB-15M-0%

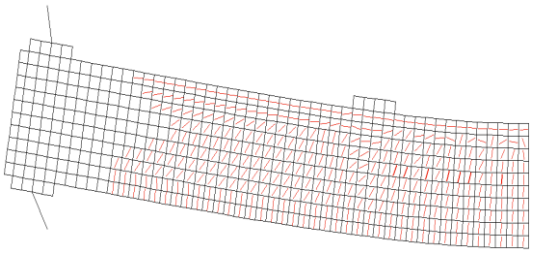
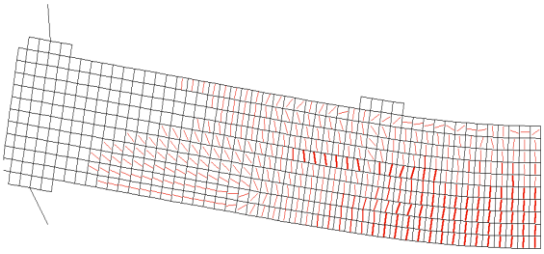
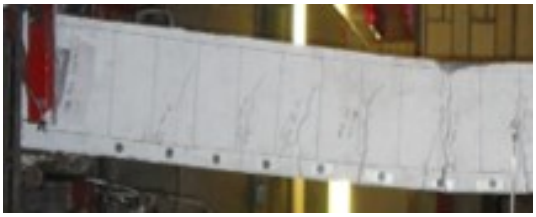
| | |
|---|---|
|  |  |
| a-17 psi (1% & 5%, DIF2-D1) | b- 50 psi (1% & 5%, DIF2-D1) |
|  |  |
| c- 17 psi | d- 50 psi |

Figure 10-13 Cracking patterns of FE model vs experimental for beam CB-10M-0%

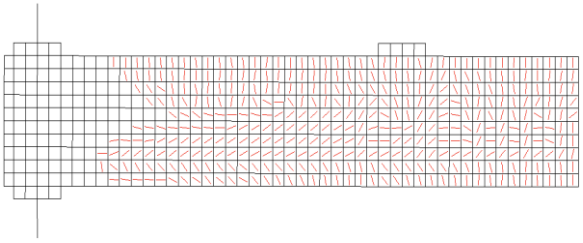
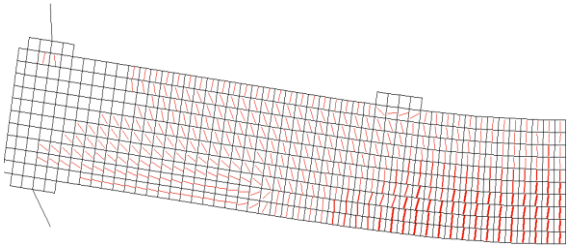
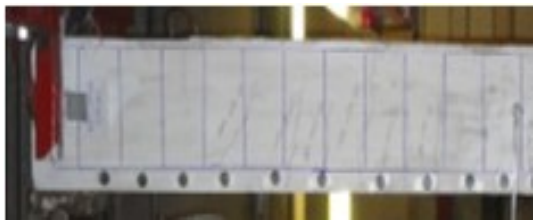
| | |
|---|---|
|  |  |
| a-17 psi (1% & 5%, DIF2-D1) | b- 70 psi (1% & 5%, DIF2-D1) |
|  |  |
| c- 17 psi | d- 70 psi |

Figure 10-14 Cracking patterns of FE model vs experimental for beam CB-15M-0%

#### 10.6.1.2 Specimens subjected to corrosion at mid-span

This section presents the FE results of beams B-MC-10M-11%, B-MC-10M-15%, B-EMC-10M-22%, B-CR-MC-10M-5%, B-MC-15M-12%, B-CR-MC-15M-4% and B-EMC-10M-17%. These beams were subjected to mid-span corrosion only. Moreover, beams of B-CR-MC-10M-5% and B-CR-MC-15M-4% were modeled without concrete cover over a length of 750 mm at mid-span in addition to adding corrosion-induced effects. The FE models used truss bar elements and smeared reinforcement for the longitudinal and transverse reinforcement, respectively. Corrosion-induced damage in each beam was modeled by modifying the steel stress-strain properties, and inducing cracking in the concrete elements surrounding the mid-span longitudinal bars over a length of 750 mm. The FE meshes for each of the beams are illustrated in **Figure 10-15**.

Beams B-MC-10M-11% and B-MC-15M-12% were analyzed considering different models for the dynamic increase factor (DIF) and two cases of damping ratios, while the remaining beams were analyzed with the default DIF, and damping ratio selected in the sensitivity analysis: DIF2-D1.

**Table 10-6** summarizes the results of the FE models and experimental results. The predicted vs experimental displacement-time history after the first and second blast shots, the dynamic reaction curves, the idealized blast pressure-time history and the cracking patterns for both the FE analysis and experimental test for each beam are shown from **Figure 10-16** to **Figure 10-43**.

Considering all beams, all blasts and all mid-span corrosion scenarios, case DIF2-D1 resulted in an average displacement ratio of 0.86 with a coefficient of variation (COV) of 24.4% (**Table 10-6**). Ignoring the two EMC beams which suffered severe failures, the prediction ratio was 0.95 with COV= 9.5%.

The FE analysis of beam B-MC-10M-11% after the first blast shot of 17 psi showed that the DIF2 option with damping case D1 (damping ratios of 1% and 5%) resulted in a maximum displacement of 15.2 mm, with a numerical-to-experimental displacement ratio of 0.84. A better prediction of 17.8 mm, with a displacement ratio of 0.99 was obtained for damping case D2 (damping ratios of 0.5% and 75%). However, the analysis of the beam subjected to a high blast shot of 50 psi gave the closest approximation to the observed maximum displacement when DIF2 option with D1 was used, with a displacement ratio of 0.97, compared to 1.11 for D2 (refer to **Figure 10-17** and **Table 10-6**). The pre-peak behaviour of the blast resistance curves when DIF2-D1 and DIF2-D2 options

were used were overestimated for the 17-psi blast shot (**Figure 10-18 (a)**); however, the post-peak behaviour when DIF2-D2 option was applied was acceptable, while the DIF2-D1 option underestimated the prediction. For the 50-psi blast shot, the pre-peak behaviour of the blast resistance curves when both DIF2-D1 and DIF2-D2 options were used were acceptable, whereas the predicted post-peak behaviour overestimated the displacements when the DIF2-D2 option was applied. In addition, the predicted maximum strength of the beam was overestimated for the first shot; however, the predicted maximum strength was acceptable after the second shot (see **Figure 10-18 (b)**). The cracking patterns predicted by the FE model for both blast shots were similar to the experimental ones observed at mid-span when using DIF2-D1, as shown in **Figure 10-19**.

The FE analysis of beam B-MC-10M-15% (analyzed using the default case: DIF2-D1) resulted in a good prediction of the maximum displacement as a result of a low blast shot of 17 psi, with a prediction ratio of 0.90; however, it underestimated the maximum displacement for the second blast shot of 50 psi, with a numerical-to-experimental ratio of 0.81 (see **Table 10-6** and **Figure 10-21**). Furthermore, this model overestimated results in terms of pre-peak and post peak responses and maximum load, with a prediction ratio of 1.58 for the first blast shot (see **Figure 10-22**). Examining **Figure 10-23**, it was observed that the cracking patterns and the failure mode of the predicted results showed good match with the experimental observations, with damage accumulated at the mid-span of the beam.

The FE results of beam B-EMC-10M-22% subjected to a blast shot of 50 psi underestimated the maximum displacement when DIF2-D1 and DIF2-D2 modelling options were used (see **Figure 10-25**), with numerical-to-experimental ratios of 0.45 and 0.52, respectively. Examining the dynamic reaction curves, the predicted maximum load reached 68.2 kN and 65.0 kN for damping cases D1 and D2, respectively, as shown in **Figure 10-26**. **Figure 10-27** shows that the predicted and the experimental results showed similar failure mode, cracking patterns, and severe damage in the beam mid-span.

The results of the FE model of beam B-CR-MC-10M-5% showed acceptable prediction in terms of displacement, with a prediction ratio of 1.07 for the default DIF2-D1 case after applying a blast shot of 50 psi (see **Table 10-6** and **Figure 10-29**). Furthermore, the FE analysis resulted in a maximum load of 79.6 kN. This FE model failed in flexure with more intense damage in the mid-span of the beam as the beam tested experimentally (refer to **Figure 10-31**).

For beam B-MC-15M-12%, the analysis of the beam subjected to a low blast shot of 17 psi showed acceptable predicted results in terms of maximum displacement for all the considered DIF cases, while that under a high blast shot of 70 psi resulted in a good prediction of the maximum displacement for the DIF2-D1 and DIF3-D1 options, with prediction ratios of 1.02 and 1.00, respectively (see **Table 10-6** and **Figure 10-33**). Considering the effect of damping, DIF2-D1 resulted in a better prediction when compared to DIF2-D2 at the 70 psi shot (ratios of 1.02 and 1.14, respectively). The blast resistance load for the first blast shot, illustrated in **Figure 10-34 (a)**, was overestimated for both damping cases, while the response under the high blast shot resulted in an acceptable pre-peak and post-peak responses of the beam for both cases, although the maximum load was over-estimated (see **Figure 10-34 (b)**). Considering DIF2-D1, it was observed in **Figure 10-35** that the predicted damage for the 17-psi blast shot showed minor cracking over the length of the beam, whereas the results for the 70-psi shot predicted significant localized cracking in the mid-span of the beam with a similar failure mode as the experimentally observed damage.

The FE results of beam B-CR-MC-15M-4% subjected to a blast shot of 70 psi described well the experimental results in terms of the maximum displacement, which reached 75 mm using DIF2 and D1, with a prediction ratio of 0.98 (refer to **Table 10-6** and **Figure 10-37**). The predicted maximum dynamic reaction load reached 137.6 kN as shown in **Figure 10-38**. **Figure 10-39** shows that the predicted cracking density happened at the mid-span of the beam, with a flexure failure as it occurred in the experiment.

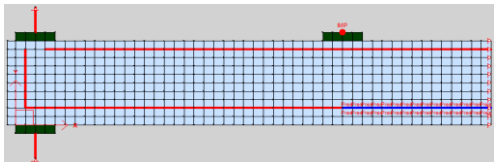
The FE results of beam B-EMC-10M-17% after a blast shot of 70 psi under-estimated the maximum displacement for both DIF2-D1 and DIF2-D2 modelling options, with prediction ratios of 0.55 and 0.62, respectively (see **Table 10-6** and **Figure 10-41**). The dynamic maximum load of the FE model reached 126.8 kN and 129.5 kN for damping cases D1 and D2, respectively, as presented in **Figure 10-42**. Also, the FE model of this beam failed in flexure with significant cracking in the mid-span, which is similar to the observed damage in the experiment (see **Figure 10-43**).

Table 10-6 Summary of FE results for specimens subjected to mid-span corrosion

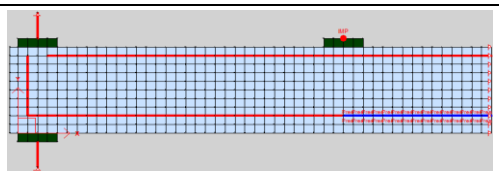
| Beam ID | Shot # | Shockwave properties | | Maximum displacements | | | | | | Displacement ratios | | | | |
|---|---|---|---|---|---|---|---|---|---|---|---|---|---|---|
| | | | | | $\delta_{num}$ (mm) | | | | | $\delta_{num}/\delta_{exp}$ | | | | |
| | | $P_r$ (kPa) | $I_r$ (kPa·msec) | $\delta_{exp}$ (mm) | DIF1-D1 | DIF2-D1 | DIF3-D1 | No DIF-D1 | DIF2-D2 | DIF1-D1 | DIF2-D1 | DIF3-D1 | No DIF-D1 | DIF2-D2 |
| B-MC-10M-11% | 1 | 27.3 | 257 | 18.0 | 14.3 | 15.2 | 15.4 | 18.8 | 17.8 | 0.79 | 0.84 | 0.85 | 1.04 | 0.99 |
| | 2 | 64.3 | 547 | 86.3 | - | 83.5 | 82.0 | 98.0 | 96.5 | - | 0.97 | 0.95 | 1.13 | 1.11 |
| B-MC-10M-15% | 1 | 27.8 | 249 | 15.6 | - | 14.1 | - | - | - | - | 0.9 | - | - | - |
| | 2 | 59.3 | 529 | 107.0 | - | 86.6 | - | - | - | - | 0.81 | - | - | - |
| B-EMC-10M-22% | 1 | 61.0 | 541 | 217.3 | - | 97.3 | - | - | 112.7 | - | 0.45 | - | - | 0.52 |
| B-CR-MC-10M-5% | 1 | 65.6 | 548 | 79.0 | - | 84.7 | - | - | - | - | 1.07 | - | - | - |
| B-MC-15M-12% | 1 | 29.0 | 251 | 11.0 | 11.0 | 11.0 | 10.8 | 12.0 | 11.7 | 1.00 | 1.00 | 0.98 | 1.09 | 1.06 |
| | 2 | 80.0 | 703 | 71.2 | 66.0 | 72.8 | 71.3 | 87.0 | 81.6 | 0.93 | 1.02 | 1.00 | 1.22 | 1.14 |
| B-CR-MC-15M-4% | 1 | 77.0 | 720 | 76.0 | - | 75.0 | - | - | - | - | 0.98 | - | - | - |
| B-EMC-15M-17% | 1 | 80.1 | 729 | 169.0 | - | 94.0 | - | - | 105 | - | 0.55 | - | - | 0.62 |
| | | | | | | | | | Average | 0.91 | 0.86 | 0.95 | 1.12 | 0.88 |
| | | | | | | | | | STDEV | 0.11 | 0.21 | 0.07 | 0.08 | 0.29 |
| | | | | | | | | | COV | 12.1% | 24.4% | 7.3% | 7.1% | 32.9% |

**Note**: $P_r$ =reflected pressure; $I_r$ = reflected impulse; $\delta_{exp}$ = experimental maximum mid-span displacement; $\delta_{num}$ = numerical maximum mid-span displacement; $\delta_{num}/\delta_{exp}$ = displacement ratio.

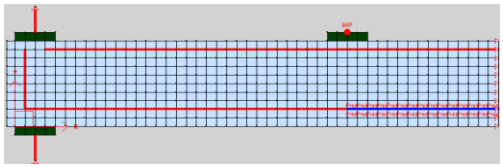
**Note**: DIF1-D1, DIF2-D1, DIF3-D1 and No DIF-D1 are run with Damping D1 (1% and 5%); DIF2-D2 is run with Damping D2 (0.5% and 0.75%).



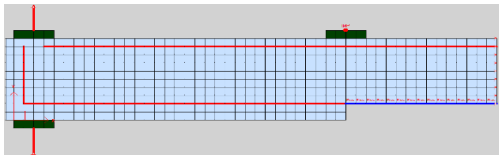
a- B-MC-10M-11%



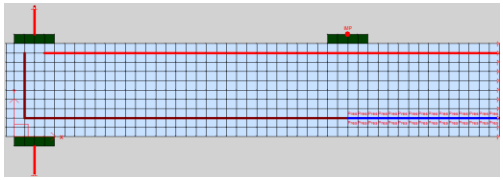
b- B-MC-10M-15%



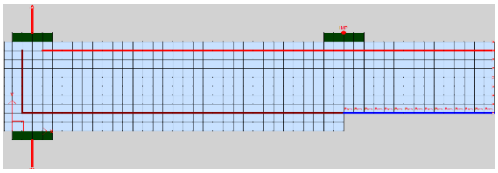
c- B-EMC-10M-22%



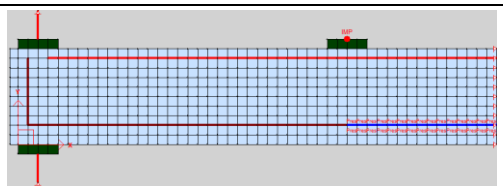
d- B-CR-MC-10M-5%



e- B-MC-15M-12%

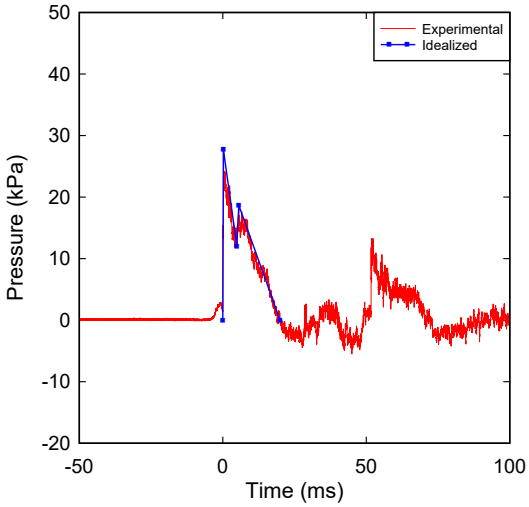


B-CR-MC-15M-4%

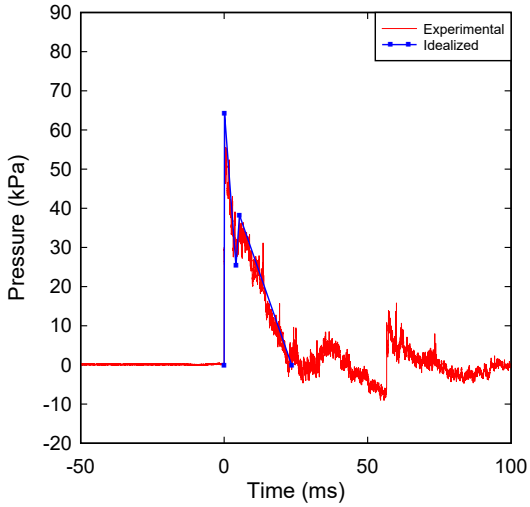


B-EMC-15M-17%

Figure 10-15 FE models for specimens with mid-corrosion

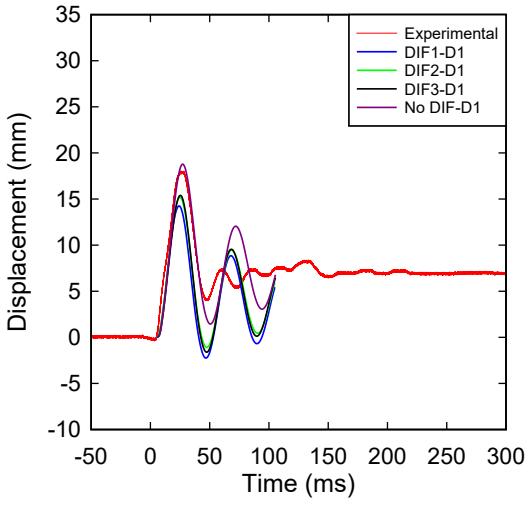



a- 17 psi

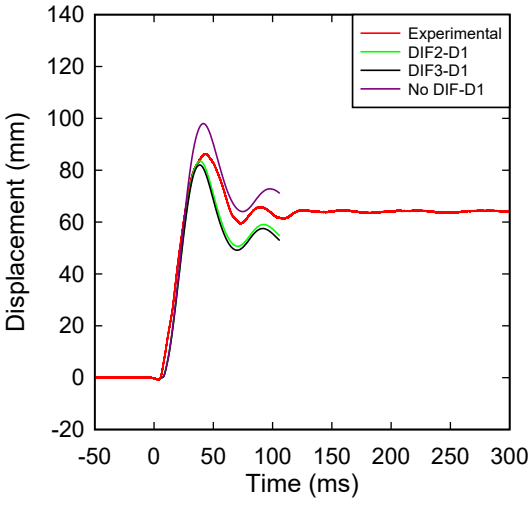



b- 50 psi

Figure 10-16 Idealized blast pressure-time history for beam B-MC-10M-11%

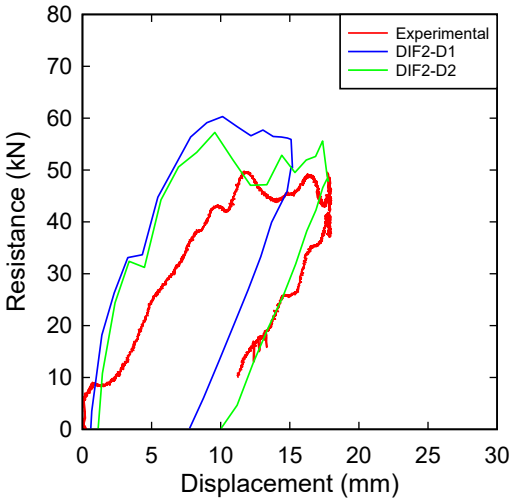



a- 17 psi

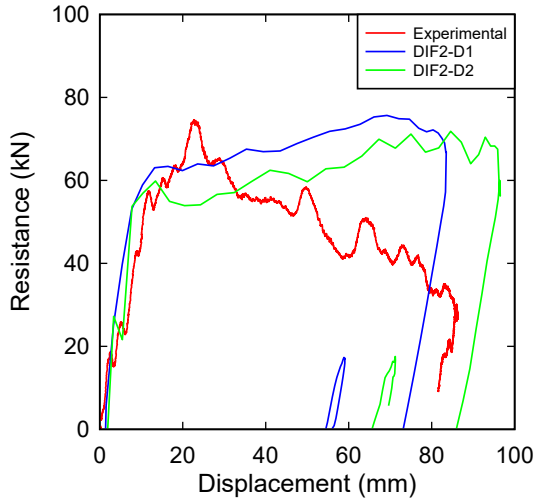



b- 50 psi

Figure 10-17 Predicted vs experimental results for beam B-MC-10M-11%

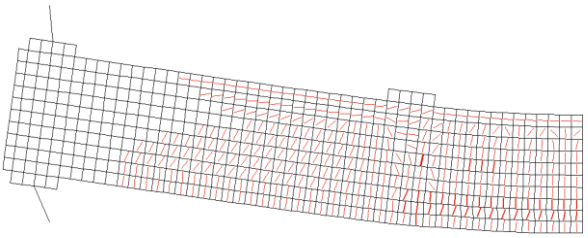



a- 17 psi

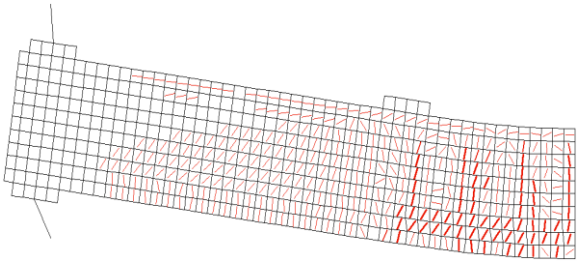



b- 50 psi

Figure 10-18 Predicted vs experimental dynamic reactions for beam B-MC-10M-11%



a- 17 psi (1% & 5%, DIF2-D1)



b- 50 psi (1% & 5%, DIF2-D1)

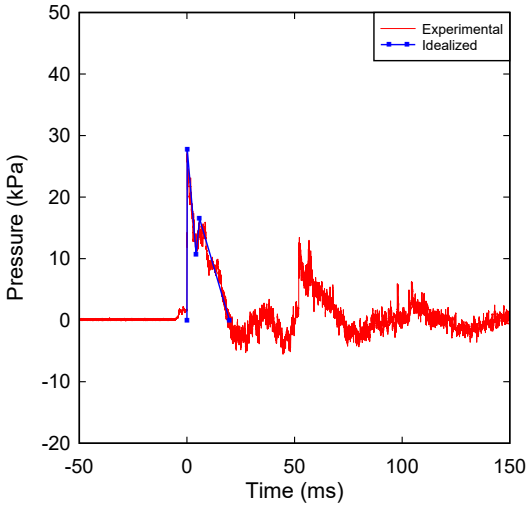


c- 17 psi

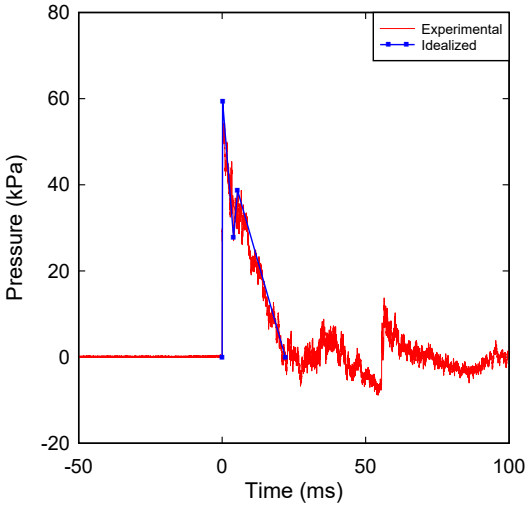


d- 50 psi

Figure 10-19 Cracking patterns of FE model vs experimental for beam B-MC-10M-11%

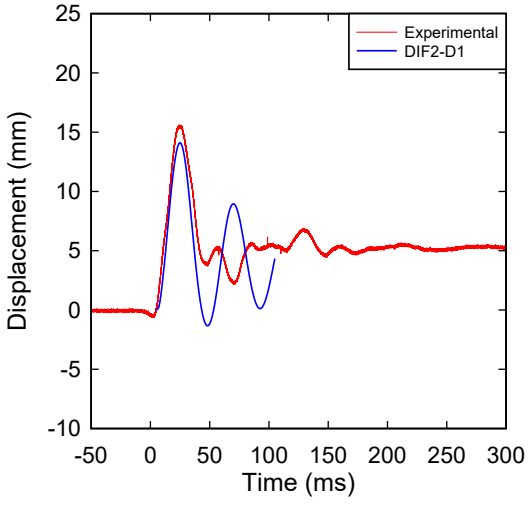



a- 17 psi

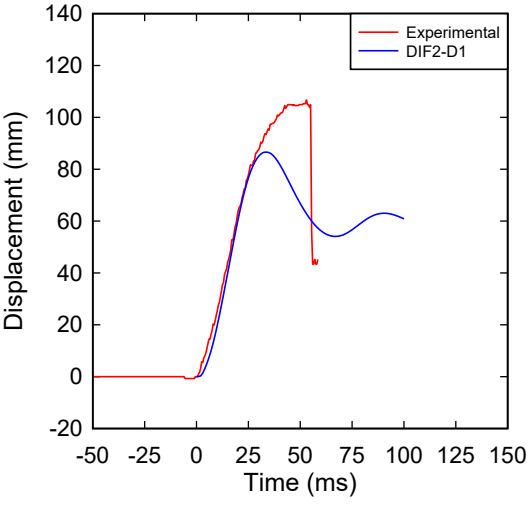



b- 50 psi

Figure 10-20 Idealized blast pressure-time history for beam B-MC-10M-15%

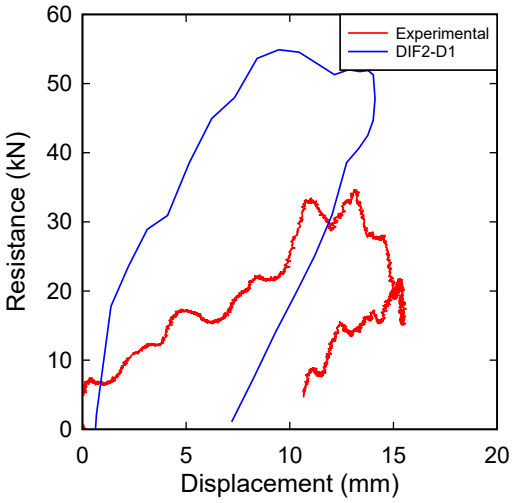



a- 17 psi

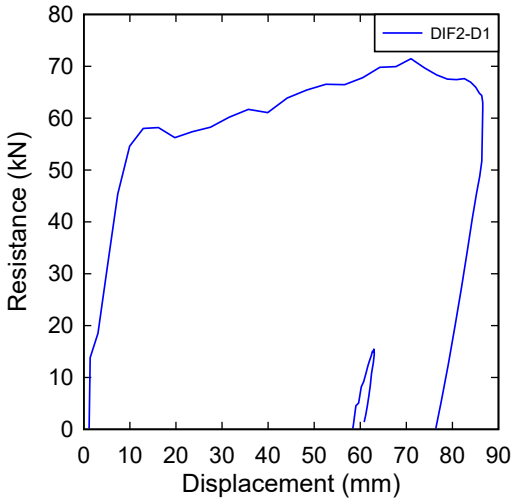



b- 50 psi

Figure 10-21 Predicted vs experimental results for beam B-MC-10M-15%

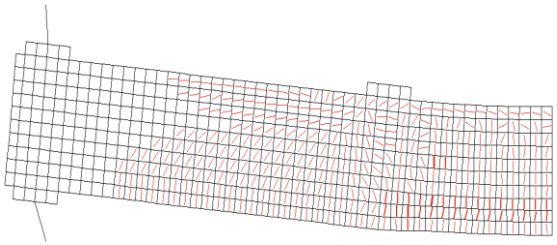



a- 17 psi

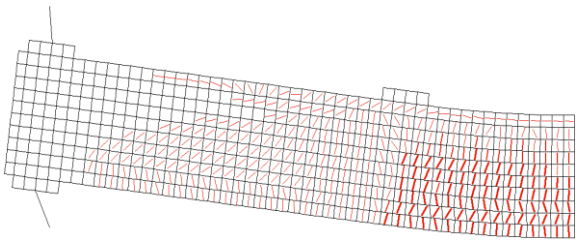



b- 50 psi
(no data captured during test)

Figure 10-22 Predicted vs experimental reactions for beam B-MC-10M-15%



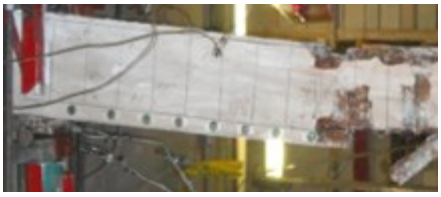
a- 17 psi (1% & 5%, DIF2-D1)



b- 50 psi (1% & 5%, DIF2-D1)

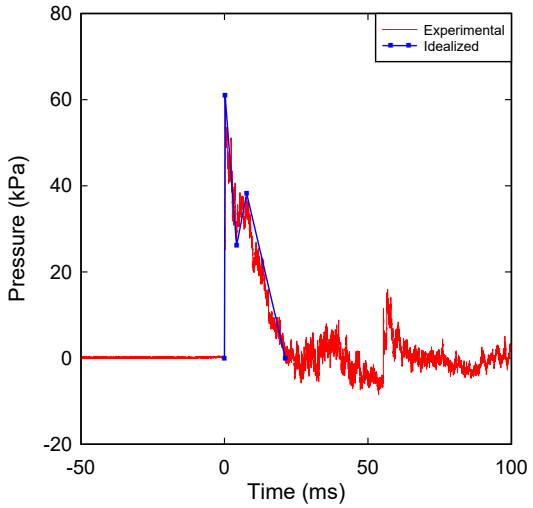


c- 17 psi



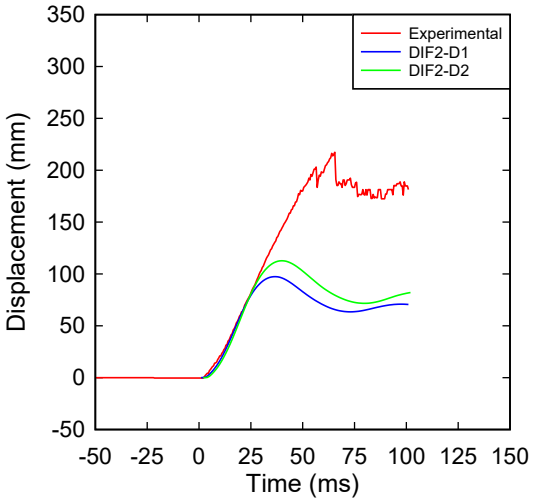
d- 50 psi

Figure 10-23 Cracking patterns of FE model vs experimental for beam B-MC-10M-15%



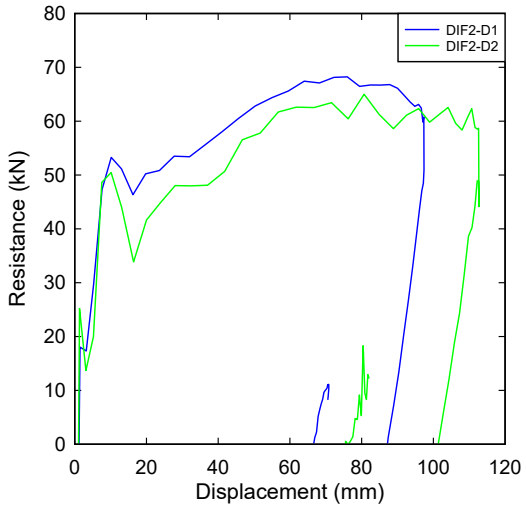

50 psi

Figure 10-24 Idealized blast pressure-time history for beam B-EMC-10M-22%



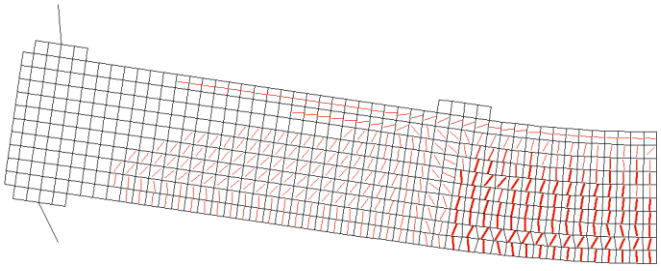

50 psi

Figure 10-25 Predicted vs experimental results for beam B-EMC-10M-22%

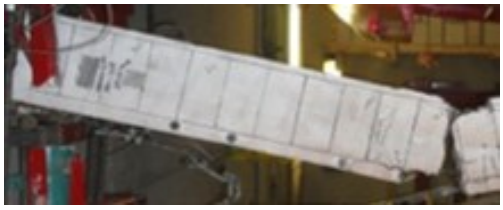



50 psi
(no data captured during test)

Figure 10-26 Predicted reactions for beam B-EMC-10M-22%

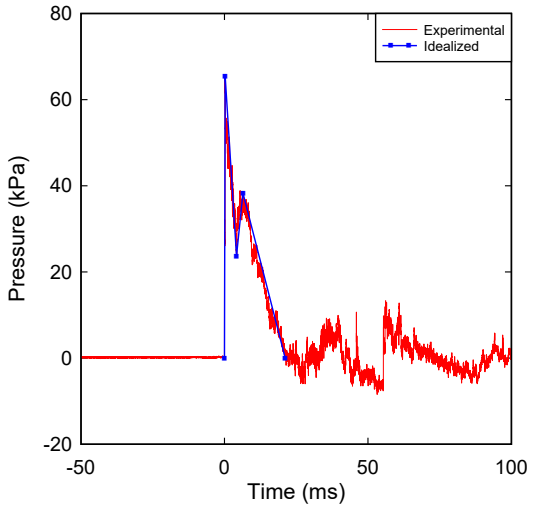


a- 50 psi (1% & 5%, DIF2-D1)



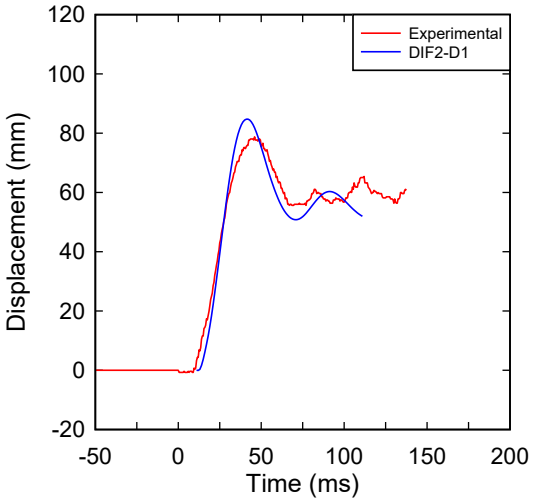
b- 50 psi

Figure 10-27 Cracking patterns of FE model vs experimental for beam B-EMC-10M-22%



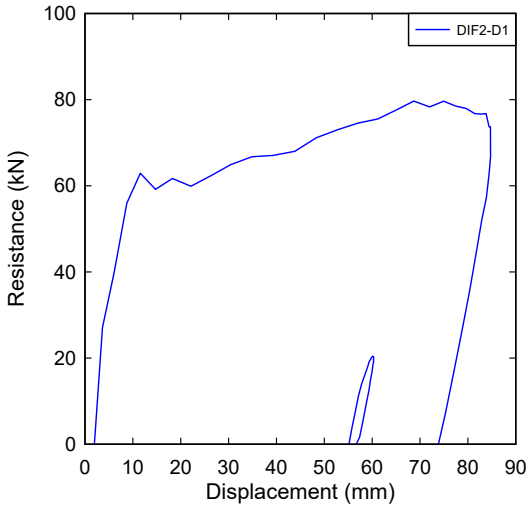

50 psi

Figure 10-28 Idealized blast pressure-time history for B-CR-MC-10M-5%



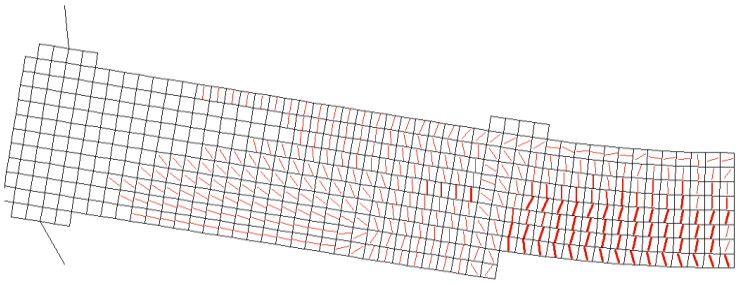

50 psi

Figure 10-29 Predicted vs experimental results for beam B-CR-MC-10M-5%




50 psi
(no data captured during test)

Figure 10-30 Predicted reactions for beam B-CR-MC-10M-5%

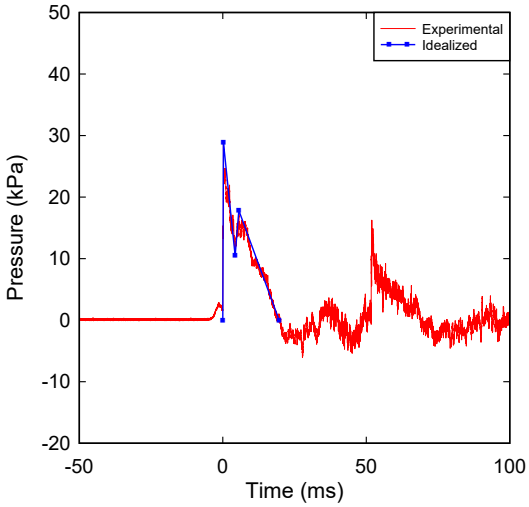


a- 50 psi (1% & 5%, DIF2-D1)

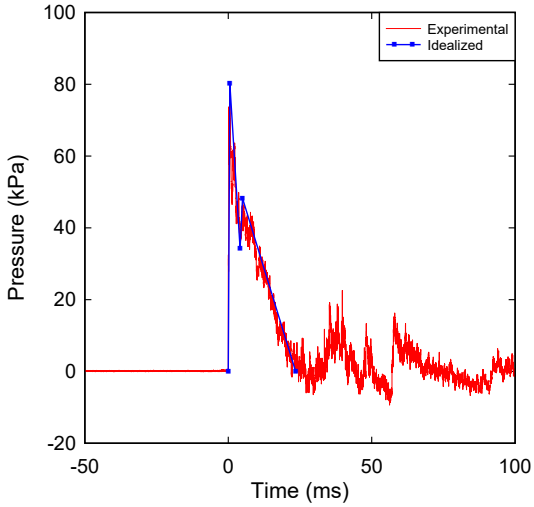


b- 50 psi

Figure 10-31 Cracking patterns of FE model vs experimental for beam B-CR-MC-10M-5%

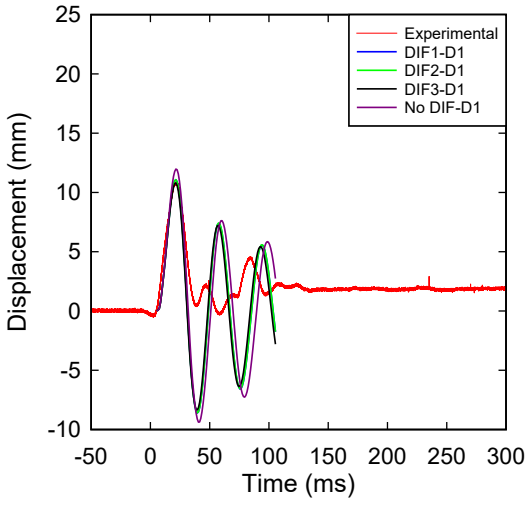



a- 17 psi

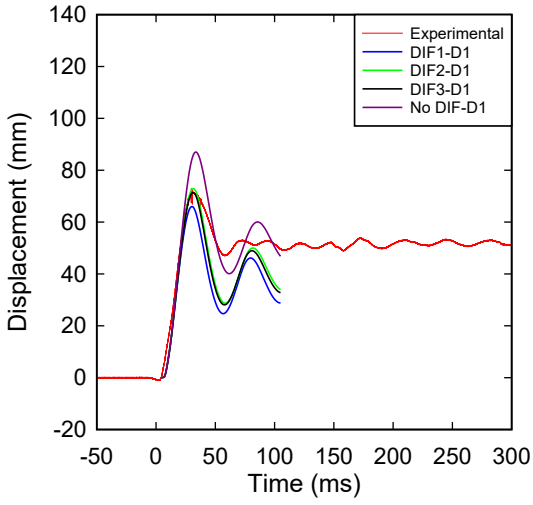



b- 70 psi

Figure 10-32 Idealized blast pressure-time history for beam B-MC-15M-12%

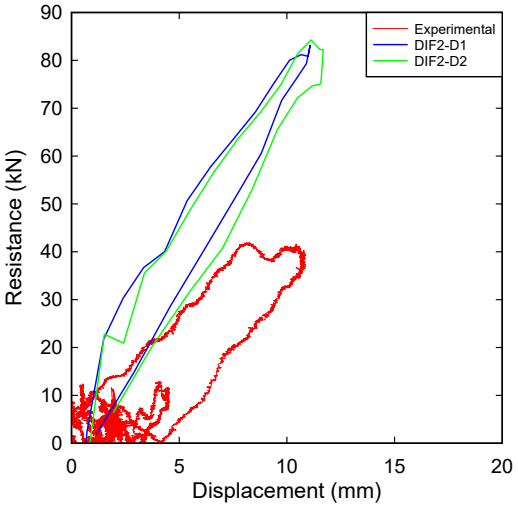



a- 17 psi

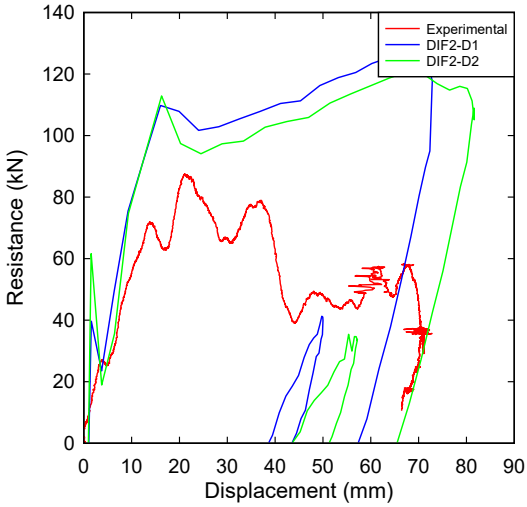



b- 70 psi

Figure 10-33 Predicted vs experimental results for beam B-MC-15M-12%

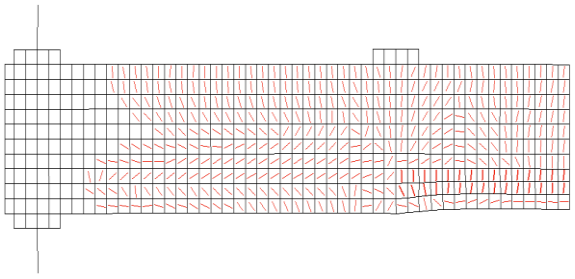



a- 17 psi

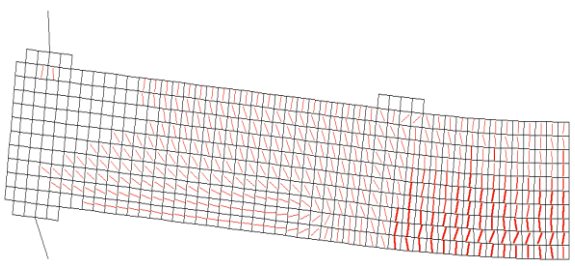



b- 70 psi

Figure 10-34 Predicted vs experimental reactions for beam B-MC-15M-12%



a- 17 psi (1% & 5%, DIF2-D1)



b- 70 psi (1% & 5%, DIF2-D1)

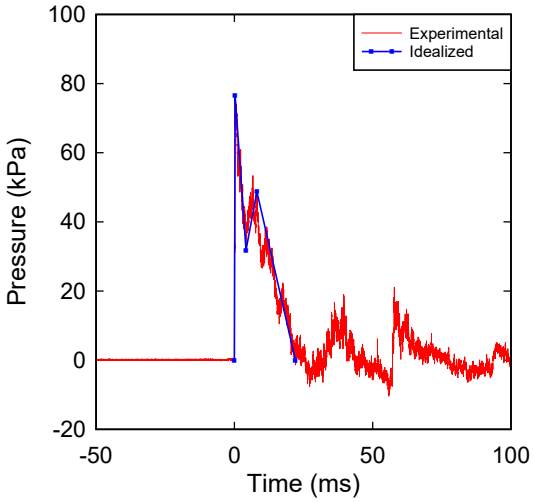


c- 17 psi



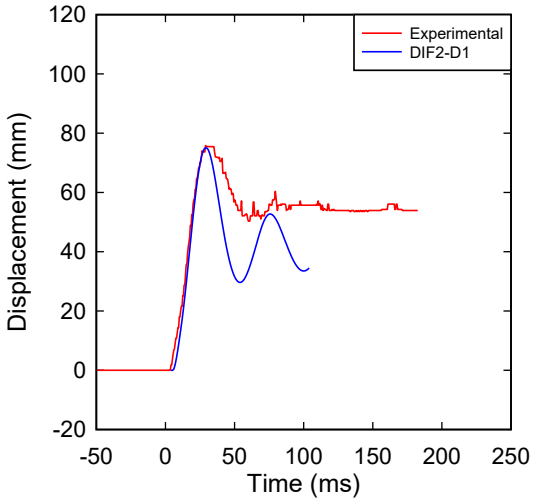
d- 70 psi

Figure 10-35 Cracking patterns of FE model vs experimental for beam B-MC-15M-12%



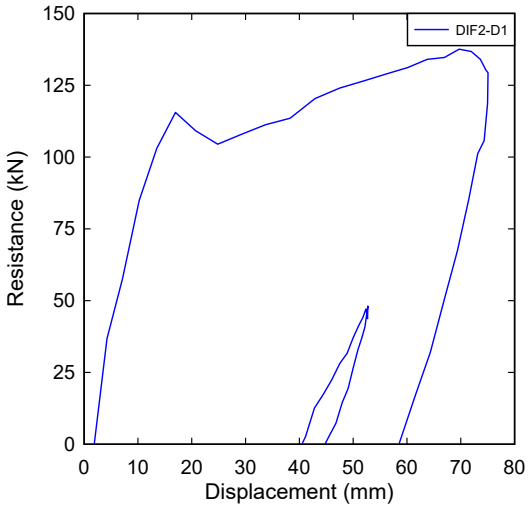

70psi

Figure 10-36 Idealized blast pressure-time history for beam B-CR-MC-15M-4%



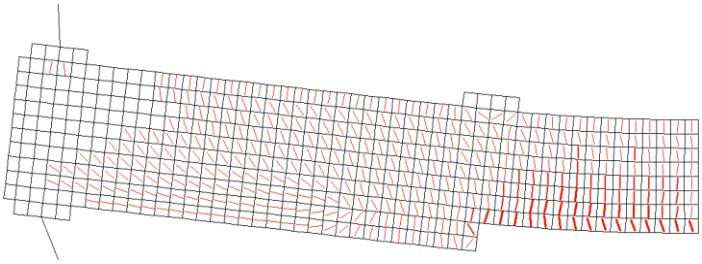

70 psi

Figure 10-37 Predicted vs experimental results for beam B-CR-MC-15M-4%




70 psi
(no data captured during test)

Figure 10-38 Predicted reactions for beam B-CR-MC-15M-4%

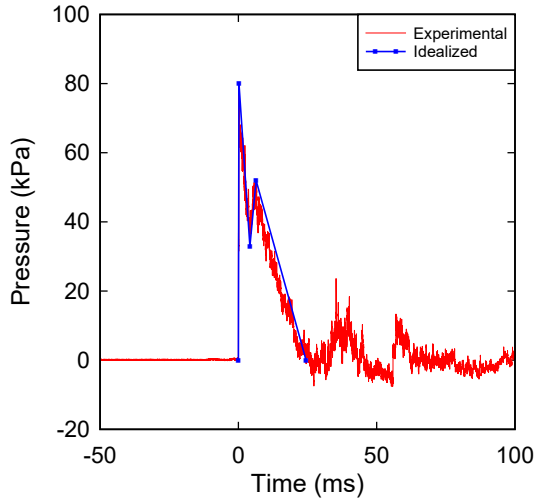


a- 70 psi (1% & 5%, DIF2-D1)



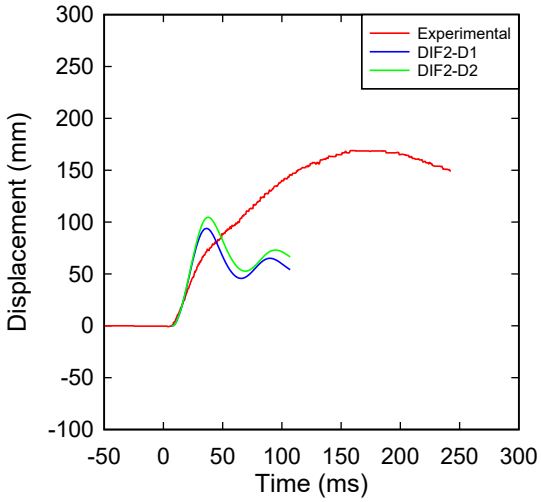
b- 70 psi

Figure 10-39 Cracking patterns of FE model vs experimental for beam B-CR-MC-15M-4%



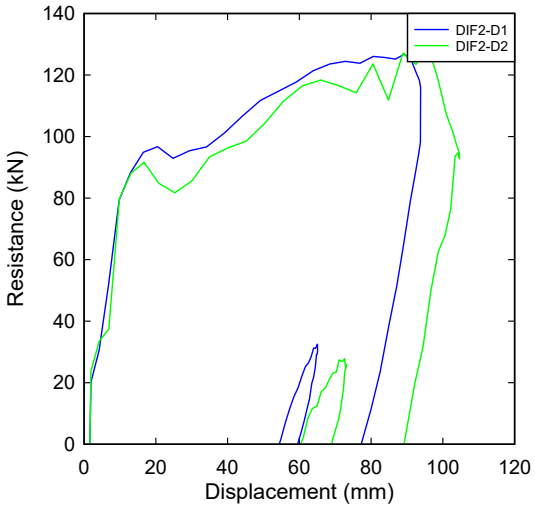

70 psi

Figure 10-40 Idealized blast pressure-time history for beam B-EMC-15M-17%



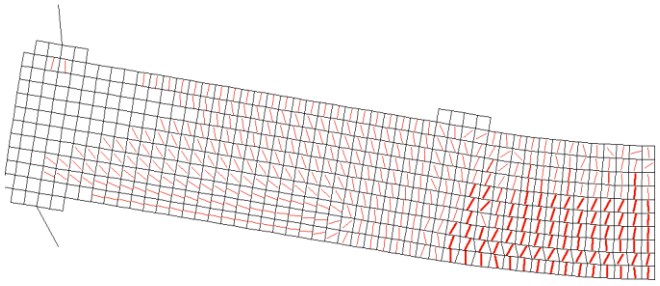

70 psi

Figure 10-41 Predicted vs experimental results for beam B-EMC-15M-17%




70 psi
(no data captured during test)

Figure 10-42 Predicted reactions for beam B-EMC-15M-17%



a- 70 psi (1% & 5%, DIF2-D1)



b- 70 psi

Figure 10-43 Cracking patterns of FE model vs experimental for beam B-EMC-15M-17%

#### 10.6.1.3 Specimen subjected to corrosion at the ends

This section presents the FE dynamic analysis of beam B-SC-10M-7%, which was corroded at its ends with a measured average mass loss of 7%. The FE model of this beam considered all the corrosion features that have been presented in Section 10.2, except that the effects of corrosion were introduced only at both ends of the beam (refer to **Figure 10-44**). The default dynamic increase factor DIF2 and damping ratio D1 were considered in most of the simulations. Considering all shots, the default DIF2-D1 case resulted in an average prediction ratio of 0.93 with a coefficient of variation (COV) of 19.3% (see **Table 10-7**). The idealized blast pressure time-history used to run the FE model of beam B-SC-10M-7% is presented in **Figure 10-45**.

**Figure 10-46** shows the calculated and experimental displacement-time histories for beam B-SC-10M-7% subjected to blast shots of 17, 35 and 50 psi when using DIF2-D1. It was observed from the figure that the prediction of maximum displacement was under-estimated for the first blast shot (17 psi) and over-estimated for the third blast shot (50 psi), with numerical-to-experimental ratios of 0.73 and 1.09, respectively. When the beam was subjected to the second blast shot of 35 psi, the predicted maximum displacement reached 31.7 mm, with a prediction ratio of 0.96, which is an acceptable estimate when compared to the experimental result (see **Table 10-7** and **Figure 10-46 (b)**). The effect of damping ratio (D2: 1% and 5% vs. D2: 0.5% and 0.75%, for modes 1 and 2, respectively) was studied for shot 1 and it can be observed that a more accurate result was obtained when using the lower damping ratio (DIF2-D2, with prediction ratio = 0.78).

**Figure 10-47** shows that the maximum dynamic load and pre-peak behavior when DIF2-D1 and DIF2-D2 were used were overestimated after applying the first blast shot; however, the post-peak response was underestimated. The beam pre-peak and post-peak behaviours in addition to the maximum dynamic load were acceptable for 35-psi and 50-psi blast shots when compared to the observed experimental behaviour.

The flexural failure mode and corresponding cracking patterns were well predicted for each blast shot when compared with the experiments and using the default DIF2-D1 case (refer to **Figure 10-48**).

Table 10-7 Summary of the FE and experimental results for beam B-SC-10M-7%

| Beam ID | Shot # | Shockwave properties | | Maximum displacements | | | | | | Displacement ratios | | | | |
|---|---|---|---|---|---|---|---|---|---|---|---|---|---|---|
| | | | | | $\delta_{num}$ (mm) | | | | | $\delta_{num}/\delta_{exp}$ | | | | |
| | | $P_r$ (kPa) | $I_r$ (kPa·msec) | $\delta_{exp}$ (mm) | DIF1-D1 | DIF2-D1 | DIF3-D1 | No DIF-D1 | DIF2-D2 | DIF1-D1 | DIF2-D1 | DIF3-D1 | No DIF-D1 | DIF1-D2 |
| B-SC-10M-7% | 1 | 29.2 | 239 | 20.4 | - | 14.85 | - | - | 15.91 | - | 0.73 | - | - | 0.78 |
| | 2 | 48.5 | 355.5 | 33 | - | 31.72 | - | - | - | - | 0.96 | - | - | - |
| | 3 | 61.5 | 554.7 | 70.1 | - | 77.09 | - | - | - | - | 1.09 | - | - | - |
| | | | | | | | | | Average | - | 0.93 | - | - | - |
| | | | | | | | | | STDEV | - | 0.18 | - | - | - |
| | | | | | | | | | COV | - | 19.3% | - | - | - |

Note: $P_r$ =reflected pressure; $I_r$ = reflected impulse; $\delta_{exp}$ = experimental maximum mid-span displacement; $\delta_{num}$ = numerical maximum mid-span displacement; $\delta_{num}/\delta_{exp}$ = displacement ratio.

Note: DIF2-D1 is run with Damping D1 (1% and 5%); DIF2-D2 is run with Damping D2 (0.5% and 0.75%).

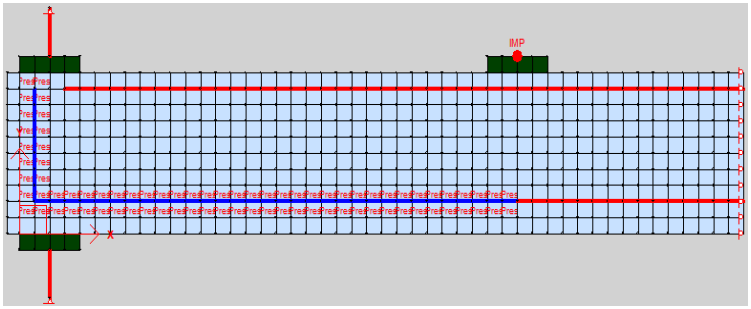



Figure 10-44 FE model of beam B-SC-10M-7%

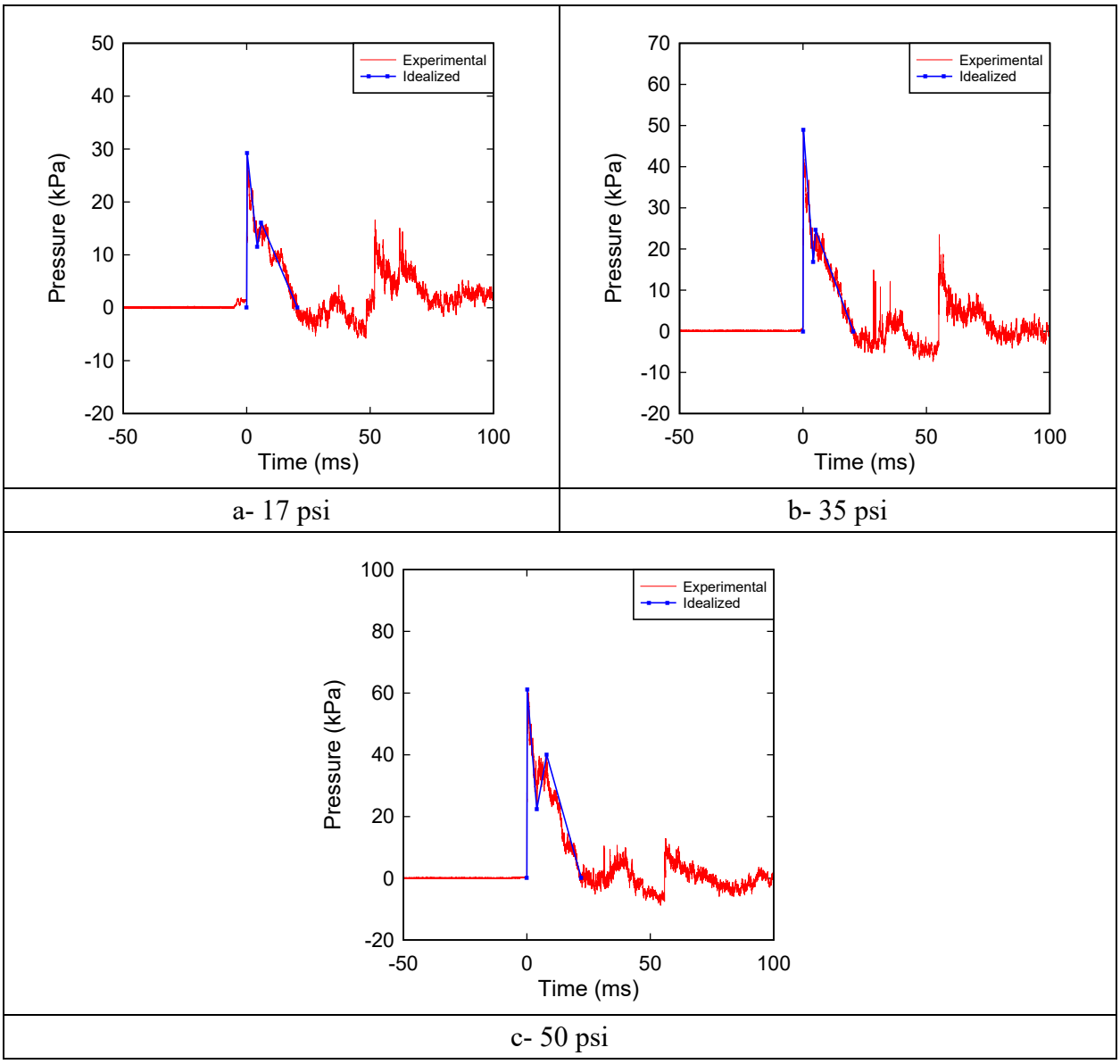



Figure 10-45 Idealized blast pressure-time history for beam B-SC-10M-7%

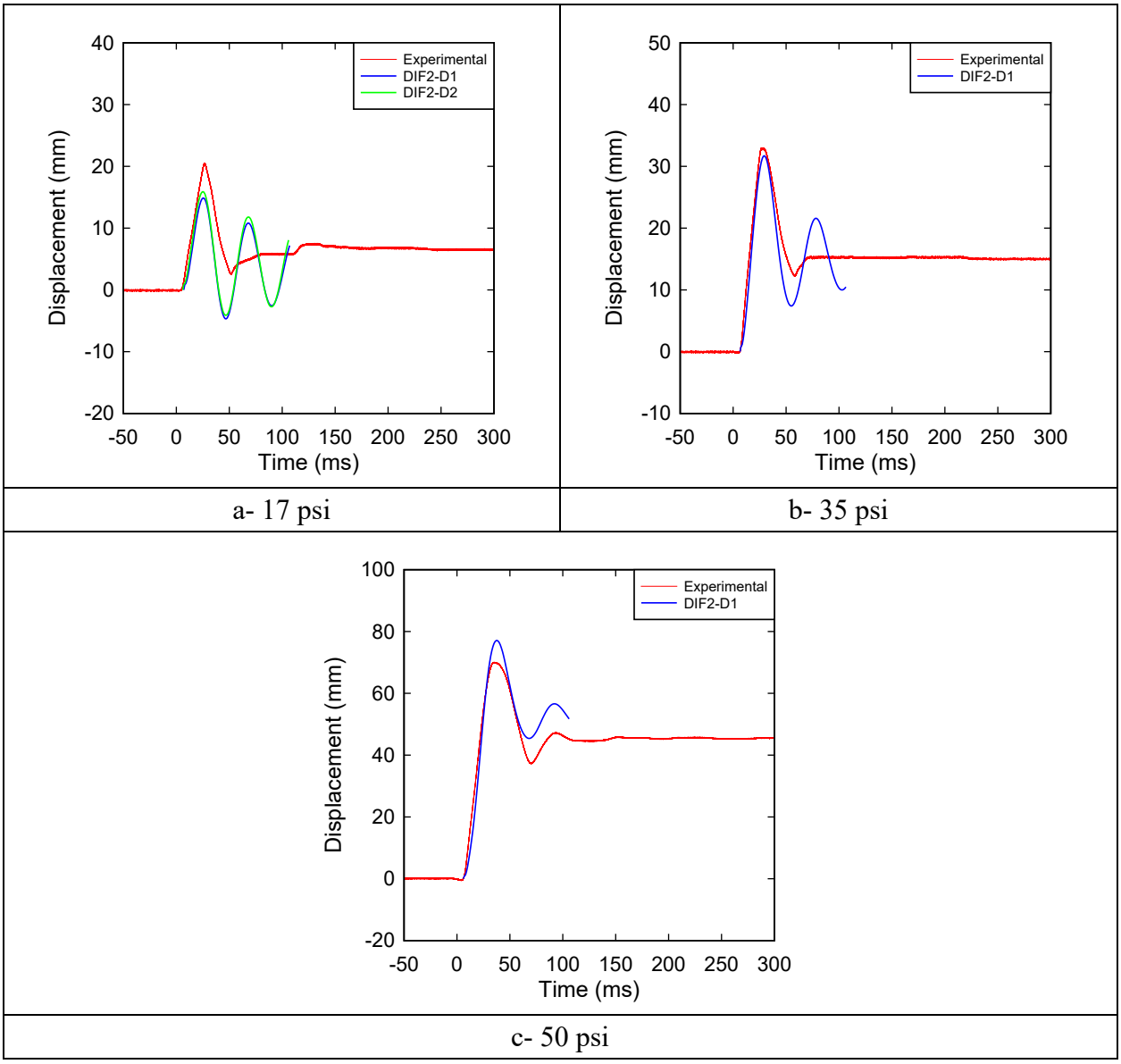
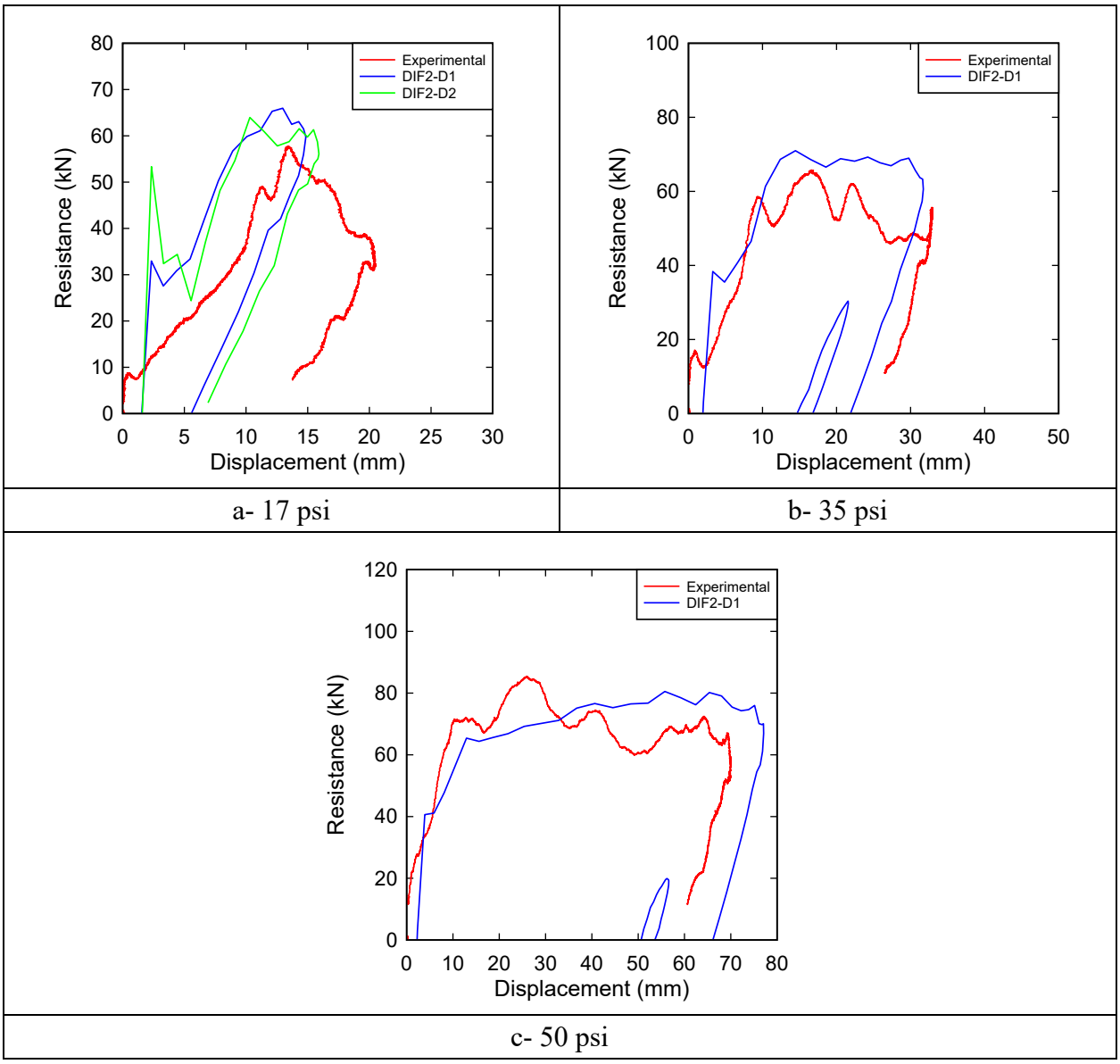



Figure 10-46 Predicted vs experimental results for beam B-SC-10M-7%




a- 17 psi

b- 35 psi

c- 50 psi

Figure 10-47 Predicted vs experimental reactions for beam B-SC-10M-7%

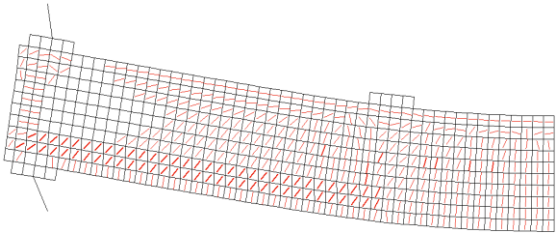
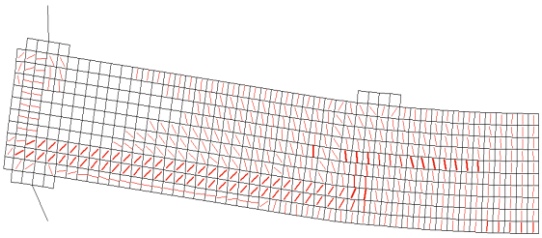
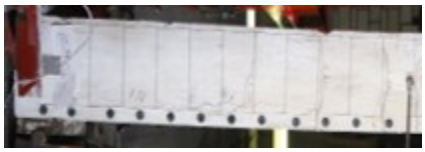
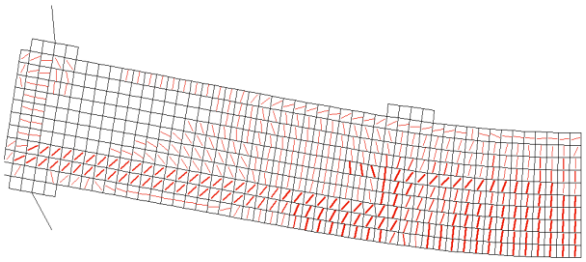
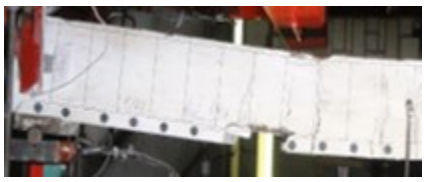
| | |
|---|---|
|  |  |
| a- 17 psi | d- 17 psi (1% & 5%, DIF2-D1) |
|  |  |
| b- 35 psi | e- 35 psi (1% & 5%, DIF2-D1) |
|  |  |
| c- 50 psi | f- 50 psi (1% & 5%, DIF2-D1) |

Figure 10-48 FE model vs experimental cracking patterns for beam B-SC-10M-7%

#### 10.6.1.4 Specimen subjected to full corrosion

The last beam in this section was subjected to corrosion of the tension reinforcement over the entire beam length, with an average mass loss of 12%. This beam, specimen B-FC-10M-12%, was modeled using the same features as the previous beams; however, the properties of the corroded bars and corrosion induced-cracking in the concrete elements were introduced over the entire tension bar length (see **Figure 10-49**). Only the default DIF2 and D1 damping ratio were applied in the FE simulation. **Figure 10-50** shows the idealized blast pressure time-history used to run the FE analysis of beam B-FC-10M-12%.

The first shot (17 psi) is not included due to lack of recorded experimental data. The calculated maximum displacement of the FE model after the second blast shot of 50 psi reached 75.8 mm, with a numerical-to-experimental ratio of 0.90, which is an acceptable result when compared with the experimental value (refer to **Table 10-8** and **Figure 10-51**).

The maximum load of the beam from the FE results was 68.8 kN (refer to **Figure 10-52**). From inspecting **Figure 10-53**, it was found that FE model failed in flexure associated with widespread cracking in the tension region with more intense cracks in the mid-span zone as observed in the experimental test.

Table 10-8 Summary of the FE results for beam B-FC-10M-12%

| Beam ID | Shot # | Shockwave properties | | Maximum displacements | | | | | | Displacement ratios | | | | |
|---|---|---|---|---|---|---|---|---|---|---|---|---|---|---|
| | | $P_r$ (kPa) | $I_r$ (kPa·msec) | $\delta_{exp}$ (mm) | $\delta_{num}$ (mm) | | | | | $\delta_{num}/\delta_{exp}$ | | | | |
| | | | | | DIF1-D1 | DIF2-D1 | DIF3-D1 | No DIF-D1 | DIF2-D2 | DIF1-D1 | DIF2-D1 | DIF3-D1 | No DIF-D1 | DIF1-D2 |
| B-FC-10M-12% | 2 | 52 | 540 | 83.7 | - | 75.8 | - | - | - | - | 0.90 | - | - | - |

Note: $P_r$ =reflected pressure; $I_r$ = reflected impulse; $\delta_{exp}$ = experimental maximum mid-span displacement; $\delta_{num}$ = numerical maximum mid-span displacement; $\delta_{num}/\delta_{exp}$ = displacement ratio.

Note: DIF2-D1 is run with Damping D1 (1% and 5%).

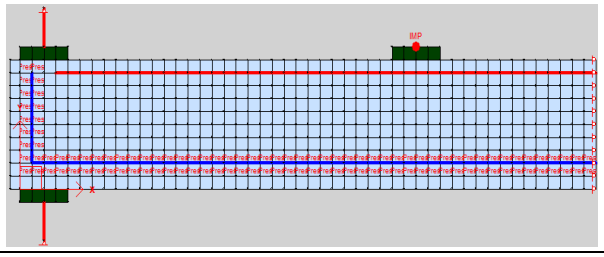
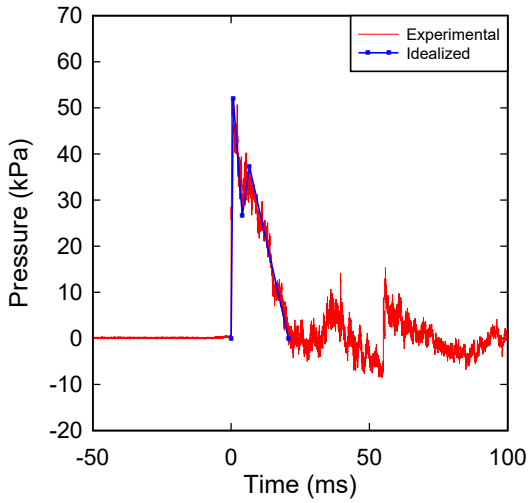
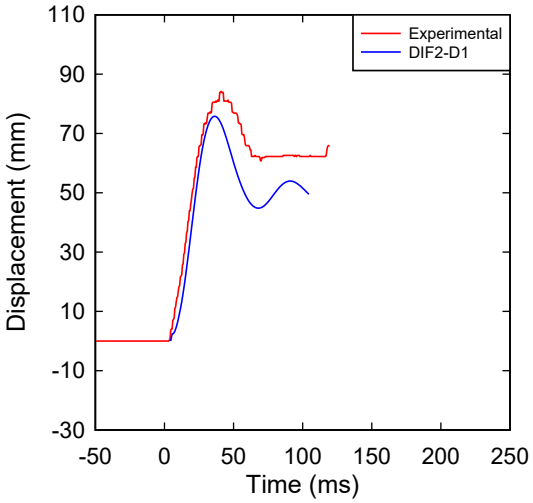


Figure 10-49 FE model of beam B-FC-10M-12%



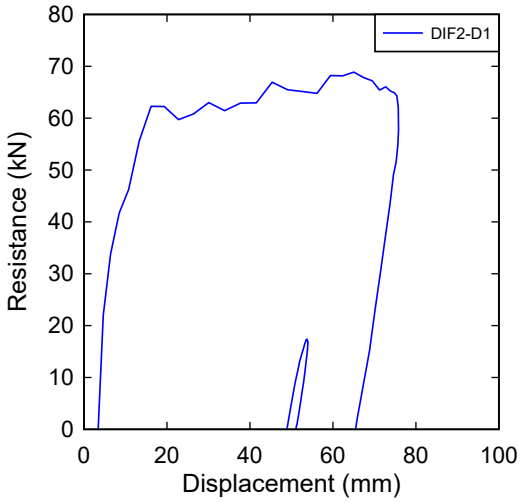

50 psi

Figure 10-50 Idealized blast pressure-time history for beam B-FC-10M-12%



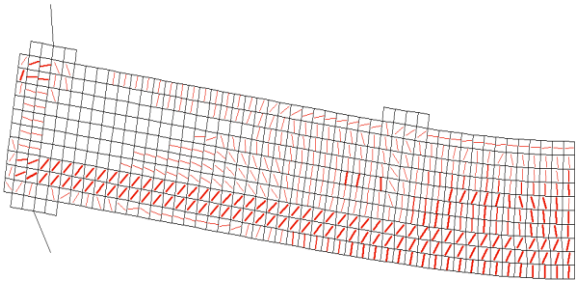

50 psi

Figure 10-51 Predicted vs experimental results for beam B-FC-10M-12%




50 psi
(no data captured during test)

Figure 10-52 Predicted reactions for beam B-FC-10M-12%



a- 50 psi (1% & 5%, DIF2-D1)



b- 50 psi

Figure 10-53 Cracking patterns of beam B-FC-10M-12%

### 10.6.2 Shear-governed beams

The following section presents the obtained results of the FE models for shear-governed beams in the 25M group. Three beams were considered in this group, one control beam and two corroded beams with different mass loss %. The FE models used a 25×25-mm mesh, with truss bar elements for both the longitudinal (25M) and transverse (6.3 mm) reinforcement.

#### 10.6.2.1 Control shear beam CB-25M-0%

Beam CB-25M-0% was the first beam modeled in the 25M group without considering the effects of corrosion. The FE model of this beam is shown in **Figure 10-54**. Two DIF cases (DIF2 and No DIF) were considered. The D1 and D2 damping ratios were also considered in the simulations. **Figure 10-55** presents the idealized blast pressure time-history used to run the FE analysis of beam CB-25M-0%.

**Table 10-9** and **Figure 10-56** show that the predicted maximum displacement for a blast shot of 90 psi was under-estimated when the DIF2-D1 modelling option was used, with a prediction ratio of 0.80, while it was over-estimated when no DIF was applied to the material properties, with a numerical-to experimental ratio of 1.08. Considering the effect of damping, DIF2-D2 (damping of 0.5% and 0.75%) resulted in an improved prediction ratio of 0.85 when compared to case DIF2-D1 (damping of 1% and 5%).

The pre-peak response and maximum strength of the FE model compare well with the experimental ones; however, the post-peak response was underestimated for both damping cases as presented in **Figure 10-57**. From examining **Figure 10-58**, it was noted that the FE model of the control beam in the 25M series resulted in a similar failure mode as the one observed in the experiment: a failure in flexure with the same cracking pattern.

Table 10-9 Summary of the FE results for beam CB-25M-0%

| Beam ID | Shot # | Shockwave properties | | Maximum displacements | | | | | | Displacement ratios | | | | |
|---|---|---|---|---|---|---|---|---|---|---|---|---|---|---|
| | | $P_r$ (kPa) | $I_r$ (kPa·msec) | $\delta_{exp}$ (mm) | $\delta_{num}$ (mm) | | | | | $\delta_{num}/\delta_{exp}$ | | | | |
| | | | | | DIF1-D1 | DIF2-D1 | DIF3-D1 | No DIF-D1 | DIF2-D2 | DIF1-D1 | DIF2-D1 | DIF3-D1 | No DIF-D1 | DIF1-D2 |
| CB-25M-0% | 1 | 91.4 | 927 | 46.0 | *- | 37.1 | - | 50.0 | 39.4 | - | 0.80 | - | 1.08 | 0.85 |

Note: $P_r$ =reflected pressure; $I_r$ = reflected impulse; $\delta_{exp}$ = experimental maximum mid-span displacement; $\delta_{num}$ = numerical maximum mid-span displacement; $\delta_{num}/\delta_{exp}$ = displacement ratio.

Note: DIF2-D1 and No DIF-D1 are run with Damping D1 (1% and 5%); DIF2-D2 is run with Damping D2 (0.5% and 0.75%).

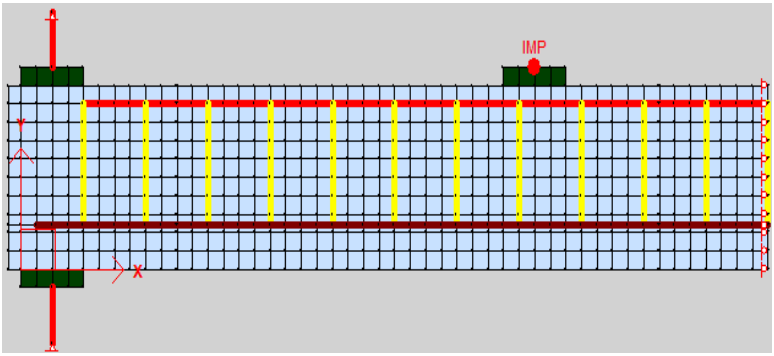
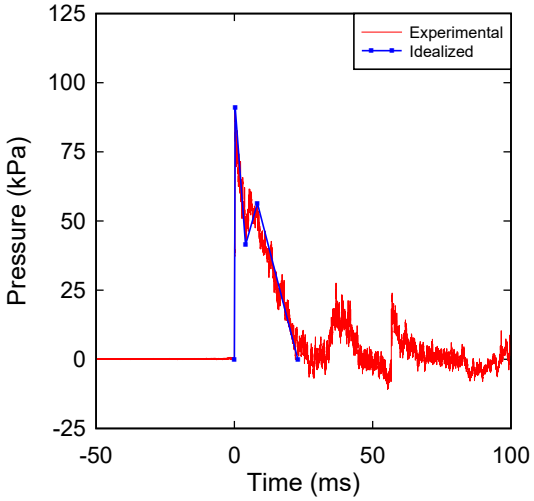
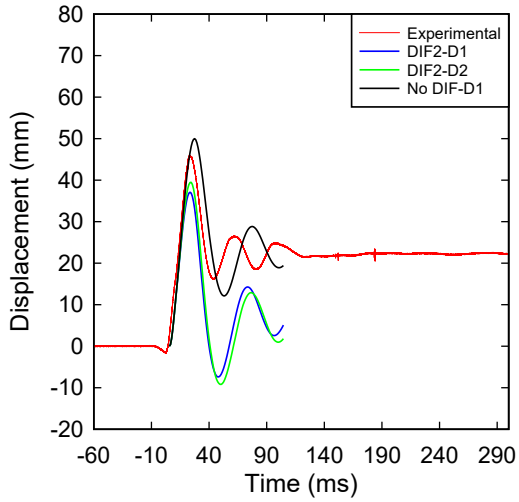



Figure 10-54 FE model for control beam CB-25M-0%



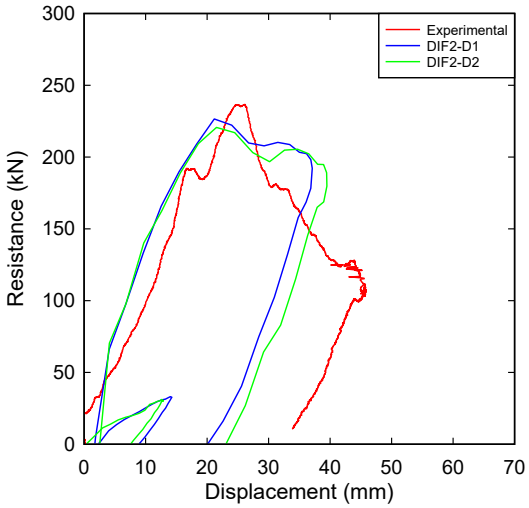

50 psi

Figure 10-55 Idealized blast pressure time-history vs experimental for beam CB-25M-0%



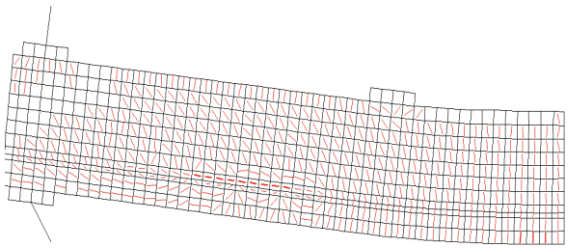

90 psi

Figure 10-56 Predicted vs experimental results for beam CB-25M-0%




50 psi

Figure 10-57 Predicted vs experimental reactions for beam CB-25M-0%



a- 90 psi (1% & 5%, DIF2-D1)



b- 90 psi

Figure 10-58 Failure mode and cracking patterns for beam CB-25M-0%

### 10.6.2.2 Corroded shear-governed beams

This section presents the FE results of the last two beams with corroded shear reinforcement in the 25M group. The FE models were the same as those used in the previous beam; however, the effects of corrosion were applied on the stirrups over the entire length of the beams by modifying their steel properties based on 11% and 12% mass loss, while corrosion-induced cracking was modeled by applying pre-strains on the concrete surrounding the transverse reinforcement as shown in **Figure 10-59**. Two DIF cases (DIF2 and No DIF) were considered. The D1 and D2 damping ratios were also considered in the simulations. **Figure 10-60** shows the idealized blast pressure time-histories used to run the FE dynamic analysis of the beams.

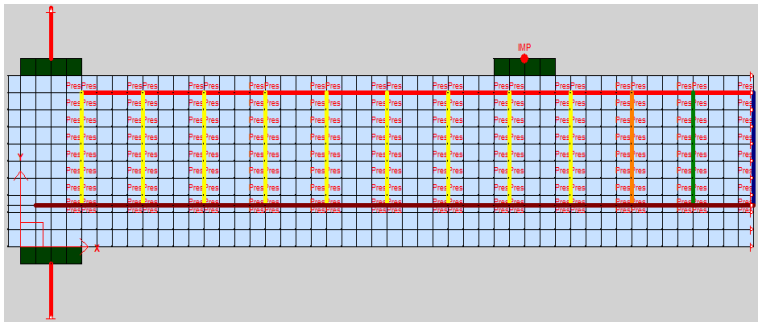
The prediction of the FE model for beams B-SHC-25M-11% and B-SHC-25M-12% considerably over-estimated the maximum displacement after applying a blast shot of 90 psi (see **Table 10-10** and **Figure 10-61**). Nonetheless, the predicted failure mode of the beams was similar to that observed in the experiments. Whereas beam B-SHC-25M-11% failed in flexure, beam B-SHC-25M-12% failed in shear, with severe cracking in both beams (see **Figure 10-62**).

Table 10-10 Summary of the FE results for corroded 25M beams

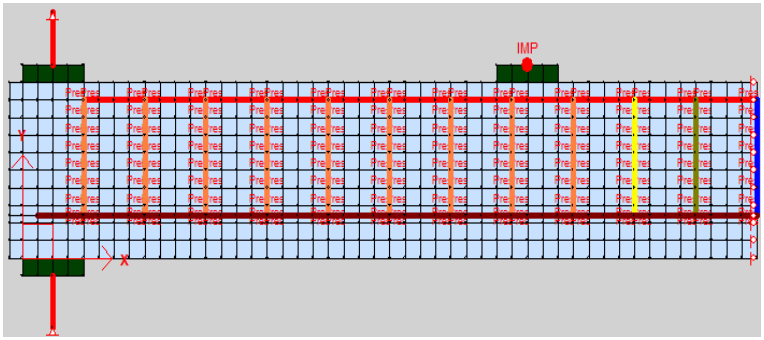
| Beam ID | Shot # | Shockwave properties | | Maximum displacements | | | | | | Displacement ratios | | | | |
|---|---|---|---|---|---|---|---|---|---|---|---|---|---|---|
| | | $P_r$ (kPa) | $I_r$ (kPa·msec) | $\delta_{exp}$ (mm) | $\delta_{num}$ (mm) | | | | | $\delta_{num}/\delta_{exp}$ | | | | |
| | | | | | DIF1-D1 | DIF2-D1 | DIF3-D1 | No DIF-D1 | DIF2-D2 | DIF1-D1 | DIF2-D1 | DIF3-D1 | No DIF-D1 | DIF1-D2 |
| B-SHC-25M-11% | 1 | 96.7 | 903 | 92.6 | - | 137.9 | - | 179.5 | 203.2 | - | 1.48 | - | 1.93 | 2.19 |
| B-SHC-25M-12% | 1 | 95.2 | 926 | 45.5 | - | 149.8 | - | 192.3 | - | - | 3.29 | - | 4.22 | - |

Note: $P_r$ =reflected pressure; $I_r$ = reflected impulse; $\delta_{exp}$ = experimental maximum mid-span displacement; $\delta_{num}$ = numerical maximum mid-span displacement; $\delta_{num}/\delta_{exp}$ = displacement ratio.

Note: DIF2-D1 and No DIF-D1 are run with Damping D1 (1% and 5%); DIF2-D2 is run with Damping D2 (0.5% and 0.75%).

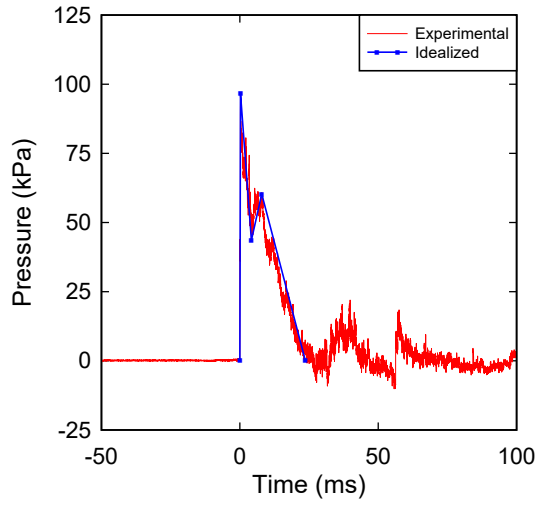



a- B-SHC-25M-11%

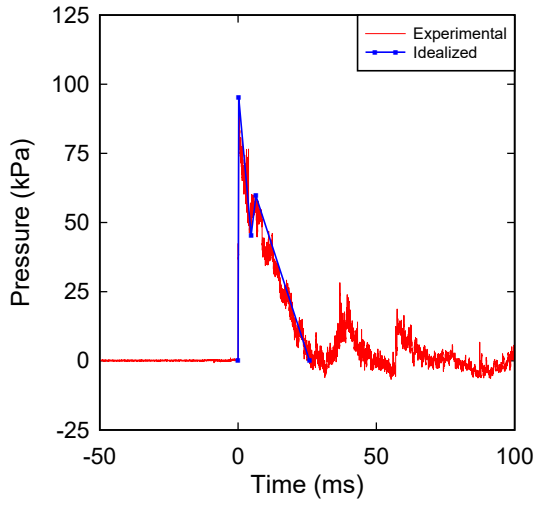



b- B-SHC-25M-12%

Figure 10-59 FE models of corroded shear-governed beams

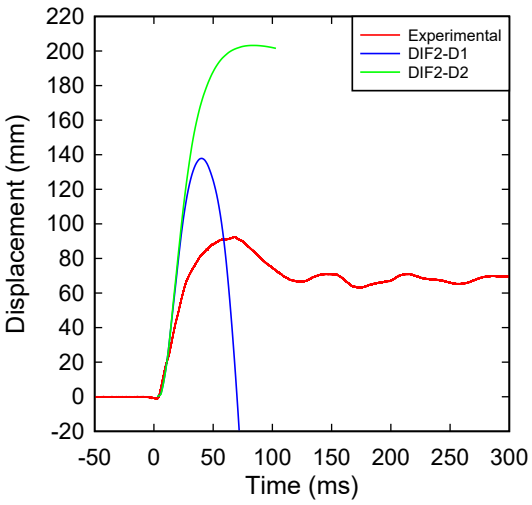



a- B-SHC-25M-11% (90 psi)

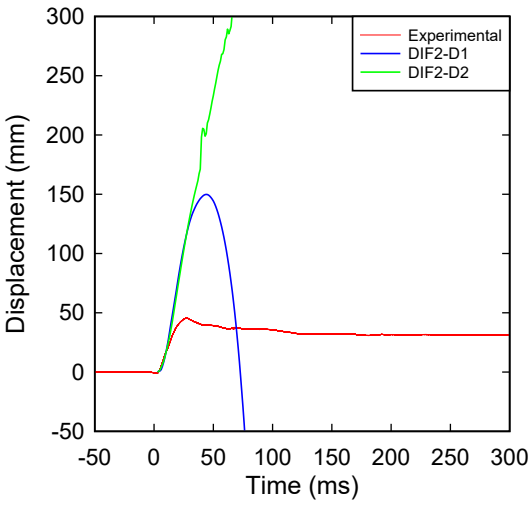



b- B-SHC-25M-12% (90 psi)

Figure 10-60 Idealized blast pressure time-history for corroded shear-governed beams

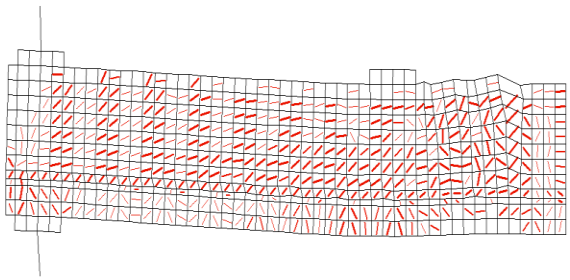



a- B-SHC-25M-11% (90 psi)




b- B-SHC-25M-12% (90 psi)

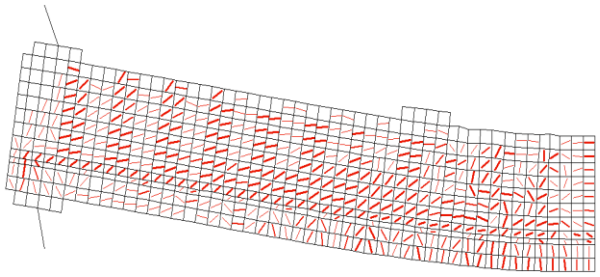
Figure 10-61 Predicted vs experimental results of corroded shear-governed beams



a- 90 psi (1% & 5%, DIF2-D1)



c- B-SHC-25M-11% (90 psi)



b- 90 psi (1% & 5%, DIF2-D1)



d- B-SHC-25M-12% (90 psi)

Figure 10-62 Failure mode and cracking patterns of corroded shear-governed beams

# Chapter 11: Conclusions and Recommendations

## 11.1 Conclusions

This thesis has presented the experimental and analytical results of a study that investigated the effects of reinforcement corrosion on the flexural, shear and blast behaviours of reinforced concrete beams. As a part of the experimental study, twenty-four reinforced concrete beams were built; ten beams were tested under four-point bending and fourteen beams were tested under simulated blast loads using the University of Ottawa Shock tube. Eighteen beams were subjected to an accelerated corrosion process to induce different amount of mass loss in the longitudinal and transverse steel reinforcement. The variables that were included in the tests include: the type of corroded reinforcement (i.e., longitudinal or transverse reinforcement), the amount of corrosion (i.e., % steel mass loss), and the extent/location of corrosion on the tension steel reinforcement (i.e., over the full length, middle span or end spans).

The following conclusions are drawn from the experimental results of the beams tested statically:

- Different levels of corrosion happening at mid-span in the 10M group resulted in a reduction of all aspects of flexural behaviour, which include the maximum and yield strengths, stiffness, maximum displacement due to occasional rupture of the 10M tension bars, ductility ($\Delta_{85}/\Delta_y$) and toughness ($A_{u85}$) and changing the failure mode from ductile to brittle due to rupture of the 10M bars.
- In the 15M group, the beam with corrosion at mid-span experienced a reduction in maximum strength, yield strength and stiffness. Also, the displacement $\Delta_{85}$, ductility ($\Delta_{max}/\Delta_y$) and toughness ($Au_{max}$) were decreased. The failure of this beam was in flexure, however, this failure was associated with more sudden crushing of concrete, buckling of the longitudinal bars and severe spalling of the cover concrete in the mid-span of the beam due to the effects of corrosion.
- Corrosion at the ends of the beam in the 10M group did not significantly affect flexural behavior, probably because the steel mass loss in the shear spans and anchorage was low.
- For the beam in the 10M group subjected to corrosion along its entire span, the most significant reduction in flexural behaviour occurred in the ductility ($\Delta_{85}/\Delta_y$) and toughness

($A_{u85}$) with a slight reduction in the maximum and yield strengths. Furthermore, this beam experienced bar rupture in the tension region.

- Examining the effect of corrosion location in the 10M group, the results showed that mid-corrosion (with a 14% mass loss) and full-corrosion (with a 13% mass loss) induced more severe damage in terms of cracking, crushing, spalling of cover concrete and rupture of bars, when compared to the beam with end-span corrosion.
- Beams with shear-corrosion in the 25M group showed similar capacities in terms of maximum strength, experiencing shear failure; however, the beam with high mass loss in the transverse reinforcement showed a more brittle failure in shear.

In addition, the following conclusions are drawn from the experimental results of beams tested dynamically under simulated blast loads:

- The corrosion affected all aspects of blast response in the 10M group when corrosion took place on the tensile 10M bars in the mid-span region, which resulted in an increase in maximum displacements and damage. The damage became more significant as the mass loss increased, leading to a severe brittle failure.
- In the 15M group, the observed results from beams in which corrosion occurred in the mid-span region showed that the increase in mass loss led to hazardous failure under blast loading and affected all aspects of the blast response.
- For the beam with corrosion at the ends in the 10M group, the observed results were consistent with the static results, with only minor effects on blast performance due to the low level and location of reinforcement corrosion.
- Full corrosion with a 12% mass loss over the entire length of the beam resulted in moderate effects in terms of displacement and damage on the beam response.
- The location of corrosion in the mid-span and full-span regions resulted in similar blast responses in terms of displacements; however, mid-span corrosion was more significant in terms of damage.
- The cover loss in the mid-span region of the beam with low intensity of corrosion had limited impact on the blast response in the 10M group, most likely because the reinforcement anchorage was not compromised. The concrete cover removal in the mid-span region of the 15M beam had minor effects on the blast response when the amount of

corrosion in the steel bars was low; the anchorage of the reinforcement at the beam ends was not compromised by corrosion.

- The blast performance of beams with corrosion in the transverse reinforcement was affected in terms of damage and failure mode.
- The residual test results on the beam with corrosion at the ends showed that the low level of corrosion had limited effects on the post-blast residual performance.
- In contrast to the ends-span corrosion beam, the residual test results on the beam with full-span corrosion significantly affected the post-blast residual performance.
- The comparison of static resistance curves vs dynamic resistance curves showed an increase in resistance under dynamic loading for flexural- and shear-governed beams. This increase was also observed in the corroded beams, implying that the strain-rate effect on the increase in strength was not affected by reinforcement corrosion.

As a part of the numerical study, the static results were predicted using 2D nonlinear finite element (FE) modelling. The effects of corrosion were considered using several modeling features including reduction in steel bar cross-sectional area, modification of the steel stress-strain response, and introducing corrosion-induced cracking using applied pre-strains. In addition, the blast results were predicted using two approaches, including: 1) single-degree of freedom (SDOF) analysis (with the resistance functions developed using FE modelling); and 2) the blast analysis capabilities of FE software VecTor2.

The following conclusions are drawn from the analytical results:

- In general, the obtained predicted results in terms of flexural and shear responses, which include maximum and yield strengths, pre-peak, and post-peak behaviours in addition to failure mode for each beam tested statically, were acceptable.
- SDOF analysis showed acceptable results in terms of ability to predict maximum displacements for flexure-governed beams (corroded and un-corroded). Using the design DIFs resulted in slightly more accurate displacement predictions when compared to those obtained using the Saatcioglu DIF model. The No DIF case resulted in poor predictions.
- The finite element blast analysis allowed for reasonable predictions of overall blast behaviour for the flexure-governed beams (corroded and un-corroded) in terms of complete displacement response, dynamic reactions, and failure mode. The prediction of the control

beam in the 25M group was acceptable in terms of displacement response and damage; however, the analysis of the beams with corrosion in the transverse reinforcement over-estimated prediction in terms of the maximum displacement, with an acceptable prediction for failure mode.

- In general, SDOF analysis can be used to reliably predict the blast response of corrosion-damaged RC beams in flexure. The use of FE modeling allows for more-in depth understanding of blast behaviour in terms of displacement response, damage, and failure mode, but requires increased computational.

## 11.2 Limitations

The following limitations apply to the conclusions from the research conducted in this thesis:

- The beams in this study were tested under simulated blast loads using a shock tube and load transfer device (LTD). This LTD results in the application of concentrated point loads at high speed and the addition of significant mass which can affect dynamic response; future tests should consider testing under uniformly distributed loading which can simulate blast loading more closely.
- Bond was ignored in the finite element analyses because the beams were well anchored at the end; however, ignoring the bond effect in the analysis also ignores the stress redistribution to neighbouring sections that occurs after bond is lost.
- The resistance functions used in the SDOF analyses were determined analytically using FE modelling instead of using the experimentally obtained ones. FE results are generally stiffer which affects the SDOF results.

## 11.3 Recommendations for future work

The following recommendations for future studies are suggested to better understand the behaviour of corroded beams under static and blast loads:

- Increasing the time of the accelerated corrosion process to reach desirable higher levels of steel mass loss.
- Studying, in depth, the effect of reinforcement corrosion at the beam ends when reinforcement anchorage is compromised by corrosion.

- Inducing corrosion, for shear-governed beams, in each stirrup separately to reach to the targeted mass loss equally.
- Studying the effect of corrosion on the blast response of beams built with high-performance concrete.
- Studying the effect of corrosion on the blast response of beams constructed with MMFX or stainless-steel bars in the tension region.
- Studying the effects of various retrofits, such as FRP and concrete jacketing, on the blast response of corrosion-damaged reinforced concrete beams.
- Using 3D finite element analysis to better capture the blast response of corroded beams.
- Comparing different steel types (carbon steel, stainless steel and high strength steel) in terms of blast behaviour with consideration of their life cycle costs.

# References


Algassem, O., Li, Y. and Aoude, H., 2019. Ability of steel fibers to enhance the shear and flexural behavior of high-strength concrete beams subjected to blast loads. Engineering Structures, 199, p.109611.

Al-Sulaimani, G. J., Kaleemullah, M., Basunbul, I. A., & Rasheeduzzafar. (1990). Influence of corrosion and cracking on bond behavior and strength of reinforced concrete members. *ACI Structural Journal*, *87*(2), 220–231. https://doi.org/10.14359/2732

Alsiwat, J. M., Saatcioglu, M. (1992). Reinforcement anchorage slip under monotonic loading. *ASCE Journal of Structural Engineering*,vol.118,no. 9, pp.2421–2438,1992.

Andrade C., Alonso C., Garcia D., Rodriguez J. Remaining Lifetime of Reinforced Concrete Structures: Effect of Corrosion in the Mechanical Properties of the Steel, *Life Prediction of Corrodible Structures*, NACE, Cambridge, UK Sept. 1991, pp. 12/1-12/11

ASCE's 2017 Infrastructure Report Card | GPA: D+, 2017, http://www.infrastructurereportcard.org. (last accessed June. 15, 2020)

ASTM C143/C143M-15. Standard Test Method for Slump of Hydraulic-Cement Concrete, 2015

ASTM G1-03 (2011). Standard Practice for Preparing, Cleaning and Evaluating Corrosion Test Specimens. ASTM Internatianal, West, Conshohocken, PA.

Azad, A. K., Ahmad, S., & Azher, S. A. (2007). Residual strength of corrosion-damaged reinforced concrete beams. *ACI Materials Journal*, *104*(1), 40–47. https://doi.org/10.14359/18493

Bastami, R. (2019). Structural Performance of High Strength Reinforced Concrete Beams Build with Synthetic Fibers. University of Ottawa. Ottawa, ON, Canada.

Bernard, S. (2013). Finite Element Modelling of Reinforced Concrete Beams with Corroded Shear Reinforcement. University of Ottawa. Ottawa, ON, Canada.

Bertolini, L., Elsener, B., Pedeferri, P., Redaelli, Elena., Polder, R. (2013) . Corrosion of Steel in Concrete: Prevension, Diagnosis, Repair. Second Edition, Wiley-VCH Verlag GmbH & Co. KGaA, Germany

Bicer, K., Yalciner, H., Pekrioglu Balkıs, A., & Kumbasaroglu, A. (2018). Effect of corrosion on flexural strength of reinforced concrete beams with polypropylene fibers. *Construction and Building Materials*, *185*, 574–588. https://doi.org/10.1016/j.conbuildmat.2018.07.021

Castel, A., François, R., & Arliguie, G. (2000). Mechanical behaviour of corroded reinforced concrete beams - Part 1: experimental study of corroded beams. *Materials and Structures/Materiaux et Constructions*, *33*(9), 539–544. https://doi.org/10.1007/bf02480533

Coronelli, D., & Gambarova, P. (2004). Structural assessment of corroded reinforced concrete beams: Modeling guidelines. *Journal of Structural Engineering*, *130*(8), 1214–1224. https://doi.org/10.1061/(ASCE)0733-9445(2004)130:8(1214)

CSA S850-12. Design and Assessment of Buildings Subjected to Blast Loads, 2012.

Dai, M., Yang, O., Xiao, Y., & Li, F. (2016). Influence of longitudinal bar corrosion on impact behavior of RC beams. *Materials and Structures/Materiaux et Constructions*, *49*(9), 3579–3589. https://doi.org/10.1617/s11527-015-0741-0

Dekoster, M., Buyle-Bodin, F., Maurel, O., & Delmas, Y. (2003). Modelling of the flexural behaviour of RC beams subjected to localised and uniform corrosion. *Engineering Structures*, *25*(10), 1333–1341. https://doi.org/10.1016/S0141-0296(03)00108-1

Dong, J., Zhao, Y., Wang, K., & Jin, W. (2017). Crack propagation and flexural behaviour of RC beams under simultaneous sustained loading and steel corrosion. *Construction and Building Materials*, *151*, 208–219. https://doi.org/10.1016/j.conbuildmat.2017.05.193

El-Sayed, A. K., Hussain, R. R., & Shuraim, A. B. (2016). Effect of stirrup corrosion on the shear strength of reinforced concrete short beams. *Journal of Civil Engineering and Management*, *22*(4), 491–499. https://doi.org/10.3846/13923730.2014.897990

El Maaddawy, T., Soudki, K., & Topper, T. (2005). Long-term performance of corrosion-damaged reinforced concrete beams. *ACI Structural Journal*, *102*(5), 649–656. https://doi.org/10.14359/14660

François, R., Castel, A., & Vidal, T. (2006). A finite macro-element for corroded reinforced concrete. *Materials and Structures/Materiaux et Constructions*, *39*(5), 571–584. https://doi.org/10.1617/s11527-006-9096-x

Hansson, C. M., Poursaee, A., Jaffer, S. J. (2012). Corrosion of Reinforcing Bars in Concrete. University of Waterloo. Waterloo, ON, Canada.

Higgins, C., & Farrow, W. C. (2006). Tests of reinforced concrete beams with corrosion-damaged stirrups. *ACI Structural Journal*, *103*(1), 133–141. https://doi.org/10.14359/15094

Hou, L., Zhou, B., Guo, S., Aslani, F., & Chen, D. (2019). Corrosion behavior and flexural performance of reinforced concrete/ultrahigh toughness cementitious composite (RC/UHTCC) beams under sustained loading and shrinkage cracking. *Construction and Building Materials*, *198*, 278–287. https://doi.org/10.1016/j.conbuildmat.2018.11.237

Imam, A., & Azad, A. K. (2016). Prediction of residual shear strength of corroded reinforced concrete beams. *International Journal of Advanced Structural Engineering*, *8*(3), 307–318. https://doi.org/10.1007/s40091-016-0133-x

Jacques. E. (2016). Characteristics of Reinforced Concrete Bond at High Strain Rates. University of Ottawa. Ottawa, ON, Canada.

Jacques. E., (2014), RCBLAST (Version. 0.5.1) (Computer program)

Juarez, C. A., Guevara, B., Fajardo, G., & Castro-Borges, P. (2011). Ultimate and nominal shear strength in reinforced concrete beams deteriorated by corrosion. *Engineering Structures*, *33*(12), 3189–3196. https://doi.org/10.1016/j.engstruct.2011.08.014

Kallias, A. N., & Imran Rafiq, M. (2010). Finite element investigation of the structural response of corroded RC beams. *Engineering Structures*, *32*(9), 2984–2994. https://doi.org/10.1016/j.engstruct.2010.05.017

Khan, I., François, R., & Castel, A. (2014). Experimental and analytical study of corroded shear-critical reinforced concrete beams. *Materials and Structures/Materiaux et Constructions*, *47*(9), 1467–1481. https://doi.org/10.1617/s11527-013-0129-y

Lachemi, M., Al-Bayati, N., Sahmaran, M., & Anil, O. (2014). The effect of corrosion on shear behavior of reinforced self-consolidating concrete beams. *Engineering Structures*, *79*, 1–12. https://doi.org/10.1016/j.engstruct.2014.07.044

Lay, S., Schießl, P. and Cairns, J. (2003). LIFECON DELIVERABLE D3.2. Service Life Models, Technical Research Centre of Finland, 169.

Li, H., Li, B., Jin, R., Li, S., & Yu, J. G. (2018). Effects of sustained loading and corrosion on the performance of reinforced concrete beams. *Construction and Building Materials*, *169*, 179–187. https://doi.org/10.1016/j.conbuildmat.2018.02.199

Li, Y., Algassem, O. and Aoude, H., 2018. Response of high-strength reinforced concrete beams under shock-tube induced blast loading. Construction and Building Materials, 189, pp.420-437.

Liu, Y., Jiang, N., Deng, Y., Ma, Y., Zhang, H., & Li, M. (2016). Flexural experiment and stiffness investigation of reinforced concrete beam under chloride penetration and sustained loading. *Construction and Building Materials*, *117*, 302–310. https://doi.org/10.1016/j.conbuildmat.2016.04.110

Lu, Y., Tang, W., Li, S., & Tang, M. (2018). Effects of simultaneous fatigue loading and corrosion on the behavior of reinforced beams. *Construction and Building Materials*, *181*, 85–93. https://doi.org/10.1016/j.conbuildmat.2018.06.028

Mangat, P. S., & Elgarf, M. S. (1999). Flexural strength of concrete beams with corroding reinforcement. *ACI Structural Journal*, *96*(1), 149–158. https://doi.org/10.14359/606

Mirza, S., 2006. Durability and sustainability of infrastructure A state-of-the-art report. Canadian Journal of Civil Engineering, 33(6), pp.639-649.

Mitchell, D., Marchand, J., Croteau, P. and Cook, W.D., 2011. Concorde overpass collapse: structural aspects. Journal of performance of constructed facilities, 25(6), pp.545-553.

Oyado, M., Kanakubo, T., Sato, T., & Yamamoto, Y. (2011). Bending performance of reinforced concrete member deteriorated by corrosion. *Structure and Infrastructure Engineering*, *7*(1), 121–130. https://doi.org/10.1080/15732471003588510

Rivera-Corral, J. O., Fajardo, G., Arliguie, G., Orozco-Cruz, R., Deby, F., & Valdez, P. (2017). Corrosion behavior of steel reinforcement bars embedded in concrete exposed to chlorides: Effect of surface finish. *Construction and Building Materials*, *147*, 815–826. https://doi.org/10.1016/j.conbuildmat.2017.04.186

Rodriguez, J., Ortega, L. M., & Casal, J. (1997). Load carrying capacity of concrete structures with corroded reinforcement. *Construction and Building Materials*, *11*(4), 239–248. https://doi.org/10.1016/S0950-0618(97)00043-3

Saatci, S., & Vecchio, F. J. (2009). Nonlinear Finite Element Modeling of Reinforced Concrete Structures under Impact Loads. *ACI Structural Journal*, V. 106, No. 5

Saatcioglu, M., Lloyd, A., Jacques, E., Braimah, A., & Doudak, G. (2011). Focused research for development of a CSA standard on design and assessment of buildings subjected to blast loads. University of Ottawa, Ottawa: Hazard Mitigation and Disaster Management Research Centre

Sánchez, P. J., Huespe, A. E., Oliver, J., & Toro, S. (2010). Mesoscopic model to simulate the mechanical behavior of reinforced concrete members affected by corrosion. *International Journal of Solids and Structures*, *47*(5), 559–570. https://doi.org/10.1016/j.ijsolstr.2009.10.023

Soltani, M., Safiey, A. and Brennan, A., (2019). A State-of-the-Art Review of Bending and Shear Behaviors of Corrosion-Damaged Reinforced Concrete Beams. *ACI Structural Journal*, V. 116, No 3, pp. 53-64

Song, Y., Wightman, E., Tian, Y., Jack, K., Li, X., Zhong, H., Bond, P. L., Yuan, Z., & Jiang, G. (2019). Corrosion of reinforcing steel in concrete sewers. *Science of the Total Environment*, *649*, 739–748. https://doi.org/10.1016/j.scitotenv.2018.08.362

Tamai, H., Sonoda, Y., Bolander, J, E. (2020). Impact resistance of RC beams with reinforcement corrosion: Experimental observations. *Construction and Building Materials,* 263, 120638. https://doi.org/10.1016/j.conbuildmat.2020.120638

Torres-Acosta, A. A., Navarro-Gutierrez, S., & Terán-Guillén, J. (2007). Residual flexure capacity of corroded reinforced concrete beams. *Engineering Structures*, *29*(6), 1145–1152. https://doi.org/10.1016/j.engstruct.2006.07.018

Vecchio, F. J., and Collins, M. P. (1986). "The modified compression-field theory for reinforced concrete elements subjected to shear." ACI Journal, 83(2), 219-231.

Wang, L., Zhang, X., Zhang, J., Ma, Y., & Liu, Y. (2015). Effects of stirrup and inclined bar corrosion on shear behavior of RC beams. *Construction and Building Materials*, *98*, 537–546. https://doi.org/10.1016/j.conbuildmat.2015.07.077

Wang, X. H., Gao, X. H., Li, B., & Deng, B. R. (2011). Effect of bond and corrosion within partial length on shear behaviour and load capacity of RC beam. *Construction and Building Materials*, *25*(4), 1812–1823. https://doi.org/10.1016/j.conbuildmat.2010.11.081

Williamson, E.B., Bayrak, O., Davis, C. and Williams, G.D., 2011. Performance of bridge columns subjected to blast loads. I: Experimental program. Journal of Bridge Engineering, 16(6), pp.693-702.

Wong, P. S., Vecchio, F. J., & Trommels, H. (2013). VecTor2 & FormWorks User's Manual (2nd edn). In *University of Toronto: Toronto, ON, Canada*.

Wood, J. G. M., 2008, "Implications of the Collapse of the de la Concorde Overpass," Structural Engineering, V. 86, No. 1, pp. 16-18.

Xia, J., Jin, W. L., & Li, L. Y. (2012). Effect of chloride-induced reinforcing steel corrosion on the flexural strength of reinforced concrete beams. *Magazine of Concrete Research*, *64*(6), 471–485. https://doi.org/10.1680/macr.10.00169

Xue, X., Seki, H., & Song, Y. (2014). Shear behavior of RC beams containing corroded stirrups.

*Advances in Structural Engineering*, *17*(2), 165–178. https://doi.org/10.1260/1369-4332.17.2.165

Yalciner, H. (2014). Structural response to blast loading: The effects of corrosion on reinforced concrete structures. *Shock and Vibration*, *2014*. https://doi.org/10.1155/2014/529892

Zhang, H., Wu, J., Jin, F., & Zhang, C. (2019). Effect of corroded stirrups on shear behavior of reinforced recycled aggregate concrete beams strengthened with carbon fiber-reinforced polymer. *Composites Part B: Engineering*, *161*(December 2018), 357–368. https://doi.org/10.1016/j.compositesb.2018.12.074

Zhang, H., Wu, J., Jin, F., & Zhang, C. (2019). Effect of corroded tension reinforcements on flexural performance of reinforced recycled aggregate concrete beams strengthened with CFRB. *Composites Part B: Engineering*, *162*(January 2019), 589–599. https://doi.org/10.1016/j.compositesb.2019.01.039

Zhang, W., Zhang, H., Gu, X., & Liu, W. (2018). Structural behavior of corroded reinforced concrete beams under sustained loading. *Construction and Building Materials*, *174*, 675–683. https://doi.org/10.1016/j.conbuildmat.2018.04.145

Zhu, W., François, R., Coronelli, D., & Cleland, D. (2013). Effect of corrosion of reinforcement on the mechanical behaviour of highly corroded RC beams. *Engineering Structures*, *56*, 544–554. https://doi.org/10.1016/j.engstruct.2013.04.017